

**OFFICE OF CIVILIAN RADIOACTIVE WASTE MANAGEMENT
ANALYSIS/MODEL COVER SHEET**
1. QA: QA

Page: 1 of 206

Complete Only Applicable Items

2. <input checked="" type="checkbox"/> Analysis Check all that apply	3. <input checked="" type="checkbox"/> Model Check all that apply																											
<table style="width:100%; border-collapse: collapse;"> <tr> <td style="width:20%;">Type of Analysis</td> <td> <input type="checkbox"/> Engineering <input type="checkbox"/> Performance Assessment <input checked="" type="checkbox"/> Scientific </td> </tr> <tr> <td>Intended Use of Analysis</td> <td> <input type="checkbox"/> Input to Calculation <input type="checkbox"/> Input to another Analysis or Model <input checked="" type="checkbox"/> Input to Technical Document </td> </tr> <tr> <td colspan="2">Describe use:</td> </tr> <tr> <td colspan="2">For the UZ PMR, provide analysis of UZ radionuclide transport, the potential impact of colloidal transport, and the contribution of daughter products to transport.</td> </tr> </table>	Type of Analysis	<input type="checkbox"/> Engineering <input type="checkbox"/> Performance Assessment <input checked="" type="checkbox"/> Scientific	Intended Use of Analysis	<input type="checkbox"/> Input to Calculation <input type="checkbox"/> Input to another Analysis or Model <input checked="" type="checkbox"/> Input to Technical Document	Describe use:		For the UZ PMR, provide analysis of UZ radionuclide transport, the potential impact of colloidal transport, and the contribution of daughter products to transport.		<table style="width:100%; border-collapse: collapse;"> <tr> <td style="width:20%;">Type of Model</td> <td> <input type="checkbox"/> Conceptual Model <input type="checkbox"/> Abstraction Model <input type="checkbox"/> Mathematical Model <input type="checkbox"/> System Model <input checked="" type="checkbox"/> Process Model </td> </tr> <tr> <td>Intended Use of Model</td> <td> <input type="checkbox"/> Input to Calculation <input type="checkbox"/> Input to another Model or Analysis <input checked="" type="checkbox"/> Input to Technical Document </td> </tr> <tr> <td colspan="2">Describe use:</td> </tr> <tr> <td colspan="2">Documents the UZ Radionuclide Transport Model for use in the UZ PMR to analyze radionuclide transport in the UZ</td> </tr> </table>	Type of Model	<input type="checkbox"/> Conceptual Model <input type="checkbox"/> Abstraction Model <input type="checkbox"/> Mathematical Model <input type="checkbox"/> System Model <input checked="" type="checkbox"/> Process Model	Intended Use of Model	<input type="checkbox"/> Input to Calculation <input type="checkbox"/> Input to another Model or Analysis <input checked="" type="checkbox"/> Input to Technical Document	Describe use:		Documents the UZ Radionuclide Transport Model for use in the UZ PMR to analyze radionuclide transport in the UZ												
Type of Analysis	<input type="checkbox"/> Engineering <input type="checkbox"/> Performance Assessment <input checked="" type="checkbox"/> Scientific																											
Intended Use of Analysis	<input type="checkbox"/> Input to Calculation <input type="checkbox"/> Input to another Analysis or Model <input checked="" type="checkbox"/> Input to Technical Document																											
Describe use:																												
For the UZ PMR, provide analysis of UZ radionuclide transport, the potential impact of colloidal transport, and the contribution of daughter products to transport.																												
Type of Model	<input type="checkbox"/> Conceptual Model <input type="checkbox"/> Abstraction Model <input type="checkbox"/> Mathematical Model <input type="checkbox"/> System Model <input checked="" type="checkbox"/> Process Model																											
Intended Use of Model	<input type="checkbox"/> Input to Calculation <input type="checkbox"/> Input to another Model or Analysis <input checked="" type="checkbox"/> Input to Technical Document																											
Describe use:																												
Documents the UZ Radionuclide Transport Model for use in the UZ PMR to analyze radionuclide transport in the UZ																												
4. Title: Radionuclide Transport Models Under Ambient Conditions																												
5. Document Identifier (including Rev. No. and Change No., if applicable): MDL-NBS-HS-000008 Rev 00																												
6. Total Attachments: <div style="text-align: center; font-size: 2em; margin-top: 20px;">13</div>	7. Attachment Numbers - No. of Pages in Each: I-12 VIII-28 II-16 IX-28 III-7 X-28 IV-7 XI-14 V-14 XII-34 VI-9 XIII-45 VII-28																											
<table border="1" style="width:100%; border-collapse: collapse;"> <thead> <tr> <th style="width:20%;"></th> <th style="width:35%;">Printed Name</th> <th style="width:35%;">Signature</th> <th style="width:10%;">Date</th> </tr> </thead> <tbody> <tr> <td rowspan="2" style="text-align: center; vertical-align: middle;">8. Originator</td> <td>G. Moridis</td> <td>SIGNATURE ON FILE</td> <td>3/12/00</td> </tr> <tr> <td>Q. Hu</td> <td>SIGNATURE ON FILE</td> <td>3/12/00</td> </tr> <tr> <td style="text-align: center; vertical-align: middle;">9. Checker</td> <td>P. Persoff</td> <td>SIGNATURE ON FILE</td> <td>3/12/00</td> </tr> <tr> <td style="text-align: center; vertical-align: middle;">10. Lead/Supervisor</td> <td>G.S. Bodvarsson</td> <td>SIGNATURE ON FILE</td> <td>3/12/00</td> </tr> <tr> <td style="text-align: center; vertical-align: middle;">11. Responsible Manager</td> <td>G.S. Bodvarsson</td> <td>SIGNATURE ON FILE</td> <td>3/12/00</td> </tr> <tr> <td colspan="4" style="padding: 5px;"> 12. Remarks: </td> </tr> </tbody> </table>			Printed Name	Signature	Date	8. Originator	G. Moridis	SIGNATURE ON FILE	3/12/00	Q. Hu	SIGNATURE ON FILE	3/12/00	9. Checker	P. Persoff	SIGNATURE ON FILE	3/12/00	10. Lead/Supervisor	G.S. Bodvarsson	SIGNATURE ON FILE	3/12/00	11. Responsible Manager	G.S. Bodvarsson	SIGNATURE ON FILE	3/12/00	12. Remarks:			
	Printed Name	Signature	Date																									
8. Originator	G. Moridis	SIGNATURE ON FILE	3/12/00																									
	Q. Hu	SIGNATURE ON FILE	3/12/00																									
9. Checker	P. Persoff	SIGNATURE ON FILE	3/12/00																									
10. Lead/Supervisor	G.S. Bodvarsson	SIGNATURE ON FILE	3/12/00																									
11. Responsible Manager	G.S. Bodvarsson	SIGNATURE ON FILE	3/12/00																									
12. Remarks:																												

**OFFICE OF CIVILIAN RADIOACTIVE WASTE MANAGEMENT
ANALYSIS/MODEL REVISION RECORD**

Complete Only Applicable Items

1. Page: 2 of 206

2. Analysis or Model Title:

Radionuclide Transport Models Under Ambient Conditions

3. Document Identifier (including Rev. No. and Change No., if applicable):

MDL-NBS-HS-000008 Rev 00

4. Revision/Change No.

5. Description of Revision/Change

REV00

Initial Issue

CONTENTS

	Page
ACRONYMS.....	11
1. PURPOSE.....	13
2. QUALITY ASSURANCE.....	15
3. COMPUTER SOFTWARE AND MODEL USAGE.....	17
4. INPUTS.....	19
4.1 DATA AND PARAMETERS.....	19
4.2 CRITERIA.....	22
4.3 CODES AND STANDARDS.....	22
5. ASSUMPTIONS.....	23
5.1 ASSUMPTIONS INVOLVED IN THE FLOW COMPONENT OF THE TRANSPORT PROCESSES.....	23
5.2 ASSUMPTIONS INVOLVED IN THE TRANSPORT PROCESSES.....	25
5.3 ASSUMPTIONS INVOLVED IN THE DUAL-CONTINUA APPROACH.....	27
5.4 ASSUMPTIONS INVOLVING INITIAL AND BOUNDARY CONDITIONS.....	28
5.5 ASSUMPTIONS INVOLVED IN THE 2-D SEMIANALYTICAL STUDIES.....	29
6. MODELS.....	31
6.1 GEOLOGICAL MODEL AND PHYSICAL PROCESSES.....	34
6.2 MATHEMATICAL MODEL OF TRANSPORT.....	51
6.3 THE NUMERICAL AND SEMIANALYTICAL MODELS.....	64
6.4 MODEL VALIDATION AND CALIBRATION.....	67
6.5 2-D TRANSPORT SIMULATIONS IN INDIVIDUAL HYDROGEOLOGIC UNITS	76
6.6 2-D TRANSPORT IN THE TS _w LAYERS.....	83
6.7 2-D TRANSPORT IN THE CH _n LAYERS.....	88
6.8 2-D TRANSPORT IN THE PP LAYERS.....	91
6.9 2-D TRANSPORT UNDERNEATH THE POTENTIAL REPOSITORY.....	94
6.10 3-D BUSTED BUTTE STUDIES.....	102
6.11 3-D TRANSPORT SIMULATIONS.....	108
6.12 3-D SIMULATIONS OF ⁹⁹ Tc TRANSPORT.....	112
6.13 3-D TRANSPORT OF ²³⁷ Np AND ITS DAUGHTERS.....	144
6.14 3-D TRANSPORT OF ²³⁹ Pu AND ITS DAUGHTERS.....	152
6.15 EFFECTS OF VARIOUS PERCHED-WATER REGIMES ON 3-D TRANSPORT.....	161
6.16 3-D SITE-SCALE TRANSPORT OF Pu COLLOIDS.....	166
6.17 ALTERNATIVE MODELS.....	177

CONTENTS (Continued)

7. CONCLUSIONS.....	181
7.1 SUMMARY OF MODELING ACTIVITY.....	181
7.2 AMR CONCLUSIONS	183
8. INPUTS AND REFERENCES.....	189
8.1 CITED DOCUMENTS	189
8.2 CODES, STANDARDS, REGULATIONS, AND PROCEDURES.....	199
8.3 SOURCE DATA, LISTED BY DATA TRACKING NUMBER	200
8.4 OUTPUT DATA, LISTED BY DATA TRACKING NUMBER	202
9. ATTACHMENTS.....	205
ATTACHMENT I	DISCUSSION OF THE EOS9nT AND FRACL MODELS I-1 to I-12
ATTACHMENT II	FIGURES FROM THE STUDY OF TRANSPORT IN THE TS _w HYDROGEOLOGIC UNIT..... II-1 to II-16
ATTACHMENT III	FIGURES FROM THE STUDY OF TRANSPORT IN THE CH _n HYDROGEOLOGIC UNIT..... III-1 to III-7
ATTACHMENT IV	FIGURES FROM THE STUDY OF TRANSPORT IN THE PP HYDROGEOLOGIC UNIT..... IV-1 to IV-7
ATTACHMENT V	FIGURES FROM THE STUDY OF TRANSPORT UNDERNEATH THE REPOSITORY..... V-1 to V-14
ATTACHMENT VI	FIGURES FROM THE BUSTED BUTTE STUDIES VI-1 to VI-9
ATTACHMENT VII	FIGURES FROM THE ²³⁷ Np 3-D TRANSPORT STUDIES..... VII-1 to VII-28
ATTACHMENT VIII	FIGURES FROM THE ²³⁹ Pu 3-D TRANSPORT STUDIES..... VIII-1 to VIII-28
ATTACHMENT IX	FIGURES FROM THE 3-D TRANSPORT STUDIES OF THE 6 nm COLLOID..... IX-1 to IX-28
ATTACHMENT X	FIGURES FROM THE 3-D TRANSPORT STUDIES OF THE 450 nm COLLOID..... X-1 to X-28
ATTACHMENT XI	FORTTRAN ROUTINES XI-1 to XI-14
ATTACHMENT XII	INPUT AND OUTPUT FILES..... XII-1 to XII-34
ATTACHMENT XIII	DOCUMENT INPUTS REFERENCE SYSTEM . XIII-1 to XIII-45

FIGURES**Page**

6.3.1.	An Example of a Layered Fractured System in FRACL Studies.....	66
6.4.1.	The Fracture-Matrix System in the Validation Study of FRACL and EOS9nT.....	68
6.4.2.	Analytical and Numerical Solutions of the Concentration Distribution in a Fracture for Three Different Grids at t=1000 Days.....	71
6.4.3.	Vertical Profile of Hydrogeologic Units at the UE-25 UZ#16 Borehole.....	72
6.4.4.	FRACL Predictions of the Cl Concentration in the Fractures of the UE-25 UZ#16 Profile.....	73
6.4.5.	Comparison of (a) EOS9nT Predictions (b) T2R3D Predictions and (c) Measurements of Cl Concentration Distribution Along the ESF.....	75
6.5.1	2-D (plan view) of the Yucca Mountain Site Identifying the Locations of Boreholes USW SD-6, SD-12 and UZ-14.....	79
6.5.2.	Hydrogeologic Units (and their layers) of the UZ Model Domain from the Potential Repository to the Groundwater in Cross Section 1 Near the USW SD-6 Borehole.....	80
6.5.3.	Hydrogeologic Units (and their layers) of the UZ Model Domain from the Potential Repository to the Groundwater Table in Cross Section 2 Near the USW SD-12 Borehole.....	81
6.5.4.	Hydrogeologic Units (and their layers) of the UZ Model Domain from the Potential Repository to the Groundwater in Cross Section 1 Near the USW UZ-14 Borehole.....	82
6.9.1.	A Conceptual Model of Transport in Cross Section 1.....	97
6.11.1.	2-D (plan view) of the UZ Model Grid Design at the Potential Repository Level.	110
6.12.1.	Normalized Relative Release R of ⁹⁹ Tc at the Water Table for Varying Present-Day Climatic Scenarios.....	114
6.12.2.	Distribution of the Relative Mass Fraction X _R of ⁹⁹ Tc in the Fractures of the Tsw39 Layer at t = 100 Years for Mean Present-Day Infiltration.....	117

FIGURES (Continued)

	Page
6.12.3. Distribution of the Relative Mass Fraction X_R of ^{99}Tc in the Matrix of the Tsw39 Layer at $t = 100$ Years for Mean Present-Day Infiltration.....	118
6.12.4. Distribution of the Relative Mass Fraction X_R of ^{99}Tc in the Fractures of the Tsw39 Layer at $t = 1,000$ Years for Mean Present-Day Infiltration.....	119
6.12.5. Distribution of the relative Mass Fraction X_R of ^{99}Tc in the Matrix of the Tsw39 Layer at $t = 1,000$ Years for Mean Present-Day Infiltration.....	120
6.12.6. Distribution of the Relative Mass Fraction X_R of ^{99}Tc in the Fractures of the Tsw39 Layer at $t = 10,000$ Years for Mean Present-Day Infiltration.....	121
6.12.7. Distribution of the Relative Mass Fraction X_R of ^{99}Tc in the Matrix of the Tsw39 Layer at $t = 10,000$ Years for Mean Present-Day Infiltration.....	122
6.12.8. Distribution of the Relative Mass Fraction X_R of ^{99}Tc in the Fractures of the Tsw39 Layer at $t = 100,000$ Years for Mean Present-Day Infiltration.....	123
6.12.9. Distribution of the Relative Mass Fraction X_R of ^{99}Tc in the Matrix of the Tsw39 Layer at $t = 100,000$ Years for Mean Present-Day Infiltration.....	124
6.12.10. Distribution of the Relative Mass Fraction X_R of ^{99}Tc in the Fractures Immediately Above the Groundwater at $t = 100$ Years for Mean Present-Day Infiltration.....	125
6.12.11. Distribution of the Relative Mass Fraction X_R of ^{99}Tc in the Matrix Immediately Above the Groundwater Table at $t = 100$ Years for a Mean Present-Day Infiltration.....	126
6.12.12. Distribution of the Relative Mass Fraction X_R of ^{99}Tc in the Fractures Immediately Above the Groundwater at $t = 1,000$ Years for Mean Present-Day Infiltration.....	127
6.12.13. Distribution of the Relative Mass Fraction X_R of ^{99}Tc in the Matrix Immediately Above the Groundwater Table at $t = 1,000$ Years for a Mean Present-Day Infiltration.....	128
6.12.14. Distribution of the Relative Mass Fraction X_R of ^{99}Tc in the Fractures Immediately Above the Groundwater at $t = 10,000$ Years for Mean Present-Day Infiltration.....	129
6.12.15. Distribution of the Relative Mass Fraction X_R of ^{99}Tc in the Matrix Immediately Above the Groundwater Table at $t = 10,000$ Years for a Mean Present-Day Infiltration.....	130

FIGURES (Continued)

	Page
6.12.16. Distribution of the Relative Mass Fraction X_R of ^{99}Tc in the Fractures Immediately Above the Groundwater at $t = 100,000$ Years for Mean Present-Day Infiltration.....	131
6.12.17. Distribution of the Relative Mass Fraction X_R of ^{99}Tc in the Matrix Immediately Above the Groundwater Table at $t = 100,000$ Years for a Mean Present-Day Infiltration.....	132
6.12.18. Mean Present-Day Infiltration Rates at the Surface.....	134
6.12.19. Percolation Fluxes at the Potential Repository Level.	135
6.12.20. Percolation Fluxes at the Water Table Level.	136
6.12.21. Mineralogy Model Plots of % Zeolites.....	138
6.12.22. Normalized Relative Release R of ^{99}Tc at the Water Table for Varying Monsoon Climatic Scenarios.	142
6.12.23. Normalized Relative Release R of ^{99}Tc at the Water Table for Varying Glacial Climatic Scenarios.....	143
6.13.1 Normalized Relative Release R of ^{237}Np at the Water Table for Varying Present-Day Climatic Scenarios.....	145
6.13.2 Relative flux Fractions M_R of the Members of the $^{237}\text{Np} \rightarrow ^{233}\text{U} \rightarrow ^{229}\text{Th}$ in the Release at the Water Table Over Time for a Mean Present-Day Infiltration.	146
6.13.3. Normalized Relative Release R of ^{237}Np at the Water Table for Varying Monsoon Climatic Scenarios	150
6.13.4. Normalized Relative Release R of ^{237}Np at the Water Table for Varying Glacial Climatic Scenarios.....	151
6.14.1. Normalized Relative Release R of ^{239}Pu at the Water Table for Varying Present-Day Climatic Scenarios.....	153
6.14.2. Relative Flux Fractions M_R of the Members of the $^{239}\text{Pu} \rightarrow ^{235}\text{U} \rightarrow ^{231}\text{Pa}$ Decay Chain in the Release at the Water Table Over Time for Varying Present-Day Climatic Conditions.....	154

FIGURES (Continued)

	Page
6.14.3. Normalized Relative Release R of ^{239}Pu at the Water Table for Varying Monsoon Climatic Scenarios.	157
6.14.4. Normalized Relative Release R of ^{239}Pu at the Water Table for Varying Glacial Climatic Scenarios.....	158
6.14.5. Relative Mass Fluxes M_R of the Members of the $^{239}\text{Pu} \rightarrow ^{235}\text{U} \rightarrow ^{231}\text{Pa}$ Decay Chain in the Release at the Water Table over Time for Varying Monsoon Climatic Conditions.	159
6.14.6. Relative Mass Fluxes M_R of the Members of the $^{239}\text{Pu} \rightarrow ^{235}\text{U} \rightarrow ^{231}\text{Pa}$ Decay Chain in the Release at the Water Table over Time for Varying Glacial Climatic Conditions.....	160
6.15.1. Normalized Relative Releases at the Water Table for Mean Present-Day Infiltration and the #1 Perched Water Model.	163
6.15.2. Normalized Relative Releases at the Water Table for Mean Present-Day Infiltration and the #2 Perched Water Model.	164
6.15.3. Normalized Relative Releases at the Water Table for Mean Present-Day Infiltration and the No-Perched Water Model.	165
6.16.1. Normalized Release at the Water Table in Case 2 of Colloidal transport for Mean Present-Day Infiltration.....	170
6.16.2. Normalized Release at the Water Table in Case 3 of Colloidal transport for Mean Present-Day Infiltration.....	174
6.16.3. Normalized Release at the Water Table in Case 4 of Colloidal transport for Mean Present-Day Infiltration.....	175
6.17.1. Normalized Relative Releases of Radioactive Solutes at the Water Table for the No-Diffusion Alternative Model	178
6.17.2. Normalized Relative Releases of Radioactive Colloids at the Water Table for the No-Diffusion Alternative Model (Mean Present-Day Infiltration, #1 Perched Water Model, Case 2 Conditions).	180

TABLES

	Page
3.1. Software Codes and Routines.....	17
4.1. Input Data.....	19
6.1. Scientific Notebooks Used for AMR U0060.....	34
6.2. Input Parameters for Model Validation Against an Analytical Solution.....	69
6.3. FRACL Input Data and Sources for Modeling the Cl ⁻ Distribution in the UE-25 UZ#16 Borehole.....	70
6.4. EOS9nT Input Data and Sources for Modeling the Cl ⁻ Distribution in the ESF.	75
6.5. Properties of the Main Radionuclides in the Transport Simulations.....	77
6.6. Distribution Coefficients K_d (in M ³ /Kg) in the 2-D FRACL Simulations.....	77
6.7. Input Parameters for the FRACL Transport Simulations in Cross Sections 1, 2 and 3.	84
6.8. Input Parameters in the FRACL Sensitivity Analysis Simulations (Transport in the Tsw35 Layer).....	86
6.9. Input Parameters for Modeling the Phase 1A Test of Busted Butte.	104
6.10. Input Parameters for Modeling the Phase 1B Test of Busted Butte.	106
6.11. Percolation Fluxes (Mm/Year) for Different Climatic Regimes and the Corresponding EOS9 Flow Simulations Used in the 3-D Site Scale Radionuclide Transport Studies.	109
6.12. Properties of the Daughter Products of Radioactive Decay in the Transport Simulations.....	111
6.13. DTNs of Input and Output Files of the 3-D Site-Scale Transport Simulations.....	113
6.14. Input Parameters for the EOS9nT 3-D Site-Scale Simulations of Solute Transport (#1 Perched-Water Model).....	115
6.15. Radionuclide Travel Times To the Water Table.....	116

TABLES (Continued)

	Page
6.16. Input Parameters for the EOS9nT 3-D Site-Scale Simulations of Solute Transport (#2 Perched-Water Model, Mean Present-Day Infiltration).....	161
6.17. Input Parameters for the EOS9nT 3-D Site-Scale Simulations of Solute Transport (No-Perched-Water Model, Mean Present-Day Infiltration).....	162
6.18. Properties of the Four Colloids in the EOS9nT Simulations.....	167
6.19. Input Parameters for the EOS9nT 3-D Site-Scale Simulations of Colloid Transport (# 1 Perched-Water Model, Mean Present-Day Infiltration).	168

ACRONYMS

2-D	two-dimensional, two dimensions
3-D	three-dimensional, three dimensions
ACC	Accession Number
AMR	Analysis/Model Report
AP	Administrative Procedure (DOE)
Bf	Bullfrog
CFR	Code of Federal Regulations
CFu	Crater Flat undifferentiated
CH	Calico Hills
CHn	Calico Hills nonwelded units
CHv	Calico Hills vitric units
CHz	Calico Hills zeolitic units
CRWMS	Civilian Radioactive Waste Management System
DIRS	Document Input Reference System
DOE	Department of Energy
DTN	Data Tracking Number
ESF	Exploratory Studies Facility
FY	Fiscal Year
LBNL	Lawrence Berkeley National Laboratory
LE	Linear Equilibrium
LIP	Linear Irreversible (Physical)
LKC	Linear Kinetic (Chemical)
LKP	Linear Kinetic (Physical)
M&O	Management and Operating Contractor
NTS	Nevada Test Site
OCRWM	Office of Civilian Radioactive Waste Management
PA	Performance Assessment
PMR	Process/Model Report
PP	Prow Pass formation
PTn	Paintbrush nonwelded formation
PW	Perched Water

ACRONYMS (CONTINUED)

Q	Qualified
QA	Quality Assurance
QAP	Quality Administrative Procedure (M&O)
QARD	Quality Assurance and Requirements Description
QIP	Quality Implementing Procedure
SN	Scientific Notebook
STN	Software Tracking Number
TBD	To Be Determined
TBV	To Be Verified
TCw	Tiva Canyon welded units
TDMS	Technical Data Management System
TSPA	Total System Performance Assessment
TSw	Topopah Spring welded units
U.S.	United States
UZ	Unsaturated Zone
YM	Yucca Mountain
YMP	Yucca Mountain Site Characterization Project

1. PURPOSE

The purpose of this Analysis/Model Report (AMR) is to evaluate (by means of 2-D semianalytical and 3-D numerical models) the transport of radioactive solutes and colloids in the unsaturated zone (UZ) under ambient conditions from the potential repository horizon to the water table at Yucca Mountain (YM), Nevada. This is in accordance with the *AMR Development Plan U0060, Radionuclide Transport Models Under Ambient Conditions* (CRWMS M&O 1999a). This AMR supports the UZ Flow and Transport Process Model Report (PMR).

This AMR documents the UZ Radionuclide Transport Model (RTM). This model considers

- the transport of radionuclides through fractured tuffs
- the effects of changes in the intensity and configuration of fracturing from hydrogeologic unit to unit
- colloid transport
- physical and retardation processes, and
- the effects of perched water.

In this AMR we document the capabilities of the UZ RTM, which can describe flow (saturated and/or unsaturated) and transport, and accounts for (a) advection, (b) molecular diffusion, (c) hydrodynamic dispersion (with full 3-D tensorial representation), (d) kinetic or equilibrium physical and/or chemical sorption (linear, Langmuir, Freundlich or combined), (e) first-order linear chemical reaction, (e) radioactive decay and tracking of daughters, (f) colloid filtration (equilibrium, kinetic or combined), and (g) colloid-assisted solute transport.

Simulations of transport of radioactive solutes and colloids (incorporating the processes described above) from the repository horizon to the water table are performed to support model development and support studies for Performance Assessment (PA). The input files for these simulations include transport parameters obtained from other AMRs (i.e., CRWMS M&O 1999d, e, f, g, h; 2000a, b, c d). When not available, the parameter values used are obtained from the literature.

The results of the simulations are used to evaluate the transport of radioactive solutes and colloids, and to determine the processes, mechanisms, and geologic features that have a significant effect on it. We evaluate the contributions of daughter products of radioactive decay to transport from the bottom of the potential repository to the water table. The effect of the various conceptual models of perched water bodies on transport is also evaluated. Note that a more thorough study of perched water bodies can be found in another AMR (CRWMS M&O 1999d, Sections 6.2 and 6.6).

The primary caveat for using the modeling results documented here is that the input transport parameters were based on limited site data. For some input parameters, best estimates were used because no specific data were available. An additional caveat is that the RTM is based on the

conceptual models and numerical approaches used for developing the flow fields and infiltration maps, and thus they share the same limitations.

2. QUALITY ASSURANCE

This AMR has been developed in accordance with procedure AP-3.10Q, Rev. 1, ICN 1, *Analyses and Models*. Accordingly, the modeling activities documented in this AMR have been conducted in accordance with the CRWMS M&O quality assurance program, using OCRWM Administrative Procedures (APs) and YMP-LBNL Quality Implementing Procedures (QIPs) identified in the *AMR Development Plan for U0060, Radionuclide Transport Models Under Ambient Conditions* (CRWMS M&O 1999a).

The activities documented in this AMR were evaluated with other related activities in accordance with QAP-2-0, Rev. 5, *Conduct of Activities* and were determined to be quality affecting and subject to the requirements of the U.S. DOE Office of Civilian Radioactive Waste Management (OCRWM) *Quality Assurance Requirements and Description* (QARD) (DOE 1998a). This evaluation is documented in *Activity Evaluation of M&O Site Investigations* (CRWMS M&O 1999b; and Wemheuer 1999 WP #1401213UM1).

INTENTIONALLY LEFT BLANK

3. COMPUTER SOFTWARE AND MODEL USAGE

The software codes and routines used in this study are listed in Table 3.1. TOUGH2 V1.4 Module EOS9 V1.4 (STN: 10007-1.4-01) and T2R3D (SN: 10006-1.4-00) were appropriate for the intended application, were used only within the range of their software validation, and were obtained from configuration management per AP-SI.1Q, Rev. 2, ICN 2, *Software Management*. TOUGH2 V1.11 Module EOS9nT V1.0 (STN: 10065-1.11MEOS9NTV1.0-00) and FRACL V1.0 (STN: 10191-1.0-00) are being qualified and Software Activity Plans for use of unqualified software and copies have been submitted to configuration management per Section 5.12 of AP-SI.1Q. The Q-status of these codes is provided in the Document Input Reference Sheet (DIRS), which is included as Attachment XIII. The software routines listed in Table 3.1 have been qualified per Section 5.1.1 of AP-SI.1Q and their source codes are included in Attachment XI.

Table 3.1: Software Codes and Routines

Software Name	Version	Software Tracking Number (STN):	Computer Platform
TOUGH2 V1.11 Module EOS9nT V1.0	1.0	10065-1.11MEOS9NTV1.0-00	Sun or DEC Workstation with Unix OS Apple Macintosh with Mac OS 8.6
TOUGH2 V1.4 Module EOS9 V1.4	1.4	10007-1.4-01	Sun or DEC Workstation with Unix OS
T2R3D	1.4	10006-1.4-00	Sun or DEC Workstation with Unix OS
FRACL	1.0	10191-1.0-00	Sun or DEC Workstation with Unix OS
Routines:			
xtract1.f	1.0	10213-1.0-00	Apple Macintosh with Mac OS 8.6
xtract2.f	1.0	10214-1.0-00	Apple Macintosh with Mac OS 8.6
xtract2a.f	1.0	10215-1.0-00	Apple Macintosh with Mac OS 8.6
xtract2b.f	1.0	10216-1.0-00	Apple Macintosh with Mac OS 8.6
xtract5.f	1.0	10217-1.0-00	Apple Macintosh with Mac OS 8.6
xtract6.f	1.0	10218-1.0-00	Apple Macintosh with Mac OS 8.6

The software code TOUGH2 V1.11 Module EOS9nT V1.0 (SN: 10065-1.11MEOS9NTV1.0-00) simulates flow (saturated and/or unsaturated) and the transport of a multiple number of radioactive solutes and/or colloids in complex subsurface systems involving porous and/or fractured media. The transport equations account for advection, molecular diffusion, hydrodynamic dispersion, kinetic or equilibrium physical and chemical sorption (linear, Langmuir, Freundlich or combined), first-order linear chemical reaction, colloid filtration, and colloid-assisted solute transport.

Industry standard graphics software programs were also used but are not subject to software quality assurance requirements under QARD per Section 2.0 of AP-SI.1Q.

This AMR documents the UZ Radionuclide Transport Model. Input and output files for the model simulations documented in this AMR are listed in Attachment XII.

4. INPUTS

The input used in this AMR consist of the following:

- Transport properties
- Calibrated fracture and matrix properties
- Base case flow fields
- Geochemical data
- Numerical grids

4.1 DATA AND PARAMETERS

Specific input data sets and their associated Data Tracking Numbers (DTNs), Accession Numbers (ACC), and sources are listed in Table 4.1. The Q-status of these data is provided in the DIRS in Attachment XIII.

Table 4.1. Input Data

Description	Parameters	Data Source
Modeling the chloride distribution in borehole UE-25 UZ#16 (Section 6.4.3)	Geological profile and rock properties at the UE-25 UZ#16 cross-section	DTN: LB990701233129.002
	Calibrated infiltration rate	DTN: LB991131233129.003
	Field measurement of the chloride concentration profile in the UE-25 UZ#16 borehole	DTN:GS950608312272.001
	Chloride diffusion coefficient	DTN: LB991220140160.019
Modeling the chloride distribution in the ESF (Section 6.4.4)	Grid and flow field	DTN: LB990701233129.002
	Calibrated infiltration rate	DTN: LB991131233129.003
	Cl ⁻ concentration measurements in the ESF	DTNs: LAJF831222AQ98.007, LA9909JF831222.010, and LA9909JF831222.012
Properties of the main radionuclides in the transport simulations (⁹⁹ Tc, ²³⁷ Np, ²³⁹ Pu, , ²³⁵ U, ²³¹ Pa, ²³³ U, and ²²⁹ Th) (Sections 6.5.2 and 6.11.3)	Molecular diffusion coefficient	DTN: LB991220140160.019
	Half-life for the first-order radioactive decay $T_{1/2}$	DTN: LB991220140160.019
	Sorption coefficient K_d	DTN: LB991220140160.019

Table 4.1. Input Data (continued)

Description	Parameters	Data Source
FRACL transport simulations in Cross Sections 1,2 and 3 (Sections 6.5, 6.6, 6.7, 6.8, 6.9)	Geologic profiles and rock properties at the three cross-sections	DTNs: LB990501233129.004
	Matrix properties (porosity ϕ , immobile water saturation S_r), fracture properties (S_r , active fracture parameter γ , frequency f_a), rock grain density ρ_s	DTN: LB997141233129.001
	Matrix (S_{wm}) and fracture water saturation (S_{wf}) at steady state	DTN: LB990801233129.003
	Fracture aperture	DTN: LB990501233129.001
	Tortuosity for each hydrogeologic layer	DTN: LB991220140160.019
Modeling the Phase1A test of Busted Butte (Section 6.10.1)	Calibrated flow parameters for base-case infiltration in the matrix of the ch1v and ch2v layers (porosity ϕ , permeability k , van Genuchten α and m parameters, residual saturation S_r , satiated saturation S_w , rock grain density ρ_s , tortuosity)	DTN: LB997141233129.001
	Matrix porosity ϕ , permeability k , initial saturation, and rock grain density ρ_s of the field samples	DTNs: GS990308312242.007 and GS990708312242.008
	Calibrated flow parameters for dual-permeability model base-case in the matrix of the ch1v and ch2v layers (porosity ϕ , permeability k , van Genuchten α and m parameters, residual saturation S_r , satiated saturation S_w , rock grain density ρ_s , tortuosity)	DTN: LB971212001254.001
	Br diffusion coefficient and sorption coefficient	DTN: LB991220140160.019

Table 4.1. Input Data (continued)

Description	Parameters	Data Source
Modeling the Phase1B test of Busted Butte (Section 6.10.2)	Calibrated flow parameters for base-case infiltration in the matrix of the tsw39 layer (porosity ϕ , permeability k , van Genuchten α and m parameters, residual saturation S_r , saturated saturation S_w , rock grain density ρ_s , tortuosity τ)	DTN: LB997141233129.001
	Matrix porosity, permeability, and initial saturation of the field samples	DTNs: GS990308312242.007 and GS990708312242.008
	Diffusion coefficient for Li^+ and 2,6-DFBA	DTN: LB991220140160.019
	Sorption coefficient for Li^+ and 2,6-DFBA	DTN: LB991220140160.019
Flow fields for 3-D site-scale radionuclide transport modeling (Sections 6.11, 6.12, 6.13, 6.14, 6.15, 6.16 and 6.17)	Present-day lower-bound infiltration (perched water model #1)	DTN: LB990801233129.001
	Present-day mean infiltration (perched water model #1)	DTN: LB990801233129.003
	Present-day upper-bound infiltration (perched water model #1)	DTN: LB990801233129.005
	Glacial lower-bound infiltration (perched water model #1)	DTN: LB990801233129.007
	Glacial mean infiltration (perched water model #1)	DTN: LB990801233129.009
	Glacial upper-bound infiltration (perched water model #1)	DTN: LB990801233129.011
	Monsoon lower-bound infiltration (perched water model #1)	DTN: LB990801233129.013
	Monsoon mean infiltration (perched water model #1)	DTN: LB990801233129.015
	Monsoon upper-bound infiltration (perched water model #1)	DTN: LB990801233129.017
	Present-day mean infiltration (no-perched-water model)	DTN: LB990801233129.019
	Present-day mean infiltration (perched-water model #2)	DTN: LB990801233129.004

Table 4.1. Input Data (continued)

Description	Parameters	Data Source
EOS9nT 3-D site-scale simulations of colloid transport (perched water model #1, mean present-day infiltration) (Sections 6.16 and 6.17)	Properties and characteristics of the geologic units, steady-state pressures, water saturations and flow fields	DTN: LB990801233129.003
	Tortuosity	DTN: LB991220140160.019
	Molecular diffusion coefficient D_0	DTN: LB991220140160.019
	Colloid density ρ_c	DTN: LB991220140160.019

4.2 CRITERIA

This AMR complies with the DOE interim guidance (Dyer 1999). Subparts of the interim guidance that apply to this modeling activity are those pertaining to the characterization of the Yucca Mountain site (Subpart B, Section 15), the definition of hydrologic parameters used in performance assessment (Subpart E, Section 114(a)) and providing the technical basis for the description of natural barriers identified as important to waste isolation (Subpart E, Sections 114(h), (i) and (j)).

4.3 CODES AND STANDARDS

No specific formally established codes or standards have been identified as applying to this AMR.

5. ASSUMPTIONS

In this section we discuss the basic assumptions in the mathematical basis of the transport model, and we provide a short discussion of the supporting rationale. This section is structured as follows:

Section 5.1 addresses the general assumptions underlying the flow component of the transport model of the Yucca Mountain (YM) unsaturated zone (UZ). Section 5.2 lists the assumptions of the transport processes. The assumptions involved in the treatment and mathematical representation of the fractured rocks using the dual-continuum approach are discussed in Section 5.3. Assumptions related to the initial and boundary conditions of the model domain are presented in Section 5.4. Sections 5.1 to 5.4 address issues related to large-scale 3-D numerical simulations. Section 5.5 discusses the assumptions involved in the semianalytical transport solution used for 2-D transport submodels.

5.1 ASSUMPTIONS INVOLVED IN THE FLOW COMPONENT OF THE TRANSPORT PROCESSES

The transport phenomena and processes in the unsaturated zone of Yucca Mountain have a flow component and a transport component, each of which are described by a set of governing equations. These conserve mass, energy and momentum in the system under study, while quantifying the system response to external mass and energy inputs and interrelationships between the various processes involved.

The basic flow assumptions are consistent with those of discussed in CRWMS M&O (1999d, Sections 5 and 6): they share identical conceptual models, which are stated below.

1. The macroscopic-continuum approach is a valid concept for the description of the flow and transport processes in the fractured UZ rocks.

Rationale: The rationale for this assumption is provided in CRWMS M&O (1999d, Section 6.1.2).

Applicability: This assumption applies to all numerical (i.e., 3-D site-scale) simulations of flow and transport in this AMR (Sections 6.4.3 and 6.11 to 6.17). No further confirmation is required for the purposes of this study.

2. Darcy's law is a valid model to describe the flow of gas and water in the matrix and fractures of the UZ.

Rationale: Given the applicability of the macroscopic continuum approach, the gaseous and aqueous flows under ambient conditions in the UZ are sufficiently slow to correspond to a

Reynolds number ≤ 10 , i.e., the upper limit of applicability of Darcy's law (Bear, p. 127, 1972).

Applicability: This assumption applies to all 3-D site-scale simulations of flow and transport in this AMR (Sections 6.4.3 and 6.11 to 6.17). No further confirmation is required for the purposes of this study.

3. Richards' equation (Richards 1931, pp. 218-233) is a valid model of unsaturated water flow in both the matrix and the fractures of the UZ.

Rationale: Under ambient conditions, the gas-phase pressure in the UZ is atmospheric, corrected for elevation. The absence of gas pressurization makes possible the adoption of Richards' equation, because the gas phase can be neglected and the aqueous phase flow occurs in response to gravitational and capillary pressure differentials.

Applicability: This assumption applies to all 3-D site-scale simulations of flow and transport in this AMR (Sections 6.4.3 and 6.11 to 6.17). No further confirmation is required for the purposes of this study.

4. Relative permeabilities and capillary pressures are assumed to follow the van Genuchten (1980) and Mualem (1978) model and are continuous functions of the effective liquid and gas saturations.

Rationale: This model is consistent with the macroscopic continuum approach, has been successfully used to determine relative permeability and capillary pressure parameters from UZ rocks (matrix blocks), and is reasonable for fractures (CRWMS M&O, 2000a, Section 6).

Applicability: This assumption applies to all 3-D site-scale simulations of flow and transport in this AMR (Sections 6.4.3 and 6.11 to 6.17). No further confirmation is required for the purposes of this study.

5. The water flow is isothermal.

Rationale: This is a reasonable approximation. The flow parameters affected by temperature are the water density and the water viscosity. The ambient temperature extremes at the domain boundaries are about 20 °C at the top and about 30 °C at the water table at the bottom (CRWMS M&O 1999d, Section 6.3). Between 20 °C and 30 °C, the water density decreases from 998.21 kg/m³ to 995.65 kg/m³ (Lide 1992, p. 6-10), i.e., the change is very small.

The effect on viscosity is more pronounced. Between 20 °C and 30 °C, the water viscosity decreases from 1.002×10^{-3} Pa·s to 7.977×10^{-4} Pa·s (Lide 1992, p. 6-10), i.e., a reduction of about 20%. Although this variation is not excessive (given the uncertainty in the values of the hydraulic properties of the UZ system), its effects are minimized by conducting the isothermal flow simulations at 25 °C.

The assumption of isothermal flow may be less valid in the immediate vicinity of the waste package because of the heat generated by the radioactive decay process. The non-isothermal flow under these conditions is the subject of another AMR (CRWMS M&O 2000b).

Applicability: This assumption applies to all 3-D site-scale simulations of flow and transport in this AMR (Sections 6.4.3 and 6.11 to 6.17). No further confirmation is required for the purposes of this study.

6. Water flow through the UZ in the numerical simulations of radionuclide transport is considered time-invariant (steady-state).

Rationale: This is a reasonable approximation, given the very long simulation periods ($\geq 100,000$ years). This approach allows the determination of the envelope of the transport behavior by considering nine different infiltration scenarios (and, consequently, flow fields), and is consistent with the flow regimes discussed in CRWMS M&O (1999d, Section 6.1.2).

Applicability: This assumption applies to all 3-D site-scale simulations of flow and transport in this AMR (Sections 6.4.3 and 6.11 to 6.17). No further confirmation is required for the purposes of this study.

5.2 ASSUMPTIONS INVOLVED IN THE TRANSPORT PROCESSES

7. The individual and combined effects of diffusion (molecular and/or colloidal), surface diffusion and hydrodynamic dispersion follow a Fickian model.

Rationale: Given the macroscopic continuum approach, this is a valid assumption (de Marsily 1986, pp. 228-277).

Applicability: This assumption applies to all studies in this AMR (Sections 6.4 to 6.17). No further confirmation is required for the purposes of this study.

8. Transport is assumed to occur isothermally at 25 °C.

Rationale: This assumption of isothermal transport at the average ambient temperature of the UZ is consistent with the assumption of isothermal flow at the same temperature. The transport parameters affected by temperature are (a) the diffusion coefficient D_0 of the dissolved or colloidal species and (b) the sorption parameters of the dissolved species or the filtration parameters of the suspended colloid. Natural temperature differentials in the undisturbed UZ profile occur because of the geothermal gradient. Substantial temperature increases over the ambient are expected after the radioactive waste emplacement in the potential repository (CRWMS M&O 2000b, Section 6.5).

An increasing temperature leads to a higher D_0 value according to the relationship discussed

in Section 6.1.2.9 of this AMR. Based on this relationship, an increase in temperature from 20 °C (at the top of the UZ domain) to 30 °C (at the water table , i.e., the bottom of the UZ domain) leads to an increase of D_0 by about 30%.

The effect of temperature on sorption and/or filtration is less well-defined. The general effect of an increasing temperature is a decrease in the sorption of anionic species and an increase in the sorption of cationic species. Theoretical and experimental studies indicate an increase of the distribution coefficient K_d with temperature when sorption follows a linear equilibrium isotherm (CRWMS M&O 1999e, Section 6.4.6).

Colloid filtration (deposition) generally follows a kinetic process (see Sections 6.2.3 and 6.16.2 in this AMR). Equation 31 in this AMR indicates that an increase in temperature increases the forward filtration coefficient κ^+ , indicating to an increase in the filtration (deposition, clogging) rate. There is no information on the effect of temperature on the reverse filtration coefficient κ^- .

Thus, an increasing temperature in the UZ enhances diffusion (a particularly important mechanism in species mass transfer from the flow-dominating fractures to the matrix) and increases sorption and/or filtration. The cumulative effect is slower transport. The assumption of isothermal transport should not be viewed as an approximation of the prevailing conditions in the UZ, but rather as a condition that reflects a worst-case transport scenario and leads to conservative estimates of radionuclide travel times to the water table . Investigation of the effect of water phase changes on transport may be included in future revisions of the present AMR.

Applicability: This assumption applies to all studies in this AMR (Sections 6.4 to 6.17). No further confirmation is required for the purposes of this study.

9. The concentration of the radioactive solutes or colloids is at a tracer level, i.e., too low to have any measurable effect on the flow regime.

Rationale: Ambient tracers and radionuclides escaping from the potential repository are expected to occur at concentrations that are too low to affect the aqueous solution density (CRWMS M&O 1999e, Section 6.3).

Applicability: This assumption applies to all studies in this AMR (Sections 6.4 to 6.17). No further confirmation is required for the purposes of this study.

10. There is no phase change, i.e., no water evaporation and condensation.

Rationale: The rationale for this assumption is covered by the discussion in assumption (5). Water evaporation and condensation due to the heat generated by the radioactive decay of the wastes is covered by CRWMS M&O (2000b, Section 6.5), in which it is shown that phase changes are not expected to last longer than the first 10,000 years after the waste placement

(i.e., a rather short time compared to the 100,000 to 1,000,000 years covered by the studies in this AMR) and are limited to a rather small volume in the immediate vicinity of the potential repository. However, investigation of the effect of water phase changes on transport may be included in future revisions of the present AMR.

Applicability: This assumption applies to all studies in this AMR (Sections 6.4 to 6.17). No further confirmation is required for the purposes of this study.

11. Filtration of colloids is limited to deep filtration, i.e., it does not affect the medium porosity and permeability.

Rationale: Pseudocolloids (i.e., colloidal waste forms) and natural pseudocolloids (such as clays) under natural conditions are present in sufficiently small concentrations (CRWMS M&O 1999f, Section 6) to make this a valid assumption. This reference also indicates that, as a result of adverse chemical conditions (e.g., pH, ionic strength) in the immediate vicinity of the potential repository, true colloids (i.e., radionuclides in colloidal form) will be released in low concentrations for a long time.

Applicability: This assumption applies to the colloid studies in this AMR (Section 6.16 and 6.17). No further confirmation is required for the purposes of this study.

These assumptions allow decoupling of the flow and transport equations. The Richards equation is first solved in the flow component of transport, followed by the sequential solution of the n independent tracer transport equations.

5.3 ASSUMPTIONS INVOLVED IN THE DUAL-CONTINUA APPROACH

The treatment of fracture-matrix interactions is a critical issue in the simulation of flow and transport under the two-phase flow conditions of the fractured UZ rocks. This AMR closely follows the approach of (CRWMS M&O 1999d, Section 6.1.2), which assumes the following:

12. The dual-permeability model is a valid approximation for flow and transport simulations in the fractured UZ rocks.

Rationale: In addition to its computational efficiency, this model has a strong conceptual basis because it describes the matrix and fractures as separate but interconnected gridblocks and permits flow and transport between matrix gridblocks, fracture gridblocks, and fractures and matrix. A more detailed discussion on the rationale for this assumption can be found in (CRWMS M&O 2000c, Section 5.3)

Applicability: This assumption applies to all 3-D site-scale studies in this AMR (Sections 6.4.3 and 6.11 to 6.17). No further confirmation is required for the purposes of this study.

5.4 ASSUMPTIONS INVOLVING INITIAL AND BOUNDARY CONDITIONS

13. The top boundary of the UZ model domain in the numerical simulations is maintained at spatially variable conditions of
- (a) temporally constant gas pressure and saturation,
 - (b) temporally constant temperature, and
 - (c) temporally constant infiltration rates (steady state).

Rationale: The spatial variations of the parameters reflect differences in elevation, climate and topography, and represent realistic approximations of the prevailing conditions. For sufficiently long simulation periods, temporal variations in these parameters tend to diminish. Moreover, at a relatively short distance below the land surface, such temporal variations diminish rapidly.

Applicability: This assumption applies to all 3-D site-scale studies in this AMR (Sections 6.4.3 and 6.11 to 6.17). No further confirmation is required for the purposes of this study.

14. The bottom boundary of the UZ model domain in the 3-D simulations coincides with the water table . It is maintained at spatially variable conditions of
- (a) temporally constant water pressure and saturation, and
 - (b) temporally constant temperature.

Rationale: This is a good representation of conditions in the saturated zone for the reasons discussed in the rationale for Assumption 13.

Applicability: This assumption applies to all 3-D site-scale studies in this AMR (Sections 6.4.3 and 6.11 to 6.17). No further confirmation is required for the purposes of this study.

15. In the numerical studies of radionuclide transport, the boundaries of the UZ domain through which flow and transport occur are the top and bottom boundaries (i.e., the ground surface and the groundwater, respectively). No lateral flow and/or transport occur across any other boundaries.

Rationale: The flow and transport through the top and bottom boundaries is consistent with the patterns of rainfall-fed infiltration and gravity-driven flow and drainage. The distance between the potential repository and these boundaries is sufficiently large to justify the assumption of no lateral flow and/or transport.

Applicability: This assumption applies to all 3-D site-scale studies in this AMR (Sections 6.4.3 and 6.11 to 6.17). No further confirmation is required for the purposes of this study.

16. The potential repository is located in the TSw hydrogeologic unit.

Rationale: This is consistent with the repository design in CRWMS M&O (1999g).

Applicability: This assumption applies to all UZ transport studies in this AMR (Sections 6.5 to 6.9 and 6.11 to 6.17). No further confirmation is required for the purposes of this study.

17. In the transport studies of radionuclides released from the wastes in the potential repository, the initial tracer (solute or colloidal species) concentrations are assumed to be
 - (a) constant in the gridblocks corresponding to the potential repository, and
 - (b) zero throughout the rest of the domain.

Rationale: This is an accurate system description. The very large mass of radionuclides stored in the potential repository and their low release rates (CRWMS M&O 1999e, Section 6.3; CRWMS M&O 1999f, Section 6) support the case for continuous constant release over the simulation periods. This is accomplished by treating the potential repository gridblocks as internal boundary gridblocks.

The radionuclides investigated in this AMR are ^{99}Tc , ^{237}Np and ^{239}Pu . These do not occur naturally. Thus the assumption of zero initial concentration in the UZ domain is accurate.

Applicability: This assumption applies to all UZ transport studies in this AMR (Sections 6.5 to 6.9 and 6.11 to 6.17). No further confirmation is required for the purposes of this study.

5.5 ASSUMPTIONS INVOLVED IN THE 2-D SEMIANALYTICAL STUDIES

The semianalytical model of transport through layered fractured media is based on some of the assumptions previously discussed. More specifically, it assumes isothermal steady-state flow and incorporates all the assumptions in Section 5.3. The additional assumptions it makes are the following:

18. Advection occurs only in the fractures. The only mechanism of radionuclide transport from the fracture to the matrix is molecular diffusion (matrix diffusion).

Rationale: This is a necessary assumption for the development of the semianalytical solution. Because of the significantly smaller magnitude of the water velocity in the matrix compared to that in the fractures (Bodvarsson et al. 1999, p. 14), this is a reasonable approximation.

Applicability: This assumption applies to all 2-D studies in this AMR (Sections 6.4 to 6.9). No further confirmation is required for the purposes of this study.

19. The upper bound of radionuclide transport predictions can be obtained by assuming that transport between the non-aligned fractures in adjacent layers is continuous, i.e., by not considering transport along the layer interface between the offset fractures.

Rationale: This is a valid assumption. By not considering transport along the layer interface,

diffusion into and sorption onto the matrices (in the case of sorbing species) of the adjacent layers are reduced. This leads to faster transport and shorter travel times to the groundwater.

Applicability: This assumption applies to all 2-D studies in this AMR (Sections 6.4 to 6.9). No further confirmation is required for the purposes of this study.

6. MODELS

The objective of this AMR is to provide a defensible and credible model of radionuclide transport in individual vertical 2-D slices of the UZ and in large 3-D systems using the flow fields submitted for use in TSPA calculations (CRWMS M&O 1999d, Section 6.6). In this section we describe the development, verification and calibration of the Radioactive Transport Model (RTM). The primary objectives of the RTM are:

- Using the comprehensive calibrated 3-D model of the unsaturated flow developed in CRWMS M&O (1999d, Section 6.2.5), to integrate the available data for the development of a comprehensive model of radionuclide transport through the UZ of the YM under a range of current and future climate conditions.
- To identify the controlling transport processes and phenomena, and to evaluate the effectiveness of matrix diffusion and sorption as retardation processes.
- To identify the geologic features that are important to radionuclide transport.
- To obtain an estimate of the migration of important radionuclide solutes and their daughter products from the potential repository toward the groundwater.
- To evaluate the effects of various climatic conditions on radionuclide transport.
- To evaluate the effect of three perched water conditions on radionuclide transport.
- To obtain an estimate of the migration of radioactive colloids from the potential repository toward the groundwater, and to determine the sensitivity of colloid transport to the kinetic coefficients of colloid filtration.
- To evaluate the effect of fracture spacing, intensity and configuration on radionuclide transport and retardation through important hydrogeologic units.

This section consists of the following subsections:

Section 6.1. Geological Model and Physical Processes. In this section we focus on (a) the geology and stratigraphy in the UZ of YM in relation the likely site for the potential repository, (b) the processes and phenomena involved in and affecting transport, and (c) important issues that may have an impact on the predictions and understanding of the transport behavior of radioactive solutes and colloids in the UZ.

Section 6.2. Mathematical Model of Transport. In this section we present the mathematical basis

and discuss the implications of the various processes and phenomena involved in the transport of solutes and colloids in the UZ.

Section 6.3. The Numerical and Semianalytical Models. In this section we discuss the codes that implement the semianalytical and numerical models developed based on the principles discussed in Section 6.2. These codes are FRACL V1.0 (STN: 10191-1.0-00, hereafter referred to as FRACL) and TOUGH2 V1.11 Module EOS9nT V1.0 (STN: 10065-1.11MEOS9NTV1.0-00, hereafter referred to as EOS9nT), respectively, and were used for the simulations discussed in Sections 6.4 to 6.9 and 6.11 to 6.17.

Section 6.4. Model Validation and Calibration. This section includes a short validation study, followed by calibration studies of FRACL and EOS9nT against field measurements and other numerical predictions.

Section 6.5. 2-D Transport Simulations in Individual Hydrogeologic Units. In this section we discuss the individual hydrogeologic units in three representative vertical cross sections (within the proposed site of the repository) that are the domains for the ensuing 2-D simulations (Section 6.6 to 6.9). The radionuclides (solute) considered in these simulations and general issues related to the application of the FRACL code are also discussed.

Section 6.6. 2-D Transport in the TSw Layers. In this section we investigate the transport patterns of three radionuclides (^{99}Tc , ^{237}Np , and ^{239}Pu) in the layers of the TSw hydrogeologic units in the three vertical cross sections.

Section 6.7. 2-D Transport in the CHn Layers. In this section we study the transport of ^{99}Tc , ^{237}Np , and ^{239}Pu in the layers of the CHn hydrogeologic units (underlying the TSw units) in the same three cross sections.

Section 6.8. 2-D Transport in the PP Layers. In this section we study the transport of ^{99}Tc , ^{237}Np , and ^{239}Pu in the layers of the PP hydrogeologic units (underlying the CHn units) in the same three cross sections.

Section 6.9. 2-D Transport Underneath the Potential Repository. In this section we discuss radionuclide transport in composite 2-D sections covering the geologic spectrum from the potential repository to the groundwater in order to evaluate the integrated transport performance of the complete geologic system beneath the potential repository. A conceptual model of transport through the various hydrogeologic units is also presented.

Section 6.10. 3-D Busted Butte Studies. In this section we conduct a modeling study to predict the concentration and water saturation distributions of various non-reactive tracers injected into Busted Butte rocks. These predictions are compared to currently available measurements from

field injections, or will be used for comparison when additional field data become available.

Section 6.11. 3-D Transport Simulations. In this section we discuss the grids, climatic conditions, perched water model, radionuclides and flow fields used in the ensuing 3-D site-scale simulations of transport through the UZ (Sections 6.12 to 6.17), as well as the conditions and general options used in these EOS9nT simulations.

Section 6.12. 3-D Simulations of ^{99}Tc Transport. In this section we study the transport of ^{99}Tc through the UZ under various climatic scenarios, and show that the 3-D EOS9nT prediction of the ^{99}Tc travel time to the groundwater is consistent with the 2-D FRACL prediction from Section 6.9. We also identify transport-controlling geologic features, transport patterns and important retardation mechanisms.

Section 6.13. 3-D Transport of ^{237}Np and its Daughters. In this section we investigate the transport of ^{237}Np through the UZ under various climatic scenarios and determine that the contribution of its daughters to releases at the water table is negligible. We identify transport-controlling geologic features and important retardation mechanisms, and we compare the concentration distributions and the transport patterns of ^{237}Np to those of ^{99}Tc . We also show that the 3-D EOS9nT site-scale prediction of the ^{237}Np travel time to the groundwater is consistent to that from the 2-D FRACL simulations from Section 6.9.

Section 6.14. 3-D Transport of ^{239}Pu and its Daughters. In this section we study the transport of ^{239}Pu through the UZ under various climatic scenarios and determine that the contribution of its daughters to releases at the water table is significant. We identify transport-controlling geologic features and important retardation mechanisms, and we compare the concentration distributions and the transport patterns of ^{239}Pu to those of ^{99}Tc and ^{237}Np . We also show that the 3-D EOS9nT site-scale prediction of the ^{239}Pu travel time to the groundwater is consistent to that from the 2-D FRACL simulations from Section 6.9.

Section 6.15. Effect of Various Perched-Water Regimes on 3-D Transport. Radionuclide transport under three different perched water models is studied in this section, and the differences in transport behavior are discussed.

Section 6.16. 3-D Site-Scale Transport of Pu True Colloids. In this section we study the transport of four radioactive colloids through the UZ for a mean present-day infiltration and the #1 perched water model. We identify transport-controlling geologic features and important retardation mechanisms, and discuss the differences between the transport patterns of the four colloids.

Section 6.17. Alternative Models. In this section we investigate an alternative model of transport that does not consider diffusion. The transport behavior and patterns of solutes and colloids under the alternative model are compared to those from the standard model of non-zero diffusion discussed

in Sections 6.12 to 6.16.

The scientific notebooks used for the activities in this AMR are listed in Table 6.1.

Table 6.1. Scientific notebooks used for AMR U0060

LBNL Scientific Notebook	YMP M&O Scientific Notebook ID	Page Numbers	Accession Number
YMP-LBNL-GJM-3	SN-LBNL-SCI-099-V1	675-768	MOL.19991221.0429
YMP-LBNL-GSB-QH-1	SN-LBNL-SCI-168-V1	1-38	MOL.19991221.0430

6.1 GEOLOGICAL MODEL AND PHYSICAL PROCESSES

6.1.1 Geological Layering

The subsurface formations at YM consist of heterogeneous layers of anisotropic, fractured volcanic rocks. There are alternating layers of welded and nonwelded ash flow and air fall tuffs. The cooling history of these volcanic rock units determines their mechanical and hydrologic properties. Beginning from the land surface, the YM geologic units are the Tiva Canyon, Yucca Mountain, Pah Canyon, and the Topopah Spring Tuffs of the Paintbrush Group. Underlying these are the Calico Hills Formation, and the Prow Pass, Bullfrog, and Tram Tuffs of the Crater Flat Group. These formations have been divided into major hydrogeologic units based roughly on the degree of welding. These are the Tiva Canyon welded (TCw); the Paintbrush nonwelded (PTn), consisting primarily of the Yucca Mountain and Pah Canyon members and the interbedded tuffs; the Topopah Spring welded (TSw); the Calico Hills nonwelded (CHn); and the Crater Flat undifferentiated (CFu) hydrogeologic units (Bodvarsson et al. 1999, p. 8; CRWMS M&O 1999h, Section 6).

Conceptual models of flow and transport at YM are described in CRWMS M&O (1999d, Section 6). In the present AMR, we focus on the subject of radionuclide transport in the hydrogeologic units beneath the potential repository horizon. A likely site for the potential repository is the TSw unit (CRWMS M&O 1999g), and more specifically the tsw34, tsw35, and tsw36 layers of the unsaturated zone (UZ), depending on the location. More information on these layers can be found in CRWMS M&O (1999h, Section 6) and CRWMS M&O (2000d, Section 6). Unsaturated flow in the TSw is primarily through the fractures, because the matrix permeability in many of the TSw layers can support flows of only a few millimeters per year, and the average fracture spacing in the TSw layers is on the order of 0.5 m (CRWMS M&O 2000d, Section 6; Bodvarsson et al. 1999, p.

13).

The CHn unit and the Prow Pass (PP) unit (formally a part of CHn, but studied separately in the present AMR) below the potential repository horizon are complex geological systems with very heterogeneous distributions of fracture and matrix hydrological properties that are expected to have pronounced effects on flow and transport of radionuclides in the UZ. There is limited information on the CHn unit, and even less on PP. The permeability of nonwelded tuffs is strongly dependent on the degree of alteration of the rock minerals into zeolites. Zeolitic alteration in the CHn (a common occurrence in its lower layers) can reduce the matrix permeability by orders of magnitude in relation to that of the welded tuffs (CRWMS M&O 2000d, Section 6). In nonwelded vitric tuffs, the matrix and fracture permeabilities are on the same order of magnitude (CRWMS M&O 2000d, Section 6). Thus, these layers behave as porous (rather than fractured) media, and flow is matrix-dominated. This has important implications for transport, as the longer contact times in these nonwelded tuff units allow increased radionuclide sorption.

The CHn major hydrogeologic unit is composed of vitric (CHv) and zeolitic (CHz) units (CRWMS M&O 1999h, Section 6). Typically, radionuclides are more strongly adsorbed onto zeolitic units than onto vitric units (DTN: LAIT831341AQ96.001). For example, the K_d (see Equation 9) of ^{237}Np in the vitrified and the zeolitic tuffs is 1 mL/g and 4 mL/g, respectively (DOE 1998b, p. 3-122). Consequently, migration of ^{237}Np is expected to be more retarded in the zeolitic than in the vitrified units, if the contact time is the same.

Flow in the CHz units is expected to be concentrated in the fractures because of low fracture density (compared to the TSw) and the large permeability contrast between matrix and fractures (CRWMS M&O 2000d, Section 6); the permeability in the fractures is about five orders of magnitude larger than in the matrix. Fracture-dominated flow is associated with short contact times, limited radionuclide removal through diffusion and sorption, and thus transport over longer distances.

6.1.2 Transport

Radioactive contaminants can escape from the wastes stored in the potential repository. These contaminants can migrate through the UZ of YM as a dissolved molecular species or in colloidal form. Transport of these radioactive solutes or colloids involves advection, hydrodynamic dispersion, sorption (solute) or filtration (colloids), matrix diffusion, and radioactive decay. The transport of radionuclides is also affected by factors such as solubility limits, the presence of perched water, and heating effects from the potential repository. In this section we briefly discuss the phenomena, processes, and factors affecting transport.

6.1.2.1 Advection

Advection is the transport of dissolved or colloidal species by flowing water. In YM, flow is

predominately downward (in response to gravitational differentials), and so is advective transport (DOE 1998b, p. 3-112). Some lateral advection is also expected in response to lateral flow diversion at the boundaries of hydrogeologic units with sharp contacts in their hydraulic properties. Such diversion occurs in the perched water bodies of the UZ (CRWMS M&O 1999d, Section 6.2.2). Laterally diverted flow ultimately finds a pathway to the water table through other, more permeable zones (e.g., faults).

Advection is probably the most important transport process in this study because it controls the speed at which radionuclides move through the UZ to reach the water table. Advection in the fractures is expected to be the dominant transport mechanism in many layers of the various hydrogeologic units. This is because the expected flow rates in the matrix exceed the matrix permeability (which gives the measure of flow capacity under the gravitational gradient). This leads inevitably to flow focusing in the more permeable fractures. Advection is the dominant transport mechanism in the fractures because of high permeability, limited fracture pore volumes, limited contact area and short contact times between the radionuclide-carrying liquid phase and the matrix (only at the fracture walls). In a few hydrogeologic units, such as the CHv, matrix flow is dominant, resulting in much slower transport velocities (compared to those in the fractures of other units) and longer contact times of the radionuclides with the matrix (DOE 1998b, pp. 3-112).

6.1.2.2 Hydrodynamic Dispersion

The hydrodynamic dispersion combines mechanical dispersion, which is caused by localized velocity variations, and molecular diffusion, which is caused by Brownian motion and is proportional to the concentration gradient. The dispersion of the radionuclides can occur both along and transverse to the average flow direction. Hydrodynamic dispersion leads to the smoothing of sharp concentration fronts and reduces the breakthrough time (which can be defined as the arrival time of the edge of the contaminant front) at the groundwater table.

There is little information on the values of the longitudinal (α_L) and transverse (α_T) dispersivity ($[L]$) in the various hydrogeologic units of the UZ. In past simulations (DOE 1998b, p. 3-122), the longitudinal dispersivity (α_L) values for both the fractures and the matrix of all units had a mean of 20 m and a standard deviation of 5 m. Dispersion is not expected, however, to play a significant role in the advective transport of radionuclides in the fractures because of the predominant role of advection as the main transport mechanism.

Dispersion is affected by the scale of observation. The value of dispersivity appears to increase with the scale of observation (Gelhar et al. 1992, p. 1955; Fetter 1993, p. 65-66). Thus, α_L increased from 10^{-2} to 10^4 m when the observation scale increased from 10^{-1} to 10^5 m, and its value does not appear to be significantly affected by the texture (porous versus fractured) of the aquifer medium (Gelhar et al. 1992, p. 1955).

The ratio α_L/α_T controls the shape of a contaminant plume in multidimensional transport. There is

a paucity of data on the relationship between α_L and α_T . Based on limited field data, Fetter (1993, p. 65-66) reported that α_L/α_T ranged between 6 and 20. Gelhar et al. (1992, p. 1955) indicated that vertical α_T is typically an order of magnitude smaller than the horizontal α_L .

6.1.2.3 Sorption

Sorption is a general term that describes a combination of chemical interactions between the dissolved radionuclides and the solid phases, that is, either the immobile rock matrix or colloids (mobile or immobile). In transport studies, the concept of sorption does not identify the specific underlying interactions, such as surface adsorption, precipitation, and ion exchange. By removing a portion of the mass of the dissolved species from the mobile liquid phase and transferring it to the immobile solid phase, sorption reduces the rate of advance of (i.e., retards) the concentration front of a dissolved or suspended species.

In YM studies, the effective K_d approach (see Equation 9) is employed to quantify the extent of radionuclide-rock interactions by measuring the overall partitioning between the aqueous and the solid phase. Three basic rock types (devitrified tuffs, vitric tuffs, and zeolitic tuffs) have been studied as having distinctively different (i.e., from each other) sorption interactions with the radionuclides (DOE 1998b, p. 3-118). The K_d values for several radionuclides in each of these rock types are listed in the TSPA conceptual model (DOE 1998b, p. 3-122). Note that sorption is not only a function of the sorptive strength (as quantified by the value of K_d), but also of the contact time of the radionuclides with the rock matrix during transport through the UZ.

Sorption kinetics could be important, especially for radionuclides sorbing onto zeolitic tuffs. Column experiments of ^{237}Np transport in tuffs (Viswanathan et al. 1998, p. 267) indicate the existence of kinetic sorption under flowing conditions, possibly as a result of the slow diffusion of ^{237}Np into the tuff pores. It is not possible to analyze these experimental data without considering a kinetic sorption model. Kinetic sorption can have a substantial effect on transport in fast fracture flow because it reduces sorption in the matrix, thus allowing larger radionuclide concentrations and migration over longer distances in the fractures. Nonlinear and irreversible sorption are evident from the diffusion and transport studies discussed in CRWMS M&O (1999e, Section 6.4).

The K_d values used in the YM studies have been estimated from batch experiments using crushed tuffs with a particle size of 75 – 500 μm under saturated conditions (CRWMS M&O 1999e, Section 6.4). There are indications that this experimental approach may overestimate the K_d values. This is because the batch experiment conditions (involving saturated crushed tuff samples) may not be representative of the UZ conditions, which are characterized by unsaturated conditions, a limited contact area and short contact times (see Section 6.1.3.1 for a more thorough discussion). The importance of kinetic, nonlinear, and irreversible sorption may need to be evaluated against the linear equilibrium isotherm assumed in UZ transport studies.

6.1.2.4 Matrix Diffusion

Diffusion can play an important role in radionuclide exchange between the fractures and the rock matrix. This process transfers radionuclides into the matrix (where water flow is slow and sorption occurs), thus removing them from (and slowing the advance of their front in) the fast fracture flow. Diffusive flux across a given interface is a function of the concentration gradient, the temperature, the size of the dissolved species and its electric charge, the matrix pore structure and the water saturation (DOE 1998b, p. 3-116 – 3-117).

Matrix diffusion is a linear function of tortuosity coefficient τ , which describes the tortuous nature of the pore networks (Grathwohl, 1998, p. 28–35), including dead-end pores and steric hindrance (in extremely narrow pores). Note that, according to the definition used in this AMR, $\tau < 1$. There are very limited experimental data on the τ distribution in the various YM hydrogeologic units. In this study, τ is approximated by the value of porosity ϕ (Farrell and Reinhard, 1994, p.64; Grathwohl, 1998, p. 28–35).

This approach was confirmed experimentally. From rock diffusion experiments using devitrified tuffs, the effective diffusion coefficient $D_e (= \phi \tau S_w D_0$, where D_0 is the molecular diffusion coefficient [$L^2 T^{-1}$] and S_w is the water saturation) for $^3\text{H}_2\text{O}$ was obtained from six tuff samples. Based on the literature value of D_0 for $^3\text{H}_2\text{O}$ (Hu and Brusseau 1995), a τ estimate of 0.0806 ± 0.035 was obtained in media in which the reported average porosity was 0.0767 ± 0.019 (DTN: LAIT831341AQ96.001 and Scientific Notebook YMP-LBNL-GSB-QH-1, p. 23). The good match between these two numbers validates the approach of using the porosity value as the tortuosity coefficient.

Even less information exists on the effect of S_w on D_e . Porter et al. (1960) reported that the $\tau \phi S_w$ product decreased consistently in medium- and fine-textured soils as the capillary pressure increased from 0.33 to 15 atm. The effect of saturation on D_e may be more complex than the linear relationship currently assumed. Supporting evidence was provided from experiments by Conca and Wright (1990), who determined D_e values for K^+ ions for a variety of water contents and grain sizes on four types of angular crushed gravel. For volumetric water contents ranging from 0.5% to 6%, the D_e ranged from 10^{-14} m²/s to 10^{-11} m²/s, i.e., the dependence was much stronger than what could be expected from the linear relationship between D_e and S_w . This subject could merit additional attention because it can provide an additional safety factor. The linear relationship assumed in this AMR results in more conservative transport estimates because diffusion from the fractures into the matrix is reduced.

6.1.2.5 Solubility

The concentration of any radionuclide (released from the stored radioactive wastes at the potential repository) in the water cannot exceed the radionuclide solubility limit, unless suspended colloids are involved. Limitations to radionuclide solubility in the water infiltrating the potential repository constitute the first barrier to transport and can reduce the extent of radionuclide migration by limiting

the available source.

The solubilities of the radionuclide of interest are reported in CRWMS M&O (1999e, Section 6). The lower solubility of many radionuclides can lead to slower and continuous release over time at the outer boundaries of engineered barrier systems surrounding the radioactive wastes because the source is not exhausted. For example, the solubility of ^{237}Np is sufficiently low to extend the period of its release to tens of thousands of years (Viswanathan et al. 1998, p. 273).

6.1.2.6 Colloids

Colloids are fine particles, between 0.001 and 1 μm in diameter, that become suspended and are transportable in a moving liquid. The generation and mobilization of colloids are considered important issues in contaminant transport, particularly the transport of radioactive true (intrinsic) colloids (e.g., colloidal Pu(IV) and Pu(V)) and the colloid-assisted transport of radioactive species (e.g., ^{239}Pu , ^{237}Np , ^{243}Am , and ^{247}Cm from high-level radionuclide wastes, or ^{137}Cs , ^{90}Sr , and ^{60}Co from low-level radioactive wastes, see CRWMS M&O (1999e, Section 6)) sorbed on pseudocolloids (e.g., naturally occurring clay colloids). See Sections 6.1.3.3 to 6.1.3.7 for a more detailed discussion.

6.1.2.7 Perched Water

Perched water is defined as a saturated zone that is located at a higher elevation than the static water table, to which it is not directly connected. Perched water usually occurs where low permeability horizons do not permit the rapid downward flow of water. Such bodies have been reported at several locations in UZ boreholes (Wu et al. 1999). The presence of perched water has implications for the travel times and flow paths of water and radionuclides through the UZ.

The majority of the perched water bodies detected in the UZ boreholes were observed in formations overlaying relatively impermeable matrix material, such as the TSw basal vitrophyre (a glassy cooling unit). Although the vitrophyre is extensively fractured, many of the fractures have been filled with zeolitic material, thus limiting flow. A portion of the Calico Hills formation has been extensively altered to zeolites, creating perched water bodies (Bodvarsson et al. 1999, p.14-15). The blockage of fracture flow which occurs in these perched water bodies can lead to lateral diversion of radionuclide migration if the percolation flux is sufficiently large.

Three perched water models, namely no perched water, perched water model #1 (flow through the perched water), and perched water model #2 (flow bypassing the perched water) have been proposed in CRWMS M&O (1999d, Sections 6.2.2 and 6.2.5). The effects of each of these perched water models on radionuclide transport will be investigated in the 3-D site-scale simulations discussed in Section 6.15.

6.1.2.8 Daughter Products

Chain-decay adds another layer of complexity because of the need to account for the transport of the

daughter products, i.e., the new radionuclides created from the decay of a parent radionuclide. The daughter products may have significantly different transport behavior than the parent radionuclide. Thus, the migration and fate of all the important members of the decay chain, rather than just the parent radionuclide, must be considered.

6.1.2.9 Effect of Heat on Transport

Radionuclide transport may also be influenced by the heat generated by the decaying radioactive waste, which affects the ambient hydrologic and chemical conditions and can thermally alter the rock near the potential repository. For example, if the zeolitic layers below the potential repository horizon are thermally altered, the sorption of radionuclides is reduced.

In addition to the thermal effect on the flow field and radionuclide sorption coefficient, temperature also enhances diffusion by increasing Brownian motion. This effect is quantified by an increase in the D_0 of radionuclides. The temperature-dependent D_0 is described by the following equation (Robin et al. 1987, p. 1105-1106):

$$\left(\frac{D_0 \mu}{T} \right)_{T_1} = \left(\frac{D_0 \mu}{T} \right)_{T_2}$$

where T is the absolute temperature and μ is the viscosity of water.

The effect of temperature on sorption has been discussed in CRWMS M&O (1999e, Section 6.4.6). In general, an increase in temperature leads to increased sorption of cationic species and decreased sorption of anionic species. In addition to theoretical predictions, CRWMS M&O (1999e, Section 6.4.6) includes a discussion of experimental data that show an increase of sorption by an order of magnitude when temperature increases from 25 °C to 75 °C.

Temperatures in the UZ increase naturally with depth because of the geothermal gradient. Additionally, heat from the stored waste is expected to lead to higher temperatures over a large volume of the UZ for as long as 100,000 years (CRWMS M&O 2000b, Section 6.5). The combined effect of higher temperatures is increased retardation of the radionuclides because of (a) increased diffusion from the fractures into the matrix and (b) increased sorption. The assumption of isothermal 25 °C conditions in the studies of the present AMR reflects a conservative approach and yields results that describe the worst-case scenario.

6.1.3 Important Transport Issues

6.1.3.1 Measurements of K_d Values

The sorption behavior of radionuclides is usually described by the distribution coefficients (K_d), which quantifies the partitioning of radionuclides between the solid and aqueous phases under a

linear equilibrium isotherm. Most of the K_d values are obtained from batch experiments using crushed rock, the particle size of which is determined only by experimental convenience and is more or less arbitrary.

Compared to intact rock samples, batch experiments using crushed rock samples may overestimate the K_d values. Crushing of the material creates new contact surfaces and also increases the radionuclide accessibility to pores that may not contribute to sorption to intact rocks. Comparison of the K_d values obtained from batch sorption experiments and from diffusion experiments (which use larger samples) show significant differences, which are attributed to differences in the size of the samples.

Bradbury and Stephen (1985) investigated the sorption of ^{85}Sr , ^{85}Tc , ^{125}I , and ^{137}Cs onto Darley Dale sandstone samples. Comparing K_d values obtained from batch (using <0.1 mm and 1-2 mm) and diffusion-sorption experiments (using disks of 25 mm indiameter and about 5 mm inthickness), they determined that crushed rock tests can overestimate sorption by as much as one or two orders of magnitude. They concluded that the magnitude of the difference in the value of K_d depends on the radionuclide, its concentration, the rock, the water/solid ratio, and the particle size distribution in the batch tests.

Holttä et al. (1997) studied the effect of specific surface area onthe sorption of ^{22}Na , ^{45}Ca and ^{85}Sr on crushed crystalline rocks of six size fractions (0.071-0.15, 0.15-0.20, 0.2-0.3, 0.3-0.85, 0.85-1.25, >1.25 mm). Sorption of ^{22}Na , ^{45}Ca and ^{85}Sr on unaltered tonalite and mica gneiss was slight and exhibited virtually no dependence on the fraction size. Considerably higher sorption of ^{22}Na and ^{85}Sr occurred on altered tonalites of smaller fractions because of their larger specific surface areas. K_d values from thin sections (0.030 mm in thickness) were in good agreement with those obtained from batch experiments, possibly because the thin-section thickness is within the range of the crushed-rock size fractions.

Johansson et al. (1997; 1998) conducted batch sorption tests of alkali- and alkaline earth metals (^{22}Na , ^{137}Cs , ^{45}Ca , ^{85}Sr , and ^{133}Ba) using six crushed size fractions (0.045-0.090, 0.090-0.25, 0.25-0.5, 0.5-1, 1-2, 2-4 mm) of medium-grained Aspö diorite and fine grained granite. The K_d increased with a decreasing particle size, and differed by approximately one order of magnitude between the largest and smallest particle because of different specific surface areas. They also determined that the the best agreement between the K_d values from diffusion experiments (using 20 mm rock disks) and from batch experiments was observed for the largest size fractions (2-4 mm) in the batch studies. They explained this observation by suggesting that, unlike the smaller fractions, the largest size fraction involved a large number of whole mineral grains.

Tachiet al. (1998)studiedthesorptionanddiffusionbehaviorofSeinTonotuffs inbatchexperiments (using crushed rock with sample sizes ranging between 0.075 and 0.355 mm) and in through-diffusion experiments (using samples 30 mm in diameter and 5 mm in thickness). The K_d values

from the diffusion experiments were one order of magnitude lower than those from the batch experiments. Correcting for the difference in the specific surface areas could not fully account for the K_d discrepancy. Mercury porosimetry suggested that the differences were caused by sorption in microscopic pores (less than 20 nm in diameter) in the crushed rock samples. When the contribution of these pores to sorption was not considered, the K_d values from the batch sorption experiments and from the diffusion experiments were consistent.

The effect of the specific area surface of ground rock samples on the sorption of ^{137}Cs , ^{85}Sr , and ^{237}Np was studied in nine size fractions (< 0.038, 0.038-0.063, 0.063-0.075, 0.075-0.106, 0.106-0.25, 0.25-0.50, 0.5-1, 1-2, 2-4 mm) of devitrified Topopah Spring tuff and zeolitized Calico Hills tuff (Rogers and Meijer 1993). They showed that the grinding process does not influence the sorption behavior for particle sizes larger than about 63 μm . They also indicated that ground samples must be washed carefully to remove very fine particles generated during the grinding process, which could lead to irreproducible or anomalously high K_d values.

6.1.3.2 Sorption of ^{129}I and ^{99}Tc

Iodine and technetium, which are represented respectively as I^- and pertechnetate (TcO_4^-) under ambient oxidizing conditions, do not sorb onto tuffs. The recommended sorption coefficient for both iodine and technetium is therefore zero for performance assessment in both saturated and unsaturated units (DOE 1998b, p. 3-122).

I^- is expected to have no significant retardation in the YM rock-water system and may even have slightly enhanced migration rates because of anion-exclusion effects. If conditions were to become sufficiently oxidizing to convert iodide to iodate, some retardation of iodine is possible. Although such conditions can occur locally for a short time (e.g., due to radiolysis), it is unlikely that they can occur over a significant volume of the flow system for an extended period of time (CRWMS M&O 1999e, Section 6).

^{99}Tc appears to show nonzero, though minimal, retardation in the YM rock-water systems, which could be important in long-term transport. If, however, sufficiently reducing conditions could be shown to occur in portions of the flow system between the potential repository and the groundwater, precipitation and sorption of the Tc^{4+} species can result in significant retardation of ^{99}Tc (CRWMS M&O 1999e, Section 6).

6.1.3.2.1 Potential Sorption of Anions

Adsorption of negatively-charged ionic species from the aqueous phase onto mineral substrates is likely to occur whenever the mineral surface exhibits a net positive surface charge. Most rock-forming aluminosilicate minerals under typical ambient conditions in shallow systems (saturated or unsaturated) have negatively charged surfaces. It is possible, however, for these surfaces to become positively charged in the presence of acids or if the surfaces dry out and only residual oligolayers of water remain.

The transition from negatively to positively charged surface occurs at the point of zero charge (PZC), where the surface charge is zero, and is usually expressed in terms of pH. The PZC differs from one mineral to another, but for most rock-forming minerals it is less than 4. However, in some materials (such as iron oxides, sulfides and some organic matter), the PZC can be as high as 8 or 9.

These minerals display a tendency to adsorb anionic species such as I^- and TcO_4^- under ambient groundwater conditions. For example, the extent of AsO_4^{3-} sorption on hydrous ferric oxide is a function of pH (Dzombak and Morel 1990, pp. 200-204). The edge sites on clays are also reported to contain positive sites. Under low pH conditions (e.g., pH = 5), significant sorption of anionic tracers occurs in systems with high concentrations of iron oxides and kaolinite (Boggs and Adams 1992; Seaman 1998).

Despite the availability of positively charged adsorption sites, $^{129}\text{I}^-$ and $^{99}\text{TcO}_4^-$ are in competition with other anionic species in solution, such as SO_4^{2-} , NO_3^- , OH^- etc, which are usually present in concentrations orders of magnitude larger than either $^{129}\text{I}^-$ or $^{99}\text{TcO}_4^-$. Because of competition, their effective sorption is minimal. There are, however, exceptions, and these should be taken into account when evaluating their retardation.

Kaplan and Serne (1995) determined that iodine sorbed on all Hanford sediments, and its K_d ranged from 0.7 to 15 mL/g, with a median value of 7 mL/g. This finding could have significant implications for radionuclide transport. Positively charged adsorption sites may exist on the edges of 2:1 clays such as smectite and illite, on Al- and Fe-oxide surfaces, and on 1:1 clays such as kaolinite. Anions may sorb onto these locally positive-charged sites, even though their numbers are limited under typical pH conditions.

Note that the study of Kaplan and Serne (1995) involved extremely low iodine concentrations (approximately 12 ppt). Therefore, only a small number of positively charged sites would be needed for the sorption of a measurable portion of the dissolved iodine. Had an initially larger concentration been used in these experiments (e.g., 1 ppm), it is reasonable to expect that a small fraction of iodine would have sorbed onto the solid phase, resulting in practically undetectable iodine sorption. It must be pointed out that the ^{129}I concentrations is expected to be in the part-per-trillion (ppt) range in a low-level waste plume (Kaplan and Serne 1995).

Similarly, significant sorption of technetium could occur in soils containing considerable amounts of natural organic matter, which tends to sorb anionic species and could reduce technetium to its +4 oxidation state, causing precipitation and/or sorption (Kaplan and Serne 1995). In the UZ of YM, however, conditions are both oxidizing and deficient in organic matter. Therefore, significant sorption is unlikely to occur until more reducing conditions are encountered within the saturated zone.

Currently, there is no information on the occurrence and extent of localized positively charged sorption sites in YM tuffs. The existence of such sites cannot be ruled out. Clays and oxides can potentially contribute to positively charged sites. Smectite is a significant constituent of some unwelded tuff horizons at Yucca Mountain. Although hematite and illite are present in minor or trace amounts in the unwelded tuffs, hematite is widely distributed in the matrix of the devitrified units. Smectite and hematite also coat fracture walls in Yucca Mountain tuffs (CRWMS M&O 1999e, Section 6). No estimate exists of the potential effects of such sites on the site-scale transport of radioactive anionic species.

6.1.3.2.2 Solute Size Effects

Another aspect about technetium and iodine transport is the exclusion effect resulting from their relatively large ionic radius and low charge density. Technetium travels faster than tritium in both diffusion and column studies (CRWMS M&O 1999e, Section 6). This is attributable to the large size of the pertechnetate anion, which is excluded from tuff pores. In contrast, in crushed-rock column experiments, anion-exclusion effects for pertechnetate are essentially negligible, except in the case of technetium transport through zeolitic tuffs in the J-13 well water. In this case, the anion-exclusion effect was small but measurable (CRWMS M&O 1999e, Section 6).

It should be emphasized that $^3\text{H}^+$ can sorb weakly onto tuffs, as TcO_4^- can. The faster TcO_4^- breakthrough curves (compared to those for $^3\text{H}^+$) reported in CRWMS M&O (1999e, Section 6.5.3.3) should not be necessarily interpreted to indicate TcO_4^- size-exclusion, but could also denote larger $^3\text{H}^+$ sorption. This is supported by the slight retardation of $^3\text{H}_2\text{O}$ reported by Hu and Brusseau (1996). The apparent sorption is in essence ion-exchange and has been postulated to occur via OH exchange on the clay lattices.

6.1.3.3 Colloidal Behavior

Radioactive true colloids or radionuclides adsorbed onto pseudocolloids can be transported over significant distances (McCarthy and Zachara 1989, pp. 496-497). The significant migration of strongly sorbing Pu and Am (more than 30 m) from a low-level waste site at Los Alamos National Laboratory through unsaturated tuff over a period of approximately 30 years is attributed to colloid and/or colloid assisted transport, a hypothesis confirmed by laboratory experiments (Buddemeier and Hunt 1988, p. 536). Using the $^{240}\text{Pu}/^{239}\text{Pu}$ isotope ratio to fingerprint the source of Pu in groundwater, Kersting et al. (1999, pp. 56-59) recently demonstrated that the soluble (ionic) Pu is practically immobile in the subsurface of the Nevada Test Site (NTS) because of its strong sorption, but can be transported over significant distances (1.3 km over a 30-year period) in a colloidal form.

Colloids are very fine particles (such as clay minerals, metal oxides, viruses, bacteria, and organic macromolecules) that range in size between 1 and 10,000 nm (McCarthy and Zachara 1989, pp. 497-498) and have high specific surface areas ($\simeq 300 \text{ m}^2/\text{g}$). Their chemical behavior is dominated by surface processes (EPRI 1999, p. 3-1), and can have a high sorptive capacity for contaminants. Colloids are deposited on porous and fractured media by surface filtration, straining filtration, and

physical-chemical filtration. Colloid transport differs from solute transport because the colloidal particle interactions (e.g., flocculation), mechanical clogging effects, and surface reactions (e.g., deposition or attachment) are substantially different from the solute processes and phenomena.

A natural colloid becomes a pseudo-colloid when a radionuclide adsorbs onto it. True (intrinsic) Pu(IV) colloids (generated from the contaminant when its concentration exceeds its solubility) have been produced by the agglomeration of hydrolyzed Pu(IV) ions under acidic conditions (EPRI 1999, p. 3-2). When immature, actinide true colloids display hydrophilic properties, but become hydrophobic with increasing age.

A complete description of colloid-facilitated radionuclide transport requires consideration of a large number of processes (EPRI 1999, pp. 4-5 – 4-6), including advection, diffusion, colloid generation, colloid stability, colloid-solute-matrix interactions, affinity of colloids for the gas-water interface, colloid filtration (surface and straining), and kinetically controlled physical-chemical filtration.

6.1.3.3.1 Colloid Generation and Stability

The formation of mobile colloidal suspensions in the subsurface is attributed to a number of mechanisms: (1) matrix dissolution caused by changes in pH or redox conditions; (2) supersaturation with respect to the inorganic species; (3) disruption of the mineral matrix by large changes in the flow regimes due to injection, pumping or large episodic rainfall infiltrations; (4) release and movement of viruses and bacteria; and (5) formation of micelles from the agglomeration of humic acids (Abdel-Salam and Chrysikopoulos 1995, pp. 199-200). Buddemeier and Hunt (1988, p. 536) indicate that submicrometer colloids can easily be released from mineral and glass surfaces that are chemically, hydrodynamically, or mechanically stressed.

Colloid stabilization/destabilization include steric stabilization by mechanisms such as organic coating of inorganic colloids, and the effects of pH and ionic strength on coagulation and precipitation. The stability of colloid suspension is very sensitive to changes in ionic strength (EPRI 1999, p. 4-6).

6.1.3.3.2 Colloid Deposition

Colloid deposition (physico-chemical filtration) during saturated flow through a porous medium is commonly assumed to occur in two steps: (1) transport of colloids to matrix surfaces by Brownian diffusion, interception, or gravitational sedimentation (i.e., colloid-matrix collision) and (2) attachment of colloids to matrix surfaces. The attachment efficiency (i.e., the fraction of collisions resulting in attachment) is strongly influenced by interparticle forces between colloids and matrix surfaces, such as van der Waals and electric double layer interactions, steric stabilization, and hydrodynamic forces (Kretzschmar et al. 1995, p. 435). Kretzschmar et al. (1997, p. 1129) demonstrated that colloid deposition generally follows a first-order kinetic rate law and experimentally determined the corresponding collision efficiencies.

6.1.3.3.3 Colloid–Contaminant–Matrix Interactions

Colloid attachment to the host rock is strongly dependent on electrostatic interactions. Once attached, colloid detachment (declogging) is generally slow to irreversible. Sorption of radionuclides on colloids is controlled by a range of chemical processes such as ion exchange, surface complexation, and organic complexation (EPRI 1999, pp. 4-9).

If sorption of metal ions onto colloids is assumed to follow an equilibrium isotherm, metals are stripped very fast from the colloids when these enter a clean part of the porous medium. This approach was incapable of explaining the long transport distances observed in field experiments (van de Weerd and Leijnse 1997, p. 246). The problem was addressed by assuming (a) kinetic sorption of radionuclides onto the humic colloids and (b) kinetic colloid deposition (van de Weerd and Leijnse 1997, pp. 245, 255).

The sorption of dissolved ionic Pu(IV) onto hematite, goethite, montmorillonite, and silica colloids in both natural and carbonate-rich synthetic groundwater was reported to be fast (CRWMS M&O 1999e, Section 6). Under equilibrium conditions, the K_d values of Pu(V) was about 100 mL/g for hematite and montmorillonite colloids. These very large values indicate that ion oxide and clay colloids in groundwater can significantly enhance the transport of ^{239}Pu .

6.1.3.3.4 Colloid Migration in Macroporous and Fractured Systems

Jacobsen et al. (1997, pp. 185-186) conducted infiltration experiments in intact structured sandy loam cores using two types of colloidal suspensions, and observed significant transport of clay and silt colloid particles through the macropores. Macropores can enhance the transport of colloids because all types of filtration are less pronounced in large pores and the large water velocities can lead to increased detachment (as the large hydrodynamic forces can overcome the colloid-grain bonding forces).

In a study of colloid-facilitated transport of radionuclides through fractured media, Smith and Degueldre (1993, pp. 143, 162-163) determined that the assumption of fast, linear, and reversible radionuclide sorption onto colloids is non-conservative. They observed that the time for radionuclide desorption (days or weeks) significantly exceeded the time for sorption (seconds or minutes). Such radionuclide-laden colloids can migrate over long distances in macropores and fractures, and the larger colloids exhibit little retardation because their size prevents them from entering the wall-rock pores. The Smith and Degueldre (1993, pp. 143, 162-163) study concluded that the transport of radionuclides sorbed irreversibly on to colloids depends strongly on the extent of colloid interaction with the fractures.

Vilks and Bachinski (1996, pp. 269, 272-278) studied particle migration and conservative tracer transport in a natural fracture within a large granite block with overall dimensions of $83 \times 90 \times 60$ cm. Flushing experiments showed that suspended particles as large as 40,000 nm could be mobilized from the fracture surface. The mobility of suspended particles with diameters of 1000-40,000 nm

was significantly less than that of colloids (<90 nm). They observed that the conservative tracer lagged slightly behind the colloid front, but colloid mobility was significantly reduced when the average groundwater velocity decreased. Compared to dissolved tracers, the migration of colloids was more affected by the flow path and flow direction. This tendency can have a significant effect in the fracture-dominated flow of the UZ in the YM system.

In field-scale colloid migration experiment, Vilks et al. (1997, pp. 203, 212-213) showed that silica colloids as small as 20 nm can migrate through open fractures over distances of 17 m when a colloidal suspension was injected at average flow velocities of 1.6 and 2.9 m/h (orders of magnitude higher than the natural flow rates at the site). Based on the analysis of the results of the study, they also suggested that although colloid migration appeared to behave conservatively, colloids may have followed different pathways than dissolved conservative tracers.

6.1.3.4 Colloidal Behavior in Unsaturated Media

Most of the available literature focuses on the behavior of colloids in saturated media. The behavior of colloids in unsaturated media is a relatively new area of study and has significant additional complexity.

6.1.3.4.1 Filtration as a Function of Water Saturation

Colloid filtration is a physical retardation process. Wan and Tokunaga (1997, p. 2413) distinguish two types of staining: conventional staining (if the colloid is larger than the pore throat diameter or the fracture-aperture width) and film straining (if the colloid is larger than the thickness of the adsorbed water film coating the grains of the rock).

Wan and Tokunaga (1997, pp. 2413, 2419) developed a conceptual model to describe colloid transport in unsaturated media as a function of water saturation S_w . If the rock S_w exceeds a critical saturation value S_c , colloids move through the system entirely within the aqueous phase. For $S_w < S_c$, colloids can only move in the thin film of water that lines the grain boundaries, and colloid transport through the water film depends on two parameters: the ratio of the colloid size to the film thickness, and the flow velocity. Temporal variations in the S_w in the subsurface profile and in the infiltration rate can lead to strongly nonlinear colloid mobility in the vicinity of S_c .

McGraw and Kaplan (1997, p. 5.2) investigated the effect of colloid size (from 52 to 1900 nm) and S_w (from 6 to 100 %) on colloid transport through unsaturated media in Hanford sediments. They showed a very strong dependence of filtration on the colloid size under unsaturated conditions. At a volumetric water content of 6%, (the expected water content in the Hanford vadose zone), colloid removal increased exponentially with the colloid size. The decrease in colloid mobility at low volumetric contents was attributed to resistance due to friction (as the colloids were dragged along the sand grains). The colloid retardation increased as the ratio between the water film thickness and colloid diameter decreased.

6.1.3.4.2 Gas–Water Interface

Under unsaturated conditions, colloid transport may be either inhibited or enhanced (compared to that under saturated conditions) because of the presence of the air-water interface. Wan and Wilson (1994, pp. 857, 863) determined that the retention of both hydrophilic and hydrophobic colloids increased with the gas content of the porous medium. They showed that colloids preferentially concentrate in the gas-water interface rather than on the matrix surface. This tendency increases with the colloid surface hydrophobicity or contact angle, with hydrophobic colloids having the strongest affinity for the gas-water interface.

The implications of this colloid behavior are important. The colloid affinity for the gas water interface may retard their transport through the unsaturated zone. Conversely, if the subsurface conditions permit the stability and migration of bubbles, colloid transport may be enhanced.

6.1.3.5 Colloids at Yucca Mountain

The available data on colloid occurrence and concentrations at the YM site are limited, and pertain to saturated zone studies. There is no published information on colloids in the unsaturated zone. The current state of understanding is that (a) the natural colloid concentrations in native waters at the YM site are low (10^6 - 10^{10} particles/mL), and (b) waste-form colloids will be the dominant colloidal species of concern to transport studies (CRWMS M&O 1999f, Section 6).

Additional information from nearby sites, however, cannot be ignored. Preliminary results of a survey of groundwater from the Nevada Test Site (NTS) have shown that, in the Pahute Mesa drainage (both on and off the NTS), have colloidal particle (>3 nm in diameter) loadings of 0.8-6.9 mg/L. Such relatively high concentrations can explain the observed transport of strongly sorbing radionuclides over significant distances, particularly because the ionic composition of the NTS groundwater is not expected to promote the coagulation of clay colloids (Buddemeier and Hunt 1988, p. 537). This is because NTS groundwater is oxygenated and low in organic matter, and a substantial fraction of the colloidal material is composed of stable natural minerals (Buddemeier and Hunt 1988, p. 543-544).

In addition to natural colloids, anthropogenic colloids may be created from the waste itself or from repository construction and sealing materials. Waste- and repository-derived colloids at Yucca Mountain are likely to include organic colloids, iron oxyhydroxides, and aluminosilicate colloids (EPRI 1999, p. 2-2, 6-22). In a 50-month experiment of simulated weathering of a high-level nuclear waste glass, spallation and nucleation were identified as the main mechanisms of colloid genesis (Bates et al. 1992, pp. 649-651). The created colloids were identified as inorganic. The same study determined that Pu and Am released from waste were predominantly in the colloidal, rather than in the dissolved, form.

6.1.3.6 Impact of Colloids on Radionuclide Transport in YM

EPRI (1999, pp. xv-xvii and 2-2) indicated that it is important for the YMP to consider the migration

of radionuclides, and assess the potential role of colloids on radionuclide transport, within both the saturated and the unsaturated systems. Furthermore, EPRI (1999, pp. 4-6 to 4-7) identified the following key areas of uncertainty for further study:

1. Colloid-matrix interactions.
2. Thermodynamic data for certain radionuclides and kinetic data to describe virtually all rate-dependent reactions.
3. Representation of the hydrological system: colloid transport differs from the transport of conservative tracers and is influenced by the details of the permeability structure, such as fracture geometry and the hydraulic conditions within the fracture zones.
4. The effects of partially-saturated conditions on colloid transport.

6.1.4 Important Points for Consideration in Colloid Transport

The assessment of the potential role of colloids in the transport of radionuclides at Yucca Mountain is particularly challenging for the reasons discussed in the previous sections, and is further complicated by the following factors:

1. Different types of colloids (minerals, organics, microbes, and polymeric actinide colloids) with substantially different characteristics and properties (e.g., hydrophobicity and surface charges) that strongly affect their behavior in the subsurface.
2. Colloid generation, growth, stability, size distribution, and concentration are dynamic. Knowledge on the temporal and spatial distributions of colloid populations in the different hydrogeologic units is difficult to obtain. Changes in the ionic strength of the aqueous solution (e.g., when percolating water in an episodic infiltration event encounters resident pore water) can affect colloid stability. There are also uncertainties about the colloid stability in the aqueous phase of the UZ and about the colloid generation from mineral-coated fracture walls (given the predominance of fracture flow in the UZ).
3. Measurements of colloid concentration in the unsaturated zone are difficult. Because of the low concentrations and low saturations in the UZ, the determination of colloid concentration in pore water is challenging, and serious questions arise about sample representativity and integrity.
4. The concentration of waste-form colloids is a key uncertainty. There is evidence to suggest that the low concentration of natural colloids in the UZ of YM will not lead to significant

colloid-assisted transport, and that waste-form colloids will be the dominant colloidal transport problem (see CRWMS M&O 1999f, Section 6). Thus, there is a need for reliable estimates of the types and generation rates of waste-form colloids. Currently, there is considerable uncertainty on this subject (EPRI 1999, p. 6-7).

Important processes to consider are:

6.1.4.1 Colloid Diffusion

Colloids diffuse slower than dissolved species because of their larger size (see Section 6.2.5, Equation 23). For the largest colloids, diffusion is approximately three orders of magnitude slower than that for molecular species (Nuttall et al. 1991, p. 189). For example, the diffusion coefficient D_0 of a $0.1 \mu\text{m}$ colloid at 20°C is $4.29 \times 10^{-12} \text{ m}^2/\text{sec}$ (see Equation 23 in the present AMR), while the D_0 of Br^- is $2.08 \times 10^{-9} \text{ m}^2/\text{sec}$ (Cussler 1984, p.147).

6.1.4.2 Pore Exclusion

Using mercury porosimetry, Roberts and Lin (1997, pp. 577-578) determined that the average pore diameters of welded and densely welded TSw tuff samples were 53.1 nm and 19.7-21.4 nm, respectively. These extremely small pores are certain to exclude a significant proportion of colloids. It is possible for colloids to accumulate on the fracture walls and thus clog the matrix pores open to the fracture. This can lead to reduction in the matrix permeability and in the colloid diffusion into the matrix. Pore exclusion is not expected to be significant in the fractures, and colloids can travel cover significant distances in the fractures (especially given the limited diffusion into the matrix).

6.1.4.3 Role of Air-Water Interface

The affinity of colloids for the air-water interface depends on their hydrophobicity and electrostatic charge. Hydrophilic colloids, such as mineral fragments, have a low affinity for the interface, in contrast to hydrophobic colloids (such as organic colloids and microbes). This affinity increases with the positive charge on the colloids (EPRI 1999, p. 6-11). The flow and saturation conditions in the UZ will determine whether this will enhance or retard transport. Note that the potential impact of the air-water interfaces on colloid transport has not been quantified yet.

6.2 MATHEMATICAL MODEL OF TRANSPORT

The mathematical model of the flow component in this AMR is included in CRWMS M&O (1999d, Section 6), in which it is thoroughly discussed. Here we focus on the mathematical model of transport and discuss the implications of the various processes it describes for radionuclide transport.

There are 8 subsections in Section 6.2. The basic mass balance equation of solutes and colloids are discussed in Section 6.2.1. Section 6.2.2 focuses on the accumulation terms of the mass balance equation. The equations of sorption (for solutes), filtration (for colloids) and colloid-assisted transport of solutes are described in Sections 6.2.3, 6.2.4, and 6.2.5, respectively. The flux terms of the mass balance equation (Section 6.2.1) are described mathematically in Section 6.2.6. Radioactive decay is discussed in Section 6.2.7, and Section 6.2.8 describes the equations of transport of the daughter products of radioactive decay.

6.2.1 General Mass Balance Equations

Following Pruess (1987, 1991), mass balance considerations in a control volume dictates that

$$\frac{d}{dt} \int_{V_n} M_\kappa dV = \int_{\Gamma_n} \mathbf{F}_\kappa \cdot \mathbf{n} d\Gamma + \int_{V_n} q_\kappa dV \quad (\text{Eq. 1})$$

where

V, V_n	=	volume, volume of subdomain n [L^3]
M_κ	=	mass accumulation term of component (tracer) κ [ML^{-3}]
Γ, Γ_n	=	surface area, surface area of subdomain n [L^2]
\mathbf{F}_κ	=	Darcy flux vector of component κ [$ML^{-2}T^{-1}$]
\mathbf{n}	=	inward unit normal vector [L^0]
q_κ	=	source/sink term of tracer κ [$ML^{-3}T^{-1}$]
t	=	time [T].

The conservation of mass for any subdomain n is given by Equation 1, which in space-discretized form assumes the form of the following ordinary differential equation:

$$\left(\frac{dM_\kappa}{dt} \right)_n = \frac{1}{V_n} \sum_m A_{nm} (F_\kappa)_{nm} + (q_\kappa)_n \quad (\text{Eq. 2})$$

where A_{nm} is the surface segment between elements n and m [L^2], $(F_\kappa)_{nm}$ is the mass flux of tracer κ between elements n and m [$ML^{-2}T^{-1}$], and $(q_\kappa)_n$ is the mass rate of the source/sink of tracer κ in element n [$ML^{-3}T^{-1}$]. Equation 2 is general, and applies to solutes and colloids.

6.2.2 Accumulation Terms

6.2.2.1 Equations of the Accumulation Terms

The accumulation term M of a tracer κ (solute or colloid) in a porous or fractured medium (PFM) is given by

$$M_{\kappa} = \begin{cases} M_{L,\kappa} + M_{Ag,\kappa} + \delta_c M_{Ac,\kappa} & \text{for solutes} \\ M_{L,\kappa} + M_{F,\kappa} & \text{for colloids} \end{cases} \quad (\text{Eq. 3})$$

where

$$\begin{aligned} M_{L,\kappa} &= \text{the mass of tracer } i \text{ in the aqueous phase } [ML^{-3}] \\ M_{Ag,\kappa} &= \text{the mass of solute tracer } i \text{ adsorbed onto the PFM grains } [ML^{-3}] \\ M_{Ac,\kappa} &= \text{the mass of solute tracer } i \text{ adsorbed onto colloidal particles } [ML^{-3}] \\ M_{F,\kappa} &= \text{the mass of filtered colloidal tracer } i [ML^{-3}] \end{aligned}$$

and the parameter

$$\delta_c = \begin{cases} 1 & \text{for "pseudocolloids"} \\ 0 & \text{otherwise.} \end{cases} \quad (\text{Eq. 4})$$

Pseudocolloids must be clearly differentiated from “true” colloids. The term “true” colloids refers to those generated from contaminants (Saltelli et al. 1984) when their concentrations exceed their solubility, and their study focuses on their transport. Colloids from other sources (e.g., clay particles naturally occurring in the subsurface) are termed “pseudocolloids” (Ibaraki and Sudicky 1995, p. 2945), and their transport behavior must include both colloid transport and sorption of contaminants onto them. A detailed discussion on the subject can be found in Ibaraki and Sudicky (1995).

Omitting for simplicity the κ subscript, M_L is obtained from

$$M_L = \phi (S_w - S_r) \rho X + \phi S_r \rho \mathcal{X}, \quad (\text{Eq. 5})$$

where

$$\begin{aligned} X &= \text{the mass fraction of the tracer in the mobile fraction of the aqueous phase } [M/M] \\ \mathcal{X} &= \text{the mass fraction of the tracer in the immobile fraction of the aqueous phase } [M/M] \\ S_r &= \text{the immobile water saturation (can be set equal to} \end{aligned}$$

$$\begin{aligned}
& \text{the irreducible) } [L^3/L^3] \\
\phi &= \text{the porosity (matrix or fracture) } [L^3/L^3] \\
\rho &= \text{the water density } [ML^{-3}].
\end{aligned}$$

Equation 5 reflects the fact that solute concentrations are different in the mobile and immobile water fractions. Because water is very strongly bound (in electric double layers) to the PFM grain surface, Brownian motion is limited and solubility in the immobile water is lower than in the mobile water fraction. The importance of this boundary layer has been recognized by de Marsily (1986, p. 234), who differentiates X and \mathcal{X} , and Moridis (1999), who used the mobile fraction of water in the analysis of diffusion experiments. Using the linear equilibrium relationship (Moridis 1999),

$$\mathcal{X} = K_i X, \quad (\text{Eq. 6})$$

where K_i is a dimensionless mass transfer coefficient. For solutes $1 \geq K_i > 0$. Because of their double layers and their relatively large size (compared to solutes), colloids are expected to concentrate in the mobile water fraction and to be practically absent from the immobile water fraction. Then, a good approximation is $K_i \simeq 0$.

Substitution into Equation 5 then leads to

$$M_L = \phi h \rho X, \quad \text{where} \quad h = S_w - S_r + K_i S_r. \quad (\text{Eq. 7})$$

6.2.2.2 Implications for Transport in the UZ

For rocks with high irreducible water saturations at the UZ of Yucca Mountain, $K_i < 1$ can lead to smaller h values, indicating lower accumulation in the liquid phase. Under conditions of steady-state release, this can result in faster breakthroughs and, consequently, shorter travel times to the groundwater.

6.2.3 Sorption Terms

The discussion in this section is limited to sorption onto the matrix and fractures. Sorption onto pseudocolloids will be discussed in Section 6.2.4.

6.2.3.1 Equilibrium Physical Sorption

Omitting again for simplicity the κ subscript, the mass of a solute sorbed onto the PFM grains and following a linear equilibrium isotherm is given by

$$M_{Ag} = (1 - \phi) \rho_s F, \quad (\text{Eq. 8})$$

where

$$\begin{aligned}
\rho_s &= \text{the rock density } [ML^{-3}]; \\
F &= F_p + F_c, \text{ the total sorbed mass of solute per unit mass} \\
&\quad \text{of the PFM } [M/M]; \\
F_p &= \text{the physically sorbed mass of solute per unit mass of the PFM } [M/M]; \\
F_c &= \text{the chemically sorbed mass of solute per unit mass of the PFM } [M/M];
\end{aligned}$$

Following the concepts of de Marsily (1986, p. 234) and considering that sorption onto the soil grains occurs as the dissolved species diffuses through the immobile water fraction (Moridis 1999), the equilibrium physical sorption is described by the equation

$$F_p = \begin{cases} K_d \rho K_i X & \text{for linear equilibrium (LE) sorption,} \\ K_F (\rho K_i X)^\beta & \text{for Freundlich equilibrium (FE) sorption,} \\ \frac{K_1 \rho K_i X}{1 + K_2 \rho K_i X} & \text{for Langmuir equilibrium (LAE) sorption} \end{cases} \quad (\text{Eq. 9})$$

where $K_d [M^{-1}L^3]$, $K_F [M^{-\beta}L^{3\beta}]$, β , $K_1 [M^{-1}L^3]$, and $K_2 [M^{-1}L^3]$ are sorption parameters specific to each solute and rock type. Of particular interest is the parameter K_d , called the distribution coefficient, which is the constant slope of the linear equilibrium adsorption isotherm of a solute in relation to the medium. The sorption of the various radionuclides in this AMR follows a linear equilibrium isotherm (See Section 5.2).

6.2.3.2 Kinetic Physical Sorption

If a kinetic isotherm is followed, then sorption is described by sorption is given by

$$\frac{dF_p}{dt} = \begin{cases} k_\ell (K_d \rho K_i X - \delta_p F_p) & \text{for linear kinetic (LKP) sorption,} \\ k_F [K_F (\rho K_i X)^\beta - F_p] & \text{for Freundlich kinetic (FKP) sorption,} \\ k_L \left(\frac{K_1 \rho K_i X}{1 + K_2 \rho K_i X} - F_p \right) & \text{for Langmuir kinetic (LAKP) sorption,} \end{cases} \quad (\text{Eq. 10})$$

where

$$\delta_p = \begin{cases} 1 & \text{for linear kinetic physical (LKP) sorption;} \\ 0 & \text{for linear irreversible physical (LIP) sorption,} \end{cases} \quad (\text{Eq. 11})$$

and k_ℓ , k_F and k_L are the kinetic constants for linear, Freundlich and Langmuir sorption, respectively $[T^{-1}]$. For $\delta_p = 0$, the linear kinetic expression in Equation 9 can also be used to describe the chemical process of salt precipitation.

6.2.3.3 Kinetic Chemical Sorption

The first-order reversible chemical sorption is represented by the linear kinetic chemical (LKC) model

$$\frac{dF_c}{dt} = k_c^+ \rho K_i X - k_c^- F_c, \quad (\text{Eq. 12})$$

where $k_c^+ [M^{-1}L^3T^{-1}]$ and $k_c^- [T^{-1}]$ are the forward and backward kinetic constants, respectively. Note that Equation 11 can be used in conjunction with the physical sorption equations to describe combined sorption (Cameron and Klute 1977), e.g., physical and chemical sorption. Combined sorption accounts for the different rates at which a species is sorbed onto different PM constituents. Thus, sorption onto organic components may be instantaneous (LE), while sorption onto mineral surfaces may be much slower and kinetically controlled (Cameron and Klute 1977).

6.2.3.4 Implications for Transport in the UZ

Sorption is the main mechanism of radionuclide mass removal from the transporting liquid phase. Nonsorbing radionuclides (such as ^3H or ^{99}Tc) will not be retarded. Strongly sorbing radionuclides (such as Np, Pu, U, Th, Am) will exhibit much longer arrival times to the groundwater. The transfer coefficient K_i is obviously quite important, because a $K_i < 1$ reduces the radionuclide sorbed onto the particle surfaces. Thus, the larger K_i is, the more the radionuclide is retarded. Although this may not be significant in the case of strong sorbers, it may be important in less-strongly sorbing tracers.

Also of interest is sorption onto the fracture surfaces, as opposed to the volume-base sorption in the matrix. Currently, no information exists on the subject. The conventional approach in fractures with $\phi = 1$ results in zero sorption. It is possible to obtain an estimate of surface sorption by (a) assuming a reasonable grain size for a matrix, (b) computing the internal surface area (available for sorption) per unit volume of the matrix, and (c) computing the surface area of a corresponding fracture for the same grain size. This approach usually produces very small surface K_d values.

6.2.4 Colloid Filtration Terms

6.2.4.1 Equations of Colloid Filtration

Colloidal particles moving through porous media are subject to filtration, the mechanisms of which have been the subject of several investigations (e.g., Herzig et al. 1970). The mass of filtered colloids is then given by

$$M_{F,\kappa} = \rho_{c,\kappa} \sigma_\kappa, \quad (\text{Eq. 13})$$

where $\rho_{c,\kappa}$ is the density of the colloidal particles of colloid $\kappa [ML^{-3}]$ and σ_κ is the filtered concentration of the colloid expressed as volume of colloids per volume of the porous medium.

When colloid deposition is a relatively fast process compared to the groundwater velocity, it is possible to describe colloid filtration as a linear equilibrium process (James and Chrysikopoulos 1999). Omitting the κ subscript, linear equilibrium filtration is then described by

$$\sigma = K_{\sigma} K_i \rho X, \quad (\text{Eq. 14})$$

where K_{σ} is a distribution coefficient [$M^{-1}L^3$].

The colloid filtration is more accurately described by a linear kinetic model (Çorapçıoglu et al. 1987, pp. 269-342), which can take the following form:

$$\frac{\partial \sigma}{\partial t} = \kappa (K_{\sigma} K_i \rho X - \delta_p \sigma) = \kappa^+ X - \kappa^- \sigma, \quad (\text{Eq. 15})$$

where $\kappa [T^{-1}]$ is a kinetic coefficient, and κ^+ and $\kappa^- [T^{-1}]$ are the kinetic forward and reverse colloid deposition rates (clogging and declogging coefficients), respectively, which are specific to each colloid and rock type. The term κ^- is commonly assumed to be zero (Bowen and Epstein 1979), but there is insufficient evidence to support this. As will be seen in Section 6.16 and 6.17 of the present AMR, colloid transport in the UZ is very sensitive to this parameter. The parameter δ_p is analogous to that for sorption in Equations 10 and 11, and describes the reversibility of filtration.

From de Marsily (1986, p. 273) and Ibaraki and Sudicky (1995, p. 2948), the following expression for the κ^+ coefficient can be derived:

$$\kappa^+ = \epsilon f u G, \quad (\text{Eq. 16})$$

where ϵ is the filter coefficient of the porous medium [L^{-1}], f is a velocity modification factor, u is the Darcy velocity [LT^{-1}], and G is a dynamic blocking function (DBF) that describes the variation of the PM porosity and specific surface with σ (James and Chrysikopoulos 1999). The factor f ($1 \leq f \leq 1.5$) accounts for the velocity of the colloidal particle flow being larger than that of water (Ibaraki and Sudicky 1995, p. 2948). This results from the relatively large size of the colloids, which tends to concentrate them in the middle of the pores where the groundwater velocity is larger than the bulk average velocity. The factor f tends to increase with decreasing ionic strength, but cannot exceed 1.5 because colloids cannot move faster than the maximum groundwater velocity (Ibaraki and Sudicky 1995, p. 2948).

For deep filtration (i.e., in the case of very dilute colloidal suspensions), there is no interaction among the colloidal particles and no effects on the medium porosity and permeability, i.e., ϕ is constant, and $G = 1$. Note that it is possible for both EOS9nT (the code of the numerical model) and FRACL (the code of the semianalytical model) to have combined filtration, in which two different types of filtration (e.g., equilibrium and kinetic, or two kinetic filtrations with different κ^+ and κ^-) occur simultaneously.

6.2.4.2 Implications for Transport in the UZ

Filtration is one of the main mechanism of radioactive colloid removal from the transporting liquid phase, the others being chemical destabilization (e.g., because of pH changes) and flocculation. Three types of filtration mechanisms may affect the transport of colloids through PFM: surface filtration, straining filtration and physical-chemical filtration. Surface filtration occurs when particles are larger than the pores, in which case a filter cake is formed.

Straining filtration is determined by the ratio $R_d = d_g/d_p$, where d_g is the diameter of the grains of the porous medium and d_p is the suspended particle diameter. Based on the experimental data of Sakthivadivel (1969), $R_d \leq 10$ leads to cake filtration, $10 < R_d \leq 20$ corresponds to substantial straining filtration (permeability reductions by a factor of 7 – 15 and particles occupying 0.3ϕ), and $R_d > 20$ results in limited straining (only 2 – 5% of ϕ occupied by particles and permeability reductions by 10-50%). Herzig et al. (1970, p. 15) indicated that little straining was expected when $R_d > 12$, and calculated that when $R_d = 50$, only 0.053% of ϕ would be occupied by particles.

A detailed discussion of the physical-chemical filtration of colloids can be found in Çorapçıoğlu et al. (1987, pp. 269-342). The physical-chemical colloidal filtration by the porous/fractured medium incorporates three mechanisms: (a) contact with the pore walls, (b) colloid fixation onto the walls, and (c) release of previously fixed colloids (Herzig et al. 1970; Çorapçıoğlu et al. 1987).

Contact with the pore walls and colloidal capture can be the result of sedimentation (caused by a density differential between the colloidal and the carrier liquid), inertia (deviation of colloidal trajectories from the liquid streamlines because of their weight), hydrodynamic effects (caused by a variation in the velocity field of the liquid), direct interception (caused by collisions with the pore walls at convergent areas) and diffusion (Brownian motion causing colloids to move toward pore walls or dead-end pores).

Fixation on the pore walls occurs at retention sites that include edges between two convex surfaces, pore throats smaller than the colloidal size, and dead-end pores or regions of near-zero liquid velocity. Fixation is caused by retentive forces, which include axial pressure of the fluid at constriction sites, friction forces, Vander Waals forces, electrical forces and chemical forces (Herzig et al. 1970, pp. 4, 11-17). Finally, remobilization of colloidal particles may be caused by a number of factors, including collision between a loosely held colloid with a moving particle, an increase in pressure as colloids constrict flow, and a change in external conditions.

All three mechanisms are expected to be present in the UZ of Yucca Mountain. The EOS9nT simulations can account for surface filtration by using a particle size versus pore size criterion, and by not allowing colloidal entry into media that do not meet this criterion. Straining filtration (pore-size exclusion) is described by using appropriate colloid accessibility factors (see Section 6.3.5), and physical-chemical filtration is represented by using appropriate parameters in Equations 14 or 15.

Note that it is not possible to account for cake filtration or for the effects of filtration on permeability and porosity, as this would violate the linearity in the models. However, these scenarios would be unlikely in the UZ of YM because (a) natural pseudocolloids (such as clays) under natural conditions occur in small concentrations, and (b) it is expected that, owing to adverse chemical conditions (e.g., pH, ionic strength) in the immediate vicinity of the potential repository, true colloids will be released at low concentrations for a long time.

6.2.5 Colloid-Assisted Transport Terms

6.2.5.1 Equations of Colloid-Assisted Transport

The mass of a tracer κ sorbed onto pseudocolloids is described by

$$M_{Ac,\kappa} = \sum_{j=1}^{N_c} (\rho_j \sigma_j + \rho X_j) \mathcal{F}_{\kappa,j} \quad (\text{Eq. 17})$$

where $\mathcal{F}_{\kappa,j}$ denotes the sorbed mass of solute κ per unit mass of the pseudocolloid j [M/M] and N_c is the total number of pseudocolloid species. The first term in the sum inside the parenthesis of Equation 17 describes the filtered (deposited) colloid concentration, and the second the concentration of the suspended colloids in the liquid phase. $\mathcal{F}_{\kappa,j}$ is computed from any combination of Equations 9–12, with the appropriate sorption parameters corresponding to each colloid. Note that Equation 17 applies to pseudocolloids only, as opposed to true colloids, onto which radionuclides are not considered to sorb.

6.2.5.2 Implications for Transport in the UZ

The formulation of Equation 17 allows consideration of the whole spectrum of sizes of a particular colloid, as each size would have different transport behavior (see Equation 16) and different sorption properties (resulting from different surface area).

Of particular interest in UZ radioactive transport models is the potential of colloid-assisted transport to significantly enhance the migration of tracers whose normally strong sorbing behavior would confine them to the vicinity of the point of release. Sorption of such a radionuclide (e.g., Pu) onto pseudocolloids renders the whole colloid radioactive. The transport of such a colloid is no longer dictated by the strong Pu sorption behavior, but by the kinetics of colloid filtration. Coupled with the fact that colloids can move at velocities up to 50% higher than the groundwater Darcy velocity (see Equation 16), this can result in travel times to the groundwater orders of magnitude shorter than the ones predicted by sorption.

6.2.6 Flux Terms

6.2.6.1 Equations of the Flux Terms

The flux term has contributions from advective, diffusive, and dispersive transport processes and is given by

$$\mathbf{F}_\kappa = \mathbf{F}_w X_\kappa - \rho \mathbf{D}_\kappa \nabla X_\kappa - \mathbf{F}_{s,\kappa} , \quad (\text{Eq. 18})$$

where $\mathbf{F}_{s,\kappa}$ is the flux due to surface diffusion and \mathbf{D}_κ is the dispersion tensor of tracer κ , a second order symmetric tensor with a principal axis aligned with the Darcy flow vector. Omitting the κ subscript, \mathbf{D} is described by the equations

$$\mathbf{D} = D^T \mathbf{I} + \frac{D^L - D^T}{u^2} \mathbf{u} \mathbf{u} , \quad (\text{Eq. 19})$$

$$D^L = \phi (S_w - S_r) \tau D_0 + \phi S_r \tau D_0 + \alpha_L u , \quad (\text{Eq. 20})$$

$$D^T = \phi (S_w - S_r) \tau D_0 + \phi S_r \tau D_0 + \alpha_T u , \quad (\text{Eq. 21})$$

where

- \mathbf{I} = the unit vector
- τ = the tortuosity coefficient of the pore paths [L/L]
- D_0 = the molecular diffusion coefficient of tracer i in water [$L^2 T^{-1}$]
- α_L, α_T = longitudinal and transverse dispersivities, respectively [L]
- \mathbf{u} = the Darcy velocity vector [LT^{-1}]

Equation 18 accounts for surface diffusion, which can be responsible for significant transport in strongly sorbing media (Moridis 1999; Cook 1989). The surface diffusion flux is given by Jahnke and Radke (1987) as

$$\mathbf{F}_s = (1 - \phi) \rho_s \tau_s D_s \nabla F_p , \quad (\text{Eq. 22})$$

where τ_s is the tortuosity coefficient of the surface path [L^0], D_s is the surface diffusion coefficient [$L^2 T^{-1}$], and F_p is the physical diffusion computed from equations (19) or (10). There is theoretical justification for the relationship $\tau_s = \frac{2}{3} \tau$ (Cook 1989, p. 10).

6.2.6.2 Application to Colloid Fluxes

Equations 17 through 20 apply to solutes, but need the following modifications to render them suitable to colloidal transport. More specifically:

1. $\mathbf{F}_s = 0$ because surface diffusion does not occur in colloids.
2. The flux \mathbf{F}_s and the Darcy velocities u are multiplied by the factor f (see Section 6.2.4.1).
3. The dispersivities α_L and α_T are generally different from those for solutes (Ibaraki and Sudicky 1995) and may be a function of the colloidal particle size.
4. The term D_0 is the colloidal diffusion coefficient in water [$L^2 T^{-1}$] and is described by the Stokes-Einstein equation, according to (Bird et al. 1960, p. 514), as

$$D_0 = \frac{k T}{3 \pi \mu_w d_p}, \quad (\text{Eq. 23})$$

where k is the Boltzmann constant ($1.38 \times 10^{-23} \text{ J K}^{-1}$ in SI units), T is the absolute water temperature [K], μ_w is the dynamic viscosity of water [$ML^{-1}T^{-1}$], and d_p is the colloid diameter [L].

5. The fluxes in Equation 18 are multiplied by the colloid accessibility factors f_c ($0 \leq f_c \leq 1$) at the interface of different media. The f_c factor describes the portion of the colloidal concentration in a medium that is allowed to enter an adjacent medium of different characteristics, and quantifies pore size exclusion (straining).

In the treatment of the general 3-D dispersion tensor, velocities are averaged by using the *projected area weighting method* (Wu et al. 1996, p. 23), in which a velocity component u_j ($j \equiv x, y, z$) of the vector \mathbf{u} is determined by vectorial summation of the components of all local connection vectors in the same direction, weighted by the projected area in that direction. This approach allows the solution of the transport problem in irregularly shaped grids, in which the velocities normal to the interface areas are not aligned with the principal axes.

6.2.6.3 Implications for Transport in the UZ

Because it is directly proportional to the water fluxes, advection in the fractures is by far the dominant mechanism of transport in the UZ of Yucca Mountain. This is further enhanced by longitudinal dispersion, molecular diffusion, and (possibly) surface diffusion (in decreasing order). Coupled with the fracture orientation and gravitational differentials, the result of the fracture and flow characteristics is a mainly downward migration of the radionuclides. Note that advection also occurs in the matrix (and is accounted for in the simulations), albeit at significantly lower rates.

Lateral spreading of the contaminants can be achieved through transverse dispersion, molecular diffusion, and (possibly) surface diffusion. As sorption occurs from the liquid phase onto the solids, and fractures are by far the main conduits of water, retardation of sorbing radionuclides

will be controlled by the rate of tracer movement from the fractures to the sorbing matrix. This is represented by the sum of diffusive, dispersive and surface diffusion fluxes, and results in the lateral migration of the contaminants.

Currently, there are no field study estimates of α_L and α_T in the UZ. When not ignored in the numerical simulations (justified by the relative magnitude of advection), reasonable α_L estimates are used, and α_T is usually set to zero (especially in the fractures). Accurate values of D_0 , coupled with estimated tortuosity coefficient values from laboratory experiments, provide a rather representative estimate of diffusive fluxes in the UZ simulations.

No information exists on whether the UZ media support surface diffusion (a possibility in zeolites). Surface diffusion can be important in tracers that exhibit strong sorption (e.g., Pu). A larger K_d clearly indicates stronger sorption, but this does not mean immobilization of the dissolved species when the porous/fractured medium supports surface diffusion. On the contrary, the stronger the sorption (i.e., the larger the K_d), the larger the diffusion rate, and practically all of it attributable to the surface process (Moridis 1999, pp. 1375–1376).

6.2.7 Radioactive Decay

6.2.7.1 Equations of Radioactive Decay

When a tracer κ undergoes radioactive decay, the rate of mass change is described by the first-order decay law

$$\frac{dM_\kappa}{dt} = -\lambda_\kappa M_\kappa, \quad \text{where} \quad \lambda_\kappa = \frac{\ln 2}{(T_{1/2})_\kappa}, \quad (\text{Eq. 24})$$

and $(T_{1/2})_\kappa$ is the half life of tracer κ . Substitution of Equations 18 and 24 into Equation 2 yields

$$\left(\frac{dM_\kappa}{dt} \right)_n + \lambda_\kappa (M_\kappa)_n = \frac{1}{V_n} \sum_m A_{nm} [F_{nm} X_\kappa - \rho \mathbf{D}_\kappa \nabla X_\kappa - \mathbf{F}_{s,\kappa}] + (q_\kappa)_n \quad (\text{Eq. 25})$$

6.2.7.2 Implications for Transport in the UZ

The decay of radioactive substance is completely predictable and well documented. Thus, the decay of radioactive substances in UZ simulations can be computed very reliably.

6.2.8 Daughter Products of Radioactive Decay

6.2.8.1 Transport Equations of Daughters

If a radioactive tracer κ is a daughter product of the decay of tracer j , then the mass accumulation terms are adjusted (de Marsily 1986, pp. 265–266) to yield the equation of transport of the daughter products as

$$\begin{aligned} \left(\frac{dM_\kappa}{dt} \right)_n + \lambda_\kappa (M_\kappa)_n - \lambda_j m_r (M_j)_n \\ = \frac{1}{V_n} \sum_m A_{nm} [F_{nm} X_\kappa - \rho \mathbf{D}_i \cdot \nabla X_\kappa - \mathbf{F}_{s,\kappa}] + (q_\kappa)_n, \end{aligned} \quad (\text{Eq. 26})$$

where $m_r = W_\kappa/W_j$, and W_κ and W_j are the molecular weights of the daughter and parent species. Equation 26 applies to radioactive solutes or radioactive true colloids.

For daughters following an isotherm other than LE, Equations 9 and 10 need to account for the generation of daughter mass from the decay of the sorbed parent, and become

$$\frac{\partial F_\kappa}{\partial t} + \lambda_\kappa F_\nu - \lambda_{\kappa-1} m_r \zeta_\kappa F_{\kappa-1} = k_A \rho X_\nu - k_B (F_\kappa + m_r \zeta_\kappa F_{\kappa-1}), \quad (\text{Eq. 27})$$

where $F_{\kappa-1}$ is the sorbed mass of the parent,

$$k_A = \begin{cases} k_\ell K_d K_i & \text{for LKP/LIP sorption,} \\ k_c^+ K_i & \text{for LKC sorption,} \end{cases} \quad k_B = \begin{cases} k_p \delta_p & \text{for LKP/LIP sorption,} \\ k_c^- & \text{for LKC sorption,} \end{cases}$$

and ζ_κ is the fraction of the mass of the decayed sorbed parent that remains sorbed as a daughter ($0 \leq \zeta_\kappa \leq 1$). The term ζ_κ is introduced to account for the different sorption behavior of parents and daughters, and the fact that daughters can be ejected from grain surfaces due to recoil (e.g., the ejection of ^{234}Th from grain surfaces during the alpha decay of ^{238}U) (Faure 1977, pp.288-289).

6.2.8.2 Implications for Transport in the UZ

If decay results in radioactive daughters, UZ simulations must compute the total radioactivity distribution, i.e., the sum of the concentrations of all the members of the radioactive chain. This is especially true if the daughters have long half lives. Intermediate chain products with short half lives relative to the simulation periods can be ignored with impunity.

Although the EOS9nT and the FRACL codes can theoretically obtain the transport scenario of any number of daughters in the radioactive chain, this is especially true for daughters with short half

lives. With longer half-lives (such as for ^{237}Np , ^{239}Pu , etc.), machine accuracy considerations and roundoff errors (with the daughter concentrations becoming increasingly smaller as we move down the radioactive chain) limit their number to a maximum of four or five with comparable half lives.

The ζ factor is a function of the type of decay, as well as of the chemical form of the sorbed cation. In alpha decay (e.g., ^{237}Np , ^{239}Pu), $\zeta = 0$. There is no information on the behavior of ζ for other types of decay. The ζ factor can have significant implications for the transport behavior of daughters if (a) the large sorbed masses of strongly sorbing parents are ejected back into the aqueous phase after decay, (b) the daughter is a much weaker sorber, and (c) its sorption is kinetically controlled. Such a possibility could arise in the kinetic sorption of radionuclides onto pseudocolloids (CRWMS M&O 1999e, Section 6). For equilibrium isotherms, this is not an issue.

6.3 THE NUMERICAL AND SEMIANALYTICAL MODELS

In mathematical simulations, the conventional meaning of the term *model* is the mathematical description of the physics governing the behavior of the simulated system, while the term *code* is the implementation of the mathematical *model* in a computer language. Because *model* and *code* are inexorably intertwined, these terms have been historically used interchangeably. In the context of EOS9nT and FRACL applications in the present AMR, when the word *model* is used, it is preceded by the qualifying words *numerical* or *semianalytical*.

6.3.1 The EOS9nT Code

The code used for the 3-D site-scale transport simulations in the AMR is TOUGH2 V1.11 Module EOS9nT V1.0 (STN: 10065-1.11MEOS9NTV1.0-00, Moridis et al. 1999), which is a member of the TOUGH2 family of codes (Pruess 1991). It can simulate flow and transport of an arbitrary number n of non volatile tracers (solutes and/or colloids) in the subsurface.

EOS9nT first solves the Richards equation, which describes saturated or unsaturated water flow in subsurface formations, and obtains the flow regime. The set of n linearly independent transport equations (corresponding to the n solutes/colloids) are then solved sequentially. The n tracer transport equations account for (a) advection, (b) molecular diffusion, (c) hydrodynamic dispersion (with full 3-D tensorial representation), (d) kinetic or equilibrium physical and chemical sorption (linear, Langmuir, Freundlich, or combined), (e) first-order linear chemical reaction, (e) radioactive decay, (f) colloid filtration (equilibrium, kinetic or combined), and (g) colloid assisted solute transport. A total of $n-1$ daughter products of radioactive decay (or of a linear, first-order reaction chain) can be tracked.

EOS9nT includes two types of Laplace transform formulations of the tracer equations, in addition to conventional timestepping. The Laplace transform is applicable to steady-state flow fields and allows a practically unlimited time step size and more accurate solution (as numerical diffusion is significantly reduced). Additional information on the EOS9nT numerical model can be found in Attachment I.

6.3.2 The FRACL Code

FRACL V1.0 (STN: 10191-1.0-00) is the FORTRAN implementation of semianalytical solutions developed to solve for the problem of transport of stable, radioactive or reactive tracers (solutes or true colloids) through a 2-D layered system of heterogeneous fractured media. (Moridis and Bodvarsson 1999). The transport equations in the matrix account for matrix and surface diffusion, mass transfer between the mobile and immobile water fractions, and physical, chemical or combined

sorption following a linear equilibrium, kinetic, or irreversible isotherm. In the case of true colloids, linear kinetic, equilibrium or combined filtration can be accounted for. Radioactive decay, first-order chemical reactions, and tracking of up to five products of radioactive decay or chemical reactions are also included in the solution. The transport equations in the fractures account for the same processes in addition to advection and hydrodynamic dispersion. The solutions are analytical in the Laplace space and are numerically inverted to provide the solution in time.

FRACL also accounts for the effects of different fracture spacing and misalignment of fractures. It can accommodate layers of fractured rocks, or a combination of fractured rock and non fractured strata (see Figure 6.3.1). It can describe fractured systems of finite fracture spacing, or single fractures in a semi-infinite medium. A complete description of the semianalytical solutions on which FRACL is based can be found in Moridis and Bodvarsson (1999). Additional information on the FRACL semianalytical model can be found in Attachment I.

6.3.3 Other Computational Tools

In addition to EOS9nT and FRACL, the following computational tools were used:

1. The TOUGH2 V1.4 Module EOS9 V1.4 (STN: 10007-1.4-00) code, to obtain the flow velocities for the various perched water and climatic scenarios discussed in CRWMS M&O (1999d, Section 6.2).
2. The T2R3D V1.4 (STN: 10006-1.4-00) code, to conduct the Busted Butte solute transport simulations.
3. The xtract1.f V1.0 routine (ACC: MOL.19991221.0431), to modify the grid system for use in the EOS9nTruns. The modifications involved (a) determining the grid elements corresponding to the potential repository, (b) moving them to the end of the element file, where (c) the upper and lower boundary elements are also moved. This was necessitated by the fact that contaminant release is considered constant and continuous in this AMR. Thus the repository elements represent internal boundary points. After moving these elements to the bottom of the element file, the volume of the first element is set to zero or a negative number. Then, these elements are considered in the determination of fluxes but are not included in mass balance computations.
4. The xtract2.f V1.0 routine (ACC: MOL.19991221.0432), to obtain initial condition files (INCON) using the SAVE files from the EOS9 runs for the EOS9nT simultaneous simulations of ^{99}Tc , ^{237}Np and ^{239}Pu transport.
5. The xtract2a.f V1.0 routine (ACC: MOL.19991220.0397), to obtain INCON files (using the

SAVE files from the EOS9 runs) for the EOS9nT simultaneous simulations of transport of the ^{237}Np and the ^{239}Pu decay-chains.

6. The xtract2b.f V1.0 routine (ACC: MOL.19991220.0398), to obtain INCON files (using the SAVE files from the EOS9 runs) for the EOS9nT simultaneous simulations of transport of ^{99}Tc , and the ^{237}Np and ^{239}Pu decay-chains.
7. The xtract5.f V1.0 routine (ACC: MOL.19991220.03900), to obtain INCON files (using the SAVE files from the EOS9 run) for the EOS9nT simulations of Cl transport in the ESF.
8. The xtract6.f V1.0 routine (ACC: MOL.19991220.0400), to extract the Cl concentrations corresponding to the ESF elements from the output of the EOS9nT simulation of Cl transport.

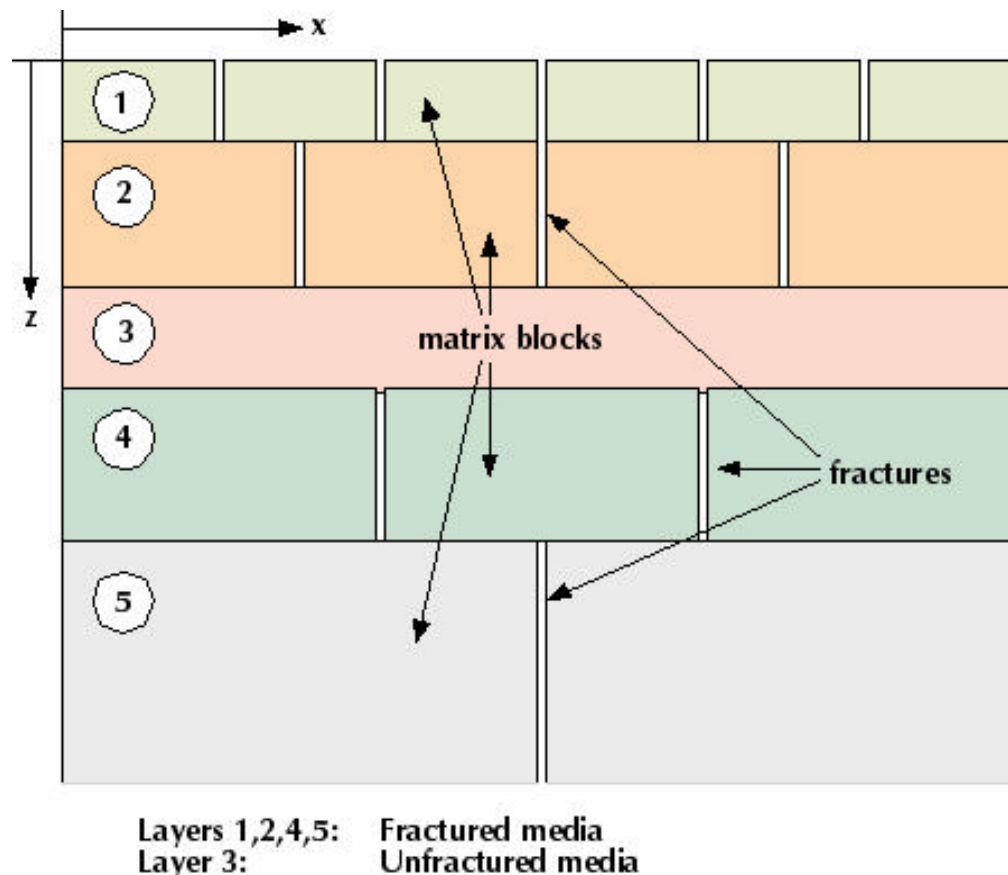


Figure 6.3.1. An example of a layered fractured system in FRACL studies. Each layer has its own distinctive geometry and fracture and matrix properties. Note that the last subdomain (layer 5) is semi-infinite.

6.4 MODEL VALIDATION AND CALIBRATION

In this section we validate and calibrate the RTM using the FRACL and EOS9nT codes. We first validate the RTM using both codes in a comparison to the analytical solution of Sudicky and Frind (1982). We then calibrate the RTM by employing FRACL and analyzing field data of Cl distribution in the UE-25 UZ#16 borehole, and compare the FRACL results to the predictions from a 3-D simulation using the T2R3D code. Finally, we calibrate the RTM by using EOS9nT and analyzing field data of Cl distribution in the ESF, and compare the results of the 3-D site-scale simulation to the T2R3D predictions for the same grid and conditions.

6.4.1 Validation and Calibration Criteria

For accurate predictions of the EOS9nT and FRACL codes, three conditions must be met:

1. The relevant physical processes must be accounted for and accurately represented by the mathematics.
2. The mathematical equations must be accurately solved by the numerical or semianalytical methods.
3. The physical properties of the rocks must be correct.

For validation of the the RTM using the EOS9nT and FRACL codes, their simulation results are compared to the analytical solution of Sudicky and Frind (1982). The criterion for validation was that the analytical solution and the FRACL and EOS9nT solutions agree within 1%. Results presented in the section show that this criterion was easily met by both codes.

Calibration and additional validation of the RTM using the FRACL and EOS9nT codes was accomplished by comparing their predictions to (a) field measurements and (b) numerical results from previously validated T2R3D V1.4 (STN: 10006-1.4-00, See Sections 3 and 6.3) simulations with the same input data. Agreement within 1% of the T2R3D predictions was the easily-met criterion for validation and matching the calibrated prediction.

6.4.2 Validation

The 2-D analytical solution of Sudicky and Frind (1982) was used to validate the RTM using the EOS9nT and the FRACL codes. This problem involves a single fracture and a matrix block of finite thickness (see Figure 6.4.1) and assumes diffusion but no advection through the matrix. Additional verification studies can be found in Moridis et al. (1999) and Moridis and Bodvarsson (1999).

The parameters (and the corresponding data sources) used in the simulations are shown in Table

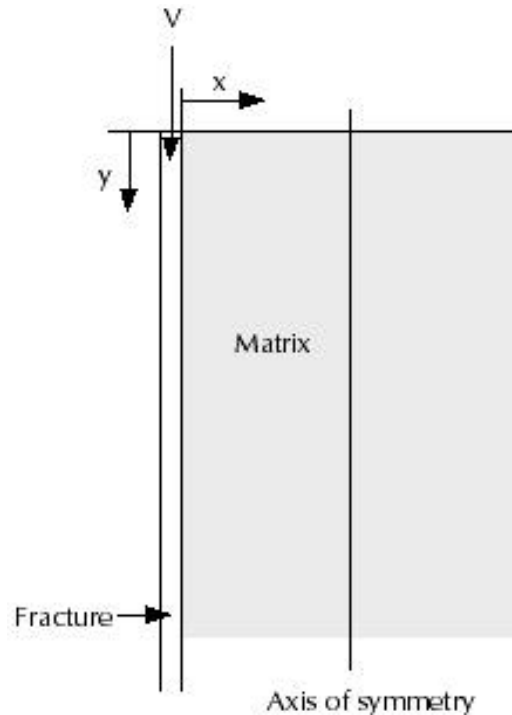


Figure 6.4.1. The fracture-matrix system in the validation study of FRACL and EOS9nT.

6.2. For the EOS9nT simulations, three different 2-D grids in (x, z) were used for the EOS9nT simulations, with increasingly finer discretization in the matrix block. The first gridblock in the x direction at any z level corresponds to the fracture; all other gridblocks at the same z level correspond to the matrix.

The discretization of the coarse grid was 2×320 in (x, z) . In the medium grid, the fracture occupied a single gridblock, and the matrix block was discretized into four gridblocks at any z level. In the fine grid, the fracture discretization was the same, but the matrix block was subdivided into 11 gridblocks. Thus, the discretization of the medium and of the fine grids were 5×320 and 12×320 in (x, z) , respectively.

Three EOS9nT simulations were conducted for each discretization, using (a) conventional timestepping, (b) the Stehfest (1970a,b) implementation of the Laplace space formulation, and (c) the De Hoog et al. (1982) implementation of the Laplace space formulation, for a total of nine EOS9nT runs. The DTN for the EOS9nT input and output data files is LB991220140160.001.

Two FRACL simulations were conducted. The first considered a single domain semi-infinite in z ; the second subdivided the domain into three segments in z , two of which were finite and the last semi-infinite. The DTN for the FRACL input and output data files is LB991220140160.002.

Table 6.2. Input parameters for model validation against an analytical solution.

Parameters	Values (*)
D_0	$1.6 \times 10^{-9} \text{ m}^2/\text{s}$
Fracture ϕ	1.0
Fracture τ	1
Fracture aperture	100 μm
Longitudinal dispersivity α_L in the fracture	0.1 m
Fracture K_d	0 m^3/kg
Fracture flow velocity V	0.1 m/day
Matrix block length	0.5 m
Matrix ϕ	0.01
Matrix τ	0.1
Matrix flow velocity	0 m/s
Matrix K_d	0 m^3/kg
Radionuclide $T_{1/2}$	12.35 years (tritium)

(*): From Sudicky and Frind (1982)

Figure 6.4.2 shows the distribution relative concentration C_R (defined as $C_R = C/C_0$, where $C = \rho X$ is the solute concentration [ML^{-3}] and the subscript 0 denotes the concentration at the release point) in the fractures at $t = 1,000$ days. The analytical and the two FRACL solutions were obtained at the same points along the z axis and were identical in the first 5 significant digits. To improve clarity, the FRACL solutions are not shown in Figure 6.4.2 because it is not possible to distinguish them from the analytical.

For the same discretization, the EOS9nT solutions for the three different time treatments are virtually indistinguishable. The coarser EOS9nT grid results in a solution that deviates significantly from the analytical solution and tends to indicate an early breakthrough. This deviation diminishes as time increases (Moridis et al. 1999). The solutions from the medium and the fine grids are very accurate, very close to each other, and exhibit very small deviations from the analytical and the FRACL solutions. These deviations are confined to the steepest portion of the curve. This indicates that there is practically no incremental benefit from refining the grid beyond the medium discretization.

6.4.3 Calibration–Cl Concentration in UE-25 UZ#16

The RTM was calibrated by using the FRACL code to analyze field measurements of aqueous chloride concentration from the UE-25 UZ#16 Borehole. The strata crossed by UE-25 UZ#16 are shown in Figure 6.4.3, which shows the simulation domain and provides the vertical thickness of the layers in the various hydrogeologic units. A total of 25 layers were involved in the simulations. The 2-D geological profiles were constructed by combining (a) fractures of known aperture and frequency (per unit of length) in each of the layers with (b) the corresponding matrix blocks (the sizes of which were obtained from data on the active fracture spacing). The input parameters (and the corresponding data sources) are shown in Table 6.3. The DTN for the FRACL input and output data files is LB991220140160.003.

Figure 6.4.4 shows (a) measurements, (b) the FRACL predictions, and (c) the T2R3D predictions of the Cl concentration in the fractures as a function of depth at various times. The curves for $t < 10000$ years show the evolution of the Cl concentration profile with depth over time. Of interest is the steady-state, which has already been reached at $t = 10,000$ years. Comparison of the FRACL predictions to the field measurements indicate a reasonable agreement.

Note that the FRACL solution is practically identical to the predictions of the T2R3D code obtained by employing a 3-D site-scale transport model and a calibrated infiltration (CRWMS M&O 1999d, Section 6.4). The two models share the same transport and infiltration data. This positive comparison supports the validation and calibration of the RTM.

Table 6.3. FRACL input data and sources for modeling the Cl distribution in the UE-25 UZ#16 borehole

Parameters	Source
Geologic profile and rock properties at the UE-25 UZ#16 cross-section	DTN: LB990701233129.002 and SN: YMP-LBNL-GSB-QH-1, page 31
Calibrated infiltration rate	DTN: LB991131233129.003
Field measurements of the Cl concentration profile in the UE-25 UZ#16 borehole	DTN: GS950608312272.001
Longitudinal dispersivity in the fracture $\alpha_L = 0.1$ m	Scientific judgement in the absence of data
D_0 of Cl: $2.03 \times 10^{-9} \text{ m}^2/\text{s}$	DTN: LB991220140160.019 (Cussler 1984, p. 147)

Relative concentration in the fracture

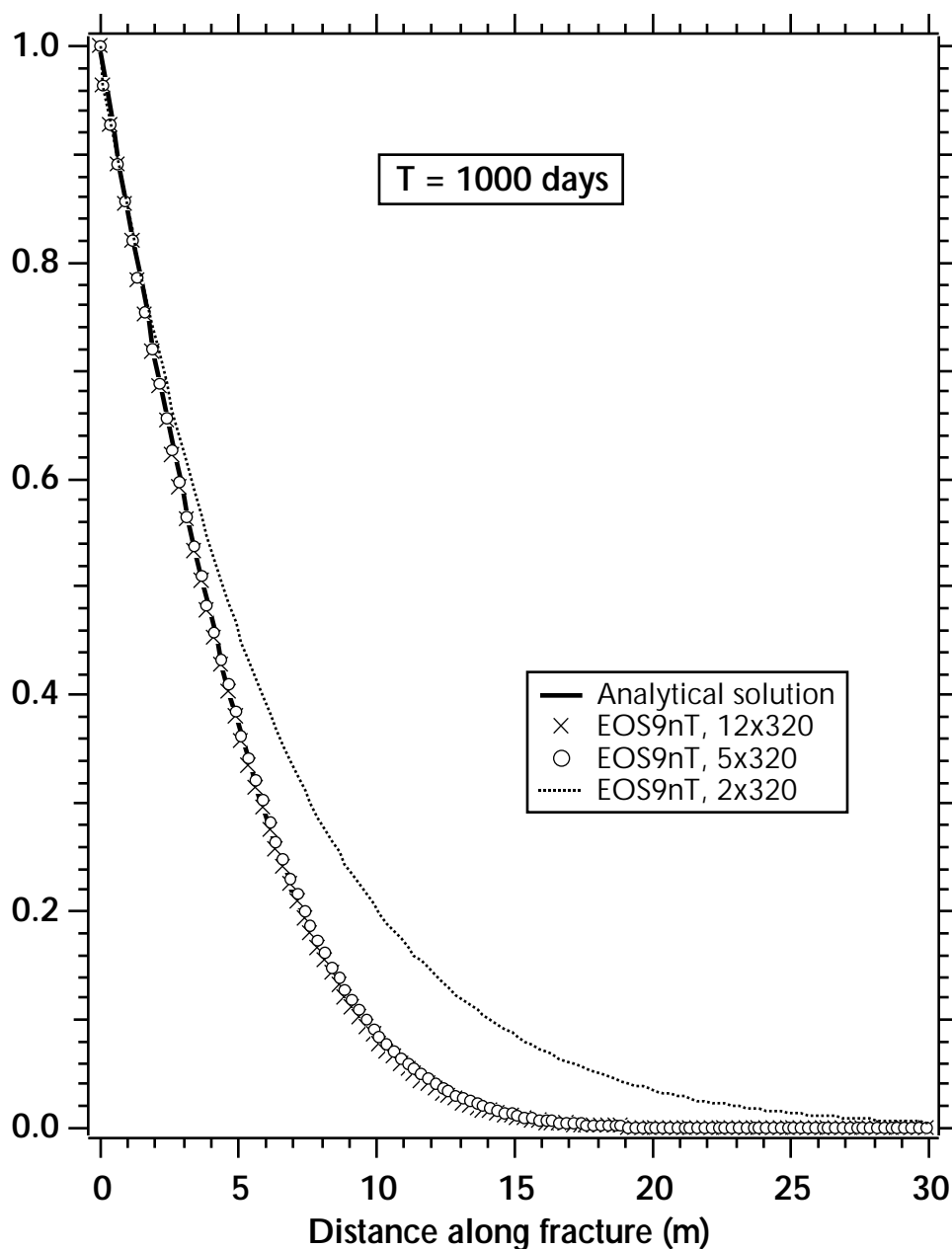


Figure 6.4.2. Analytical and numerical solutions of the concentration distribution in a fracture for three different grids at $t=1000$ days. The error caused by the coarse discretization accuracy is significant. The solutions for a medium and coarse grid are indistinguishable. The two FRACL solutions are identical to the analytical and are not differentiated (DTN: LB991220140160.001 and LB991220140160.002, data submitted with this AMR).

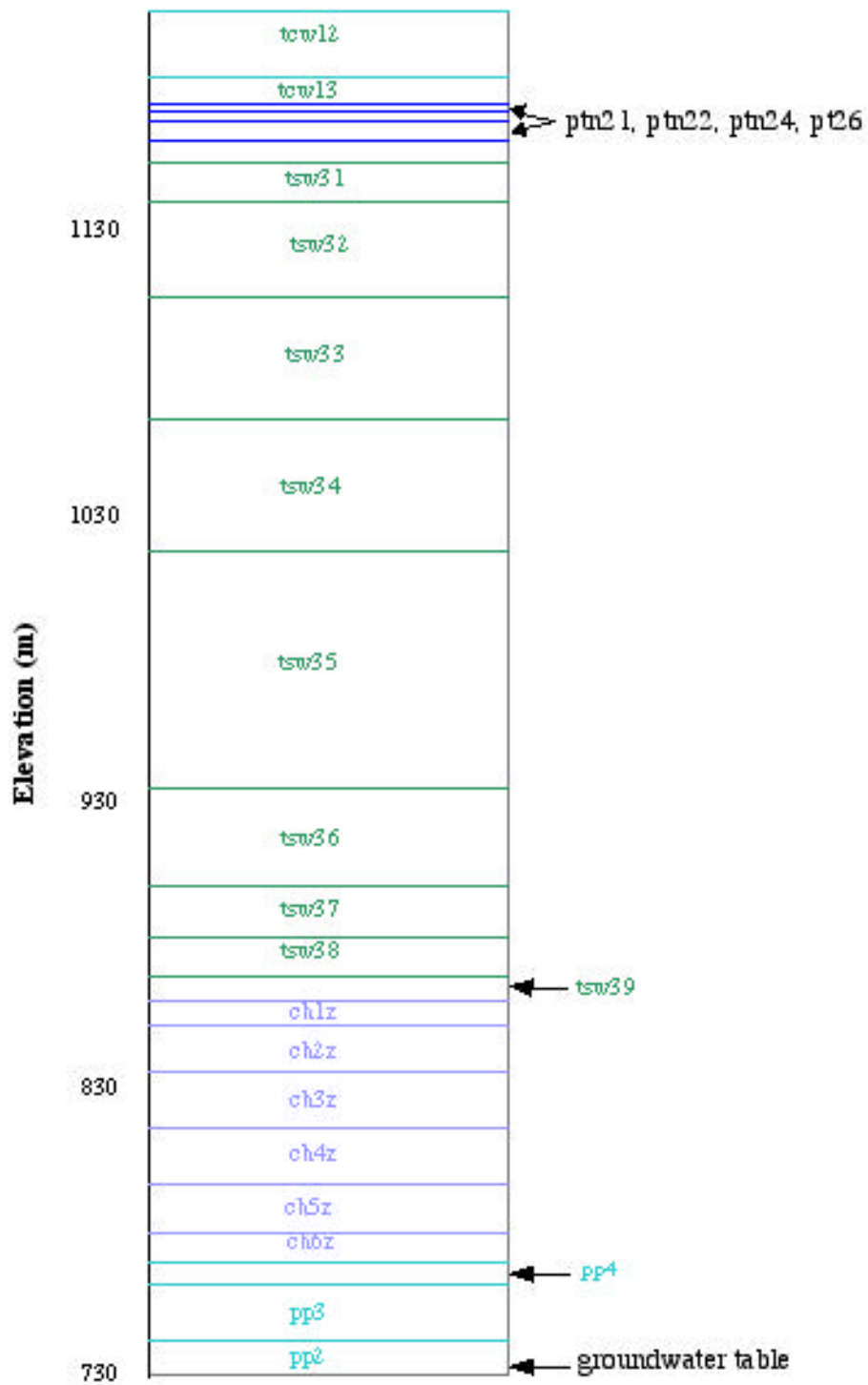


Figure 6.4.3. Vertical profile of hydrogeologic units at the UE-25 UZ#16 borehole (CRWMS M&O 1999h, Table III-1).

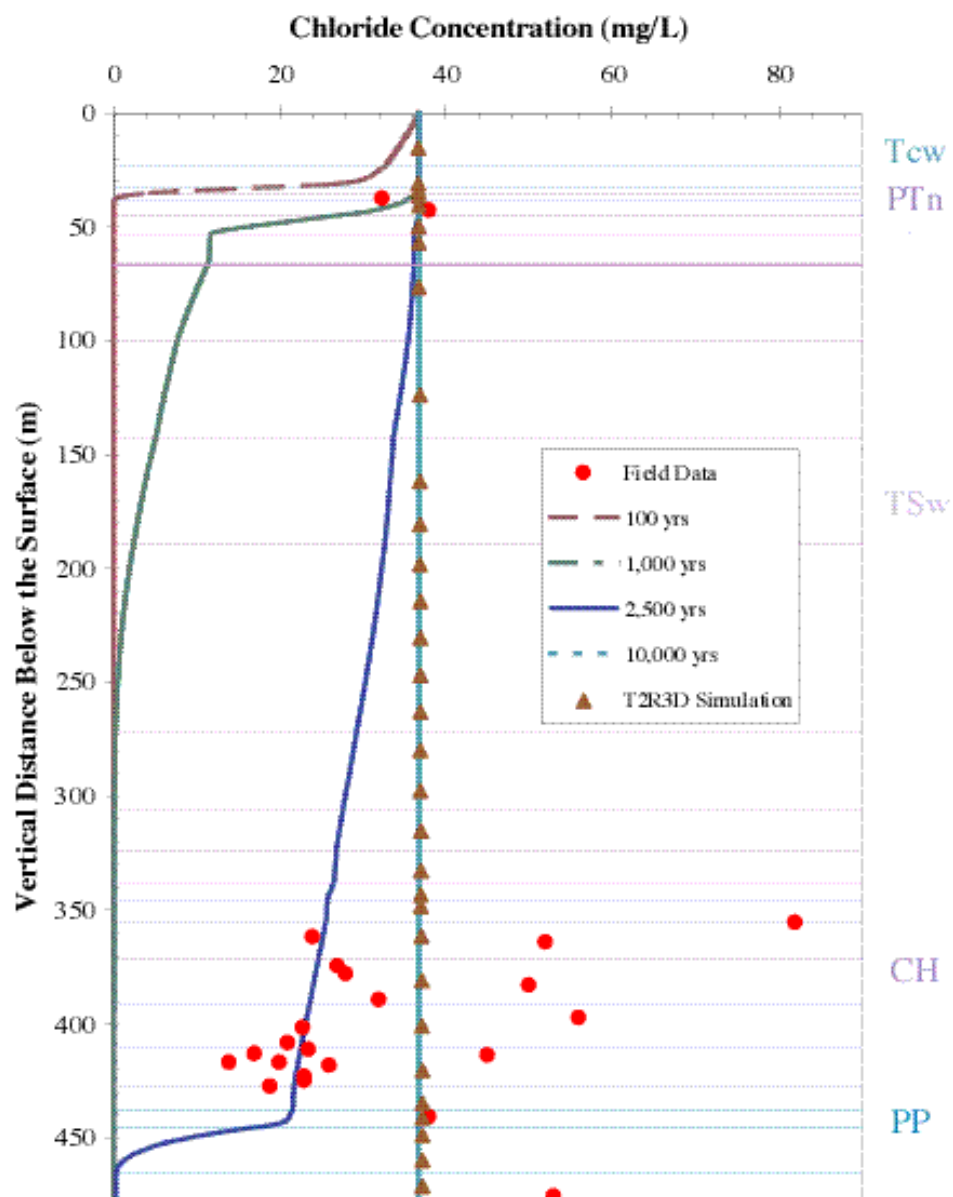


Figure 6.4.4. FRACL predictions of the Cl concentration in the fractures of the UE-25 UZ#16 profile (DTN: LB991220140160.003, data submitted with this AMR). Measurements are also shown (DTN: GS950608312272.001). The T2R3D predictions from a 3-D site-scale model are shown for comparison (DTN: LB991131233129.003).

6.4.4 Calibration - Cl Concentration in the ESF

The RTM was calibrated through comparison of the EOS9nT predictions to (a) field measurements of chloride concentration in the ESF and (b) numerical predictions obtained by using the T2R3D code (CRWMS M&O 1999d, Sections 3, 6.4 and 6.7). For this EOS9nT simulation, the site-scale 3-D grid, the initial and boundary conditions, and the water flow velocities were obtained from the EOS9 simulation using the calibrated infiltration data (CRWMS M&O 1999d, Section 6.4.4). The Cl sources (and their areally nonuniform distribution) in the EOS9nT model reflected the calibrated Cl source conditions used in the T2R3D simulation (CRWMS M&O 1999d, Section 6.4.4 and Figure 6.4.8). The parameters (and the corresponding data sources) used in this simulation are listed in Table 6.4. The DTN for the EOS9nT input and output data files is LB991220140160.004.

Figure 6.4.5 shows (a) the measured and (b) the predicted Cl concentration distribution along the ESF from both the EOS9nT and the T2R3D runs. The EOS9nT results were obtained using the De Hoogetal . (1982) implementation of the Laplace space formulation at $t = 10,000,000$ years, at which time Cl concentrations are expected to have reached steady state. This 3-D site-scale simulation takes only about 12 minutes to complete because the Laplace-space formulation eliminates the need for solutions at any intermediate times.

Comparison between the EOS9nT predictions and the field measurements in Figure 6.4.5 shows a satisfactory agreement and helps support the validation of EOS9nT. In the same figure, note the practical identity of the EOS9nT and the T2R3D predictions. This further supports the RTM calibration.

Table 6.4. EOS9nT input data and sources for modeling the Cl distribution in the ESF

Parameters	Source
Grid and 3-D flow field	DTN: LB990701233129.002
Calibrated infiltration rate	DTN: LB991131233129.003
Measurements of the Cl concentration distribution in the ESF	DTN: LAJF831222AQ98.002 DTN: LAJF831222AQ98.010 DTN: LAJF831222AQ98.015

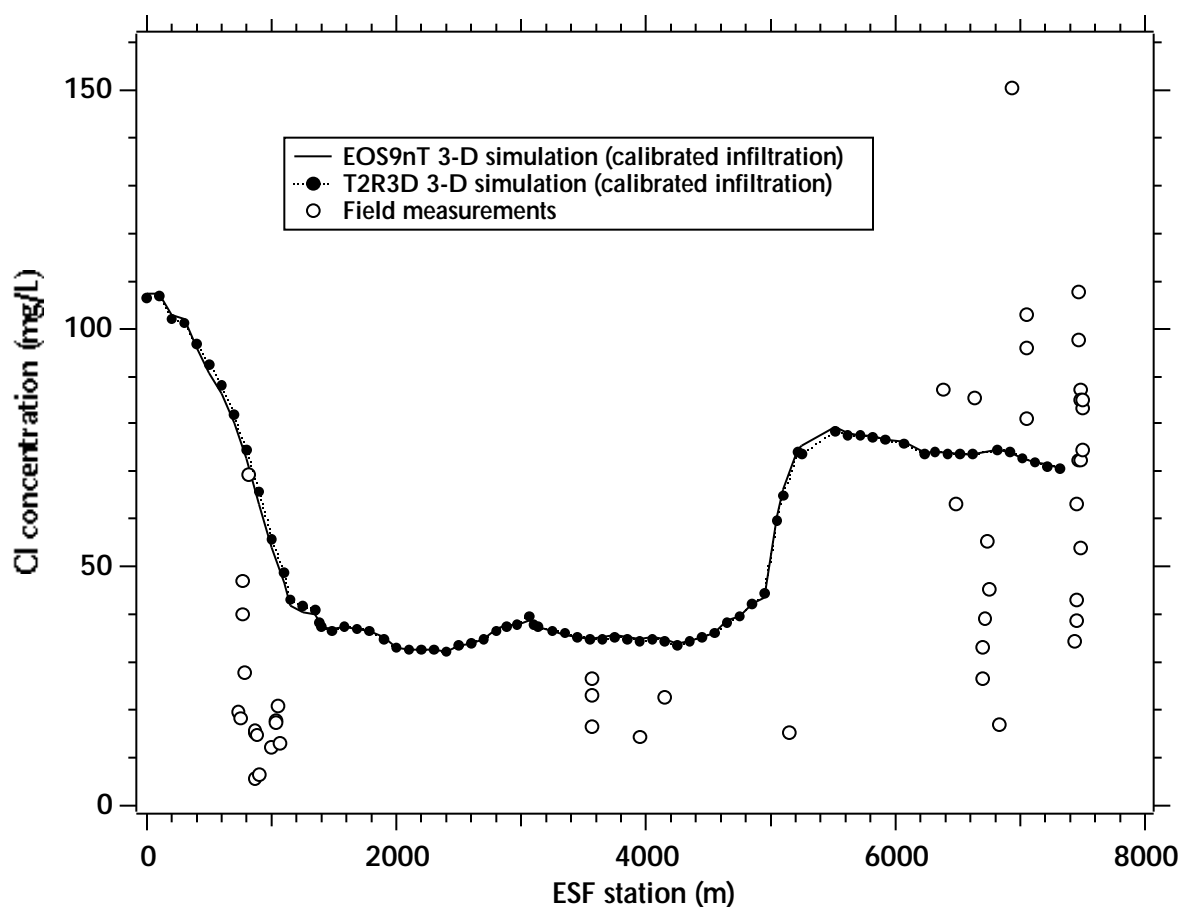


Figure 6.4.5. Comparison of (a) EOS9nT predictions (DTN: LB991220140160.003, data submitted with this AMR), (b) T2R3D predictions and (c) measurements of Cl concentration distribution along the ESF.

6.5 2-D TRANSPORT SIMULATIONS IN INDIVIDUAL HYDROGEOLOGIC UNITS

6.5.1 General Issues

In Sections 6.6 to 6.8 we study radionuclide transport in 2-D systems that are representative of the individual hydrogeologic units present at the site of the potential repository. The focus of these studies is to determine the important processes and the effect of differences in geology on the transport of radionuclides with different transport and decay properties.

In all the 2-D studies in Sections 6.6 to 6.8, water infiltrates at a rate of 6 mm/year. This is close to the mean present-day infiltration rate (see Table 6.11).

6.5.2 Radionuclides Considered

Three radionuclides are considered: ^{99}Tc (nonsorbing), ^{237}Np (moderately sorbing) and ^{239}Pu (strongly sorbing). Their properties are listed in Table 6.5. When occurring, sorption follows a linear equilibrium isotherm. The distribution coefficient K_d values used in the FRACL simulations in Sections 6.6 through 6.9 are listed in Table 6.6.

The scenario being investigated here is the fate and transport of radionuclides that manage to enter the layers of the TSw, CHn, and PP hydrogeologic units. In the TSw hydrogeologic unit, the radionuclides are released at an elevation corresponding to the bottom of the potential repository; in the the CHn and PP hydrogeologic units, the radionuclides are released at the top of the units. The contaminant distribution is then monitored over time. For purposes of discussion and comparison among cases, breakthrough is defined as the point at which the relative concentration C_R (see Section 6.4.2) exceeds 10^{-12} at the bottom of the domain under investigation.

6.5.3 Hydrogeologic Profiles

Transport was studied in three hydrogeologic profiles called Cross Sections 1, 2 and 3. These profiles are two-dimensional in the sense that concentrations are computed in both the vertical (z) and horizontal (x) directions in the fractures and the matrix blocks of each layer in the hydrogeologic units in the cross sections (see Figure 6.4.1). It must be pointed out that the use of the term *Cross Section* does not imply a (x, z) profile that spans a considerable distance in the x direction, but a 2-D simulation domain of limited width in the x direction. This limited width is the minimum necessary to describe the simulation stencil of the matrix-fracture system, i.e., the basic repeatable element of a representative hydrogeologic profile at the given location.

Table 6.5. Properties of the main radionuclides in the transport simulations

Radionuclide	D_0 (m ² /s)*	$T_{1/2}$ (years) [†]	$\lambda = \frac{\ln 2}{T_{1/2}}$ (s)	Decay mode [†]
⁹⁹ Tc	4.55×10^{-10}	2.13×10^5	1.031×10^{-13}	β^-
²³⁷ Np	7.12×10^{-10}	2.14×10^6	1.026×10^{-14}	α
²³⁹ Pu	6.08×10^{-10}	2.41×10^4	9.114×10^{-13}	α

*: From DTN: LB991220140160.019 and DTN: LAIT831341AQ96.001

[†]: From Lide (1992, pp. 11-53, 11-125, 11-126)Table 6.6. Distribution Coefficients K_d (in m³/kg) in the 2-D FRACL simulations

Model Layer	⁹⁹ Tc	²³⁷ Np	²³⁹ Pu
tsw35, tsw36, tsw37, tsw38, tsw39	0.000	0.001	0.100
ch1v, ch2v, ch3v, ch4v, ch5v	0.000	0.001	0.100
ch1z, ch2z, ch3z, ch4z, ch5z, ch6z	0.000	0.004	0.100
pp4, pp1	0.000	0.004	0.100
pp3, pp2	0.000	0.001	0.100
bf3	0.000	0.001	0.100
bf2	0.000	0.004	0.100

DTN: LB991220140160.019 and DTN: LAIT831341AQ96.001

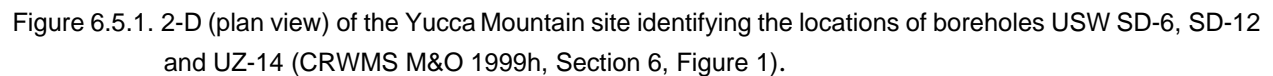
The three cross sections are located in the vicinity of the USW SD-6, SD-12, and UZ-14 boreholes, respectively. The locations of the three boreholes in the context of the UZ site- scale model are shown in Figure 6.5.1. Thus, Cross Section 3 is located in the northern part of the potential repository site, while Cross Sections 1 and 2 are located in the southern part. The geologic profiles in Cross Sections 1, 2 and 3, including the layers of all the hydrogeologic units involved in radionuclide transport, and their elevations and thicknesses, are shown in Figures 6.5.2 through 6.5.4.

The domains for the 2-D semianalytic FRACL simulations were constructed by combining (a) fractures of known aperture and frequency (per unit of length) in each of the layers in the hydrogeologic units with (b) the corresponding matrix blocks (the sizes of which were determined from the active fracture spacing) at each location.

6.5.4 The 2-D FRACL Transport Simulations

All the 2-D simulations were conducted using the FRACL code. The DTN for the FRACL input and output data files is LB991220140160.005. Because they are based on a semianalytical solution of the transport problem, FRACL simulations are very fast, needing less than a minute of computational time on any of the computing platforms used in the simulations.

Note that misalignment of fractures is not accounted for in the simulations discussed in Sections 6.5–6.8. Thus, the results represent the worst case scenario, yield the shortest possible breakthrough times, and provide the upper limit of radionuclide transport. By assuming fracture alignment, transport between the offset fractures at the interface of adjacent layers (and the corresponding delay in the breakthrough curves) is not considered.



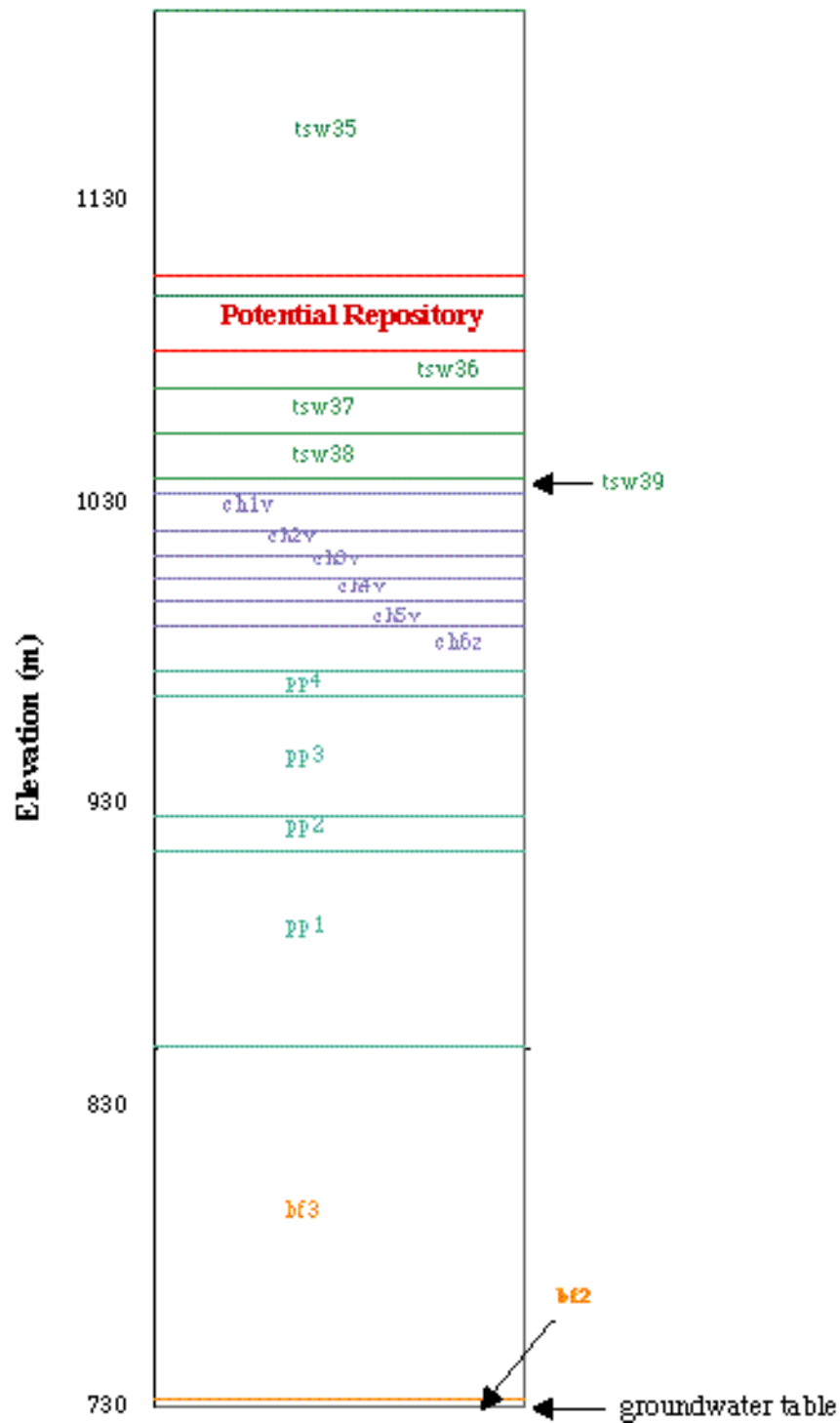


Figure 6.5.2. Hydrogeologic units (and their layers) of the UZ model domain from the potential repository to the groundwater in Cross Section 1 near the USW SD-6 borehole (CRWMS M&O 1999h, Table III-1).

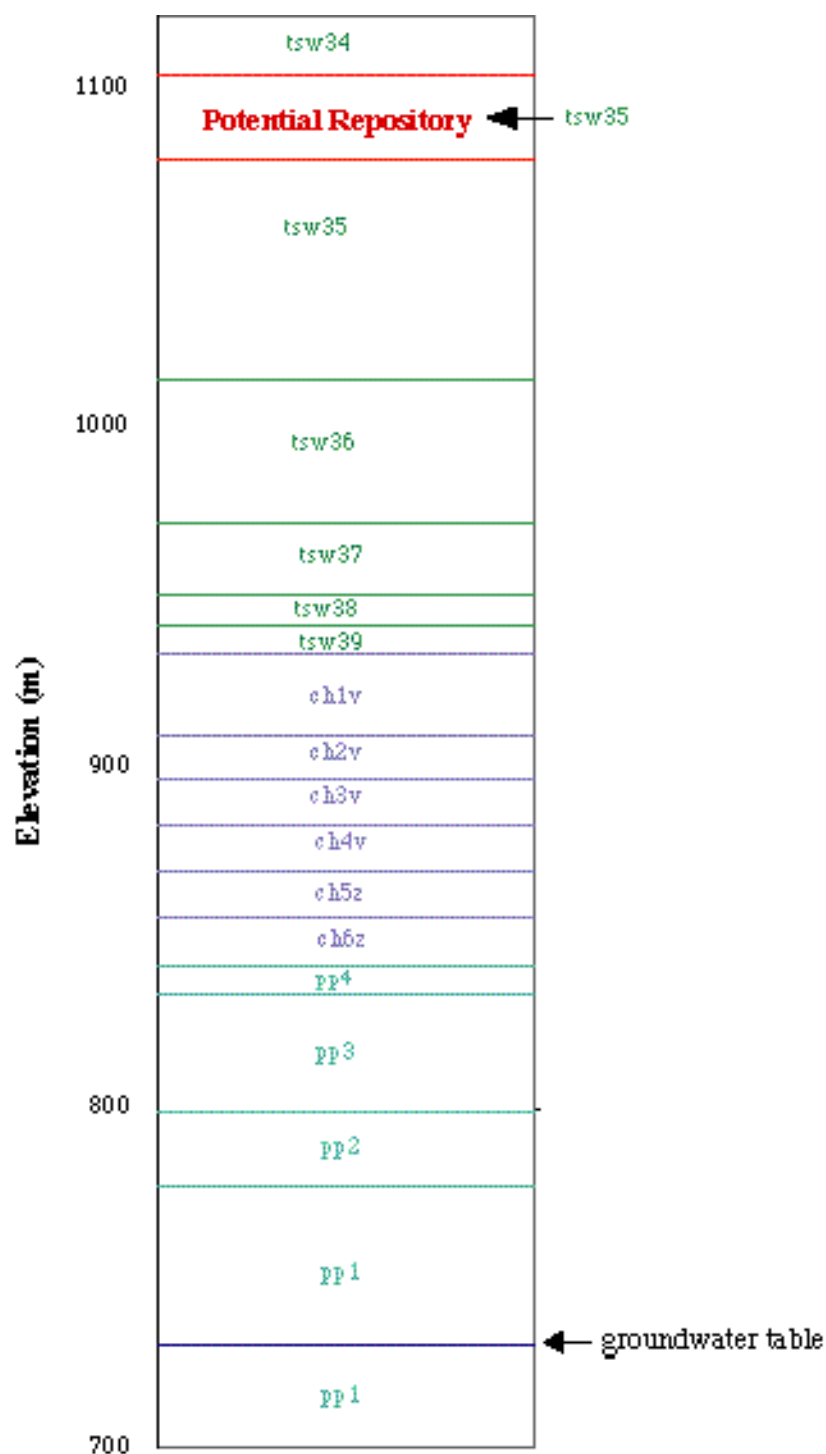


Figure 6.5.3. Hydrogeologic units (and their layers) of the UZ model domain from the potential repository to the groundwater table in Cross Section 2 near the USW SD-12 borehole (DTN:LB990501233129.004).

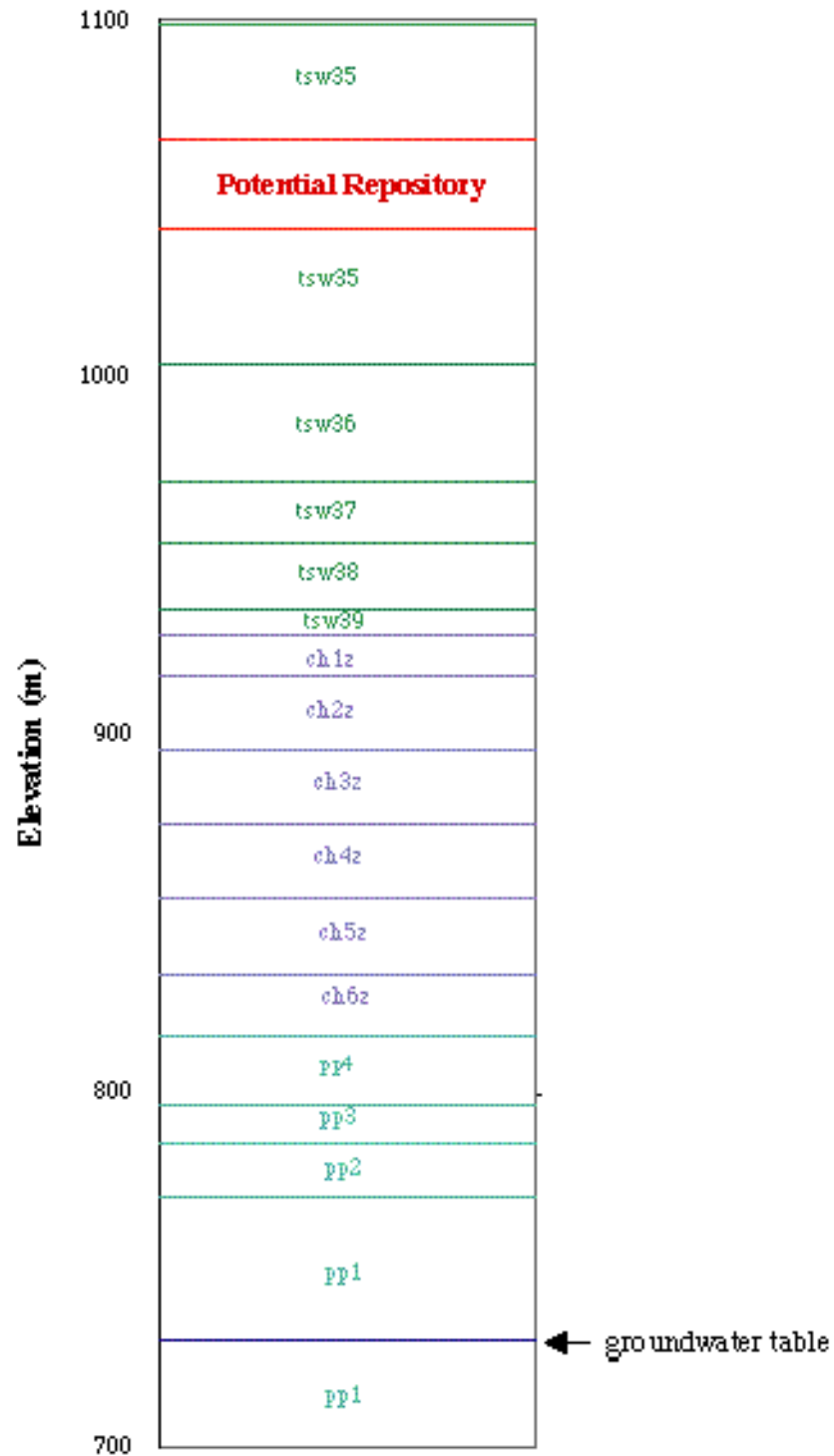


Figure 6.5.4. Hydrogeologic units (and their layers) of the UZ model domain from the potential repository to the groundwater in Cross Section 1 near the USW UZ-14 borehole (CRWMS M&O 1999h, Table III-1).

6.6 2-D TRANSPORT IN THE TSw LAYERS

This section focuses on radionuclide transport in 2-D vertical cross sections of the TSw hydrogeologic unit under the conditions discussed in Section 6.5, and is subdivided in five subsections. Section 6.6.1 discusses the transport of ^{99}Tc , ^{237}Np and ^{239}Pu through the TSw at Cross Section 1. The results of the study appear in Figures II.1 to II.4 (Attachment II). The subject of Section 6.6.2 is the transport of the same radionuclides through the TSw at Cross Sections 2 and 3 (Figures II.5 to II.10).

Sections 6.6.3 to 6.6.5 involve sensitivity analysis studies, in which we evaluate the importance of various parameters on the transport of the three radionuclides. The effect of the transfer coefficient K_i is discussed in Section 6.6.3 (Figures II.11 to II.15). Section 6.6.4 addresses the effect of matrix tortuosity coefficient τ (Figures II.16 to II.21). The sensitivity of transport to the longitudinal dispersivity α_L in the fractures is discussed in Section 6.6.5 (Figures II.22 to II.25).

6.6.1 2-D Transport in TSw, Cross Section 1

6.6.1.1 Results and Discussion

The parameters and the data sources for this simulation are listed in Table 6.7. The distribution of relative concentration (with respect to the concentration at the release point) of the three radionuclides in the fractures along the z-axis are shown in Figures II.1-II.3 in Attachment II. Figure II.4 shows the concentration distributions in the matrix at a depth of 10 m from the top of the TSw (in the tsw36 geologic layer).

The lack of retardation of ^{99}Tc is obvious from Figure II.1, which shows breakthrough occurring in less than a year. At $t = 1$ year, significant concentrations of ^{99}Tc are observed at the lower TSw boundary at this location. The moderately sorbing ^{237}Np reaches the bottom boundary of the TSw at this location in about 35 years, but appears to have a transport behavior similar to that of ^{99}Tc after $t \geq 100$ years. The concentration profile of ^{239}Pu in the fractures is consistent with expectations because of its high K_d values. ^{239}Pu reaches the bottom boundary at about $t = 300$ years.

Because of the limited thickness of the TSw unit, even ^{239}Pu exhibits substantial transport at $t \geq 100$ years. The relative sorption behavior of the three radionuclides is demonstrated by their distribution in the matrix along the x axis at a depth of $z = 10$ m from the top of the TSw (Figure II.4).

6.6.1.2 Synopsis of Important Findings

The TSw unit at the location of Cross Section 1 does not effectively retard the radionuclide transport because of its fractured nature and its limited thickness. This is true even for a strong sorber such as Pu.

Table 6.7. Input parameters for the FRACL transport simulations in Cross Sections 1, 2 and 3

Parameters	Source
Geologic profiles and rock properties at the three cross-sections	CRWMSM&O 1999h, TableIII-1, DTN:LB990501233129.004
Percolation rate (6 mm/yr)	Reasonable value of current mean percolation flux for present-day climate (see Table 6.11)
Matrix properties (porosity ϕ , immobile water saturation S_r), fracture parameters (ϕ , S_r , active fracture parameter γ and frequency f_a), rock grain density ρ_s	DTN: LB997141233129.001
Matrix (S_{wm}) and fracture water saturation (S_{wf}) at steady state	DTN: LB990801233129.003
Fracture apertures	DTN: LB990501233129.001
Active interface area fraction $[=S_{wf}^{1-\gamma}]$, active fracture spacing $[=1/(f_a S_{wf}^{1-\gamma})]$	Liu et al. (1998, pp. 2637-2638)
Sorption coefficients K_d	DTN: LAIT831341AQ96.001
Tortuosity $\tau \simeq \phi$	DTN: LB991220140160.019 and DTN: LAIT831341AQ96.001, Grathwohl (1998, pp. 28-35), Farrell and Reinhard (1994, p. 64)
Transfer coefficient $K_i = 1$	Conventionally used value
Longitudinal dispersivity $\alpha_L = 1$ m in the fractures, 0.1 m in the matrix	Scientific judgement in the absence of available data

6.6.2 2-D Transport in TSw, Cross Sections 2 and 3

6.6.2.1 Results and Discussion

The parameters for this simulation and the data sources are listed in Table 6.7. Compared to Cross Section 1, TSw is substantially thicker in Cross Sections 2 and 3, and the effect of the longer (in the z direction) domain is evident in Figures II.5 to II.10 in Attachment II. The figures also denote the configuration and thickness of the various TSw layers.

The transport of the non sorbing ^{99}Tc in Cross Section 2 (Figure II.5) is fast, and reaches the lower boundary of the TSw unit in about 20 years. For $t \geq 100$ years, the relative concentration of ^{99}Tc in the fracture water reaches high levels, and is equal to 1 at $t \geq 1,000$ years. The transport of ^{99}Tc in Cross Section 3 (Figure II.8) is analogous to that in Cross Section 2 and shows an earlier breakthrough, consistent with the thinner TSw at this location.

Breakthrough of the moderately sorbing ^{237}Np takes about 60 years in Cross Section 2 (Figure II.6) and about 40 years in Cross Section 3 (Figure II.9). In both cases, significant amounts are released from the bottom of the TSw for $t \geq 100$ years. The ^{239}Pu breakthrough occurs at about 6,000 years in Cross Section 2 (Figure II.7) and 4,000 years in Cross Section 3 (Figure II.10).

6.6.2.2 Synopsis of Important Findings

The TSw layers at the location of Cross Sections 2 and 3 retard radionuclide transport more effectively than in Cross Section 1 because of larger total horizon thickness.

6.6.3 Effect of the Transfer Coefficient K_i

6.6.3.1 Results and Discussion

The effect of the transfer coefficient K_i (Section 6.2.1, Equation 6) is investigated here. Although this effect is not expected to be significant in non sorbing and weakly sorbing radionuclides, it can be substantial in strong sorbers. Smaller K_i values correspond to weaker sorption, thus contaminant retardation and/or removal is reduced, leading to larger concentrations in the fractures and increased transport.

This semi-infinite system in these simulations (as well as in those in Sections 6.6.4 and 6.6.5) consists of a fracture and a matrix block corresponding to the properties of TSw35. The parameters for this FRACL simulation set (and the corresponding data sources) are listed in Tables 6.7 and 6.8. The DTN for the input and output data files is LB991220140160.006. Relative concentration profiles in the fractures were obtained for $t = 1,000$ years.

The relative concentration of ^{99}Tc in the fractures as shown in Figure II.11 (see Attachment II) conforms with the expectation of limited effect of K_i on the transport of a non-sorbing radionuclide. Significant differences are observed at very large distances from the point of release. The effect on the transport of ^{237}Np , shown in Figure II.12, is much more pronounced. It is obvious that a lower K_i corresponds to weaker sorption (because it leads to a lower effective K_d), thus larger concentrations in the fractures at the same point. This is supported by Figure II.13, which shows the relative concentration profiles in the matrix at $z = 50$ m. The reduced sorption onto the matrix leads to higher concentration in the liquid phase of the matrix.

Table 6.8. Input parameters in the FRACL sensitivity analysis simulations
(transport in the TSw35 layer)

Parameters	Source
Transfer coefficient $K_i = 1, 0.5, 0.1$	Reasonable value range for sensitivity analysis
Tortuosity $\tau \simeq \phi, 0.2\phi, 5\phi$	Reasonable value range for sensitivity analysis
Longitudinal dispersivity in the fractures $\alpha_L = 1 \text{ m}, 0.1 \text{ m}, 10 \text{ m}$	Reasonable value range for sensitivity analysis

The ^{239}Pu transport in Figures II.14 and II.15 show the most pronounced effect of K_i . Lower K_i results in significantly higher Pu concentrations both in the fractures and in the matrix, and, consequently, in transport over longer distances.

6.6.3.2 Synopsis of Important Findings

The transfer coefficient K_i may be important in the migration of strongly sorbing radionuclides (such as Pu) from possible releases from the potential repository. Currently it is not known whether the effects of the K_i variations in the UZ are within the PA tolerances.

6.6.4 Effect of the Matrix Tortuosity

6.6.4.1 Results and Discussion

The RTM sensitivity to tortuosity coefficient ($\tau \leq 1$) is investigated in this section. The parameters for this FRACL simulation set (and the corresponding data sources) are listed in Tables 6.7 and 6.8. The simulations were conducted under the same conditions discussed in Section 6.6.3, from which they differed only in that the matrix tortuosity coefficient was varied. Increasing matrix tortuosity coefficient leads to more pronounced diffusion in the matrix, which in turn results in lower concentrations in the fractures, increased sorption in the matrix, and thus delayed breakthroughs. The effect of tortuosity coefficient is therefore expected to be more pronounced in strongly sorbing systems.

The DTN of the FRACL input and output data files is LB991220140160.006. Relative concentration profiles in the fractures and in the matrix were obtained at $t = 1,000$ years. The FRACL simulations indicate that the effect of matrix tortuosity coefficient on the transport of ^{99}Tc is substantial. Larger tortuosity coefficient values (as multiples of porosity) lead to lower relative concentrations and

delayed breakthroughs in the fractures (Figure II.16, see Attachment II), and larger concentrations in the matrix (Figure II.17).

The tortuosity coefficient effect becomes increasingly important as sorption (quantified by the K_d value) increases. With increasing tortuosity coefficient, transport of ^{237}Np in the fractures is greatly retarded (Figure II.18), and its concentration profile in the matrix (Figure II.19) shows a more uniform distribution, consistent with the higher matrix diffusion. A low tortuosity coefficient value ($= 0.2 \times \phi$) leads to a dramatically faster transport of ^{239}Pu in the fractures (Figure II.20), while a high tortuosity coefficient value ($= 5 \times \phi$) reduces ^{239}Pu concentrations to practically non detectable levels in the matrix (Figure II.21).

6.6.4.2 Synopsis of Important Findings

The sensitivity analysis study in this section indicates that tortuosity can have a significant effect on transport, and the issue of obtaining accurate τ data merits attention. Currently it is not known whether the effects of the τ variations in the UZ are within the PA tolerances.

6.6.5 Effect of Dispersion in the Fractures

6.6.5.1 Results and Discussion

The RTM sensitivity to the longitudinal dispersion α_L is investigated in this section. The FRACL simulations in this study were conducted under the same conditions discussed in Section 6.6.3, from which they differed only in that the longitudinal dispersivity α_L of the fracture was varied. The parameters for this FRACL simulation set (and the corresponding data sources) are listed in Tables 6.7 and 6.8. The DTN for the input and output data files is LB991220140160.006. The FRACL simulations indicate that at $t = 1,000$ years the effect of α_L is minimal on the ^{99}Tc transport (Figure II.22) and marginal on the ^{237}Np transport (Figure II.23).

Conversely, variations in the magnitude of α_L have a pronounced effect on the transport of ^{239}Pu . A larger α_L value significantly enhances transport in the fractures, and leads to earlier breakthroughs (Figure II.24) and higher concentrations in the matrix (Figure II.25).

6.6.5.2 Synopsis of Important Findings

Knowledge of α_L can be important in reliably predicting the transport of strongly sorbing radionuclides. Currently it is not known whether the effects of the α_L variations in the UZ are within the PA tolerances.

6.7 2-D TRANSPORT IN THE CH_n LAYERS

This section focuses on radionuclide transport in 2-D vertical cross sections of the CH_n hydrogeologic unit under the conditions discussed in Section 6.5. It is subdivided in three subsections.

In Section 6.7.1 we address general issues. In Section 6.7.2 we investigate the transport of ⁹⁹Tc, ²³⁷Np and ²³⁹Pu at Cross Sections 1 and 2. The results of the study appear in Figures III.1 to III.6 (Attachment III). The subject of Section 6.7.3 is the transport of the same radionuclides at Cross Section 3 (Figures III.7 to III.9).

6.7.1 General Issues

6.7.1.1 The FRACL Simulations

The simulations in Section 6.7 were conducted using the FRACL code and involved ⁹⁹Tc, ²³⁷Np, and ²³⁹Pu (Table 6.5). The parameters and the data sources for these simulations are listed in Tables 6.6 and 6.7. The DTN for the FRACL input and output data files is LB991220140160.007. The radionuclide release scenario was the same as in the TSw unit (Section 6.6). Transport was studied in the CH_n layers at the three locations (Cross Sections 1, 2 and 3) discussed in Section 6.5.

6.7.1.2 Perched Water Considerations

Note that the perched water at the TSw/CH_n interface is not considered in this 2-D study, which focuses on transport exclusively within the CH_n hydrogeologic unit and not at (or through) its interfaces. This subject is addressed in the study of transport underneath the potential repository in Section 6.9, in which we discuss transport across all the hydrogeologic units from the stratigraphic horizon of the potential repository to the groundwater.

The 3-D site-scale studies in Sections 6.11 to 6.14 account for the complexities of the effects of perched water on transport. Additionally, Section 6.15 focuses exclusively on the effect of three different conceptual models of perched water on the transport behavior of ⁹⁹Tc, ²³⁷Np and ²³⁹Pu. The 3-D studies in Sections 6.11 to 6.15 can address complex issues of flow bypassing and focusing (and their effect on transport) that are beyond the capabilities of the 2-D FRACL code. The discussion in this section should be viewed as strictly an investigation of the fate and transport of radionuclides that manage to enter the CH_n Formation.

6.7.2 2-D Transport in CH_n, Cross Sections 1 and 2

6.7.2.1 Results and Discussion

Cross Sections 1 and 2 are located in the southern part of the potential repository. Their location relative to the potential repository is discussed in Section 6.5.3 and is shown in Figure 6.5.1. The stratigraphy of the CH_n unit in Cross Sections 1 and 2 is dominated by vitric layers (Figures 6.5.2

and 6.5.3).

The CHn hydrogeologic unit in Cross Section 1 (see Figure 6.5.2) consists of five vitric layers (ch1v, ch2v, ch3v, ch4v, and ch5v) and one zeolitic layer (ch6z). The CHn unit in Cross Section 2 (see Figure 6.5.3) consists of four vitric layers (ch1v, ch2v, ch3v, ch4v, and ch5v) and two zeolitic layers (ch5z and ch6z). Transport is studied in Cross Sections 1 and 2 together because of the similarity of geology and transport behavior.

Transport in the vitric layers is expected to be substantially different from that in the zeolitic layers because of the distinctively different properties and characteristics of these layers. The permeabilities of the fractures and of the matrix of the vitric layers are similar in magnitude (CRWMS M&O 2000a, Section 6). This permeability parity, coupled with a large fracture spacing, result in a behavior similar to that of a nonfractured porous medium (CRWMS M&O 2000a, Section 6).

In contrast, the zeolitic layers in the northern part of the potential repository (Cross Section 3) have similar fracture spacing and fracture permeability, but the matrix permeability is about five orders of magnitude lower than that in the fractures (CRWMS M&O 2000a, Section 6). Thus, matrix flow in the zeolitic layers of Cross Section 3 is extremely slow and practically all the flow occurs in the fractures, leading to relatively fast transport.

In Cross Section 1, the distribution of relative concentration (with respect to the concentration at the release point) of the three radionuclides in the fractures along the z-axis are shown in Figures III.1 to III.3 (see Attachment III), which also denote the various layers of the CHn hydrogeologic unit involved in transport. Figures III.4 to III.6 show the radionuclide concentration in the fractures of the CHn unit in Cross Section 2.

As expected, an increasing K_d results in transport over a longer distance for a given time. The strong sorptive tendency of ^{239}Pu is demonstrated in Figures III.3 and III.6, which indicate that the advancement of the Pu front is limited to a few meters (<10 m) from the point of release. The different (fracture-controlled) transport properties of the zeolitic zone ch6z are shown in Figures III.1 and III.2, and are denoted by the almost flat (i.e., constant) concentration (characteristic of fast transport) once the zeolitic layer is reached. The same (and even more pronounced) pattern of constant concentration is observed in the thickest zeolitic layers (ch5z and ch6z) of Cross Section 2 (Figure III.4 and III.5).

Figures III.1 and III.4 show that the ^{99}Tc front reaches the bottom of the CHn unit in a few hundred years (<1,000 years). The ^{237}Np takes several thousand years (<10,000 years) in Cross Section 1 (Figure III.2), and over 10,000 years in the thicker CHn unit of Cross Section 2 (Figure III.5). In either column, the ^{239}Pu front does not escape ch1v, i.e., the first layer in the unit, within 100,000 years (Figures III.3 and III.6).

6.7.2.2 Synopsis of Important Findings

It appears that, at Cross Sections 1 and 2, the CHn unit is an effective transport barrier. This results from the dominant presence of vitric layers, which act as a porous (rather than fractured) medium by virtue of their infrequent fracture spacing and similar permeabilities in the matrix and in the fractures.

6.7.3 2-D Transport in CHn, Cross Section 3

6.7.3.1 Results and Discussion

The CHn unit in Cross Section 3 presents an entirely different geologic picture than at Cross Sections 1 and 2. It is characterized by the absence of vitric layers (see Figure 6.5.4). This hydrogeologic unit consists of six zeolitic layers (ch1z, ch2z, ch3z, ch4z, ch5z, and ch6z). Because the fracture permeability is about five orders of magnitude larger than that in the matrix (CRWMS M&O 2000a, Section 6) of the zeolitic layers, radionuclide transport through the unit is expected to be advection-controlled and rapid at this location. Thus, the greater potential adsorption of radionuclides onto the zeolitic matrix (as quantified by the K_d values) does not result in increased retardation because the fracture-dominated flow does not allow significant contact of the water with the matrix.

The simulation results are entirely consistent with the expected transport behavior. Despite the relatively large thickness of the unit at this location, ^{99}Tc and ^{237}Np reach the bottom boundary in less than 10 years (Figures III.7 and III.8, Attachment III). The stronger-sorbing ^{239}Pu needs more than 1,000 years (but less than 10,000 years) to cover this distance (Figures III.9), a relatively short time compared to its half-life of 2.41×10^4 years (Table 6.5).

6.7.3.2 Synopsis of Important Findings

At the location of Cross Section 3, the CHn unit is extremely inefficient in retarding transport despite its relatively large thickness. This is caused by the uniformly zeolitic nature of the unit at this location, the layers of which are characterized by high fracture permeability and a nearly impermeable matrix.

6.8 2-D TRANSPORT IN THE PP LAYERS

This section focuses on radionuclide transport in 2-D vertical cross sections of the PP hydrogeologic unit under the conditions discussed in Section 6.5. Section 6.8 is subdivided in three subsections.

In Section 6.8.1 we address general issues. In Section 6.8.2 we investigate the transport of ^{99}Tc , ^{237}Np and ^{239}Pu at Cross Sections 1 and 2. The results of the study appear in Figures IV.1 to IV.6 (Attachment V). The subject of Section 6.8.3 is the transport of the same radionuclides at Cross Section 3 (Figures IV.7 to IV.9).

6.8.1 General Issues

The simulations in Section 6.8 were conducted using the FRACL code and involved ^{99}Tc , ^{237}Np and ^{239}Pu (Table 6.5). The parameters and the data sources for these simulations are listed in Table 6.6 and 6.7. The DTN for the input and output data files is LB991220140160.008.

The radionuclide-release scenario was the same as in the TSw and the CHn units (see Sections 6.5 to 6.7). The purpose of this study was to investigate the fate and transport of radionuclides that manage to migrate through the overlaying TSw and CHn hydrogeologic units and enter the PP unit at the three locations (Cross Sections 1, 2 and 3) discussed in Section 6.5 (Figures 6.5.2 to 6.5.4). Note that layer numbering in the PP units decrease with depth.

As indicated in the previous sections, Cross Sections 1 and 2 are located in the southern part of the potential repository. At these locations, the PP hydrogeologic units directly underlie the vitric layers of the CHn unit. Cross Section 3 is in the northern part of the potential repository, at a location where the PP hydrogeologic unit underlie the highly-permeable (compared to the matrix) fractures of the zeolitic layers of the CHn unit. More complex phenomena and processes (such as transport in fault zones, transport across geologic interfaces, flowdiversion, and funnel flow through the areally shrinking (with depth) vitric layers of the CHn hydrogeologic unit overlying the PP unit near Cross Section 1) cannot be resolved by the 2-D nature of FRACL. These are investigated in the 3-D studies discussed in Sections 6.11 to 6.15.

6.8.2 2-D Transport in PP, Cross Sections 1 and 2

6.8.2.1 Results and Discussion

The PP hydrogeologic units in Cross Sections 1 and 2 are similar in terms of geologic structure, relative thickness of the various PP layers, and total thickness. Thus, they are studied together. At these two locations, PP consists of (a) a rather thin zeolitic layer (pp4), (b) a thick devitrified layer (pp3) followed by a thinner devitrified layer (pp2), and (c) a thick zeolitic layer (pp1). These layers

are denoted in Figures 6.5.2 and 6.5.3. Note that the groundwater table occurs in the pp1 layer in Cross Section 2 and 3.

In terms of flow and transport, the devitrified layers are similar to the vitric layers in the CHn (CRWMSM&O2000a, Section6). Consequently, transport in the PP is expected to be characterized by (a) a rapid transport phase in the fractures of the zeolitic pp4 layer, followed by (b) slower transport in the devitrified pp3 and pp2 layers (whose behavior is akin to porous, rather than fractured, media), and (c) by rapid transport again once the pp1 layer is reached.

The relative concentrations of the three radionuclides in the fractures of the PP layers along the z-axis in Cross Section 1 are shown in Figures IV.1 to IV.3 in Attachment IV. Figures IV.4 to IV.6 show the radionuclide concentration in the fractures of the PP unit in Cross Section 2.

The simulations confirm the expected transport pattern. Figures IV.1 to IV.6 show that pp4 (i.e., the top zeolitic layer) at both locations is breached in a short time, and then radionuclide transport is controlled by the devitrified layers. These layers are quite efficient in retarding transport even for the nonsorbing ^{99}Tc (Figures IV.1 and IV.4), which takes over 1000 years to cross the devitrified layers.

Once the advancing solute front reaches pp1 (i.e., the bottom zeolitic layer), transport is fast and practically unretarded, as evidenced by the constant concentration (indicated by the flatness of the relative concentration curve) in this layer in the transport of ^{237}Np (Figures IV.2 and IV.5). It takes several thousand (<10,000) years to reach the pp1 layer, after which time the radionuclide front advances rapidly.

Although the ^{239}Pu front crosses the pp4 layer in a relatively short time, the devitrified layers appear to be very effective in retarding its transport. This is indicated by the steepness of the Pu relative concentration curve in pp3, and the fact that the Pu front does not reach the pp3 boundary even after 100,000 years (Figures IV.3 and IV.6).

6.8.2.2 Synopsis of Important Findings

At the location of Cross Sections 1 and 2, transport is practically uninhibited in the top zeolitic layer of the PP hydrogeologic unit, but is effectively retarded by the underlying devitrified layers. Once the radionuclide solute front reaches the bottom of the devitrified layers, transport becomes very fast because of the fast, fracture-dominated flow in the pp1 zeolitic layer.

6.8.3 2-D Transport in PP, Cross Section 3

6.8.3.1 Results and Discussion

Although the PP hydrogeologic unit in Cross Section 3 consists of the same layers as in Cross

Sections 1 and 2, they differ in the relative thickness of the zeolitic and devitrified layers and in the total PP unit thickness. Thus, (a) pp4 is much thicker (than in Locations 1 and 2), (b) the devitrified layers are thinner, and (c) the combined thickness of the zeolitic pp4 and pp1 layers in Cross Section 3 constitute over half the PP unit thickness (which is shorter than that in Cross Sections 1 and 2).

The layers in the PP hydrogeologic unit in Cross Section 3 are shown in Figure 6.5.4. Because of the geologic differences, transport in the PP in Cross Section 3 is expected to be substantially faster than in Cross Sections 1 and 2, owing to the predominant presence of the zeolitic layers and the limited thickness of the devitrified layers.

The relative concentrations of the three radionuclides in the fractures of the PP layers along the z-axis in Cross Section 3 are shown in Figures IV.7 to IV.9 in Attachment IV. The simulation results are entirely consistent with the expected transport behavior. The ^{99}Tc front reaches the bottom of the PP hydrogeologic unit much faster than in Cross Sections 1 and 2 (Figure IV.7), after which time transport in the pp1 layer is very fast (denoted by the virtually constant concentration in this layer).

A similar pattern emerges in the transport of ^{237}Np , which reaches the bottom of the PP unit much earlier (<10,000 years) than in Cross Sections 1 and 2 (Figure IV.8), and exhibits constant concentration in the pp1. The ^{239}Pu transport is marked by its strongly sorbing property. Although the relatively thick pp4 layer is crossed by the Pu front relatively quickly, the devitrified layers are very effective in retarding its advance (Figure IV.9). This is indicated by the steepness of the concentration curve in the devitrified layers, and the fact that radionuclides do not emerge from them until after 100,000 years.

6.8.3.2 Synopsis of Important Findings

At the location of Cross Section 3, the transport of ^{99}Tc and ^{237}Np is much faster than in Cross Sections 1 and 2 because of the greater thickness of the zeolitic layers relative to the devitrified layers. The ^{239}Pu transport, however, is effectively retarded at this location because after 100,000 years it had not yet reached the pp1 layer.

6.9 2-D TRANSPORT UNDERNEATH THE POTENTIAL REPOSITORY

This section focuses on radionuclide transport in 2-D vertical cross sections that include all the hydrogeologic units from the potential repository horizon to the water table. Section 6.9 includes nine subsections.

In Section 6.9.1 we address general issues. In Sections 6.9.2 and 6.9.3 we discuss the transport of ^{99}Tc , ^{237}Np and ^{239}Pu at Cross Section 1 for a (a) mean present-day infiltration (Figures V.1 to V.3, see Attachment V) and (b) high glacial infiltration (Figures V.4 to V.6), respectively (see Table 6.11).

In Sections 6.9.4 and 6.9.5 we investigate transport at Cross Section 2 for a (a) mean present-day (Figures V.7 to V.9) and (b) high glacial infiltration (Figures V.10 to V.12), respectively. Similarly, in Sections 6.9.6 and 6.9.7 we investigate transport at Cross Section 3 for a (a) mean present-day (Figures V.13 to V.15) and (b) high glacial infiltration (Figures V.16 to V.19), respectively.

In Section 6.9.8 we evaluate the effect of perched water bodies on transport at Cross Section 3 for a mean present-day infiltration. Finally, in Section 6.9.9 we discuss some important results and their implications.

6.9.1 General Issues

In Sections 6.5 through 6.8 we focused on the study of transport in individual hydrogeologic units. More specifically, we investigated the fate and migration of radionuclides that entered each of the three major hydrogeologic units underlying the potential repository horizon, and we identified mechanisms and geological properties that affect transport.

6.9.1.1 Focus of the Study

In the present section, we study radionuclide transport in composite 2-D sections covering the entire geologic profile from the potential repository to the groundwater table. The purpose of these simulations is to evaluate the integrated transport performance of all the hydrogeologic units beneath the potential repository, accounting for changes in fracture aperture, frequency, active spacing, and saturation distribution (in the fractures and the matrix) across layer interfaces.

6.9.1.2 Radionuclides Considered

The transport of ^{99}Tc , ^{237}Np and ^{239}Pu (Table 6.5) was studied. The transport model simulates continuous and time-invariant release at the location of the potential repository. The radionuclide concentration distribution in the profile is monitored over time. When occurring, sorption is described by a linear equilibrium equation (Equation 9, Section 6.2.3.1).

6.9.1.3 The 2-D FRACL Simulations

Transport was studied in the three 2-D geological profiles of Cross Sections 1, 2 and 3 (see Section 6.5). The FRACL code was used for the simulations, each of which needed less than a minute of execution time to complete. The parameters and the data sources for these simulations are listed in Tables 6.6 and 6.7. The DTN for the input and output data files is LB991220140160.009.

6.9.1.4 Perched Water

Perched water is not an important issue in Cross Sections 1 and 2, but can be more relevant in Cross Section 3, at which location perched water was encountered (CRWMS M&O, 1999d, Section 6.2.2). Thus, the effect of perched water bodies was confined to a limited comparative study in Cross Section 3 (see Section 6.9.8), but was not considered in the rest of the simulations.

The rationale for this approach is that the focus of the simulations in Section 6.9 was to investigate the worst-case scenario (shortest possible breakthrough times) and to provide the upper limit of the rate and extent of radionuclide transport. An additional reason is that there is very little direct information on the hydrogeologic properties and conditions that lead to the emergence of perched water in these low-permeability zones, i.e., the zeolitic CHn or the densely welded basal vitrophyre of the TSw (CRWMS M&O, 1999d, Section 6.2.2). The effect of perched water bodies, however, is thoroughly addressed in the 3-D site-scale simulations discussed in Sections 6.11 to 6.16.

6.9.2 2-D Radionuclide Transport in Cross Section 1, Mean Present-Day Infiltration

6.9.2.1 Results and Discussion

A cross section of the 2-D domain in Cross Section 1, indicating the layers of all the hydrogeologic units involved in the transport, their elevation, and their thickness, was shown in Figure 6.5.2. Note that at this location the Bullfrog (BF) hydrogeologic unit is present. The total distance between the bottom of the potential repository and the water table at this location is about 350 m.

The infiltration rate in these simulations was 6 mm/year, i.e., about the mean present-day infiltration (see Table 6.11). Figure V.1 in Attachment V shows the relative concentration profile of the non sorbing ^{99}Tc over a period of 100,000 years. The ^{99}Tc front takes several thousand (but <10,000) years to reach the water table. As expected (due to its different sorption behavior), the ^{237}Np breakthrough at the water table takes longer than 10,000 (but <100,000) years (Figure V.2). The same figure clearly denotes the presence of the highly permeable (compared to the matrix) fractures in the zeolites, indicated by the near-constant concentration profile in ch6z and pp4. The strongly sorbing ^{239}Pu does not advance past the ch1v layer, less than 60 m from the point of release, even after $t = 100,000$ years (Figure V.3).

6.9.2.2 Conceptual Model of Transport in Cross Section 1

Figure 6.9.1 illustrates a conceptual model of transport in Cross Section 1 that incorporates the findings from Sections 6.5 through 6.9. Water-borne radionuclides enter the TSw formation through the bottom of the potential repository. Radionuclide transport in the TSw hydrogeologic unit is occurs mostly in the fractures (see Section 6.7).

The vitric layers in the underlying CHn unit at this location (i.e., layers ch1v through ch5v) behave as porous (rather than fractured) media because of the parity of permeability in the matrix and in the fractures (CRWMS M&O 2000a, Section 6). Thus transport occurs in both the matrix and the fractures, and the contact times between the radionuclides and the media is longer. The vitric layers are effective transport barriers because of the increased sorption (for sorbing radionuclides) and retardation (see Section 6.7). Once the radionuclide reaches the zeolitic ch6z unit, flow becomes again fracture-dominated, and, consequently, so does transport.

Transport in the pp4 layer, the top layer in the PP hydrogeologic unit, is controlled by its zeolitic nature, which leads to fractured-dominated flow and transport. The next two layers (i.e., pp3 and pp2) are devitrified and behave similarly to the vitric layers in the CHn unit. Transport in the thick zeolitic pp1 layer (the last layer in the PP unit) is again fractured-dominated, as is transport in the underlying layers of the BF unit (see Section 6.8).

6.9.3 2-D Radionuclide Transport in Cross Section 1, High Glacial Infiltration

The simulations discussed in Section 6.9.2 were repeated for an infiltration rate of 33.5 mm/year, i.e., the high glacial infiltration (See Table 6.11). As Figures V.4 to V.6 in Attachment V show, the effect on transport is significant.

The breakthrough of the non sorbing ^{99}Tc (Figure V.4) occurs much earlier, i.e., after less than 1,000 years. The ^{237}Np front reaches the groundwater in more than 10,000 years (Figure V.5). Despite an infiltration rate over 5 times that in the mean present-day case, the ^{239}Pu front advances only slightly in the profile (to a distance of 82 m from the point of release), but is still far from reaching the groundwater at $t = 100,000$ years (Figure V.6).

6.9.4 2-D Radionuclide Transport in Cross Section 2, Mean Present-Day Infiltration

A cross section of the domain at this location, indicating the layers of all the hydrogeologic units involved in the transport, their elevation, and their thickness, is shown in Figure 6.5.3. The total distance between the bottom of the potential repository and the water table at this location is about 350 m. The infiltration rate in the simulations was 6 mm/year, i.e., about the mean present-day infiltrations (see Table 6.11).

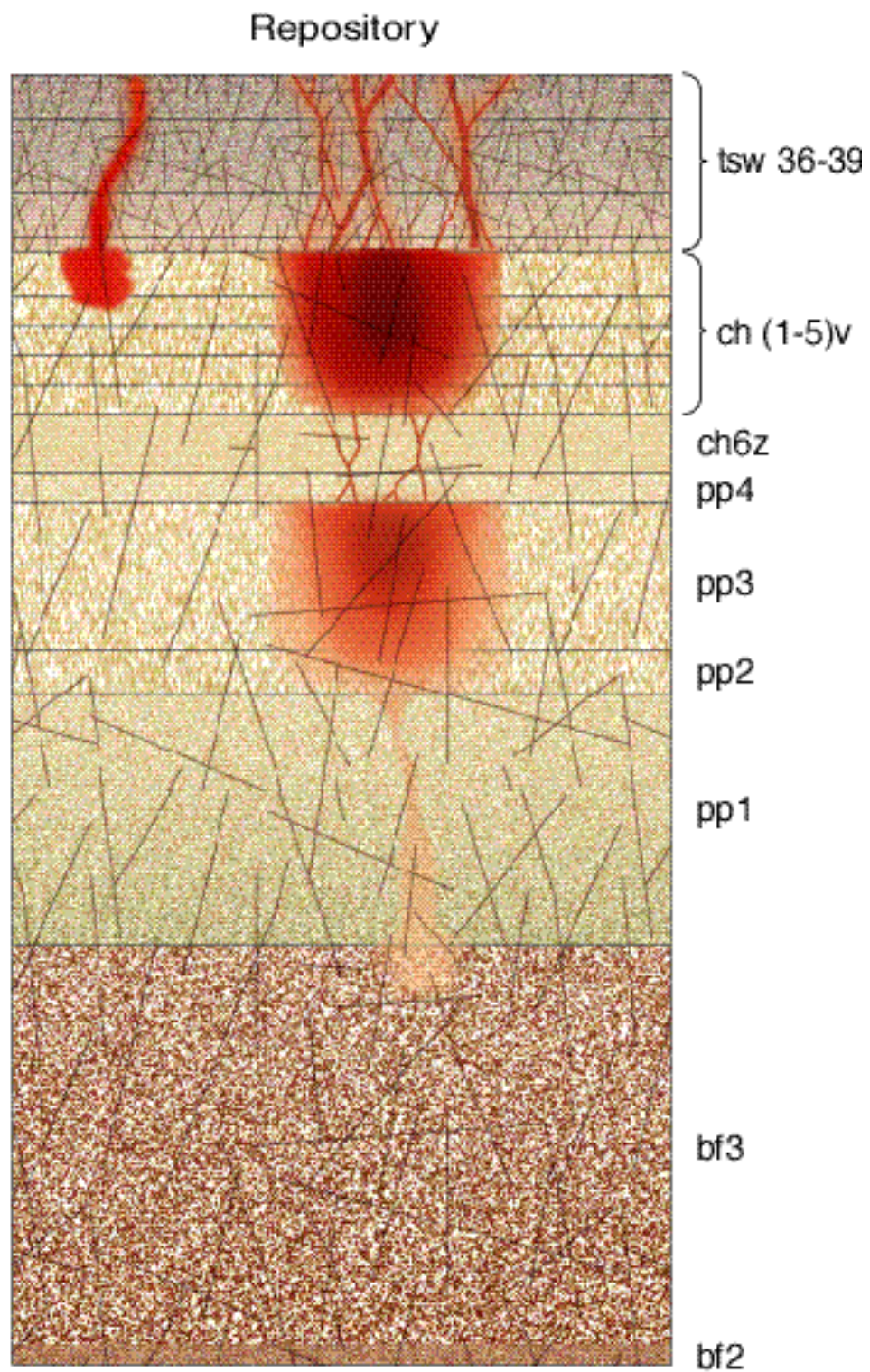


Figure 6.9.1. A conceptual model of transport in Cross Section 1.

Figure V.7 in Attachment V shows the relative concentration profile of ^{99}Tc over a period of 100,000 years. The ^{99}Tc front takes several thousand (but $<10,000$) years to reach the water table. Note the near-constant concentration in the zeolitic layers of the CHn and the PP hydrogeologic units. As in Cross Section 1, the ^{237}Np breakthrough at the water table takes longer than 10,000 (but $<100,000$) years (Figure V.8). Because of the relatively large thickness of the highly fractured TSw unit in Cross Section 2, the strongly sorbing ^{239}Pu migrates much further than in Cross Section 1, reaching a distance of about 150 m from the release point (Figure V.9). It does not, however, advance past the ch1v layer after 100,000 years.

6.9.5 2-D Radionuclide Transport in Cross Section 2, High Glacial Infiltration

The simulations discussed in Section 6.9.4 were repeated for an infiltration rate of 33.5 mm/year. The increase in contaminant transport observed here is analogous to that observed in Cross Section 1.

The breakthrough of ^{99}Tc (Figure V.10) occurs much earlier than for the mean present-day infiltration case, i.e., after several hundred years, while at 1,000 years its concentration at the water table equals that at the release point. This is the same behavior observed in the much shorter Cross Section 1 domain. The ^{237}Np front reaches the groundwater in less than 10,000 years (Figure V.11), while the incremental advance of ^{239}Pu is relatively small (about 180 m from the point of release) compared to the mean present-day infiltration case, but is still far from reaching the groundwater at $t = 100,000$ years (Figure V.12).

6.9.6 2-D Radionuclide Transport in Cross Section 3, Mean Present-Day Infiltration

A cross section of the domain at this location, indicating the layers of all the hydrogeologic units involved in the transport, their elevation, and their thickness, is shown in Figure 6.5.4. The total distance between the bottom of the potential repository and the water table at this location is about 310 m.

Inspection of the ^{99}Tc profile in Figure V.13 (see Attachment V) shows a drastically different profile from those in Cross Sections 1 and 2. The extensive zeolitic zones at this location result in very rapid transport, and the ^{99}Tc front reaches the water table in significantly less time than 1,000 years. Note the near-constant concentration in the extensive zeolitic layers of the CHn and PP hydrogeologic units.

Similarly, the ^{237}Np breakthrough at the water table takes substantially less than 10,000 (Figure V.14). Even the strongly sorbing ^{239}Pu shows drastically enhanced migration, reaching a distance of about 255 m from the release point (Figure V.15). The large portions of near-constant concentrations

indicate the substantial impact of zeolites on transport. Although Pu in Cross Section 3 advances much further than in either Cross Section 1 or 2, it does not migrate past the devitrified pp3 layer within 100,000 years.

6.9.7 2-D Radionuclide Transport in Cross Section 3, High Glacial Infiltration

The simulations discussed in Section 6.9.6 were repeated for an infiltration rate of 33.5 mm/year. Figure V.16 shows that, at $t = 100$ years, the ^{99}Tc front has reached the upper boundary of the extremely permeable (and conducive to transport) zeolitic layer pp1. Thus, ^{99}Tc breakthrough at the water table is expected at a little more than 100 years.

The ^{237}Np breakthrough occurs at $t < 1,000$ years (Figure V.17), indicating a clear acceleration of transport over the climatic scenario of mean present-day infiltration. Under these conditions, even the strongly sorbing ^{239}Pu exhibits a significantly enhanced migration and reaches the groundwater in less than 100,000 years (Figure V.18).

6.9.8 2-D Radionuclide Transport in Cross Section 3 with Perched Water, Mean Present-Day Infiltration

There is evidence to suggest that perched water occurs at the interface of the TSw and CHn units at location of Cross Section 3 (CRWMS M&O 1999d, Section 6.2.5). In this section, the effect of perched water on transport is investigated. As field data from this location are very limited, reasonable approximations (stated and justified in Sections 6.7.1.2 and 6.9.8.1) had to be made in the FRACL simulations.

6.9.8.1 Representation of the Perched Water in the FRACL Simulations

The fracture and matrix water saturations were set to 1 in the tsw38 and tsw39 layers, i.e., the layers immediately above the TSw-CHn interface. Although there are no supporting field measurements, this configuration corresponded to the prediction of the perched water depth from the simulations in CRWMS M&O (1999d, Section 6.2.5). Additionally, the fractures in the chlz (the top zeolitic layer of CHn at this location) were assumed to be filled and to have the same (a) saturation and (b) transport properties with the matrix in the same layer. Thus, the chlz layer was acting as a porous, rather than a fractured, medium.

6.9.8.2 Results and Discussion

The effect of the perched water body itself (i.e., the saturated tsw38 and tsw39 layers) on transport appears to be minimal, as is demonstrated by a comparison of the concentration profiles in the tsw38 and tsw39 layers of the perched and no-perched water regimes in Figure V.19 and V.13, respectively. On the other hand, the effect of the geological conditions that lead to the perched

water body, namely the filled fractures in ch1z, is dramatic and is more pronounced at earlier times. Figure V.19 shows that, at $t = 10$ and $t = 100$ years, the edge of the ^{99}Tc front has advanced about 130 m less than the front in Figure V.13, in which the perched water body is not considered (i.e., when the ch1z layer is treated as a fractured and unsaturated medium). Once the ch1z layer is breached, ^{99}Tc travels fast in the underlying fractured layers. At $t = 1,000$ years, the ^{99}Tc concentration is beginning to appear at the water table, although (a) its arrival is delayed, and (b) its concentration is lower in all the layers below the tsw39 layer compared to those for no-perched water in Figure V.13. The concentration profiles of ^{99}Tc for the perched and the no-perched water models (Figures V.19 and V.13, respectively) coincide for $t \geq 10,000$ years.

Because of its stronger sorption, at $t = 10$ years there is no difference between the ^{237}Np distributions for the perched water regime in Figure V.20 and the no-perched water model in Figure V.14. This is because the advancing front has not yet reached the ch1z layer. The maximum effect is observed at $t = 100$ years, at which time the front is more than 100 m above its position for no-perched water. At $t = 1,000$ years, the front (a) has already breached the ch1z layer and (b) is at the same location as that for the no-perched water regime (i.e., the bottom of the pp3 layer), but (c) the ^{237}Np concentrations in the fractured ch2z to ch6z layers are 150 times (or less) lower than that for no-perched water in Figure V.14. At $t = 10,000$ years, the ^{237}Np distributions show differences in magnitude only in the bottom (above the water table) two layers pp2 and pp1, with the perched water concentrations being lower. At $t = 100,000$ years, the distributions coincide.

The concentration profile of strongly sorbing ^{239}Pu in the perched water regime (Figure V.21) does not show any differences from those for no-perched water (Figure V.15) for $t \leq 1,000$ years because the advancing front has not yet reached the ch1z layer. For $t \geq 10,000$ years, the ^{239}Pu fronts in Figures V.21 and V.14 are at about the same location, but the concentrations in the fractured ch2z to pp4 layers are lower in the perched water regime.

6.9.8.3 An Important Point

Note that these results were obtained by considering a single geologic layer acting as a permeability barrier (i.e., the ch1z layer acting as a porous, rather than fractured, medium). If this barrier involves more than one CHn and/or PP layers, then the additional retardation effect on transport is expected to be significant.

6.9.9 Synopsis of Findings

A review of the results in Sections 6.9.2 through 6.9.8 indicates that while the geological profiles in Cross Sections 1 and 2 afford good retardation of radionuclide transport (and especially of the strongly sorbing ^{239}Pu), this is not the case in the domain of Cross Section 3 because of the preponderance of highly permeable (compared to the matrix) fractures of the zeolitic layers at this location. The enhancement of transport increases rapidly with a decreasing K_d of the radionuclide,

but is far less important in the case of the strongly sorbing ^{239}Pu .

Increases in the infiltration rate, brought about by possible changes in climatic patterns, can have a substantial impact on breakthrough times, especially at the Cross Section 3 location. The effect of changes in infiltration becomes more pronounced with weaker-sorbing radionuclides.

Conditions leading to the occurrence of perched water bodies can lead to significant retardation. Their effect appears to be more pronounced for weaker-sorbing radionuclides at earlier times.

6.10 3-D BUSTED BUTTE STUDIES

The Busted Butte Unsaturated Zone Transport Test (UZTT) is a long-term experiment conducted in Busted Butte, Yucca Mountain (CRWMS M&O 1999e, Section 6.8) to investigate flow and transport issues in the UZ site-process models for Yucca Mountain, including

1. The effect of heterogeneities on flow and transport under unsaturated conditions in the CHn hydrogeologic unit, particularly fracture-matrix interactions and permeability contrast boundaries;
2. The migration behavior of colloids in the CHn layers;
3. The validation of laboratory sorption results;
4. Scaling effects (from laboratory to field to site) on 3-D site-scale flow and transport simulations.

The site was selected because of the presence of a readily accessible interface of the TSw and CHv units, and the similarity of these layers to those beneath the potential repository horizon. The study of the Tsw/CHv interface is important because of the important role that the vitric layers of the CHv unit play in radionuclide retardation (see Section 6.7). The test proceeded in two phases, which differ in design, purpose, and experimental scales, among other factors. A detailed description of the tests can be found in CRWMS M&O (1999e, Section 6.8).

The Busted Butte studies reported in this AMR were limited to numerical simulations of two sets of tests in the the first phase of the experiment, namely the Phase 1A and 1B tests (see discussion in Sections 6.9.1 and 6.9.2). The field work on these phases has been completed, but the analysis of the experimental results is not yet complete.

6.10.1 Numerical Simulation of the Phase 1A Test

6.10.1.1 Purpose

The purpose of this modeling study was to predict the concentration and water saturation distributions after the injection of a non-reactive tracer into the ch1v and ch2v layers. Of the four tracers injected during the field experiment, only the injection of a non-sorbing Br^- solution was simulated because no other data were available at the time of this study.

6.10.1.2 Procedure and Layout

A schematic of the borehole layout in the Phase 1A test is shown in Figure VI.1 (see Attachment VI). The layout does not include distances because these were unavailable at the time of preparation of this report. The test involved injection rates of 10 mL/hr into boreholes 1 and 3 (located in the

ch1v layer of the CHn unit), and of 1 mL/hr into boreholes 2 and 4 (located in the ch2v layer of the CHn unit). Injections were conducted continuously for 285 days, starting April 2, 1998.

Mineback of the Phase1A test block took place from January 15, 1999 to March 3, 1999. During mineback, successive layers were being removed, digital photographs under visible and ultraviolet light were taken, rock samples were collected by augering, and the exposed plane was accurately surveyed. When the tracer distribution and moisture content data from this experiment become available, they will be used for the calibration of the simulation results discussed in the present section.

Borehole 3 is located in the ch1v layer and is about 20 cm above the ch1v-ch2v interface. Borehole 1 is also located in the ch1v layer, but is further away from the interface. Injection into boreholes 2 and 4 is not expected to be strongly affected by the interface because of the very low injection rates into these boreholes.

6.10.1.3 Conceptual and Numerical Model

For this 3-D numerical study, the underlying geologic model considered a homogeneous, unfractured rock matrix with the properties of the ch1v and ch2v layers. The initial saturation distribution was based on *in situ* measurements (Table 6.9). The T2R3D code (V1.4, STN: 10006-1.4-00, see Section 3; Wu et al. 1996) was used for the simulation. Each borehole was simulated separately. The DTN of the input and output files for this simulation set is DTN LB991220140160.010. Table 6.9 includes the input parameters for the Phase 1A simulations.

Three different sources of flow parameters were used in the simulations (Table 6.9): Source 1 (hereafter referred to as S1A) was the UZ99 calibrated flow parameter set; Source 2 (referred to as S2A) was hydraulic property measurements from field-collected samples, and Source 3 (referred to as S3A) was the parameter set included in DTN: LB971212001254.001 (Table 6.9).

6.10.1.4 Simulation Results and Discussion

Figure VI.2 shows the distribution of the nonsorbing Br^- tracer on a 2-D cross section (parallel to the face of the rock surface) that includes the injection point ($y = 1.5$ m) corresponding to borehole 3 at $t = 285$ days. These results are obtained using the S1A parameters for both the ch1v and ch2v layers (see Table 6.9). The observed flattening of tracer distribution occurs as the tracer moves preferentially laterally along the interface.

When the S2A properties are used, the Br^- distribution on the same plane (Figure VI.3) follows a different, far more uniform pattern, which exhibits little flattening. This indicates that the permeability from core measurements is significantly smaller than that suggested from the S1A parameters. Predictions using the S3A parameters (see Table 6.9) are similar to the results from the run with S1A parameters because the hydraulic and transport properties are not very different in the two data sets (figure not shown, see Scientific Notebook YMP-LBNL-GSB-QH-1, p. 31-33).

Table 6.9. Input parameters for modeling the Phase 1A test of Busted Butte

Parameters	Source
Test design, test implementation, tracers, injection rates, test duration, etc.	CRWMS M&O 1999e, Section 6.8
3-D grid (X:Y:Z = 3 m:3m:3m)	SN: YMP-LBNL-GSB-QH-1, pages 5-35
Data set S1A: UZ99 calibrated flow parameters in matrix of the ch1v and ch2v layers (porosity ϕ , permeability k , vanGenuchten α and m parameters, residual saturation S_r , water saturation S_w , rock grain density ρ_s , tortuosity coefficient τ)	DTN: LB997141233129.001
Data set S2A: Matrix porosity ϕ , permeability k , initial water saturation S_w , rock grain density ρ_s of the field samples	DTNs: GS990308312242.007 and GS990708312242.008
Data set S3A: VA97 calibrated flow parameters in matrix of the ch1v and ch2v layers (porosity ϕ , permeability k , vanGenuchten α and m parameters, residual saturation S_r , water saturation S_w , rock grain density ρ_s , tortuosity coefficient τ)	DTN: LB971212001254.001
Longitudinal dispersivity $\alpha_L = 0.1$ m and transverse dispersivity $\alpha_T = 0.01$ m in the matrix	Scientific judgement in the absence of available data
Br^- sorption coefficient $K_d = 0 \text{ m}^3/\text{kg}$	DTN: LB991220140160.019 (Boggs et al. 1992, p. 3285)
Br^- diffusion coefficient $D_0 = 2.03 \times 10^{-9} \text{ m}^2/\text{s}$	DTN: LB991220140160.019 (Cussler 1984, p. 147)
Percolation flux: 1 mm/yr	Scientific judgement

The Br^- distribution in boreholes 1 and 4 for the S1A parameters (see Table 6.9) is shown in Figures VI.4 and VI.5, respectively. Both distributions exhibit similar symmetric, near-circular patterns, and indicate the dominance of capillary over gravitational forces. The extent of the tracer distribution is more limited in borehole 4 because of the smaller injection rate (1 mL/hr vs. 10 mL/hr in Borehole 1).

6.10.2 Numerical Simulation of the Phase 1B Test

6.10.2.1 Purpose

The purpose of this modeling study was to predict the breakthrough curves of three tracers injected into the tsw39 layer. The three tracers were Br^- (nonsorbing), 2,6-difluorobenzoate (2,6-DFBA, nonsorbing, used to evaluate possible molecular size effects on transport) and Li^+ (sorbing). Two parameter sets were used in the simulations: the S1A data set (see Section 6.10.1.1) and a modified S2B set, which included porosity and permeability data from core measurements, and all other parameters from the S1A data set (because no other measured parameters were available). Of the five tracers injected during the field experiment, only the three for which reliable data were available were simulated.

6.10.2.2 Procedure and Layout

In the Phase 1B field test, the tracers were injected into the lower portion of the Topopah Spring basal vitrophyre (Ttpv2 in the lithostratigraphic units; tsw39 in the UZ99 layers of the hydrogeologic units), which is a relatively low-permeability fractured rock. The design, configuration, and important dimensions of the Phase 1B test are shown in Figure VI.6, which depicts the injection/collection pair of boreholes 5 and 6. The layout of boreholes 7 and 8 is identical, and is not shown.

Two such pairs were involved in the experiment, i.e., (a) boreholes 5 and 6, and (b) boreholes 7 and 8. The tracer solution was injected at the location $x = 1.30$ m from the rock surface into boreholes 5 and 7 at a rate of 10 mL/hr and 1 mL/hr, respectively. Injections began on May 12, 1998, and ceased on November 9, 1998 (borehole 5) and November 18, 1998 (borehole 7). Water samples from the collection boreholes 6 and 8 were obtained and analyzed regularly during the injection period. A detailed description of the experiment can be found in CRWMS M&O (1999e, Section 6.8).

6.10.2.3 Conceptual and Numerical Model

The input parameters of flow and transport for the simulation of the Phase 1B test are listed in Table 6.10. For this 3-D numerical study, the geologic model treated the domain as a homogeneous, unfractured rock matrix. Although this geologic layer is known to have fractures, the use of unfractured rock matrix as the domain model in the simulation was made possible by the system behavior during the injections, which did not show evidence of fracture flow. The DTN of the input and output files for this simulation is LB991220140160.010.

6.10.2.4 Simulation Results and Discussion

Breakthrough data (measured in borehole 6) for the three tracers discussed in Section 6.10.2.1 can be found in DTN: LA9909WS831372.001 and DTN: LA9909WS831372.002. As expected, peak concentrations are observed at $x = 1.3$ m from the rock face, i.e., directly beneath the injection point in borehole 5.

Table 6.10. Input parameters for modeling the Phase 1B test of Busted Butte

Parameters	Source
Test design, test implementation, tracers applied, injection rates, sample collection duration, test duration, measured tracer concentration, etc.	CRWMSM&O 1999e, Section 6.8, and DTNs: LA9909WS831372.001 and LA9909WS831372.002
3-D grid ($X \times Y \times Z = 4 \text{ m} \times 2 \text{ m} \times 2 \text{ m}$)	SN: YMP-LBNL-GSB-QH-1, pp. 15-35
S1A data set: UZ99 calibrated flow parameters in matrix of the ch1v and ch2v layers (porosity ϕ , permeability k , van Genuchten α and m parameters, residual saturation S_r , water saturation S_w , rock grain density ρ_s , tortuosity coefficient τ)	DTN: LB997141233129.001
S2B data set: Matrix porosity ϕ , permeability k , initial water saturation S_w of the field samples	DTNs: GS990308312242.007 and GS990708312242.008
Longitudinal dispersivity $\alpha_L = 0.1 \text{ m}$ and transverse dispersivity $\alpha_T = 0.01 \text{ m}$ in the matrix	Scientific judgement in the absence of available data
Sorption coefficient of Br^- and 2,6-DFBA $K_d = 0 \text{ m}^3/\text{kg}$	DTN: LB991220140160.019 (Boggs et al. 1992, p. 3285, Benson and Bowman 1994, pp. 1123-1129)
Sorption coefficient of Li^+ $K_d = 0.001 \text{ m}^3/\text{kg}$	CRWMS M&O (1999e, Table 37)
Br^- diffusion coefficient $D_0 = 2.08 \times 10^{-9} \text{ m}^2/\text{s}$ Li^+ diffusion coefficient $D_0 = 1.03 \times 10^{-9} \text{ m}^2/\text{s}$	DTN: LB991220140160.019 (Cussler 1984, p. 147)
2,6-DFBA diffusion coefficient $D_0 = 7.6 \times 10^{-10} \text{ m}^2/\text{s}$	DTN: LB991220140160.019 (Benson and Bowman 1994, p. 1125)
Percolation flux: 1 mm/yr	Scientific judgement

No tracer breakthrough was detected in collection borehole 8 (CRWMS M&O 1999e, Section 6.8) because of the small (1 mL/hr) injection rate into the overlying borehole 7. The measured concentrations indicated transport consistent with flow in the matrix (rather than in the fractures), which appeared to imbibe the injected solution quickly.

The predicted Br^- breakthrough curves for the S1A and the S2B data sets at several locations in borehole 6 are shown in Figures VI.7 and VI.8, respectively. Because of symmetry about the $x = 1.3 \text{ m}$ axis, only the curves at $x \geq 1.3 \text{ m}$ are shown in the figures. The figures show the

predicted relative pore-water tracer concentrations over time in the collection pads in borehole 6. Visual inspection indicates that these results are in good agreement with the measured data (CRWMS M&O 1999e, Section 6.8.5.3.2).

The differences between the two sets of Br^- curves and the even larger differences between the predicted saturation profiles (Figures VI.9 and VI.10 for the S1A and S2B data sets, respectively), were attributed to the significant differences in the values of porosity and permeability between the two data sets. For example, the S2B (measured) permeability of $3.06 \times 10^{-14} \text{ m}^2$ was significantly larger than the S1A value of $5.46 \times 10^{-19} \text{ m}^2$.

The effect of solute size on dispersion can be evaluated by comparing the predicted breakthrough curves of 2,6-DFBA (Figure VI.11) and of Br^- (Figure VI.7) in borehole 6. The only difference between the two simulations was the value of the molecular diffusion coefficient D_0 , which was $7.6 \times 10^{-10} \text{ m}^2/\text{s}$ for the large 2,6-DFBA molecule, and $2.08 \times 10^{-9} \text{ m}^2/\text{s}$ for Br^- (Benson and Bowman 1994, p. 1125; Cussler 1984, p. 147). The higher relative concentrations of 2,6-DFBA at the same observation times resulted from lower diffusion into the matrix, as this process was hampered by the larger molecular size of 2,6-DFBA. These simulation results are consistent with laboratory studies of ^3H and pentafluorobenzoate (PFBA) transport in columns (Hu and Brusseau 1994).

The breakthrough curves of the sorbing Li^+ tracer follow a distinctively different pattern. This is caused by sorption, which results in maximum relative concentrations (in borehole 6) significantly lower than the ones observed in the non-sorbing Br^- and 2,6-DFBA. Predictions based on the measured $K_d = 1 \text{ mL/g}$ (CRWMS M&O 1999e, Table 36) in Figure VI.12 are consistently higher than the measured concentrations in CRWMS M&O (1999e, Section 6.8.5.3). In the same section, it is indicated that the Li^+ K_d measurements are preliminary, and that more thorough sorption measurements are in progress. When K_d is increased to 2 mL/g , predictions are consistent with measurements (Figure VI.13).

6.11 3-D TRANSPORT SIMULATIONS

In this section we study radionuclide transport in the entire Yucca Mountain system using large-scale 3-D grids. The development and features of the 3-D grids for this numerical modeling effort are documented in CRWMS M&O (1999h, Section 6) and further discussed in CRWMS M&O (1999d, Section 6.6).

6.11.1 Climatic Conditions

The three climatic scenarios investigated here are identical to those discussed in CRWMS M&O (1999d, Sections 6.1 and 6.6): present-day, monsoon and glacial. For each climatic scenario, a high, mean and low infiltration case was studied. The annual infiltration rates corresponding to each of the nine climatic cases are listed in Table 6.11, which also lists the DTN numbers of the data files involved in the EOS9 (V1.4, STN: 10007-1.4-00) flow simulations of each climatic case in CRWMS M&O (1999d, Section 6.6).

6.11.2 Grids and Flow Simulations

The input data files of the EOS9 (V1.4, STN: 10007-1.4-00, see Section 3) simulations listed in Table 6.11 were slightly modified. The modification involved a very minor rearrangement of the element order number, which moved the elements corresponding to the location of the potential repository near the bottom of the element file, and immediately above the top and bottom boundary elements of the 3-D domain. This modification was made because the release rate in the ensuing EOS9nT simulations was considered constant over time, a condition which necessitated treating the repository elements as internal boundary elements with time-invariant flow and concentration profiles. Moving them to the bottom of the element file made use of the ability of the TOUGH2 family of codes to treat them (after a small change discussed at the end of this section) as inactive elements (i.e., elements that have time-invariant properties and conditions and do not contribute to mass and energy balances).

Using the modified input files, all the EOS9 (V1.4, STN: 10007-1.4-00) simulations listed in Table 6.11 were repeated to obtain the steady-state flow fields to be used in the EOS9nT simulations. The DTNs for the EOS9 input (modified) and output files is LB991220140160.011. A 2-D (plan view) of the grid at the potential repository level is shown in Figure 6.11.1.

After each EOS9 simulation, the output files SAVE were compared to those from the simulations using the unmodified grids to confirm that they were identical. Note that EOS9nT (V1.0, STN: 110065-1.11MEOS9NTV1.0-00) shares identical flow solution routines with EOS9, and confirmatory tests confirmed the identity of the flow solutions predicted by both EOS9 and EOS9nT

Table 6.11. Percolation fluxes (mm/year) for different climatic regimes and the corresponding EOS9 flow simulations used in the 3-D site scale radionuclide transport studies*

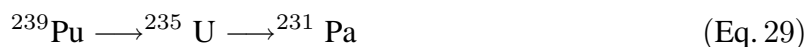
Value	Present-Day Infiltration	Glacial Infiltration	Monsoon Infiltration
Lower bound	1.2013 mm/yr DTN: LB990801233129.001	2.4042 mm/yr DTN: LB990801233129.007	4.5956 mm/yr DTN: LB990801233129.013
Mean	4.5956 mm/yr DTN: LB990801233129.003	17.9614 mm/yr DTN: LB990801233129.009	12.3589 mm/yr DTN: LB990801233129.015
Upper bound	11.2408 mm/yr DTN: LB990801233129.005	33.5185 mm/yr DTN: LB990801233129.011	20.1222 mm/yr DTN: LB990801233129.017

*: The percolation fluxes and the corresponding flow fields are from the DTNs at the same table location.

(YMP-LBNL-GJM-3, p. 742). It was decided, however, to use the EOS9 module in the TOUGH2 flow simulations to ensure complete compatibility with the results in CRWMS M&O (1999d, Section 6.6). For the EOS9nT simulations, the 3-D grids from the EOS9 simulations were used, after making the volume of the first repository element negative. This rendered all the following repository elements and the top and bottom boundary elements inactive, thus maintaining their properties and conditions constant throughout the simulations.

6.11.3 Radionuclides Considered

Three radionuclides are considered: ^{99}Tc (non sorbing), ^{237}Np (moderately sorbing) and ^{239}Pu (strongly sorbing). Their properties are listed in Table 6.5. The radionuclides are released at the gridblocks corresponding to the location of the potential repository. For the large scale simulations, all the important members in the decay chains of ^{237}Np and ^{239}Pu were considered, according to the decay equations (Pigford et al. 1980)



Note that only the most important members of the radioactive chain members are included in these equations, which omit daughters with short half lives. The properties of the daughters of ^{237}Np and ^{239}Pu are listed in Table 6.12. As alpha is the decay mode of all the members in the ^{237}Np and ^{239}Pu chains, $\zeta = 0$ (Equation 27) in all the simulations because the daughters are ejected from grain surfaces due to recoil (Faure 1977, pp. 288-289).

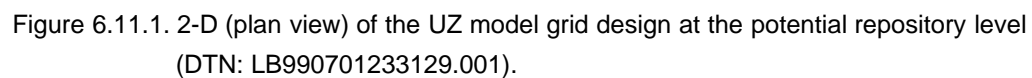


Table 6.12. Properties of the daughter products of radioactive decay in the transport simulations

Radionuclide	D_0 (m ² /s)*	$T_{1/2}$ (years) [†]	$\lambda = \frac{\ln 2}{T_{1/2}}$ (s)	Decay mode [†]
²³³ U	7.123×10^{-10}	1.59×10^5	1.3814×10^{-13}	α
²²⁹ Th	7.123×10^{-10}	7.90×10^3	2.7803×10^{-12}	α
²³⁵ U	6.08×10^{-10}	7.08×10^8	3.1023×10^{-17}	α
²³¹ Pa	6.08×10^{-10}	3.25×10^4	6.7583×10^{-13}	α

*: DTN: LB991220140160.019

†: From Lide (1992, pp. 11-122, 11-123, 11-124)

6.11.4 Important Geologic Features

As will be clearly shown in the ensuing Sections 6.12 through 6.16, the role of faults in the 3-D site-scale transport model is very important because faults provide fast pathways for the radionuclide migration to the water table. In the EOS9 and EOS9nT simulations, the faults are represented as thin vertical domains characterized by large permeabilities. More detailed description of the faults, their properties and their role in water flow can be found in CRWMS M&O (1999d, Sections 6.3 and 6.6), CRWMS M&O (2000d, Sections 6.4) and CRWMS M&O (2000e, Sections 6.2 and 6.3).

6.11.5 Transport Simulation Options

All the 3-D simulations were conducted by using the De Hoog et al. (1982) implementation of the Laplace transform formulation of EOS9nT. This was selected because of the speed and accuracy of this formulation, its ability to provide information over the whole spectrum of the simulation period, and its ability to drastically reduce numerical diffusion. The resulting matrices were very well behaved, requiring no more than 10-15 conjugate gradient iterations to reduce residuals to below the 10^{-11} level in a matrix of order of about 200,000. Thus, simulations were very fast and efficient, requiring 1,800-2,200 seconds of execution time to cover a simulation period of 1,000,000 years.

EOS9nT allows the simultaneous solution of the concentration profiles of any number of radionuclides. Thus, all three parents (⁹⁹Tc, ²³⁷Np, ²³⁹Pu) were considered simultaneously in the runs. Similarly, and exploiting the fact that EOS9nT allows the tracking of any daughter products, the solutions for each of the parent radionuclides and its two daughters in the decay Equations 28 and 29 were obtained simultaneously. In the perched water model# 2 and the no-perched water models, five radionuclides (⁹⁹Tc, ²³⁷Np, ²³⁹Pu, ²³⁵U and ²³¹Pa) were considered together.

6.12 3-D SIMULATIONS OF ^{99}Tc TRANSPORT

In this section we investigate the transport of ^{99}Tc by means of EOS9nT 3-D site-scale simulations representing the entire UZ system of Yucca Mountain. Section 6.12 includes four subsections.

In Section 6.12.1 we address the issue of the perched water model assumed in the simulations. In Section 6.12.2 we discuss the transport of the non-sorbing ^{99}Tc for three levels of present-day infiltration. The results of this study are shown in Figures 6.12.1 to 6.12.17. In Section 6.12.3 we study the transport of ^{99}Tc for three levels of monsoon infiltration (Figure 6.12.18). Finally, in Section 6.12.4 we study the transport of ^{99}Tc for three levels of glacial infiltration (Figure 6.12.19).

6.12.1 Perched-Water Model

The grids, flow fields and conditions discussed in Section 6.11.2 correspond to the #1 conceptual model of perched water (CRWMS M&O 1999d, Section 6.2). This is the permeability barrier model, which uses the calibrated perched water parameters for fractures and matrix in the northern part of the model domain, and modified property layers (including the tsw38, tsw39, ch1z and ch2z layers) where the lower basal vitrophyre of the TSw is above the zeolites of the CHn. A detailed discussion of this perched water model can be found in CRWMS M&O (1999d, Section 6.2).

6.12.2 ^{99}Tc Transport Under Present-Day Infiltration

The DTNs of the input and output files for the three present-day infiltration scenarios are listed in Table 6.13. The input parameters used in the EOS9nT simulations of 3-D transport of the nonsorbing ^{99}Tc are listed in Table 6.14.

6.12.2.1 Breakthrough Curves

As the ^{99}Tc concentration in the potential repository and in the bottom boundary elements (corresponding to the water table) remain constant over time, the breakthrough concept was based on the normalized release rate R , which is defined as

$$R = \frac{\text{Mass release rate at the groundwater boundary } [MT^{-1}]}{\text{Mass release rate at the potential repository } [MT^{-1}]}$$

The normalized release rate at the potential repository in Figure 6.12.1 shows a very strong dependence on the infiltration regime.

As the infiltration rate increases from low to mean, the t_{10} time, defined as the time at which $R = 0.1$, decreases from about 10,000 years to about 300 years. The t_{50} , defined as the time at which

Table 6.13. DTNs of input and output files of the 3-D site-scale transport simulations

Item	DTN
EOS9 input & output files for 3-D UZ flow simulations (3 perched-water models, 3 infiltration regimes)	LB991220140160.011
EOS9nT input & output files for the 3-D transport simulations of radioactive solutes (#1 perched-water model, present-day infiltration)	LB991220140160.012
EOS9nT input & output files for the 3-D transport simulations of radioactive solutes (#1 perched-water model, monsoon infiltration)	LB991220140160.013
EOS9nT input & output files for the 3-D transport simulations of radioactive solutes (#1 perched-water model, glacial infiltration)	LB991220140160.014
EOS9nT input & output files for the 3-D transport simulations of radioactive solutes (#2 perched-water model, present-day infiltration)	LB991220140160.015
EOS9nT input & output files for the 3-D transport simulations of radioactive solutes (no-perched-water model, present-day infiltration)	LB991220140160.016
EOS9nT input & output files for the 3-D transport simulations of radioactive colloids (#1 perched-water model, present-day infiltration)	LB991220140160.017

$R=0.5$, decreases from about 45,000 years to about 4,000 years. Further increase of infiltration to high present-day levels leads to a decrease of t_{10} to about 45 years, and of t_{50} to 1,000 years. The t_{10} and t_{50} of ^{99}Tc , ^{237}Np and ^{239}Pu for three levels of the three climatic scenarios (present-day, monsoon and glacial) are listed in Table 6.15. It should be kept in mind that the term R is relative, and these findings are only important if the magnitude of the release rate at the potential repository becomes significant.

Figure 6.12.1 also shows that the maximum attainable R increases with the infiltration rate. This is expected because lower infiltration results in lower velocities and longer travel times, thus higher radioactive decay.

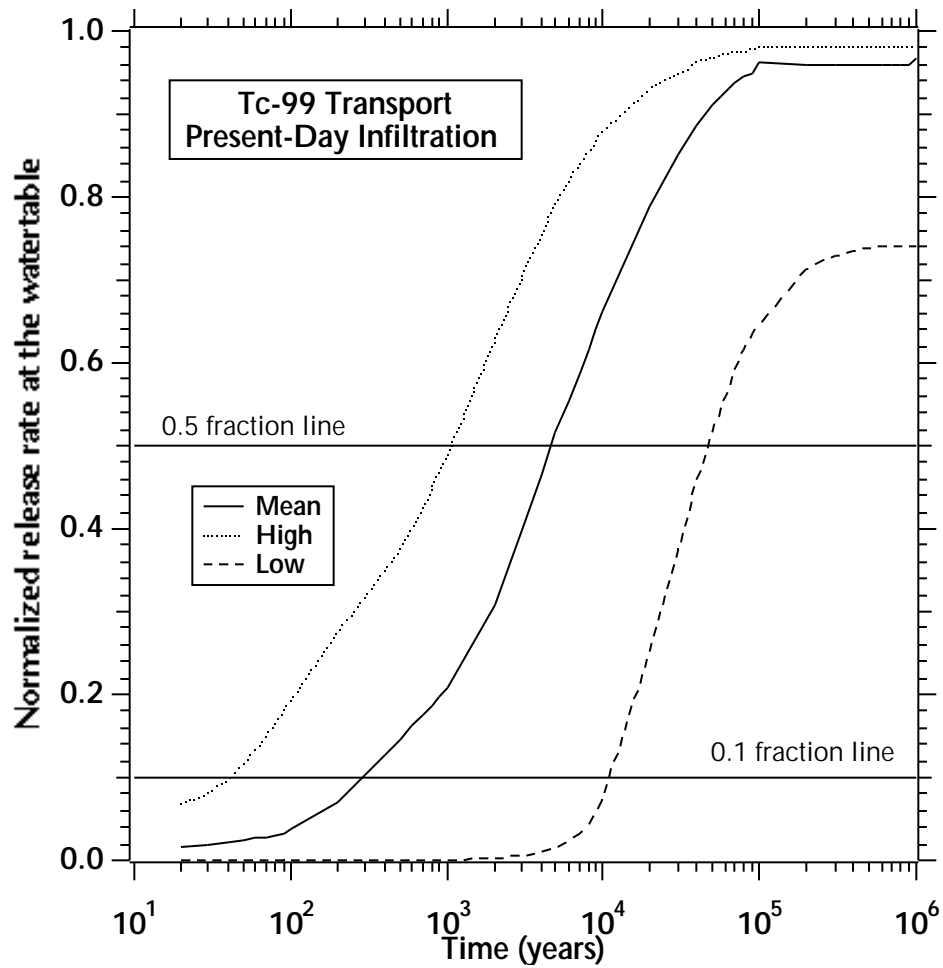


Figure 6.12.1. Normalized relative release R of ^{99}Tc at the water table for varying present-day climatic scenarios (DTN: LB991220140160.012, data submitted with this AMR)

Table 6.14. Input parameters for the EOS9nT 3-D site-scale simulations of solute transport (#1 perched-water model)

Parameters	Source
Transfer coefficient $K_i = 1$	Conventionally used value
Tortuosity $\tau \simeq \phi$	DTN: LB991220140160.019 and DTN: LAIT831341AQ96.001, Grathwohl (1998, pp. 28–35), Farrell and Reinhard (1994, p. 64)
Longitudinal dispersivity $\alpha_L = 1$ m in the fractures, 0.1 m in the matrix	Scientific judgement in the absence of available data
Properties and characteristics of the geologic units, steady-state pressures, water saturations and flow fields	Table 6.11
Sorption coefficients K_d for Tc, Np, Pu, U, Th, Pa	DTN: LB991220140160.019 and DTN: LAIT831341AQ96.001
Fracture porosity $\phi = 0.99$	A reasonable estimate that allows limited sorption in the fractures.

6.12.2.2 Transport-Controlling Features

In the study of the radionuclide transport, we use the relative mass fraction X_R , defined as

$$X_R = \frac{X}{X_0} = \frac{C}{C_0} = C_R$$

where the subscript 0 denotes the value of the subscripted parameter in the water released from the potential repository. For mean present-day infiltration, the distribution of the ^{99}Tc X_R in the aqueous phase in the fractures and in the matrix in the gridblocks directly above the TSw-CHn interface (i.e., at the bottom of the TSw, corresponding to the tsw39 layer) is given in Figures 6.12.2 through 6.12.9 for $t = 100, 1,000, 10,000$ and $100,000$ years. Note that the X_R distributions in Figures 6.12.2 through 6.12.9 do not correspond to a plan view from a horizontal cross section, but follow the uneven topography of the bottom of the tsw39 layer. The X_R distributions of ^{99}Tc in the aqueous phase in the fractures and in the matrix immediately above the water table at the same times are given in Figures 6.12.10 through 6.12.17.

From the inspection of these figures, it becomes apparent that transport in the RTM is both dominated and controlled by the faults. From the distribution of the fracture X_R at the bottom of the TSw at a time $t = 100$ years (Figure 6.12.2), it is evident that, immediately above the TSw-CHn interface

Table 6.15. Radionuclide travel times to the water table

Infiltration Level	^{99}Tc		^{237}Np		$^{239}\text{Pu} + ^{235}\text{U} + ^{231}\text{Pa}$	
	t_{10}	t_{50}	t_{10}	t_{50}	t_{10}	t_{50}
PD* Low	10,000	45,000	220,000	>1,000,000	600,000	>1,000,000
PD Mean	300	4,000	10,000	120,000	40,000	250,000
PD High	45	1,000	1,700	22,000	12,000	90,000
M [†] Low	920	3,500	17,000	70,000	60,000	280,000
M Mean	50	1,000	1,400	21,000	14,000	75,000
M High	25	400	650	9,000	8,500	50,000
G [‡] Low	2,200	9,000	40,000	200,000	105,000	1,000,000
G Mean	23	500	800	10,000	10,000	60,000
G High	10	160	260	2,000	5,100	38,000

*: PD = Present-day; [†]: M = Monsoon ; [‡]: G = Glacial

(i.e., in the tsw39 layer), Splay G of the Solitario Canyon fault is the main transport-facilitating feature. Once contamination reaches the interface, it moves primarily in an easterly direction, moving with the draining water that hugs the downward sloping (in this direction) low-permeability TSw-CHn interface. The importance of this fault as a transport conduit is confirmed by the X_R distribution in Figure 6.12.10. As shown in this figure, ^{99}Tc begins to register a faint signature at the water table in the general location of the Solitario Canyon Splay G at the relatively early time of $t = 100$ years.

The Ghost Dance fault splay identified in Figure 6.12.2 is the next most important transport-facilitating feature in the tsw39 layer, and is also important at the water table (Figure 6.12.10). It is remarkable that, though it facilitates downward migration, this fault as modeled appears to act as a barrier to the lateral migration of radionuclides. This is evidenced both at the bottom of the TSw (Figures 6.12.2 through 6.12.9), and also at the water table (Figures 6.12.12 through 6.12.17).

The Sundance fault and the Drill Hole Wash fault are also important transport-facilitating geologic features. The Drill Hole Wash fault appears to act as a barrier to lateral radionuclide migration across it, while providing pathways for relatively fast transport to the water table. Even at $t = 100,000$ years, very limited migration is observed across it in the tsw39 layer (Figures 6.12.8 and 6.12.9) and at the water table (Figures 6.12.16 and 6.12.17).

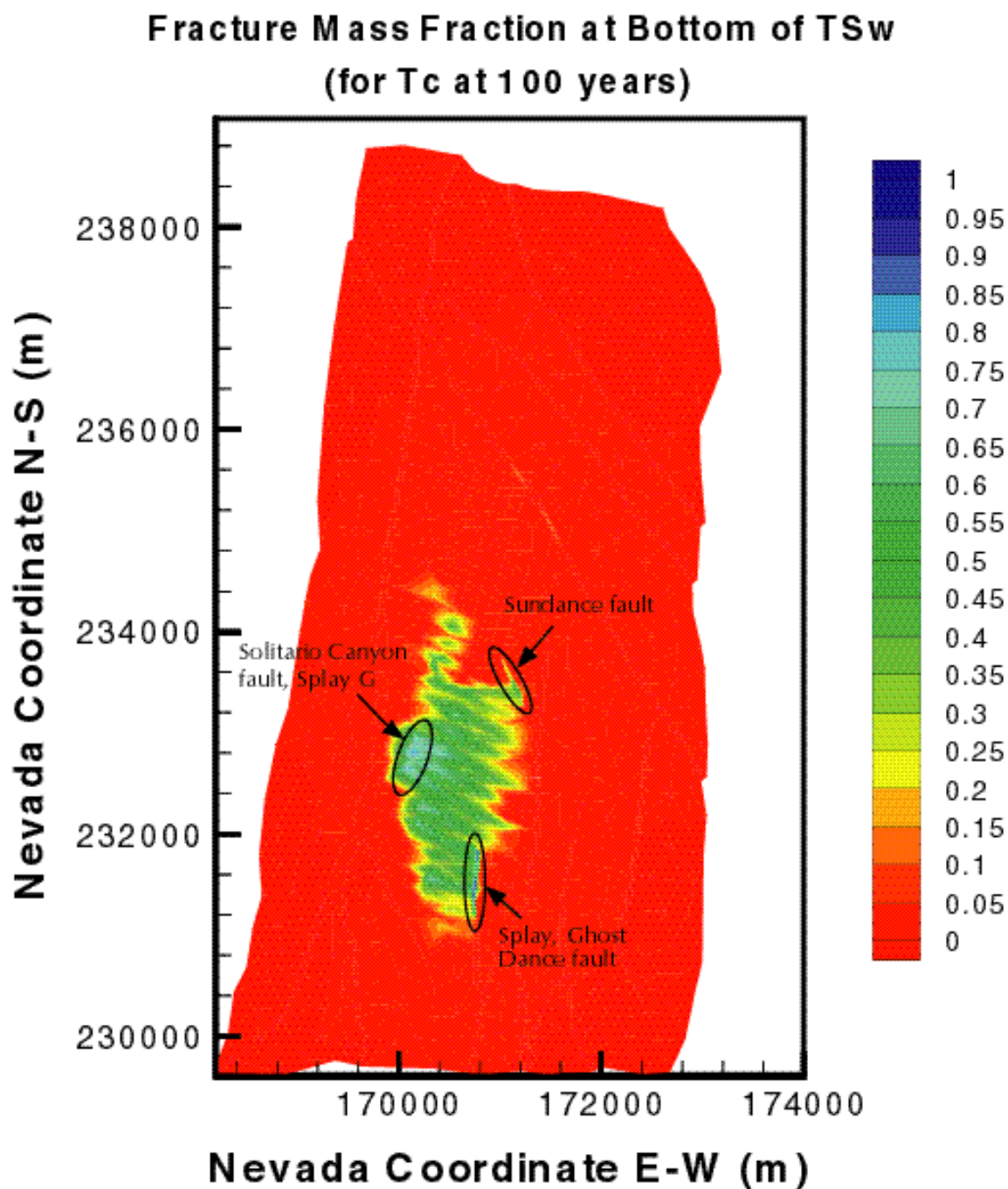


Figure 6.12.2. Distribution of the relative mass fraction X_R of ^{99}Tc in the fractures of the tsw39 layer at $t = 100$ years for mean present-day infiltration (DTN: LB991220140160.012, data submitted with this AMR).

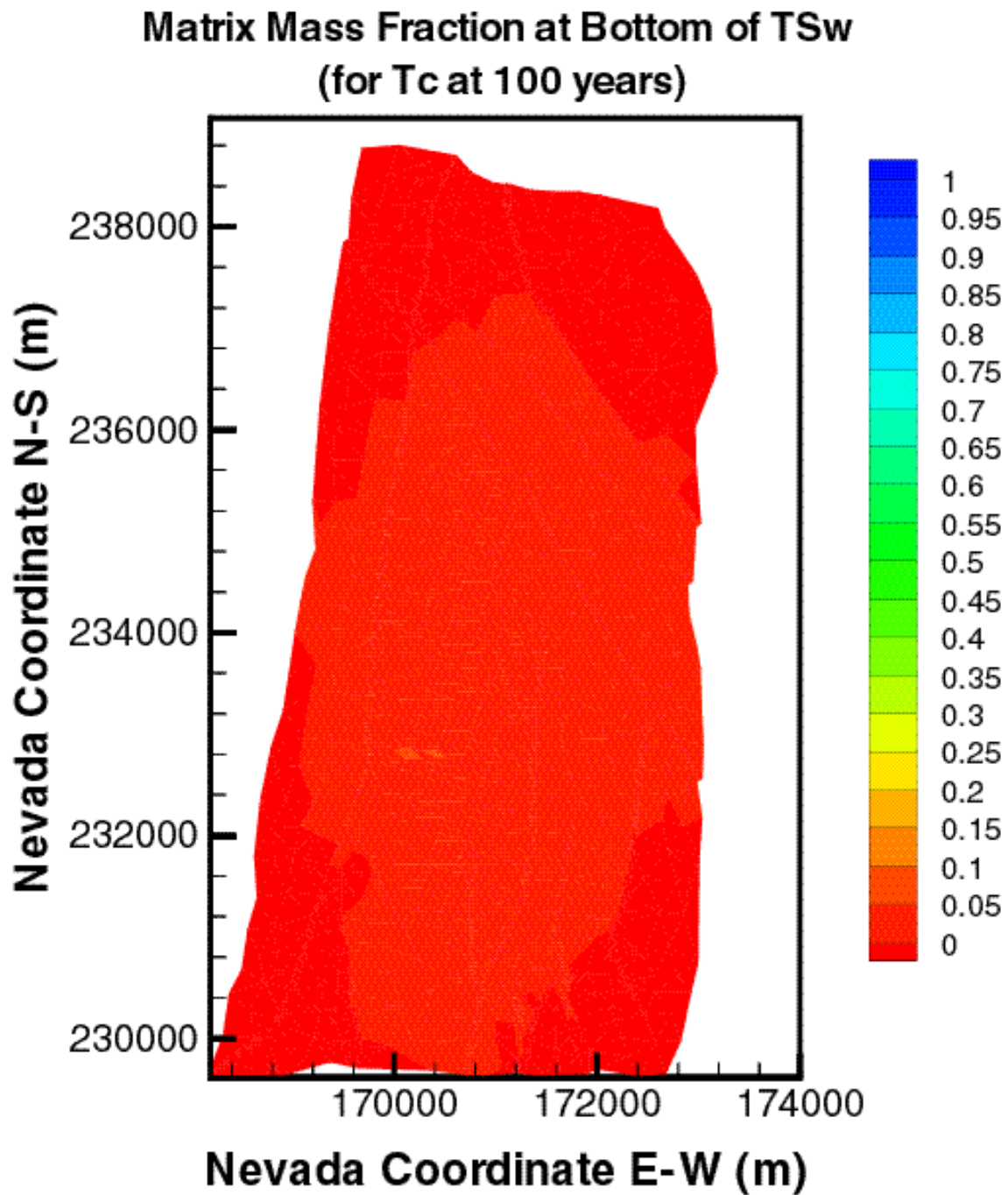


Figure 6.12.3. Distribution of the relative mass fraction X_R of ^{99}Tc in the matrix of the tsw39 layer at $t = 100$ years for mean present-day infiltration (DTN: LB991220140160.012, data submitted with this AMR).

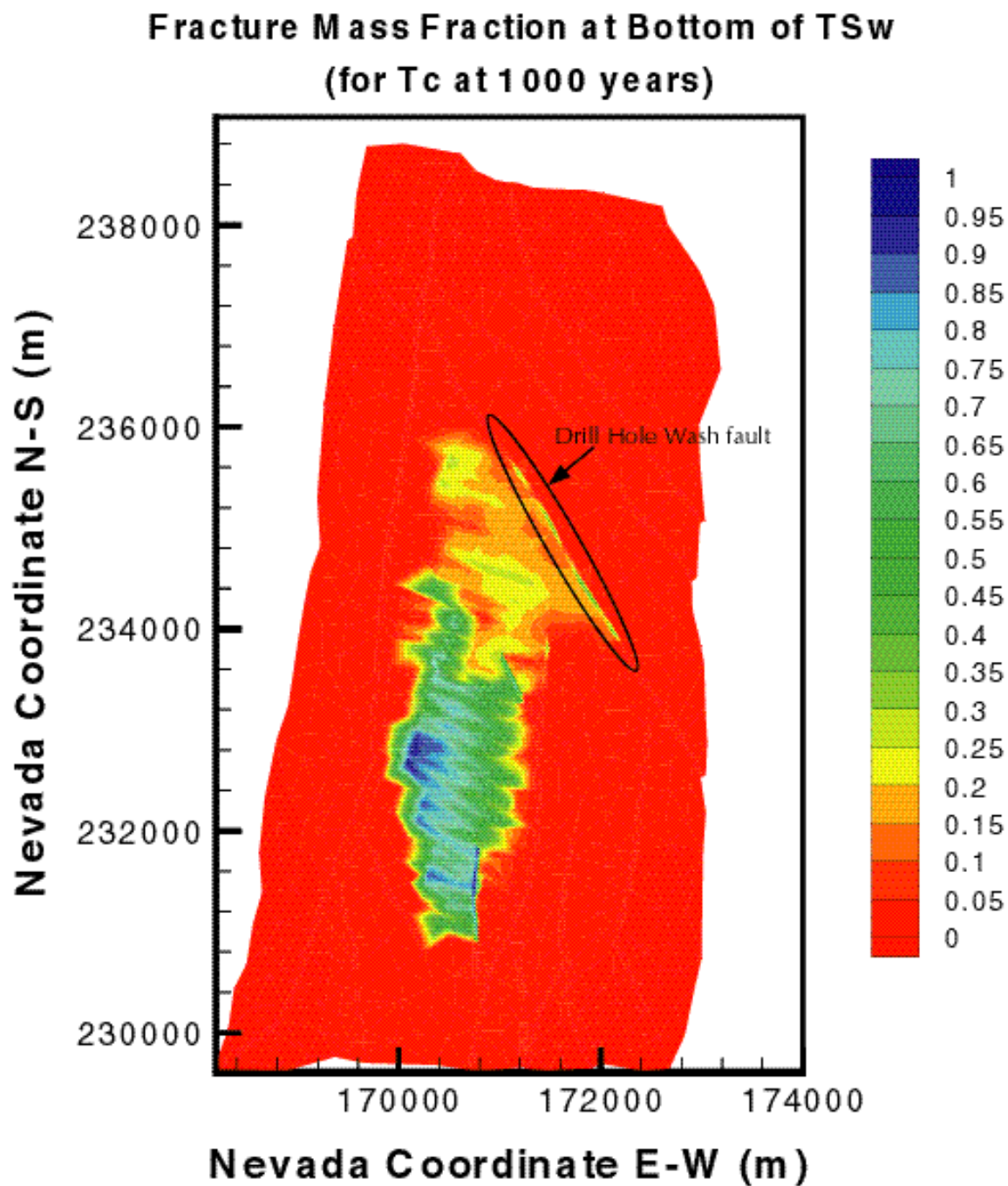


Figure 6.12.4. Distribution of the relative mass fraction X_R of ^{99}Tc in the fractures of the tsw39 layer at $t = 1,000$ years for mean present-day infiltration (DTN: LB991220140160.012, data submitted with this AMR).

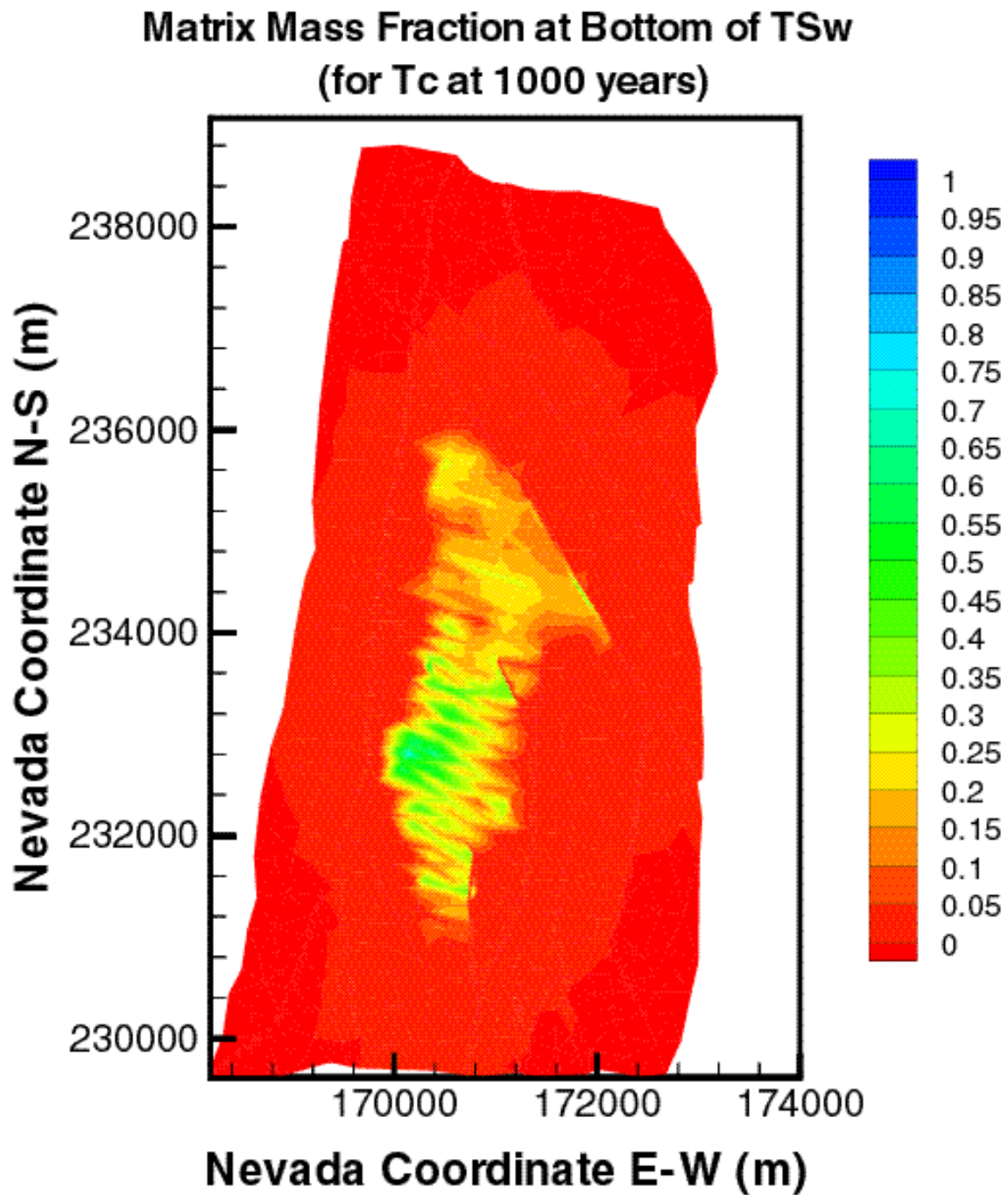


Figure 6.12.5. Distribution of the relative mass fraction X_R of ^{99}Tc in the matrix of the TSw layer at $t=1,000$ years for mean present-day infiltration (DTN: LB991220140160.012, data submitted with this AMR).

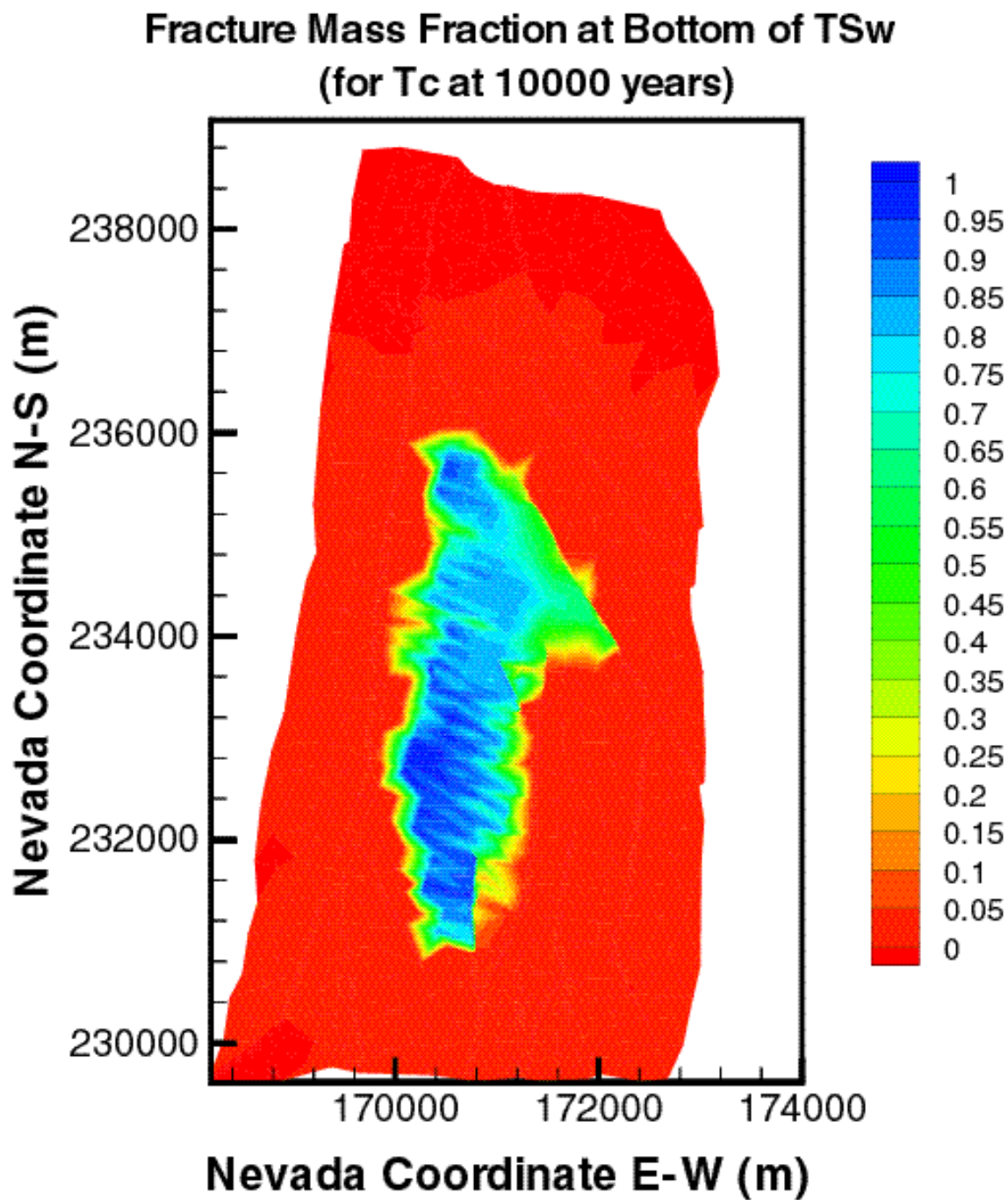


Figure 6.12.6. Distribution of the relative mass fraction X_R of ^{99}Tc in the fractures of the tsw39 layer at $t = 10,000$ years for mean present-day infiltration (DTN: LB991220140160.012, data submitted with this AMR).

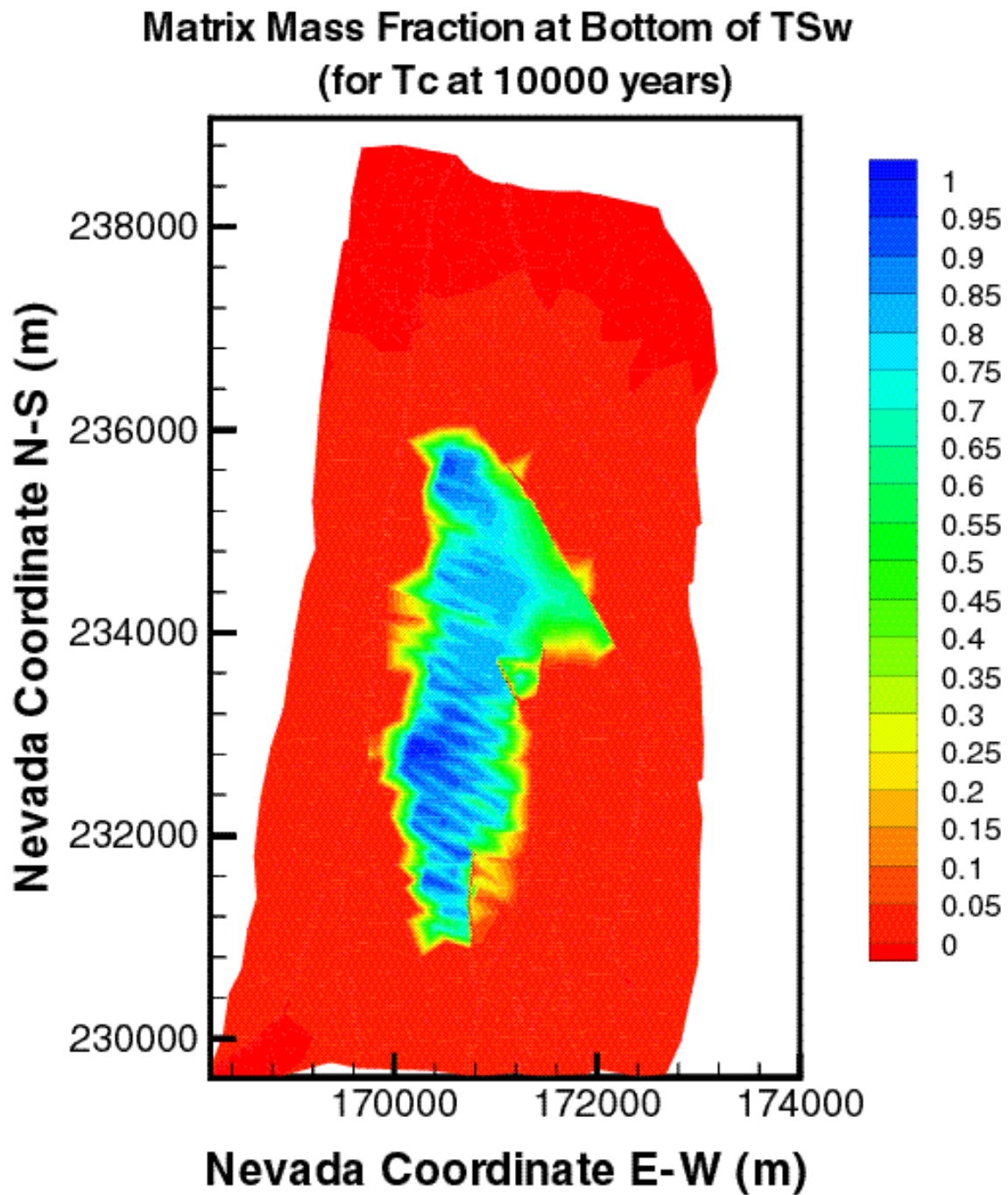


Figure 6.12.7. Distribution of the relative mass fraction X_R of ^{99}Tc in the matrix of the tsw39 layer at $t = 10,000$ years for mean present-day infiltration (DTN: LB991220140160.012, data submitted with this AMR).

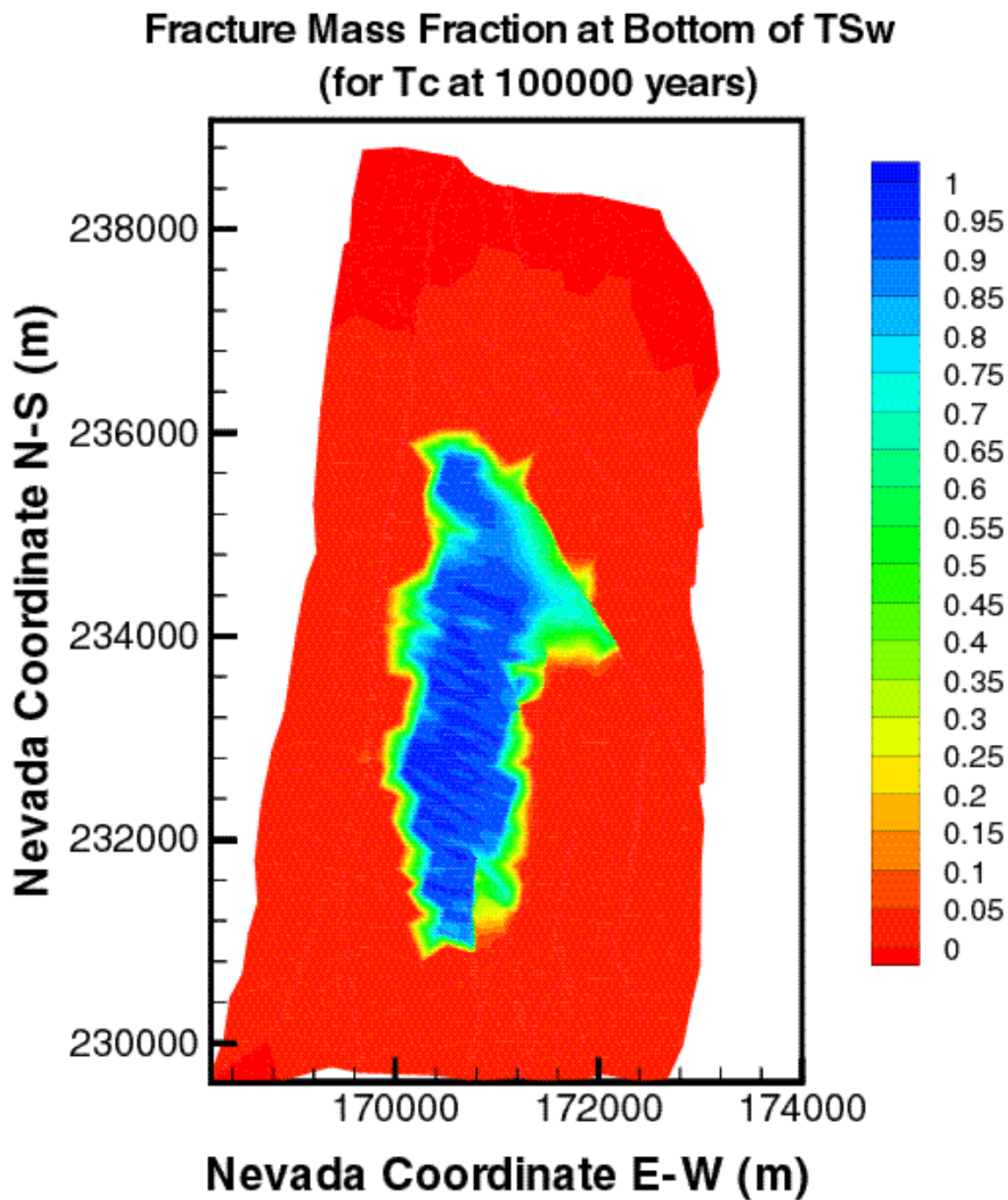


Figure 6.12.8. Distribution of the relative mass fraction X_R of ^{99}Tc in the fractures of the tsw39 layer at $t = 100,000$ years for mean present-day infiltration (DTN: LB991220140160.012, data submitted with this AMR).

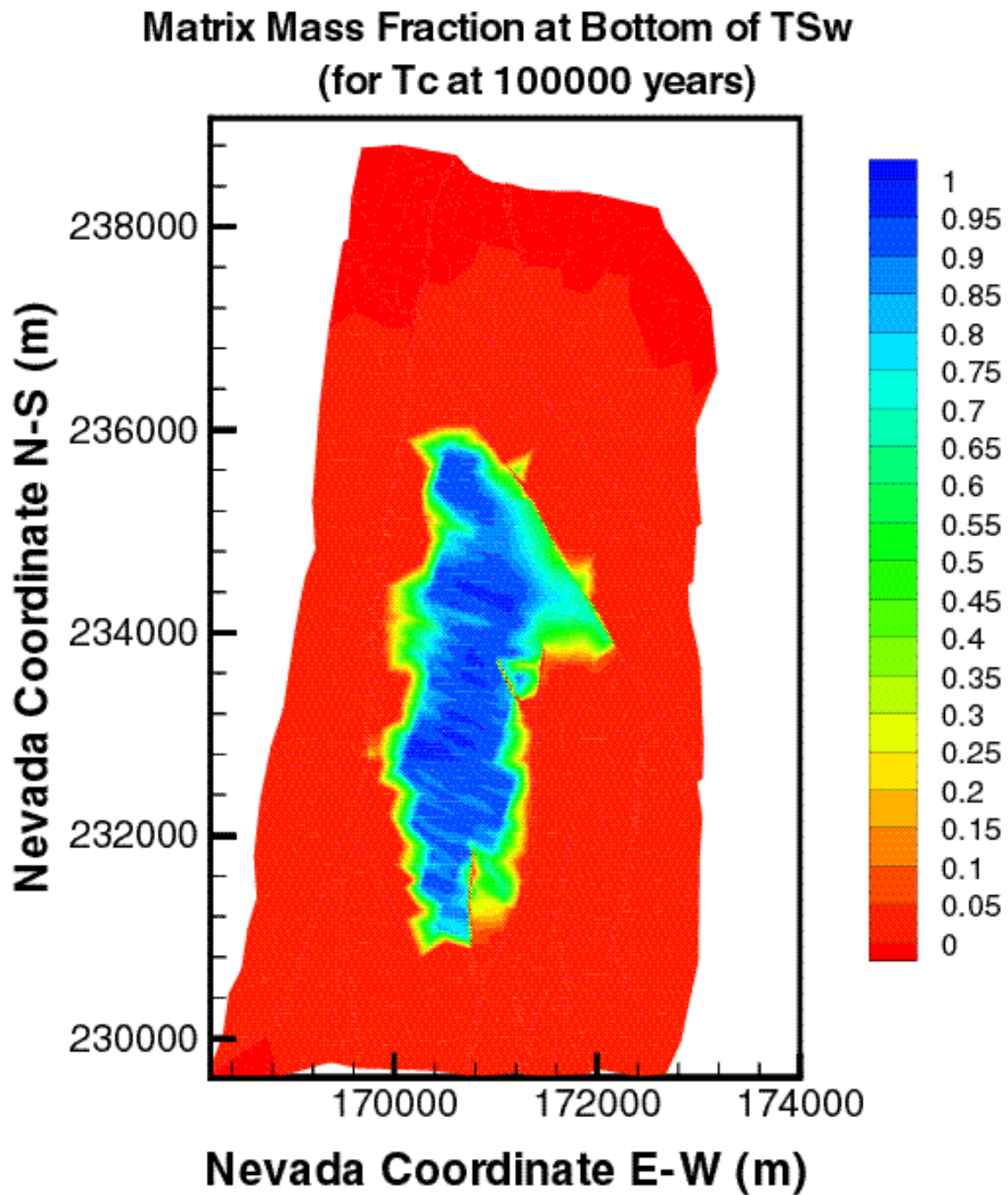


Figure 6.12.9. Distribution of the relative mass fraction X_R of ^{99}Tc in the matrix of the tsw39 layer at $t = 100,000$ years for mean present-day infiltration (DTN: LB991220140160.012, data submitted with this AMR).

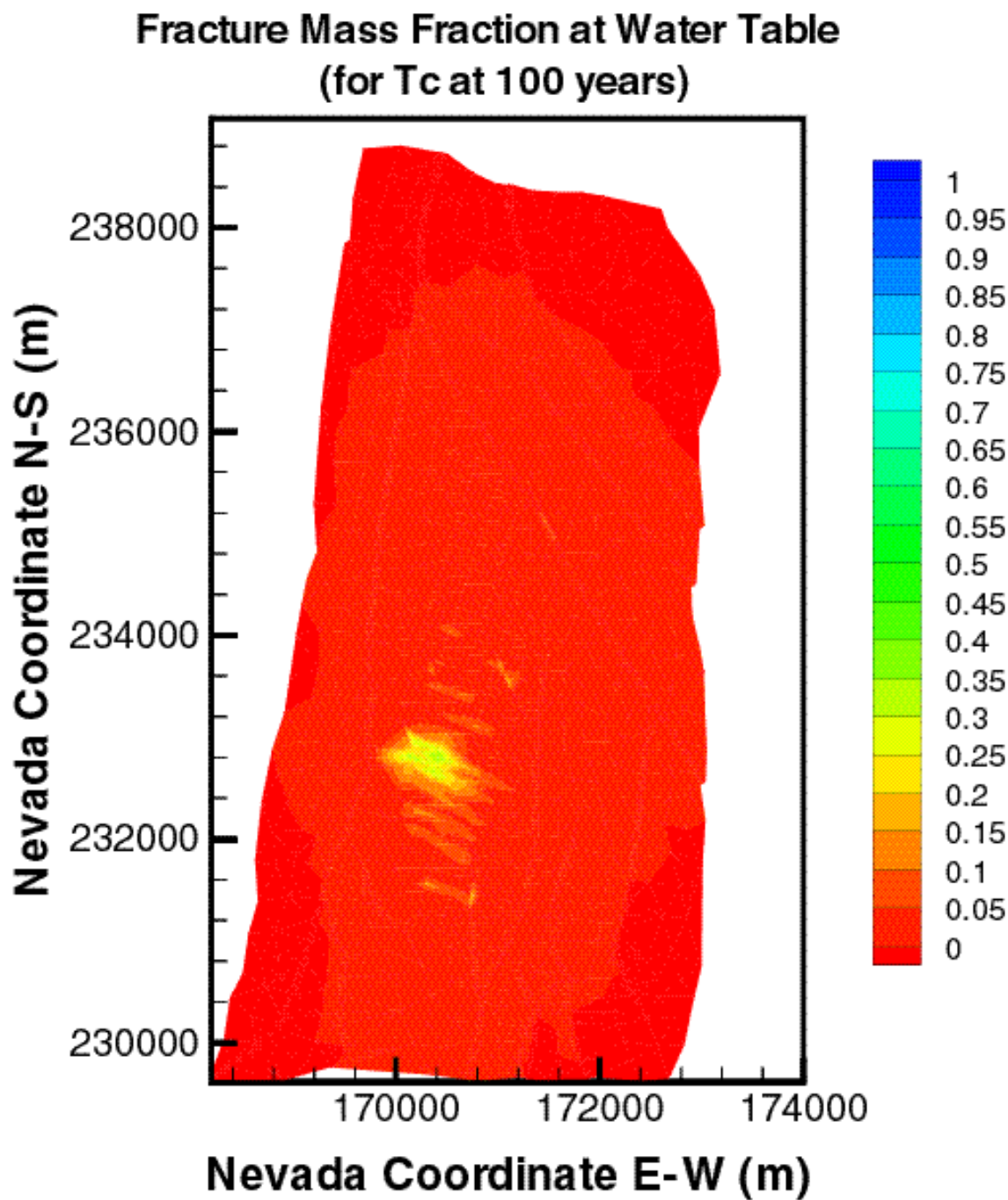


Figure 6.12.10. Distribution of the relative mass fraction X_R of ^{99}Tc in the fractures immediately above the groundwater at $t = 100$ years for mean present-day infiltration (DTN: LB991220140160.012, data submitted with this AMR).

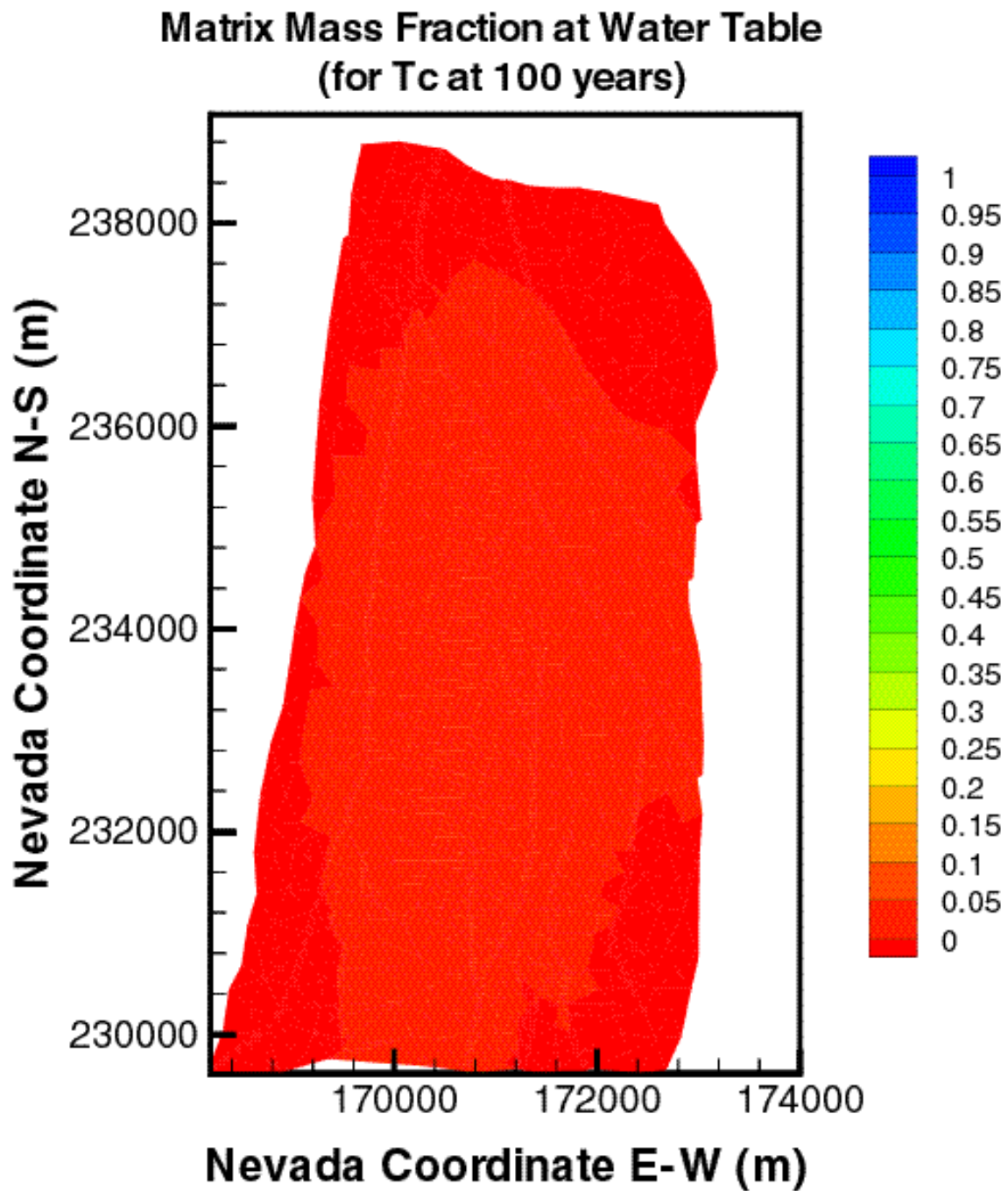


Figure 6.12.11. Distribution of the relative mass fraction X_R of ^{99}Tc in the matrix immediately above the groundwater table at $t = 100$ years for a mean present-day infiltration (DTN: LB991220140160.012, data submitted with this AMR).

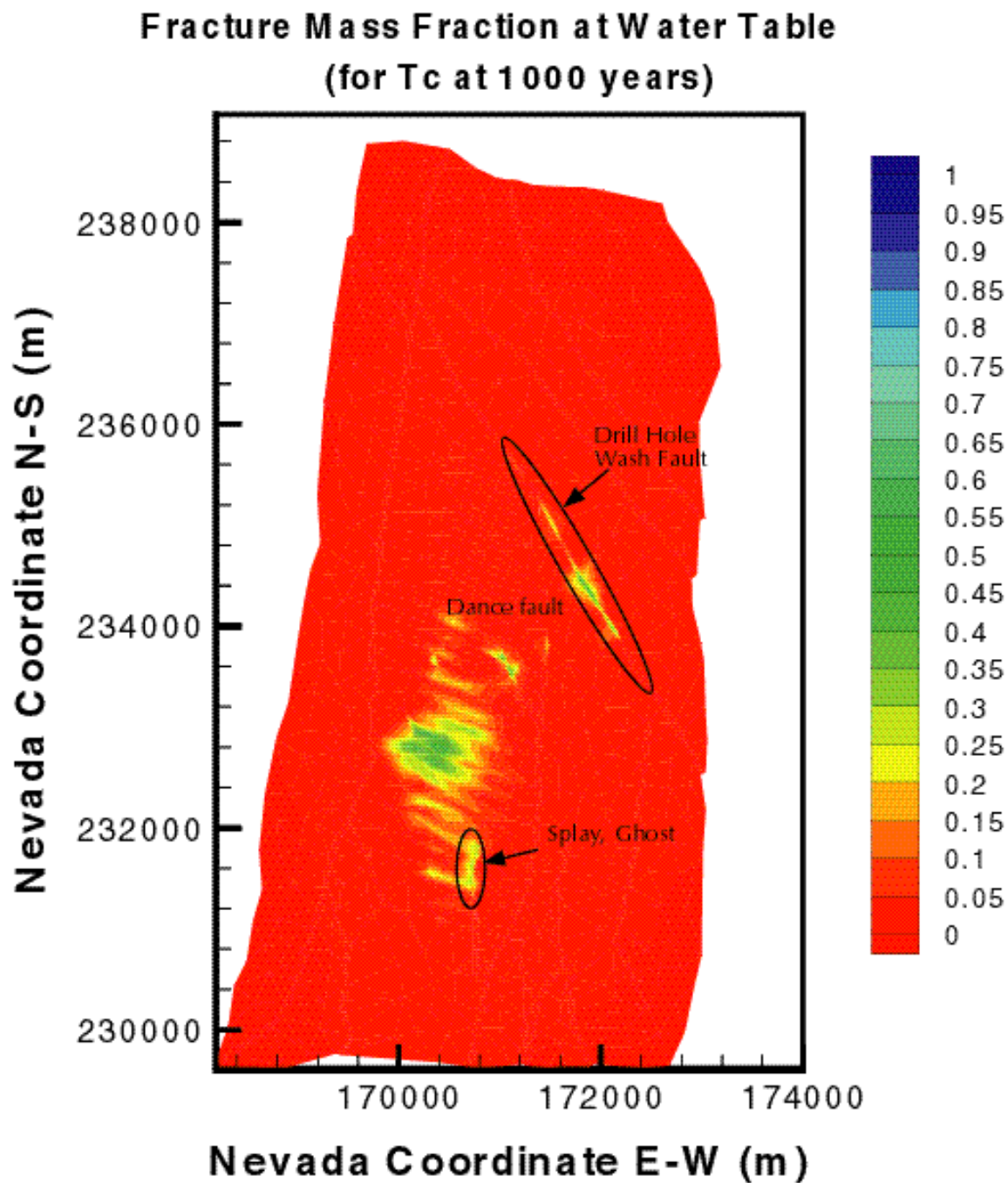


Figure 6.12.12. Distribution of the relative mass fraction X_R of ^{99}Tc in the fractures immediately above the groundwater at $t = 1,000$ years for mean present-day infiltration (DTN: LB991220140160.012, data submitted with this AMR).

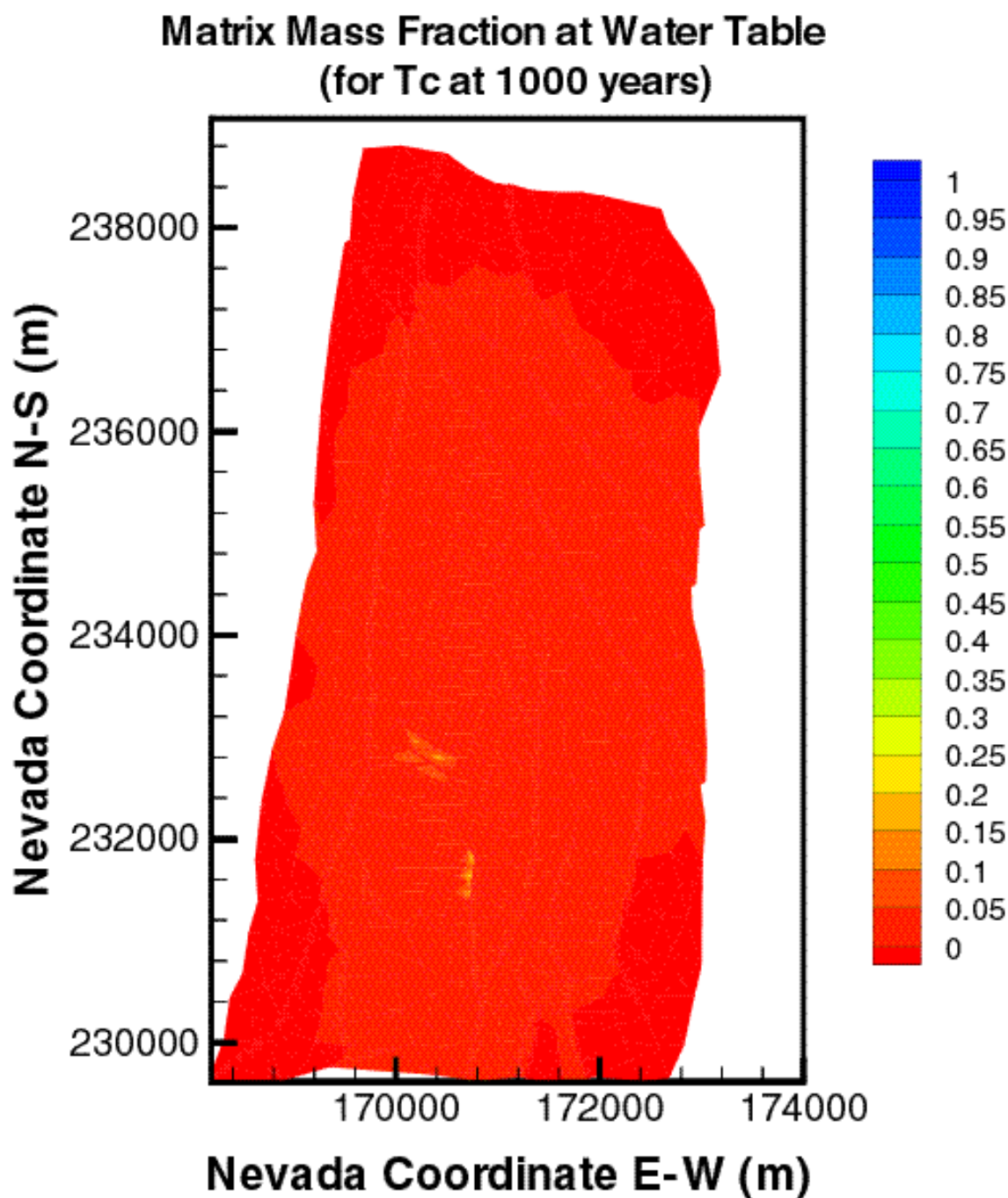


Figure 6.12.13. Distribution of the relative mass fraction X_R of ^{99}Tc in the matrix immediately above the ground-water table at $t = 1,000$ years for a mean present-day infiltration (DTN: LB991220140160.012, data submitted with this AMR).

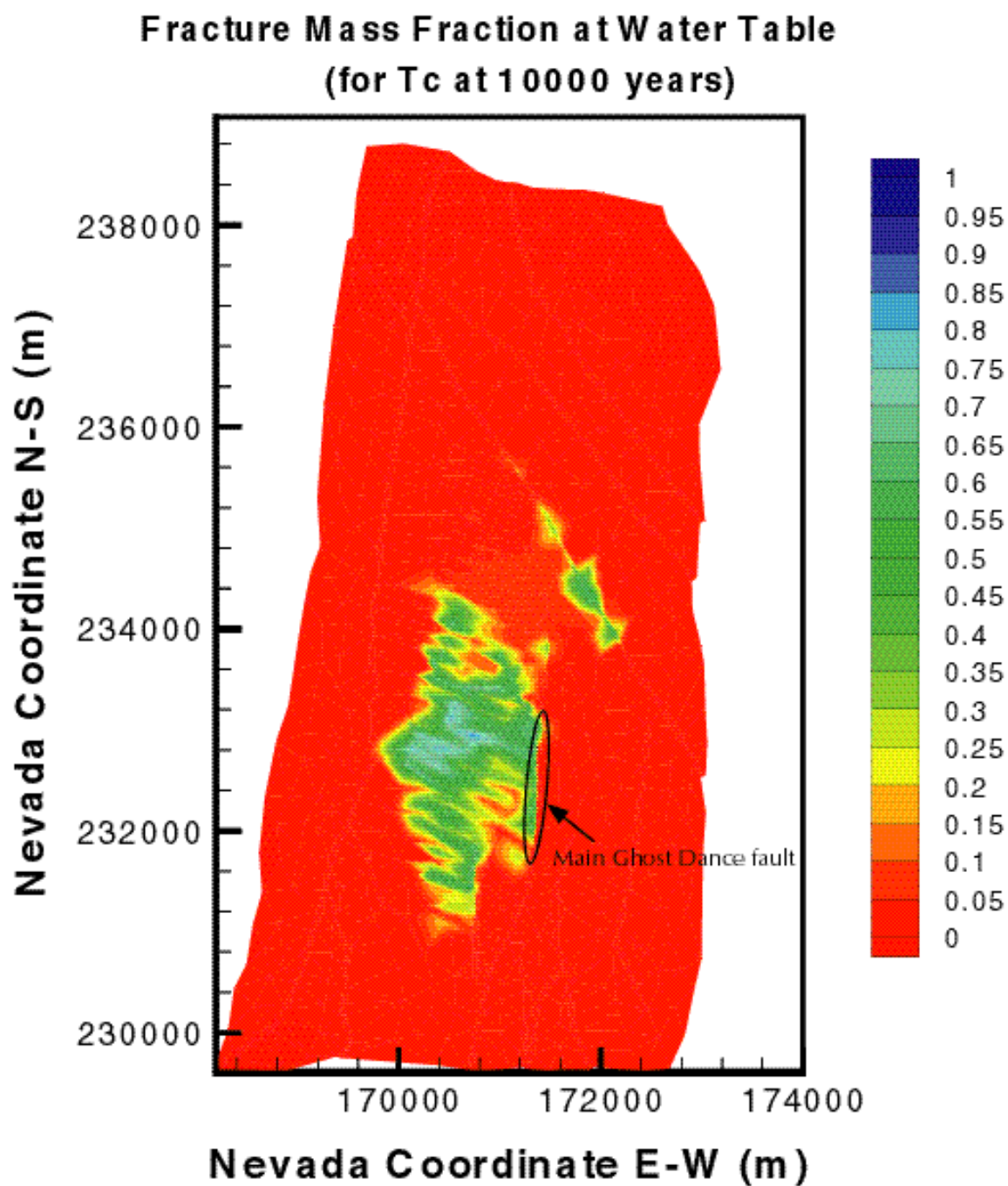


Figure 6.12.14. Distribution of the relative mass fraction X_R of ^{99}Tc in the fractures immediately above the groundwater at $t = 10,000$ years for mean present-day infiltration (DTN: LB991220140160.012, data submitted with this AMR).

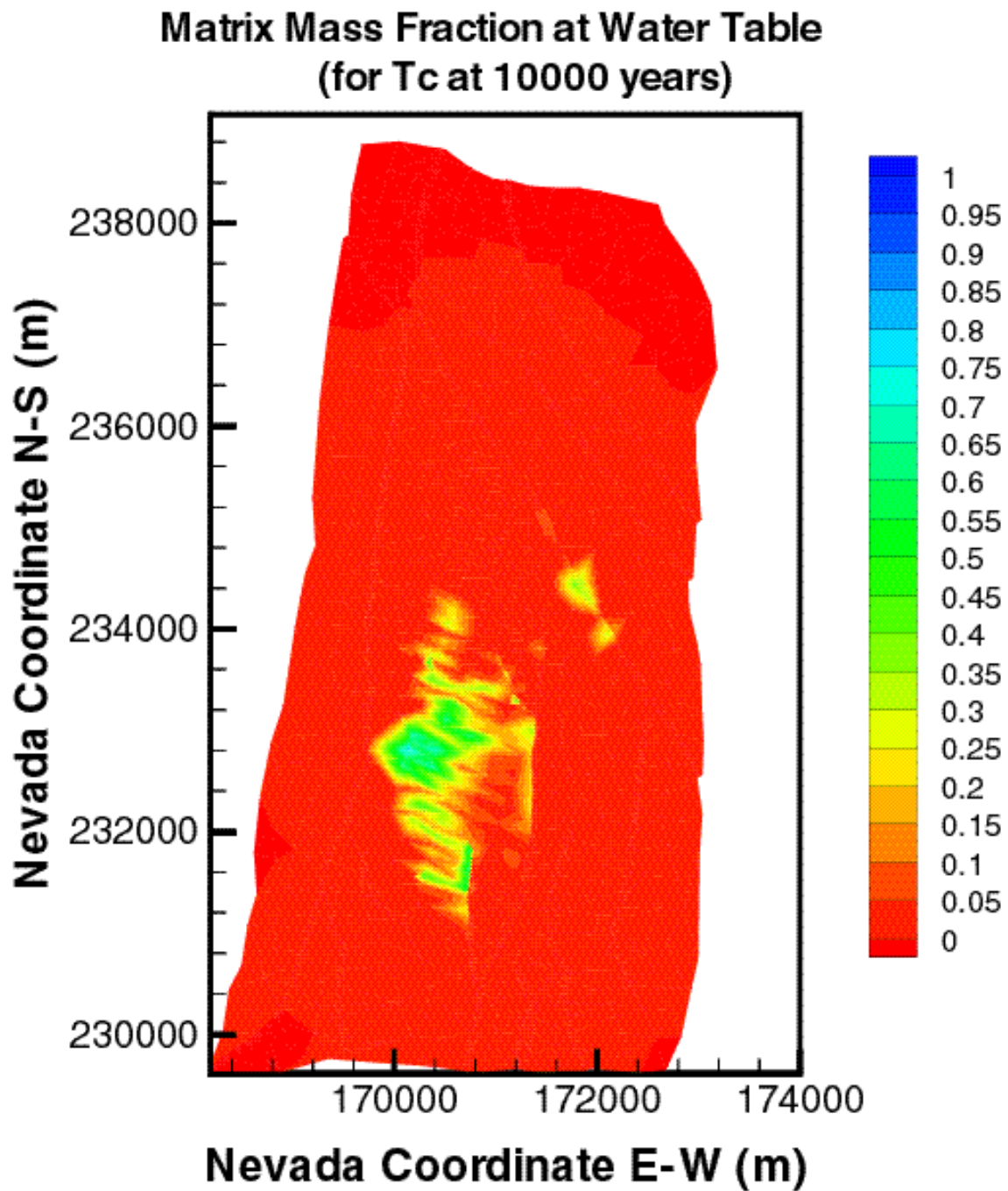


Figure 6.12.15. Distribution of the relative mass fraction X_R of ^{99}Tc in the matrix immediately above the groundwater table at $t = 10,000$ years for a mean present-day infiltration (DTN: LB991220140160.012, data submitted with this AMR).

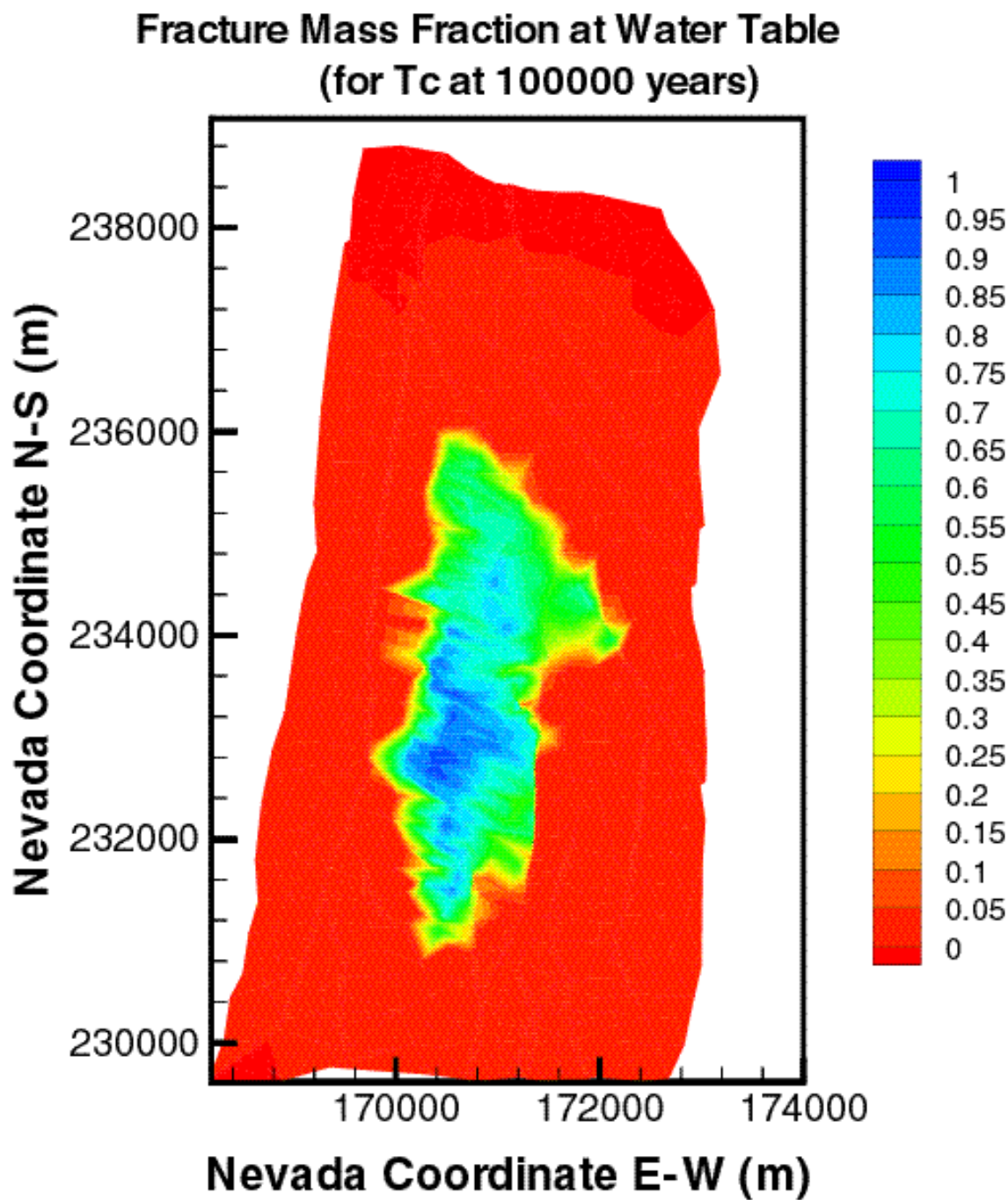


Figure 6.12.16. Distribution of the relative mass fraction X_R of ^{99}Tc in the fractures immediately above the groundwater at $t = 100,000$ years for mean present-day infiltration (DTN: LB991220140160.012, data submitted with this AMR).

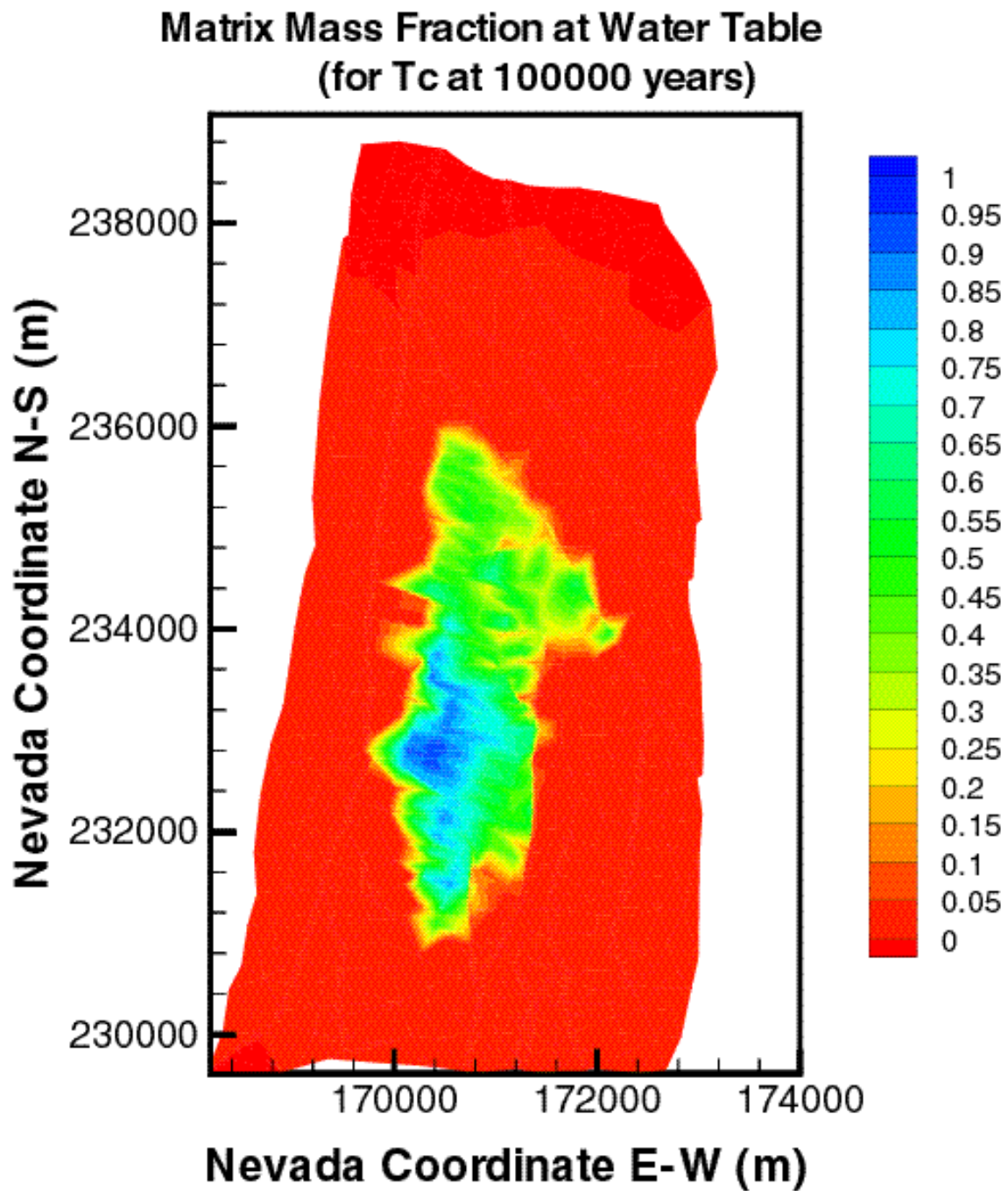


Figure 6.12.17. Distribution of the relative mass fraction X_R of ^{99}Tc in the matrix immediately above the groundwater table at $t = 100,000$ years for a mean present-day infiltration (DTN: LB991220140160.012, data submitted with this AMR).

The main Ghost Dance fault does not play an important role in transport in the tsw39 layer, as the ^{99}Tc does not reach the fault at this level even after 100,000 years (Figures 6.12.8 and 6.12.9). This fault (identified in Figure 6.12.14) is more important at the water table, where it evidently acts as a barrier to transport across it while facilitating downward migration into the groundwater. Its presence in Figures 6.12.14 and 6.12.17 is denoted by the sharp contrast between the non-moving boundary of the concentration front along the fault and the adjacent uncontaminated rock mass. This boundary has the shape of the main Ghost Dance fault (see Figures 6.11.1)

6.12.2.3 Transport Patterns

Of particular interest is the emerging transport pattern, which indicates that radionuclide transport to the groundwater is faster in the southern part of the potential repository, where it is also areally concentrated. This appears to be counterintuitive and in conflict with expectations, based on the properties of the layers beneath the potential repository. It would be reasonable to expect that the general area of fastest, largest and most extensive transport would be in the northern part of the potential repository site, where the highly conductive fractures of the zeolitic CHz layers occur. Such an expectation appears to be supported by the 2-D studies of transport in vertical cross sections discussed in Section 6.9.

The 3-D site-scale simulations indicate that the opposite occurs, i.e., radionuclide transport is significantly slower in the northern part despite the preponderance of the zeolitic CHz hydrogeologic units. The relatively large permeability contrast between the matrix and the fractures in the CHz unit does not appear to lead to the expected fast fracture-dominated flow (compared to that in the vitric CHv units in the south) and to a correspondingly fast advective transport.

There are four reasons for this transport pattern. The first reason is the infiltration and percolation distributions. A review of the infiltration pattern (Figure 6.12.18) at the surface, the percolation flux at the repository level (Figure 6.12.19) and the percolation flux at the groundwater level (Figure 6.12.20) indicates that they closely reflect the transport patterns in Figures 6.12.2 through 6.12.17. Thus, the water flow pattern dictates the advective transport pattern. In the #1 perched-water model of these studies, the maximum water flow within the footprint of the potential repository is in its southern part.

The presence of the highly conductive (a) Splay G of the Solitario Canyon fault and (b) Ghost Dance fault splay are the second reason (and related to the percolation patterns) for the dominance of the southern part of the potential repository as the pathway of transport, despite the vitric CHv layers having fewer fractures (than the overlying TSw) and acting as porous (rather than fractured) media (with relatively lower water velocities). The permeability of the fractures in the faults can be as high as hundreds of darcies (CRWMS M&O 2000a, Section 6; Bodvarsson et al. 1999, p. 15), i.e., orders of magnitude larger. The resulting fast advective transport is the reason for the transport pattern observed in Figures 6.12.2 through 6.12.17.

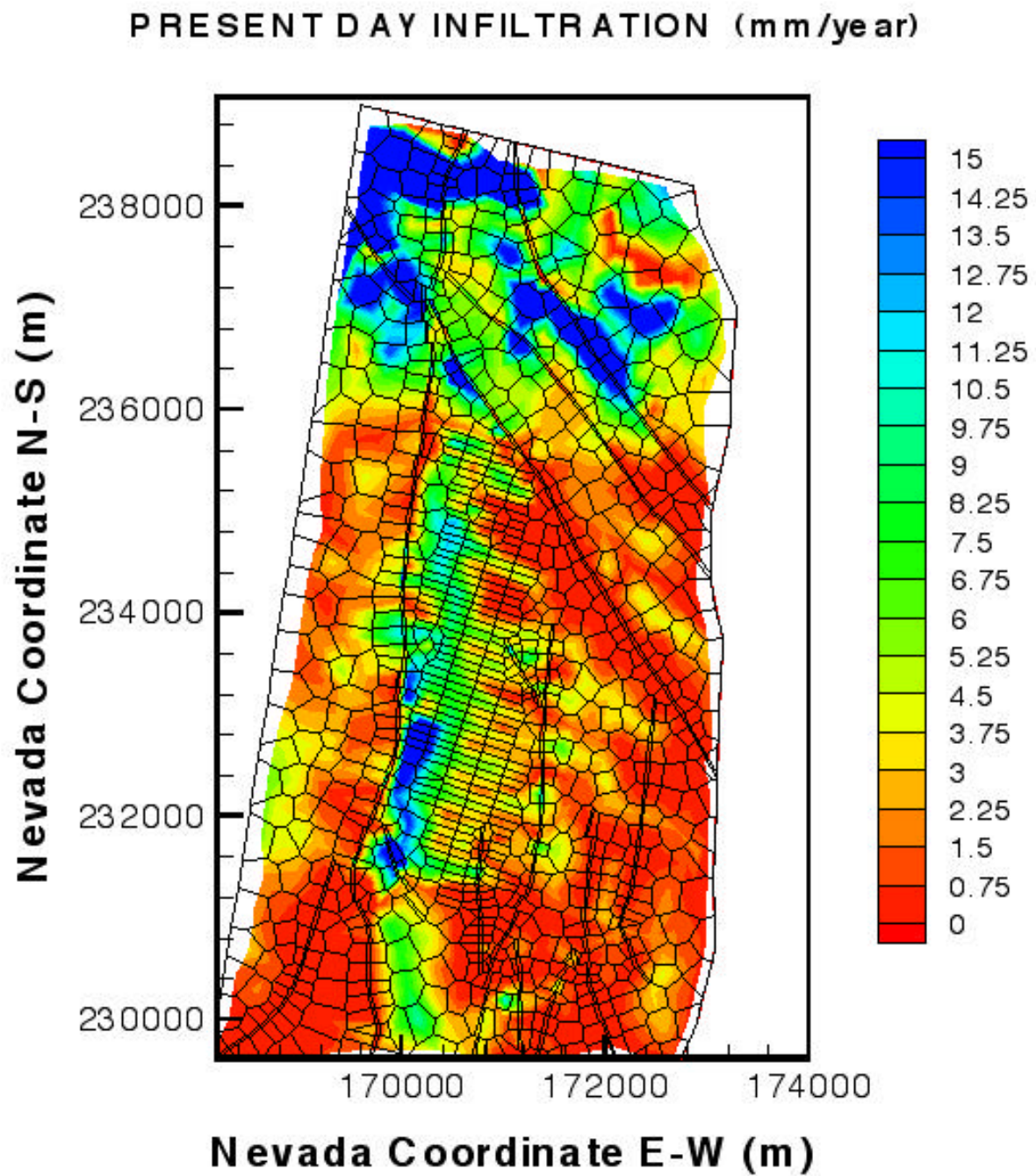


Figure 6.12.18. Mean present-day infiltration rates at the surface (CRWMS M&O 1999d, Section 6.6, DTN: LB990801233129.003).

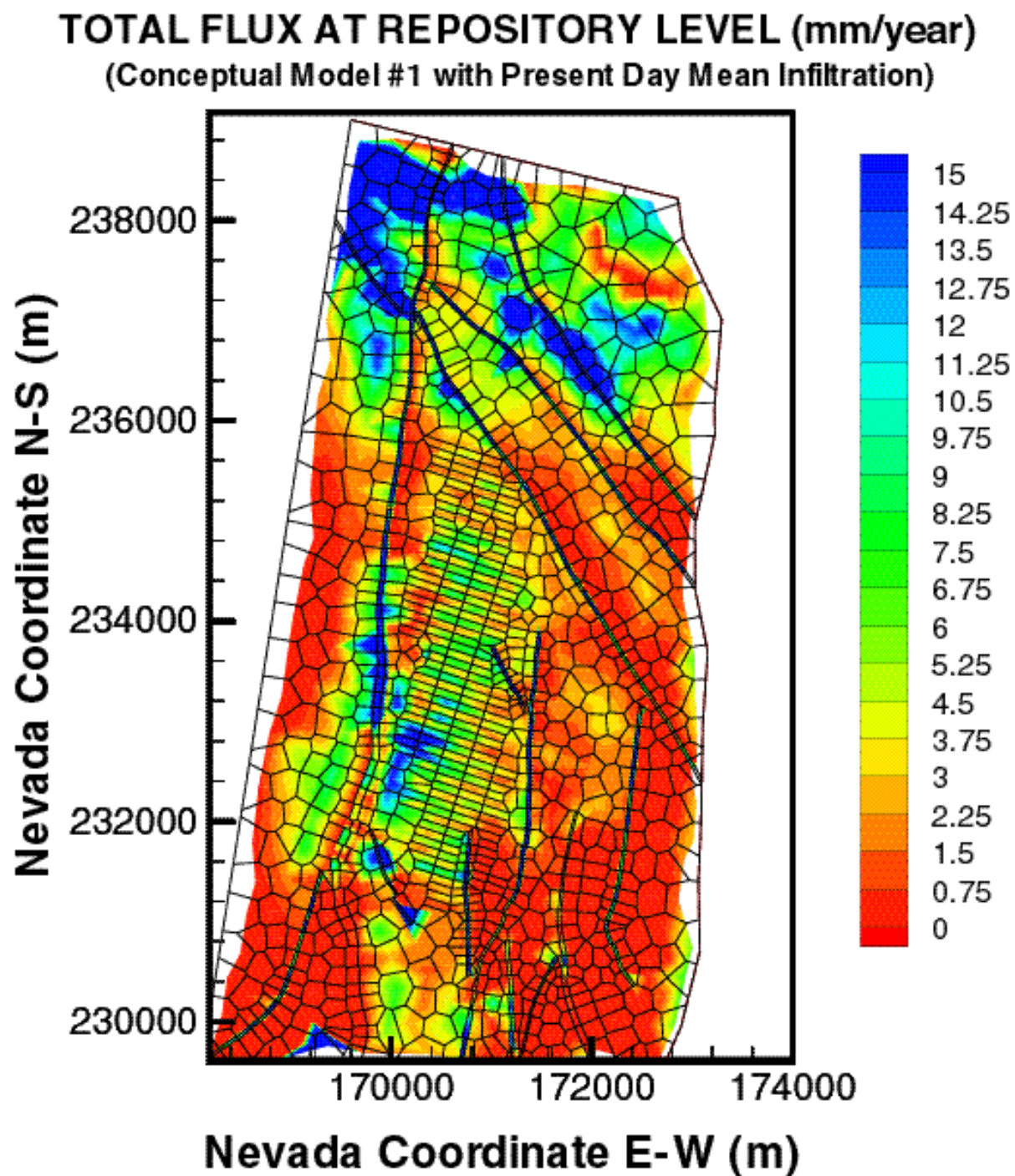


Figure 6.12.19. Percolation fluxes at the potential repository level (CRWMS M&O 1999d, Section 6.6, DTN: LB990801233129.003).

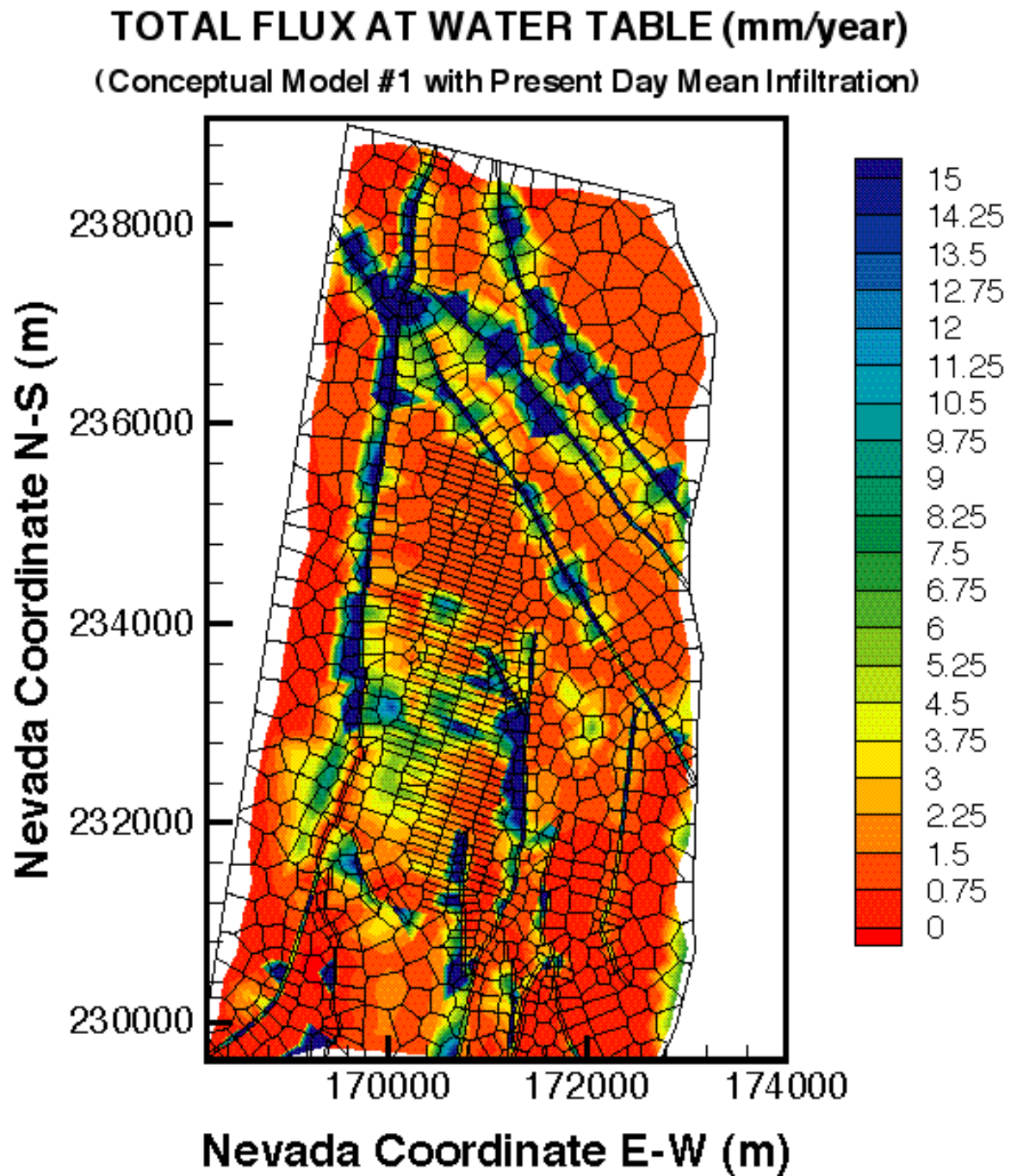


Figure 6.12.20. Percolation fluxes at the water table level (CRWMS M& O 1999d, Section 6.6, DTN: LB990801233129.003).

This may be further facilitated by the contraction of the areal extent of the vitrified tuffs (the third reason), whose vertical distribution shows a funnel-type structure in the southern part of the potential repository. Thus, as depth from the potential repository increases, an increasing portion of the water flow occurs through the zeolites, in which the fractured dominated flow (and consequently, transport) is fast. Figure 6.12.21 shows the areally diminishing extent of the vitrified tuffs with depth (DTN: MO9910MWDISMMM.003). In this figure, the zeolites are indicated by the yellow color in the layers of the CHn and PP hydrogeologic units, while the vitric tuffs are indicated by a purple color. Note also the contrast at the interface of the TSw and CHn units (layers tsw39 and ch1 in Figure 6.12.21).

The fourth reason is the low-permeability zones at the TSw-CHn interface in the northern part of the potential repository in the #1 perched water model (CRWMS M&O, 1999d, Sections 6.2 and 6.6). These zones are barriers to drainage, and lead to low water velocities and perched water bodies. Radionuclides move slowly through the perched water before reaching the underlying highly permeable zeolite fractures; hence the delay in transport.

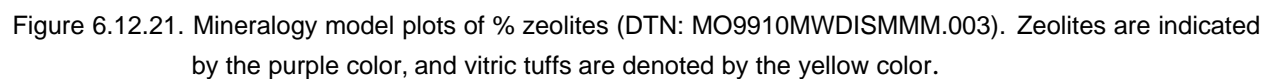
Note that the importance of faults and perched water bodies in transport are directly dependent on the underlying geologic and perched water conceptual models. In the simulations discussed in this section, the TSPA geologic model and the #1 perched water model (Table 6.13) were assumed. It is reasonable to expect that changing geologic and perched water models may lead to substantially different results, given the sensitivity of transport to these geologic features.

The fourth reason is the low-permeability zones at the TSw-CHn interface in the northern part of the potential repository in the #1 perched water model (CRWMS M&O, 1999d, Sections 6.2 and 6.6). These zones are barriers to drainage, and lead to low water velocities and perched water bodies. Radionuclides move slowly through the perched water before reaching the underlying highly permeable zeolite fractures; hence the delay in transport.

Note that the importance of faults and perched water bodies in transport are directly dependent on the underlying geologic and perched water conceptual models. In the simulations discussed in this section, the TSPA geologic model and the #1 perched water model (Table 6.13) were assumed. It is reasonable to expect that changing geologic and perched water models may lead to substantially different results, given the sensitivity of transport to these geologic features.

6.12.2.4 Transport Processes and Mechanisms

The importance of fractures in the transport becomes evident in Figure 6.12.2, which shows the areal distribution of the ^{99}Tc X_R in the aqueous phase in the tsw39 layer at $t = 100$ years. Compared to the distribution of X_R in the matrix (Figure 6.12.3), which shows practically no ^{99}Tc presence, it is evident that fractures are the main pathways of transport at this relatively early stage. Figure 6.12.2 clearly shows distinctive transport patterns corresponding to the geologic features discussed in Section 6.12.2.2.



As time progresses, the same pattern persists, although the differences in the X_R distribution between the fractures and the matrix become less pronounced with time. This is evidenced at $t = 1,000$ years (Figures 6.12.4 and 6.12.5), where the matrix $^{99}\text{Tc } X_R$ is significant, but substantially lower than the fracture X_R of ^{99}Tc . It is obvious that the $^{99}\text{Tc } X_R$ distribution in the matrix follows the X_R distribution in the fractures, indicating that diffusion from the fractures into the matrix is the main mechanism for the ^{99}Tc presence in the matrix. The distinctive transport patterns, corresponding to identifiable geologic features, are now even more pronounced. At $t = 10,000$ years, X_R is still higher in the fractures (Figure 6.12.6) than in the matrix (Figure 6.12.7), but the differences are smaller. Finally, at $t = 100,000$ years, X_R differences between the fractures (Figure 6.12.8) and the matrix (Figure 6.12.9) can be barely distinguished by visual inspection of the figures.

The X_R distribution immediately above the water table further attests to the importance of fractures for transport. For mean present-day infiltration, the fracture X_R immediately above the water table shows evidence of measurable transport at $t = 100$ years (Figure 6.12.10), while the corresponding matrix X_R shows no evidence of ^{99}Tc (Figure 6.12.11). At $t = 1,000$ years, X_R is significant in fractures and denotes the geological features that facilitate transport (Figure 6.12.12), but the corresponding matrix X_R is just beginning to show faint signs of ^{99}Tc presence (Figure 6.12.13).

At $t = 10,000$ years, the differences between the matrix and the fracture X_R (Figures 6.12.14 and 6.12.15) lessen. The general observation is that the matrix X_R distribution follows the same pattern as fracture X_R distribution, but lags in time. Their patterns confirm the earlier observation that matrix diffusion from the fractures into the matrix is the main mechanism for the ^{99}Tc presence in the matrix. The distinctive transport patterns, corresponding to the faults discussed in Section 6.12.2.2, are now even more pronounced. At $t = 100,000$ years, only small X_R differences between the fractures (Figure 6.12.16) and the matrix (Figure 6.12.17) persist.

6.12.2.5 Comparison to the Semianalytical 2-D FRACL Predictions

The fracture X_R distributions above the water table at $t = 1,000$ and $t = 10,000$ years in Figures 6.12.12 and 6.12.14 provide confirmation of the travel times predicted by the 2-D semianalytical solutions in Section 6.9. From Figures V.1, V.7, V.13 and V.19 (see Attachment V), it appears that, for mean present-day infiltration, ^{99}Tc transport through the fractures and matrix (but not accounting for faults) takes over 1,000, but less than 10,000 years, to reach the water table.

The fracture X_R in Figures 6.12.12 and 6.12.14 are consistent with this prediction. Figure 6.12.12 shows limited ^{99}Tc presence in the fractures, all of which is attributed to transport through the faults. Figure 6.12.12 shows that the Splay G of the Solitarion Canyon Fault is the earliest and most significant contributor of ^{99}Tc in the fractures at the water table. At $t = 10,000$ years (Figure 6.12.14), the fracture X_R shows an extensive distribution, which is consistent with ^{99}Tc arrivals through the bulk of the fractures in addition to contributions from faults.

Note that the observation of faster transport in the southern part of the potential repository from the EOS9nT 3-D site-scale simulations does not contradict the FRACL 2-D predictions, which appear to indicate faster transport in the northern part (despite the presence of permeability conditions that lead to the formation of perched water bodies). There are several reasons for this.

The FRACL predictions and the EOS9nT predictions do not describe the same problem. The FRACL problems involve a thin 2-D cross section at a representative location. The FRACL semianalytical model cannot account for 3-D processes (such as flow diversion, focusing, and advective transport from outside its narrow 2-D domain) and the effects of faults. The FRACL and EOS9nT results would be comparable if the same limited 2-D domain were simulated for the same infiltration rate.

In the dual permeability approach of the EOS9nT simulations, the matrix and fracture components of a fractured rock are represented by a fracture subdomain and a matrix subdomain. As simulated, the FRACL results approximate transport at a vertical column of the EOS9nT 3-D domain (involving a single fracture and a single matrix system) at the locations of Cross Sections 1, 2 and 3 (see Section 6.5). Note that the two are not fully comparable because the effects of 3-D flow and transport in the EOS9nT domain columns and the areal differences of infiltration and percolation (Figures 6.12.18 to 6.12.20).

FRACL describes transport in the fracture-matrix system of Cross Sections 1, 2 and 3 (i.e., 2-D domains such as that in Figure 6.9.1) without accounting for the 3-D effects of the faults. It is these fault effects that are first noticed in the transport patterns of Figures 6.12.2 to 6.12.17, from which it is not possible to separate the transport component through the bulk matrix and fractures and the effects of lateral advective transport. Thus, Figures 6.12.1 to 6.12.17 do not provide sufficient information to ascertain that, excluding the effects of the faults, bulk transport through the fractures and matrix is faster in the southern part of the potential repository.

6.12.3 ⁹⁹Tc Transport Under Monsoon Infiltration

The DTNs of the input and output files for the three monsoon infiltration scenarios are listed in Table 6.13. The monsoon infiltration rate is higher than that for present-day infiltration of the same level (Table 6.11). The simulation results are consistent with the observations made in Section 6.12.2.

The higher infiltration rates result in lower t_{10} and t_{50} values (Table 6.15) than those for present-day infiltration. Thus, for low, mean, and high monsoon infiltration, the t_{10} is 920, 50 and 15 years, respectively (Figure 6.12.22). For the same infiltration regimes, the corresponding t_{50} is 3,500, 1,000, and 400 years. These times are significantly smaller than the ones for the present-day infiltration scenario (Figure 6.12.1), indicating faster transport through the system and earlier appearance of ⁹⁹Tc at the water table.

Because transport is faster than under present-day infiltration, travel times to the water table are shorter and thus the amount of ^{99}Tc lost to radioactive decay is smaller. This is evident in Figure 6.12.22, in which the maximum attainable R values are shown (a) to increase with the infiltration rate and (b) to be higher and closer to each other than those for present-day infiltration (Figure 6.12.1).

6.12.4 ^{99}Tc Transport Under Glacial Infiltration

The DTNs of the input and output files for the three glacial infiltration scenarios are listed in Table 6.13. The high and mean glacial infiltration are higher than the present-day and monsoon infiltration of the same level (Table 6.11), and result in lower t_{10} and t_{50} values (Table 6.15).

Figure 6.12.23 shows that the t_{10} values for high and mean glacial infiltration are only 10 (extrapolated from the figure) and 23 years, respectively, while the corresponding t_{50} values are 160 and 500 years. As in the case of monsoon infiltration (Figure 6.12.18), the maximum attainable R for high and mean glacial infiltration is almost 1, indicating fast transport through the 3-D system. The t_{10} and t_{50} values for low glacial infiltration are 2,200 and 9,000 years respectively.

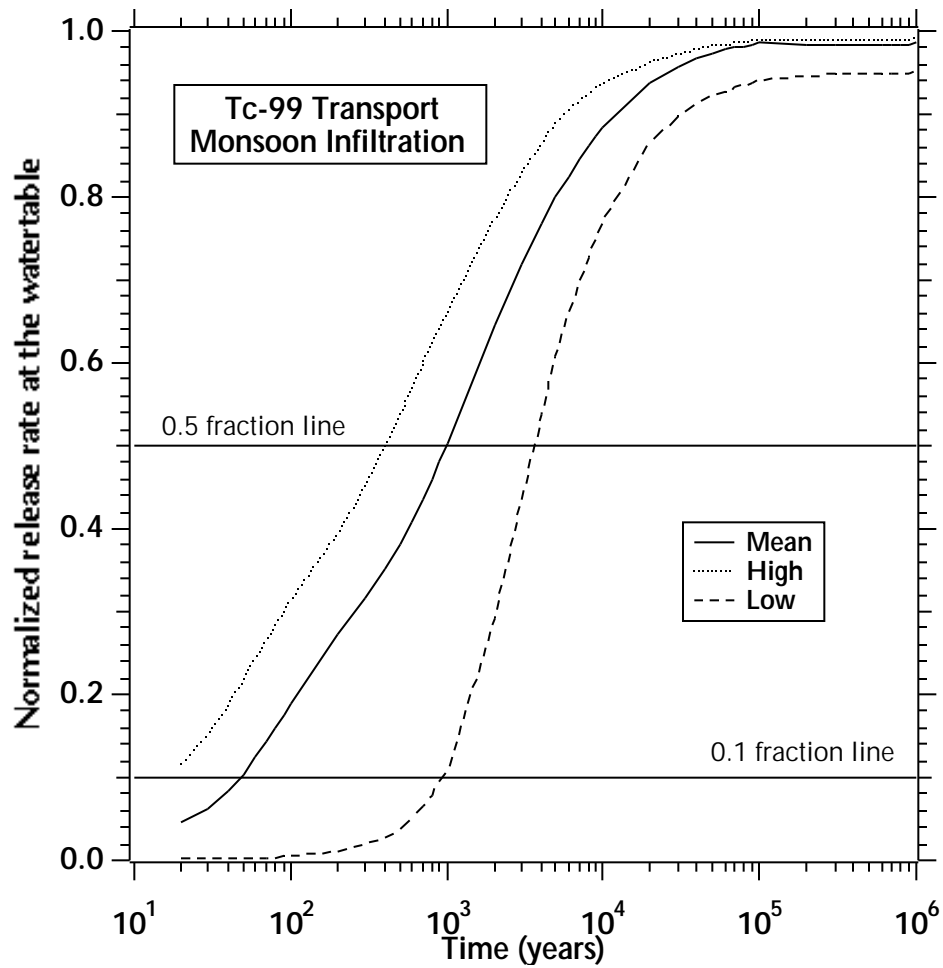


Figure 6.12.22. Normalized relative release R of ^{99}Tc at the water table for varying monsoon climatic scenarios (DTN: LB991220140160.013, data submitted with this AMR).

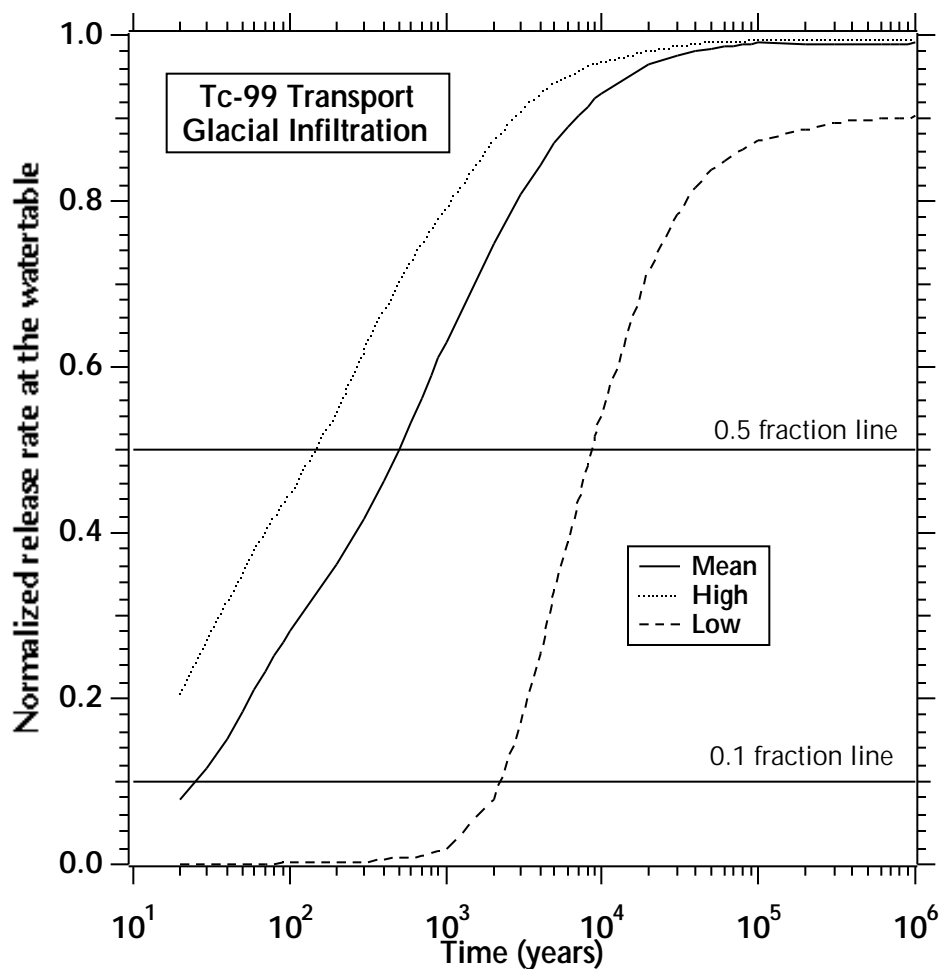


Figure 6.12.23. Normalized relative release R of ^{99}Tc at the water table for varying glacial climatic scenarios (DTN: LB991220140160.014, data submitted with this AMR).

6.13 3-D TRANSPORT OF ^{237}Np AND ITS DAUGHTERS

In this section we investigate the transport of ^{237}Np by means of EOS9nT 3-D site-scale simulations of the entire UZ system of Yucca Mountain. Section 6.13 includes three subsections.

In Section 6.13.1 we discuss the transport of the moderately-sorbing ^{237}Np and its daughters for three levels of present-day infiltration. The results of this study are shown in Figures 6.13.1 to 6.13.2, and in Figures VII.1 to VII.24 of Attachment VII. In Section 6.13.2 we study the transport of ^{237}Np for three levels of monsoon infiltration (Figure 6.13.3). Finally, in Section 6.13.3 we study the transport of ^{237}Np for three levels of glacial infiltration (Figure 6.13.4).

6.13.1 Transport of ^{237}Np and its Daughters Under Present-Day Infiltration

The grids, flow fields and conditions discussed in Section 6.11.2 corresponded to the #1 conceptual model of perched water (CRWMS M&O 1999d, Sections 6.2 and 6.6) and are used in the simulation of all infiltration regimes. The parameters used in the EOS9nT simulations of 3-D transport of the moderately sorbing ^{237}Np are listed in Table 6.14. The DTN of the input and output files for the three present-day infiltration scenarios is DTN: LB991220140160.012 (Table 6.13).

6.13.1.1 Breakthrough Curves

The moderate sorption of ^{237}Np results in retardation of its transport through the UZ system, as the normalized release rate R at the water table in Figure 6.13.1 indicates. A comparison of this figure to that for the non sorbing ^{99}Tc (Figure 6.12.1) reveals a drastically different pattern. Thus, the moderate sorption of ^{237}Np is sufficient to effect a large increase in t_{10} and t_{50} compared to those for the non-sorbing ^{99}Tc (Table 6.15).

Increased infiltration rate leads to faster transport and shorter travel times to the repository. When infiltration increases from mean to high, t_{10} and t_{50} are reduced to 1,700 and 22,000 years, respectively. Reduction of infiltration to the low present-day level results in analogous increase of t_{10} and t_{50} to 220,000 and over 1,000,000 years, respectively.

Because of significant retardation, the maximum attainable R varies over a larger value range and does not necessarily reach a plateau within the simulation period. At $t = 1,000,000$ years, R for mean and low infiltration is 0.86 and 0.42, respectively, and the maximum possible values for either infiltration are not yet reached. At the same time, the R for high infiltration is approaching its maximum at $R = 0.95$.

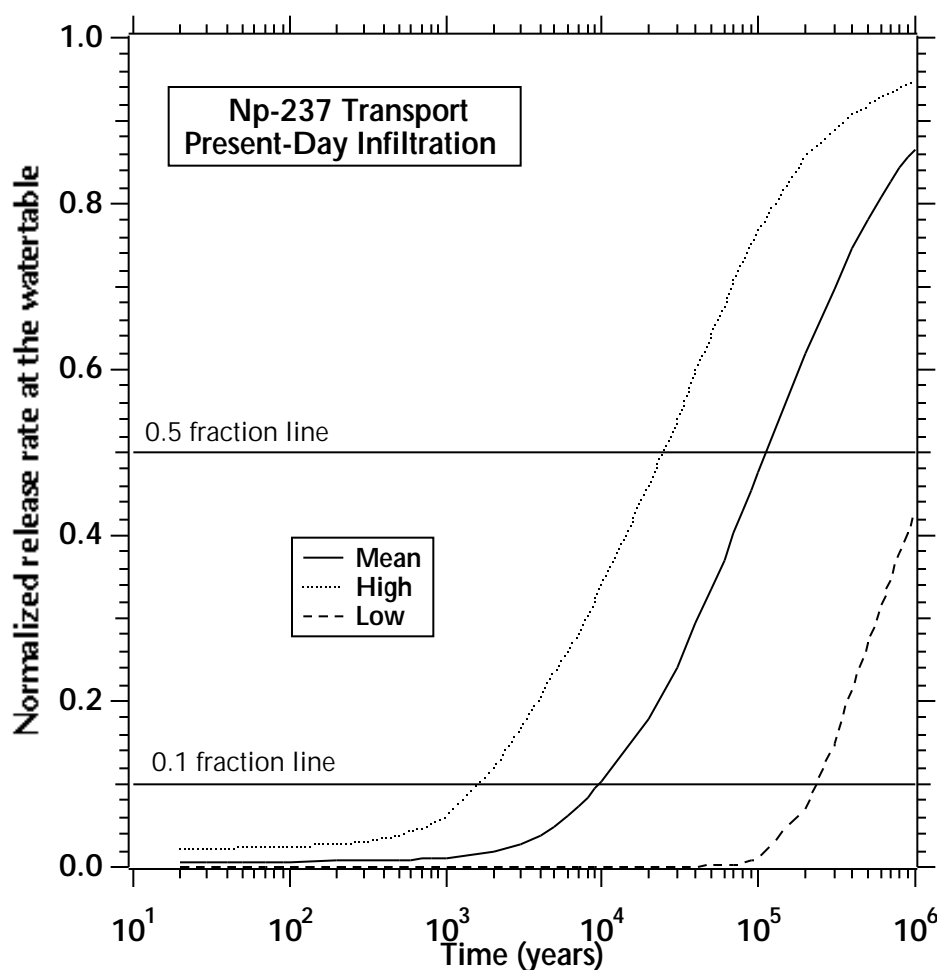


Figure 6.13.1. Normalized relative release rate of ^{237}Np at the watertable for varying present-day climatic scenarios (DTN: LB991220140160.012, data submitted with this AMR).

6.13.1.2 Daughter Contributions

The effect of daughter generation on radionuclide transport was investigated by accounting for the contributions of ^{237}Np and its two daughters (^{233}U and ^{229}Th) to the release rate at the water table. The relative flux fraction M_R of each member of the chain, defined as

$$M_R = \frac{\text{Flux of the member of the } ^{237}\text{Np} \text{ chain at the water table}}{\text{Sum of fluxes of all members of the } ^{237}\text{Np} \text{ chain at the water table}},$$

is shown in Figure 6.13.2. The M_R of both ^{233}U and ^{229}Th increase monotonically with time, and at $t = 1,000,000$ years, they reach values of 0.02 and 10^{-5} , respectively. Contributions of the daughters are obviously rather insignificant and can be safely ignored.

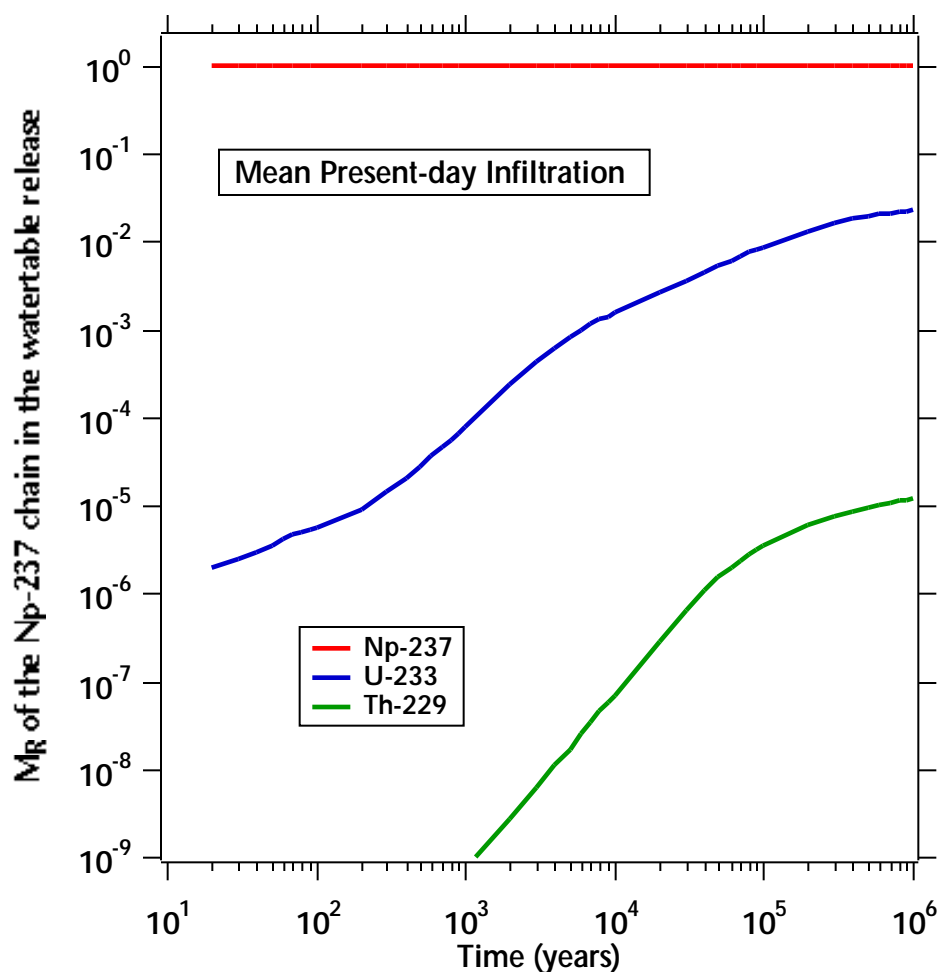


Figure 6.13.2. Relative flux fractions M_R of the members of the $^{237}\text{Np} \rightarrow ^{233}\text{U} \rightarrow ^{229}\text{Th}$ in the release at the water table over time for a mean present-day infiltration (DTN: LB991220140160.012, data submitted with this AMR).

6.13.1.3 Transport Mechanisms and Patterns

The importance of fractures on the ^{237}Np transport becomes evident in Figure VII.1 (see Attachment VII), which shows the areal distribution of X_R (see Section 6.12.2.2) in the aqueous phase in the fractures immediately above the TSw-CHn interface (i.e., in the tsw39 layer) at $t = 100$ years (under mean present-day infiltration). The contrast with the distribution of X_R in the aqueous phase of the matrix (Figure VII.2), which shows no discernible difference from the background $X_R = 0$, is dramatic.

Of particular interest is the distribution of the relative sorbed or filtered concentration $F_R [ML^{-3}]$,

defined as

$$F_R = \frac{F}{X_0},$$

where X_0 is the species mass fraction in the water released from the potential repository. Figure VII.3 shows a sizable ^{237}Np F_R distribution, which has an areal extent significantly larger than that of the fracture X_R at the same time, and denotes geologic features (i.e., the section of the Drill Hole Wash fault shown in Figure VII.3) that do not appear in the fracture X_R (Figure VII.1).

Figures VII.1 through VII.3 indicate the efficiency of the matrix as a ^{237}Np sink. The small amounts of ^{237}Np that diffuse from the fractures into the matrix are immediately sorbed and are thus removed from the matrix aqueous phase. The X_R in the matrix aqueous phase shows no discernible signs of ^{237}Np presence because its magnitude is so low that it cannot be differentiated from the zero background level when using a linear X_R scale. The logarithmic scale of relative sorbed concentrations in Figure VII.3 shows the extent of ^{237}Np presence in the matrix.

Figures VII.4 to VII.6 show the fracture X_R distribution, the matrix X_R , and the matrix F_R in the tsw39 layer of ^{237}Np at $t = 1,000$ years. Note the very large differences in the areal extents of the ^{237}Np footprints in these three figures. The effect of the Drill Hole Wash fault, clearly denoted in its entirety by the F_R distribution in Figure VII.6, is absent from the fracture and matrix X_R distributions in Figures VII.4 and Figures VII.5, respectively.

The fracture X_R , matrix X_R , and the matrix F_R at $t = 10,000$ years are shown in Figures VII.7 to VII.9, respectively; the distribution of these parameters at $t = 100,000$ years is shown in Figures VII.10 to VII.12. Compared to the fracture X_R , matrix X_R levels appear to be particularly low. This is caused by sorption onto the matrix.

From Figures VII.1 to VII.12, we deduce that matrix diffusion from the fractures into the matrix, and subsequent sorption onto the matrix grains are the main mechanisms for ^{237}Np removal from the fractures and transport retardation. As the relative sorbed concentration distributions indicate, matrix diffusion leads to the removal of substantial contaminant mass from the fast-flowing fractures. The fracture X_R of ^{237}Np is substantially lower than that of ^{99}Tc at the same locations and times (Section 6.12) and further confirms this observation.

The X_R distribution immediately above the water table provides another indication of the importance of fractures. For mean present-day infiltration, the fracture and matrix X_R immediately above the water table show practically no signs of ^{237}Np at $t = 100$ years (Figures VII.13 and VII.14), but the corresponding matrix F_R (Figure VII.15) is easily detectable and demonstrates the effectiveness of sorption in radionuclide removal from the solution. At $t = 1,000$ years, the X_R distribution in the fractures (Figure VII.16) and in the matrix (Figure VII.17) remain practically unchanged from those at $t = 100$ years (Figures VII.13 and VII.14). On the other hand, the matrix F_R in Figure VII.18 exhibits large values, and clearly identifies all the transport-facilitating faults

discussed in Section 6.13.2.2.

The fracture X_R , matrix X_R and matrix F_R distributions of ^{237}Np at $t = 10,000$ years are shown in Figures VII.19 to VII.21; the same distributions at $t = 100,000$ years are shown in Figures VII.22 to VII.24. The fracture X_R is beginning to register above background at $t = 10,000$ (Figure VII.19) and reaches a significant level at $t = 100,000$ years (Figure VII.22). The matrix X_R has at last become differentiable from the background at $t = 100,000$ (Figure VII.23). The matrix F_R at $t = 10,000$ years and $t = 100,000$ years in Figures VII.21 and VII.24, respectively, show that ^{237}Np is sorbed onto the rocks over a large area, which increases over time. Comparison of the X_R (matrix and fracture) to the matrix F_R distributions provides further evidence of the efficiency of the matrix as a ^{237}Np sink, which leads to the significant retardation (over that of the non-sorbing ^{99}Tc , see Figure 6.12.1) indicated in Figure 6.13.1.

6.13.1.4 Transport-Controlling Features

Review of Figures VII.1 through VII.24 (see Attachment VII), and comparison to the corresponding ^{99}Tc figures (Figures 6.12.2 through 6.12.17) indicate that transport is both dominated and controlled by the same faults identified and discussed in Section 6.12.1.2. Thus, Splay G of the Solitario Canyon fault is the main transport-facilitating feature and leads to the early appearance of ^{237}Np in the tsw39 layer and at the water table. Once ^{237}Np reaches the TSw-CHn interface, it is transported along the eastward-sloping and relatively impermeable interface with the draining water.

The Ghost Dance fault splay appears to play a more significant role in ^{237}Np transport than in the ^{99}Tc transport. This fault is very clearly identified in Figures VII.1, VII.4, VII.7 and VII.22 as a conduit of very fast transport to the water table. The Sundance fault is the next fault (in terms of time at which contributions to transport become significant), followed by the Drill Hole Wash fault, and finally the main Ghost Dance fault. These faults appear to act as barriers to the lateral migration of radionuclides across them, as the fracture and matrix X_R indicate. Note, however, that the sorbed ^{237}Np distributions straddle the faults, especially at long times. Of interest is the observation that at $t \geq 10,000$ years, the F_R distribution appears to have reached the main Solitario Canyon fault both in the tsw39 layer and at the water table. This can have important implications in the long-term transport of ^{237}Np , given its long half-life (2.14×10^6 years).

As in the case of ^{99}Tc transport, radionuclide transport to the groundwater is faster in the southern part of the potential repository, where it is also areally concentrated. This is caused by (a) the infiltration and percolation patterns, (b) the fast conduit to transport provided by the faults (and especially the Splay G of the Solitario Canyon fault and the Ghost Dance fault splay); (c) the permeability barriers to flow (and, consequently, to transport) in the northern part, where perched water bodies occur and through which water is forced to flow slowly; and (d) the distribution of the vitric CHv layers. A detailed discussion on the subject of transport pattern can be found in Section 6.12.2.3.

6.13.1.5 Comparison to the ^{99}Tc Transport

The obvious difference between the ^{99}Tc and the ^{237}Np transport is sorption. This results in (a) the universally lower (than ^{99}Tc) concentrations of ^{237}Np in the fractures and in the matrix at the same times, and (b) the slower breakthroughs indicated by Figures VII.13 through VII.24 and Table 6.15.

6.13.1.6 Comparison to the Semianalytical 2-D FRACL Predictions

The fracture X_R distributions of ^{237}Np above the water table at $t = 10,000$ and $t = 100,000$ years in Figures VII.19 and VII.22 (obtained from the EOS9nT simulations) are generally consistent with the travel times predicted by the 2-D semianalytical FRACL solutions in Section 6.9. Figures V.2 and V.8 (see Attachment V) show that, for mean present-day infiltration, ^{237}Np transport through the fractures and matrix (but not accounting for faults) in Cross Sections 1 and 2 (See Section 6.5) takes over 10,000 years, but less than 100,000 years, to reach the water table. Figure VII.19 shows only limited, fault-related transport at 10,000 years. At $t = 100,000$ years, Figure VII.22 shows a fracture X_R distribution consistent with ^{237}Np arrivals through the bulk of the fractures (i.e., fractures not related to the faults), in addition to the earlier fault contributions.

The transport of ^{237}Np in Column 3 (Figures V.14 and V.20) does not appear to be consistent with the results of the 3-D simulations. The main reason for this apparent discrepancy is the inability of the 2-D FRACL semianalytical model to account for 3-D effects on flow and transport. A detailed discussion on the subject can be found in Section 6.12.2.5. Note that caution should be exercised in comparing the EOS9nT and FRACL results for the reasons discussed in Section 6.12.2.5.

6.13.2 ^{237}Np Transport Under Monsoon Infiltration

The DTN of the input and output files for the three monsoon infiltration scenarios is DTN: LB991220140160.013 (Table 6.13). The higher monsoon infiltration rates (compared to those in present-day regimes, see Table 6.11) lead to the faster transport indicated in Figure 6.13.3, compared to that shown in Figure 6.13.1. The corresponding shorter t_{10} and t_{50} values are listed in Table 6.15.

The t_{10} for low, mean, and high monsoon infiltration is 17,000, 1,400, and 650 years, respectively. The corresponding t_{50} are 70,000, 21,000, and 9,000 years, respectively. These times are significantly lower than the ones for the present-day infiltration scenario, as the faster transport through the system would warrant. Because transport is faster than under present-day infiltration, radioactive decay of the released ^{237}Np has a less pronounced effect in the reduction of the R at a given time.

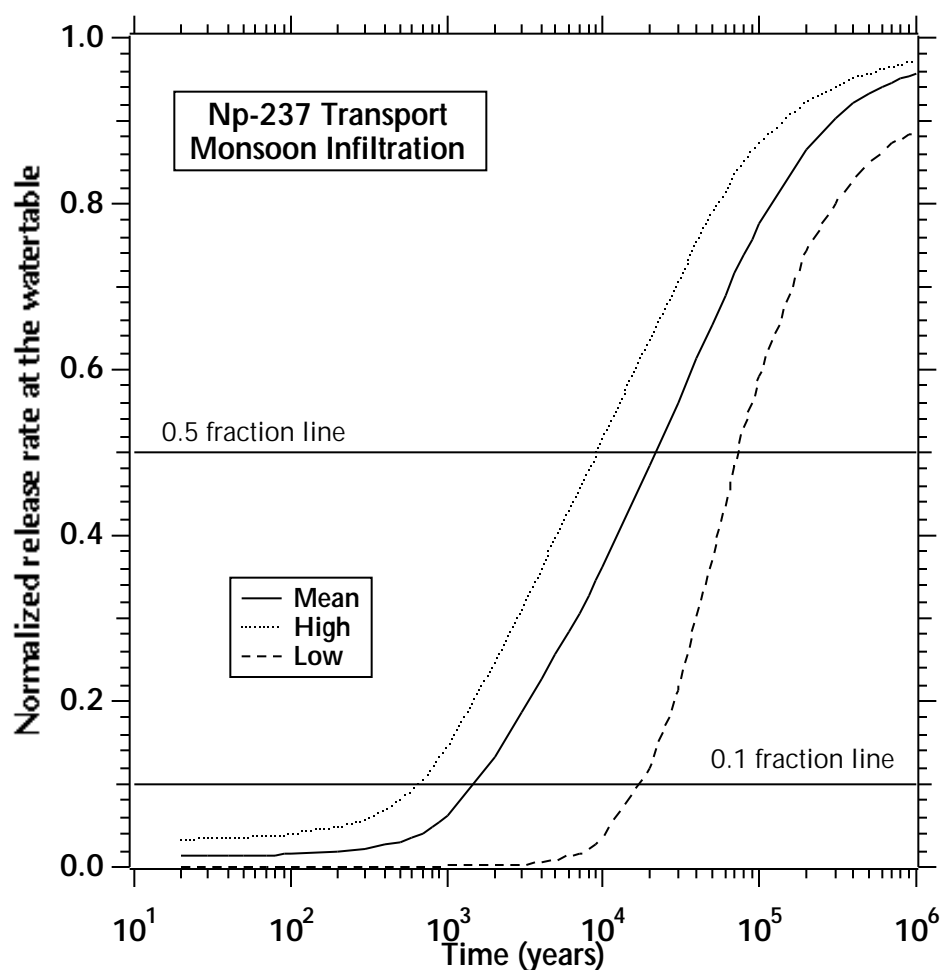


Figure 6.13.3. Normalized relative release R of ^{237}Np at the water table for varying monsoon climatic scenarios (DTN: LB991220140160.013, data submitted with this AMR).

6.13.3 ^{237}Np Transport Under Glacial Infiltration

The DTN of the input and output files for the three glacial infiltration scenarios is DTN: LB991220140160.014 (Table 6.13). The high and mean glacial infiltration infiltration rates are the highest in the three regimes (Table 6.11) and result in the breakthrough pattern shown in Figure 6.13.4. The corresponding shorter t_{10} and t_{50} values are listed in Table 6.15.

The t_{10} for low, mean, and high glacial infiltration is 40,000, 800 and 260 years, respectively. The corresponding t_{50} are 200,000, 10,000, and 3,000 years, respectively. For high and mean glacial infiltration, the t_{10} and t_{50} times are the shortest in the three infiltration regimes.

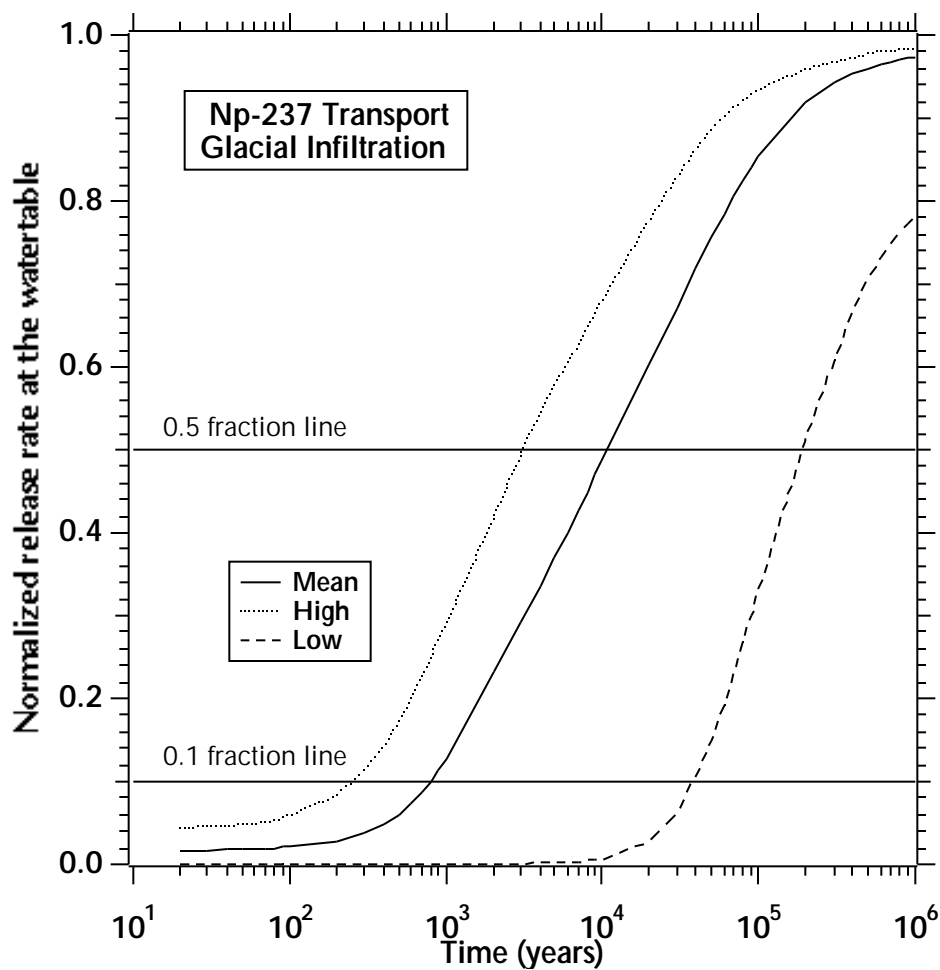


Figure 6.13.4. Normalized relative release R of ^{237}Np at the water table for varying glacial climatic scenarios (DTN: LB991220140160.014, data submitted with this AMR).

6.14 3-D TRANSPORT OF ^{239}Pu AND ITS DAUGHTERS

In this section we investigate the transport of ^{239}Pu by means of EOS9nT 3-D site-scale simulations of the entire UZ system of Yucca Mountain. Section 6.14 includes two subsections.

In Section 6.14.1 we discuss the transport of the strongly sorbing ^{239}Pu and its daughters for three levels of present-day infiltration. The results of this study are shown in Figures 6.14.1–6.14.2, and in Figures VIII.1 to VIII.24 of Attachment VIII. In Section 6.14.2 we study the transport of ^{239}Pu and its daughters for three levels of monsoon infiltration and three levels of glacial infiltration (Figures 6.14.3 to 6.14.6).

6.14.1 Transport of ^{239}Pu and its Daughters Under Present-Day Infiltration

The grids, flow fields, and conditions discussed in 6.11.2 corresponded to the #1 conceptual model of perched water (CRWMS M&O 1999d, Sections 6.2 and 6.6) and are used in the simulation of all infiltration regimes. The parameters used in the EOS9nT simulation of 3-D transport of the strongly sorbing ^{239}Pu are listed in Table 6.14. The DTN of the input and output files for the three present-day infiltration scenarios is DTN: LB991220140160.012 (Table 6.13). The distribution coefficients K_d of the ^{239}Pu daughters (i.e., ^{235}U and ^{231}Pa) can be found in DTN: LAIT831341AQ96.001 (see Table 6.14).

6.14.1.1 Breakthrough Curves

The normalized release rate R at the water table for present-day infiltration is shown in Figure 6.14.1. If the contributions of the daughter products (i.e., ^{235}U and ^{231}Pa) are not accounted for, R does not reach the 0.1 level even after 1,000,000 years of continuous release. This is due to the strong sorption of ^{239}Pu .

The picture changes dramatically, however, if the daughter contributions are included in the computations. The R of the sum of the parent and daughter contributions exhibits a delayed breakthrough. Thus, t_{10} is 12,000, 40,000, and 600,000 years for high, mean, and low present-day infiltration. The corresponding t_{50} values are 90,000, 250,000, and over 1,000,000 years (Table 6.15). Given the long half life of ^{239}Pu and the much longer half life of ^{235}U (see Tables 6.5 and 6.12), the daughter contributions are very important and cannot be neglected with impunity under the high infiltration regime. The daughter contributions are even more important under the wetter monsoon and glacial conditions (see Figures 6.13.3 to 6.13.6).

6.14.1.2 Daughter Contributions

The relative flux fractions M_R for present-day infiltration are shown in Figure 6.14.2. The interesting realization is that the ^{239}Pu contribution to the release rate starts declining rapidly after 1,000 years, and ^{235}U is by far the dominant species after $\geq 10,000$ years. Lower infiltration rates are associated

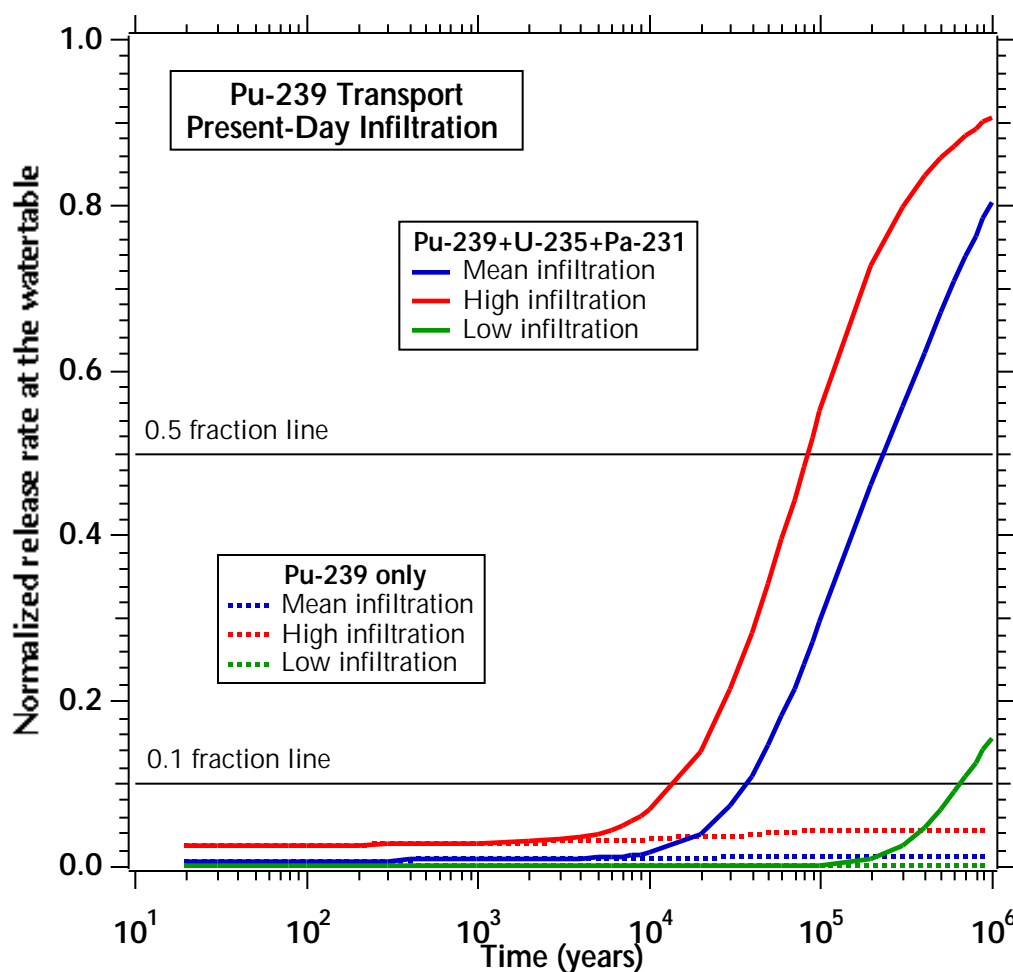


Figure 6.14.1. Normalized relative release rate of ^{239}Pu at the watertable for varying present-day climatic scenarios (DTN: LB991220140160.012, data submitted with this AMR).

with the earlier emergence of ^{235}U as the dominant species released at the water table. For example, at $t = 10,000$ years, water table releases consist mostly (over 95%) of ^{235}U under low present-day infiltration conditions. This is expected because, under a low infiltration regime, less ^{239}Pu reaches the water table on account of strong sorption. Note that the ^{231}Pa contribution is negligible because of the very long half life of ^{235}U .

6.14.1.3 Transport Mechanisms and Patterns

The importance of fractures on the ^{239}Pu transport is evident in Figure VIII.1 (see Attachment VIII), which shows the areal distribution of X_R in the aqueous phase in the fractures in the tsw39 layer at $t = 100$ years (under mean present-day infiltration). The contrast with the distribution of

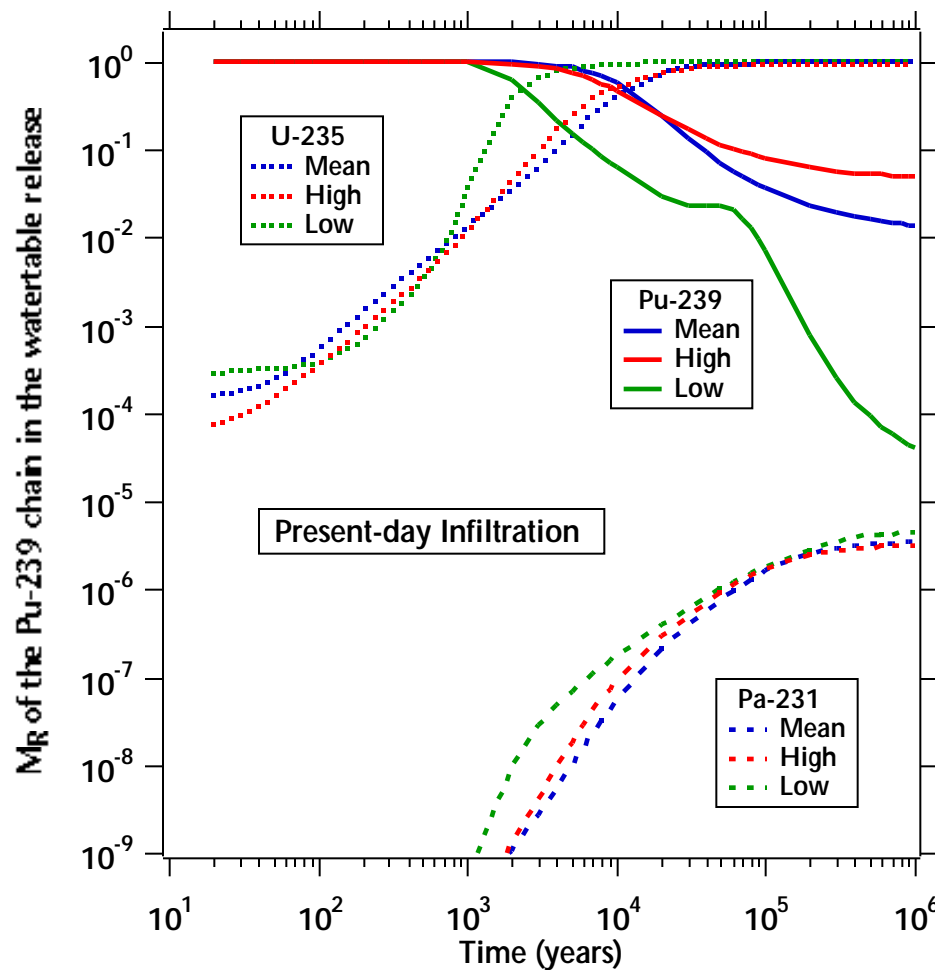


Figure 6.14.2. Relative flux fractions M_R of the members of the $^{239}\text{Pu} \rightarrow ^{235}\text{U} \rightarrow ^{231}\text{Pa}$ decay chain in the release at the water table over time for varying present-day climatic conditions (DTN: LB991220140160.012, data submitted with this AMR). Note that the ^{231}Pa contribution is negligible because of the very long half life of ^{235}U .

X_R in the matrix (Figure VIII.2), which shows no discernible difference from the background $X_R = 0$, is dramatic. The same difference between the X_R in the fractures and matrix in the tsw39 layer is observed at $t = 1,000$ years (Figure VIII.4 and VIII.5), $t = 10,000$ years (Figure VIII.7 and VIII.8), and $t = 100,000$ years (Figure VIII.10 and VIII.11).

As in the case of ^{237}Np , the distribution of matrix F_R at $t = 100$ years shows a sizable ^{239}Pu presence sorbed onto the matrix of the tsw39 layer (Figure VIII.3). The area of non-zero F_R is significantly larger than that of the fracture X_R footprint at the same time. The same pattern persists as time

increases (see Figures VIII.6, VIII.9 and VIII.12), with the fracture X_R distribution showing only slight expansion and the F_R distribution continuously expanding.

The transport pattern is similar above the water table (Figures VIII.13 to VIII.24), where (a) the fracture X_R shows faint signs of ^{239}Pu presence (in the vicinity of Splay G of the Solitario canyon fault distribution), which remains practically unchanged over time, (b) the matrix X_R does not register any measurable ^{239}Pu presence (for a linear X_R scale), and (c) the footprint of the measurable F_R distribution keeps expanding.

Figures VIII.1 through VIII.24 indicate the efficiency of the matrix as a ^{239}Pu sink. ^{239}Pu diffusion from the fractures into the matrix is followed by immediate sorption and thus removal from the matrix aqueous phase. The X_R in the matrix aqueous phase shows no discernible signs of ^{239}Pu presence because of the very strong sorption of ^{239}Pu . The logarithmic scale of the F_R distributions allows delineation of the extent of the measurable ^{239}Pu presence sorbed onto the matrix.

6.14.1.4 Transport-Controlling Features

Review of Figures VIII.1 through VIII.24 (see Attachment VIII) and comparison to the corresponding ^{237}Np figures (Figures VII.1 to VII.24) indicate that transport is both dominated by the faults identified and discussed in Sections 6.12.1.2 and 6.12.1.3. Thus, Splay G of the Solitario Canyon fault is the main transport-facilitating feature and leads to the early appearance of ^{239}Pu in the tsw39 layer and above the water table .

The Ghost Dance fault splay appears to play a significant role. This fault is very clearly identified in Figures VIII.7 and VIII.10 as a conduit of very fast transport to the water table . The Sundance fault is the next fault (in terms of time at which contributions to transport become significant). The Drill Hole Wash fault does not appear to have any contributions in the fracture or matrix X_R distributions at any time in either the tsw39 layer or at the water table , but is discernible in the F_R distributions at late times.

The main Ghost Dance fault becomes discernible in the F_R distributions at $t \geq 10,000$ in tsw39, and marginally so above the water table at $t = 100,000$. Note that at $t \geq 10,000$ years, the F_R distribution appears to have reached the main Solitario Canyon fault both in the tsw39 layer and above the water table .

6.14.1.5 Comparison to the ^{99}Tc and ^{237}Np Transport

The obvious difference between the transport of ^{239}Pu and those of ^{99}Tc and ^{237}Np is the strong sorption of ^{239}Pu . This results in (a) ^{239}Pu relative concentrations X_R in the fractures and the matrix that are universally lower than those for ^{99}Tc (Figures 6.12.2 to 6.12.17) and ^{237}Np (Figures VII.1 to VII.24 in Attachment VII) at the same times, and (b) no arrival at the water table of significant ^{239}Pu amounts even after $t = 100,000$ years (see Figure 6.14.1). Note that the matrix X_R of ^{239}Pu (at any location and time) does not show any discernible difference from the background

zero concentration.

The strong sorption of ^{239}Pu results in fracture and matrix X_R distributions that do not change significantly over time. This is observed in both the tsw39 layer and immediately above the water table. This is not the case in the weaker-sorbing ^{237}Np , in which these distributions increase measurably over time. The sorbed concentrations of ^{239}Pu in tsw39 or above the water table at any time are lower than the corresponding ones for ^{237}Np . This is because the strong sorption of ^{239}Pu removes a large portion of the radionuclide mass in the overlaying layers, leading to lower concentrations in the underlying layers, and hence lower sorbed concentrations.

6.14.1.6 Comparison to the Semianalytical 2-D FRACL Predictions

The fracture X_R distributions of ^{239}Pu above the water table at $t = 100,000$ years in Figures 6.14.1 and VIII.22 indicate no breakthrough (other than the fast transport in the faults) at this time. This is consistent with the predictions of the 2-D semianalytical model in Section 6.9 (see Attachment V, Figures V.3, V.9, V.15, and V.21).

6.14.2 ^{239}Pu Transport Under Monsoon and Glacial Infiltration

The DTNs of the input and output files for the three monsoon and glacial infiltration scenarios are LB991220140160.013 and LB991220140160.014 (Table 6.13). The faster transport depicted in Figures 6.14.3 and 6.14.4 is the result of the higher monsoon and glacial infiltration rates, respectively.

The changes in the climatic conditions lead to breakthrough curves that follow the same pattern established in the Tc and Np transport. Thus, higher infiltration corresponds to faster breakthroughs (Table 6.15). The daughter contributions under monsoon and glacial conditions are shown in Figures 6.14.5 and 6.14.6, respectively. As in the present-day infiltration regime, ^{235}U becomes by far the dominant species released at the groundwater after about 7,000 years, and the contribution of ^{239}Pu becomes practically negligible after 10,000 years. Lower infiltration rates are also associated with (a) earlier significant contributions of ^{235}U to releases at the groundwater table and (b) a faster, steeper and larger decline of the ^{239}Pu contributions. The ^{231}Pa contribution is negligible.

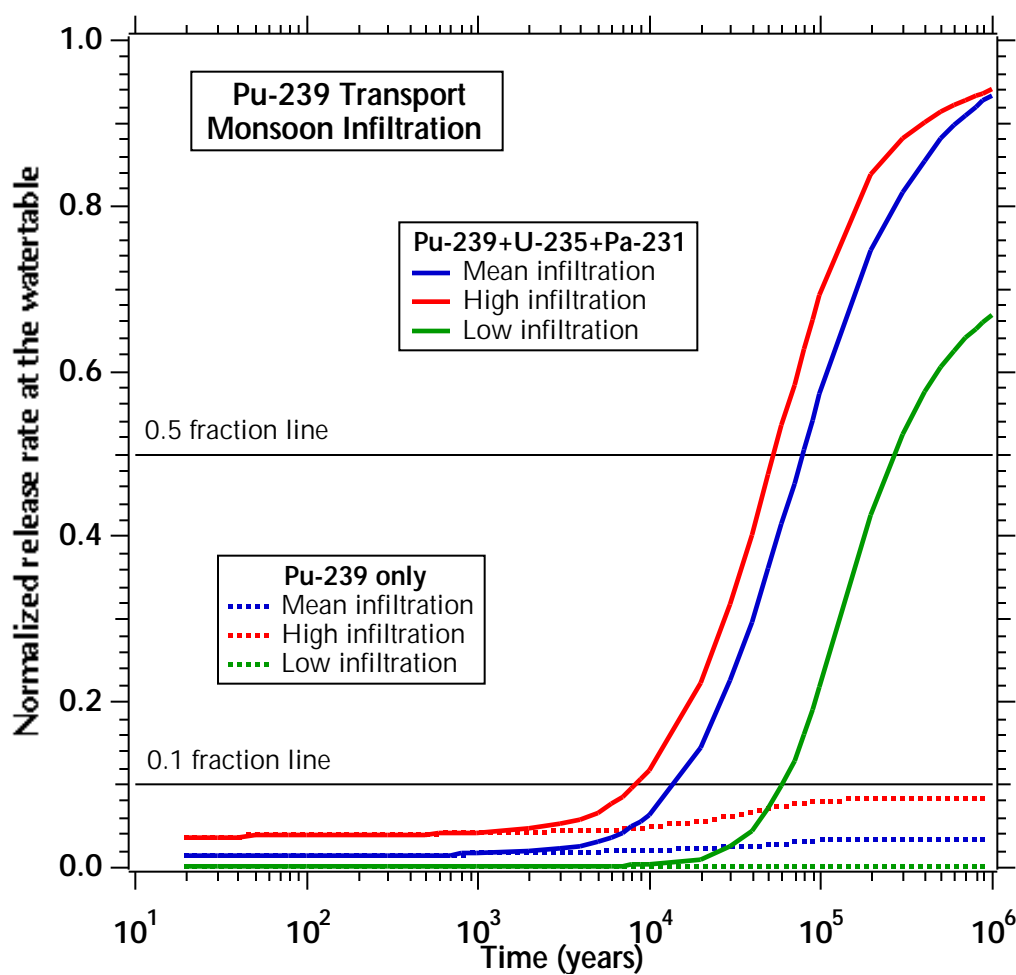


Figure 6.14.3. Normalized relative release R of ^{239}Pu at the water table for varying monsoon climatic scenarios (DTN: LB991220140160.013, data submitted with this AMR).

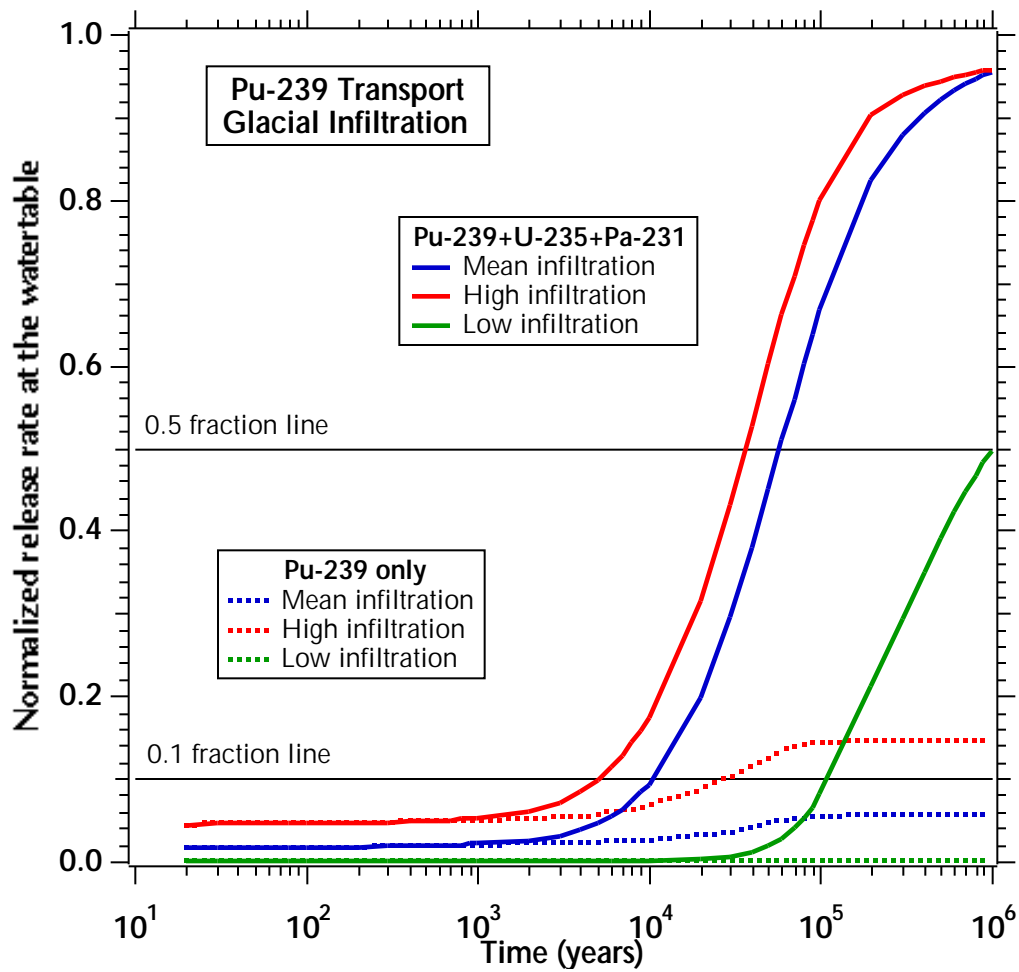


Figure 6.14.4. Normalized relative release R of ^{239}Pu at the water table for varying glacial climatic scenarios (DTN: LB991220140160.014, data submitted with this AMR).

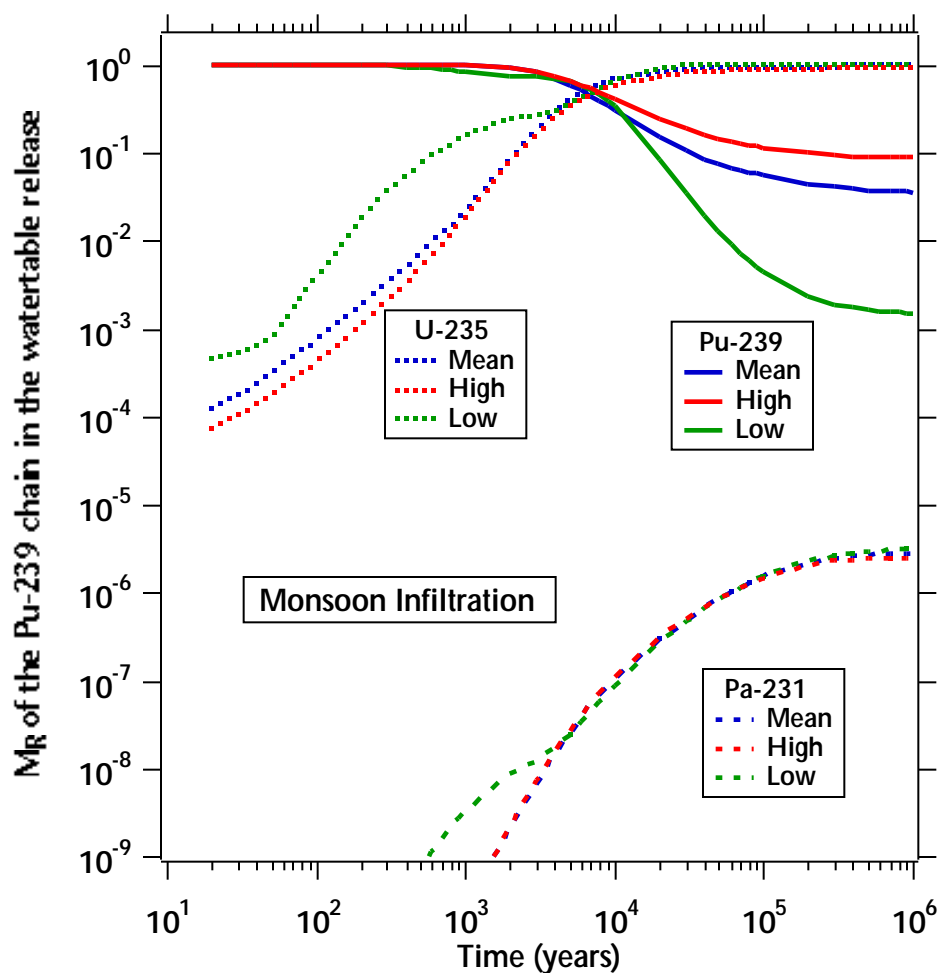


Figure 6.14.5. Relative mass fluxes M_R of the members of the $^{239}\text{Pu} \rightarrow ^{235}\text{U} \rightarrow ^{231}\text{Pa}$ decay chain in the release at the water table over time for varying monsoon climatic conditions (DTN: LB991220140160.013, data submitted with this AMR).

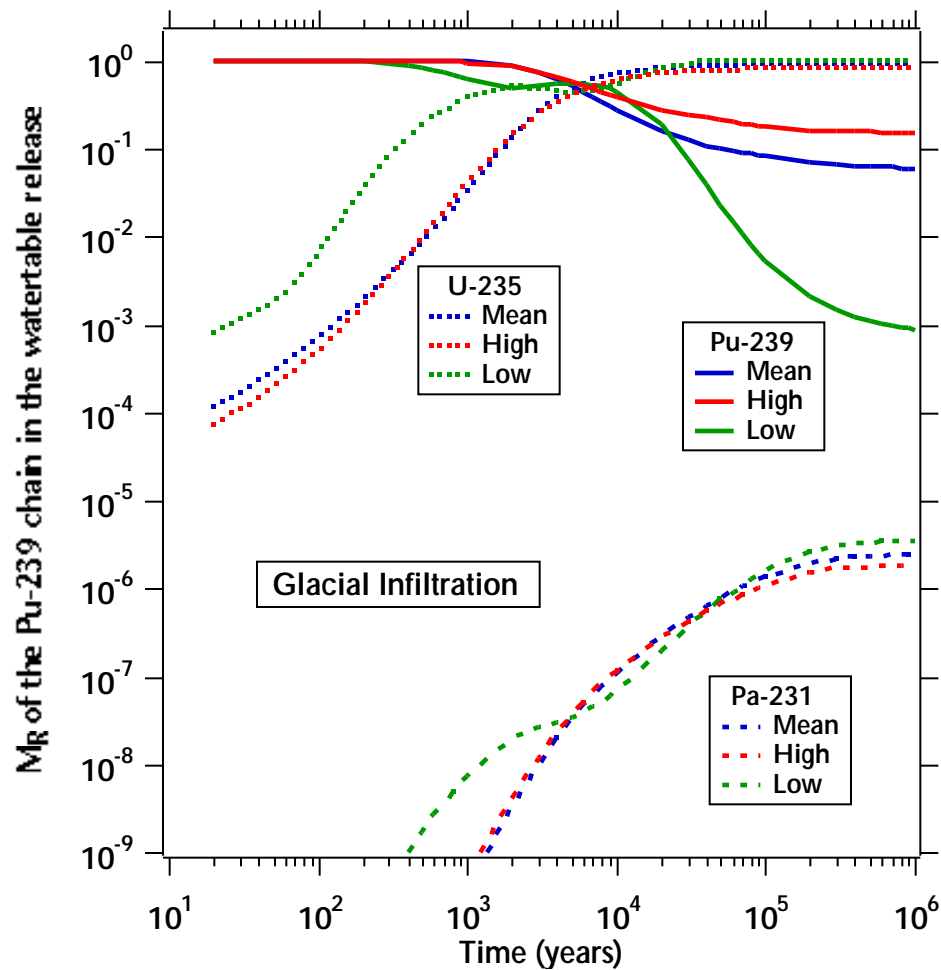


Figure 6.14.6. Relative mass fluxes M_R of the members of the $^{239}\text{Pu} \rightarrow ^{235}\text{U} \rightarrow ^{231}\text{Pa}$ decay chain in the release at the water table over time for varying glacial climatic conditions (DTN: LB991220140160.014, data submitted with this AMR).

6.15 EFFECTS OF VARIOUS PERCHED-WATER REGIMES ON 3-D TRANSPORT

Three conceptual perched water models were defined and studied in CRWMS M&O (1999d, Sections 6.2 and 6.6). Here we investigate the effect of differences in the three perched water models on radionuclide transport under mean present-day conditions. The DTNs of the input and output files for the #2 perched water model (involving flow bypassing) and for the no perched water model are listed in Table 6.13. The parameters used in the EOS9nT simulations are listed in Tables 6.16 and 6.17.

For reference, we show in Figure 6.15.1 the normalized release rate of the important radionuclides for the #1 perched water model under mean present-day infiltration (summarized from Sections 6.12 to 6.14). Figures 6.15.2 and 6.15.3 show the R for the same radionuclides under the same climatic conditions and for the other two perched water models.

Table 6.16. Input parameters for the EOS9nT 3-D site-scale simulations of solute transport (#2 perched-water model, mean present-day infiltration)

Parameters	Source
Transfer coefficient $K_i = 1$	Conventionally used value
Tortuosity $\tau \simeq \phi$	DTN: LB991220140160.019 and DTN: LAIT831341AQ96.001, Grathwohl (1998, pp. 28-35), Farrell and Reinhard (1994, p. 64)
Longitudinal dispersivity $\alpha_L = 1$ m in the fractures, 0.1 m in the matrix	Scientific judgement in the absence of available data
Properties and characteristics of the geologic units, steady-state pressures, water saturations and flow fields	DTN: LB990801233129.004
Sorption coefficients K_d for Tc, Np, Pu, U, Th, Pa	DTN: LB991220140160.019 and DTN: LAIT831341AQ96.001
Fracture porosity $\phi = 0.99$	A reasonable estimate that allows limited sorption in the fractures.

Table 6.17. Input parameters for the EOS9nT 3-D site-scale simulations of solute transport (no-perched-water model, mean present-day infiltration)

Parameters	Source
Transfer coefficient $K_i = 1$	Conventionally used value
Tortuosity $\tau \simeq \phi$	DTN: LB991220140160.019 and DTN: LAIT831341AQ96.001, Grathwohl (1998, pp. 28-35), Farrell and Reinhard (1994, p. 64)
Longitudinal dispersivity $\alpha_L = 1$ m in the fractures, 0.1 m in the matrix	Scientific judgement in the absence of available data
Properties and characteristics of the geologic units, steady-state pressures, water saturations and flow fields	DTN: LB990801233129.004
Sorption coefficients K_d for Tc, Np, Pu, U, Th, Pa	DTN: LB991220140160.019 and DTN: LAIT831341AQ96.001
Fracture porosity $\phi = 0.99$	A reasonable estimate that allows limited sorption in the fractures.

The grids, flow fields and conditions discussed in 6.10.2 corresponded to the #1 conceptual model of perched water (CRWMS M&O 1999d, Sections 6.2 and 6.6). This is the permeability barrier model, which uses the calibrated perched water parameters for fractures and matrix in the northern part of the model domain, and modified property layers (including the tsw38, tsw39, ch1z and ch2z layers) where the lower basal vitrophyre of the TSw is above the zeolites of the CHn. A detailed discussion of this perched water model can be found in CRWMS M&O (1999d, Section 6.2.2).

The differences between the breakthrough curves from the #1 and the #2 perched water models (Figures 6.15.1 and 6.15.2, respectively) are very small. For all practical purposes, the two models result in the same transport behavior.

A different picture emerges from Figure 6.15.3 of the no-perched water model, which exhibits a somewhat slower breakthrough. The t_{10} are 400, 17,000, and 45,000 years for ^{99}Tc , ^{237}Np , and the ^{239}Pu chain members. The corresponding t_{50} for the same radionuclides are 6,000, 140,000, and 300,000 years, respectively.

Note that caution should be exercised in attempting to compare these EOS9nT results (obtained

from a 3-D site-scale simulations) to the 2-D FRACL predictions in Section 6.9 because the latter cannot account for 3-D effects such as flow under varying perched water scenarios. A discussion on this subject can be found in Section 6.12.2.5.

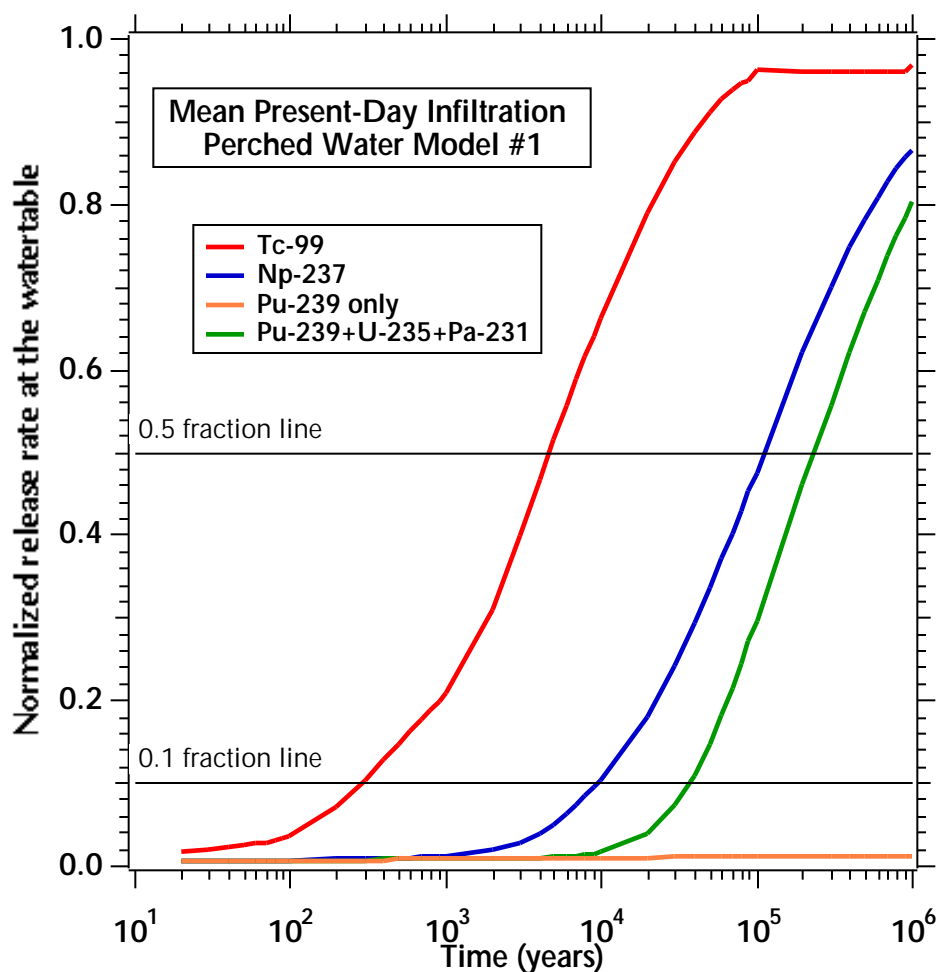


Figure 6.15.1. Normalized relative releases at the watertable for mean present-day infiltration and the #1 perched water model (DTN: LB991220140160.012, data submitted with this AMR).

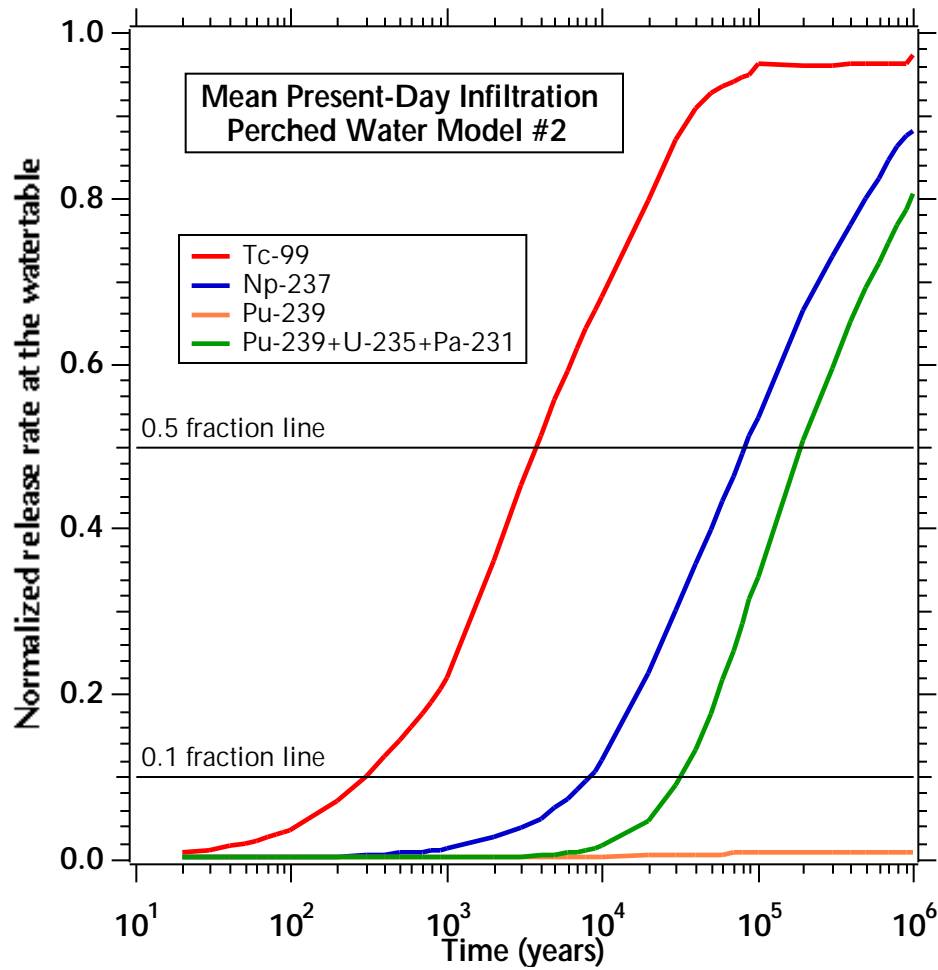


Figure 6.15.2. Normalized relative releases at the watertable for mean present-day infiltration and the #2 perched water model (DTN: LB991220140160.015, data submitted with this AMR).

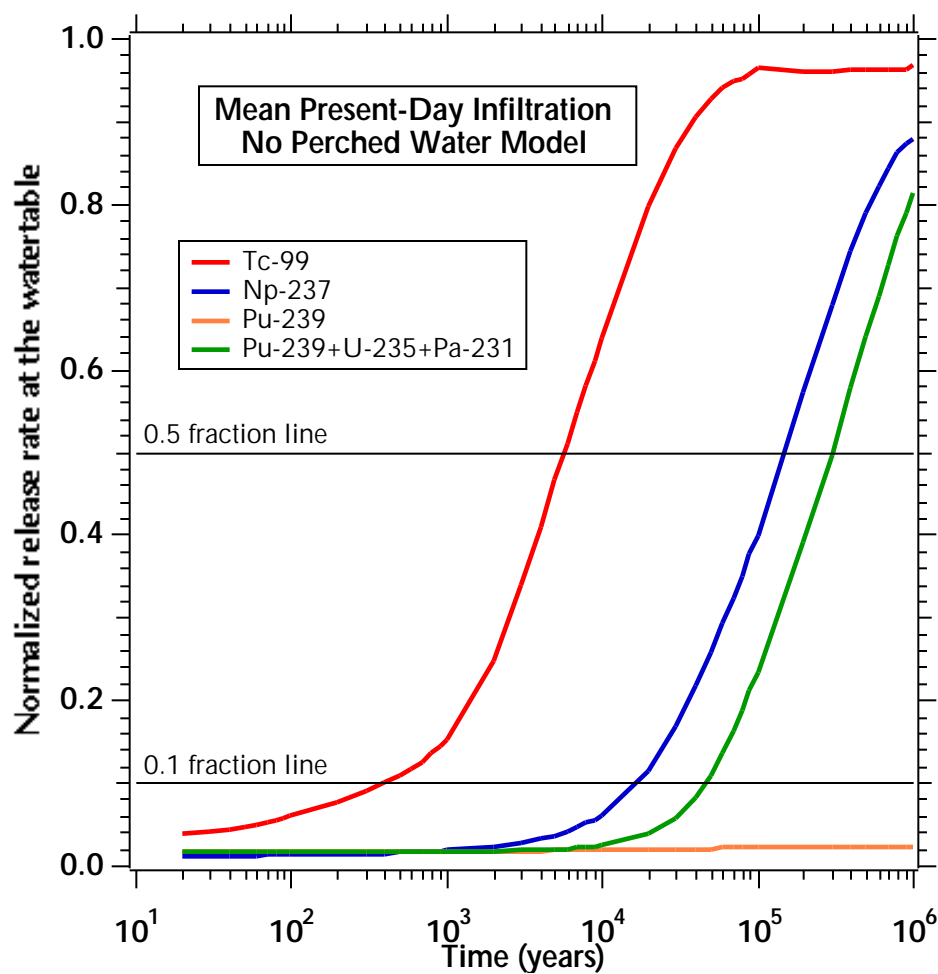


Figure 6.15.3. Normalized relative releases at the watertable for mean present-day infiltration and the no-perched water model (DTN: LB991220140160.016, data submitted with this AMR).

6.16 3-D SITE-SCALE TRANSPORT OF Pu COLLOIDS

In this section, we study the transport of true colloids in the entire Yucca Mountain system using large-scale 3-D grids. The infiltration regime is that of mean present-day. In these simulations, the flow field and the 3-D grid are identical to the ones discussed in the sections on transport of dissolved species under the same climatic conditions (Sections 6.11 to 6.14).

Section 6.16 includes eight subsections. In Section 6.16.1 we discuss the colloidal forms considered in the simulations. In Section 6.16.2 we present the mathematical model of filtration used in EOS9nT, and discuss its parameters for the four colloids of various sizes (450 nm, 200 nm, 100 nm and 6 nm) we discuss in the ensuing sections. In Section 6.16.3 we list the four cases of colloid transport of the four colloids we investigated.

In Section 6.16.4 we study colloid transport for irreversible filtration. In Section 6.16.5 we investigate colloid transport with kinetic filtration and fast colloid declogging (detachment). The results of this study are shown in Figure 6.16.1, in Figures IX.1 to IX.24 of Attachment IX, and in Figures X.1 to X.24 of Attachment X. In Section 6.16.6 we discuss colloid transport with kinetic filtration and slow colloid declogging (Figure 6.16.2). In Section 6.16.7 we evaluate the importance of fractures in colloid transport with kinetic filtration and fast colloid declogging (Figure 6.16.3). Finally, in Section 6.16.8 we discuss some important observations from the colloid studies in Section 6.16.

6.16.1 Colloidal Forms and Properties

As there are indications that colloid-assisted transport (i.e., transport by pseudocolloids) in the UZ of Yucca Mountain will not be significant because of the low concentrations of naturally occurring colloids such as clays (CRWMS M&O 1999f, Section 6), only true colloids were considered in the simulation. Those were taken to have the properties of PuO_2 and are subject to radioactive decay.

Four colloids of different sizes were considered. Their sizes and their accessibility factors were taken from CRWMS M&O (1999f, Table 1, Section 6), and are shown in Table 6.18. The parameters used in the EOS9nT simulations of 3-D transport of the colloids are listed in Table 6.19. The DTN of the input and output files for the three present-day infiltration scenarios is DTN: LB991220140160.017 (Table 6.13).

6.16.2 Colloid Filtration Model and Coefficients

Pore-size exclusion (straining filtration) was described using the accessibility factors shown in Table 6.18. The linear kinetic model of colloid filtration described by Equation 15 was used in the simu-

Table 6.18. Properties of the four colloids in the EOS9nT simulations

Parameter	450 nm	200 nm	100 nm	6 nm
Diffusion coefficient [*] D_0 (m ² /s)	9.53×10^{-13}	2.15×10^{-12}	4.29×10^{-12}	7.15×10^{-11}
Velocity adjustment factor [†] f	1.5	1.2	1.1	1.0
Accessibility factor [‡] f_c in the TSw	0.05	0.10	0.20	0.65
Accessibility factor [‡] f_c in the CHv	0.45	0.50	0.55	0.80
Accessibility factor [‡] f_c in the CHz	0.20	0.25	0.25	0.65

*: From DTN: LB991220140160.019

†: Reasonable estimates, see p. 54

‡: From AMR U0070, Table 1

lations. The forward kinetic coefficient κ^+ was computed from Equation 16, in which the velocity coefficients are as shown in Table 6.18, and ϵ is computed using Equation 2 of Harvey and Garabedian (1991), which, in our nomenclature, is

$$\epsilon = 1.5 \frac{1 - \phi}{d_m} \alpha_c \eta_c, \quad (\text{Eq. 30})$$

where d_m is the particle size of the medium grains or the fracture aperture $[L]$, α_c is the single collector efficiency, and

$$\eta_c = 0.9 \left(\frac{k_B T}{\mu_w d_c d_m u} \right)^{2/3} + 1.5 \left(\frac{d_c}{d_m} \right)^2 + (\rho_c - \rho) \frac{g d_c^2}{18 \mu u} \quad (\text{Eq. 31})$$

in which k_B is the Boltzman constant, d_c is the colloid diameter $[L]$, T is the absolute temperature, and all other terms remain as previously defined. The clogging (forward) kinetic coefficients κ^+ are computed internally in EOS9nT.

No information exists on the kinetic declogging (reverse) coefficient κ^- . To alleviate the problem, κ^- in the EOS9nT coefficients was entered as a fraction of κ^+ . We believe that this is a sounder

Table 6.19. Input parameters for the EOS9nT 3-D site-scale simulations of colloid transport
(# 1 perched-water model, mean present-day infiltration)

Parameters	Source
Transfer coefficient $K_i = 1$	Conventionally used value
Tortuosity $\tau \simeq \phi$	DTN: LB991220140160.019 and DTN: LAIT831341AQ96.001, Farrell and Reinhard (1994, p. 64)
Longitudinal dispersivity $\alpha_L = 0.5$ m in the fractures, 0.05 m in the matrix	Scientific judgement in the absence of available data
Properties and characteristics of the geologic units, steady-state pressures, water saturations and flow fields	DTN: LB990801233129.003 (see Table 6.11)
Colloid density $\rho_c = 11,640$ kg/m ³ (PuO ₂)	Lide (1992, p. 4-83)
Forward kinetic filtration (clogging) coefficient κ^+ : from Equations 6, 30 and 31, parameters computed at 25 °C	Harvey and Garabedian, p. 180, Equation 6, 1991
Backward (reverse) kinetic filtration (declogging) coefficient $\kappa^- = 100\kappa^+; 0.1\kappa^+; 0$	Reasonable estimates bracketing the range of κ^-
Fracture porosity $\phi = 0.99$	A reasonable estimate that allows limited colloid filtration (attachment) in the fractures.

approach than the constant κ^- employed in CRWMS M&O (1999f, Section 6) because it maintains dependence on the flow velocity. Because the kinetic coefficient κ^+ is a linear function of the flow velocity, dependence of κ^- on velocity is conceptually sounder than the constant value approach.

6.16.3 The Colloid Transport Simulation Cases

The following four cases were investigated:

1. $\kappa^- = 0$. This corresponds to a case of no declogging, in which colloids, once filtered, do not detach from the pore/fracture walls.

2. $\kappa^-/\kappa^+ = 100$. This corresponds to strong kinetic declogging and will provide an estimate of maximum colloidal transport.
3. $\kappa^-/\kappa^+ = 0.1$. This corresponds to weak kinetic declogging and approaches equilibrium filtration behavior.
4. Same as in Case 2, but the fractures are assumed to have the same colloidal transport properties as the corresponding matrix. This study provides an estimate of the importance of fractures in the transport of colloids. Note that the change in the filtration properties affects only 1% of the fracture pore volume (because $\phi = 0.99$ in the fractures, see Equation 30).

6.16.4 Colloid Transport Case 1

The results of this simulation indicate no colloid breakthrough at any time. This is consistent with the underlying clogging-only model.

6.16.5 Colloid Transport Case 2

6.16.5.1 Breakthrough Curves

Figure 6.16.1 shows the relative release rate R of the four colloids at the water table. Two observations appear particularly important. The first is the very fast breakthrough of the larger colloids (characterized by a rapid rise of the breakthrough curve), the rapidity of which increased slightly with the colloid size. The t_{10} for the three larger colloids is only about 15 years, and 30 years for the 6 nm colloid; t_{50} is about 60 years for the 450 nm and the 200 nm colloid, about 80 years for the 100 nm colloid, and 1,200 years for the 6 nm colloid. The second observation is that, counter to expectations, the smallest colloid (6 nm) exhibits the slowest breakthrough. This behavior results from a combination of the following factors:

1. The larger transport velocity of larger colloids, which, by virtue of their size, can only move in the center of pores/fractures where velocities are larger than the average water velocity. In this case, the 450 nm colloid moves at 1.5 times the water velocity (i.e., $f = 1.5$, see Equation 16 in Section 6.2.4.1).
2. The inability of larger colloids to penetrate into the matrix from the fractures because of size exclusion. Thus, the colloid mass in the fractures is not reduced through colloidal diffusion and/or hydrodynamic dispersion, and practically all of it moves exclusively in the fractures. The 6 nm colloid is capable of diffusing into the matrix, a process which in Figure 6.16.1 manifests itself by the substantially slower breakthrough, the milder rise of the curve, and its lower maximum R value.

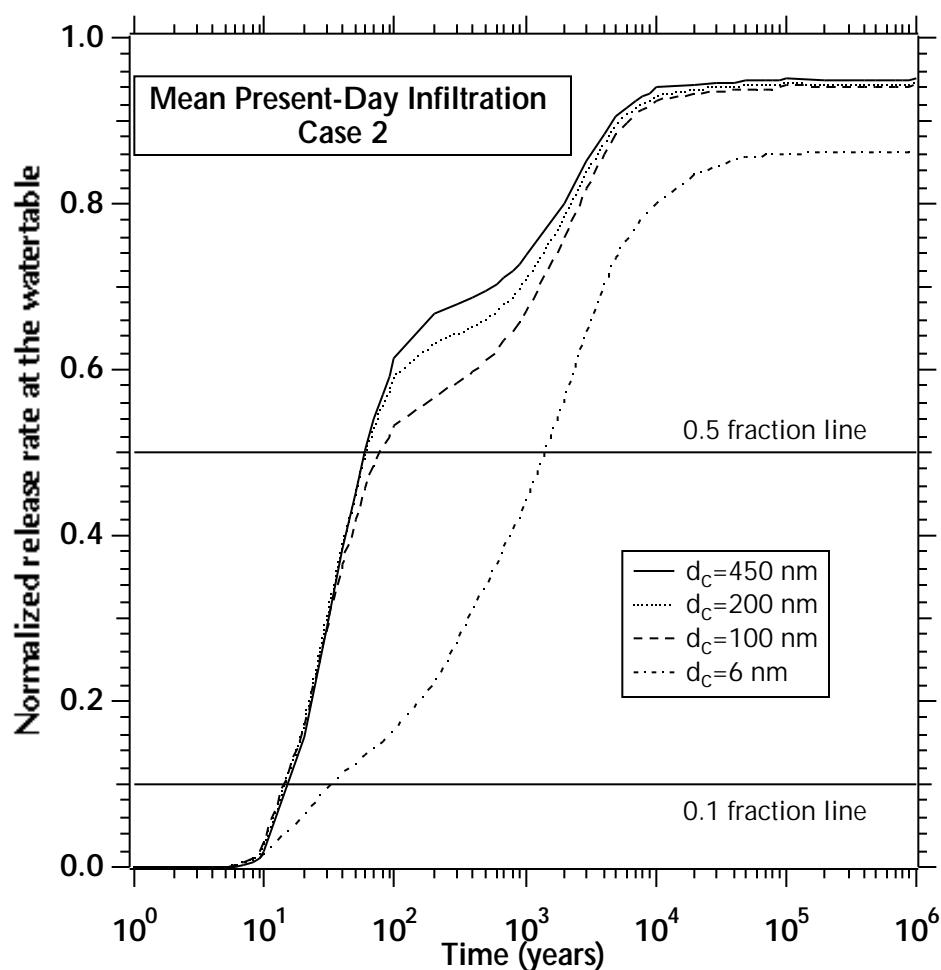


Figure 6.16.1. Normalized release at the water table in Case 2 of colloidal transport for mean present-day infiltration (DTN: LB991220140160.017, data submitted with this AMR).

6.16.5.2 Transport Mechanisms and Patterns of the 6 nm Colloid

The importance of fractures on the transport of the 6 nm colloid (Co0060) is evident in Figure IX.1 (see Attachment IX), which shows the areal distribution of X_R in the aqueous phase in the fractures in the tsw39 layer at $t = 10$ years (under mean present-day infiltration). Despite the very early time, the colloid concentration in the fracture is substantial, and it approaches the release concentration ($X_R = 0.965$) at its maximum.

The reasons for the significant presence (in terms of areal extent and level of concentration) of the 6 nm colloid are that (a) diffusion into the matrix is limited because of its relatively large size (compared to solutes) and pore-exclusion, and (b) the tsw39 layer is above the TSw-CHn interface,

where significant filtration occurs. Note that the distribution pattern of the fracture X_R in Figure IX.1 indicates that the colloids (transported in the fractures) accumulate at the TSw-CHn interface and, unable to cross it, move along the sloping interface in an easterly direction. This transport is more pronounced in the 6-nm colloid than in the solutes (see Sections 6.11 to 6.14, and Attachments VII and VIII).

In contrast to Figure IX.1, the matrix X_R in Figure IX.2 shows no discernible difference from the background at the same time. In Figure IX.3, the distribution of matrix F_R at $t = 10$ years shows a sizable presence of the 6 nm colloid filtered onto the matrix of the tsw39 layer. As in the case of sorbing solutes, the area of nonzero F_R (Figure IX.3) is larger than that of the fracture X_R footprint (Figure IX.3) at the same time, and shows presence of filtered 6 nm colloids at locations where there appear to be no colloids suspended in the aqueous phase in the fractures.

At $t = 100$ years, the fracture X_R in Figure IX.4 is significant over a large area (larger than that for solutes at the same time) and is at its maximum value over a large portion of this area. Although the matrix X_R (Figure IX.5) does not register a measurable difference from the UZ background, the matrix F_R (Figure IX.6) shows a significant presence of the 6 nm colloid over an area larger than that covered by the fracture X_R (Figure IX.4). Note that the matrix F_R distribution indicates more filtration in the northern part of the potential repository. This is consistent with the permeability barriers that result in the perched water bodies at this location.

A comparison of the matrix F_R of the 6 nm colloid (Figure IX.6) to that of the dissolved ^{239}Pu (Figure VIII.3) shows a drastically different pattern. While the matrix F_R distribution of ^{239}Pu shows concentration of sorption in the southern part of the potential repository, the F_R of the 6 nm colloid shows filtration in both the northern and the southern part, i.e., colloids and sorbing radioactive solutes (Sections 6.12 to 6.15) are not similarly affected under the #1 perched water model. The reason for the different behavior is attributed to (a) the lower diffusion of the colloid into (and the lack of its sorption onto) the matrix (thus the faster transport of larger amounts to the TSw-CHn interface), (b) the lack of sorption and (b) the combined effects of pore-size exclusion and filtration at the interface that are quantitatively larger than the effects of sorption of the limited amounts of the dissolved ^{239}Pu (Figure VIIi.3).

The fracture X_R , matrix X_R , and matrix F_R distributions at $t = 1,000$ years and $t = 10,000$ years are shown in Figures IX.7 to IX.12, and they follow the same pattern. The matrix X_R registers measurable deviations from background at $t = 1,000$ years (Figure IX.8), and it shows extensive areas of relatively high concentrations at $t = 10,000$ years (Figure IX.11). At $t = 10,000$ years, the concentration in the fractures exceeds that in the water released from the potential repository (i.e., $X_R = 1.07$ in tsw39). This is caused by pore-exclusion (straining) at the TSw-CHn interface, which leads to the accumulation of the 6 nm colloid in the tsw39.

Transport at the water table is shown in Figures IX.13 to IX.24, and follows patterns analogous to those in the tsw39 layer. The high concentrations at the water table at early times ($t \leq 100$ years)

are noteworthy. The matrix X_R begins to show signs of colloid presence at $t = 1000$ years, and shows highly localized areas of large concentration at $t = 10,000$ years. The nonzero area of the matrix F_R is consistently larger than that for fracture X_R .

Note that the fracture X_R above the water table exceeds that in the water released from the potential repository, and the differences between the two increases with time. At $t = 10,000$ years, the maximum fracture $X_R > 2$, i.e., the concentration of the 6 nm colloid in the fractures above the water table is more than double that in the water released at the potential repository. This occurs because of the fast transport of the colloids in the fractures (where limited attachment occurs because of the large fracture porosity, i.e., $\phi = 0.99$) and their accumulation. This accumulation is caused by the very significant pore-size exclusion and kinetic (physical-chemical) filtration at the water table, which prevent colloids from entering the saturated zone while allowing water to flow into it. This occurs because the saturated zone behaves as a porous (rather than a fractured) medium with the properties of the TSw matrix.

Review of Figures IX.1 through IX.24 indicates that transport of the 6 nm colloid is dominated by the faults identified and discussed in Sections 6.12 to 6.14. Diffusion from the fractures into the matrix is delayed for the reasons discussed earlier, but the areal extent and the magnitude of the filtered concentration (indicated by the F_R distribution) indicates that its effect is sizable.

6.16.5.3 Transport Mechanisms and Patterns of the 450 nm Colloid

The fracture X_R , matrix X_R and matrix F_R distributions of the 450 nm colloid (Co450) in the tsw39 and above the water table are shown in Figures X.1–X.24 (see Attachment X). These figures correspond to the same times discussed in the 6 nm colloid.

Comparison of the Figures in Attachment X to those for the 6 nm colloid in Attachment IX indicates that fractures are far more important to the transport of the 450 nm colloid. Supporting evidence is provided by (a) the larger areal extent and values of the fracture X_R , (b) the smaller areal extent and lower values of the matrix F_R , and (c) the substantial delay in the appearance of 450 nm colloids in the matrix aqueous phase, when compared to the 6 nm case.

Thus, the fracture X_R in Figure X.4 ($t = 100$ years) indicates contributions from the whole area (at least) of the potential repository, and shows a much larger footprint than the corresponding 6 nm figure (Figure IX.4). Additionally, the maximum X_R exceeds 1 (= 1.40) because of accumulation behind the TSw-CHn interface caused by straining (pore-size exclusion). Because of its larger size, the straining is more pronounced in the 450 nm colloid, rather than in the 6 nm colloid, and leads to higher concentrations at earlier times behind the interface (see Figures X.4, X.7 and X.10). The same phenomenon occurs above the water table (Figures X.13, X.16, X.19 and X.29), where it is far more pronounced, and the fracture X_R reaches values as high as 72. Note that, while this indicates a significant colloid accumulation, it does not necessarily mean clogging and decrease in permeability (at least for a long time) if the concentrations of the colloid waste form are sufficiently

low. The reasons for this behavior at the water table were discussed in Section 6.16.5.2.

Compared to the 6 nm colloid, the 450 nm colloid exhibits consistently lower matrix F_R values over smaller areas (see Figures X.3, X.6, X.9, X.12, X.15, X.18, X.21, X.24). This is consistent with the expectation of lower diffusion from the fractures into the matrix and increased straining because of its larger size.

6.16.6 Colloid Transport Case 3

The change in the magnitude of the reverse kinetic filtration coefficient κ^- (as a fraction of κ^+) has a rather dramatic effect on colloid transport (Figure 6.16.2). This case is closer to equilibrium filtration and results in a breakthrough that occurs at a time about three orders of magnitude larger than that of Case 2 (see Figure 6.16.1). Thus, t_{10} is 12,000 years for the 450nm, the 200 nm and the 100 nm colloids, and infinity for the 6 nm colloid; t_{50} is infinity for all colloids because the maximum normalized release rate at the water table never exceeds 0.3.

Repeating the pattern discussed in Section 6.16.5, the larger three colloids reach the groundwater first. The 6 nm colloid reaches the groundwater slightly later, but it has a substantially different R curve, with a maximum value that is only one third that for the 450 nm colloid. This stems from both larger diffusion (compared to that of the larger colloids) into the matrix and the resulting slower transport, which allows radioactive decay to reduce the colloid mass. Note that the R of the 6 nm colloid reaches a plateau at only about $R = 0.097$, i.e., it does not even attain the 0.1 level.

6.16.7 Colloid Transport Case 4

Setting the fracture filtration properties equal to those of the matrix results leads to the transport scenario depicted in Figure 6.16.3. The effect of limited diffusion on transport (because of pore-size exclusion and filtration) becomes more obvious in this case. Thus, the 6 nm colloids are the first to reach the groundwater, the 450 nm are the last, and the first arrival times of the rest increase with their diameter.

The reason for this study was to obtain a measure of the relative importance of the fractures in UZ colloid transport. The t_{50} of the three larger colloids is about 1,000 years, and 2,000 years for the smallest colloid. Given that the significant difference between Figure 6.16.3 and 6.16.1 is due solely to assigning matrix filtration properties to only 1% of the pore volume of the fractures, the significant retardation of the colloids gives a measure of the importance of fractures and their relative contribution to the total colloid transport through the UZ system.

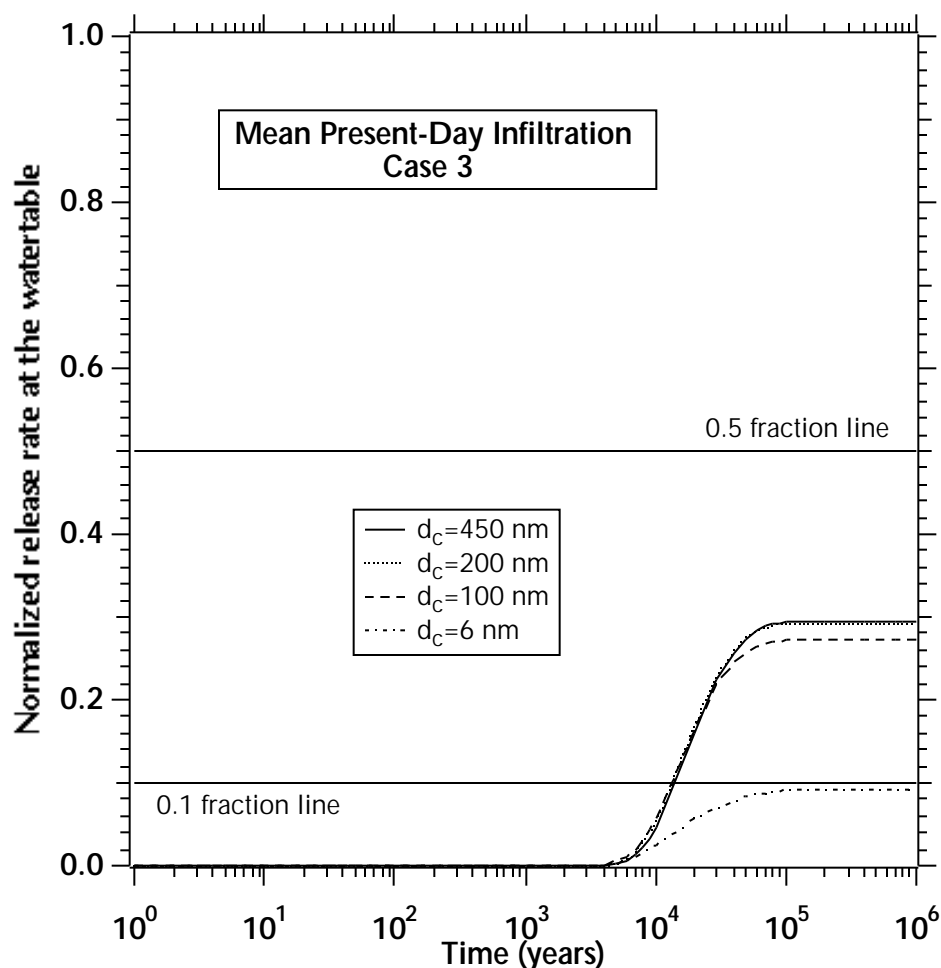


Figure 6.16.2. Normalized release at the water table in case 3 of colloidal transport for mean present-day infiltration (DTN: LB991220140160.017, data submitted with this AMR).

6.16.8 Uncertainties and Limitations

While the results in this section provide some elucidation of colloid transport, caution should be exercised in the interpretation of the simulation results. The reason for this notice of restraint is the realization of the substantial knowledge gaps that hamper the study of colloid behavior.

Thus, the tremendous variation in behavior with the change in the kinetic declogging coefficient κ^- should only serve to indicate the sensitivity of transport to κ^- . Similarly, the change in transport behavior when 1% of the fracture volume is given the attributes of the matrix should be viewed as indicative and qualitative, rather than quantitative and predictive. In essence, the sensitivity of the model to these parameters is evidenced by the change in t_{10} of the larger colloids from 15 years to

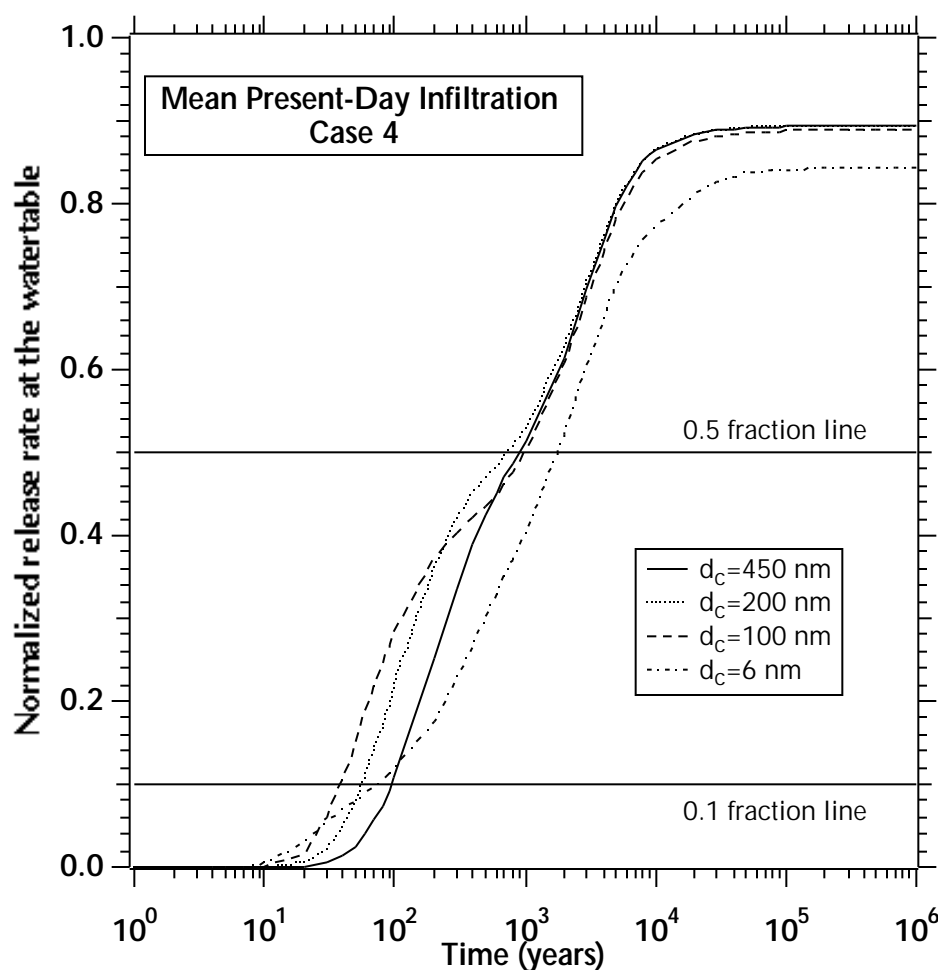


Figure 6.16.3. Normalized release at the water table in case 4 of colloidal transport for mean present-day infiltration (DTN: LB991220140160.017, data submitted with this AMR).

about 12,000 years to infinity as the value of κ^- changes from $100\kappa^+$ (fast declogging) to $0.1\kappa^+$ (slow declogging) to 0 (no declogging).

There are significant uncertainties in colloid modeling. It is not known if the applicability limits of the currently available kinetic models, developed from theoretical principles (Herzig et al. 1970) and tested in uniform sandy laboratory experiments (van de Weerd and Leijnse 1997) or small-scale field tests (Harvey and Garabedian 1991), are not breached under the UZ conditions at Yucca Mountain. The affinity of colloids for air-water interfaces can have a significant effect on their transport. The limitations of the equations for the prediction of the forward kinetic filtration (clogging coefficient) have not been tested under the UZ conditions, and the subject of kinetic declogging coefficient has

barely been raised (let alone studied). Additionally, it is unclear how representative the current size-exclusion (straining filtration) models are. Additional challenges and uncertainties are discussed in detail in Section 6.1.3.

6.17 ALTERNATIVE MODELS

In this section, we investigate an alternative conceptual model and its effect on transport. This conceptual model assumes no diffusion. All simulations in this section assume a mean present-day infiltration.

Section 6.17 includes two subsections. In Section 6.17.1 we study solute transport using the alternative conceptual model of no diffusion. The results of this study appear in Figure 6.17.1. In Section 6.17.2 we investigate colloid transport under the alternative model.

6.17.1 Solutes

As shown in Sections 6.11 to 6.15, the main mechanism of radionuclide retardation in the UZ is diffusion from the fracture into the matrix. This process transfers radionuclides from the fractures (the pathways of fast flow and the main conduits of transport) to the matrix, where their transport is retarded because of the much slower water velocities and matrix sorption.

In this section we investigate an alternative conceptual model that does not allow diffusion into the matrix. Thus, there is no mechanism for radionuclide removal from the fractures other than the relatively small sorption on the fracture walls. For non- and moderately sorbing radionuclides, this means that there is no means of retardation, and the contaminants in the fractures are transported virtually unhindered to the groundwater.

For mean present-day infiltration, the breakthrough curves in Figure 6.17.1 confirms this expectation. The nonsorbing ^{99}Tc and the moderately sorbing ^{237}Np move unhindered in the fractures, and their breakthrough curves to $t = 50$ years practically coincide. Transport in this case is extremely fast, and their t_{10} and t_{50} are about 5 and 30 years, respectively. The early behavior (i.e., to $t = 100$ years) reflects fracture transport exclusively, and the identity of the breakthrough curves of ^{99}Tc and ^{237}Np results from the absence of diffusion into the matrix and the limited ^{237}Np sorption onto the fracture walls, which is insufficient to have a measurable effect on transport. Note that the breakthrough curves reach a plateau at $t = 50$ years. The flat portion of the breakthrough curves indicates a constant radionuclide release rate at the water table, all of which is attributable to fracture flow.

The effects of the matrix become evident for $t > 100$ years, when matrix flow (and the contaminants it transports) begins to arrive at the water table. The arrival of matrix flow is indicated by the rising portion of the breakthrough curve after the fracture-associated R plateau. The nonsorbing ^{99}Tc is not retarded and arrives at the water table earlier than the moderately sorbing ^{237}Np . The phase of constant ^{237}Np release from fracture flow lasts from 50 to about 2,000 years, after which time the matrix flow (and the ^{237}Np it transports) arrive at the water table.

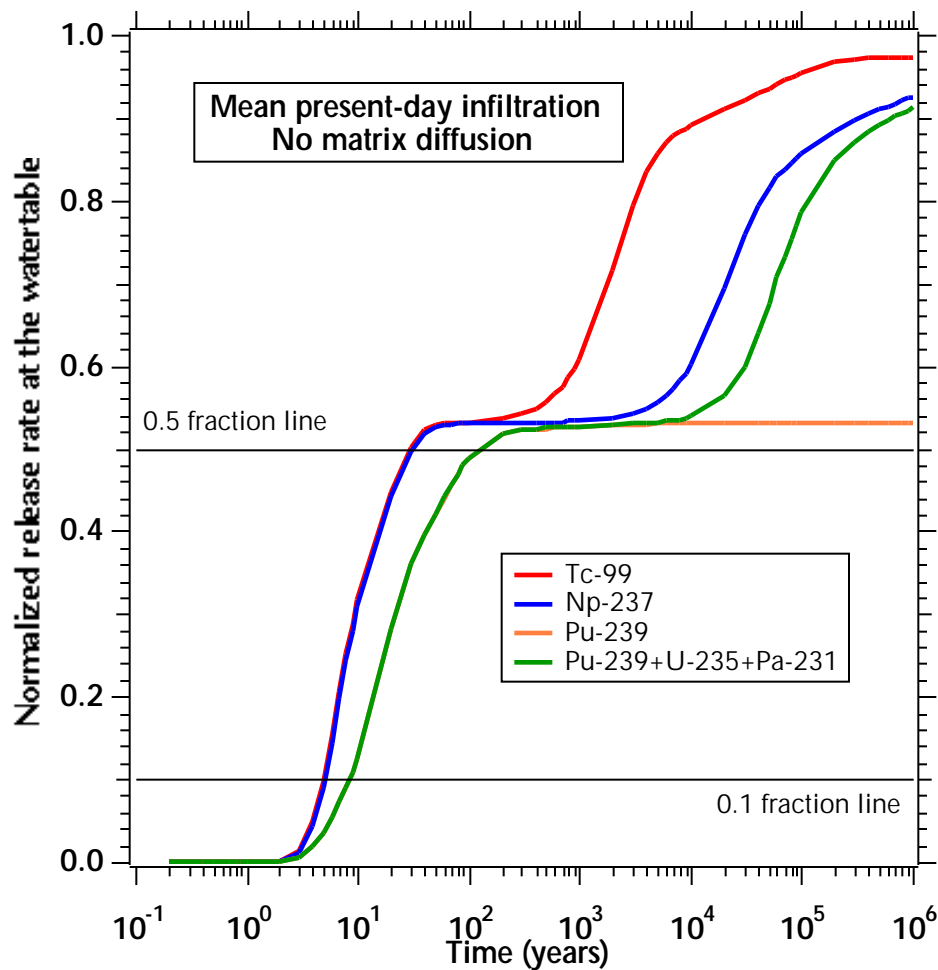


Figure 6.17.1. Normalized relative releases of radioactive solutes at the watertable for the no-diffusion alternative model (mean present-day infiltration, #1 perched water model—DTN:LB991220140160.012, data submitted with this AMR).

The picture is somewhat different for the strongly sorbing ^{239}Pu . The limited sorption on the fracture walls (attained by setting $\phi = 0.99$ in the fractures) is sufficiently high to retard transport in the fractures. If only ^{239}Pu is considered, the fracture release rate reaches a plateau at about 300 years, i.e., a very short time considering its half-life. Its constant (and at $R = 0.52$, very significant) value indicates only fracture contributions to the release at the water table, as the matrix acts as sink for the ^{239}Pu in the matrix flow. Thus, there is no matrix contribution to the groundwater release of ^{239}Pu in the first 10^6 years.

Accounting for the ^{239}Pu daughters leads to matrix contributions to the water table after $t = 10,000$

years. These are attributed (almost exclusively) to the release of the ^{235}U daughter (see Section 6.13), which sorbs less strongly and has a longer half-life than ^{239}Pu .

The results of this study emphasize the importance of diffusion from the fractures into the matrix as the main mechanism for retardation of radionuclide transport. When this process is not considered in the simulations, very fast travel times are observed, and radionuclides reach the water table in less than 10 years.

6.17.2 Colloids

For the conditions of Case 2 (see Section 6.16.6), the breakthrough curves for no diffusion in Figure 6.17.2 are quite similar to the ones obtained when colloid diffusion is considered (see Figure 6.16.1). This was expected because (a) colloid diffusion is smaller than molecular diffusion because of the larger colloid size, and (b) size exclusion (straining) effects at the interfaces of different layers further limit entry through diffusion into the matrix (especially for larger colloids).

The early portions (to 70 years) of the breakthrough curves for the 450, 200 and 100 nm colloids are identical, indicating the same filtration behavior. Colloid straining is the reason for the larger t_{10} (= 15 years) and t_{50} (= 100 years for the 6 nm colloid, 60 years for the 450, 200, and 100 nm colloids) compared to those for solutes. These times are practically the same as those observed for the 450 and 200 nm colloids in Figure 6.15.1, indicating the limited importance of diffusion to larger colloids.

Comparison of the curves in Figures 6.17.2 and 6.16.1 shows the increasing importance of diffusion as the colloid size decreases. Thus, inclusion of diffusion leads to limited retardation of the transport of the 100 nm colloid, but the effect is more pronounced in the case of the 6 nm colloid. Its t_{10} and t_{50} are reduced from 300 and 1,500 years to 15 and 100 years, respectively.

Note that the colloid breakthrough curves do not exhibit the plateaus (denoting pure fracture transport with no matrix contribution) of the solute curves in Figure 6.17.1, but rather a section of milder slope. This is attributed to the slower transport in the fractures (as a result of straining at the hydrogeologic layer interfaces) and the resulting evolution of concentrations larger than that in the water released from the potential repository. Hence the concentration gradients keep increasing over time, and do not reach a steady-state as in solutes.

The conclusion drawn from this study is that diffusion is less significant in the transport of colloids than in solute transport. Its effect, however, becomes increasingly important for a decreasing colloid size.

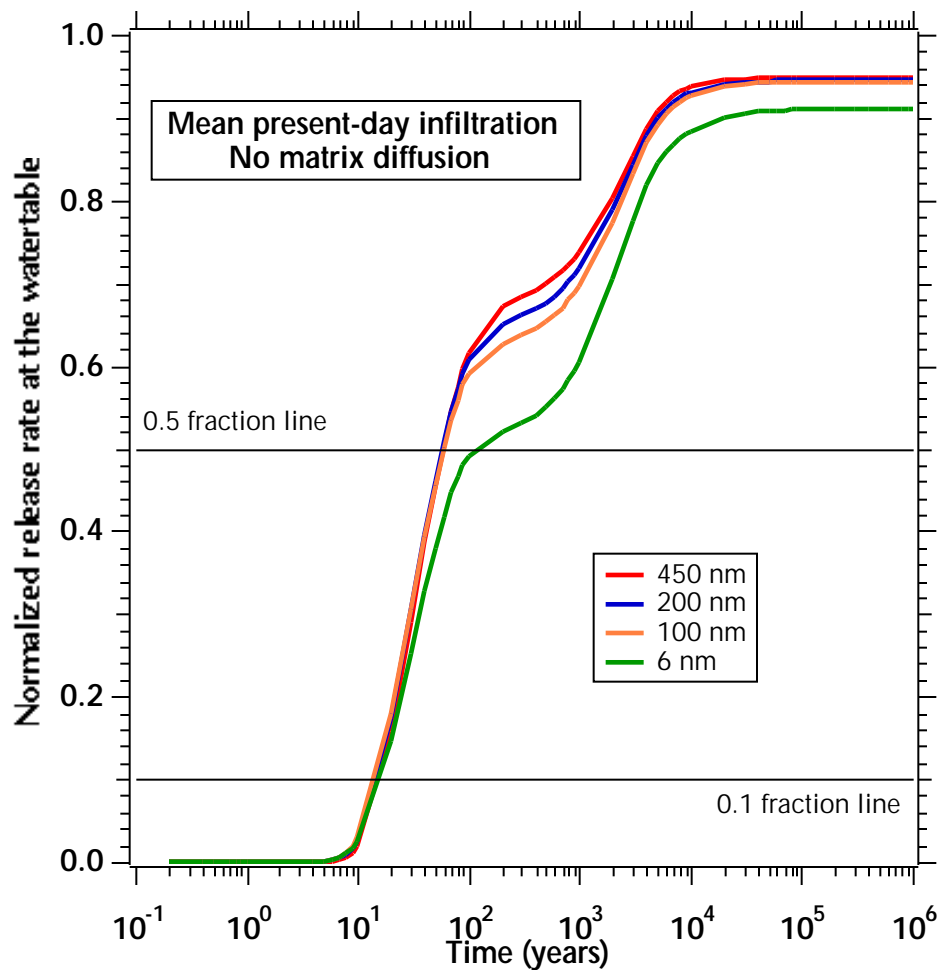


Figure 6.17.2. Normalized relative releases of radioactive colloids at the water table for the no-diffusion alternative model (mean present-day infiltration, #1 perched water model, Case 2 conditions – DTN: LB991220140160.017, data submitted with this AMR).

7. CONCLUSIONS

7.1 SUMMARY OF MODELING ACTIVITY

In Section 6.4 modeling activity focused on the validation and calibration of the RTM using the 2-D semianalytical FRACL code and the 3-D numerical EOS9nT code. We first validated the RTM by comparing the predictions of both codes to the analytical solution of Sudicky and Frind (1982). We then calibrated the RTM by using FRACL to analyze field data of Cl distribution in the UE-25 UZ#16 borehole, and compared the FRACL results to the predictions from a 3-D simulation using the T2R3D code. Finally, we calibrated the RTM by using EOS9nT to analyze field data of Cl distribution in the ESF, and compared the results of the 3-D site-scale simulation to the T2R3D predictions for the same grid and conditions.

Modeling activity in Sections 6.6, 6.7 and 6.8 involved the application of the FRACL code to simulate the transport of the radioactive solutes ^{99}Tc (nonsorbing), ^{237}Np (moderately sorbing) and ^{239}Pu (strongly sorbing) in three vertical cross sections that are representative of the individual hydrogeologic units (i.e., TSw, CHn and PP) present at the site of the potential repository. The focus of these studies was to determine the important processes and the effect of differences in geology on the transport of radionuclides with different transport and decay properties.

Modeling activity in Section 6.9 involved the application of the FRACL code to simulate the transport of ^{99}Tc , ^{237}Np and ^{239}Pu in three vertical cross sections covering the entire geologic profile from the potential repository to the groundwater table. The purpose of these simulations is to evaluate the integrated transport performance of all the hydrogeologic units beneath the potential repository.

The modeling activity in Section 6.10 involved the application of the T2R3D code to predict the concentration and water saturation distributions after the injection of various tracers into the ch1v and ch2v layers. The studies were numerical simulations of two sets of tests in the first phase of an experiment conducted in Busted Butte, Yucca Mountain (CRWMS M&O 1999e, Section 6.8). The field work on these phases has been completed, but the analysis of the experimental results is not yet complete.

Modeling in Section 6.11 involved the application of TOUGH2 V1.4 Module EOS9 V1.4 (STN: 10007-1.4-01) to obtain the flow fields in the 3-D site-scale YM domains to be used in subsequent transport simulations. Flow fields for a total of nine climatic scenarios were obtained.

In Sections 6.12 to 6.14, modeling activity involved the application of EOS9nT to study the transport of ^{99}Tc , ^{237}Np , and ^{239}Pu in the entire Yucca Mountain system using large-scale 3-D grids. Additionally, (a) the contributions of the daughters of ^{237}Np and ^{239}Pu to transport to the water table and (b) the effects of varying infiltration were modeled. Modeling in Section 6.15

involved the EOS9nT code and focused on the effects of various perched water table bodies to the transport of ^{99}Tc , ^{237}Np , and ^{239}Pu and their important daughters.

The modeling activity in Section 6.16 involved the application of EOS9nT to study the transport of four true colloids of different sizes and properties in the entire Yucca Mountain system using large-scale 3-D grids. Modeling using the EOS9nT code in Section 6.17 aimed at evaluating the YM UZ system performance under a different conceptual model that does not consider diffusion.

7.2 AMR CONCLUSIONS

The following conclusions can be drawn from this study:

1. The transfer coefficient K_i may be important in the migration of strongly sorbing radionuclides (such as ^{239}Pu), as lower K_i values enhance transport.
2. Increasing matrix tortuosity coefficient ($\tau \leq 1$) values lead to increased matrix diffusion, lower relative concentrations and delayed breakthroughs in the fractures, and larger concentrations and sorption in the matrix.
3. The importance of the longitudinal dispersivity α_L in accurately predicting the transport of radionuclides increases with the sorption affinity of the radionuclide (i.e., with the distribution coefficient K_d).
4. Transport in the TSw hydrogeologic unit is strongly dependent on the thickness of the unit (measured from the bottom of the potential repository) and its spatial variability over the area of the potential repository.
5. Transport in the CHn hydrogeologic unit is strongly dependent on the spatial variability of the distribution of the vitric and zeolitic layers over the area of the potential repository. Occurrence of zeolitic layers leads to fast advective transport due to flow focusing caused by the large fracture permeability (compared to that in the matrix). The parity of the fracture and matrix permeability in the vitric layers leads to behavior akin to that of a porous (rather than a fractured) medium. The vitric layers of the CHn hydrogeologic unit are shown to be effective barriers to radionuclide transport, and their effectiveness increases with the sorptive tendencies of the radionuclides.
6. Radionuclide transport appears to be practically uninhibited in the top zeolitic layers (pp4) of the PP hydrogeologic unit, but is effectively retarded by the underlying devitrified layers. The retardation is a function of the relative thickness of the zeolitic and devitrified layers.
7. Results from 2-D semi-analytic FRACLS simulations of transport from the bottom of the potential repository to the water table show that the times to reach the water table from the release point are (a) 1,000 years or more for ^{99}Tc , (b) 10,000 or more for ^{237}Np , and (c) over 100,000 years for ^{239}Pu . The arrival times are consistent at three different locations within the domain of the potential repository. Note that these 2-D simulations predict fracture and matrix transport, but do not account for the possible effects of faults.
8. The 2-D FRACLS simulations indicate that increasing infiltration rates lead to fast erradionuclide transport to the water table. The largest increase was observed for the non-sorbing ^{99}Tc , and

the smallest for the strongly sorbing ^{239}Pu .

9. The 2-D FRACL simulations indicate that conditions leading to the emergence of perched water bodies (i.e., permeability barriers) in the #1 perched water model lead to retardation of radionuclide transport. The effect is more pronounced in less strongly sorbing radionuclides (such as ^{99}Tc and ^{237}Np) at relatively early times and is less important for stronger-sorbing radionuclides and longer times.
10. 3-D site-scale simulations using EOS9nT indicate that, under the #1 perched water model, radionuclide transport from the bottom of the potential repository to the water table is both dominated and controlled by the faults. These provide fast pathways to downward migration to the water table, but also limit lateral transport past them.
11. The 3-D site-scale EOS9nT simulations indicate that radioactive solutes from the potential repository move faster and reach the water table earlier and over a larger area in the southern part of the potential repository. This appears to be counterintuitive, as it would be reasonable to expect that the general area of fastest, largest, and most extensive transport would be in the northern part of the potential repository site, where the highly conductive fractures of the zeolitic CHn layers occur. There are four reasons for this transport pattern.
12. The first reason is the infiltration and percolation distributions. A review of the infiltration pattern at the surface, the percolation flux at the repository level and the percolation flux at the groundwater level indicates that they closely reflect the transport patterns discussed in Conclusion (11). Thus, the water flow pattern dictates the advective transport pattern. In the #1 perched-water model of these studies, the maximum water flow within the footprint of the potential repository is in its southern part.

The presence of the highly conductive (a) Splay G of the Solitario Canyon fault and (b) Ghost Dance fault splay are the second reason (and related to the percolation patterns) for the dominance of the southern part of the potential repository as the pathway of transport, despite the vitric CHv layers having fewer fractures (than the overlying TSw) and acting as porous (rather than fractured) media (with relatively lower water velocities). Once contamination migrating through the Splay G of the Solitario Canyon fault reaches the TSw-CHn interface, it moves primarily in an easterly direction, moving with the draining water that hugs the downward sloping (in this direction) low-permeability interface.

Additionally, the Sundance fault, the Drill Hole Wash fault, and the main Ghost Dance fault are transport-facilitating geologic features. Of these, the Drill Hole Wash fault and the main Ghost Dance fault act as barriers to the northward and eastward radionuclide movement, while providing pathways for relatively fast transport to the water table.

The transport pattern discussed in Conclusion (11) may be further facilitated by the contraction of the areal extent of the vitrified tuffs (the third reason), whose vertical distribution shows a funnel-type structure in the southern part of the potential repository. Thus, as depth from the potential repository increases, an increasing portion of the water flow occurs through the zeolites, in which the fracture-dominated flow (and, consequently, transport) is fast. The fourth reason is the low-permeability zones at the TSw-CHn interface in the northern part of the potential repository in the #1 perched water model. These zones are barriers to drainage, and lead to low water velocities and perched water bodies. Radionuclides move slowly through the perched water before reaching the underlying highly permeable zeolite fractures; hence the delay in transport.

13. Fractures are the main pathways of radionuclide transport. Diffusion from the fractures into the matrix is the main retardation process in radionuclide transport. By sorbing onto the matrix into which they diffuse, the migration of sorbing radionuclides is retarded. The same process leads to retardation in the fractures by resulting in larger concentration gradients (thus enhanced diffusion) between the liquid phases in the fractures and in the matrix.
14. The importance of faults and perched water bodies in transport is directly dependent on the underlying geologic and perched water conceptual models. It is reasonable to expect that changing geologic and perched water models may lead to substantially different results, given the sensitivity of transport to these geologic features. This realization underlines the importance of representative conceptual models.
15. From the 3-D EOS9nT simulations we determine that, under present-day climatic conditions (infiltration of 6 mm/year) and the #1 perched water model, the t_{10} (see definition in Section 6.12) of the non-sorbing ^{99}Tc for low, mean and high infiltration is 10,000, 300, and 45 years, and the t_{50} (see definition in Section 6.12) is 45,000, 4,000 and 1,000 years, respectively. Under the same conditions, the t_{10} of the moderately sorbing ^{237}Np for low, mean and high infiltration is 220,000, 10,000, and 1,700 years, and the corresponding t_{50} is over 1,000,000, 120,000, and 22,000 years, respectively. The contributions of the ^{237}Np daughters to releases at the water table are trivial and can be safely ignored.
16. In the 3-D site-scale simulation of transport of the strongly sorbing ^{239}Pu , the members of the decay chain may have to be considered (i.e., ^{239}Pu , ^{235}U , and ^{231}Pa) if the ^{239}Pu release rate at the repository is significant. Although the t_{10} for ^{239}Pu transport is always larger than 1,000,000 years, ^{235}U becomes the main contributor in the radionuclide release at the water table after 10,000 years (at most) because of its weaker sorption onto the matrix and its longer half-life. The contributions of ^{231}Pa are not important. Under present-day climatic conditions and the #1 perched water model, the t_{10} of the members of the ^{239}Pu chain for low, mean and high infiltration is computed from the 3-D simulations as 600,000, 40,000, and 12,000 years, and the t_{50} is >1,000,000, 250,000, and 9,000 years, respectively.

17. The 3-D site-scale simulations indicate that a change in the future climatic conditions can have a significant effect on transport. Increasing infiltration (as the climatic regime changes from present-day to monsoon and glacial conditions and its level changes from low to mean to high) leads to faster radionuclide transport to the water table. The acceleration in transport increases with decreasing sorption.

Thus, for the extreme case of high glacial infiltration (about 33.5 mm/year), the t_{10} of the non-sorbing ^{99}Tc is reduced to about 10 years, and t_{50} is 160 years. For the same infiltration, the t_{10} and t_{50} of ^{237}Np are reduced to 260 and 2,000 years, respectively, while the t_{10} and t_{50} of ^{239}Pu are reduced to 5,100 and 38,000 years, respectively

18. The 3-D site-scale simulations indicate that, for a mean present-day infiltration, radionuclide transport does not appear to be significantly affected by the conceptual model used to describe the perched water bodies, as the three models studied (i.e., the #1 perched water model, the #2 perched water model and the no-perched water model, see CRWMS M&O 1999d, Sections 6.2 and 6.6) show similar results.
19. The predictions of radionuclide transport obtained using the 2-D semi-analytical FRACL model are generally consistent with those from the 3-D site-scale numerical model. Note that caution should be exercised in the comparison of these results because of the conceptual differences between the 2-D and the 3-D problems. Thus, FRACL is capable of providing a good first-order estimate of radionuclide concentration distributions and travel times from the bottom of the potential repository to the water table at a particular narrow cross section of the UZ. Further refinements, accounting for faults and the effects of 3-D systems and phenomena, can then be obtained from the 3-D EOS9nT simulations.
20. For a mean present-day infiltration and a given kinetic clogging (forward filtration) coefficient κ^+ , the transport of radioactive true colloids is strongly influenced by the kinetic declogging (reverse filtering) coefficient κ^- . When no declogging is allowed, no colloids reach the groundwater. Low values of κ^- (i.e., slow declogging) lead to long travel times to the water table (and thus significant retardation). For $\kappa^-/\kappa^+ = 0.1$, t_{10} is 12,000 years for the 450, 200 and 100 nm colloids, and infinity for the 6 nm colloid; t_{50} is infinity for all colloids because the maximum normalized release rate at the water table never exceeds 0.3.

Large values of κ^- lead to a dramatically different behavior, with very fast travel times of the radioactive colloids to the water table. For $\kappa^-/\kappa^+ = 100$, the t_{10} is 15 years for the 450 nm, the 200 nm and the 100 nm colloids, and 30 years for the 6 nm colloids. The t_{50} is about 60 years for the 450 nm and 200 nm colloids, about 80 years for the 100 nm colloid, and 1,200 years for the 6 nm colloid. The extreme sensitivity of colloid filtration (deposition) on κ^- and the dearth of any representative information on its value in the various UZ hydrogeologic units underline the need for attention to this subject.

21. For a given κ^- , the colloid size has a significant effect on transport. Given the fact that fractures are the main transport conduit in YM, the inability of larger colloids to diffuse into the matrix because of smaller D_0 values and size exclusion (straining) result in faster transport to the groundwater. Smaller colloidal particles can diffuse easier into the matrix, and their transport is thus retarded.
22. Size exclusion (straining) at the interfaces of different hydrogeologic layers leads to colloid concentrations immediately above the interface that can be significantly higher than that in the water released from the potential repository. This phenomenon is more pronounced in larger colloids.
23. Assuming an alternative conceptual model of no diffusion from the fractures into the matrix, the transport of radioactive solutes to the water table is dramatically accelerated, and t_{10} and t_{50} can be as low as 5 and 30 years, respectively. A characteristic plateau marks the period between constant steady-state fracture release and the arrival at the water table of the radionuclide front in the fracture flow.

The analysis of the alternative model indicates that diffusion is less significant in colloid transport than in solute transport. Its effect, however, becomes increasingly important as the colloid size decreases.

This document and its conclusions may be affected by technical product input information that requires confirmation. Any changes to the document or its conclusions that may occur as a result of completing the confirmation activities will be reflected in subsequent revisions. The status of the input information quality may be confirmed by review of the DIRS Database.

INTENTIONALLY LEFT BLANK

8 INPUTS AND REFERENCES

8.1 CITED DOCUMENTS

Abdel-Salam, A., and C.V. Chrysikopoulos. 1995. Modeling of colloid and colloid-facilitated contaminant transport in a two-dimensional fracture with spatially variable aperture. *Transport in Porous Media*, 20:197-221. TIC: applied for.

Bates, J.K.; Bradley, J.P.; Teetsov, A.; Bradley, C.R.; and ten Brink, M.B. 1992. "Colloid Formation during Waste Form Reaction: Implications for Nuclear Waste Disposal." *Science*, 256, 649–651. Washington, D.C.: American Association for the Advancement of Science. TIC: 239138.

Bear, J. 1972. *Dynamics of Fluid in Porous Media*. New York, New York: Dover Publications. TIC: 217568.

Benson, C.F. and Bowman, R.S. 1994. "Tri- and Tetrafluorobenzoates as Nonreactive Tracers in Soil and Groundwater." *Soil Science Society of America Journal*, 58, 1123–1129. Madison, Wisconsin: Soil Science Society of America. TIC: applied for.

Bird, R.B.; Stewart, W.E.; and Lightfoot, E.N. 1960. *Transport Phenomena*. New York: John Wiley & Sons. TIC: 208957.

Bodvarsson, G.S.; Boyle, W.; Patterson, R.; and Williams, D. 1999. "Overview of Scientific Investigations at Yucca Mountain the Potential Repository for High-Level Nuclear Waste." *Journal of Contaminant Hydrology* 38 (1–3), 3–24. Amsterdam, The Netherlands: Elsevier Science Publishers. TIC: 244160.

Boggs, J.M. and Adams, E.E. 1992. "Field Study in a Heterogeneous Aquifer. 4: Investigation of Adsorption and Sampling Bias." *Water Resources Research*, 28, 3325–3336. Washington, D.C.: American Geophysical Union. TIC: applied for.

Bowen, B.D. and Epstein, N. 1979. "Fine Particle Deposition in Smooth Parallel-Plate Channels." *Journal of Colloid and Interface Science*, 72, 81–97. Orlando, Florida: Academic Press. TIC: 224935.

Bradbury, M.H. and Stephen, I.G. 1985. "Diffusion and Permeability Based Sorption Measurements in Intact Rock Samples." *Scientific Basis for Nuclear Waste Management IX*, 81–90. Werme, L.O., ed. Boston, Massachusetts: Materials Research Society. TIC: 236384.

Buddemeier, R.W. and Hunt, J.R. 1988. "Transport of Colloidal Contaminants in Groundwater: Radionuclide Migration at the Nevada Test Site." *Applied Geochemistry*, 3, 535–548. Amsterdam, The Netherlands: Elsevier Science Publishers. TIC: 224116.

Cameron, D.R. and Klute, A. 1977. "Convective-Dispersive Solute Transport with a combined Equilibrium and Kinetic Adsorption Model." *Water Resources Research*, 13 (1), 183–188. Washington, D.C.: American Geophysical Union. TIC: 246265.

Conca, J.L. and Wright, J. 1990. "Diffusion Coefficients in Gravel under Unsaturated Conditions." *Water Resources Research*, 26 (5), 1055–1066. Washington, D.C.: American Geophysical Union. TIC: 237421.

Corapcioglu, M.Y.; Abboud, N.M.; and Haridas, A. 1987. "Governing Equations for Particle Transport in Porous Media." *Advances in Transport Phenomena in Porous Media*. Bear, J. and Corapcioglu, M.Y., eds. Series E.: Applied Sciences Series 128. Dordrecht, The Netherlands: Martinus Nijhoff. TIC: applied for.

Cook, A.J. 1989. *A Desk Study of Surface Diffusion and Mass Transport in Clay*. Report WE/88/34. Luxembourg, Luxembourg: Commission of the European Communities. TIC: applied for.

Crump, K.S. 1976. "Numerical Inversion of Laplace Transforms Using a Fourier Series Approximation." *Journal of the Association of Computing Machinery*, 23 (1), 89–96. New York, New York: The Association of Computing Machinery. TIC: applied for.

CRWMS M&O (Civilian Radioactive Waste Management System Management & Operating Contractor) 1999a. *M&O Site Investigations*. Activity Evaluation. Las Vegas, Nevada: CRWMS M&O. ACC: MOL.19990317.0330.

CRWMS M&O 1999b. *M&O Site Investigations*. Activity Evaluation. Las Vegas, Nevada: CRWMS M&O. ACC: MOL.19990928.0224.

CRWMS M&O 1999c. *Analysis & Modeling Development Plan (DP) for U0060, Radionuclide Transport Models under Ambient Conditions, Rev. 00*. TDP-NBS-HS-000013. Las Vegas, Nevada: CRWMS M&O. ACC: MOL.19990830.0381.

CRWMS M&O 1999d. *UZ Flow Models and Submodels*. MDL-NBS-HS-000006. Las Vegas, Nevada: CRWMS M&O. ACC: MOL.19990721.0527. URN-0030.

CRWMS M&O 1999e. *Unsaturated Zone and Saturated Zone Transport Properties*. ANL-NBS-HS-000019. Las Vegas, Nevada: CRWMS M&O. URN-0038.

CRWMS M&O 1999f. *UZ Colloid Transport Model*. ANL-NBS-HS-000028. Las Vegas, Nevada: CRWMS M&O. URN-0031.

CRWMS M&O 1999g. *Enhanced Design Alternative (EDA) II Repository Layout for 10 cm/s Ventilation Plan*. Las Vegas, Nevada: CRWMS M&O. ACC: MOL.19990409.0102.

CRWMS M&O 1999h. *Development of Numerical Grids for UZ Flow and Transport Modeling*. ANL-NBS-HS-000015. Las Vegas, Nevada: CRWMS M&O. ACC: MOL.19990721.0517.

CRWMS M&O 2000a. *Calibrated Properties Model*. MDL-NBS-HS-000003. Las Vegas, Nevada: CRWMS M&O. ACC: MOL.19990721.0520. URN-0028. URN-0053.

CRWMS M&O 2000b. *Drift-Scale Coupled Processes (DST and THC Seepage) Models*. MDL-NBS-HS-000001. Las Vegas, Nevada: CRWMS M&O. ACC: MOL.19990721.0523. URN-0054.

CRWMS M&O 2000c. *Seepage Calibration Model and Seepage Testing Data*. MDL-NBS-HS-000004. Las Vegas, Nevada: CRWMS M&O. ACC: MOL.19990721.0521.

CRWMS M&O 2000d. *Analysis of Hydrologic Properties Data*. ANL-NBS-HS-000002. Las Vegas, Nevada: CRWMS M&O. ACC: MOL.19990721.0519. URN-0055.

CRWMS M&O 2000e. *Geologic Framework Model (GFM3.1) Analysis Model Report*. Las Vegas, Nevada: CRWMS M&O.

Cussler, E.L. 1984. *Diffusion: Mass Transfer in Fluid Systems*. New York, New York: Cambridge University Press. TIC: applied for.

DeHoog, F.R.; Knight, J.H.; and Stokes, A.N. 1982. "An Improved Method for Numerical Inversion of Laplace Transforms." *SIAM Journal on Scientific and Statistical Computing*, 3 (3), 357–366. Philadelphia, Pennsylvania: Society for Industrial and Applied Mathematics. TIC: applied for.

de Marsily, G. 1986. *Quantitative Hydrogeology: Groundwater Hydrology for Engineers*. Orlando, Florida: Academic Press. TIC: 226335.

DOE (U.S. Department of Energy) 1998b. *Viability Assessment of a Repository at Yucca Mountain*. Volume 3 of *Total System Performance Assessment*. DOE/RW-0508. Washington D.C.: DOE OCRWM. ACC: MOL.19981007.0030.

Dyer, J.R. 1999. "Revised Interim Guidance Pending Issuance of New U.S. Nuclear Regulatory Commission (NRC) Regulations (Revision 01, July 22, 1999), for Yucca Mountain, Nevada." Letter from J.R. Dyer (DOE) to D.R. Wilkins (CRWMS M&O), September 9, 1999, OL&RC:SB-1714, with enclosure, "Interim Guidance Pending Issuance of New U.S. Nuclear Regulatory Commission (NRC) Regulations (Revision 01)." ACC: MOL.19990910.0079.

Dzombak, D.A. and Morel, F.M.M. 1990. *Surface Complexation Modeling: Hydrous Ferric Oxide*. New York, New York, John Wiley & Sons. TIC: 224089.

EPRI 1999. *Colloids in Saturated and Partially-Saturated Porous Media: Approaches to the Treatment of Colloids in Yucca Mountain Total System Performance Assessment*. TR-112135. Palo Alto, California: Electric Power Research Institute. TIC: applied for.

Farrell, J. and Reinhard, M. 1994. "Desorption of Halogenated Organics from Model Solids, Sediments, and Soil under Unsaturated Conditions. 2: Kinetics." *Environmental Science and Technology*, 28 (1), 63–72. Washington, D.C.: American Chemical Society. TIC: applied for.

Faure, G. 1977. *Principles of Isotope Geology*. New York, New York: John Wiley and Sons. TIC: 3332.

Fetter, C.W. 1993. *Contaminant Hydrogeology*. Upper Saddle River, New Jersey: Prentice Hall. TIC: 240691.

Gelhar, L.W.; Welty, C.; and Rehfeldt, K.R. 1992. "A Critical Review of Data on Field-Scale Dispersion in Aquifers." *Water Resources Research*, 28 (7), 1955–1974. Washington, D.C.: American Geophysical Union. TIC: 235780.

Grathwohl, P. 1998. *Diffusion in Natural Porous Media: Contaminant Transport, Sorption/Desorption and Dissolution Kinetics*. Kluwer Academic Publishers, Boston, MA. TIC: applied for.

Harvey, R.W. and Garabedian, S.P. 1991. "Use of Colloid Filtration Theory in Modeling Movement of Bacteria through a Contaminated Sandy Aquifer." *Environmental Science and Technology*, 25 (1), 178–185. Washington, D.C.: American Chemical Society. TIC: 245733.

Herzig, J.P.; Leclerc, D.M.; and Le Goff, P. 1970. "Flow of Suspension through Porous Media." *Industrial and Engineering Chemistry Research*, 62 (5), 129–157. Washington, D.C.: American Chemical Society. TIC: applied for.

Holttä, P.; Siitani-Kauppi, M.; Huikuri, P.; Lindberg, A.; and Hautajarvi, A. 1997. "The Effect of Specific Surface Area on Radionuclides Sorption on Crushed Crystalline Rock." *Material Resources Society Symposium Proceedings*, 465, 789–796. Pittsburgh, Pennsylvania: Materials Resources Society of America. TIC: applied for.

Hu, Q. and Brusseau, M.L. 1994. "Effect of Solute Size on Diffusive-Dispersive Transport in Porous Media." *Journal of Hydrology*, 158, 305–317. Amsterdam, The Netherlands: Elsevier Science Publishers. TIC: applied for.

Hu, Q. and Brusseau, M.L. 1995. "The Effect of Solute Size on Transport in Structured Porous Media." *Water Resources Research*, 31 (7), 1637–1646. Washington, D.C.: American Geophysical Union. TIC: applied for.

Hu, Q. and Brusseau, M.L. 1996. "Transport of Rate-Limited Sorbing Solutes in an Aggregated Porous Medium: A Multiprocess Non-Ideality Approach." *Journal of Contaminant Hydrology*, 24 (1), 53–73. Amsterdam, The Netherlands: Elsevier Science Publishers. TIC: applied for.

Ibaraki, M. and Sudicky, E.A. 1995. "Colloid-Facilitated Contaminant Transport in Discretely Fractured Media: 1. Numerical Formulation and Sensitivity Analysis." *Water Resources Research*, 31 (12), 2945–2960. Washington, D.C.: American Geophysical Union. TIC: 245719.

Jacobsen, O.H.; Moldrup, P.; Larsen, C.; Konnerup, L.; and Peterson, L.W. 1997. "Particle Transport in Macropores of Undisturbed Soil Columns." *Journal Of Hydrology*, 196, 185–203. Amsterdam, The Netherlands: Elsevier Science Publishers. TIC: applied for.

Jahnke, F.M. and Radke, C.J. 1987. "Electrolyte Diffusion in Compacted Montmorillonite Engineered Barriers." *Coupled Processes Associated With Nuclear Waste Repositories*, 287–297. Orlando, Florida: Academic Press. TIC: applied for.

James, S.C. and Chrysikopoulos, C.V. 1999. "Transport of Polydisperse Colloid Suspensions in a Single Fracture." *Water Resources Research*, 35 (3), 707–718. Washington, D.C.: American Geophysical Union. TIC: 245938.

Johansson, H.; Byegard, J.; Skarnemark, G.; and Skalberg, M. 1997. "Matrix Diffusion of Some Alkali and Alkaline Earth Metals in Granitic Rock." *Material Resources Society Symposium Proceedings*, 465, 871–878. Pittsburgh, Pennsylvania: Materials Resources Society of America. TIC: applied for.

Johansson, H.; Siitari-Kauppi, M.; Skalberg, M.; and Tullborg, E.L.. 1998. "Diffusion Pathways in Crystalline Rock-Examples from Äspö-Diorite and Fine-Grained Granite." *Journal of Contaminant Hydrology*, 35, 41–53. Amsterdam, The Netherlands: Elsevier Science Publishers. TIC: applied for.

Kaplan, D.I. and Serne, R.J. 1995. *Distribution Coefficient Values Describing Iodine, Neptunium, Selenium, Technetium, and Uranium Sorption to Hanford Sediments*. PNL-10379. Richland, Washington: Pacific Northwest National Laboratory. TIC: applied for.

Kersting, A.B.; Efurud, D.W.; Finnegan, D.L.; Rokop, D.J.; Smith, D.K.; and Thompson, J.L. 1999. "Migration of Plutonium in Ground Water at the Nevada Test Site." *Nature*, 397, 56–59. London, England: Macmillan Magazines. TIC: 243597.

Kretzschmar, R.; Robarge, W.P.; and Amoozegar, A. 1995. "Influence of Natural Organic Matter on Colloid Transport through Saporlite." *Water Resources Research*, 31 (3), 435–445. Washington, D.C.: American Geophysical Union. TIC: applied for.

Kretzschmar, R.; Barmettler, K.; Grolimund, D.; Yan, Y.; Borkovec, M.; and Sticher, H. 1997. "Experimental Determination of Colloid Deposition Rates and Collision Efficiencies in Natural Porous Media." *Water Resources Research*, 33 (5), 1129–1137. Washington, D.C.: American Geophysical Union. TIC: applied for.

Lide, D.R. 1992. *CRC Handbook of Chemistry and Physics*. 73rd Edition. Boca Raton, Florida: CRC Press. TIC: 3595.

Liu, H.H.; Doughty, C.; and Bodvarsson, G.S. 1998. "An Active Fracture Model for Unsaturated Flow and Transport in Fractured Rocks." *Water Resources Research*, 34 (10), 2633–2646. Washington, D.C.: American Geophysical Union. TIC: 243012.

McCarthy, J.F. and Zachara, J.M. 1989. "Subsurface Transport of Contaminants." *Environmental Science and Technology*, 23 (5), 496–502. Washington, D.C.: American Chemical Society. TIC: 224876.

McGraw, M.A. and Kaplan, D.I. 1997. *Colloid Suspension Stability and Transport Through Unsaturated Porous Media*. PNNL-11565. Richland, Washington: Pacific Northwest National Laboratory. TIC: applied for.

Moridis, G. J. 1992. "Alternative Formulations of the Laplace Transform Boundary Element (LTBE) Numerical Method for the Solution of Diffusion-Type Equations." *Boundary Element Technology VII*, 815–833. Boston, Massachusetts: Computational Mechanics Publications. TIC: applied for.

Moridis, G. J. 1999. "Semianalytical Solutions for Parameter Estimation in Diffusion Cell Experiments." *Water Resources Research*, 35 (6), 1729–1740. Washington, D.C.: American Geophysical Union. TIC: 246266.

Moridis, G.J., and Pruess, K. 1995. *Flow and Transport Simulations Using T2CG1, a Package of Conjugate Gradient Solvers for the TOUGH2 Family of Codes*. Report LBL-36235. Berkeley, California: Lawrence Berkeley National Laboratory. TIC: 220015.

Moridis, G.J. and Pruess, K. 1998. "T2SOLV: An Enhanced Package of Solvers for the TOUGH2 Family of Reservoir Simulation Codes." *Geothermics*, 27 (4), 415–444. Amsterdam, The Netherlands: Elsevier Science Publications. TIC: applied for.

Moridis, G.J. and Bodvarsson, G.S. 1999. *Semianalytical Solutions of Radioactive or Reactive Tracer Transport in Layered Fractured Media*. LBNL-44155. Berkeley, California: Lawrence Berkeley National Laboratory. TIC: applied for.

Moridis, G.; Wu, Y.; and Pruess, K. 1999. *EOS9nT: A TOUGH2 Module for the Simulation of Flow and Solute/Colloid Transport*. Report LBL-42351. Berkeley, California: Lawrence Berkeley National Laboratory. TIC: applied for.

- Mualem, Y. 1976. "A New Model for Predicting the Hydraulic Conductivity of Unsaturated Porous Media." *Water Resources Research*, 12, 513–522. Washington, D.C.: American Geophysical Union. TIC: 217339.
- Nuttall, H.E.; Jain, R.; and Fertelli, Y. 1991. "Radiocolloid Transport in Saturated and Unsaturated Fractures." *High Level Radioactive Waste Management, Proceedings of the Second Annual International Conference, Las Vegas, Nevada, April 28–May 3, 1991*, 189–196. La Grange Park, Illinois: American Nuclear Society. ACC: NNA.19930625.0031.
- Pigford, T. H.; Chambre, P. L.; Albert, M.; Foglia, M.; Harada, M.; Iwamoto, F.; Kanki, T.; Leung, D.; Masuda, S.; Muraoka, S.; and Ting, D. 1980. *Migration of Radionuclides through Sorbing Media, Analytical Solutions*. Report LBL-11616. Berkeley, California: Lawrence Berkeley National Laboratory. TIC: 211541.
- Porter, L.K.; Kemper, W.D.; Jackson, R.D.; and Stewart, B.A. 1960. "Chloride Diffusion in Soils as Influenced by Moisture Content." *Soil Science Society of America Proceedings*, 24, 460–463. Madison, Wisconsin: Soil Science Society of America. TIC: applied for.
- Pruess, K. 1987. *TOUGH User's Guide*. Nuclear Regulatory Commission, Report NUREG/CR-4645, Report LBL-20700. Berkeley, California: Lawrence Berkeley National Laboratory. ACC: MOL.19960314.0434.
- Pruess K. 1991. *TOUGH2—A General Purpose Numerical Simulator for Multiphase Fluid and Heat Flow*. Report LBL-29400, UC-251. Berkeley, California: Lawrence Berkeley National Laboratory. ACC: NNA.19940202.0088.
- Richards, L.A. 1931. "Capillary Conduction of Liquids through Porous Mediums." *Physics*, 1, 318–333. Washington, D.C.: American Physical Society. TIC: 225383.
- Roberts, J.J. and Lin, W. 1997. "Electrical Properties of Partially Saturated Topopah Spring Tuff: Water Distribution as a Function of Saturation." *Water Resources Research*, 33 (4), 577–587. Washington, DC: American Geophysical Union. ACC: MOL.19961014.0060.
- Robin, M.J.L.; Gillham, R.W.; and Oscarson, D.W. 1987. "Diffusion of Strontium and Chloride in Compacted Clay-Based Materials." *Soil Science Society of America Journal*, 51, 1102–1108. Madison, Wisconsin: Soil Science Society of America. TIC: applied for.
- Rogers, P.S.Z. and Meijer, A. 1993. "Dependence of Radionuclide Sorption on Sample Grinding Surface Area, and Water Composition." *High Level Radioactive Waste Management, Proceedings of the Fourth Annual International Conference, Las Vegas, Nevada*, 1509–1516. LaGrange Park, Illinois: American Nuclear Society. TIC: 226357.

Sakthivadivel, R. 1969. *Clogging of Granular Porous Medium by Sediment*. Report No. HEL 15-7. Berkeley, California: Hydraulic Engineering Laboratory. TIC: applied for.

Saltelli, A.; Avogadro, A.; and Bidoglio, G. 1984. "Americium Filtration in Glauconitic Sand Columns." *Nuclear Technology*, 67, 245–254. LaGrange Park, Illinois: American Nuclear Society. TIC: 223230.

Seaman, J.C. 1998. "Retardation of Fluorobenzoate Tracers in Highly Weathered Soil and Groundwater Systems." *Soil Science Society America of Journal*, 62, 354–361. Madison, Wisconsin: Soil Science Society of America. TIC: applied for.

Smith, P.A. and Degeldre, C. 1993. "Colloid-Facilitated Transport of Radionuclides through Fractured Media." *Journal of Contaminant Hydrology*, 13, 143–166. Amsterdam, The Netherlands: Elsevier Science Publishers. TIC: 224863.

Stehfest, H. 1970a. "Algorithm 368, Numerical Inversion of Laplace Transforms." *Journal of the Association of Computing Machinery*, 13 (1), 47–49. New York, New York: Association of Computing Machinery. TIC: applied for.

Stehfest, H. 1970b. "Algorithm 368, Remark on Algorithm 368 [D5], Numerical Inversion of Laplace Transforms. *Journal of the Association of Computing Machinery*, 13 (1), 56. New York, New York: Association of Computing Machinery. TIC: applied for.

Sudicky, E.A. 1989. "The Laplace Transform Galerkin Method: A Time-Continuous Finite Element Theory and Application to Mass Transport in Groundwater." *Water Resources Research*, 25 (8), 1833–1846. Washington, D.C.: American Geophysical Union. TIC: applied for.

Sudicky, E.A.; Frind, E.O. 1982. "Contaminant Transport in Fractured Porous Media: Analytical Solutions for a System of Parallel Fractures." *Water Resources Research*, 18 (6), 1634–1642. Washington, D.C.: American Geophysical Union. TIC: 217475.

Tachi, Y.; Shibutani, T.; Sato, H.; and Yui, M. 1998. "Sorption and Diffusion Behavior of Selenium in Tuff. *Journal of Contaminant Hydrology*, 35, 77–89. Amsterdam, The Netherlands: Elsevier Science Publications. TIC: applied for.

van Genuchten, M. 1980. "A Closed-Form Equation for Predicting the Hydraulic Conductivity of Unsaturated Soils." *Soil Science Society of America Journal*, 44 (5), 892–898. Madison, Wisconsin: Soil Science Society of America. TIC: 217327.

Vilks, P. and Bachinski, D.B. 1996. "Colloid and Suspended Particle Migration Experiments in a Granite Fracture." *Journal of Contaminant Hydrology*, 21, 269–279. Amsterdam, the Netherlands: Elsevier Science Publishers. TIC: 245730.

Vilks, P.; Frost, L.H.; Bachinski, D.B. 1997. "Field-Scale Colloid Migration Experiments in a Granite Fracture." *Journal of Contaminant Hydrology*, 26, 203–214. Amsterdam, the Netherlands: Elsevier Science Publishers. TIC: 245732.

Viswanathan, H.S.; Robinson, B.A.; Valocchi, A.J.; and Triay, I.R. 1998. "A Reactive Transport Model of Neptunium Migration from the Potential Repository at Yucca Mountain." *Journal of Hydrology*, 209, 251–280. Amsterdam, the Netherlands: Elsevier Science Publishers. TIC: 243441.

Wan, J., and J.L. Wilson. 1994. "Colloid Transport in Unsaturated Porous Media." *Water Resources Research*, 30 (4), 857–864. TIC: 222359.

Wan, J. and Tokunaga, T.K. 1997. "Film Straining of Colloids in Unsaturated Porous Media: Conceptual Model and Experimental Testing." *Environmental Science and Technology*, 31 (8), 2413–2420. Washington, D.C.: American Chemical Society. TIC: 234804.

Wemheuer, R.F. 1999. "First Issue of FY00 NEPO QAP-2-0 Activity Evaluations." Interoffice correspondence from R.F. Wemheuer (CRWMS M&O) to R.A. Morgan (CRWMS M&O), October 1, 1999, LV.NEPO.RTPS.TAG.10/99-155, with attachments, Activity Evaluation for Work Package #1401213UM1. ACC: MOL.19991028.0162.

van de Weerd, H. and Leijnse, A. 1997. "Assessment of the Effect of Kinetics on Colloid Facilitated Radionuclide Transport in Porous Media." *Journal of Contaminant Hydrology*, 26, 245–256. Amsterdam, the Netherlands: Elsevier Science Publishers. TIC: 245731.

Wu, Y.S.; Ritcey, A.C.; and Bodvarsson, G.S. 1999. "A Modeling Study of Perched Water Phenomena in the Unsaturated Zone at Yucca Mountain." *Journal of Contaminant Hydrology*, 38 (1-3), 157–184. Amsterdam, the Netherlands: Elsevier Science Publishers. TIC: 244160.

Wu, Y.S.; Ahlers, C.F.; Fraser, P.; Simmons, A.; and Pruess, K. 1996. *Software Qualification of Selected TOUGH2 Modules*. Report LBL-39490. Berkeley, California: Lawrence Berkeley National Laboratory. ACC: MOL.19970219.0104.

Software Cited

Software Code: TOUGH2 V1.4 Module EOS9 V1.4. STN: 10007-1.4-01.

Software Code: TOUGH2 V1.11 Module EOS9nT V1.0. CSCI: 10065-1.11MEOS9NTV1.0-00.

Software Code: T2R3D V1.4. STN: 10006-1.4-00.

Software Code: FRACL V1.0. STN: 10191-1.0-00.

Software routine: xtrqct1.f V1.0. STN: 10213-1.0-00.

Software routine: xtrqct2.f V1.0. STN: 10214-1.0-00.

Software routine: xtract2a.f V1.0. STN: 10215-1.0-00.

Software routine: xtract2b.f V1.0. STN: 10216-1.0-00.

Software routine: xtract5.f V1.0. STN: 10217-1.0-00.

Software routine: xtract6.f V1.0. STN: 10218-1.0-00.

8.2 CODES, STANDARDS, REGULATIONS AND PROCEDURES

64 FR (Federal Register) 8640. Disposal of High-Level Radioactive Waste in a Proposed Geologic Repository at Yucca Mountain. Proposed rule 10 CFR (Code of Federal Regulations) 63. Readily available.

AP-3.10Q, Rev. 1, ICN 1. *Analyses and Models*. Washington, D.C.: U.S. Department of Energy, Office of Civilian Radioactive Waste Management. ACC: MOL.19991019.0467.

AP-SI.1Q, Rev. 2, ICN 2. *Software Management*. Washington, D.C.: U.S. Department of Energy, Office of Civilian Radioactive Waste Management. ACC: MOL.19991214.0627.

DOE 1998a. *Quality Assurance Requirements and Description*. DOE/RW-0333P, REV 8. Washington D.C.: DOE OCRWM. ACC: MOL.19980601.0022.

QAP-2-0, Rev. 5. *Conduct of Activities*. Las Vegas, Nevada: CRWMS M&O. ACC: MOL.19980826.0209.

8.3 SOURCE DATA, LISTED BY DATA TRACKING NUMBER

GS950608312272.001. Chemical Data for Pore Water from Tuff Cores of USW NRG-6, NRG7/7A, UZ-14 AND UZ-N55, and UE-25 UZ#16. Submittal date: 05/30/1995.

GS990308312242.007. Laboratory And Centrifuge Measurements Of Physical And Hydraulic Properties Of Core Samples From Busted Butte Boreholes UZTT-BB-INJ-1, UZTT-BB-INJ-3, UZTT-BB-INJ-4, UZTT-BB-INJ-6, UZTT-BB-COL-5 and UZTT-BB-COL-8. Submittal date: 03/22/1999.

GS990708312242.008. Physical and Hydraulic Properties of Core Samples from Busted Butte Boreholes. Submittal date: 07/01/1999.

LAIT831341AQ96.001. Radionuclide Retardation. Measurements of Batch Sorption Distribution Coefficients for Barium, Cesium, Selenium, Strontium, Uranium, Plutonium, and Neptunium. Submittal date: 11/12/1996.

LAJF831222AQ98.007. Chloride, Bromide, and Sulfate Analyses of Salts Leached from ECRB-CWAT#1, #2, and #3 Drill core. Submittal date: 09/09/1998.

LA9909JF831222.010. Chloride, Bromide, Sulfate, and Chlorine-36 Analyses of ESF Pore Waters. Submittal date: 09/29/1999.

LA9909JF831222.012. Chloride, Bromide, and Sulfate Analyses of Porewater Extracted from ESF Niche 3566 (Niche #1) and ESF 3650 (Niche #2) Drillcore. Submittal date: 09/29/1999.

LA9909WS831372.001. Busted Butte UZ Transport Test: Phase I Collection Pad Extract Concentrations. Submittal date: 09/29/1999.

LA9909WS831372.002. Busted Butte UZ Transport Test: Phase I Collection Pad Tracer Loading And Tracer Concentrations. Submittal date: 09/30/1999.

LA9909WS831372.011. Preliminary Measured Sorption Coefficients. Submittal date: 10/13/1999.

LB971212001254.001. DKM Base Case Parameter Set For UZ Model with Mean Fracture Alpha, Present Day Infiltration, and Estimated Welded, Non-Welded and Zeolitic FMX. Submittal date: 12/12/1997.

LB990501233129.001. Fracture Properties for the UZ Model Grids and Uncalibrated Fracture and Matrix Properties for the UZ Model Layers for AMR U0090, "Analysis of Hydrologic Properties Data." Submittal date: 08/25/1999.

LB990701233129.002. 3-D Model Calibration Grid for Calculation of Flow Fields using #3 Perched Water Conceptual Model (Non-Perched Water Model). Submittal date: Will be submitted with AMR.

LB990501233129.004. 3-D UZ Model Calibration Grids for AMR U0000, "Development of Numerical Grids of UZ Flow and Transport Modeling." Submittal date: 9/24/1999

LB990801233129.001. TSPA Grid Flow Simulations for AMR U0050, "UZ Flow Models and Submodels." (Flow Field #1). Submittal date: 11/29/1999.

LB990801233129.003. TSPA Grid Flow Simulations for AMR U0050, "UZ Flow Models and Submodels." (Flow Field #3). Submittal date: 11/29/1999.

LB990801233129.004. TSPA Grid Flow Simulations for AMR U0050, "UZ Flow Models and Submodels." Submittal date: 11/29/1999.

LB990801233129.005. TSPA Grid Flow Simulations for AMR U0050, "UZ Flow Models and Submodels." (Flow Field #5). Submittal date: 11/29/1999.

LB990801233129.007. TSPA Grid Flow Simulations for AMR U0050, "UZ Flow Models and Submodels." (Flow Field #7). Submittal date: 11/29/1999.

LB990801233129.009. TSPA Grid Flow Simulations for AMR U0050, "UZ Flow Models and Submodels." (Flow Field #9). Submittal date: 11/29/1999.

LB990801233129.011. TSPA Grid Flow Simulations for AMR U0050, "UZ Flow Models and Submodels." (Flow Field #11). Submittal date: 11/29/1999.

LB990801233129.013. TSPA Grid Flow Simulations for AMR U0050, "UZ Flow Models and Submodels." (Flow Field #13). Submittal date: 11/29/1999.

LB990801233129.015. TSPA Grid Flow Simulations for AMR U0050, "UZ Flow Models and Submodels." (Flow Field #15). Submittal date: 11/29/1999.

LB990801233129.017. TSPA Grid Flow Simulations for AMR U0050, "UZ Flow Models and Submodels." (Flow Field #17). Submittal date: 11/29/1999.

LB990801233129.019. TSPA Grid Flow Simulations for AMR U0050, "UZ Flow Models and Submodels." Flow Field #19: Present Day Mean Infiltration Map for Non-Perched Water Conceptual Model. Submittal date: will be submitted with AMR.

LB991131233129.003. Analytical and Simulation Results of Chloride and Chlorine-36 Analysis. Submittal date: Will be submitted with AMR U0050 (CRWMS M&O, 1999d)

LB997141233129.001. Calibrated Base Case Infiltration 1-D Parameter Set for the UZ Flow and Transport Model, FY99. Submittal date: 07/21/1999.

8.4 OUTPUT DATA, LISTED BY DATA TRACKING NUMBER

LB991220140160.001. Model Validation using EOS9nT Input and Output file.
Submittal date: Will be submitted with AMR.

LB991220140160.002. Model Validation using FRACL Input and Output files. Will be submitted with AMR.

LB991220140160.003. Model Calibration of Chloride in UZ-16 using FRACL Input and Output files. Will be submitted with AMR.

LB991220140160.004. Model Calibration of Chloride in the ESF using FRACL Input and Output files. Will be submitted with AMR.

LB991220140160.005. Model Prediction of Transport in TSw using FRACL Input and Output files. Will be submitted with AMR.

LB991220140160.006. Model Prediction of Sensitivity Studies in tsw35 using FRACL Input and Output files. Will be submitted with AMR.

LB991220140160.007. Model Prediction of Transport in CHn using FRACL Input and Output files. Will be submitted with AMR.

LB991220140160.008. Model Prediction of Transport in PP using FRACL Input and Output files. Will be submitted with AMR.

LB991220140160.009. Model Prediction of Transport Underneath Repository using FRACL Input and Output files. Will be submitted with AMR.

LB991220140160.010. Model Prediction of Busted Butte Using T2R3D Input and Output files. Will be submitted with AMR.

LB991220140160.011. Model Prediction of 3-D Flow using T2R3D Input and Output files. Will be submitted with AMR.

LB991220140160.012. Model Prediction of 3-D Transport, Present-Day Infiltration, #1 Perched Water Model, using EOS9nT Input and Output files. Will be submitted with AMR.

LB991220140160.013. Model Prediction of 3-D Transport, Monsoon Infiltration, #1 Perched Water Model, using EOS9nT Input and Output files. Will be submitted with AMR.

LB991220140160.014. Model Prediction of 3-D Transport, Glacial Infiltration, #1 Perched Water Model, using EOS9nT Input and Output files. Will be submitted with AMR.

LB991220140160.015. Model Prediction of 3-D Transport, Present-Day Infiltration, #2 Perched Water Model, using EOS9nT Input and Output files. Will be submitted with AMR.

LB991220140160.016. Model Prediction of 3-D Transport, Present-Day Infiltration, No Perched Water Model, using EOS9nT Input and Output files. Will be submitted with AMR.

LB991220140160.017. Model Prediction of 3-D Colloid Transport, Present-Day Infiltration, #1 Perched Water Model, using EOS9nT Input and Output files. Will be submitted with AMR.

LB991220140160.018. Model Prediction of 3-D Site-Scale Radionuclide Transport, Present-Day Infiltration, #1 Perched Water Model, using EOS9nT Input and Output files. Will be submitted with AMR.

LB991220140160.019. Parameter values taken and/or computed from information in the scientific literatures. These parameter values are used for radionuclide transport analysis. Will be submitted with AMR.

INTENTIONALLY LEFT BLANK

ATTACHMENTS

INTENTIONALLY LEFT BLANK

ATTACHMENT I
DISCUSSION OF THE EOS_{9nT} AND FRACL MODELS

INTENTIONALLY LEFT BLANK

I.1 THE EOS9nT AND FRACL MODELS

I.1 TREATMENT OF SPACE AND TIME IN THE MODELS

I.1.1 Treatment of Space

The space derivatives in the transport equations of EOS9nT (the numerical 3-D model) are discretized following the Integrated Finite Difference method of the TOUGH2 family of codes (Pruess 1991). For unconditional monotonicity, upstream weighting is always employed in EOS9nT. No space discretization is needed in FRACL, as the solutions are analytical in space.

I.1.2 Treatment of Time

FRACL, the 2-D semianalytical model, employs Laplace transforms for the treatment of the time derivative. The Laplace space solutions are then inverted numerically to obtain the solution in time. EOS9nT allows both conventional timestepping and Laplace transform formulations.

Using the conventional timestepping approach of TOUGH2 (Pruess 1991), time in EOS9nT is discretized using a first-order, fully implicit finite-difference approximation. Radioactive decay can be computed either at the middle or the end of the timestep. The residuals are determined, and the elements of the Jacobian matrix are computed following the approach described in detail by Pruess (1987;1991). The Jacobian is then solved using a set of preconditioned conjugate gradient solvers available in TOUGH2 (Moridis and Pruess 1995;1998). The evolution of the timestep size in the flow component of EOS9nT is internally controlled by the Newtonian convergence criteria (Pruess 1991).

The timestep size in the n transport equations is specific to each tracer, and is controlled by inputs which place limitations on its magnitude based on (a) the user-defined maximum allowed grid Courant number and (b) the maximum allowable fraction of the half-life $(T_{1/2})_{\kappa}$ (if radioactive) of tracer κ . It must be pointed out that the fully implicit formulation of EOS9nT with upstream weighting does not place any limitations on the Courant number. This is a consideration only in explicit schemes. A user-defined maximum allowed Courant number in EOS9nT is a means of setting an upper boundary to the timestep magnitude in the transport equations.

Under transient flow conditions, the time-stepping process in EOS9nT is shown in Figure I.1, in which Δt_f is the timestep in the flow equation and $\Delta t_{t,\kappa}$ is the timestep in the transport equation of tracer κ . A total of $n + 1$ separate simulation times are independently tracked in EOS9nT (one for the flow equation and n for the n tracer transport equations).

After the flow solution at $t + \Delta t_f$ is obtained, the water saturations, flow velocities and flow rates

across the element interfaces are recorded. The time is then reset to t in the transport equation of tracer κ , and the maximum allowable $\Delta t_{t,\kappa}$ is determined from limitations on the grid Courant number and the tracer half life. The tracer transport in the Δt_f interval is simulated using a total of k_κ generally unequal time steps, where $k_\kappa \geq \Delta t_f / \Delta t_{t,\kappa}$. The process is repeated for all n independently-tracked tracers. The time step sizes of the various tracers are not generally equal.

As the flow field becomes invariant, the size of the Δt_f in TOUGH2 increases, and convergence is achieved after a single Newtonian iteration. When this occurs, EOS9nT prints the steady state flow solution and continues solving the tracer equations. The time step in the solute transport equations becomes uniform and equal to the shortest of the $\Delta t_{t,\kappa}$, $\kappa = 1, \dots, n$ after the flow has reached a steady state.

EOS9nT also allows tracer transport simulations when the initial flow field is time-invariant. In this case, EOS9nT solves the flow field only once in order to obtain the constant water saturations, flow velocities and flow rates across the element interfaces. After printing the flow data, only the tracer transport equations are solved.

The Courant number limitations may result in a situation where the smallest gridblock controls the $\Delta t_{t,i}$, and may result in inefficient simulations and excessive computational times. To partially alleviate this problem, EOS9nT determines the $\Delta t_{t,\kappa}$ from limitation on the Courant numbers at gridblocks at which the changes in X_κ are within 5% of the maximum change. This allows timestep adjustment by tracking moving front, and limits Courant number considerations to elements where measurable changes occur.

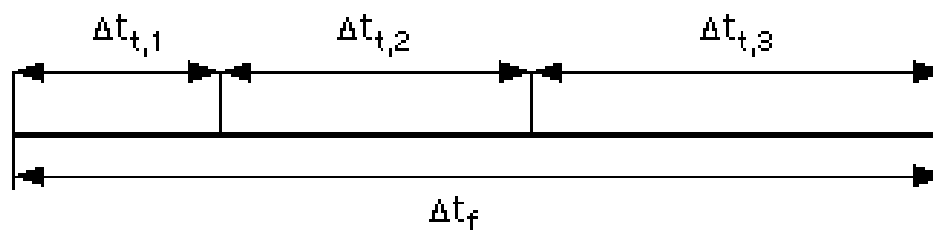


Figure I.1. Timestepping in EOS9nT.

I.2 THE LAPLACE TRANSFORM FORMULATION IN EOS9nT

I.2.1 Applicability

This is a EOS9nT option in problems in which the flow field is invariant and solutions are required at very large times, the Courant and half-life limitations in conventional timestepping may result in $\Delta t_{t,i}$ which are too short for an efficient simulation, thus requiring impractically long execution times.

Application of the Laplace space formulation demands strict linearity of (or ability to linearize the) problem. Thus, the Laplace formulation in EOS9nT can be invoked under the following conditions:

- (a) The flow field is time-invariant.
- (b) Sorption (physical and/or chemical) follows a linear equilibrium or linear kinetic isotherm.
- (c) Colloid filtration is governed by a linear equilibrium or linear kinetic model.
- (d) Colloid-assisted solute transport is not considered.

I.2.2 Advantages of the Laplace Transform Formulation

The major advantage of this formulation is that it eliminates the need for time discretization. It yields solutions semi-analytical in time and numerical in space by solving the transformed PDEs in the Laplace space, and numerically inverting the solution vectors. Concerns over the effects of the numerical treatment of the time dependency on accuracy and stability, which necessitate a large number of small time steps between successive observation times in conventional timestepping solutions, are rendered irrelevant because time is no longer a consideration. An unlimited time step size is thus possible without loss of accuracy or stability.

Additionally, the Laplace transform formulation significantly reduces numerical dispersion by practically eliminating the error associated with the treatment of the time derivative. Sudicky (1989, pp. 1844-1845) reported very accurate solutions with grid Peclet numbers in excess of 33 (more than an order of magnitude larger than the maximum recommended value of 2), and indicated that much coarser grid can be employed without loss of accuracy.

I.2.3 The Laplace Space Transport Equations in EOS9nT

In its most general form, the Laplace transform of the derivative of the accumulation terms of a daughter product κ from the decay of parent j (i.e. the left-hand side) in Equation 26 (after the incorporation of Equations (3), (7) and (8), see Section 6.3) yields

$$\begin{aligned}
& \mathcal{L}\left\{\frac{dM_\kappa}{dt} + \lambda_\kappa M_\kappa - \lambda_j m_r M_j\right\} \\
&= \left[\phi h \rho \widehat{X}_\kappa + (1 - \phi) \rho_s \widehat{F}_\kappa\right] (s + \lambda_\kappa) - \lambda_j m_r \widehat{M}_j \\
&\quad - [\phi h \rho X_{\kappa,0} + (1 - \phi) \rho_s F_{\kappa,0}] ,
\end{aligned} \tag{Eq. I.1}$$

where s is the Laplace space parameter, $\hat{\alpha} = \mathcal{L}\{\alpha\}$, $\mathcal{L}\{\}$ denotes the Laplace transform of the term within the brackets, and the subscript 0 of X_κ and F_κ denotes their values at $t = 0$.

From a slight manipulation of the equations in Moridis and Bodvarsson (1999),

$$\widehat{F} = \gamma \widehat{X} + \theta , \tag{Eq. I.2}$$

where

$$\gamma = \begin{cases} w & \text{for LE sorption,} \\ u & \text{for LKP or LIP sorption,} \\ v & \text{for LKC sorption,} \\ w + u & \text{for combined LE and LKP/LIP sorption,} \\ w + v & \text{for combined LE and LKC sorption,} \\ u + v & \text{for combined LKP/LIP and LKC sorption,} \end{cases} \tag{Eq. I.3}$$

$$\theta = \begin{cases} 0 & \text{for LE sorption,} \\ u_1 & \text{for LKP or LIP sorption,} \\ v_1 & \text{for LKC sorption,} \\ u_1 & \text{for combined LE and LKP/LIP sorption,} \\ v_1 & \text{for combined LE and LKC sorption,} \\ u_1 + v_1 & \text{for combined LKP/LIP and LKC sorption,} \end{cases} \tag{Eq. I.4}$$

$$w = K_d K_i \rho, \quad u = \frac{k_p K_d K_i \rho}{s + \lambda + \delta_p k_p}, \quad v = \frac{k_c^+ K_i \rho}{s + \lambda + k_c^-}, \tag{Eq. I.5}$$

and

$$u_1 = \frac{F_{p,0}}{s + \lambda + \delta_p k_p}, \quad v = \frac{F_{c,0}}{s + \lambda + k_c^-}, \tag{Eq. I.6}$$

where the 0 subscript of F_p and F_c denotes their values at $t = 0$. For non-radioactive substances, $\lambda = 0$, and Equation I.1 through I.6 apply unchanged. The Moridis and Bodvarsson (1999) equation $\widehat{F} = p \widehat{C} + \theta$, is equivalent to Equation I.2 for $p = \gamma \rho$. The ρ term is directly incorporated in the γ expression, as seen from Equations I.3 and I.5.

For colloids, the term $(1 - \phi) \rho_s \widehat{F}$ in Equation 8 is replaced by $\rho_c \widehat{\sigma}$, where

$$\widehat{\sigma} = \frac{\overbrace{\kappa^+ K_\sigma \rho}^{\gamma}}{s + \kappa^- + \lambda} \widehat{X} + \frac{\overbrace{\sigma_0}^{\theta}}{s + \kappa^- + \lambda} . \quad (\text{Eq. I.7})$$

Thus, Equation I.2 applies after substituting σ for F . The 0 subscript in Equation I.6 and I.7 denotes the value at $t = 0$. This formulation allows simulation of radioactive true colloids. For pseudocolloids, $\lambda = 0$ in Equation I.7.

Taking Laplace transform in the right-hand side of Equation 26 (Section 6.3) and combining it with Equation I.1 yields

$$\mathcal{M}_\kappa \widehat{X}_\kappa - \frac{1}{V_n} \sum_m A_{nm} \left[F_{nm} \widehat{X}_\kappa - \mathbf{D}_\kappa^* \nabla \widehat{X}_\kappa \right] = \mathcal{H}_\kappa - \lambda_j m_r \widehat{M}_j, \quad (\text{Eq. I.8})$$

where

$$\mathcal{M}_\kappa = [\phi h \rho + (1 - \phi) \rho_s \gamma_\kappa] (s + \lambda_\kappa) \quad (\text{Eq. I.9})$$

$$\mathbf{D}_\kappa^* = \rho \mathbf{D}_\kappa + (1 - \phi) \rho_s \tau_s D_s \gamma_\kappa, \quad (\text{Eq. I.10})$$

$$\mathcal{H}_\kappa = - \left\{ \phi h \rho X_{\kappa,0} + (1 - \phi) \rho_s [1 - \theta_\kappa (s + \lambda_i)] F_{i,0} + \widehat{Q}_\kappa \right\}, \quad (\text{Eq. I.11})$$

$$\widehat{Q}_\kappa = \mathcal{L}\{q_\kappa\} = \begin{cases} q_w X_{q,\kappa}/s & \text{for a source,} \\ q_w (\widehat{X}_\kappa)_n & \text{for a sink,} \end{cases} \quad (\text{Eq. I.12})$$

q_w is the water mass injection or withdrawal rate, and $X_{q,\kappa}$ is the mass fraction of tracer i in the injected stream. In EOS9nT the terms \widehat{M}_j are saved from the simulation of the parent, and are subsequently used in the computation of the distribution of any parent. Equations I.8 through I.12 apply to both solute and colloid transport by employing the appropriate γ and θ values, i.e., Equations I.3 through I.6 for solutes, or Equation I.7 for colloids.

I.2.4 Implications for UZ Transport Simulations

One of the obvious advantages that the Laplace transform formulation affords is that, in the Laplace space, it completely linearizes all the kinetic transport equations, which are nonlinear in time for conventional timestepping. Thus, the Laplace transform formulation does not increase the order of the matrix to be solved. For an implicit solution in conventional timestepping, each kinetic equation must be solved separately, in addition to the general transport equation. Thus, the order of the matrix increases linearly with the number of kinetic equations.

For example, to obtain the concentration distribution of a species that follows simultaneously two separate kinetic sorption isotherms (combined sorption) in a particular porous medium, the solution of a matrix of order $3N_e$ would be needed, where N_e is the number of elements into which the domain is subdivided. Because of the linearity of equations (I.2) to (I.7), the order of the matrix in the Laplace space formulation is only N_e . Additionally, the Laplace transforms alleviate accuracy problems which may arise from the inaccurate time-weighting of the radioactive decay. More specifically, in conventional timestepping, it is not known a-priori whether the mass accumulation is correctly represented by using its value at the midpoint or at the end of the timestep.

I.2.5 The Laplace Space Solutions

Equation I.8 is the Laplace space equation of transport in EOS9nT. The resulting algebraic equations may be written in a general matrix form as:

$$\mathbf{T} \vec{\tilde{X}} = \vec{\tilde{B}}, \quad (\text{Eq. I.13})$$

where \mathbf{T} is the coefficient matrix, $\vec{\tilde{X}}$ is the vector of the unknowns, and $\vec{\tilde{B}}$ is the composite vector of knowns.

The Laplace space equations in FRACL are also of the form of the matrix Equation I.13. The computation of \mathbf{T} and $\vec{\tilde{B}}$ necessitates values for the s parameter of the Laplace space. These are provided by two numerical inversion schemes: the Stehfest algorithm (Stehfest 1970a, b) and the De Hoog et al. (1982) method.

I.3 NUMERICAL INVERSION METHODS OF THE LAPLACE SPACE SOLUTIONS

I.3.1 The Stehfest Algorithm

For a desired observation time t , the s in the Stehfest algorithm (Stehfest 1970a; 1970b) is real and given by

$$s_\nu = \frac{\ln 2}{t} \cdot \nu, \quad \nu = 1, \dots, N_S \quad (\text{Eq. I.14})$$

where N_S is the number of summation terms in the algorithm and is an even number.

The unknown vector \vec{X} at any time t is obtained by numerically inverting the Laplace space solutions $\vec{X}(s_\nu)$ according to the equation

$$\vec{X}(t) = \frac{\ln 2}{t} \sum_{\nu=1}^{N_S} W_\nu \vec{X}(s_\nu), \quad (\text{Eq. I.15})$$

where

$$W_\nu = (-1)^{\frac{N_S}{2} + \nu} \sum_{k=\frac{1}{2}(\nu+1)}^{\min\{\nu, \frac{N_S}{2}\}} \frac{k^{\frac{N_S}{2}} (2k!)}{(\frac{N_S}{2} - k)! k! (k-1)! (\nu - k)! (2k - \nu)!}. \quad (\text{Eq. I.16})$$

Although the accuracy of the method is theoretically expected to improve with increasing N_S , Stehfest (1970a, b) showed that with increasing N_S the number of correct significant figures increases linearly at first and then, due to roundoff errors, decreases linearly. He determined that the optimum N_S is 10 for single-precision variables (8 significant figures) and 18 for double-precision variables (16 significant figures). Our experience with T2E9nT indicates that $N_s = 16$ or $N_s = 18$ provide the best results.

A very important issue on the Stehfest algorithm concerns its behavior in the solution of the transport of daughters of radioactive decay. Because the Stehfest s includes only real components, the algorithm deteriorates in the solution of the daughter equations (Moridis et al. 1999). Thus, its use should be limited to simulations of parents only.

I.3.2 The De Hoog Method

In the method of De Hoog et al. (1982), hereafter referred to as the De Hoog method, s is a complex number given by Crump (1976) as

$$s_\nu = s_0 + \frac{\nu\pi}{T} j, \quad s_0 = \mu - \frac{\ln(E_R)}{2T}, \quad \nu = 1, \dots, N_H \quad (\text{Eq. I.17})$$

where $2T$ is the period of the Fourier series approximating the inverse function in the interval $[0, 2T]$, $j = \sqrt{-1}$, and $N_H = 2M_H + 1$ is an odd number. Moridis (1992, pp. 815-832) showed that very accurate solutions were obtained when $\mu = 0$, $10^{-12} \leq E_R \leq 10^{-9}$, and $0.9 t_{max} \leq T \leq 1.1 t_{max}$, where t_{max} is the maximum simulation time.

The inversion of the Laplace space solution obtained with the De Hoog method is far more complicated than in the Stehfest algorithm. The solution $\vec{X}(t)$ is given by

$$\vec{X}(t) = \frac{1}{T} \exp(s_0 t) \operatorname{Re} \left[\frac{A_{2M_H}}{B_{2M_H}} \right], \quad (\text{Eq. I.18})$$

where

$$A_n = A_{n-1} + d_n z A_{n-2}, \quad B_n = B_{n-1} + d_n z B_{n-2}, \quad n = 1, \dots, 2M_H, \quad (\text{Eq. I.19})$$

$$z = \exp \left(\frac{j \pi t}{T} \right), \quad (\text{Eq. I.20})$$

$$A_{-1} = 0, \quad A_0 = d_0, \quad B_{-1} = B_0 = 1, \quad (\text{Eq. I.21})$$

$$d_0 = a_0, \quad d_{2m-1} = -q_m^{(0)}, \quad d_{2m} = -e_m^{(0)}, \quad m = 1, \dots, M_H, \quad (\text{Eq. I.22})$$

$$\begin{aligned} \text{for } \ell = 1, \dots, M_H, \quad e_\ell^{(k)} &= q_\ell^{(k+1)} - q_\ell^{(k)} + e_{\ell-1}^{(k+1)}, \quad k = 0, \dots, 2M_H - 2\ell, \\ \text{for } \ell = 2, \dots, M_H, \quad q_\ell^{(k)} &= q_{\ell-1}^{(k+1)} e_{\ell-1}^{(k+1)} / e_{\ell-1}^{(k)}, \quad k = 0, \dots, 2M_H - 2\ell - 1, \end{aligned} \quad (\text{Eq. I.23})$$

$$e_0^{(k)} = 0 \text{ for } k = 0, \dots, 2M_H \quad \text{and} \quad q_1^{(k)} = a_{k+1}/a_k \text{ for } k = 0, \dots, 2M_H - 1, \quad (\text{Eq. I.24})$$

and

$$a_0 = \frac{1}{2} X(s_0), \quad a_k = X(s_k). \quad (\text{Eq. I.25})$$

A convergence acceleration is obtained if, on the last evaluation of the recurrence relations, $d_{2M_H} z$ in (I.19) is replaced by $R_{2M_H}(z)$,

$$R_{2M_H}(z) = -h_{2M_H} \left[1 - \sqrt{(1 + d_{2M_H} z / h_{2M_H})} \right], \quad (\text{Eq. I.26})$$

where

$$h_{2M_H} = \frac{1}{2} [1 + z (d_{2M_H-1} - d_{2M_H})], \quad (\text{Eq. I.27})$$

giving

$$\hat{A}_{2M_H} = A_{2M_H-1} + R_{2M_H} A_{2M_H-2}, \quad \hat{B}_{2M_H} = B_{2M_H-1} + R_{2M_H} B_{2M_H-2}, \quad (\text{Eq. I.28})$$

in which case the accelerated solution at a time t is given by replacing A_{2M_H} and B_{2M_H} by \hat{A}_{2M_H} and \hat{B}_{2M_H} , respectively, in (I.18).

Moridis (1992, p. 825) determined that the minimum M_H for an acceptable accuracy is 5 ($N_H = 11$), and that $M_H \geq 6$ ($N_H \geq 13$) provides very accurate solutions. All the operations in Equations I.17 through I.27 involve complex variables. Because both the real and the imaginary parts of the Laplace space solutions are needed to obtain the solution in time, the DeHoog method results in a matrix of order $2N_e$, i.e., twice as large than the matrix for the Stehfest algorithm. An efficient set of Preconditioned Conjugate Gradient (PCG) methods is used to solve the equations. Details on the PCG methods and their preconditioning can be found in Moridis and Pruess (1995;1998).

The increase in the order of the matrix may be outweighed by the unique advantages of the De Hoog formulation: is (a) it is capable of accurately inverting very steep solution surfaces (even the step function) by increasing M_H , (b) produces a very accurate solution, which allows accurate tracking of daughter transport (a capability which the Stehfest algorithm does not have), and (c) a whole range of solutions at times t in the range $[0, T]$ can be obtained from a single set of solutions X , i.e., Equation I.13 need not be solved for each t of interest. This drastically reduces the number of times the equations need to be solved to cover the desired simulation period. The superior accuracy of the De Hoog method allows the very accurate solution of the daughter equations.

INTENTIONALLY LEFT BLANK

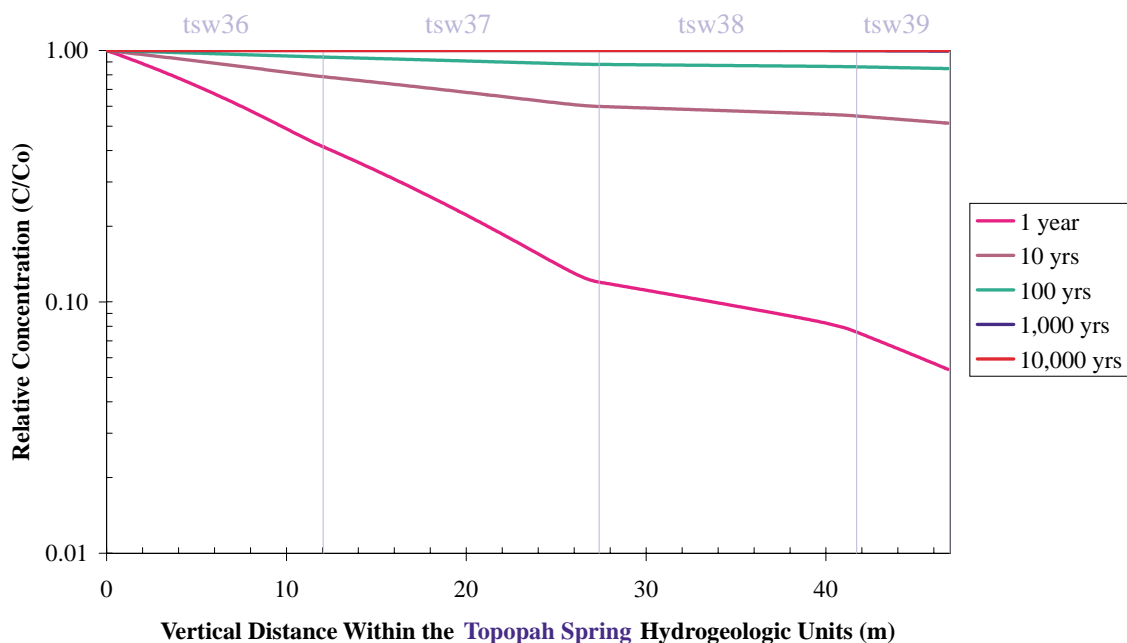
ATTACHMENT II
FIGURES FROM THE STUDY OF TRANSPORT IN THE TS_w
HYDROGEOLOGIC UNIT

FIGURES

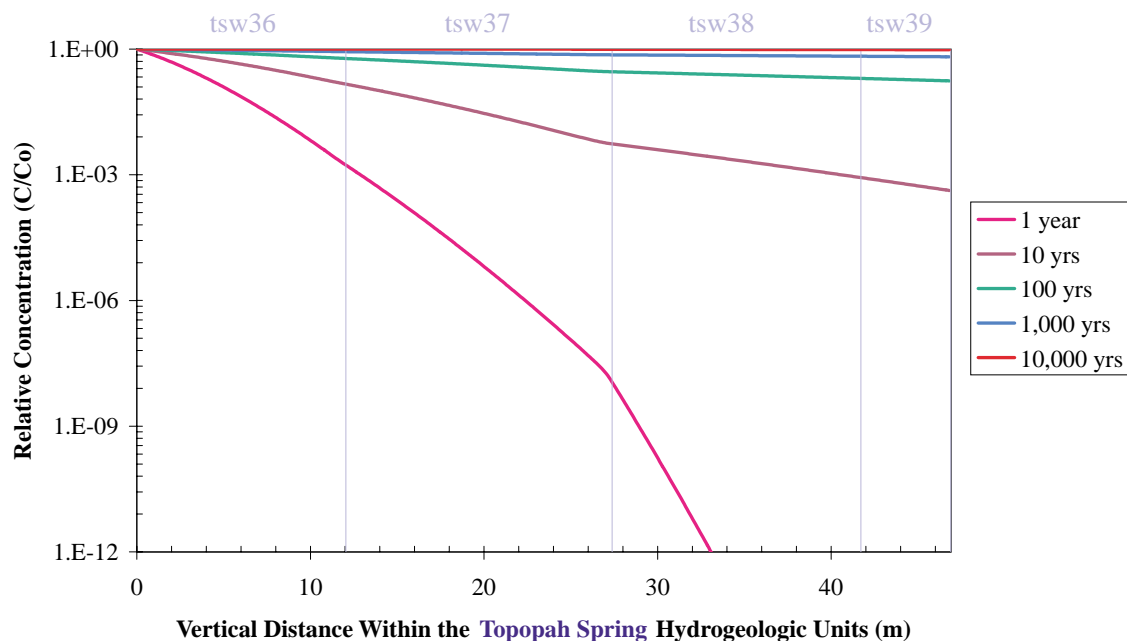
Page

II.1.	^{99}Tc Concentration Profile in TSw in Cross Section 1. Results for 1,000 years and 10,000 years overlap.	II-4
II.2.	^{237}Np Concentration Profile in TSw in Cross Section 1.	II-4
II.3.	^{239}Pu Concentration Profile in TSw in Cross Section 1..	II-5
II.4.	Concentration Profiles in the Matrix at $z=10$ m and $t=1,000$ Years.....	II-5
II.5.	^{99}Tc Concentration Profile in TSw in Cross Section 2. Results for 1,000 years and 10,000 years overlap.	II-6
II.6.	^{237}Np Concentration Profile in TSw in Cross Section 2.	II-6
II.7.	^{239}Pu Concentration Profile in TSw in Cross Section 2.	II-7
II.8.	^{99}Tc Concentration Profile in TSw in Cross Section 3. Results for 1,000 years and 10,000 years overlap.	II-7
II.9.	^{237}Np Concentration Profile in TSw in Cross Section 3.	II-8
II.10.	^{239}Pu Concentration Profile in TSw in Cross Section 3.	II-8
II.11	Effect of K_i on ^{99}Tc Concentration Profiles Along the z -axis in the Fractures at $t = 1,000$ Years.	II-9
II.12.	Effect of K_i on ^{237}Np Concentration Profiles Along the z -axis in the Fractures at $t = 1,000$ Years.	II-9
II.13.	Effect of K_i on ^{237}Np Concentration Profiles Along the x -axis in the Matrix at $z=50$ m and $t=1,000$ Years.	II-10
II.14.	Effect of K_i on ^{239}Pu Concentration Profiles along the z -axis in the Fractures at $t=1,000$ Years.	II-10
II.15.	Effect of K_i on ^{239}Pu Concentration Profiles Along the x -axis in the Matrix at $z=50$ m and $t=1,000$ Years.	II-11

II.16. Effect of Matrix Tortuosity on ^{99}Tc Concentration Profiles Along the z-axis in the Fractures at t=1,000 Years.	II-11
II.17. Effect of Matrix Tortuosity on ^{99}Tc Concentration Profiles Along the x-axis in the Matrix at z=50 m and t=1,000 Years.	II-12
II.18. Effect of Matrix Tortuosity on ^{237}Np Concentration Profiles Along the z-axis in the Fractures at t=1,000 Years.	II-12
II.19. Effect of Matrix Tortuosity on ^{237}Np Concentration Profiles Along the x-axis in the Matrix at z=50 m and t=1,000 Years.....	II-13
II.20. Effect of Matrix Tortuosity on ^{239}Pu Concentration Profiles Along the z-axis in the Fractures at t=1,000 Years.	II-13
II.21. Effect of Matrix Tortuosity on ^{239}Pu Concentration Profiles Along the x-axis in the Matrix at z=50 m and t=1,000 Years.	II-14
II.22. Effect of α_L on ^{99}Tc Concentration Profiles Along the z-axis in the Fractures at t=1,000 Years.	II-14
II.23. Effect of α_L on ^{237}Np Concentration Profiles Along the z-axis in the Fractures at t=1,000 Years.	II-15
II.24. Effect of α_L on ^{239}Pu Concentration Profiles Along the z-axis in the Fractures at t=1,000 Years.	II-15
11.25 Effect of α_L on ^{239}Pu Concentration Profiles Along the x-axis in the Matrix at z=50 and t=1,000 Years.....	II-16

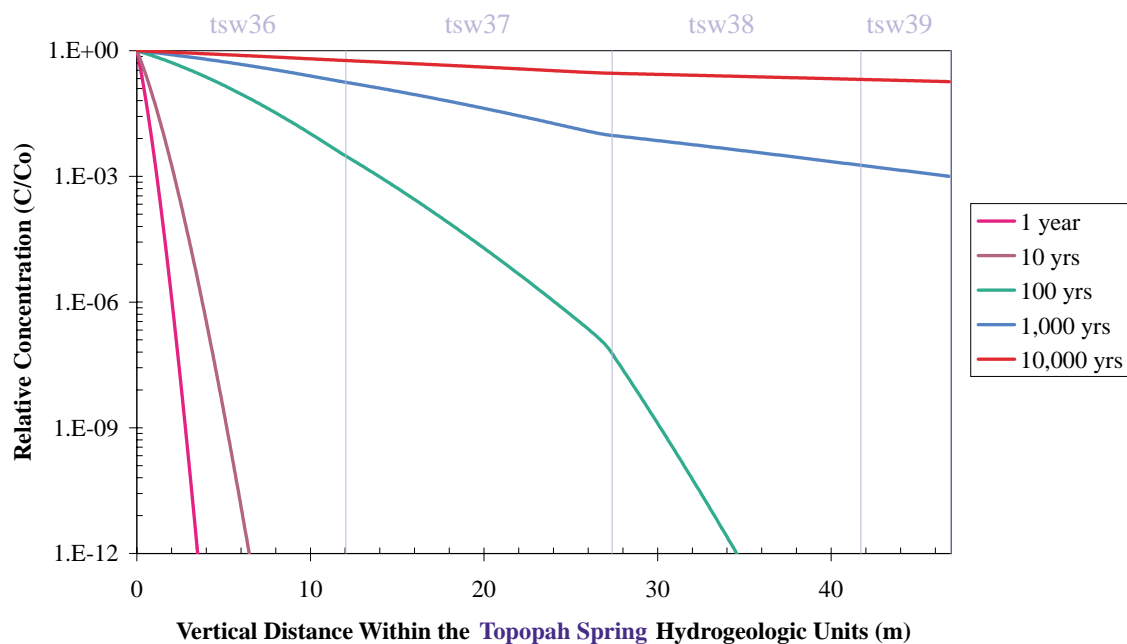


DTN: LB991220140160.005

Figure II.1. ^{99}Tc Concentration Profile in TSw in Cross Section 1. Results for 1,000 years and 10,000 years overlap.

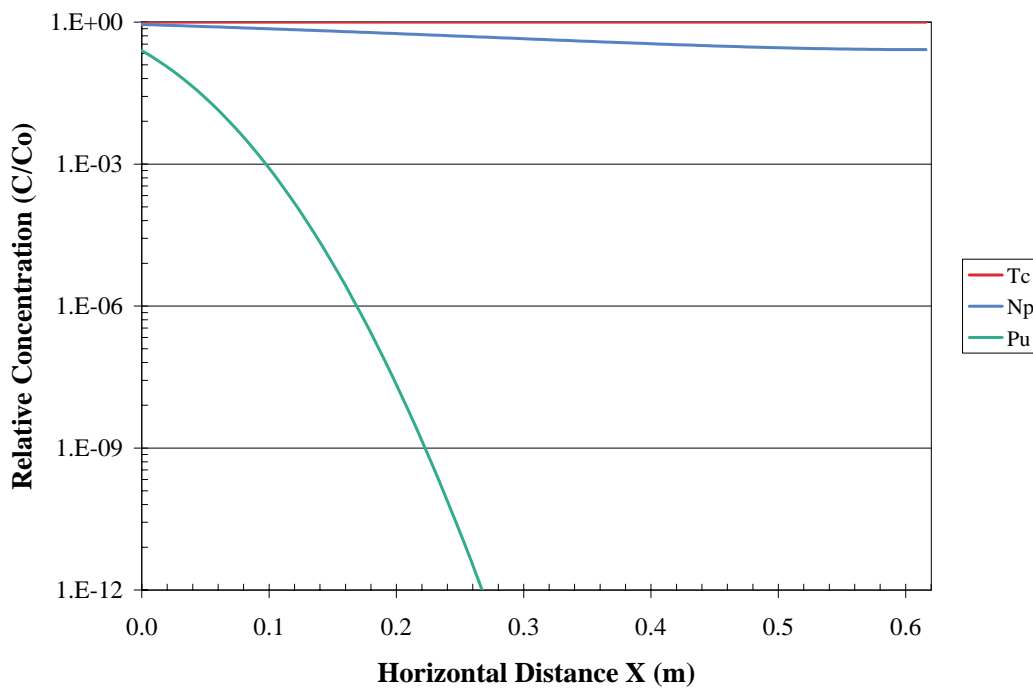
DTN: LB991220140160.005

Figure II.2. ^{237}Np Concentration Profile in TSw in Cross Section 1.



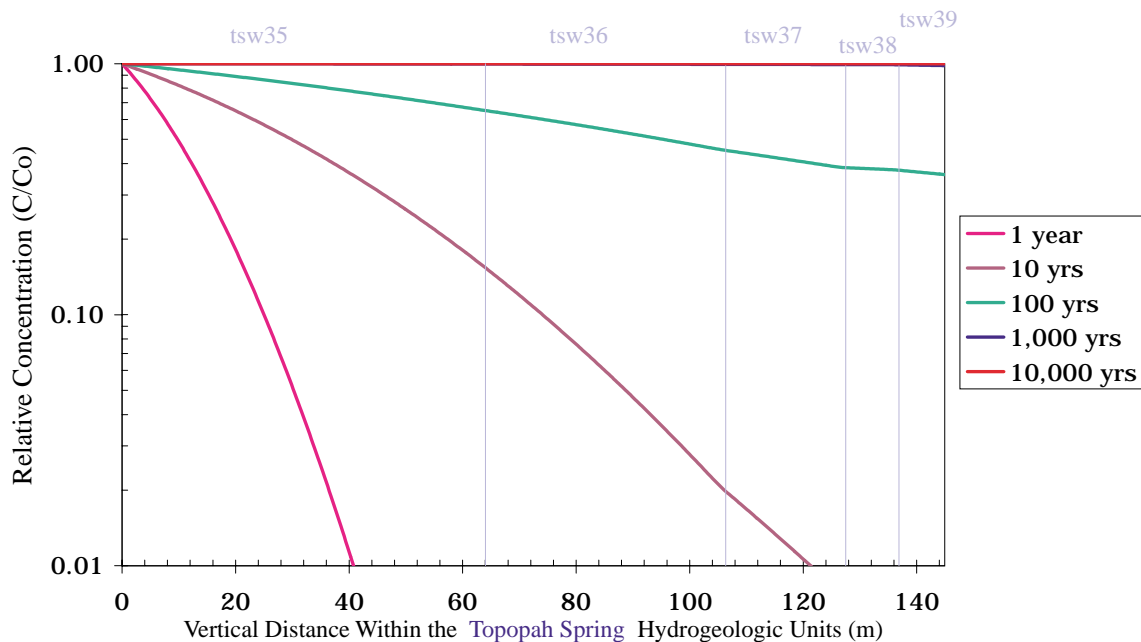
DTN: LB991220140160.005

Figure II.3. ^{239}Pu Concentration Profile in TSw in Cross Section 1.

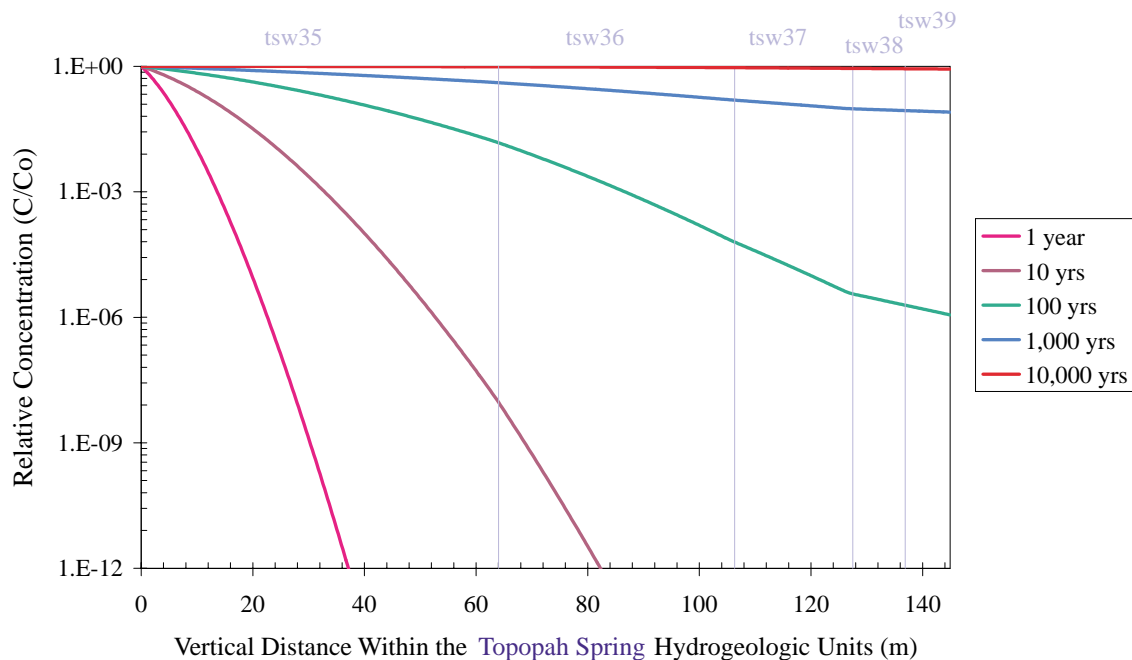


DTN: LB991220140160.005

Figure II.4. Concentration Profiles in the Matrix at $z=10$ m and $t=1,000$ Years.

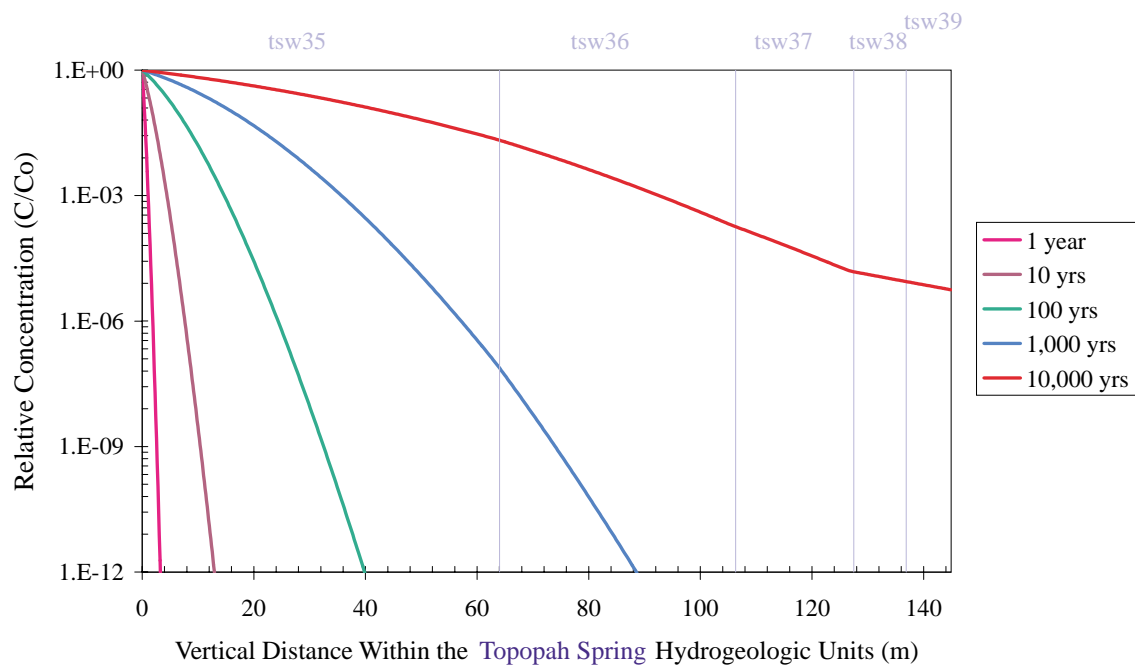


DTN: LB991220140160.005

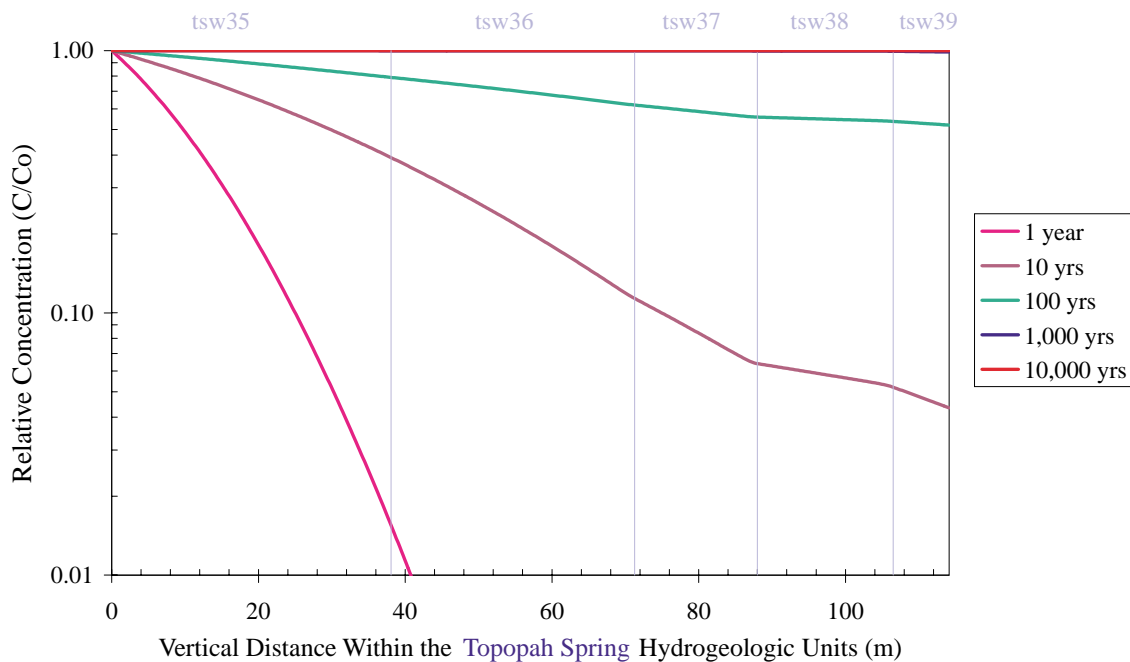
Figure II.5. ^{99}Tc Concentration Profile in TSw in Cross Section 2. Results for 1,000 years and 10,000 years overlap.

DTN: LB991220140160.005

Figure II.6. ^{237}Np Concentration Profile in TSw in Cross Section 2.

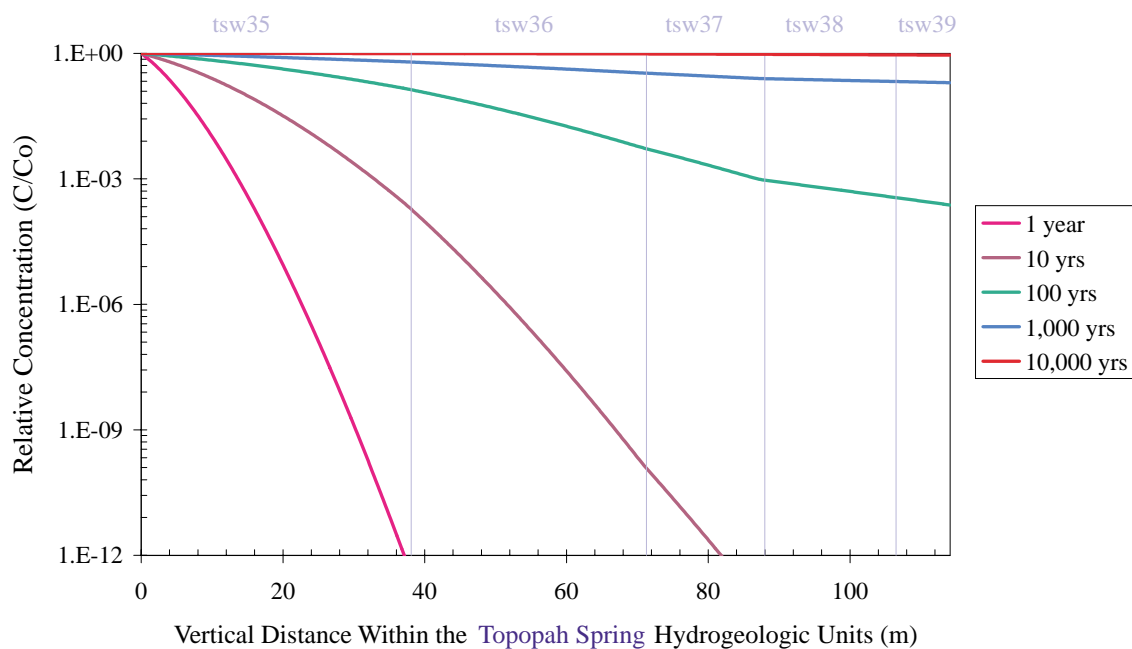


DTN: LB991220140160.005

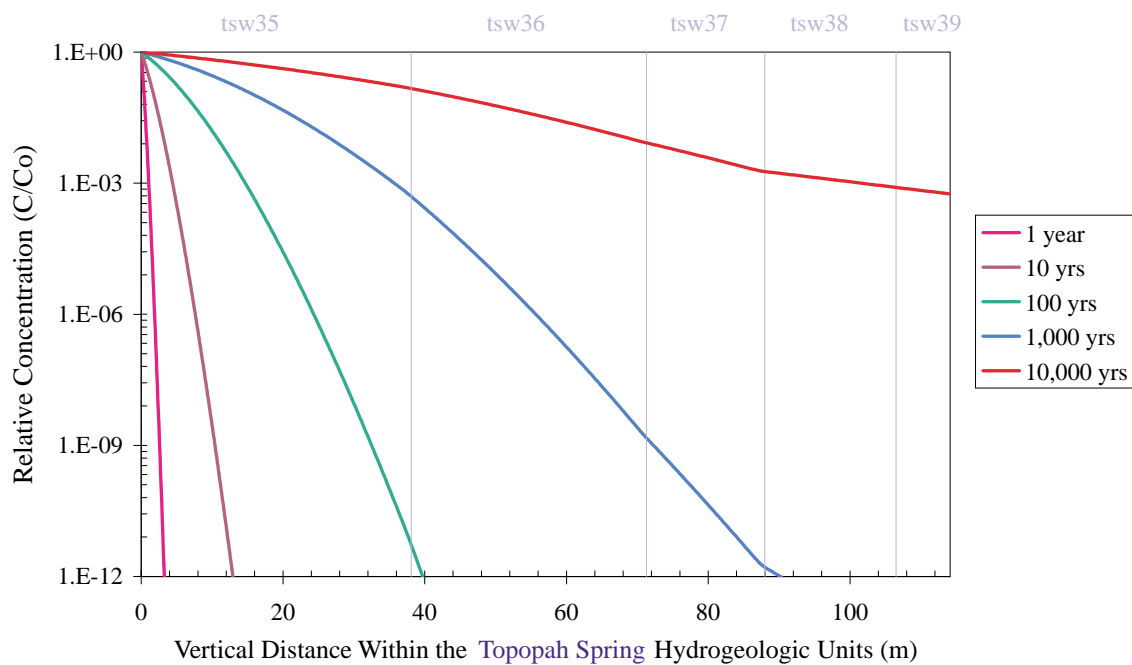
Figure II.7. ^{239}Pu Concentration Profile in TSw in Cross Section 2.

DTN: LB991220140160.005

Figure II.8. ^{99}Tc Concentration Profile in TSw in Cross Section 3. Results for 1,000 years and 10,000 years overlap.

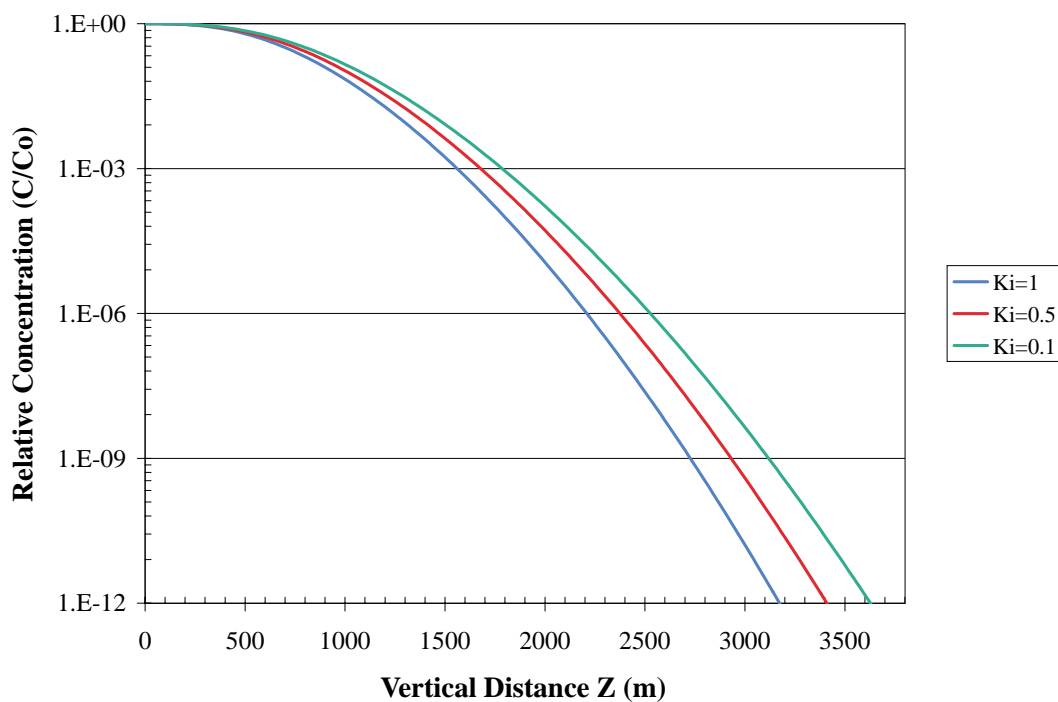


DTN: LB991220140160.005

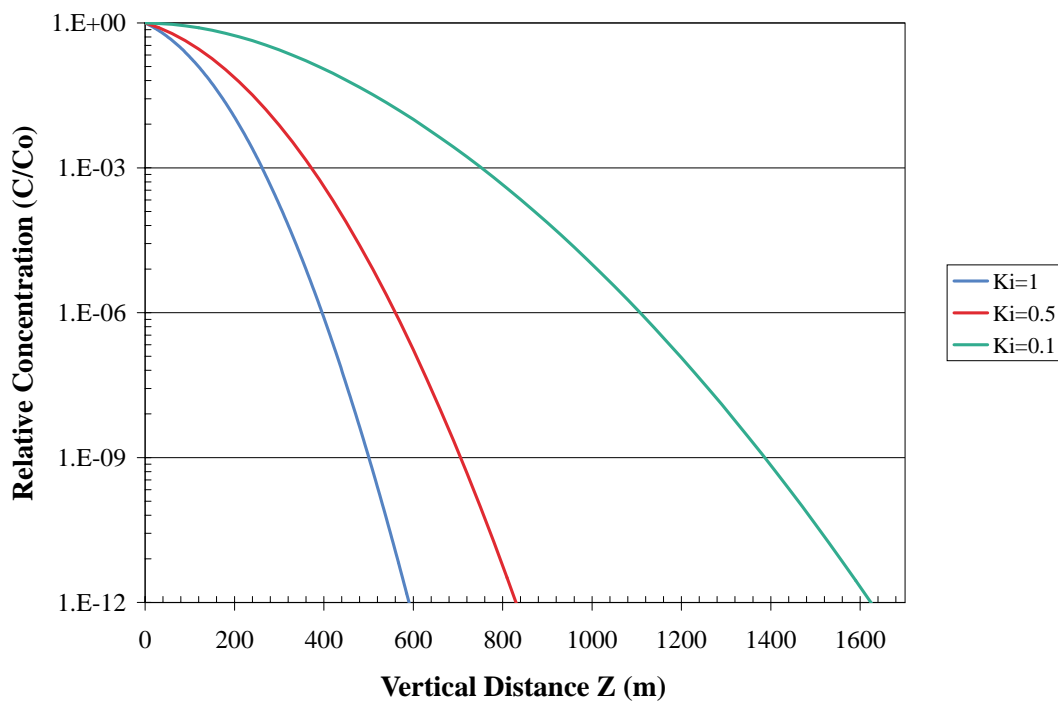
Figure II.9. ^{237}Np Concentration Profile in TSw in Cross Section 3.

DTN: LB991220140160.005

Figure II.10. ^{239}Pu Concentration Profile in TSw in Cross Section 3.

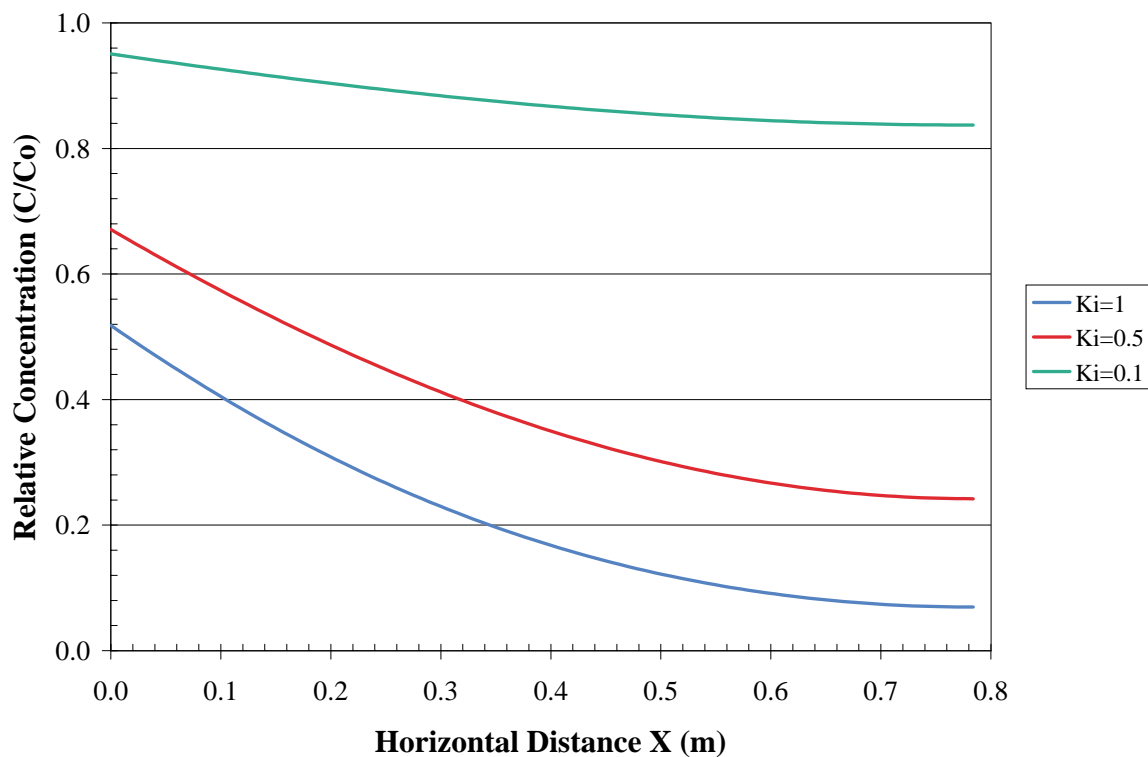


DTN: LB991220140160.006

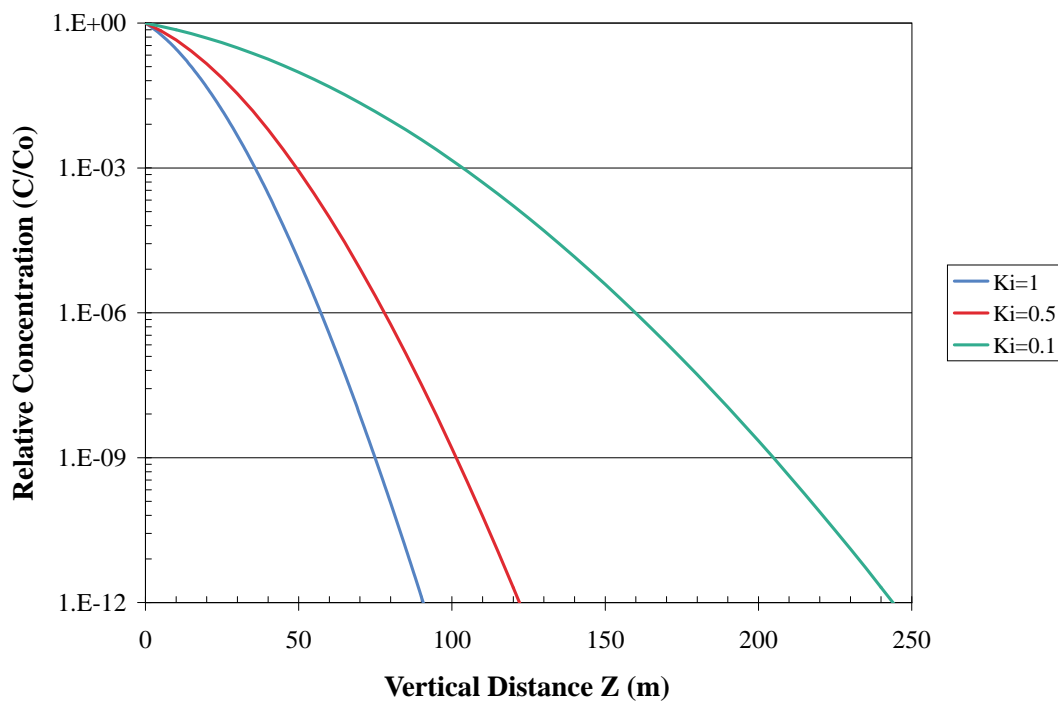
Figure II.11 Effect of K_i on ^{99}Tc Concentration Profiles Along the z-axis in the Fractures at $t = 1,000$ Years.

DTN: LB991220140160.006

Figure II.12. Effect of K_i on ^{237}Np Concentration Profiles Along the z-axis in the Fractures at $t = 1,000$ Years.

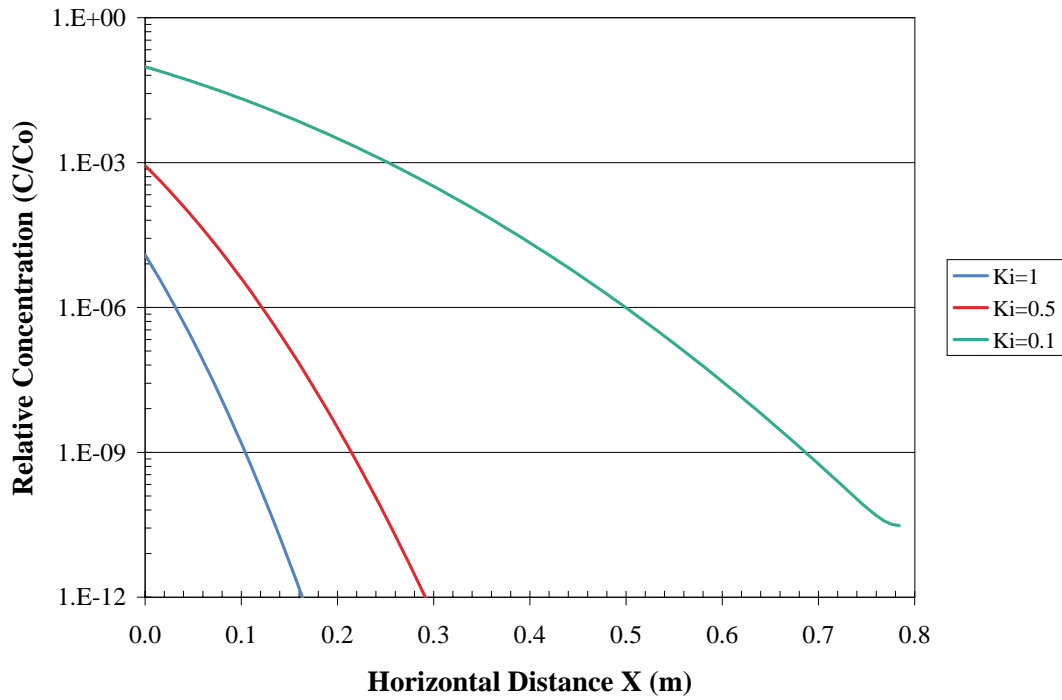


DTN: LB991220140160.006

Figure II.13. Effect of K_i on ^{237}Np Concentration Profiles Along the x-axis in the Matrix $z=50\text{m}$ and $t=1,000$ Years.

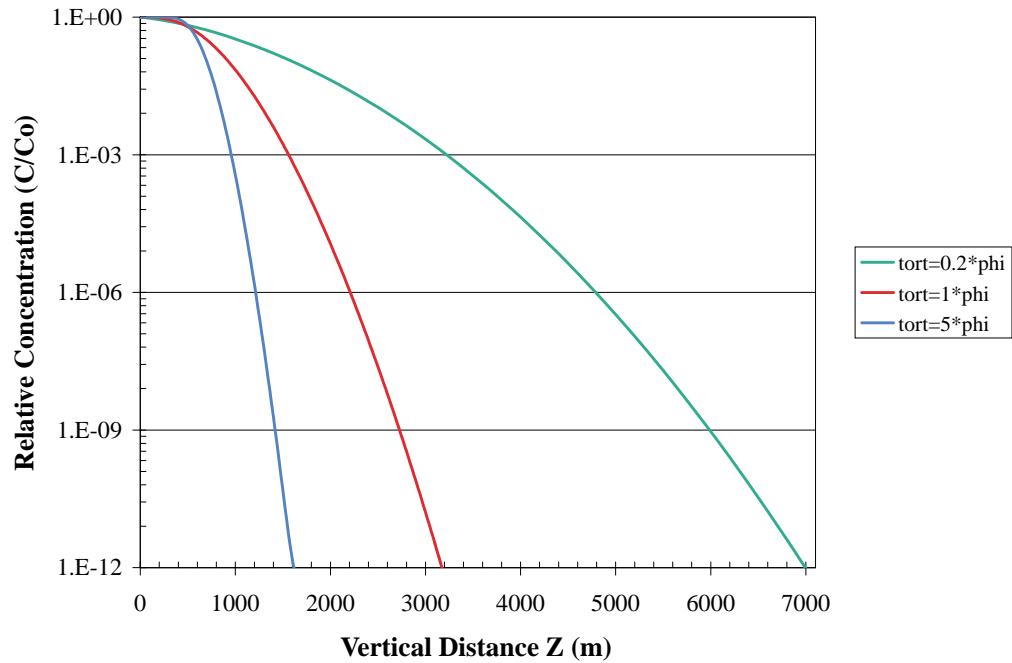
DTN: LB991220140160.006

Figure II.14. Effect of K_i on ^{239}Pu Concentration Profiles Along the z-axis in the Fractures at $t=1,000$ Years.



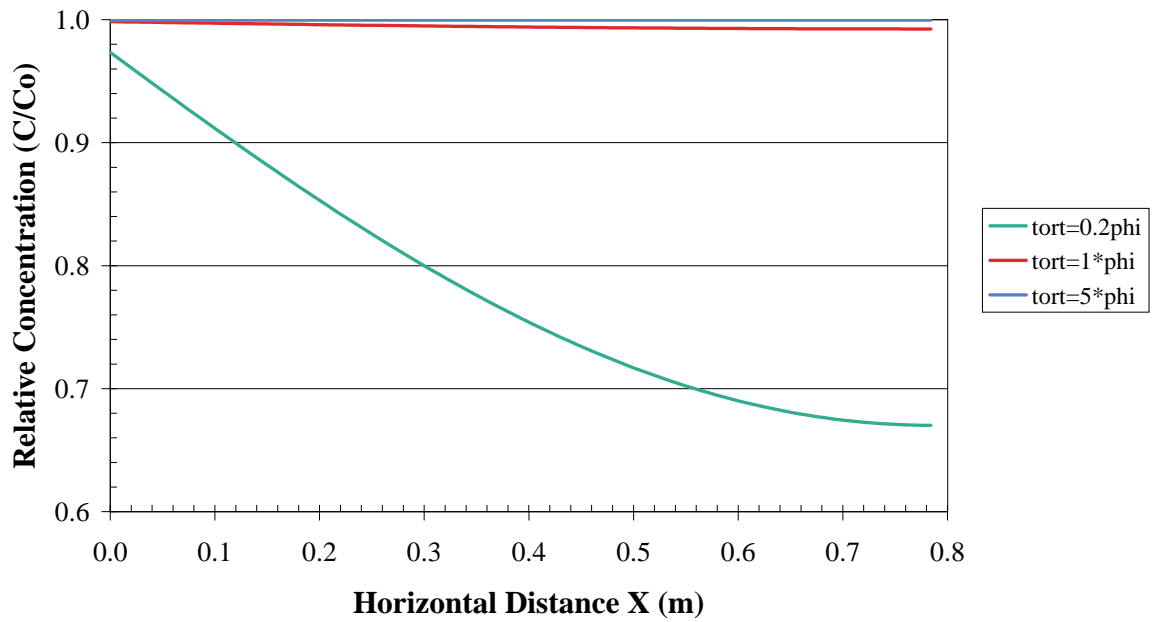
DTN: LB991220140160.006

Figure II.15. Effect of K_i on ^{239}Pu Concentration Profiles Along the x-axis in the Matrix at $z=50$ m and $t=1,000$ Years.



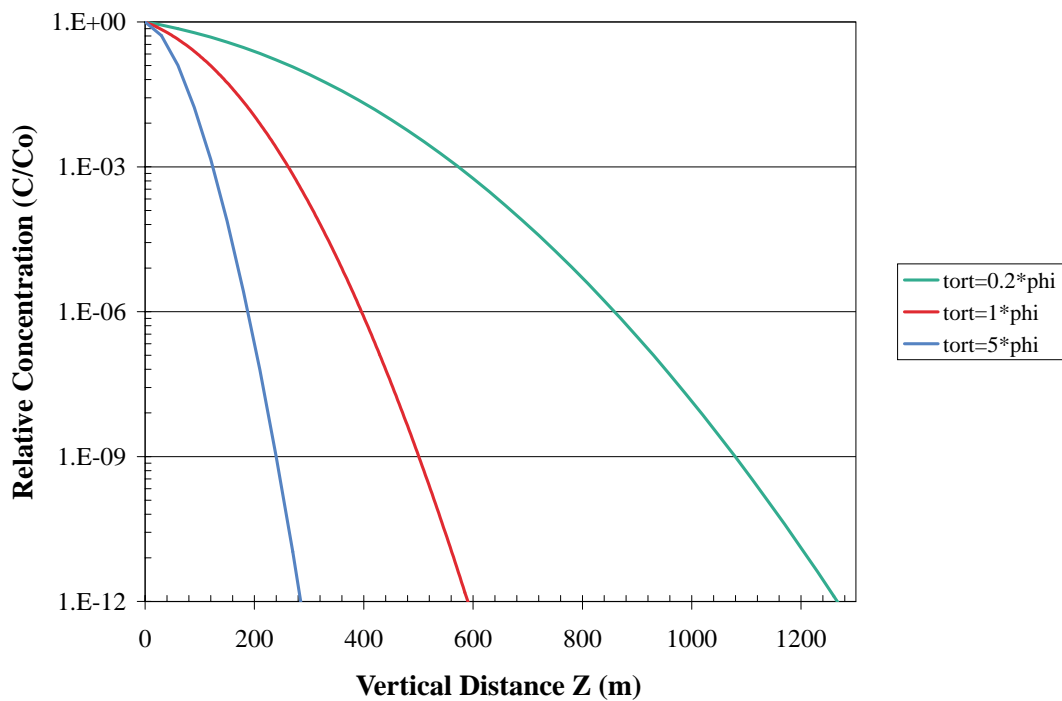
DTN: 991220140160.006

Figure II.16. Effect of Matrix Tortuosity on ^{99}Tc Concentration Profiles Along the z-axis in the Fractures at $t=1,000$ Years.



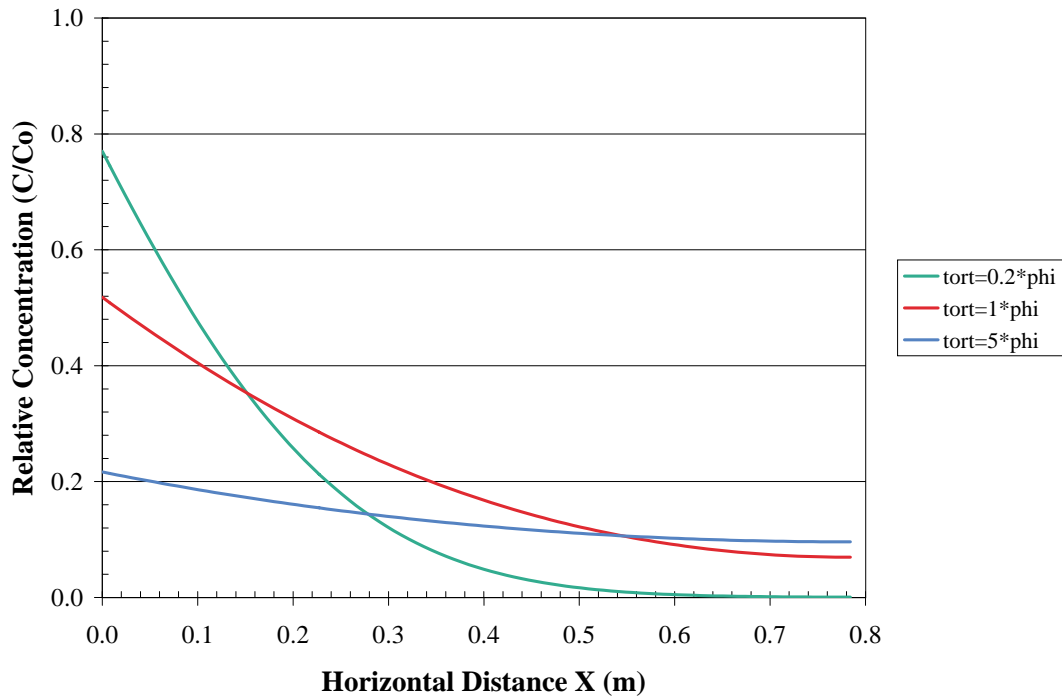
DTN: LB991220140160.006

Figure II.17. Effect of Matrix Tortuosity on ^{99}Tc Concentration Profiles Along the x-axis in the Matrix at Z=50 m and t=1,000 Years.



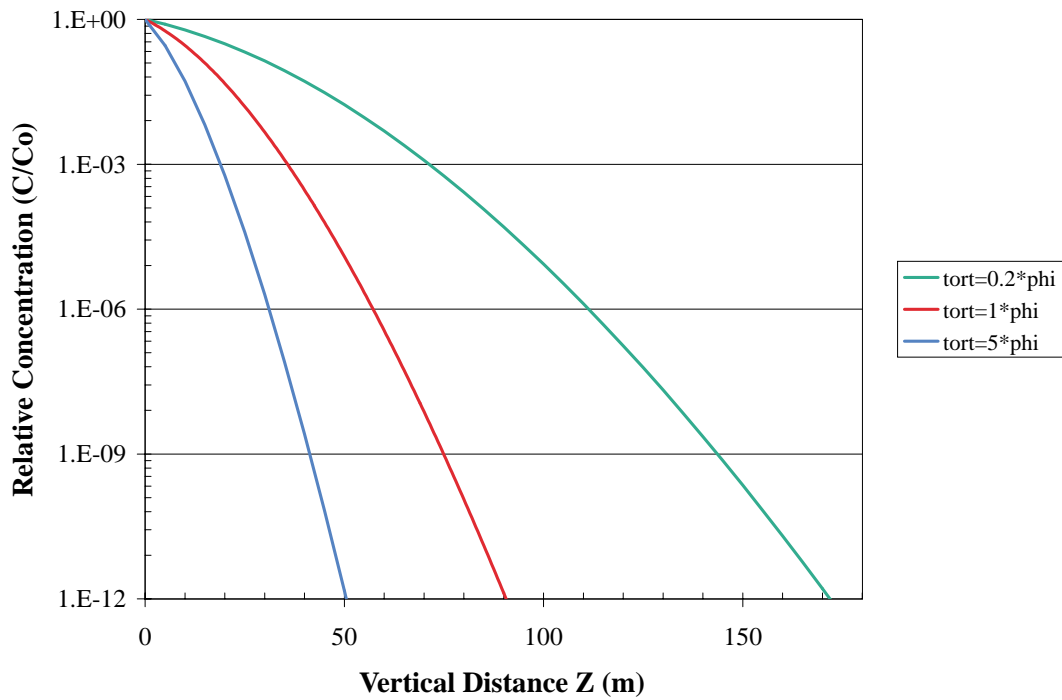
DTN: LB991220140160.006

Figure II.18. Effect of Matrix Tortuosity on ^{237}Np Concentration Profiles Along the z-axis in the Fractures at t=1,000 Years.



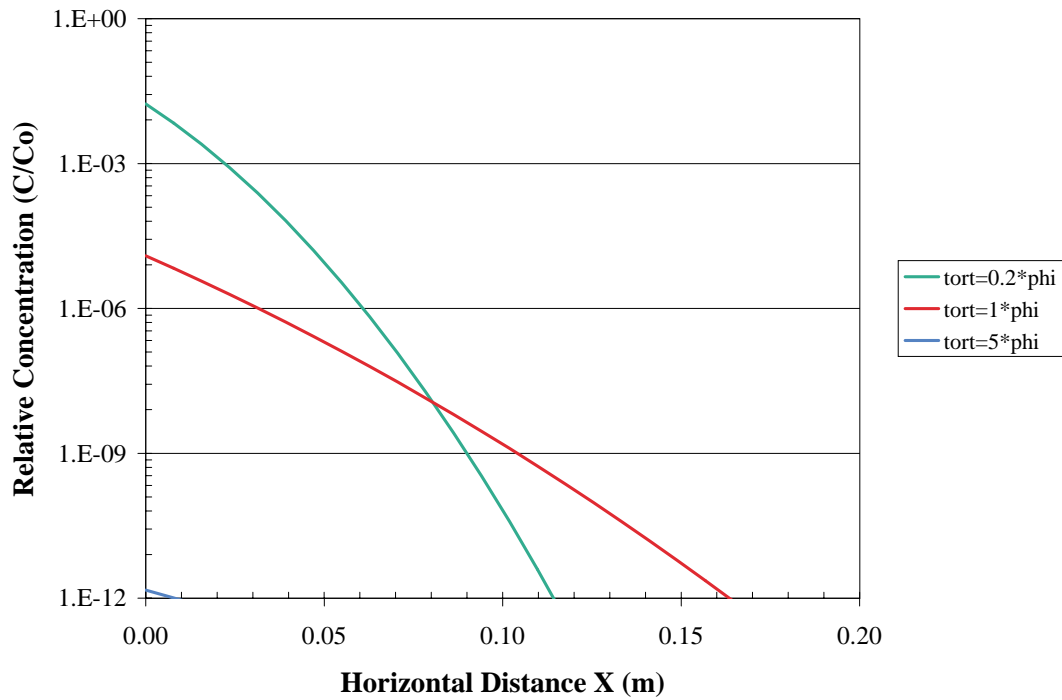
DTN: LB991220140160.006

Figure II.19. Effect of Matrix Tortuosity on ^{237}Np Concentration Profiles Along the x-axis in the Matrix at $Z=50$ m and $t=1,000$ Years



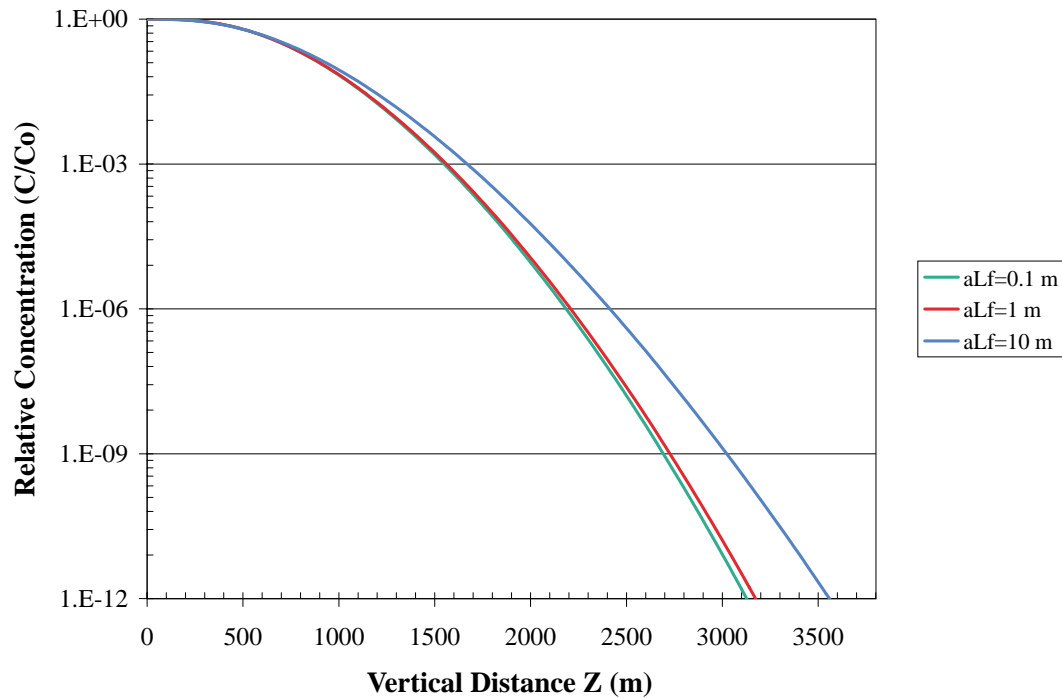
DTN: LB991220140160.006

Figure II.20. Effect of Matrix Tortuosity on ^{239}Pu Concentration Profiles Along the z-axis in the Fractures at $t=1,000$ Years



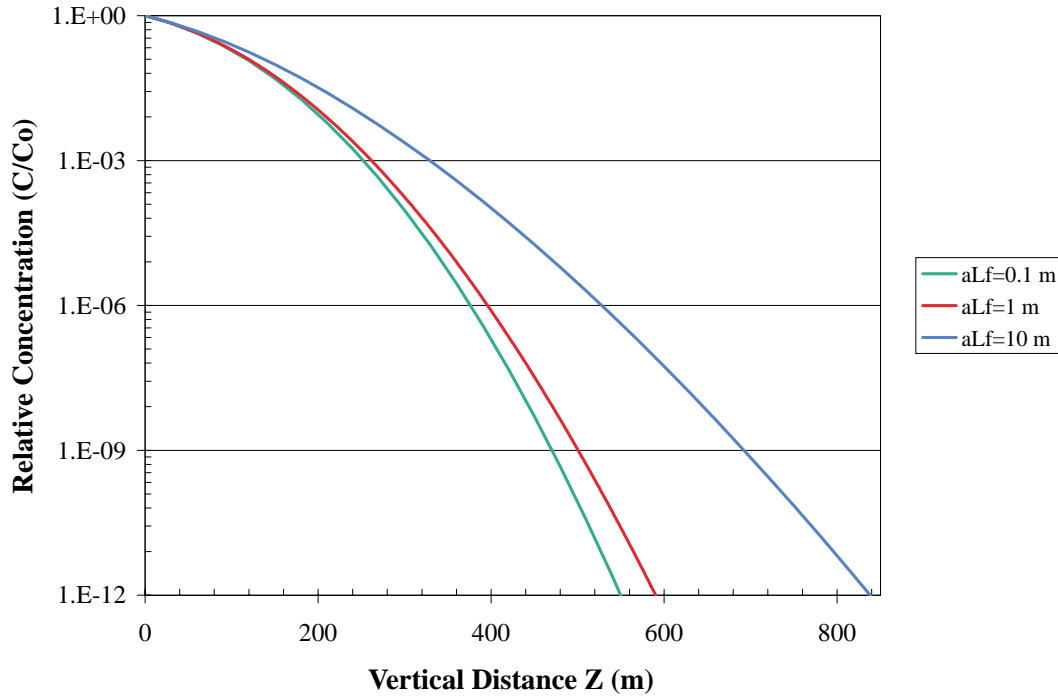
DTN: LB991220140160.006

Figure II.21. Effect of Matrix Tortuosity on ^{239}Pu Concentration Profiles Along the z-axis in the Matrix at Z=50 m and t=1,000 Years.



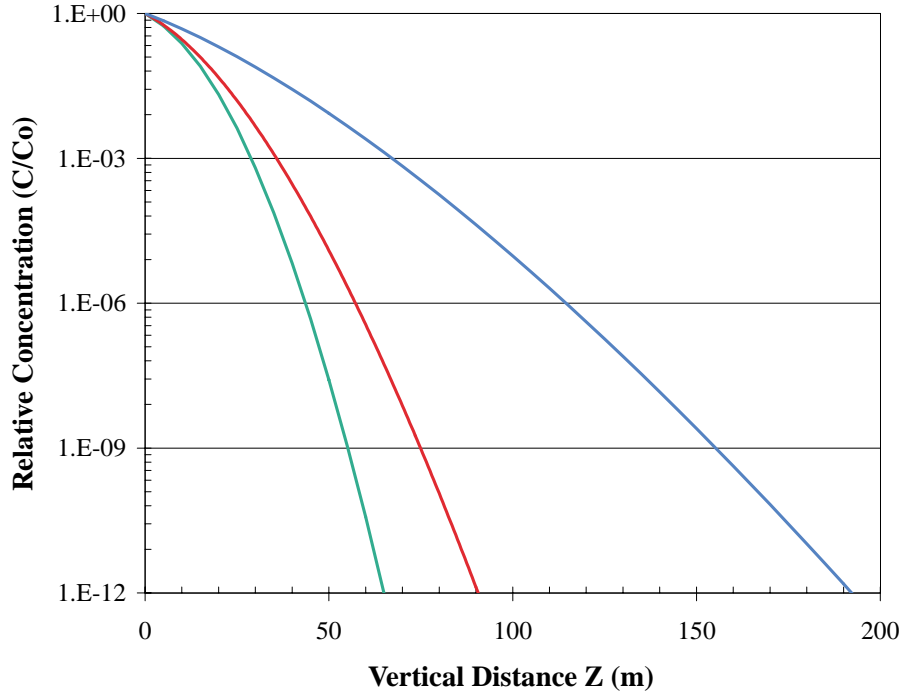
DTN: LB991220140160.006

Figure II.22. Effect of α_L on ^{99}Tc Concentration Profiles Along the z-axis in the Fractures at t=1,000 Years.



DTN: LB991220140160.006

Figure II.23. Effect of α_L on ^{237}Np Concentration Profiles Along the z-axis in the Fractures at $t=1,000$ Years.



DTN: LB991220140160.006

Figure II.24. Effect of α_L on ^{239}Pu Concentration Profiles Along the z-axis in the Fractures at $t=1,000$ Years.

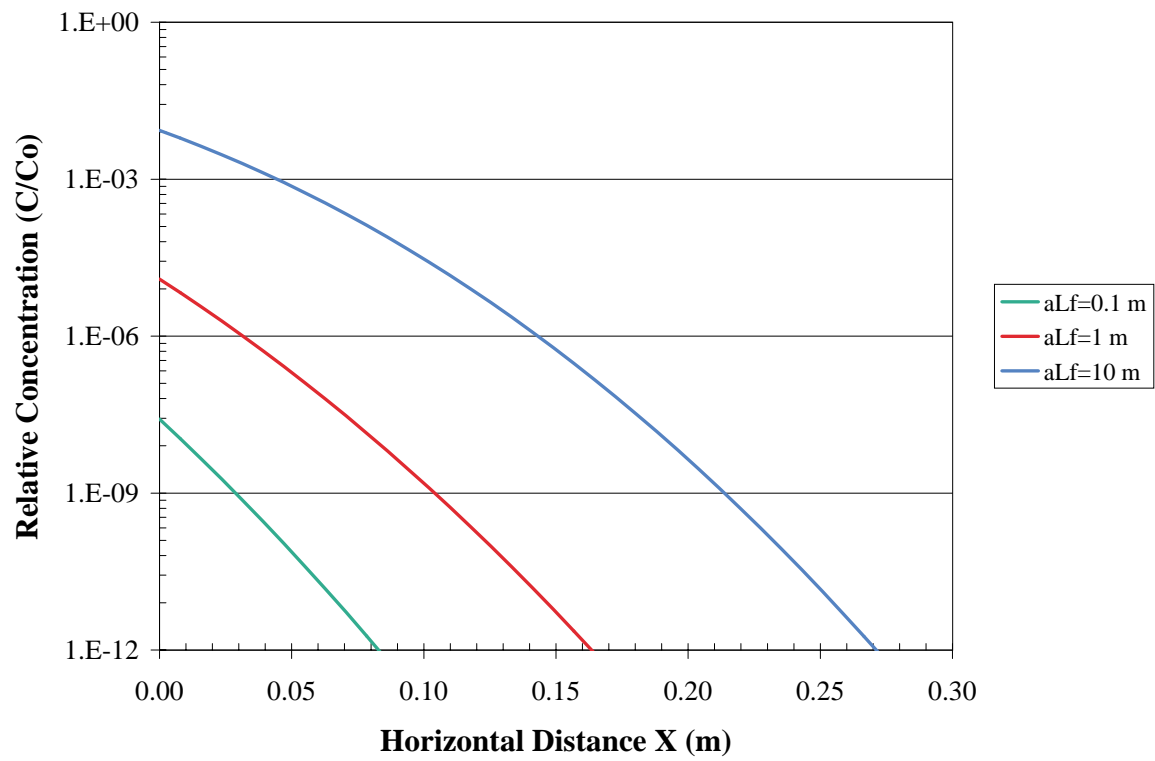
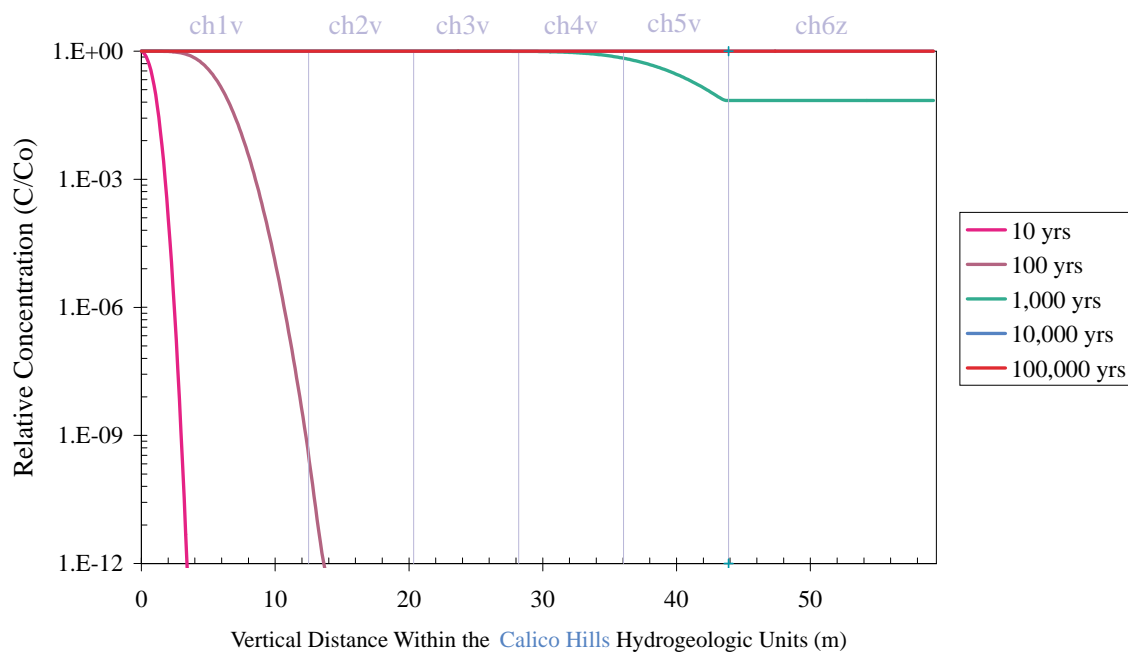


Figure II.24. Effect of α_L on ^{239}Pu Concentration Profiles Along the X-axis in the Matrix at $z=50$ m and $t=1,000$ Years.

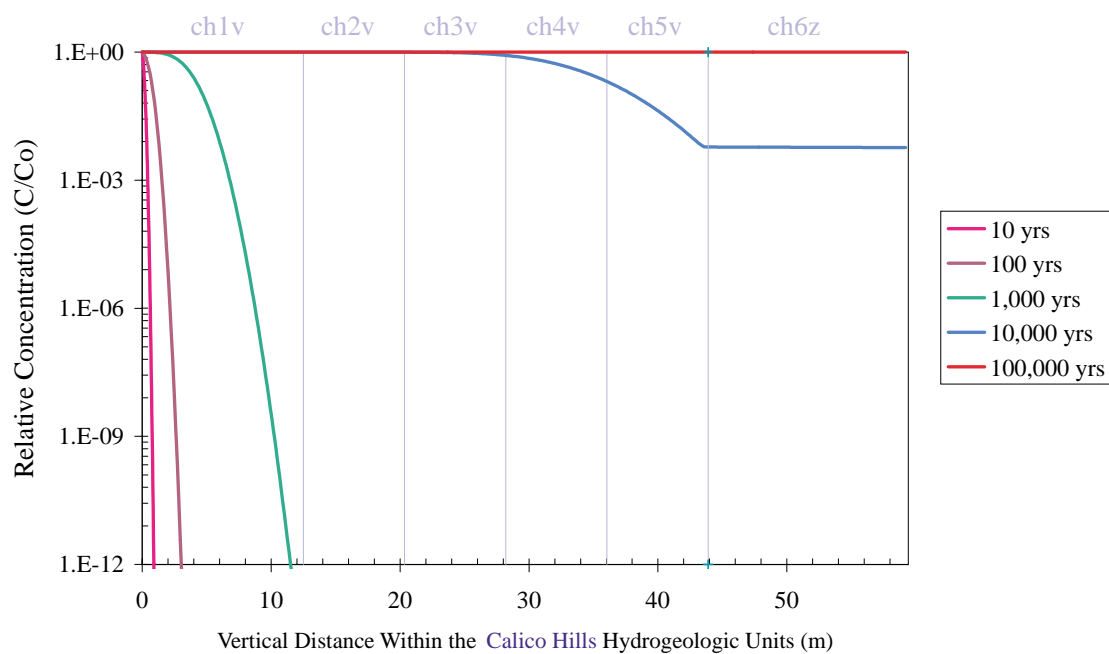
ATTACHMENT III
FIGURES FROM THE STUDY OF TRANSPORT IN THE CH_n
HYDROGEOLOGIC UNIT

FIGURES**Page**

III.1	⁹⁹ Tc Concentration Profile in CHn in Cross Section 1. Results for 10,000 Years and 100,000 Years Overlap.....	III-3
III.2	²³⁷ Np Concentration Profile CHn in Cross Section 1	III-3
III.3	²³⁹ Pu Concencentration Profile in CHn in Cross Section 1.....	III-4
III.4	⁹⁹ Tc Concentration Profile in CHn in Cross Section 2. Results for 10,000 Years and 100,000 Years Overlap	III-4
III.5	²³⁷ Np Concentration Profile in CHn in Cross Section 2	III-5
III.6	²³⁹ Pu Concentration Profile in CHn in Cross Section 2. Results for 10 Years and 100 Years Overlap	III-5
III.7	⁹⁹ Tc Concentration Profile in CHn in Cross Section 3. Results for 10,000 Years and 100,000 Years Overlap.....	III-6
III.8	²³⁷ Np Concentration Profile in CHn in Cross Section 3. Results for 10,000 Years and 100,000 Years Overlap	III-6
III.9	²³⁹ Pu Concentration Profile in CHn in Cross Section 3	III-7

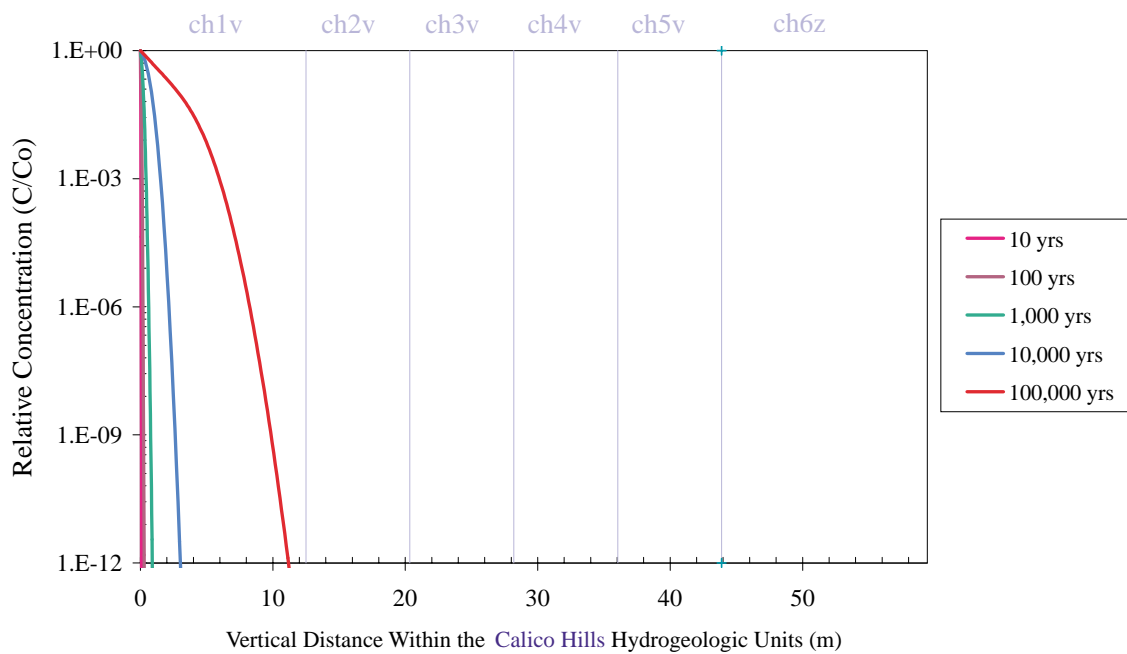


DTN: LB991220140160.007

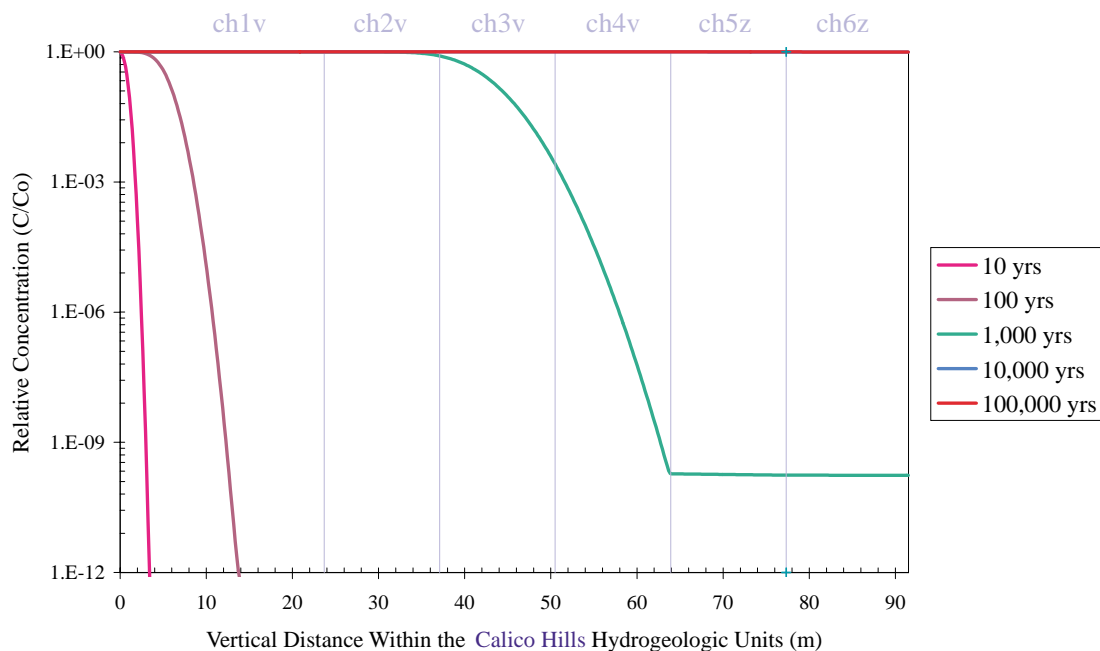
Figure III.1. ^{99}Tc Concentration Profile in CHn in Cross Section 1. Results for 10,000 years and 100,000 years overlap.

DTN: LB991220140160.007

Figure III.2. ^{237}Np Concentration Profile in CHn in Cross Section 1.

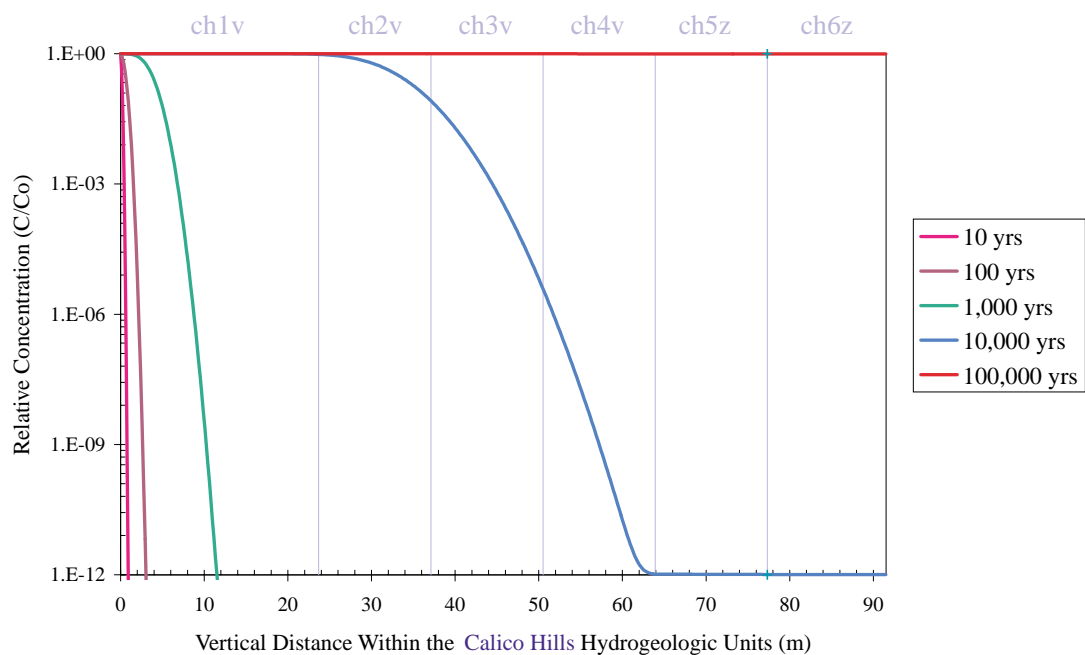


DTN: LB991220140160.007

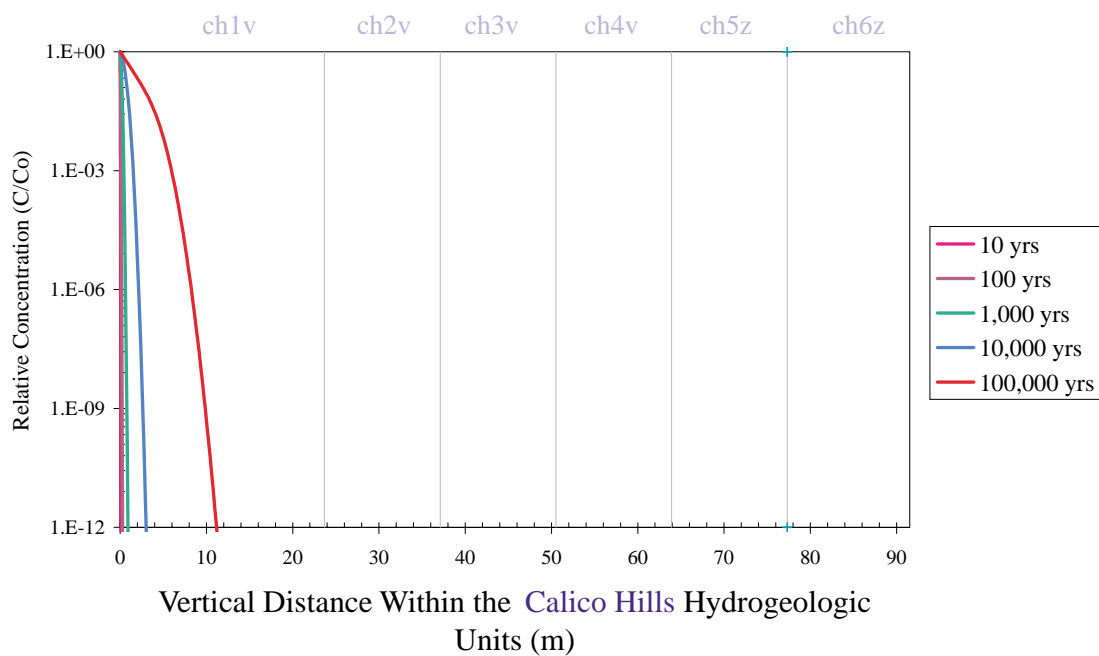
Figure III.3 ^{239}Pu Concentration Profile CHn in Cross Section 1.

DTN: LB991220140160.007

Figure III.4. ^{99}Tc Concentration Profile in CHn in Cross Section 2. Results for 10,000 years and 100,000 years overlap.

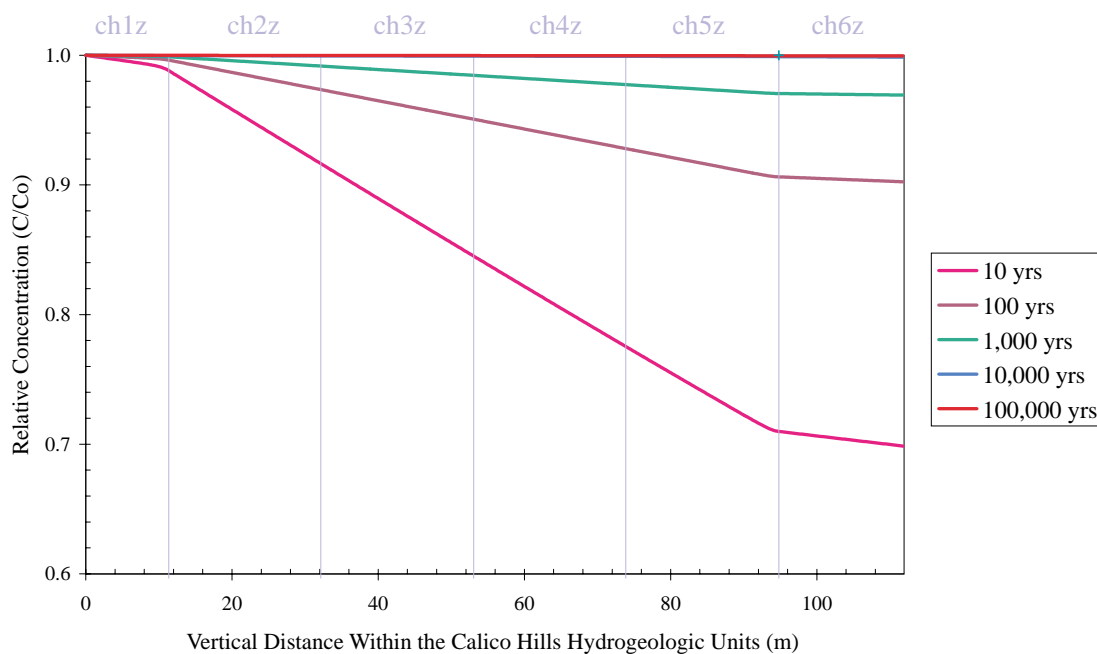


DTN: LB991220140160.007

Figure III.5. ^{237}Np Concentration Profile CHn in Cross Section 2.

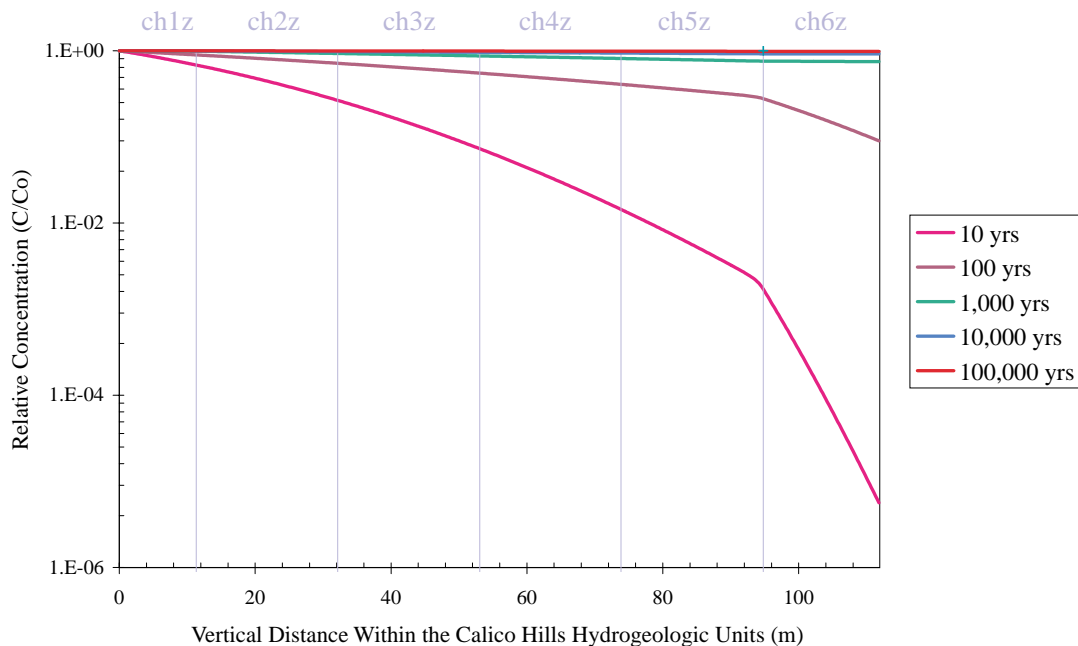
DTN: LB991220140160.007

Figure III.6. ^{239}Pu Concentration Profile in CHn in Cross Section 2. Results for 10 years and 100 years overlap.



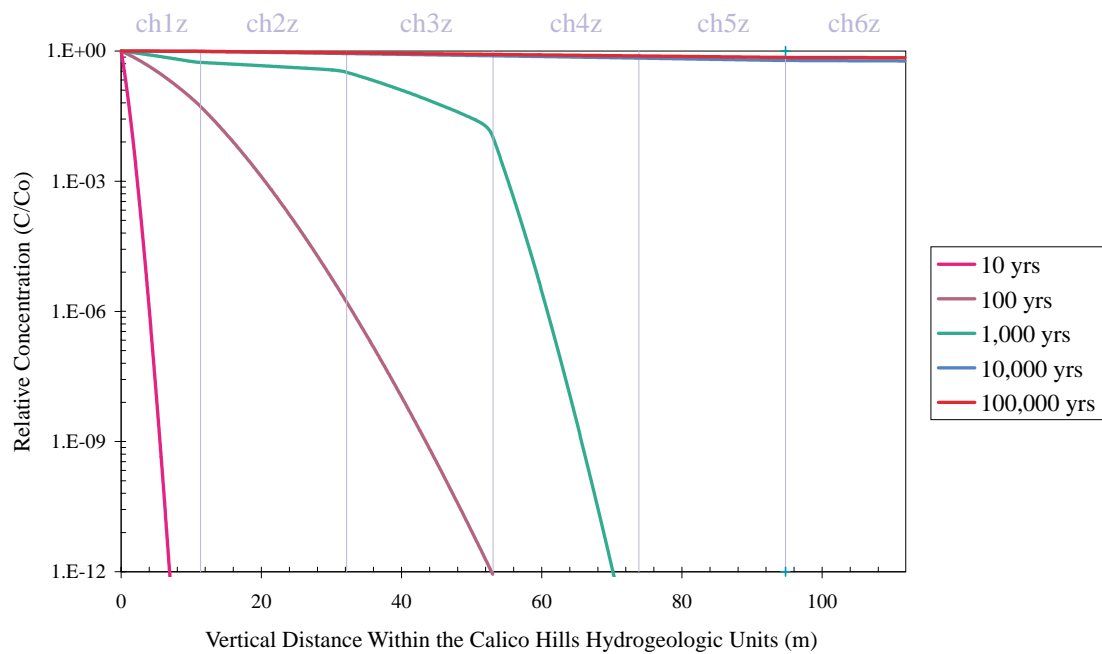
DTN: LB991220140160.007

Figure III.7. ^{99}Tc Concentration Profile in CHn in Cross Section 3. Results for 10,000 years and 100,000 years overlap.



DTN: LB991220140160.007

Figure III.8. ^{237}Np Concentration Profile in CHn in Cross Section 3. Results for 10,000 years and 100,000 years overlap.



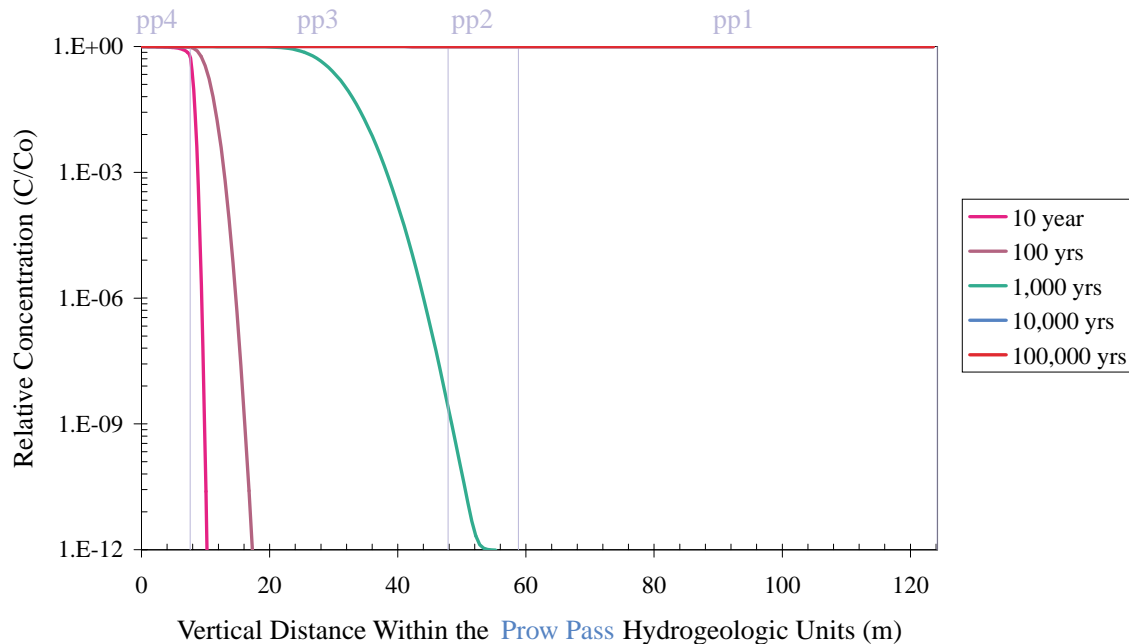
DTN: LB991220140160.007

Figure III.9. ^{239}Pu Concentration Profile in CHn in Cross Section 3.

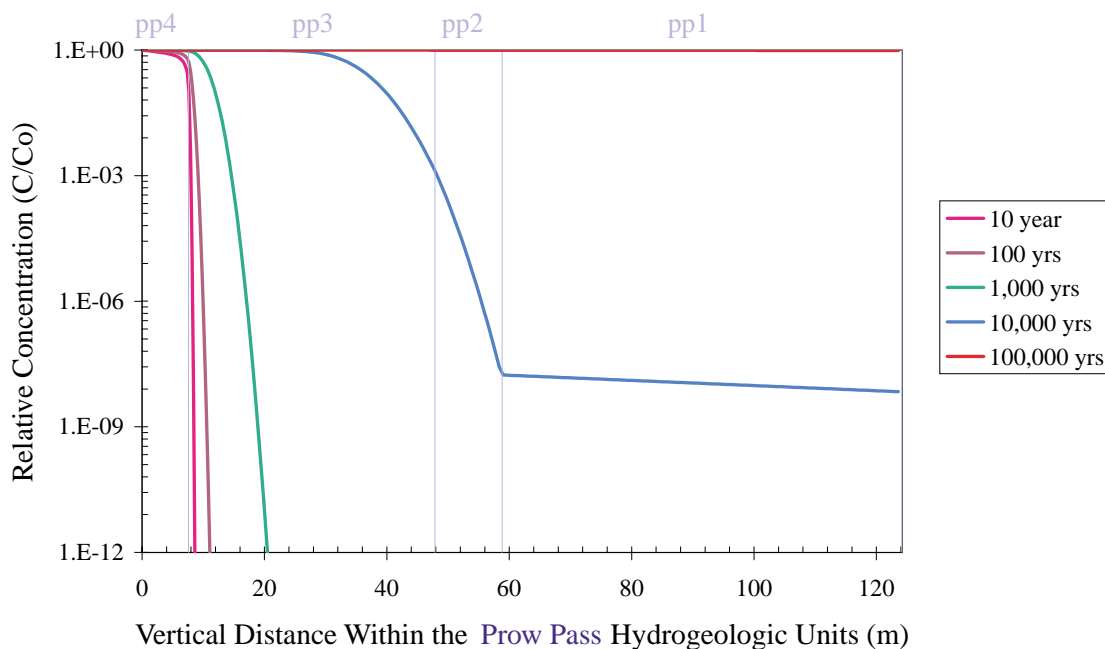
ATTACHMENT IV
FIGURES FROM THE STUDY OF TRANSPORT IN THE PP
HYDROGEOLOGIC UNIT

FIGURES**Page**

IV.1	^{99}Tc Concentration Profile in PP in Cross Section 1. Results for 10,000 years and 100,000 years overlap.	IV-3
IV.2	^{237}Np Concentration Profile in PP in Cross Section 1.	IV-3
IV.3	^{239}Pu Concentration Profile in PP in Cross Section 1.	IV-4
IV.4	^{99}Tc Concentration Profile in PP in Cross Section 2. Results for 10,000 years and 100,000 years overlap.	IV-4
IV.5	^{237}Np Concentration Profile in PP in Cross Section 2.....	IV-5
IV.6	^{239}Pu Concentration Profile in PP in Cross Section 2.	IV-5
IV.7	^{99}Tc Concentration Profile in PP in Cross Section 3. Results for 10,000 years and 100,000 years overlap.	IV-6
IV.8	^{237}Np Concentration Profile in PP in Cross Section 3.....	IV-6
IV.9	^{239}Pu Concentration Profile in PP in Cross Section 3.	IV-7

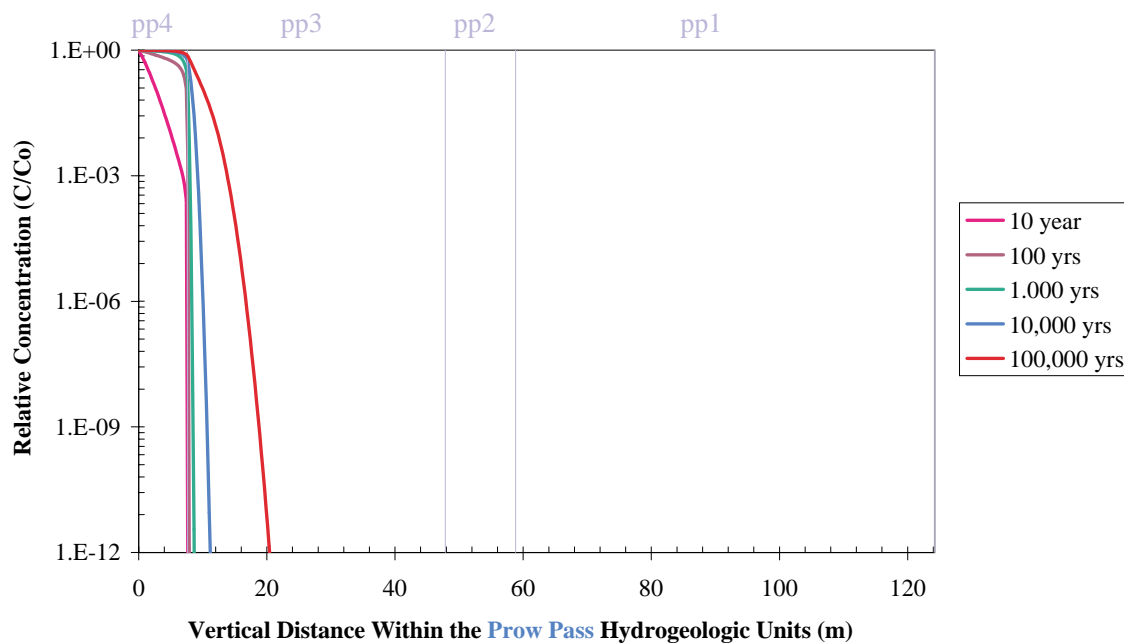


DTN: LB991220140160.008

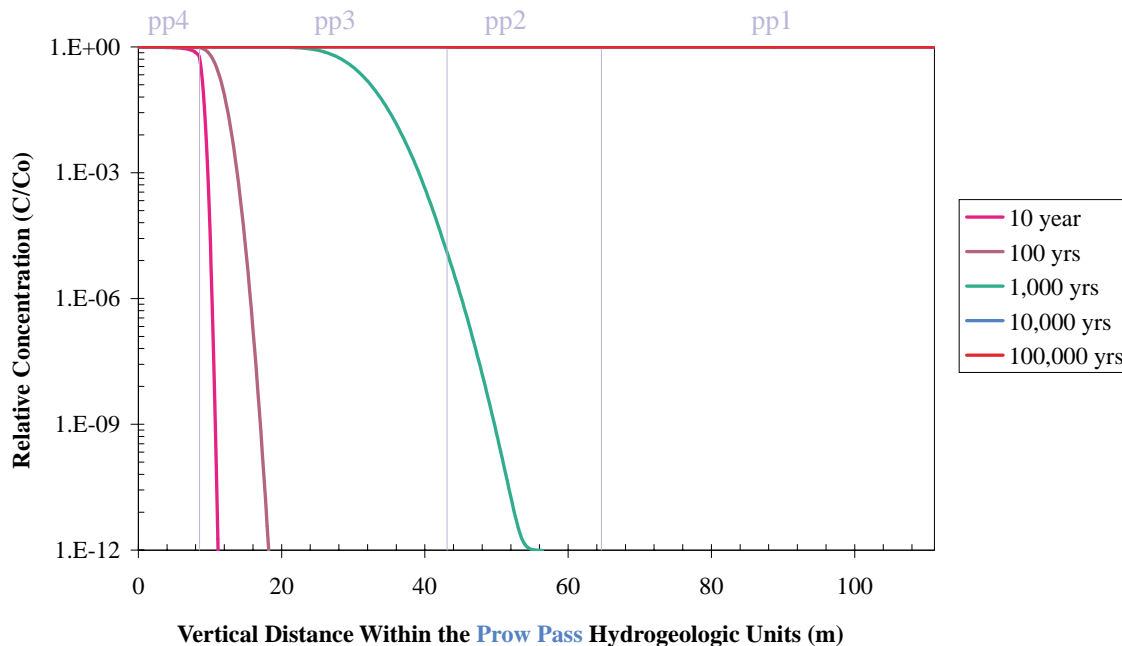
Figure IV.1. ^{99}Tc Concentration Profile in PP in Cross Section 1. Results for 10,000 years and 100,000 years overlap.

DTN: LB991220140160.008

Figure IV.2. ^{237}Np Concentration Profile in PP in Cross Section 1.

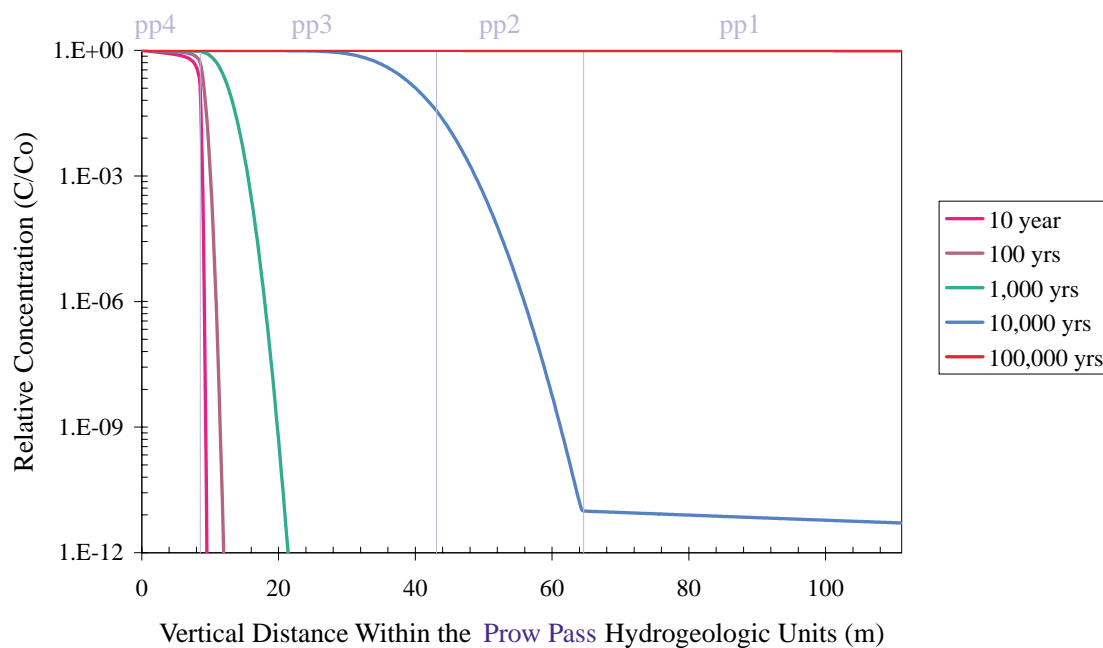


DTN: LB991220140160.008

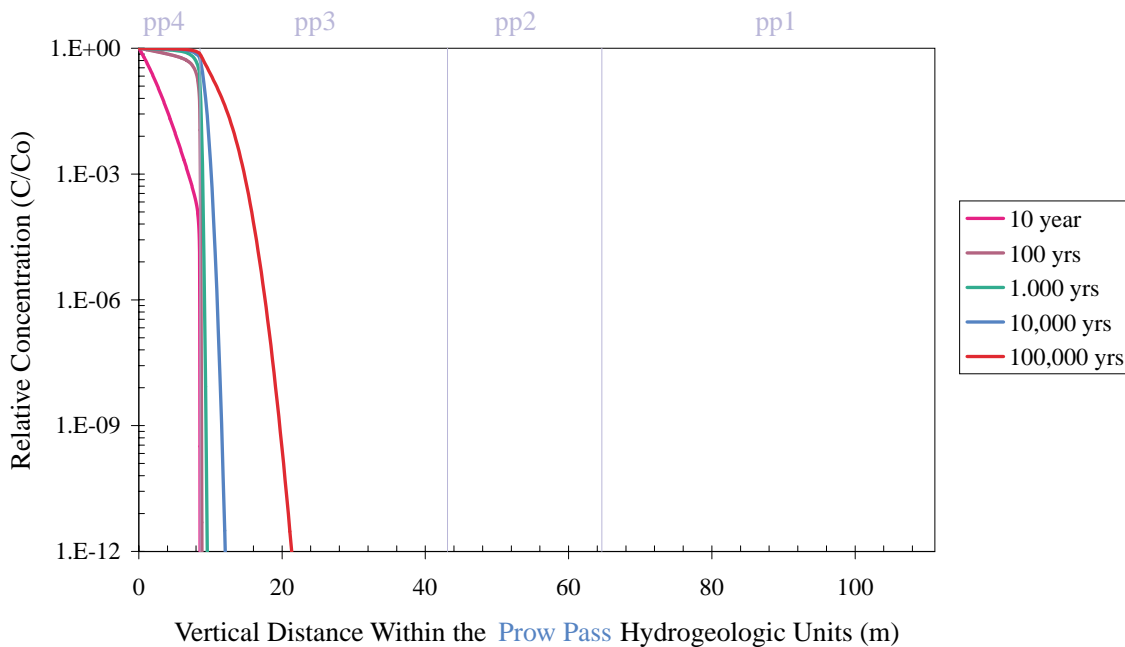
Figure IV.3. ^{239}Pu Concentration Profile in PP in Cross Section 1.

DTN: LB991220140160.008

Figure IV.4. ^{99}Tc Concentration Profile in PP in Cross Section 2. Results for 10,000 years and 100,000 years overlap.

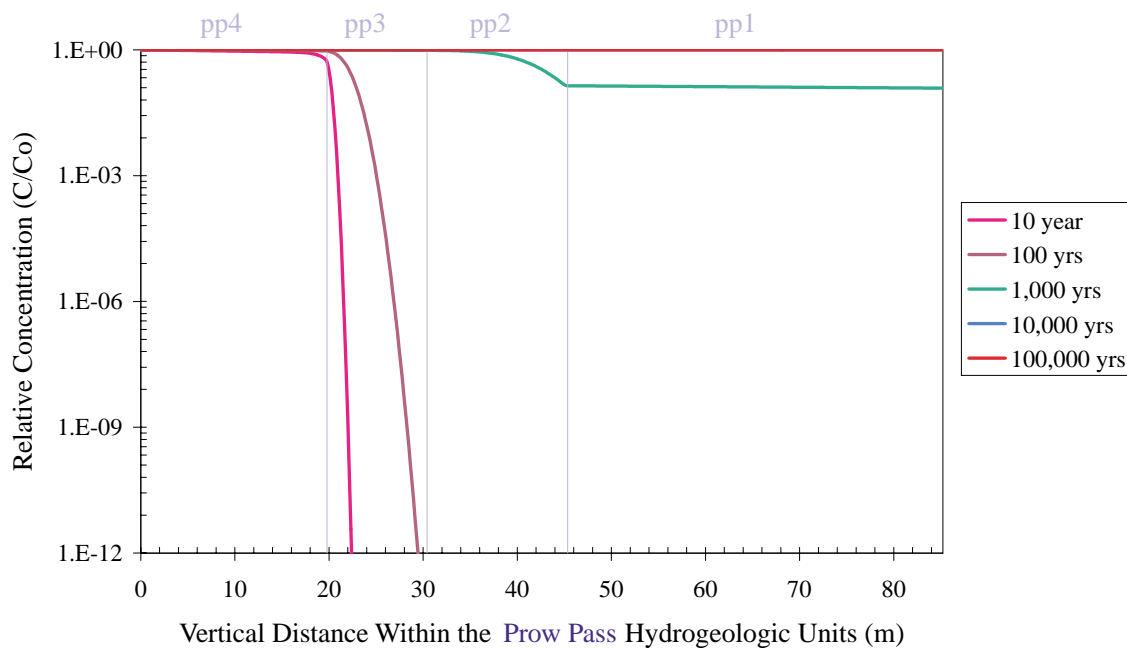


DTN: LB991220140160.008

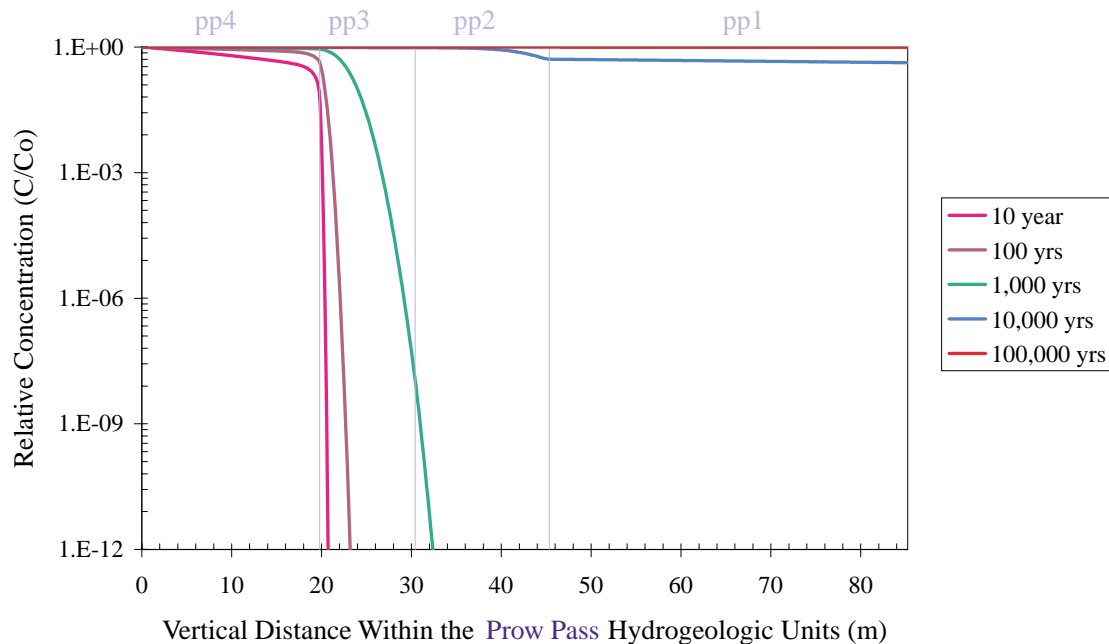
Figure IV.5. ^{237}Np Concentration Profile in PP in Cross Section 2.

DTN: LB991220140160.008

Figure IV.6. ^{239}Pu Concentration Profile in PP in Cross Section 2.

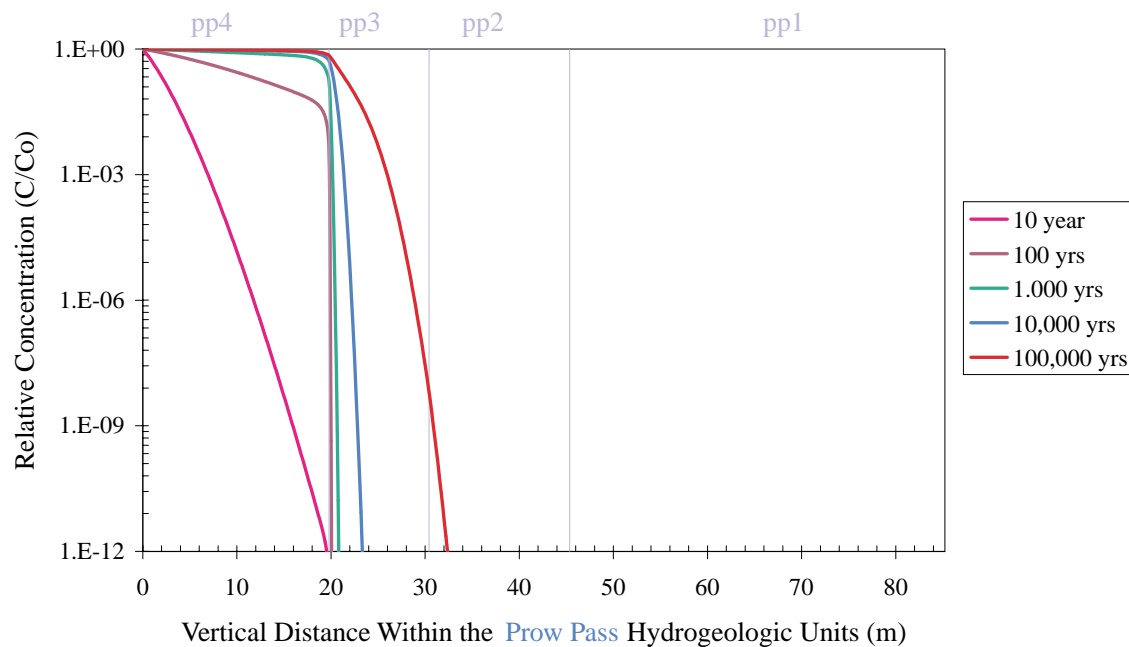


DTN: LB991220140160.008

Figure IV.7. ^{99}Tc Concentration Profile in PP in Cross Section 3. Results for 10,000 years and 100,000 years overlap.

DTN: LB991220140160.008

Figure IV.8. ^{237}Np Concentration Profile in PP in Cross Section 3.



DTN: LB991220140160.008

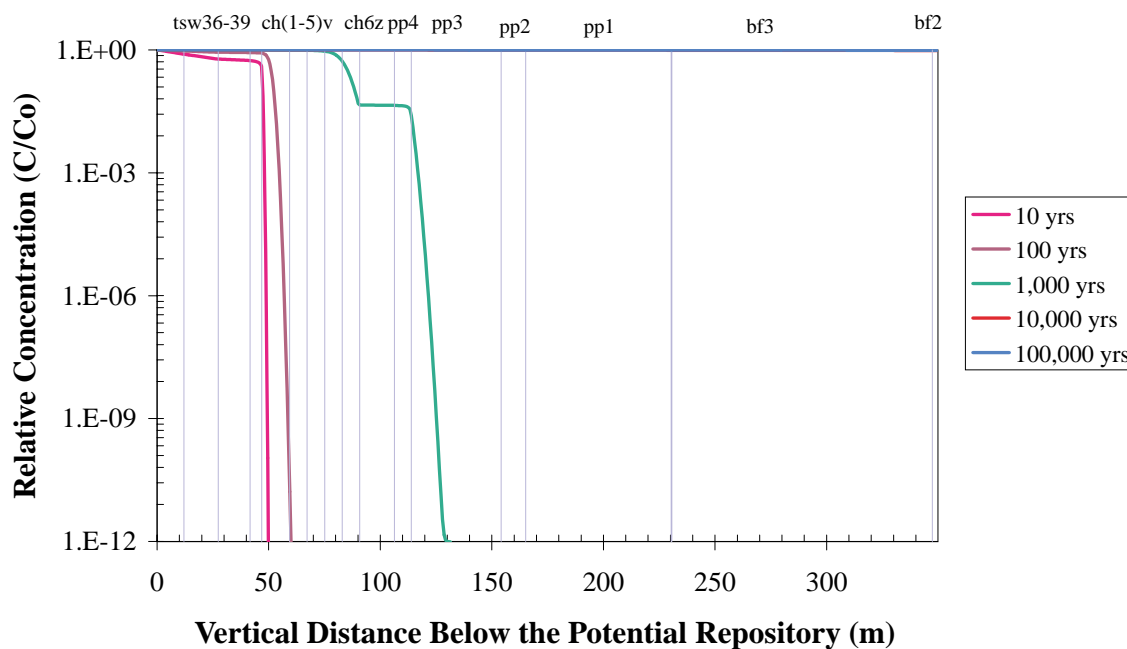
Figure IV.9. ^{239}Pu Concentration Profile in PP in Cross Section 3.

ATTACHMENT V
FIGURES FROM THE STUDY OF TRANSPORT UNDERNEATH THE REPOSITORY

FIGURES

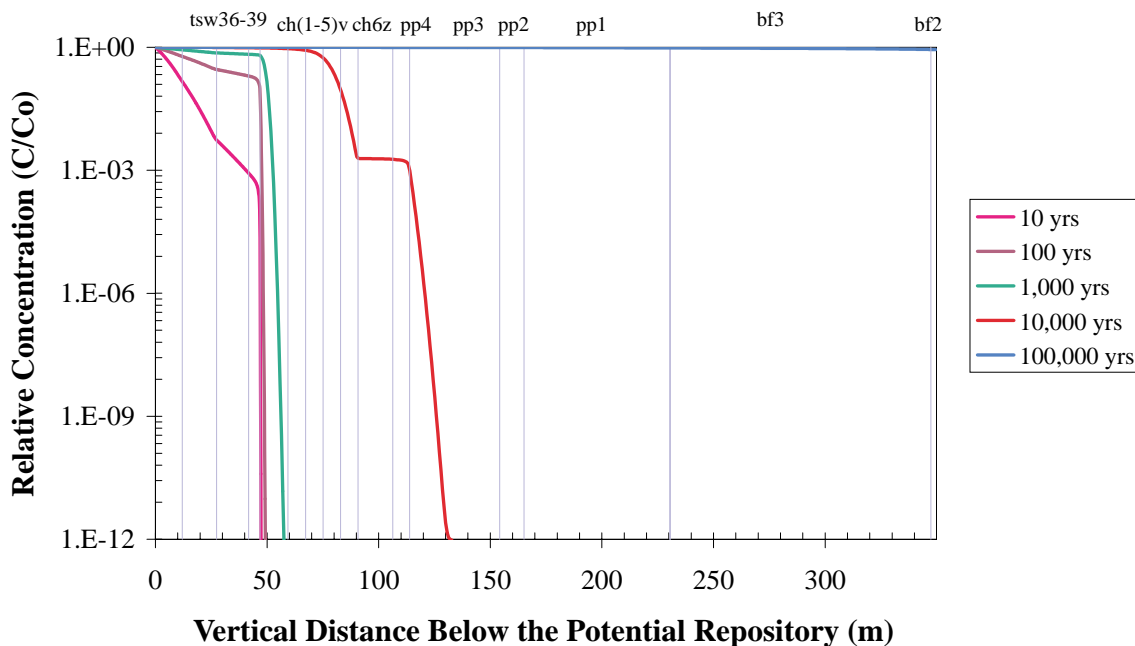
		Page
V.1.	⁹⁹ Tc Concentration Profile Under the Potential Repository in Cross Section 1 (Mean Present-Day Infiltration, No Perched Water). Results for 10,000 years and 100,000 years overlap.	V-4
V.2.	²³⁷ Np Concentration Profile Under the Potential Repository in Cross Section 1 (Mean Present-Day Infiltration, No Perched Water).	V-4
V.3.	²³⁹ Pu Concentration Profile Under the Potential Repository in Cross Section 1 (Mean Present-Day Infiltration, No Perched Water).	V-5
V.4.	⁹⁹ Tc Concentration Profile Under the Potential Repository in Cross Section 1 (High Glacial Infiltration, No Perched Water). Results for 10,000 years and 100,000 years overlap.	V-5
V.5.	²³⁷ Np Concentration Profile Under the Potential Repository in Cross Section 1 (High Glacial Infiltration, No Perched Water).	V-6
V.6.	²³⁹ Pu Concentration Profile Under the Potential Repository in Cross Section 1 (High Glacial Infiltration, No Perched Water).	V-6
V.7.	⁹⁹ Tc Concentration Profile Under the Potential Repository in Cross Section 2 (Mean Present-Day Infiltration, No Perched Water). Results for 10,000 years and 100,000 years overlap.	V-7
V.8.	²³⁷ Np Concentration Profile Under the Potential Repository in Cross Section 2 (Mean Present-Day Infiltration, No Perched Water).	V-7
V.9.	²³⁹ Pu Concentration Profile Under the Potential Repository in Cross Section 2 (Mean Present-Day Infiltration, No Perched Water).	V-8
V.10.	⁹⁹ Tc Concentration Profile Under the Potential Repository in Cross Section 2 (High Glacial Infiltration, No Perched Water). Results for 1,000 years, 10,000 years and 100,000 years overlap.	V-8
V.11.	²³⁷ Np Concentration Profile Under the Potential Repository in Cross Section 2 (High Glacial Infiltration, No Perched Water). Results for 10,000 years and 100,000 years almost overlap.	V-9

V.12.	^{239}Pu Concentration Profile Under the Potential Repository in Cross Section 2 (High Glacial Infiltration, No Perched Water).	V-9
V.13.	^{99}Tc Concentration Profile Under the Potential Repository in Cross Section 3 (Mean Present-Day Infiltration, No Perched Water). Results for 10,000 years and 100,000 years overlap.	V-10
V.14.	^{237}Np Concentration Profile Under the Potential Repository in Cross Section 3 (Mean Present-Day Infiltration, No Perched Water).	V-10
V.15.	^{239}Pu Concentration Profile Under the Potential Repository in Cross Section 3 (Mean Present-Day Infiltration, No Perched Water).	V-11
V.16.	^{99}Tc Concentration Profile Under the Potential Repository in Cross Section 3 (High Glacial Infiltration, No Perched Water). Results for 1,000 years, 10,000 and 100,000 years overlap.	V-11
V.17.	^{237}Np Concentration Profile Under the Potential Repository in Cross Section 3 (High Glacial Infiltration, No Perched Water). Results for 10,000 and 100,000 years overlap.	V-12
V.18.	^{239}Pu Concentration Profile Under the Potential Repository in Cross Section 3 (High Glacial Infiltration, No Perched Water).	V-12
V.19.	^{99}Tc Concentration Profile Under the Potential Repository in Cross Section 3 for a Perched Water Regime (Mean Present-Day Infiltration). Results for 10,000 years and 100,000 years overlap.	V-13
V.20.	^{237}Np Concentration Profile Under the Potential Repository in Cross Section 3 for a Perched Water Regime (Mean Present-Day Infiltration).	V-13
V.21.	^{239}Pu Concentration Profile Under the Potential Repository in Cross Section 3 for a Perched Water Regime (Mean Present-Day Infiltration).	V-14



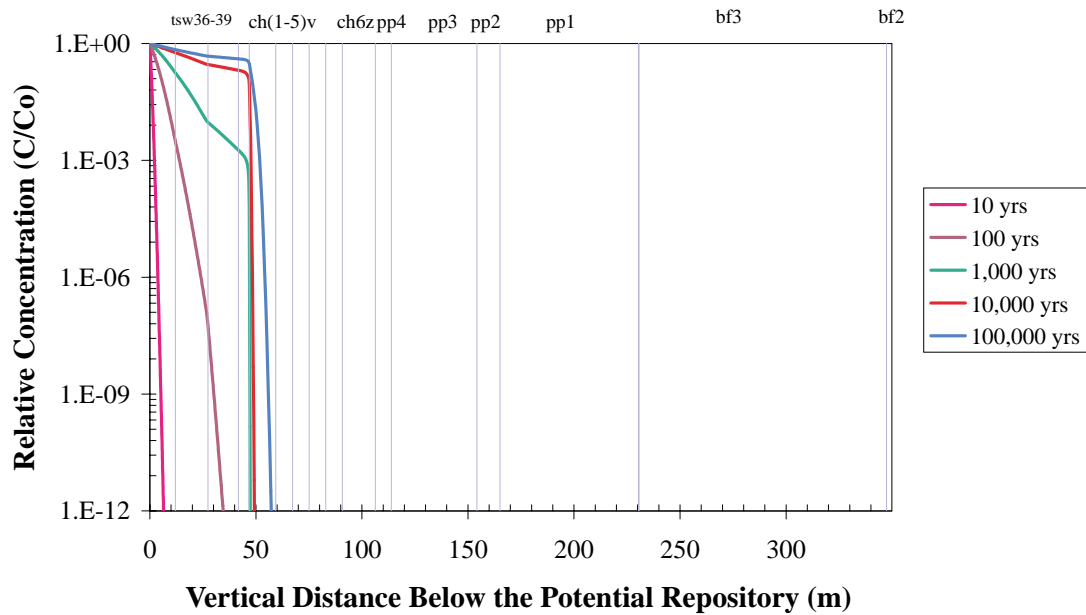
DTN: LB991220140160.009

Figure V.1. ^{99}Tc Concentration Profile Under the Potential Repository in Cross Section 1 (Mean Present-Day Infiltration, No Perched Water). Results for 10,000 years and 100,000 years overlap.



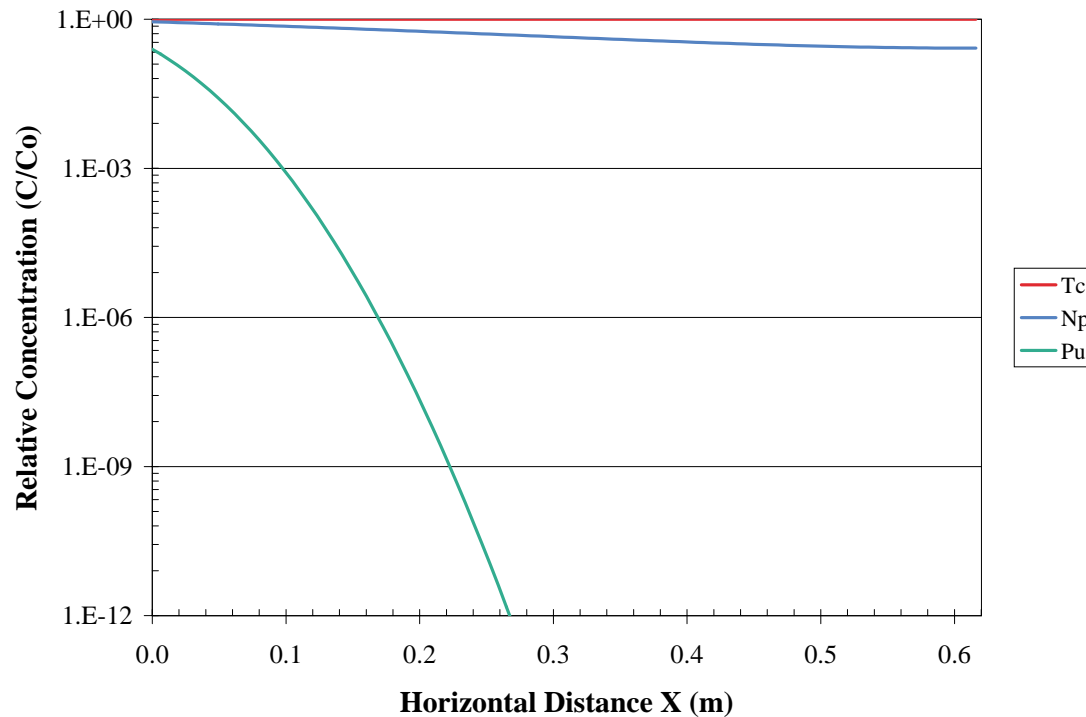
DTN: LB991220140160.009

Figure V.2. ^{237}Np Concentration Profile Under the Potential Repository in Cross Section 1 (Mean Present-Day Infiltration, No Perched Water).



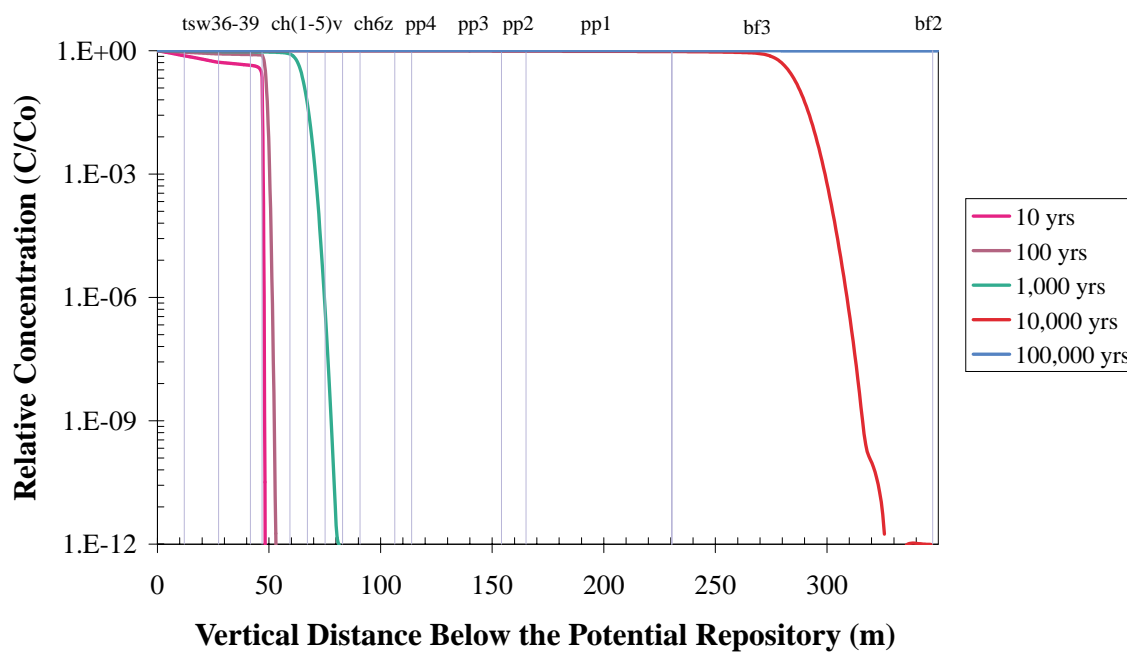
DTN: LB991220140160.009

Figure V.3. ^{239}Pu Concentration Profile Under the Potential Repository in Cross Section 1 (Mean Present-Day Infiltration, No Perched Water).



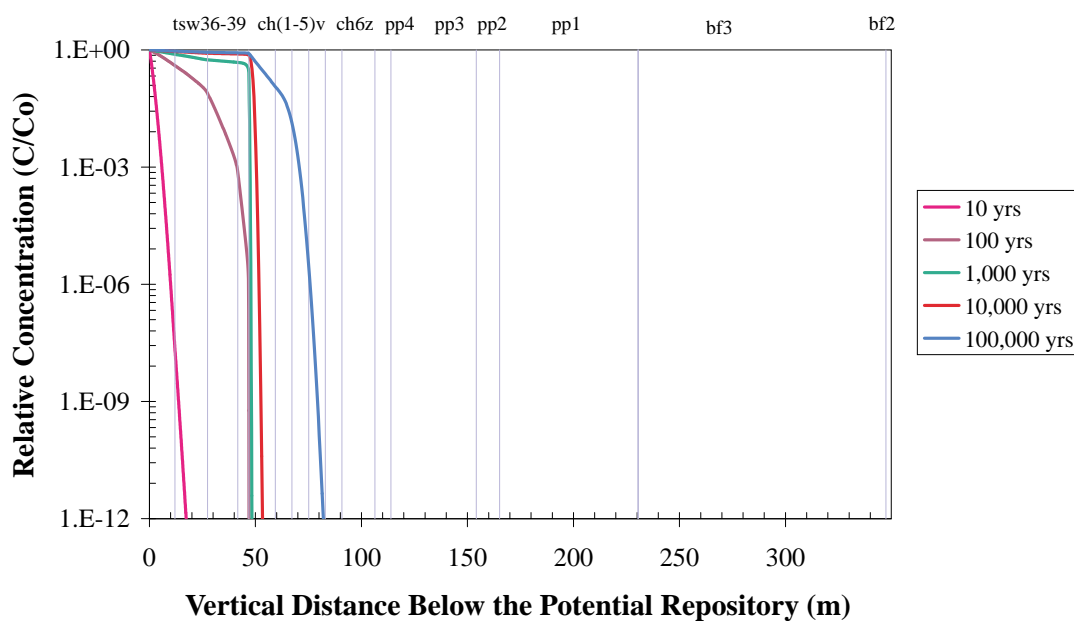
DTN: LB991220140160.009

Figure V.4. ^{99}Tc Concentration Profile Under the Potential Repository in Cross Section 1 (High Glacial Infiltration, No Perched Water). Results for 10,000 years and 100,000 years overlap.



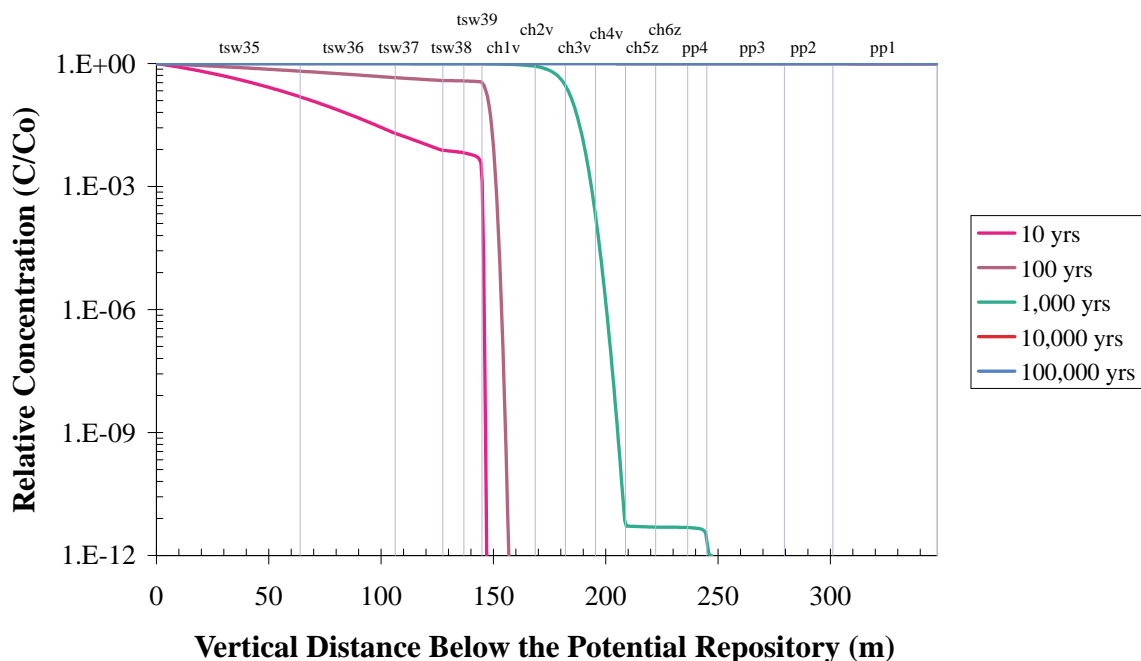
DTN: LB991220140160.009

Figure V.5. ^{237}Np Concentration Profile Under the Potential Repository in Cross Section 1 (High Glacial Infiltration, No Perched Water).



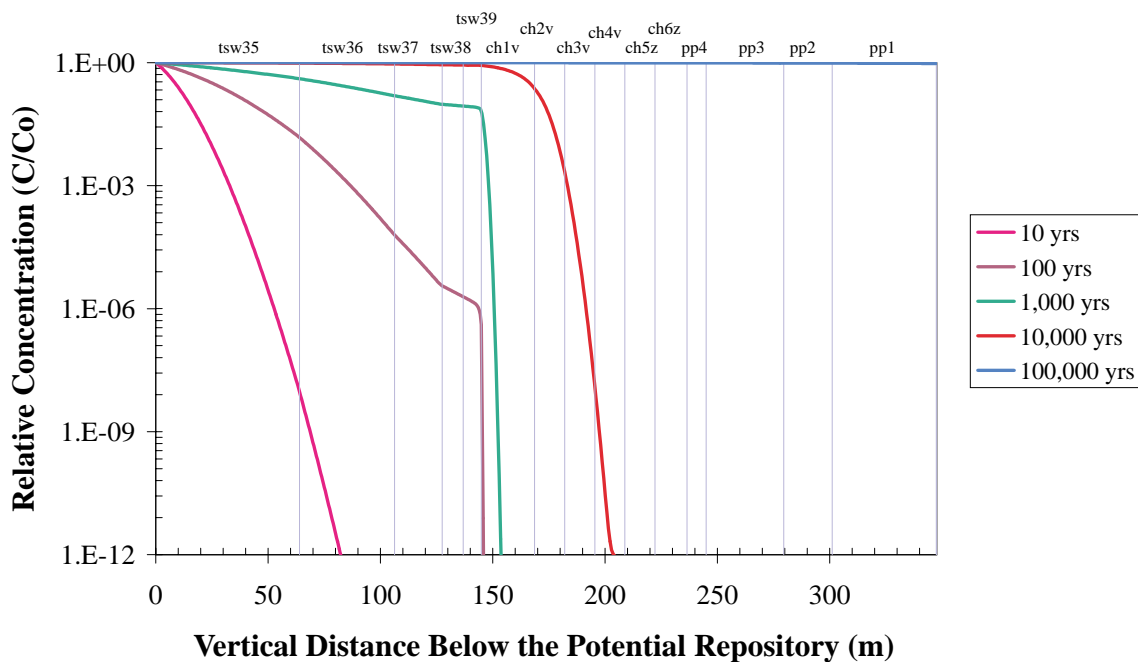
DTN: LB991220140160.009

Figure V.6. ^{239}Pu Concentration Profile Under the Potential Repository in Cross Section 1 (High Glacial Infiltration, No Perched Water).



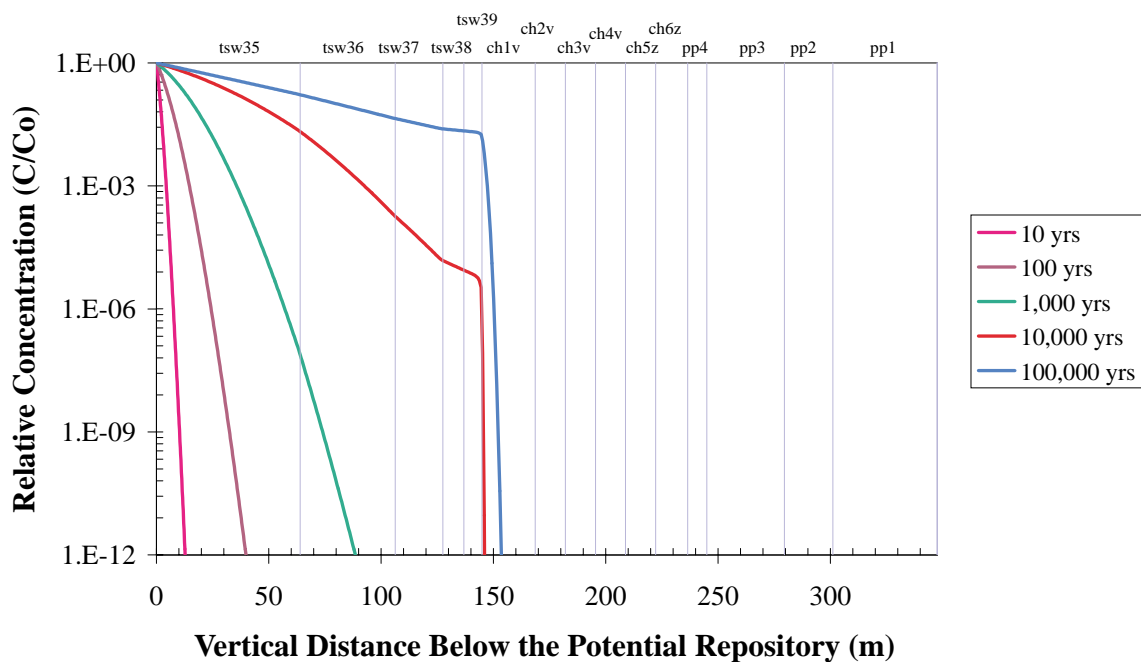
DTN: LB991220140160.009

Figure V.7. ^{99}Tc Concentration Profile Under the Potential Repository in Cross Section 2 (Mean Present-Day Infiltration, No Perched Water). Results for 10,000 years and 100,000 years overlap.



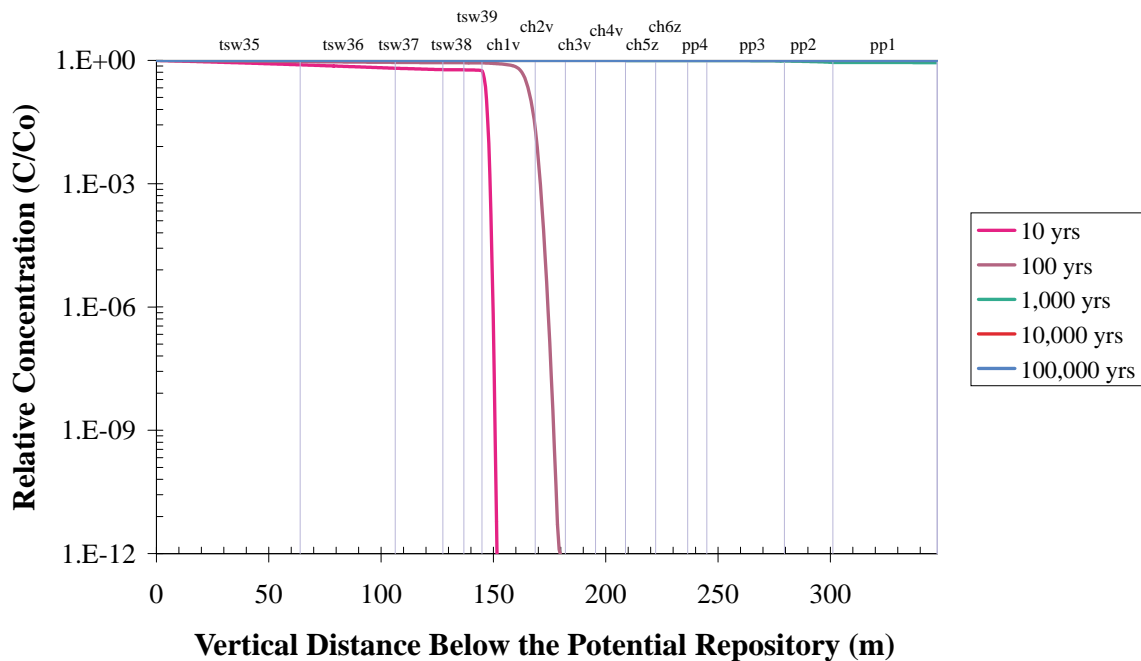
DTN: LB991220140160.009

Figure V.8. ^{237}Np Concentration Profile Under the Potential Repository in Cross Section 2 (Mean Present-Day Infiltration, No Perched Water).



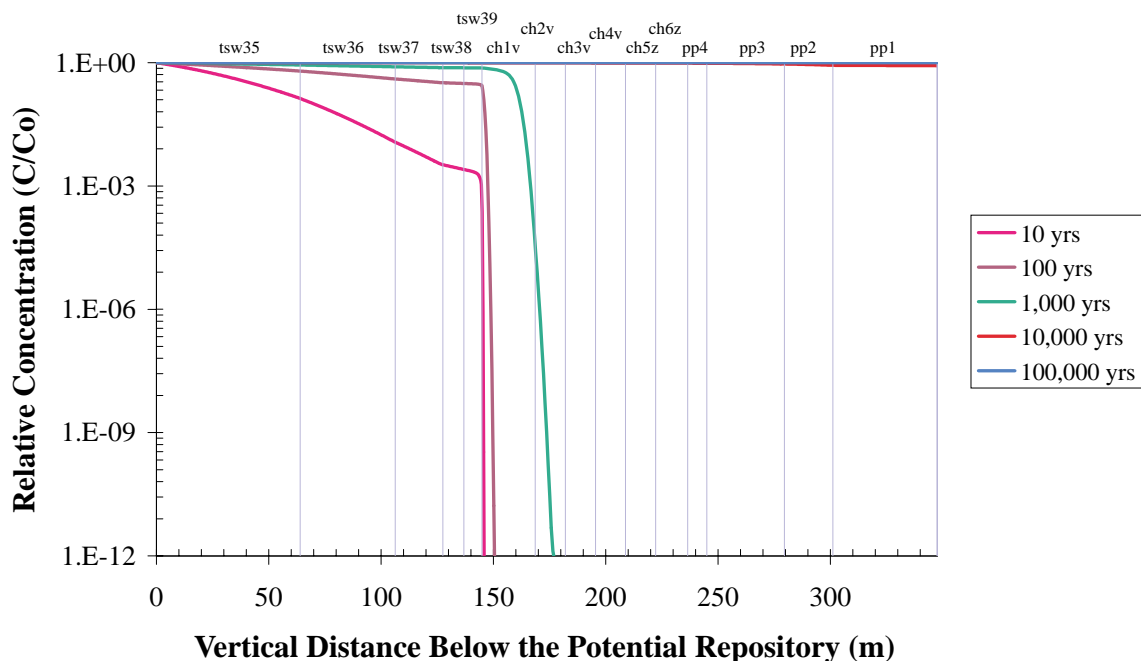
DTN: LB991220140160.009

Figure V.9. ^{239}Pu Concentration Profile Under the Potential Repository in Cross Section 2 (Mean Present-Day Infiltration, No Perched Water).



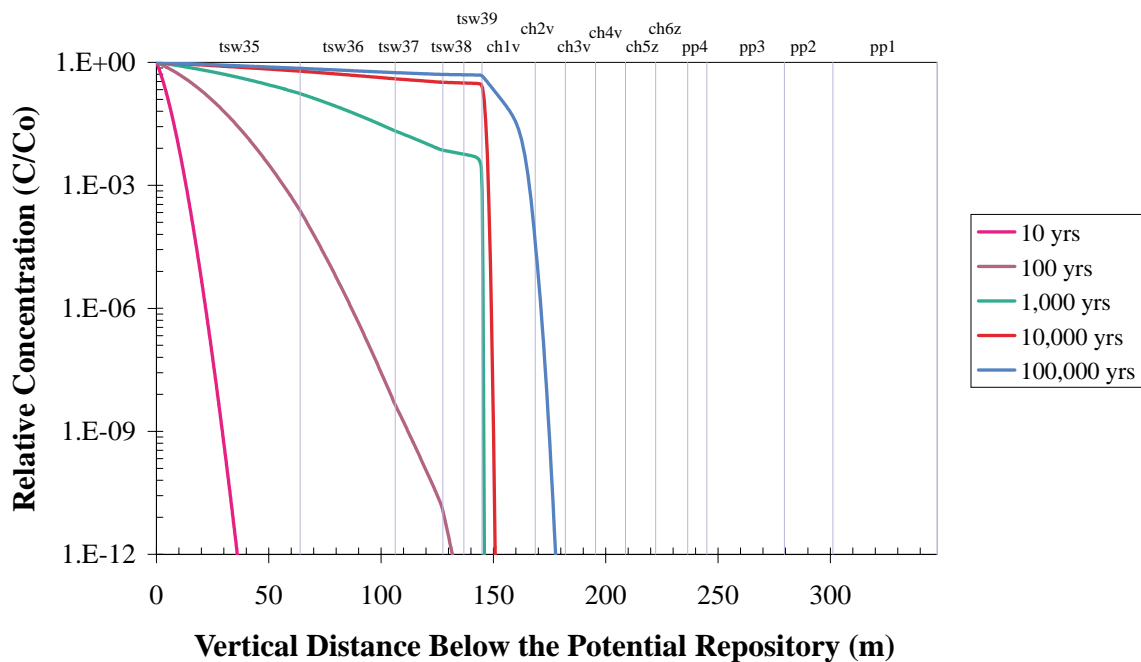
DTN: LB991220140160.009

Figure V.10. ^{99}Tc Concentration Profile Under the Potential Repository in Cross Section 2 (High Glacial Infiltration, No Perched Water). Results for 1,000 years, 10,000 years and 100,000 years overlap.



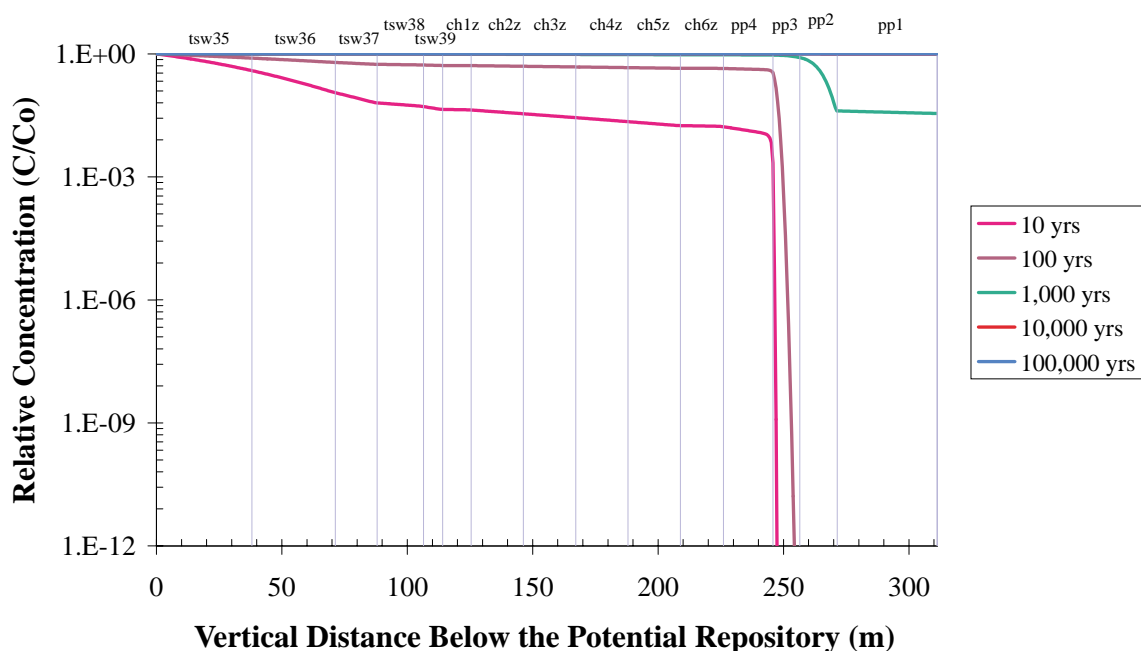
DTN: LB991220140160.009

Figure V.11. ^{237}Np Concentration Profile Under the Potential Repository in Cross Section 2 (High Glacial Infiltration, No Perched Water). Results for 10,000 years and 100,000 years almost overlap.



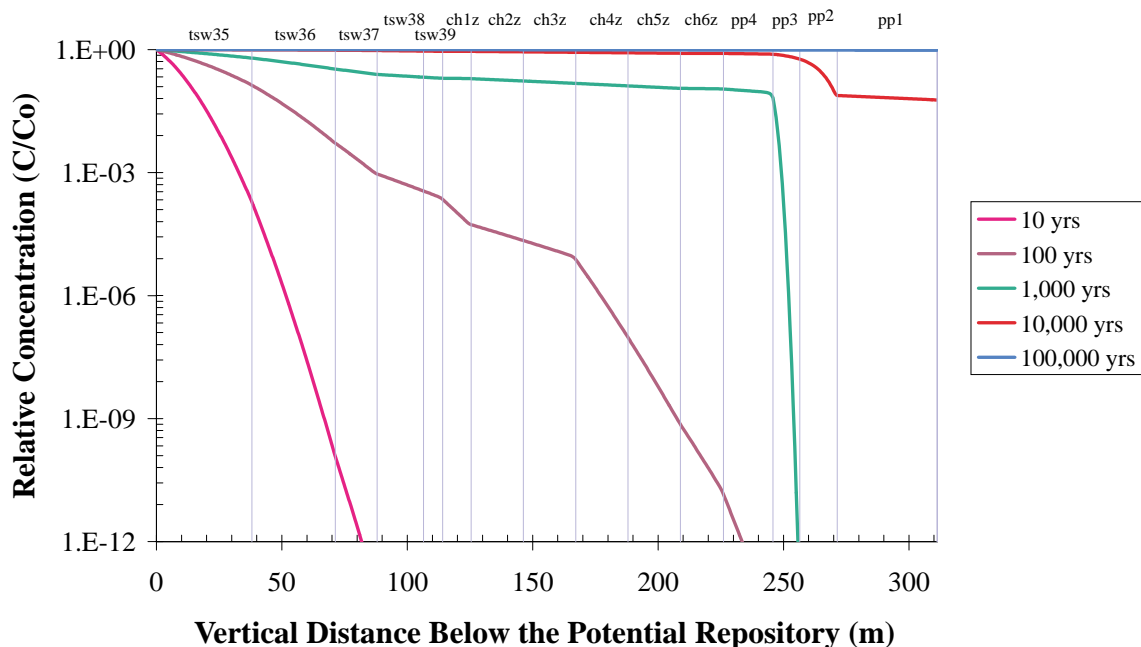
DTN: LB991220140160.009

Figure V.12. ^{239}Pu Concentration Profile Under the Potential Repository in Cross Section 2 (High Glacial Infiltration, No Perched Water).



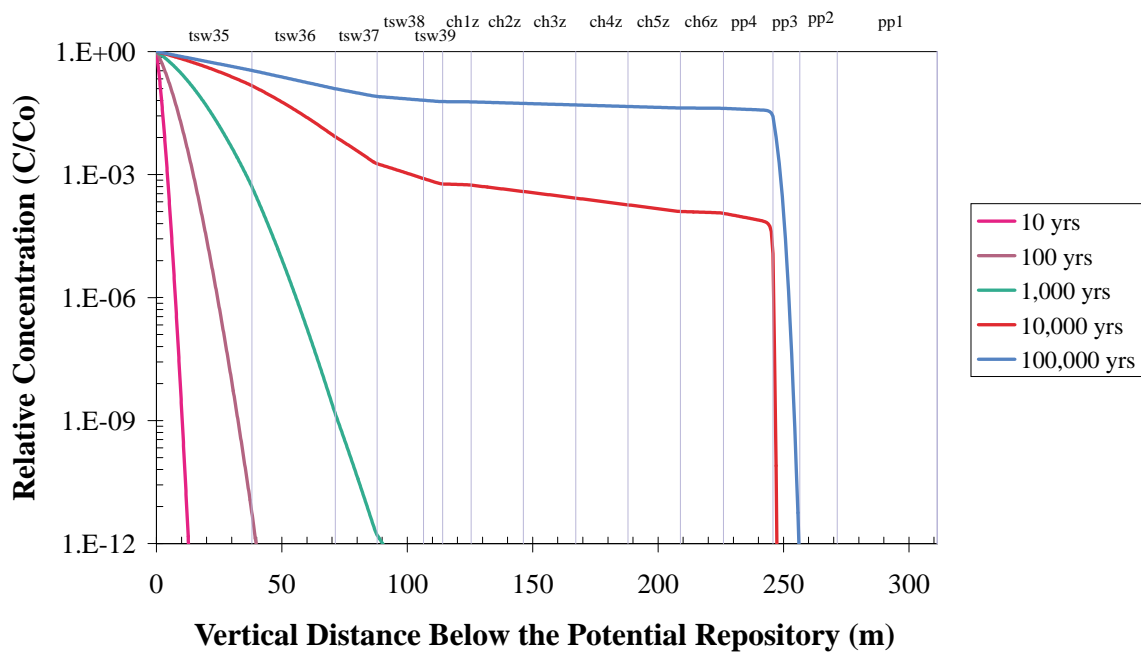
DTN: LB991220140160.009

Figure V.13. ^{99}Tc Concentration Profile Under the Potential Repository in Cross Section 3 (Mean Present-Day Infiltration, No Perched Water). Results for 10,000 years and 100,000 years overlap.



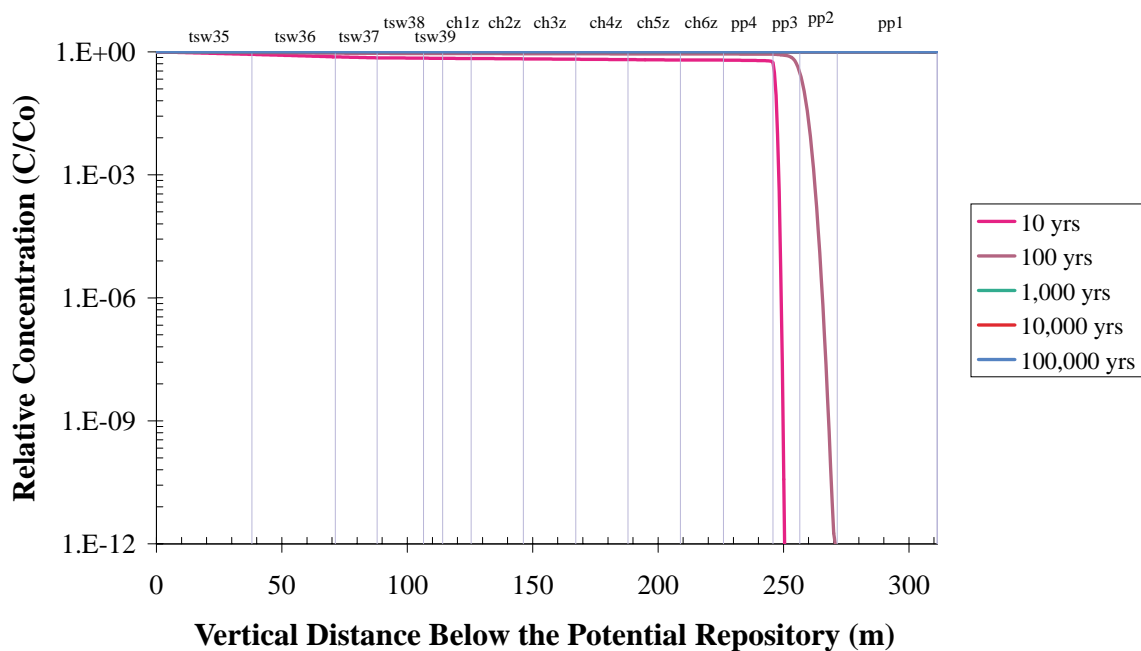
DTN: LB991220140160.009

Figure V.14. ^{237}Np Concentration Profile Under the Potential Repository in Cross Section 3 (Mean Present-Day Infiltration, No Perched Water).



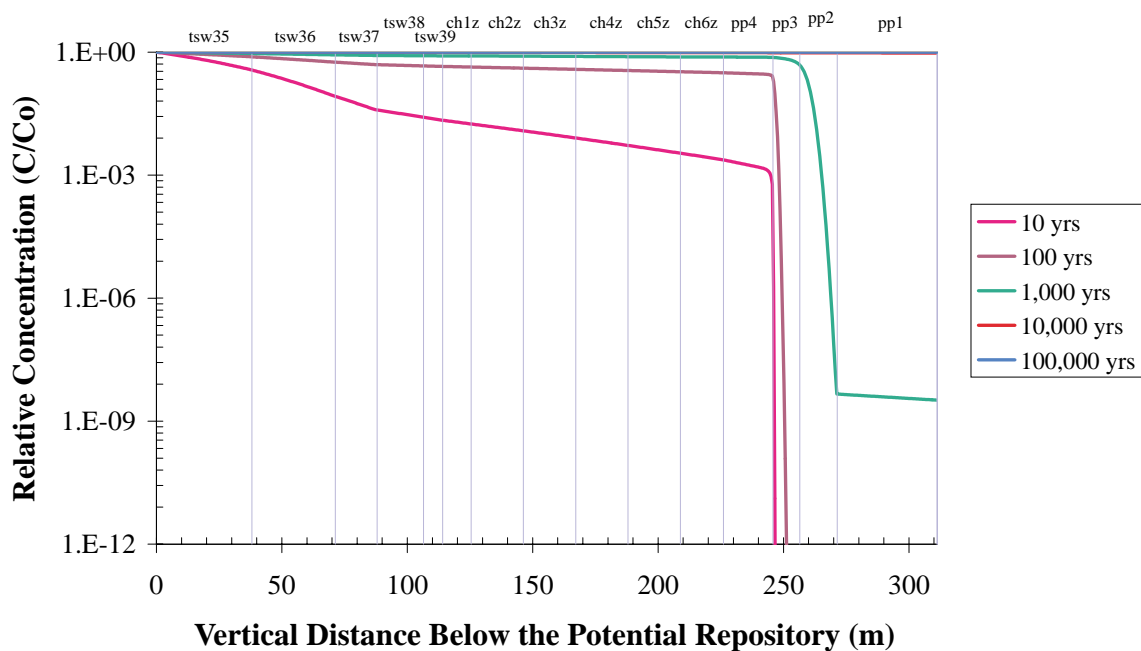
DTN: LB991220140160.009

Figure V.15. ^{239}Pu Concentration Profile Under the Potential Repository in Cross Section 3 (Mean Present-Day Infiltration, No Perched Water).



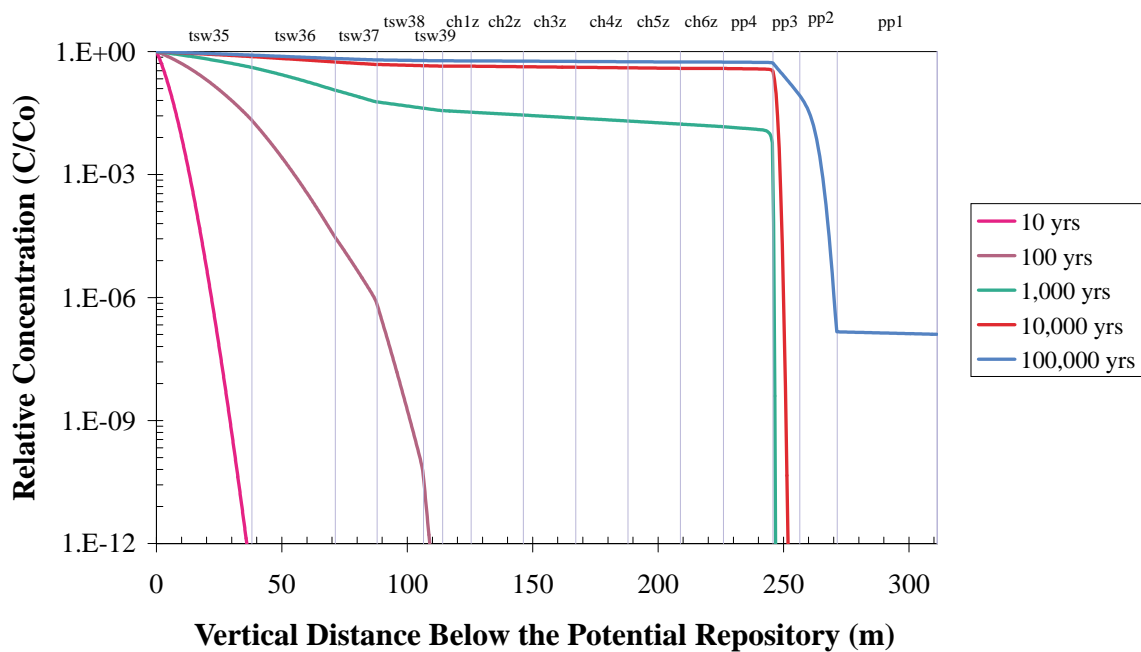
DTN: LB991220140160.009

Figure V.16. ^{99}Tc Concentration Profile Under the Potential Repository in Cross Section 3 (High Glacial Infiltration, No Perched Water). Results for 1,000 years, 10,000 and 100,000 years overlap.



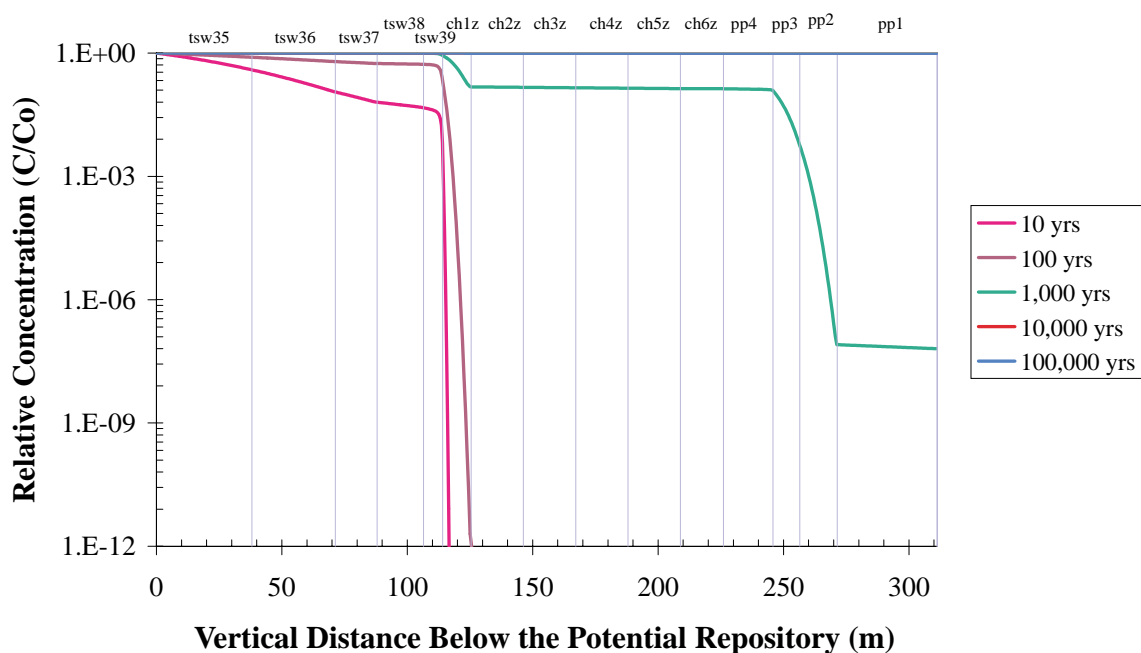
DTN: LB991220140160.009

Figure V.17. ^{237}Np Concentration Profile Under the Potential Repository in Cross Section 3 (High Glacial Infiltration, No Perched Water). Results for 10,000 and 100,000 years overlap.



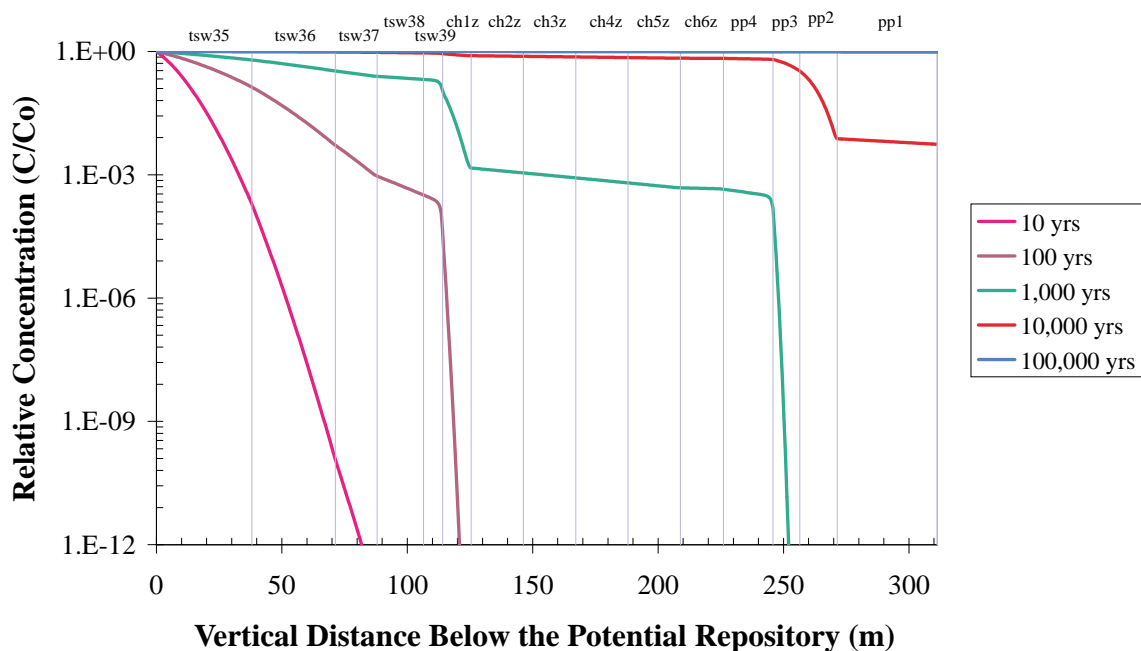
DTN: LB991220140160.009

Figure V.18. ^{239}Pu Concentration Profile Under the Potential Repository in Cross Section 3 (High Glacial Infiltration, No Perched Water).



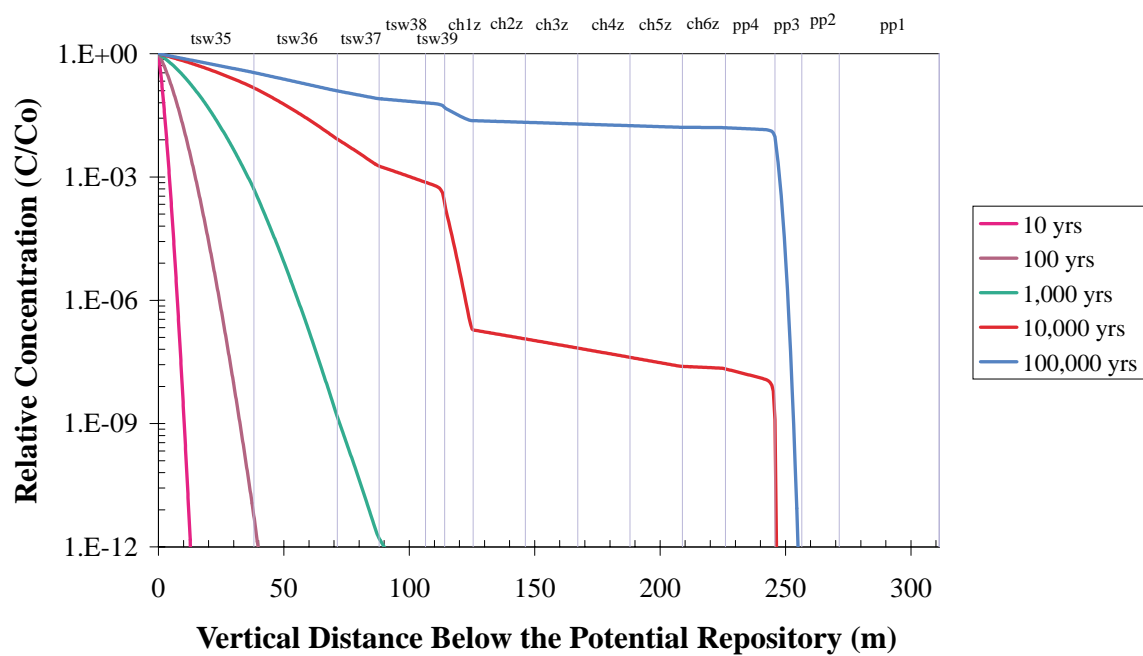
DTN: LB991220140160.009

Figure V.19. ^{99}Tc Concentration Profile Under the Potential Repository in Cross Section 3 for a Perched Water Regime (Mean Present-Day Infiltration). Results for 10,000 years and 100,000 years overlap.



DTN: LB991220140160.009

Figure V.20. ^{237}Np Concentration Profile Under the Potential Repository in Cross Section 3 for a Perched Water Regime (Mean Present-Day Infiltration).



DTN: LB991220140160.009

Figure V.21. ^{239}Pu Concentration Profile Under the Potential Repository in Cross Section 3 for a Perched Water Regime (Mean Present-Day Infiltration).

ATTACHMENT VI
FIGURES FROM THE BUSTED BUTTE STUDIES

FIGURES

Page

VI.1	Schematic Illustration of Borehole Layout in the Phase 1A Test, Busted Butte (Not to Scale)	VI-3
VI.2	Predicted Nonsorbing Bromide Tracer Distribution after 285 Days for Borehole 3 (S1A Flow Parameters)	VI-3
VI.3	Predicted Nonsorbing Bromide Tracer Distribution after 285 Days for Borehole 3 (S2A Flow Parameters)	VI-4
VI.4	Predicted Nonsorbing Bromide Tracer Distribution after 285 Days for Borehole 1 (S1A Flow Parameters)	VI-4
VI.5	Predicted Nonsorbing Bromide Tracer Distribution after 285 days for Borehole 4 (S1A Flow Parameters)	VI-5
VI.6	Schematic Illustration of Injection/Collection Boreholes 5 and 6 and Collection Locations in Borehole 6 in the Phase 1B Test, Busted Butte (Not to Scale)	VI-5
VI.7	Predicted Bromide Breakthrough Curves at Different Collection Locations in Borehole 6 (S1A Flow Parameters)	VI-6
VI.8	Predicted Bromide Breakthrough Curves at Different Collection Locations in Borehole 6 (S2B Flow Parameters)	VI-6
VI.9	Predicted Liquid Saturation at Different Collection Locations in Borehole 6 (S1A Flow Parameters)	VI-7
VI.10	Predicted Liquid Saturation at Different Collection Locations in Borehole 6 (S2B Flow Parameters)	VI-7
VI.11	Predicted 2,6-DFBA Breakthrough Curve at Different Collection Locations in Borehole 6 (S1A Flow Parameters)	VI-8
VI.12	Predicted Lithium Breakthrough Curve at Different Collection Locations in Borehole 6 ($K_d=2$ mL/mg; S1A Flow Parameters)	VI-8
VI.13	Predicted Lithium Breakthrough Curve at Different Collection Locations in Borehole 6 ($K_d=2$ mL/mg; S2B Flow Parameters).....	VI-9

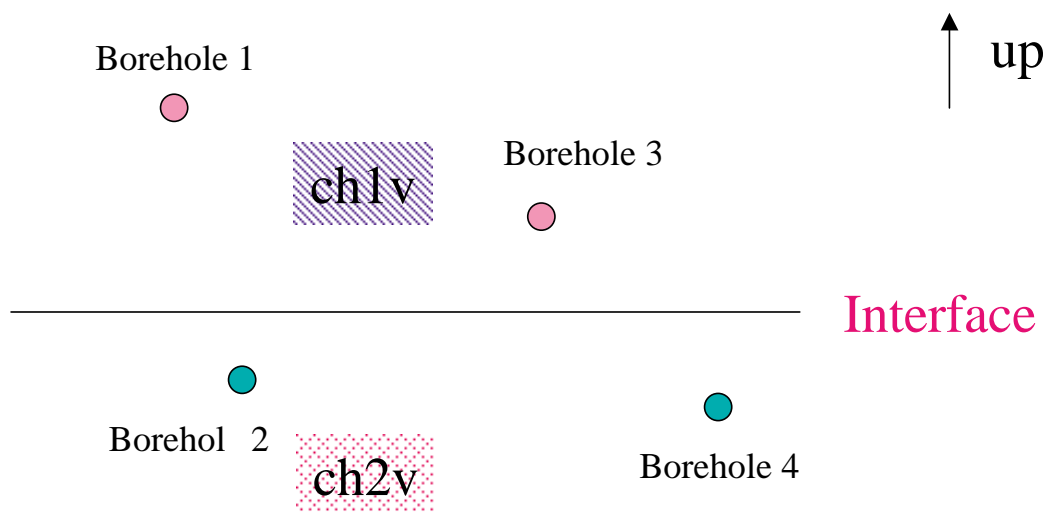
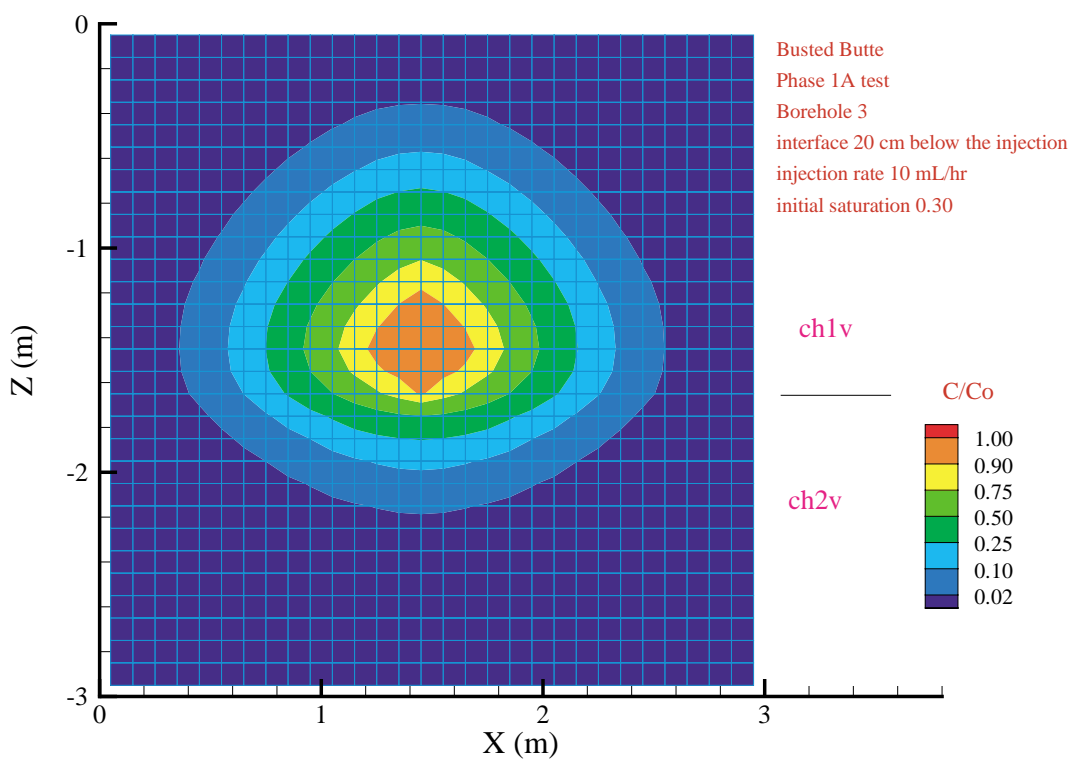


Figure V1.1. Schematic Illustration of Borehole Layout in the Phase 1A Test, Busted Butte (Not to Scale).



DTN: LB991220140160.010

Figure VI.2. Predicted Nonsorbing Bromide Tracer Distribution after 285 Days for Borehole 3 (S1A Flow Parameters).

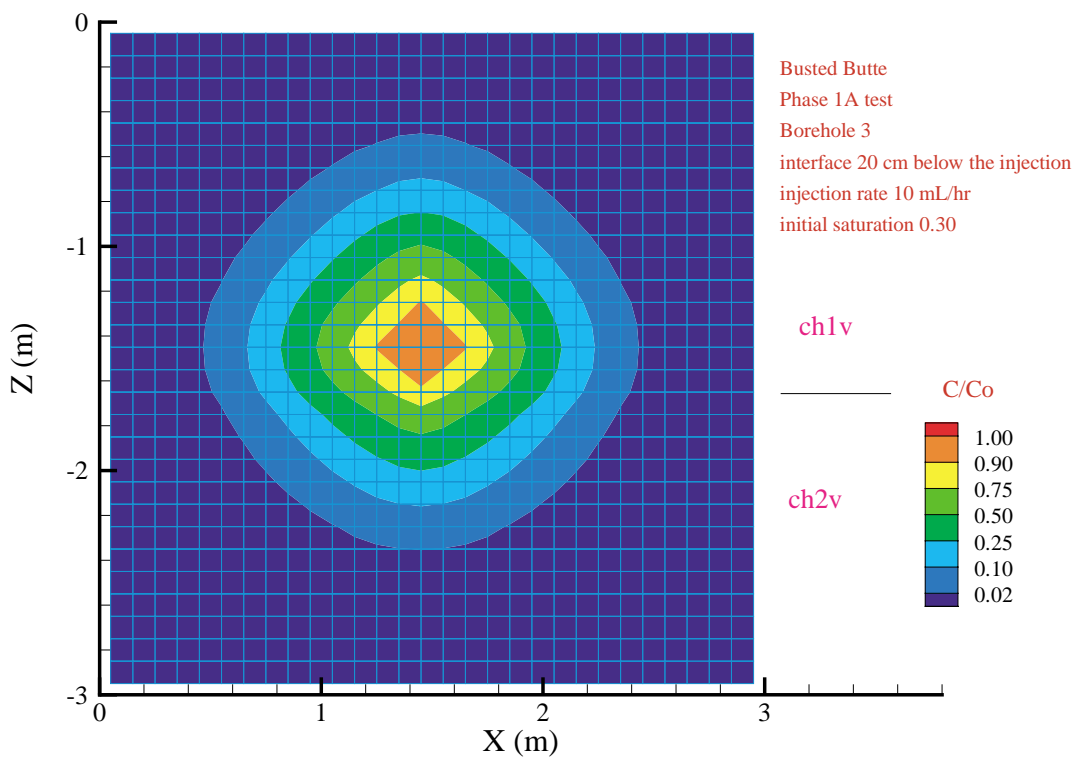


Figure VI. 3 Predicted Nonsorbing Bromide Tracer Distribution after 285 Days for Borehole 3 (S2A Flow Parameters).

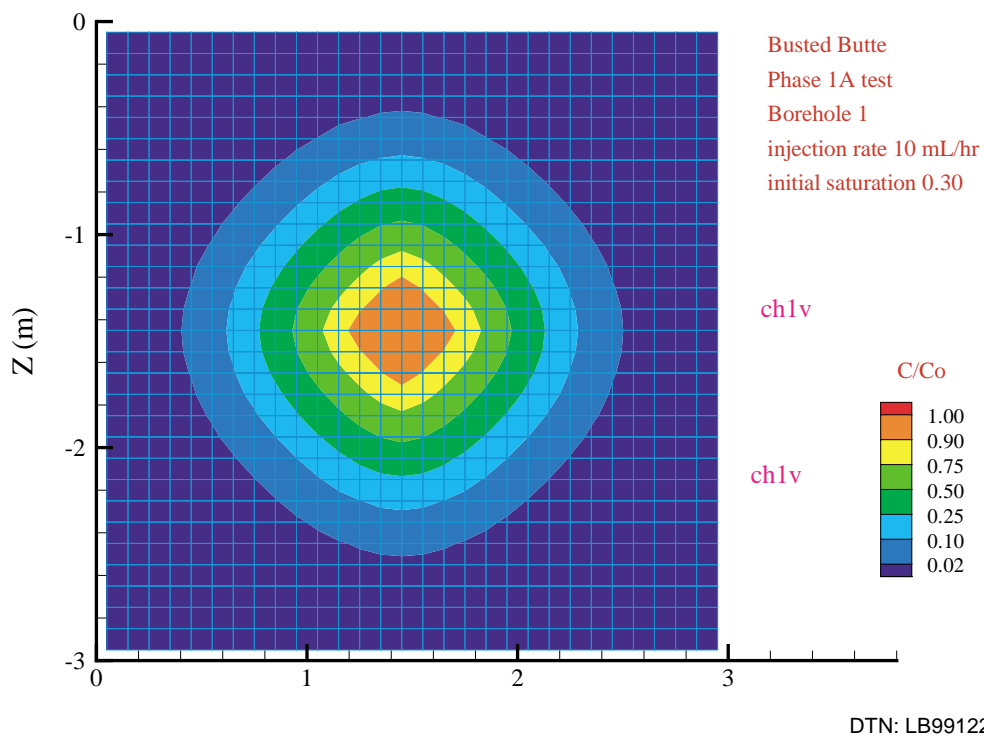


Figure VI.4. Predicted Nonsorbing Bromide Tracer Distribution after 285 Days for Borehole 1 (S1A Flow Parameters).

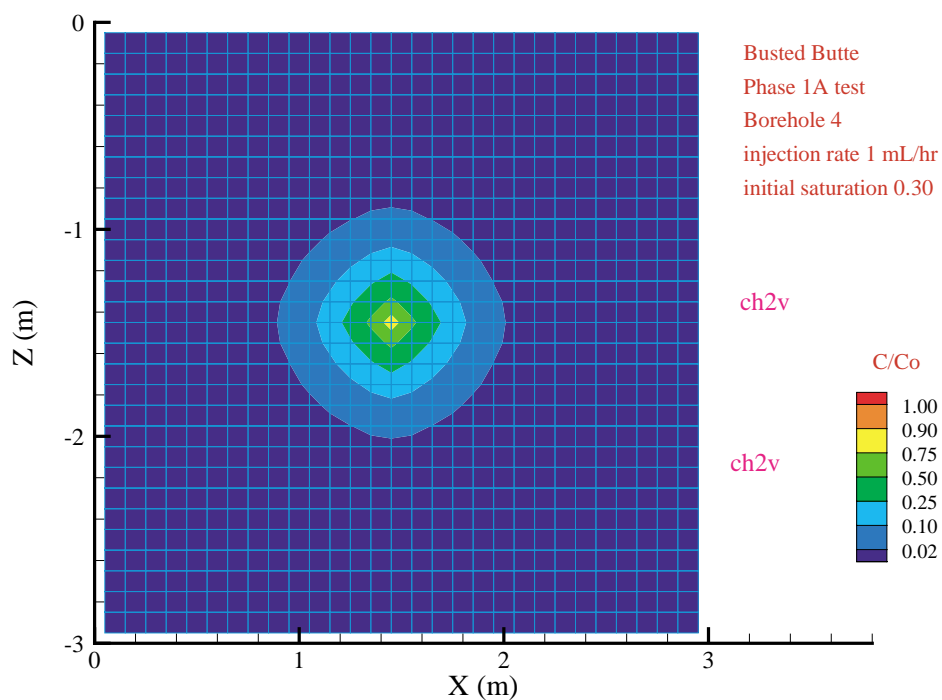


Figure VI. 5. Predicted Nonsorbing Bromide Tracer Distribution after 285 days for Borehole 4 (S1A Flow Parameters).

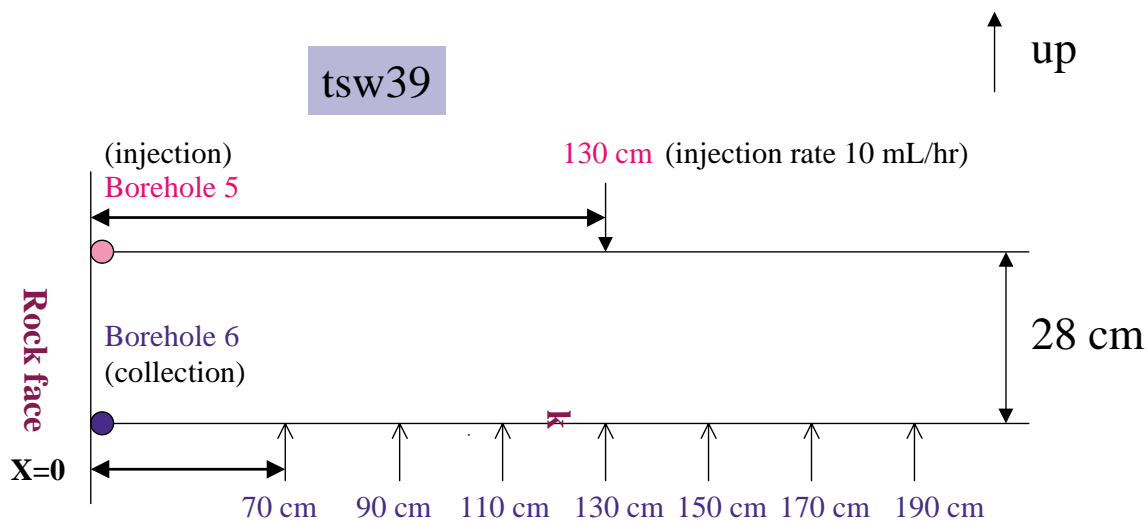
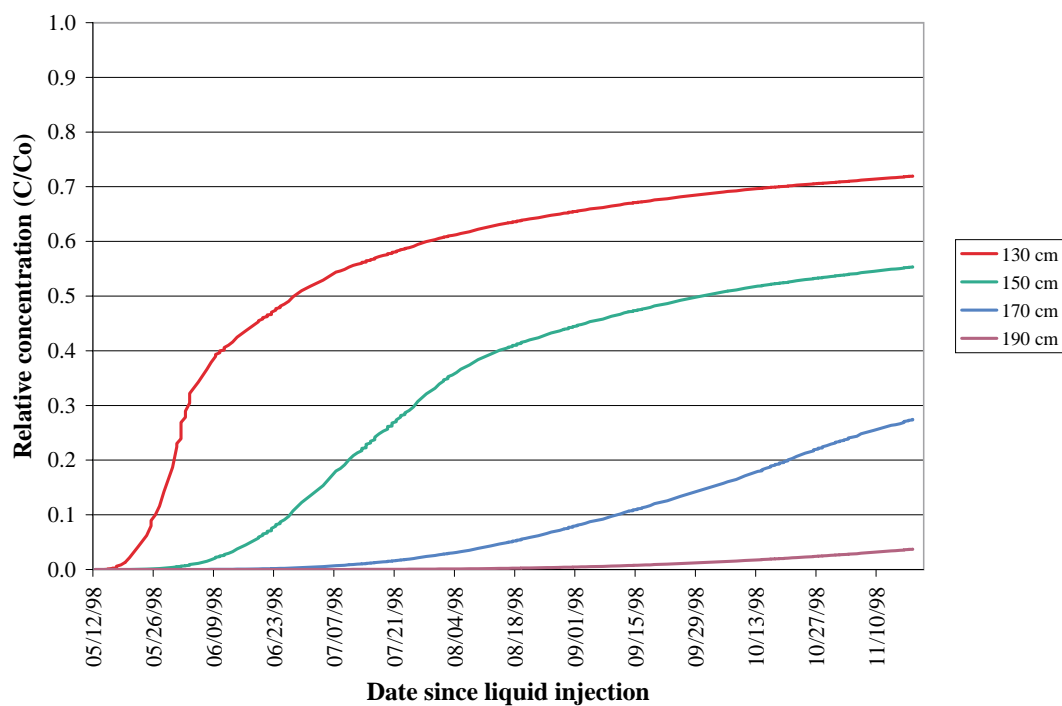
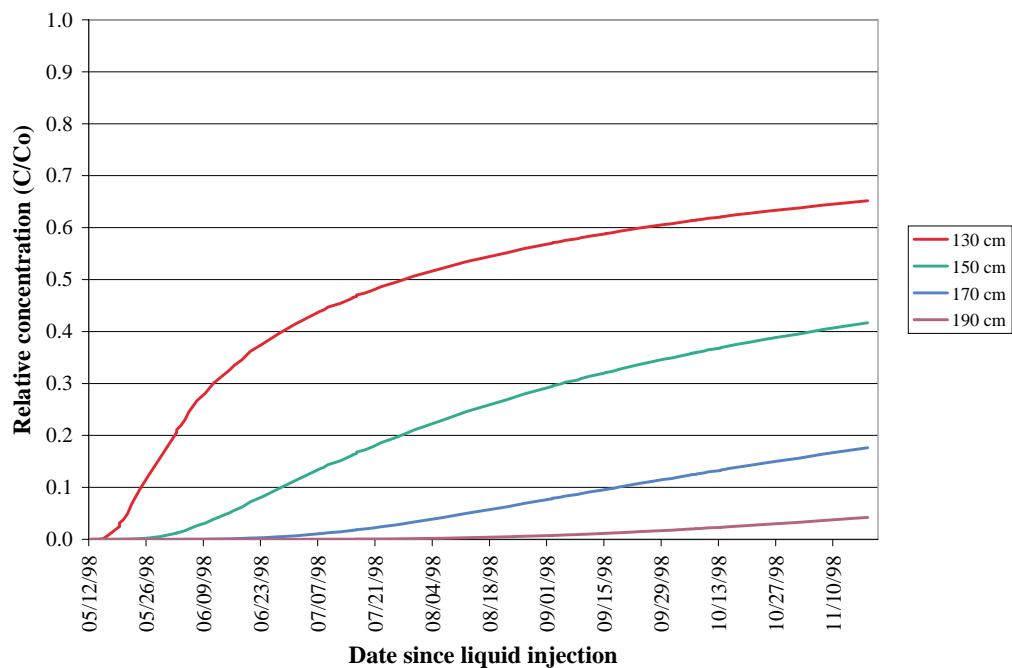


Figure VI.6. Schematic Illustration of Injection/Collection Boreholes 5 and 6 and Collection Locations in Borehole 6 in the Phase 1B Test, Busted Butte (Not to Scale).



DTN: LB991220140160.010

Figure VI.7. Predicted Bromide Breakthrough Curves at Different Collection Locations in Borehole 6 (S1A Flow Parameters).



DTN: LB991220140160.010

Figure VI.8. Predicted Bromide Breakthrough Curves at Different Collection Locations in Borehole 6 (S2B Flow Parameters).

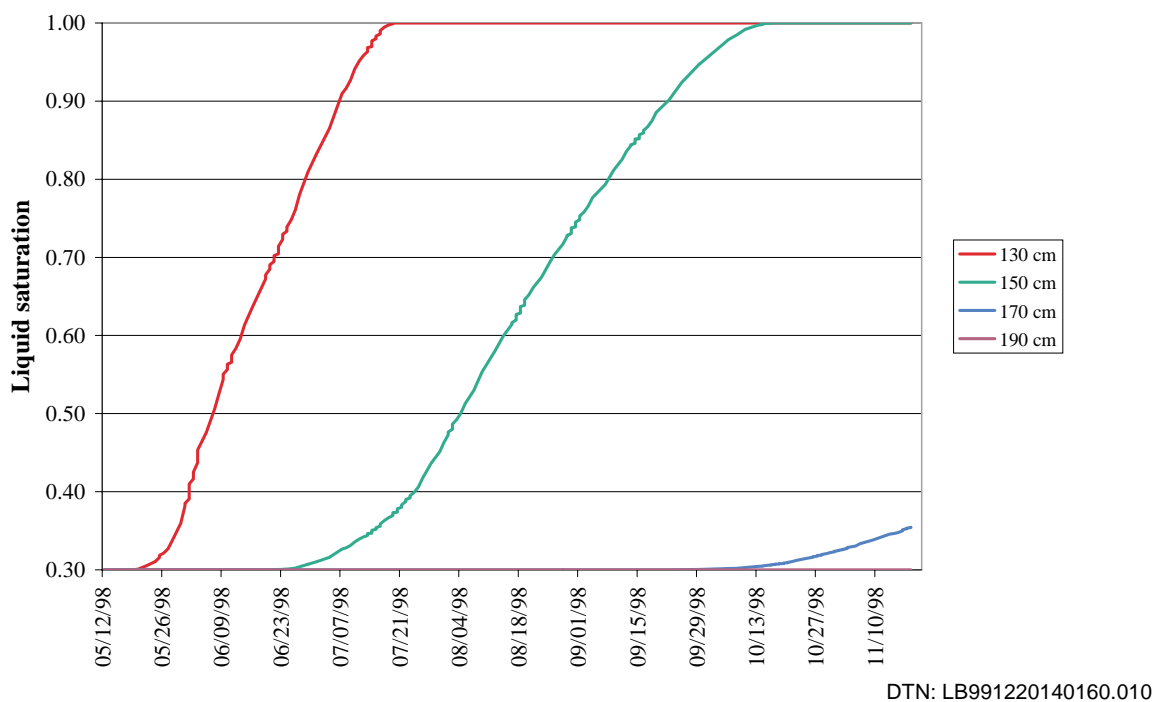


Figure VI.9. Predicted Liquid Saturation at Different Collection Locations in Borehole 6 (S1A Flow Parameters).

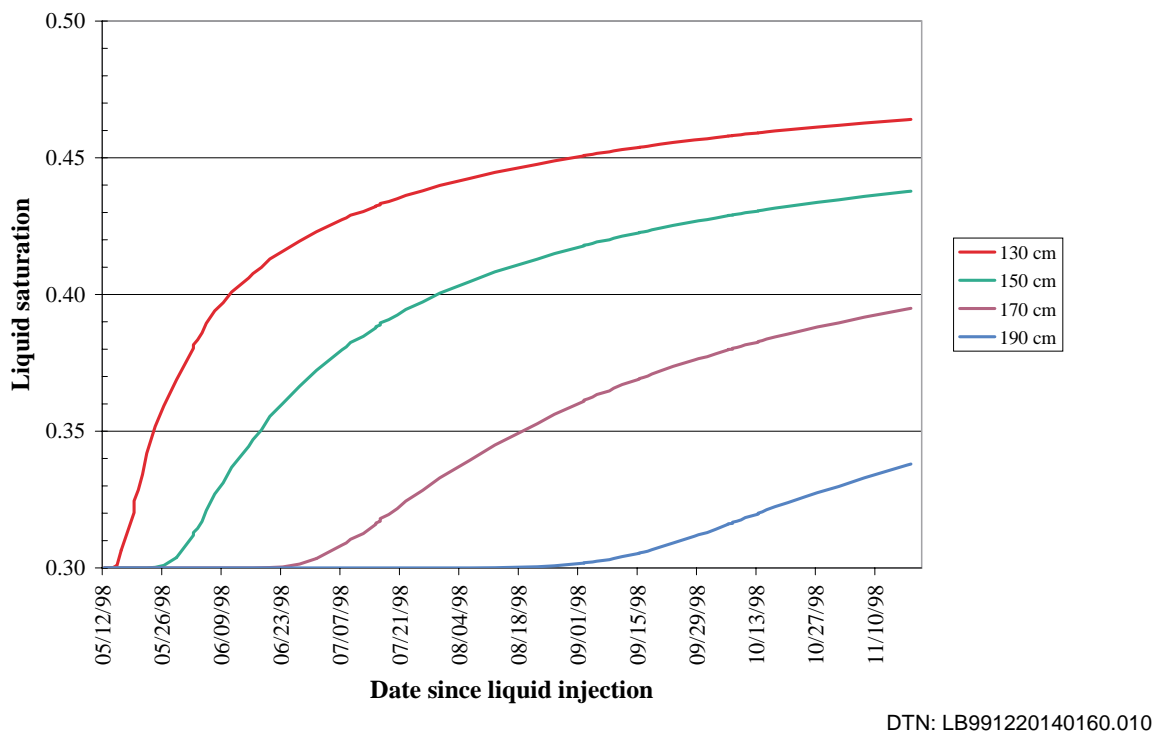
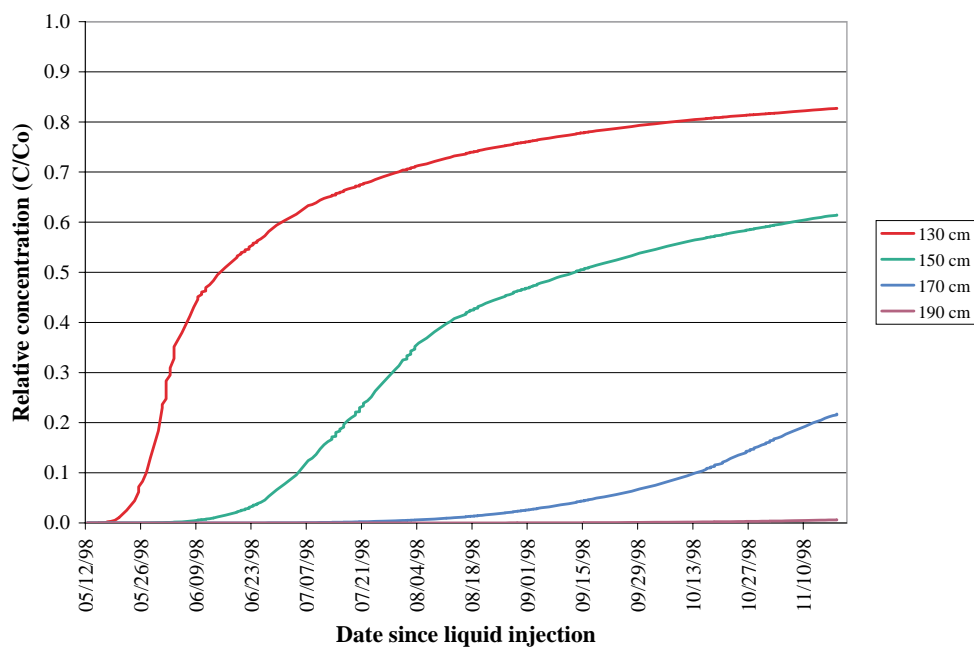
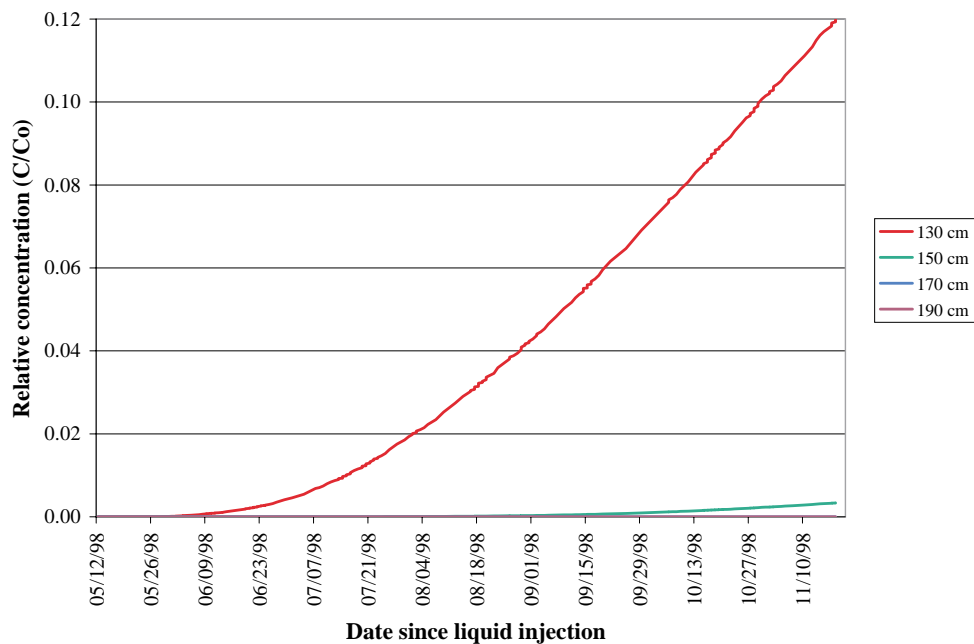


Figure VI.10. Predicted Liquid Saturation at Different Collection Locations in Borehole 6 (S2B Flow Parameters).



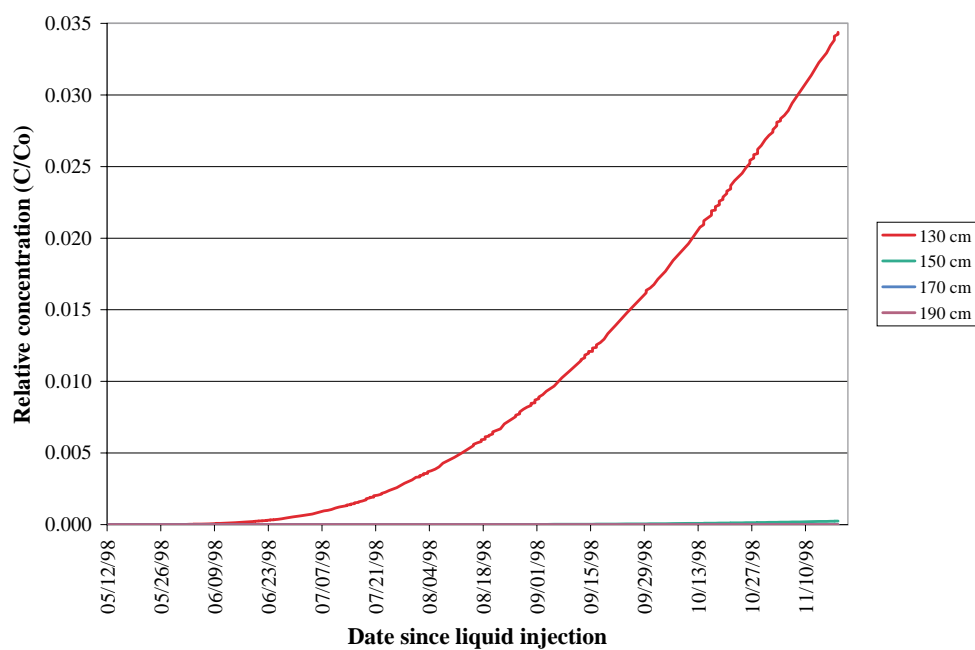
DTN: LB991220140160.010

Figure VI.11. Predicted 2,6-DFBA Breakthrough Curve at Different Collection Locations in Borehole 6 (S1A Flow Parameters).



DTN: LB991220140160.010

Figure VI.12. Predicted Lithium Breakthrough Curve at Different Collection Locations in Borehole 6 ($K_d=2$ mL/mg; S1A Flow Parameters).



DTN: LB991220140160.010

Figure VI.13. Predicted Lithium Breakthrough Curve at Different Collection Locations in Borehole 6 ($K_d=2$ mL/mg; S2B Flow Parameters).

ATTACHMENT VII.

FIGURES FROM THE ^{237}Np 3-D TRANSPORT STUDIES

INTENTIONALLY LEFT BLANK

FIGURES

Page

VII.1.	Distribution of the Relative Mass Fraction X_R of ^{237}Np in the Fractures of the Tsw39 Layer at $t = 100$ Years for Mean Present-Day Infiltration.....	VII-5
VII.2.	Distribution of the Relative Mass Fraction X_R of ^{237}Np in the Matrix of the Tsw39 Layer at $t = 100$ Years for Mean Present-Day Infiltration.....	VII-6
VII.3.	Distribution of the Relative Sorbed Concentration F_R of ^{237}Np in the Matrix of the Tsw39 Layer at $t = 100$ Years for Mean Present-Day Infiltration.....	VII-7
VII.4.	Distribution of the Relative Mass Fraction X_R of ^{237}Np in the Fractures of the Tsw39 Layer at $t = 1,000$ Years for Mean Present-Day Infiltration.....	VII-8
VII.5.	Distribution of the Relative Mass Fraction X_R of ^{237}Np in the Matrix of the Tsw39 Layer at $t = 1,000$ Years for Mean Present-Day Infiltration.....	VII-9
VII.6.	Distribution of the Relative Sorbed Concentration F_R of ^{237}Np in the Matrix of the Tsw39 Layer at $t = 1,000$ Years for Mean Present-Day Infiltration.....	VII-10
VII.7.	Distribution of the Relative Mass Fraction X_R of ^{237}Np in the Fractures of the Tsw39 Layer at $t = 10,000$ Years for Mean Present-Day Infiltration.....	VII-11
VII.8.	Distribution of the Relative Mass Fraction X_R of ^{237}Np in the Matrix of the Tsw39 Layer at $t = 10,000$ Years for Mean Present-Day Infiltration.....	VII-12
VII.9.	Distribution of the Relative Sorbed Concentration F_R of ^{237}Np in the Matrix of the Tsw39 Layer at $t = 10,000$ Years for Mean Present-Day Infiltration.....	VII-13
VII.10.	Distribution of the Relative Mass Fraction X_R of ^{237}Np in the Fractures of the Tsw39 Layer at $t = 100,000$ Years for Mean Present-Day Infiltration.....	VII-14
VII.11.	Distribution of the Relative Mass Fraction X_R of ^{237}Np in the Matrix of the Tsw39 Layer at $t = 100,000$ Years for Mean Present-Day Infiltration.....	VII-15
VII.12.	Distribution of the Relative Sorbed Concentration F_R of ^{237}Np in the Matrix of the Tsw39 Layer at $t = 100,000$ Years for Mean Present-Day Infiltration.....	VII-16
VII.13.	Distribution of the Relative Mass Fraction X_R of ^{237}Np in the Fractures Immediately Above the Groundwater at $t = 100$ Years for Mean Present-Day Infiltration.....	VII-17

FIGURES (Continued)

	Page
VII.14. Distribution of the Relative Mass Fraction X_R of ^{237}Np in the Matrix Immediately Above the Groundwater Table at $t = 100$ Years for a Mean Present-Day Infiltration.....	VII-18
VII.15. Distribution of the Relative Sorbed Concentration F_R of ^{237}Np in the Matrix Immediately Above the Groundwater Table at $t = 100$ Years for a Mean Present-Day Infiltration.....	VII-19
VII.16. Distribution of the Relative Mass Fraction X_R of ^{237}Np in the Fractures Immediately Above the Groundwater at $t = 1,000$ Years for Mean Present-Day Infiltration.....	VII-20
VII.17. Distribution of the Relative Mass Fraction X_R of ^{237}Np in the Matrix Immediately Above the Groundwater Table at $t = 1,000$ Years for a Mean Present-Day Infiltration.....	VII-21
VII.18. Distribution of the Relative Sorbed Concentration F_R of ^{237}Np in the Matrix Immediately Above the Groundwater Table at $t = 1,000$ Years for a Mean Present-Day Infiltration.....	VII-22
VII.19. Distribution of the Relative Mass Fraction X_R of ^{237}Np in the Fractures Immediately Above the Groundwater at $t = 10,000$ Years for Mean Present-Day Infiltration.....	VII-23
VII.20. Distribution of the Relative Mass Fraction X_R of ^{237}Np in the Matrix Immediately Above the Groundwater Table at $t = 10,000$ Years for a Mean Present-Day Infiltration.....	VII-24
VII.21. Distribution of the Relative Sorbed Concentration F_R of ^{237}Np in the Matrix Immediately Above the Groundwater Table at $t = 10,000$ Years for a Mean Present-Day Infiltration.....	VII-25
VII.22. Distribution of the Relative Mass Fraction X_R of ^{237}Np in the Fractures Immediately Above the Groundwater at $t = 100,000$ Years for Mean Present-Day Infiltration.....	VII-26
VII.23. Distribution of the Relative Mass Fraction X_R of ^{237}Np in the Matrix Immediately Above the Groundwater Table at $t = 100,000$ Years for a Mean Present-Day Infiltration.....	VII-27
VII.24. Distribution of the Relative Sorbed Concentration F_R of ^{237}Np in the Matrix Immediately Above the Groundwater Table at $t = 100,000$ Years for a Mean Present-Day Infiltration.....	VII-28

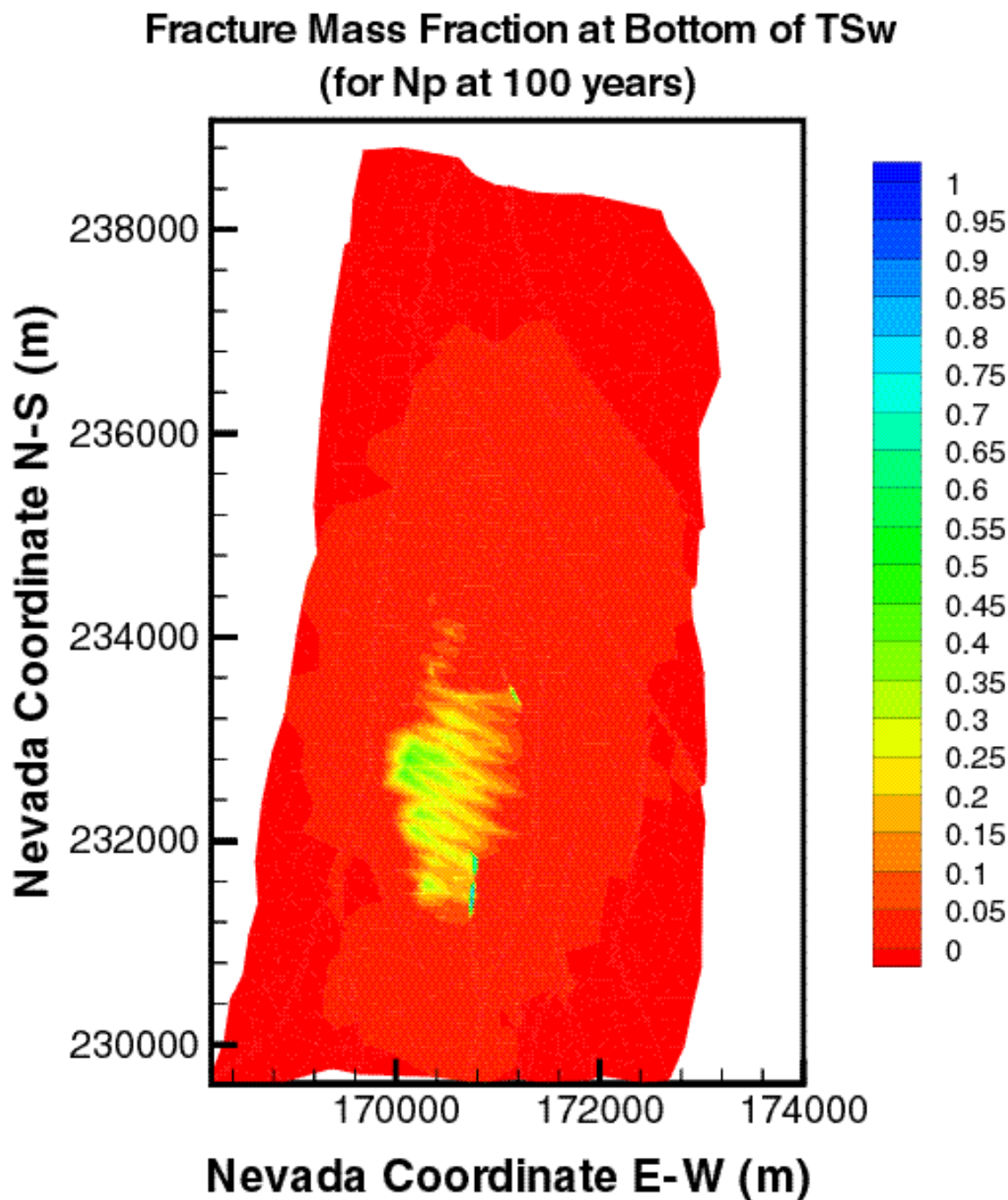


Figure VII.1. Distribution of the relative mass fraction X_R of ^{237}Np in the fractures of the tsw39 layer at $t = 100$ years for mean present-day infiltration (DTN: LB991220140160.012, data submitted with this AMR).

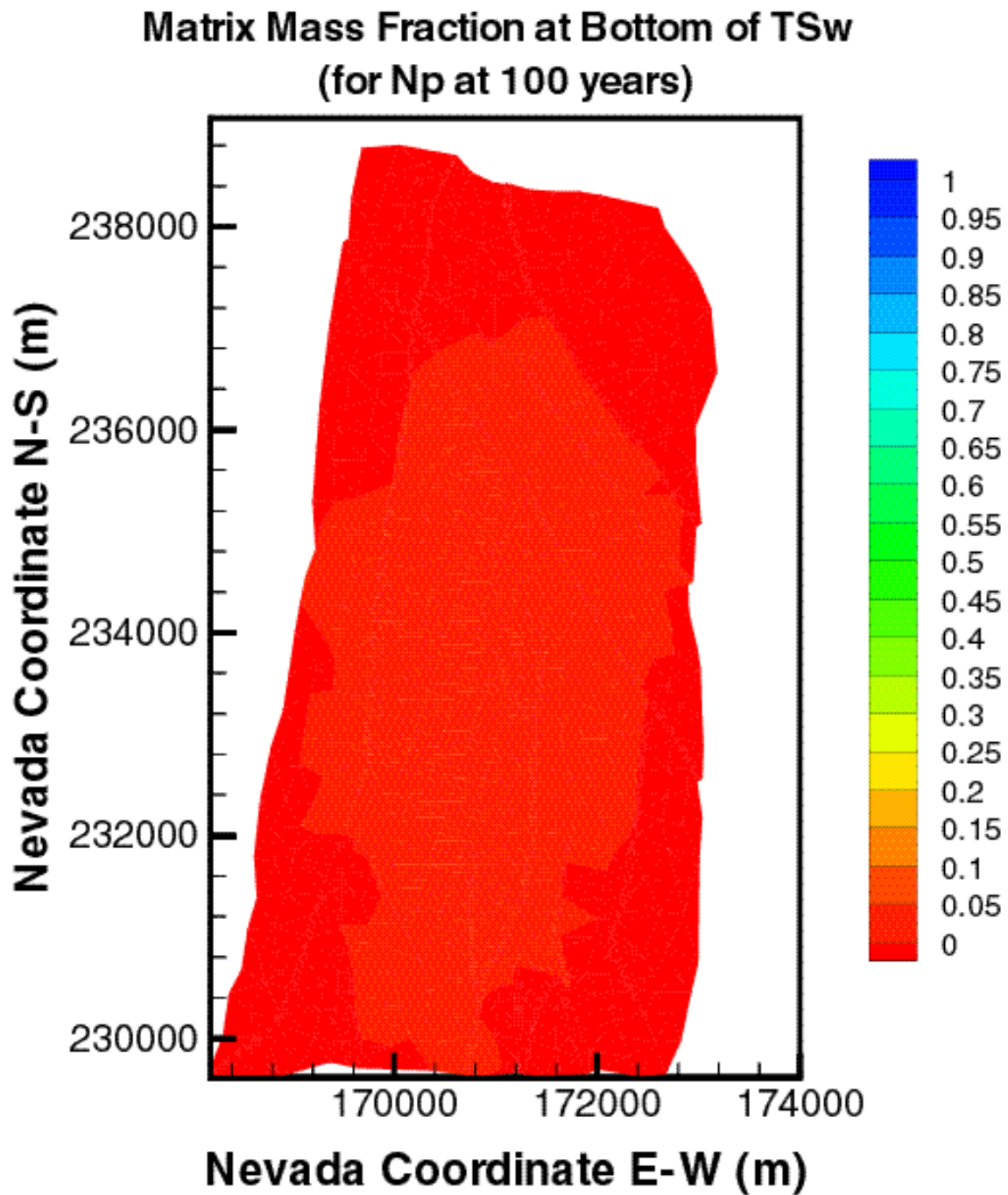


Figure VII.2. Distribution of the relative mass fraction X_R of ^{237}Np in the matrix of the tsw39 layer at $t = 100$ years for mean present-day infiltration (DTN: LB991220140160.012, data submitted with this AMR).

**Matrix Sorbed Concentration at Bottom of TSw (kg/m³)
(for Np at 100 years)**

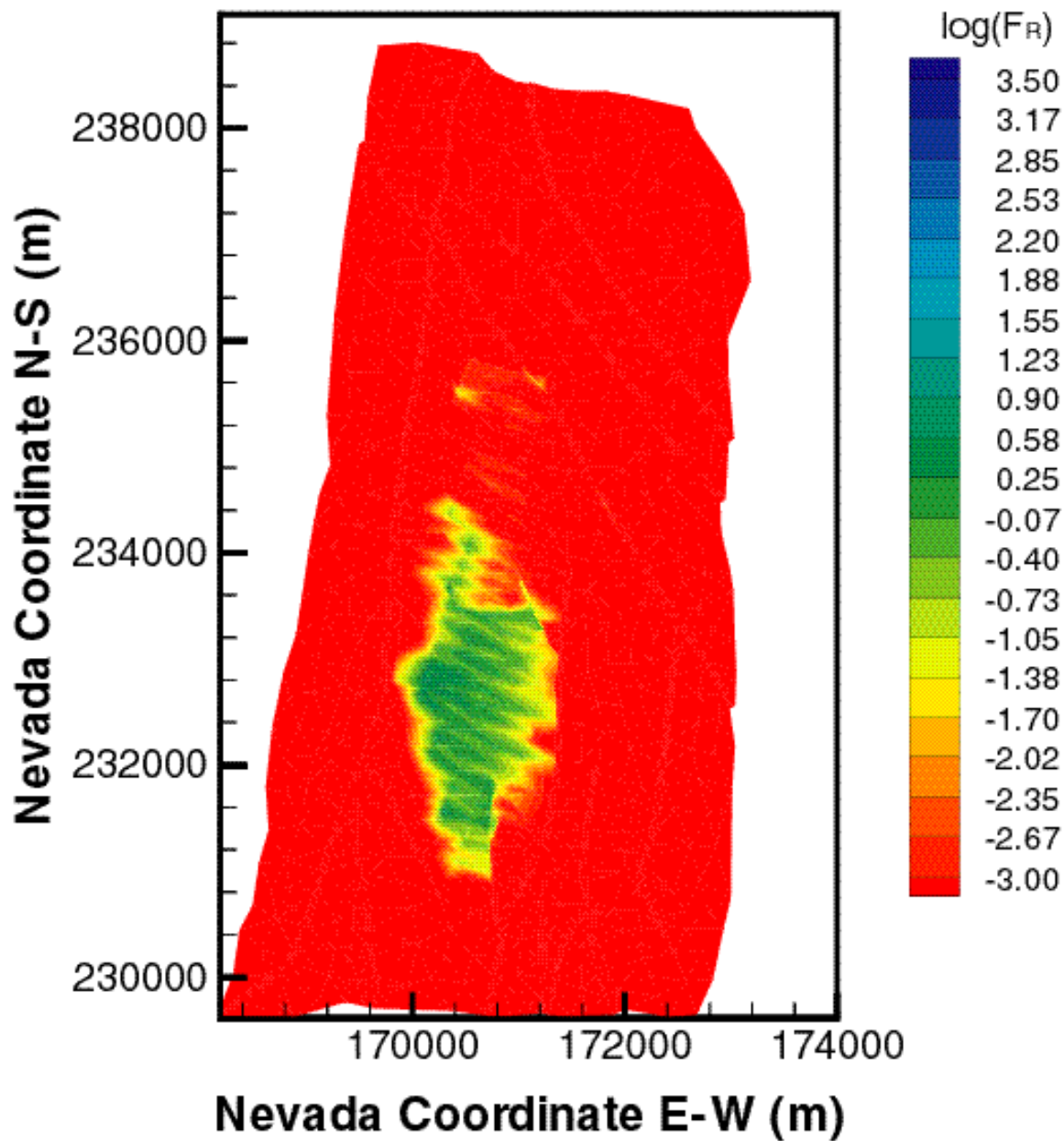


Figure VII.3. Distribution of the relative sorbed concentration F_R of ^{237}Np in the matrix of the tsw39 layer at $t = 100$ years for mean present-day infiltration (DTN: LB991220140160.012, data submitted with this AMR).

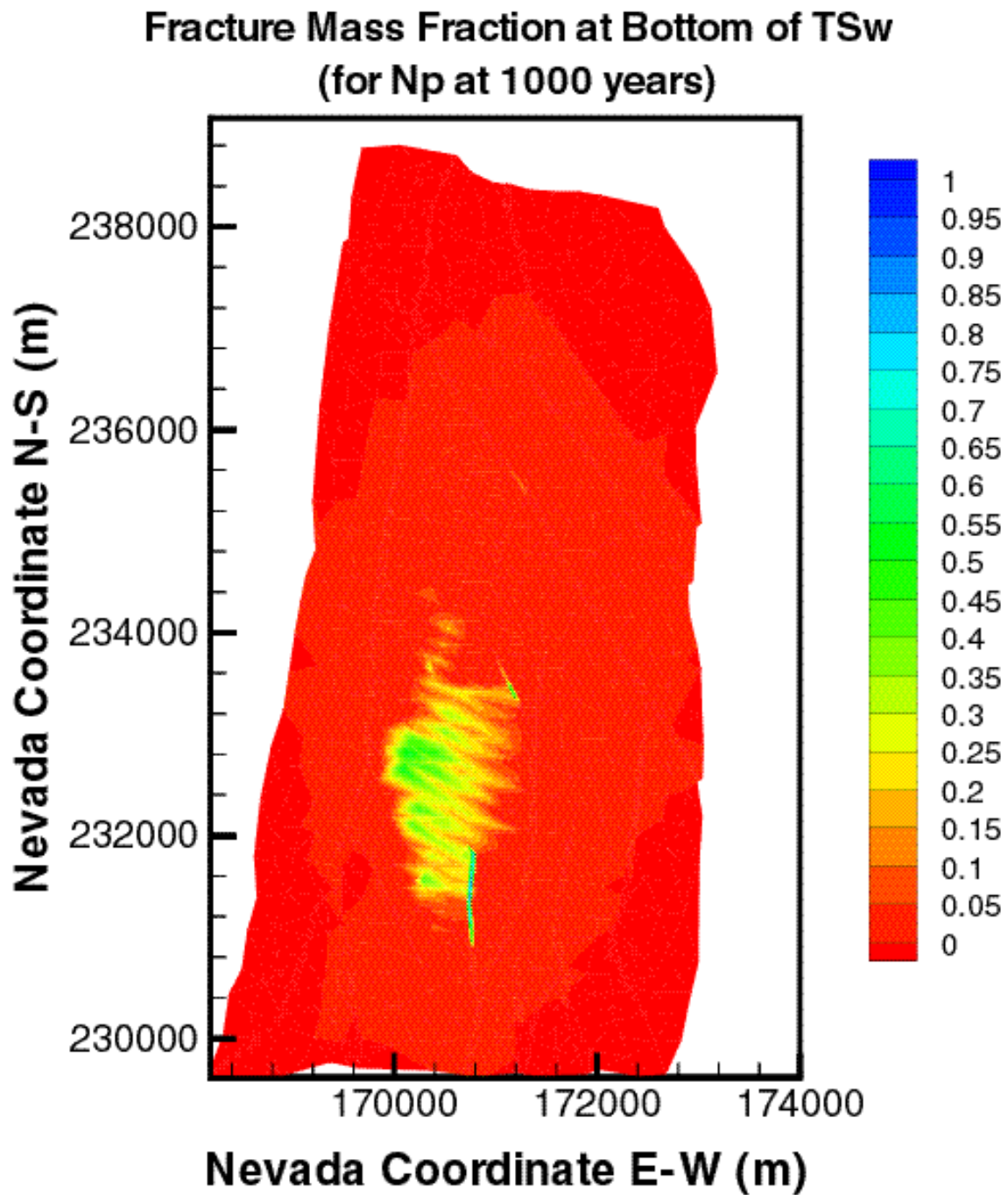


Figure VII.4. Distribution of the relative mass fraction X_R of ^{237}Np in the fractures of the tsw39 layer at $t = 1,000$ years for mean present-day infiltration (DTN: LB991220140160.012, data submitted with this AMR).

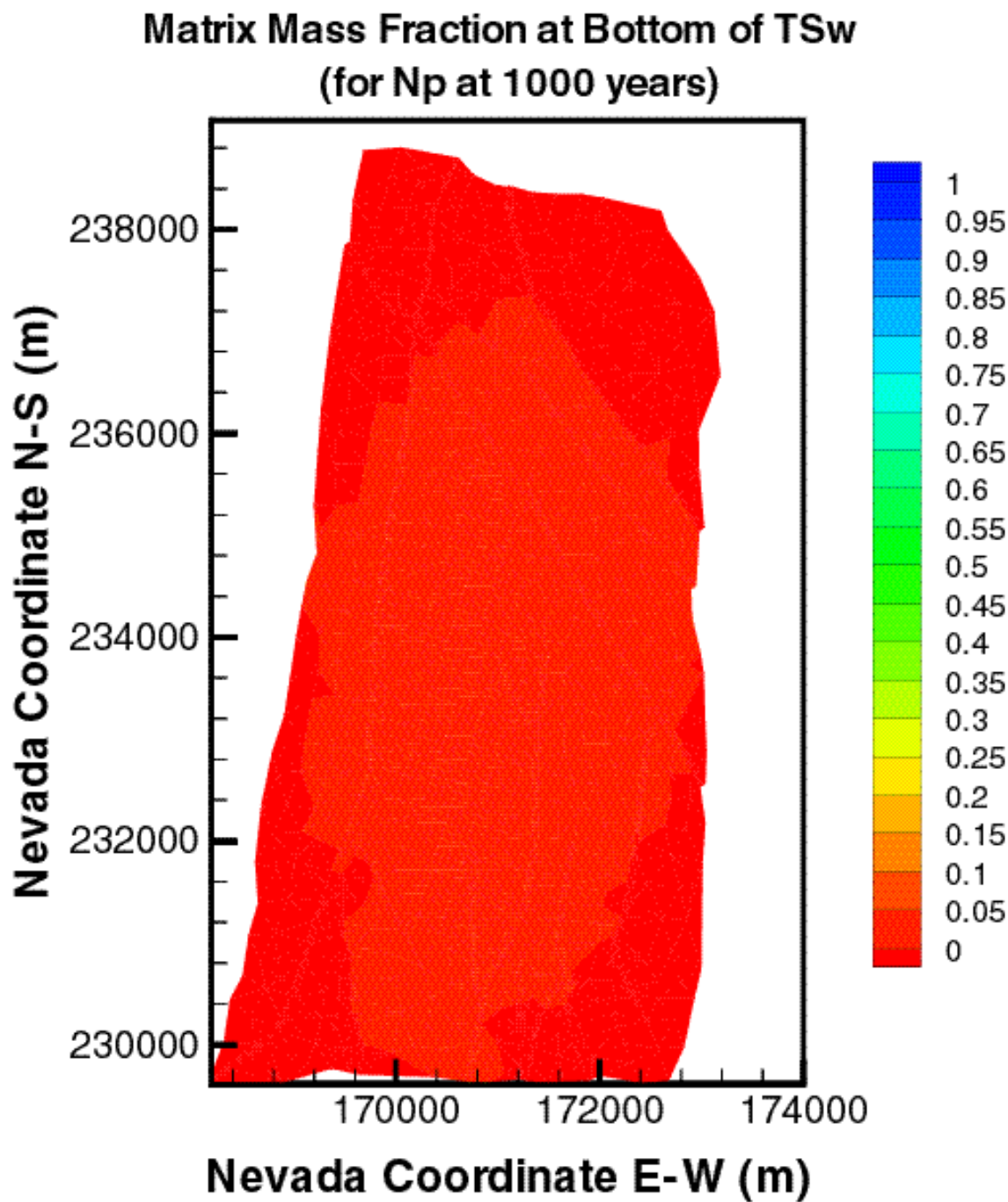


Figure VII.5. Distribution of the relative mass fraction X_R of ^{237}Np in the matrix of the tsw39 layer at $t = 1,000$ years for mean present-day infiltration (DTN: LB991220140160.012, data submitted with this AMR).

**Matrix Sorbed Concentration at Bottom of TSw (kg/m³)
(for Np at 1000 years)**

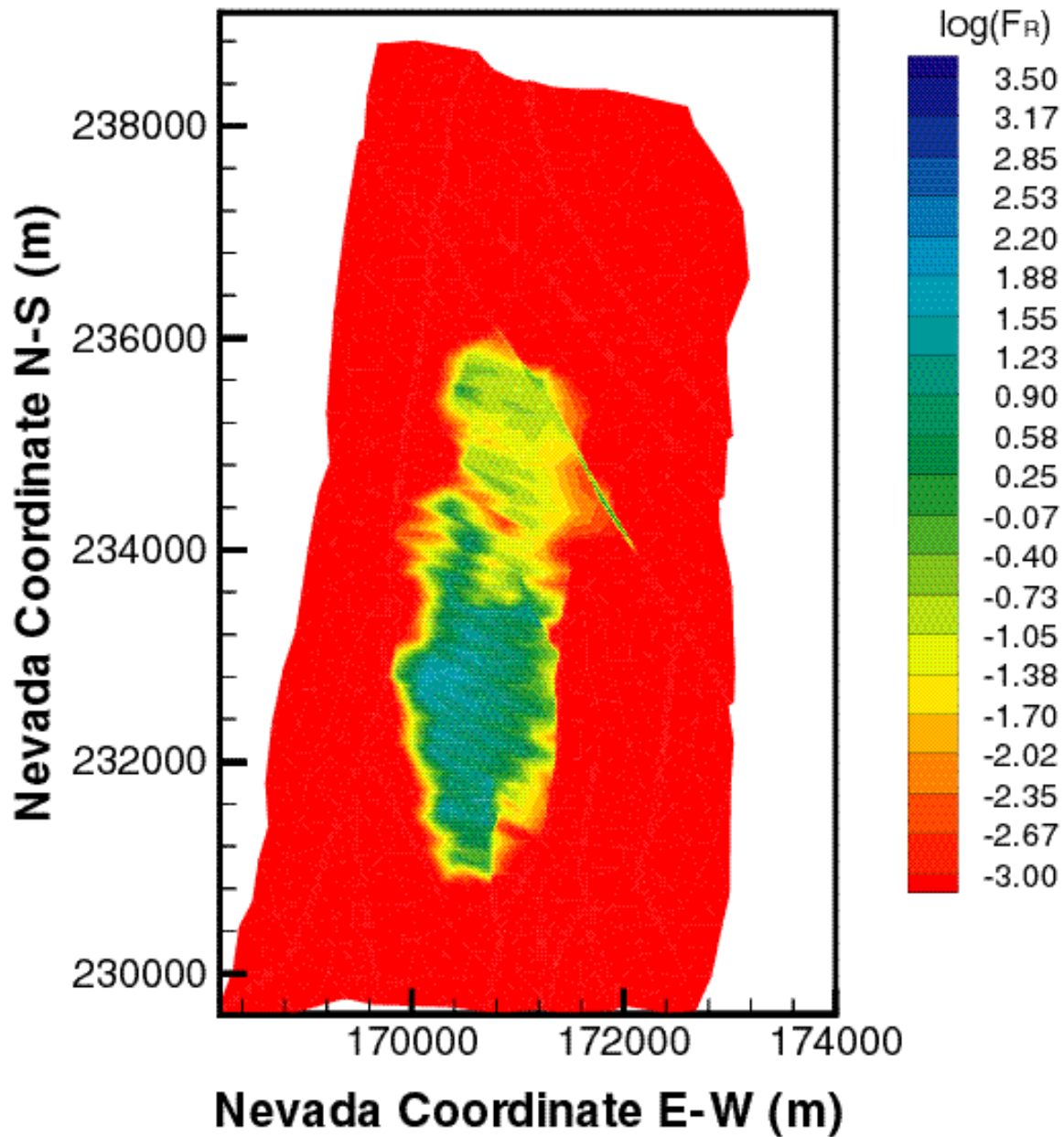


Figure VII.6. Distribution of the relative sorbed concentration F_R of ^{237}Np in the matrix of the tsw39 layer at $t = 1,000$ years for mean present-day infiltration (DTN: LB991220140160.012, data submitted with this AMR).

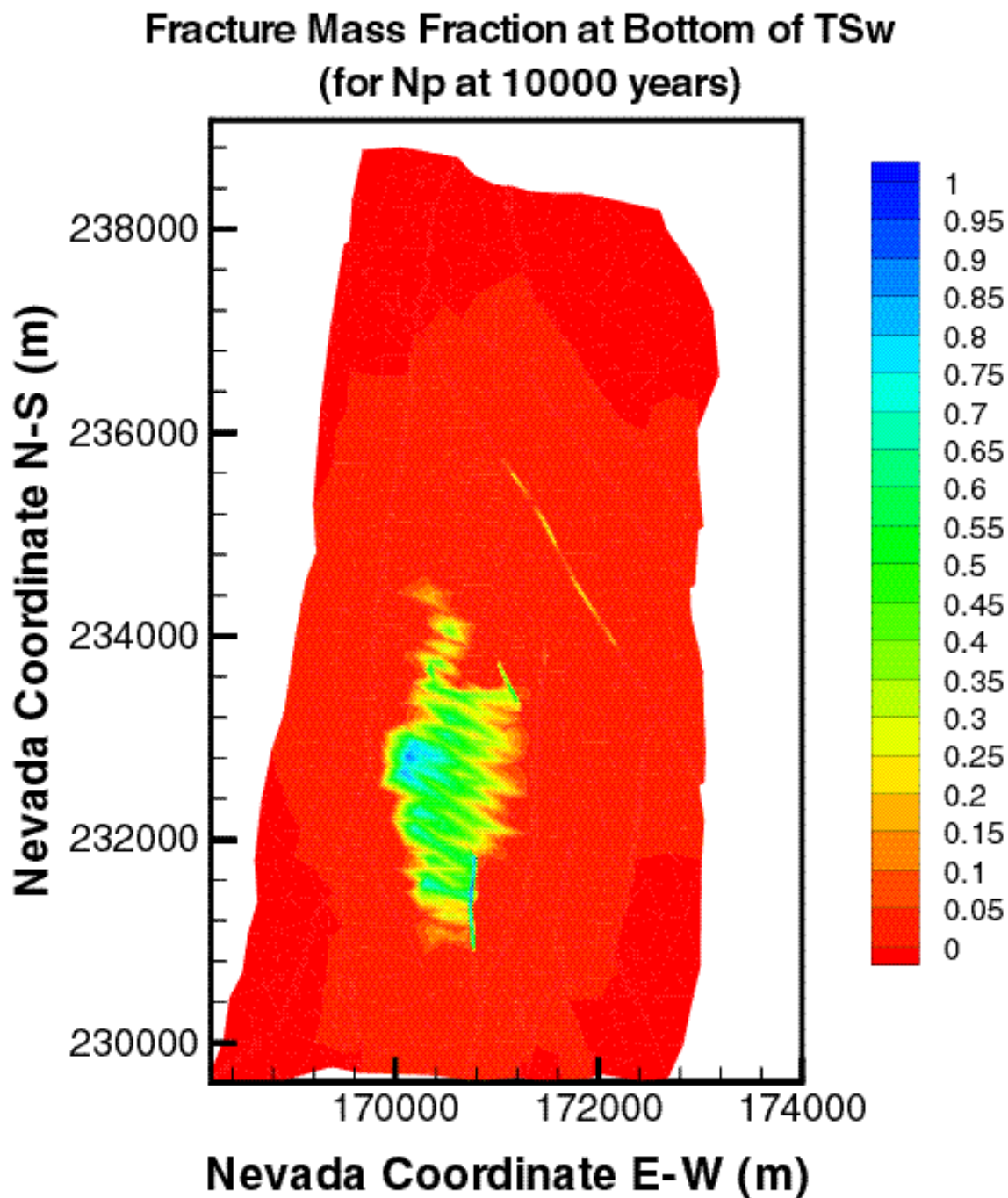


Figure VII.7. Distribution of the relative mass fraction X_R of ^{237}Np in the fractures of the tsw39 layer at $t = 10,000$ years for mean present-day infiltration (DTN: LB991220140160.012, data submitted with this AMR).

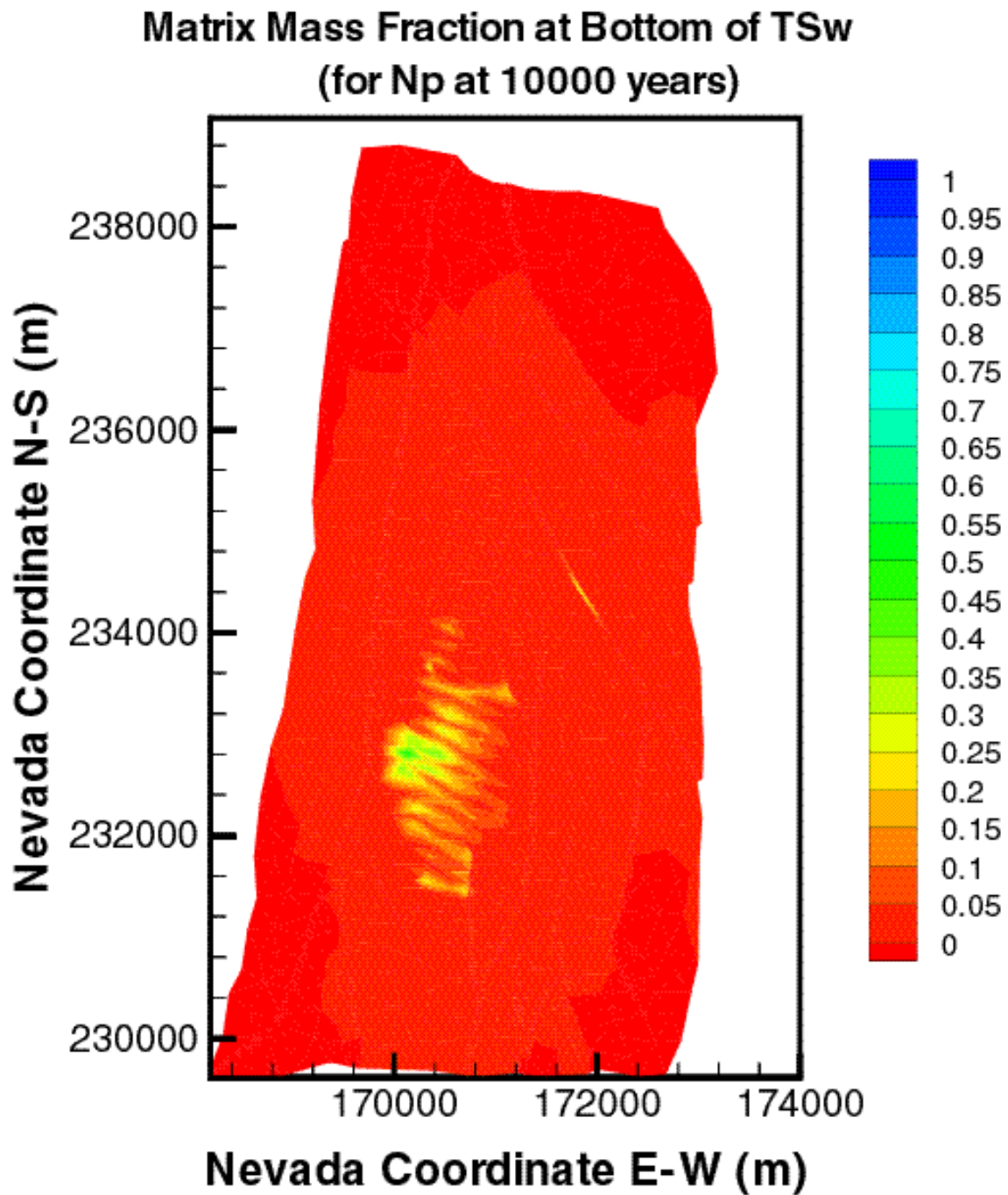


Figure VII.8. Distribution of the relative mass fraction X_R of ^{237}Np in the matrix of the tsw39 layer at $t = 10,000$ years for mean present-day infiltration (DTN: LB991220140160.012, data submitted with this AMR).

**Matrix Sorbed Concentration at Bottom of TSw (kg/m³)
(for Np at 10000 years)**

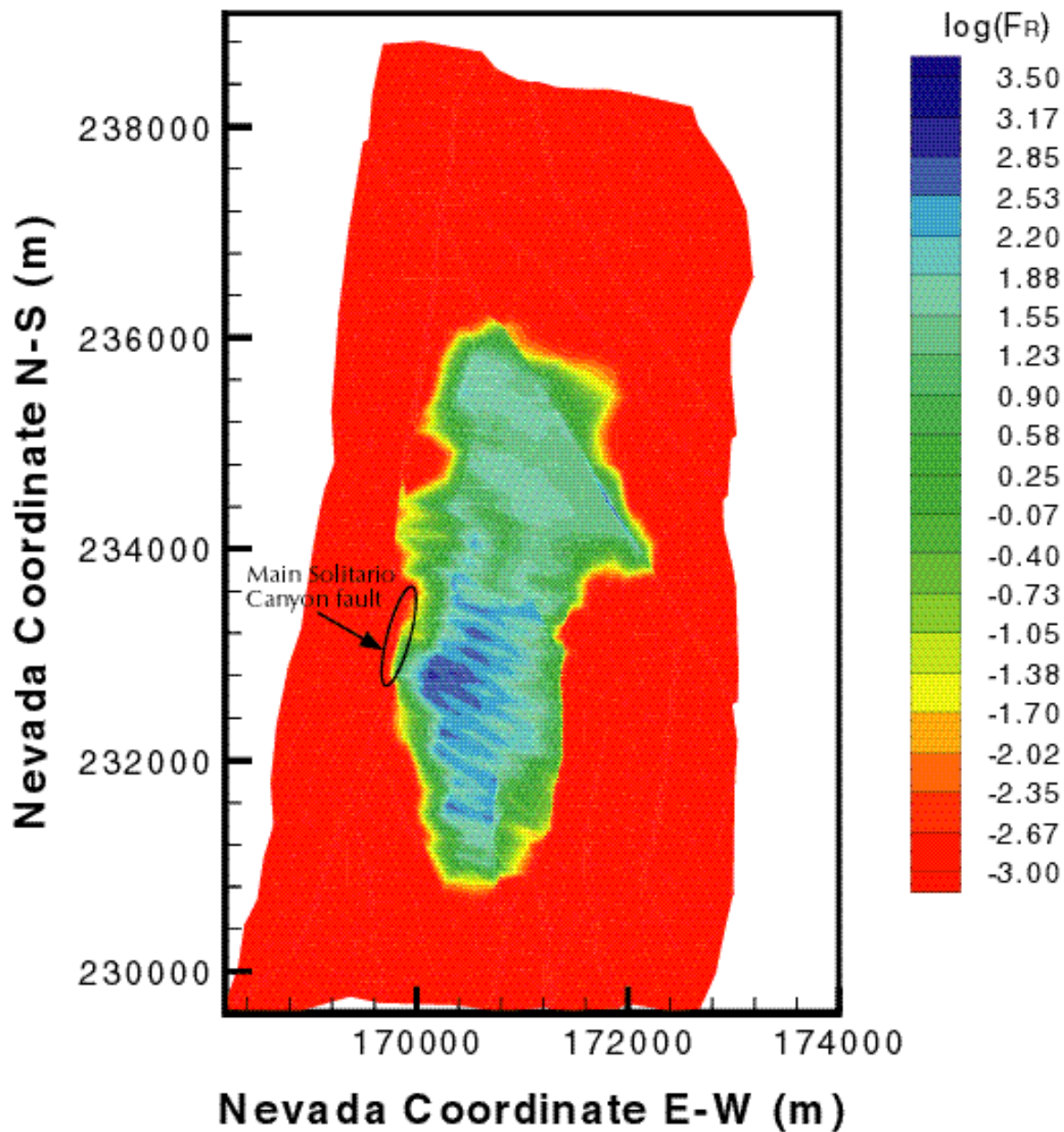


Figure VII.9. Distribution of the relative sorbed concentration F_R of ^{237}Np in the matrix of the tsw39 layer at $t = 10,000$ years for mean present-day infiltration (DTN: LB991220140160.012, data submitted with this AMR).

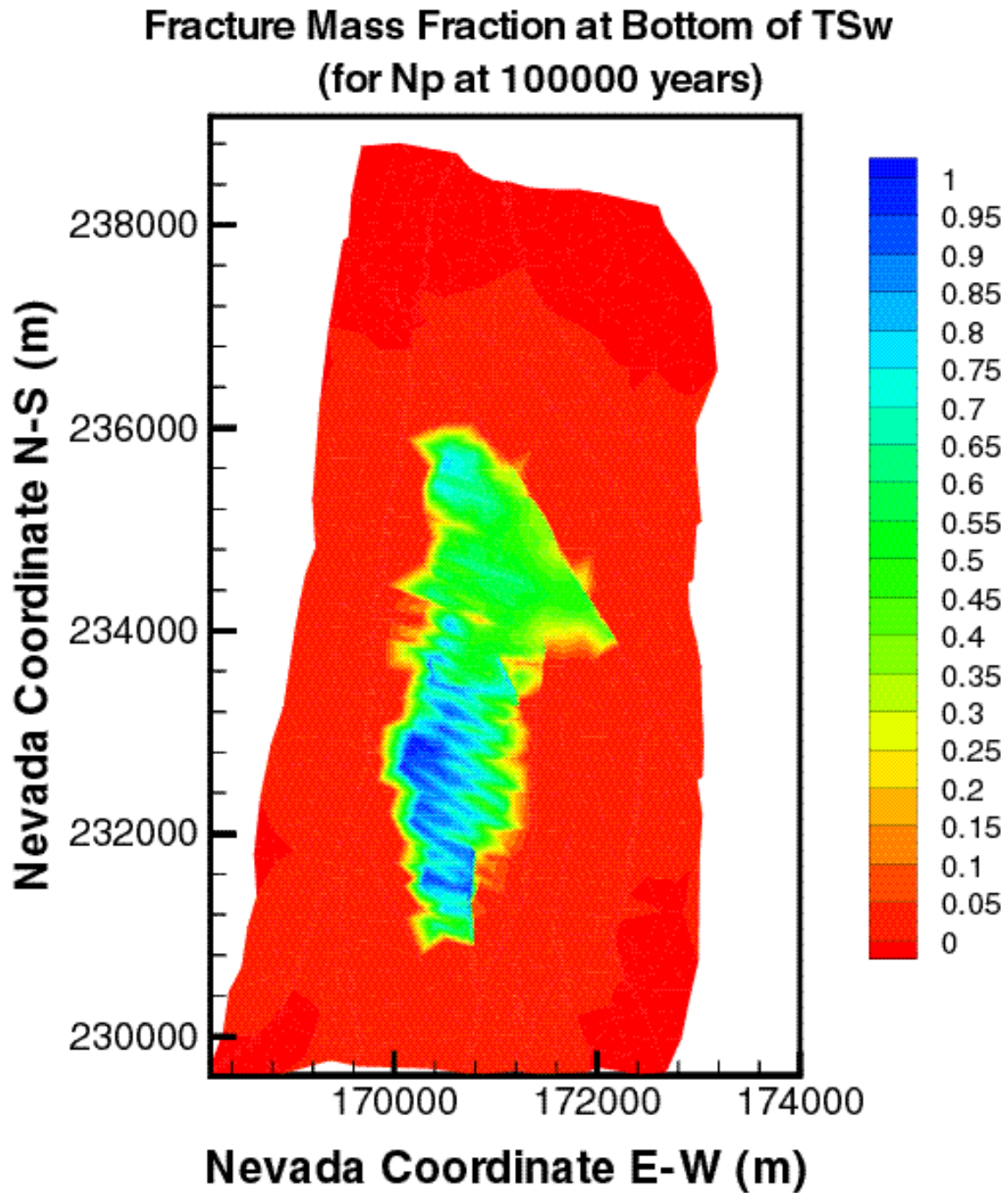


Figure VII.10. Distribution of the relative mass fraction X_R of ^{237}Np in the fractures of the tsw39 layer at $t = 100,000$ years for mean present-day infiltration (DTN: LB991220140160.012, data submitted with this AMR).

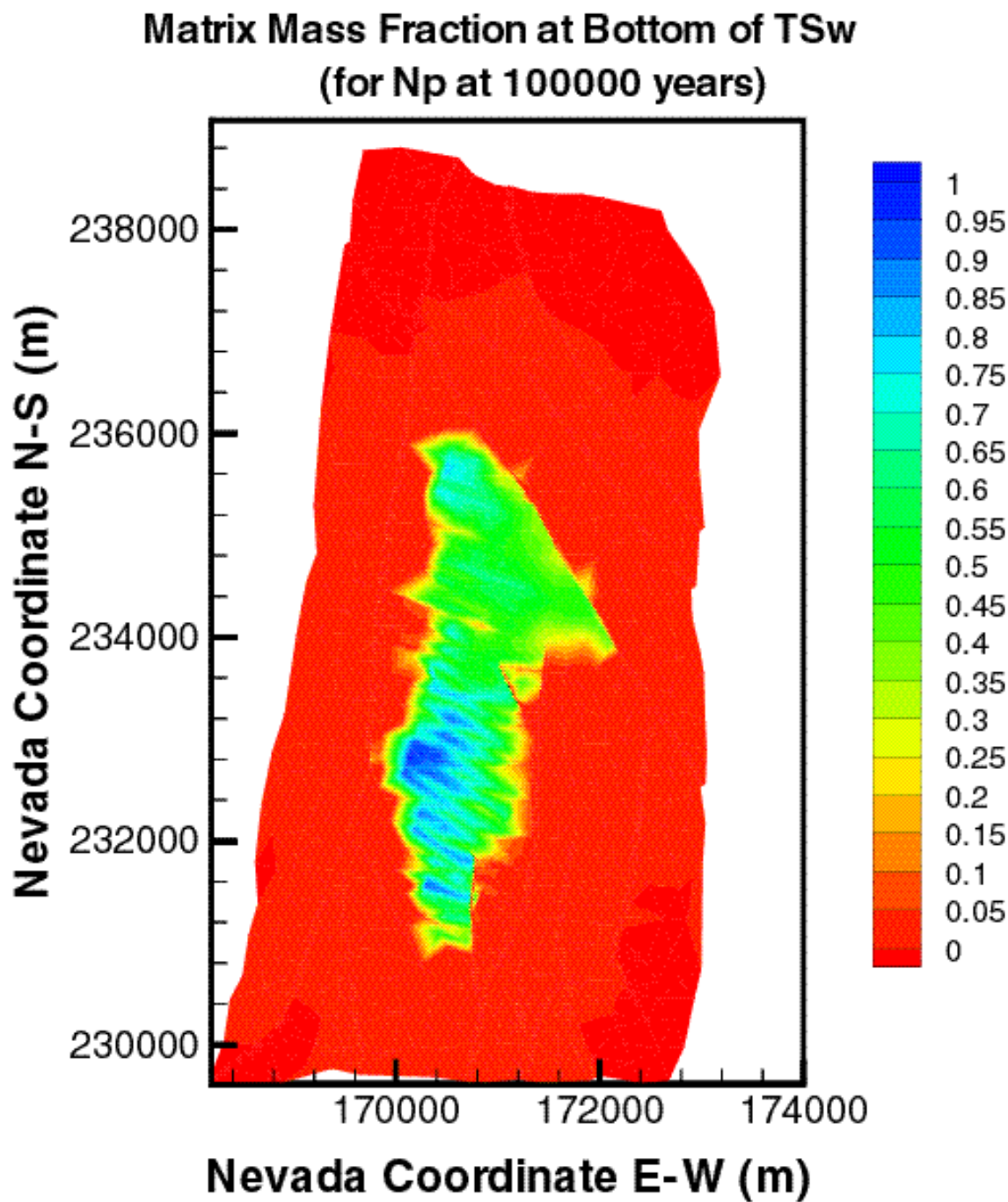


Figure VII.11. Distribution of the relative mass fraction X_R of ^{237}Np in the matrix of the tsw39 layer at $t = 100,000$ years for mean present-day infiltration (DTN: LB991220140160.012, data submitted with this AMR).

**Matrix Sorbed Concentration at Bottom of TSw (kg/m³)
(for Np at 100000 years)**

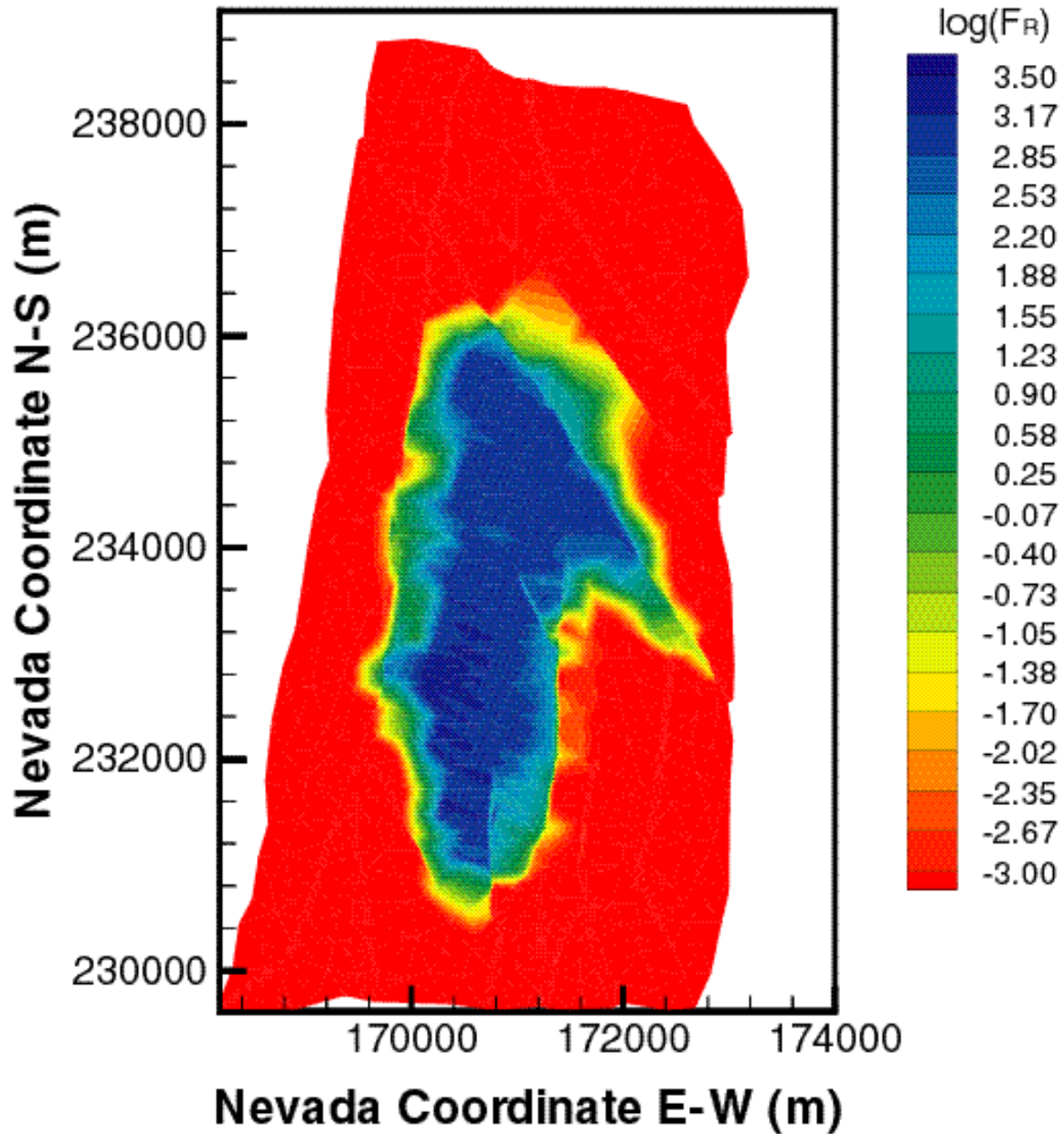


Figure VII.12. Distribution of the relative sorbed concentration F_R of ^{237}Np in the matrix of the tsw39 layer at $t = 100,000$ years for mean present-day infiltration (DTN: LB991220140160.012, data submitted with this AMR).

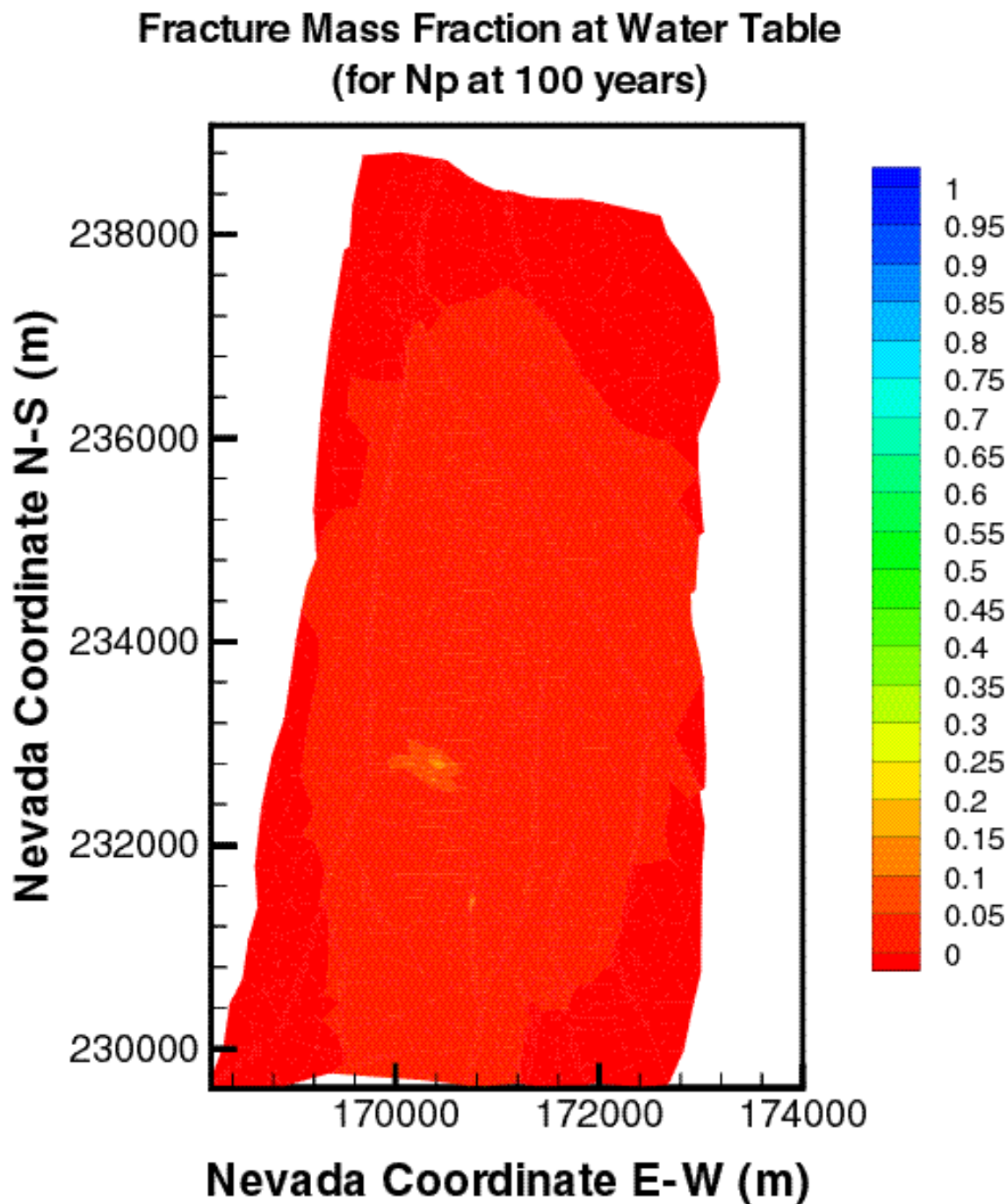


Figure VII.13. Distribution of the relative mass fraction X_R of ^{237}Np in the fractures immediately above the groundwater table at $t = 100$ years for mean present-day infiltration (DTN: LB991220140160.012, data submitted with this AMR).

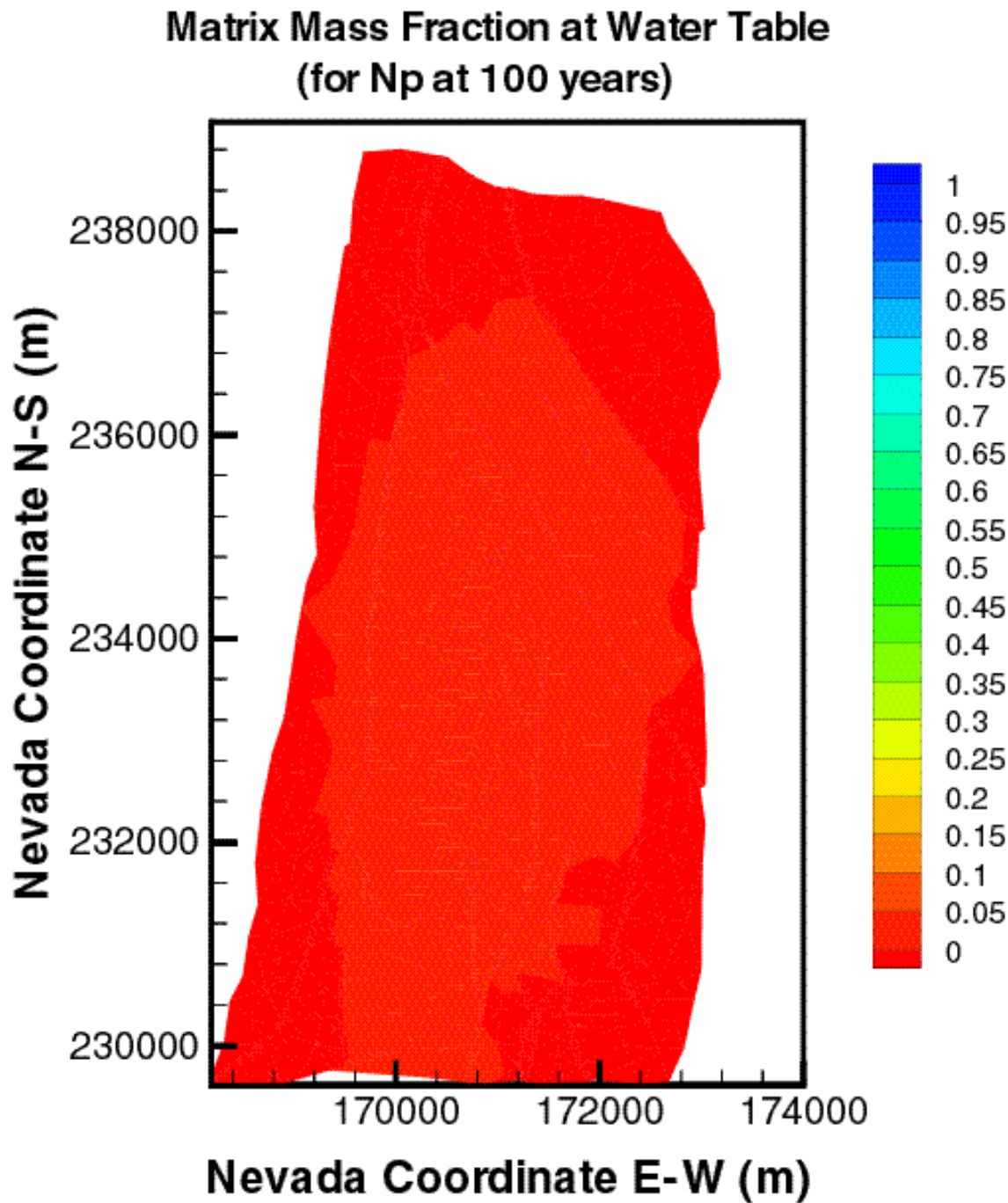


Figure VII.14. Distribution of the relative mass fraction X_R of ^{237}Np in the matrix immediately above the groundwater at $t = 100$ years for mean present-day infiltration (DTN: LB991220140160.012, data submitted with this AMR).

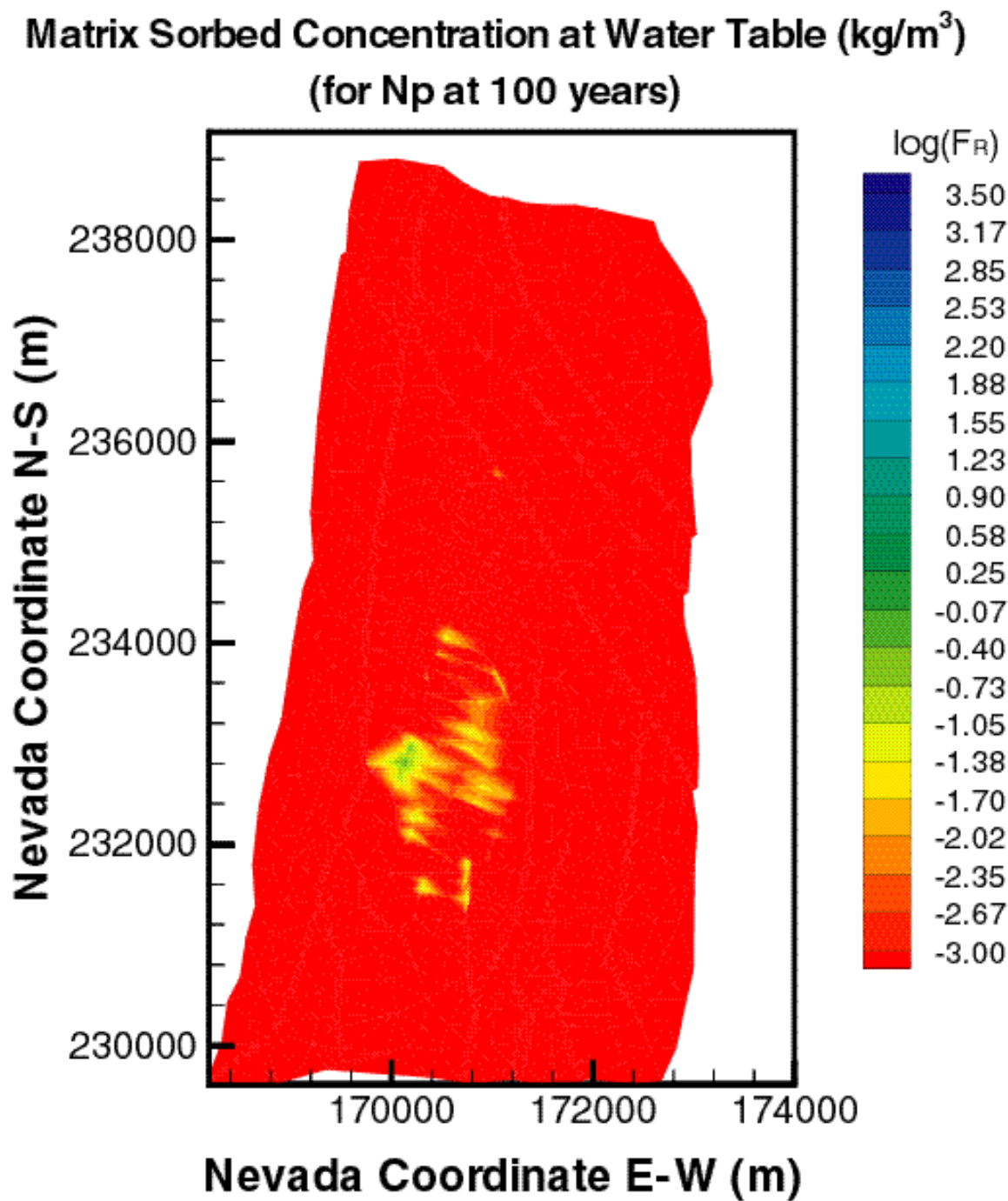


Figure VII.15. Distribution of the relative sorbed concentration F_R of ^{237}Np in the matrix immediately above the groundwater at $t = 100$ years for mean present-day infiltration (DTN: LB991220140160.012, data submitted with this AMR).

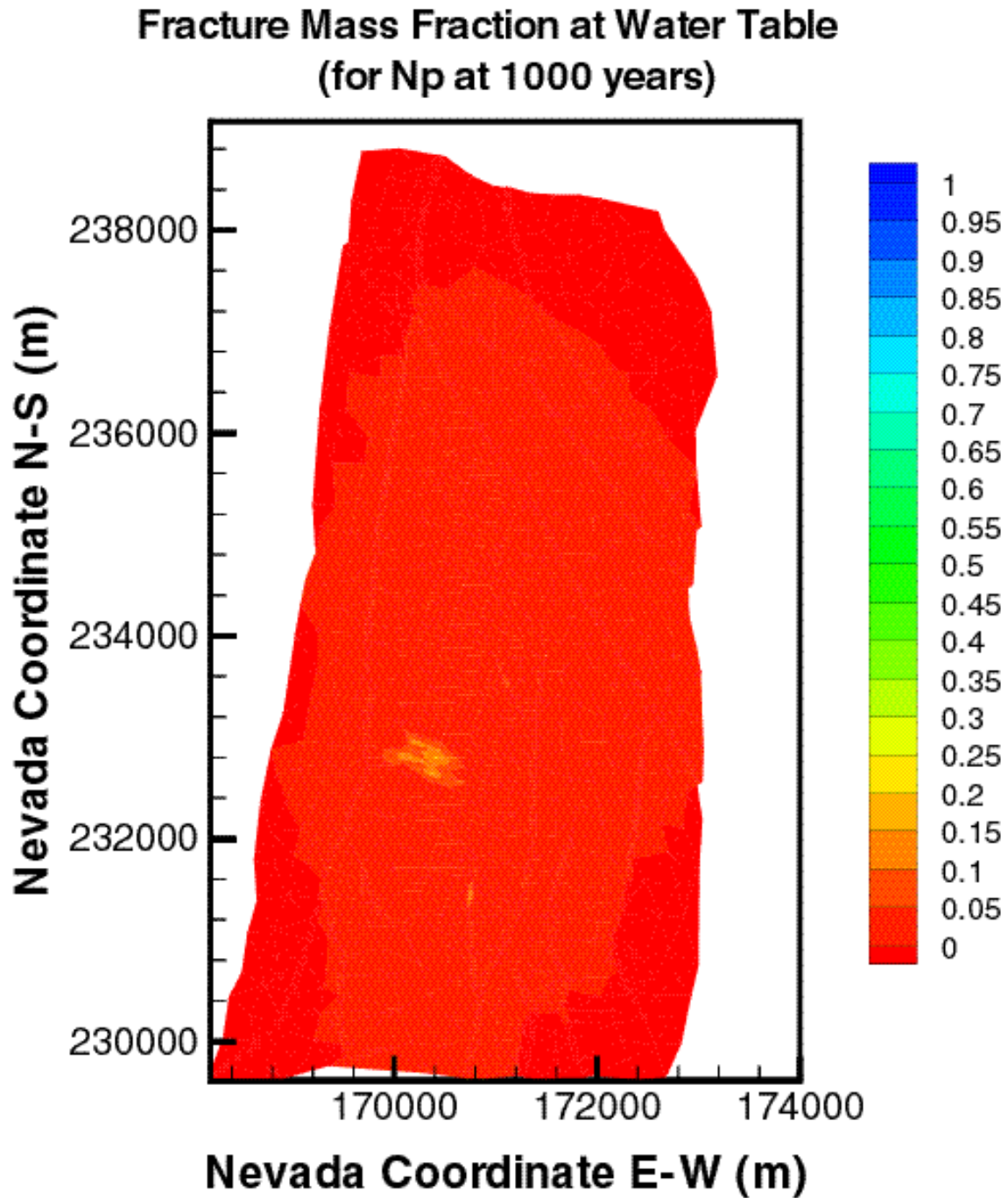


Figure VII.16. Distribution of the relative mass fraction X_R of ^{237}Np in the fractures immediately above the groundwater at $t = 1,000$ years for mean present-day infiltration (DTN: LB991220140160.012, data submitted with this AMR).

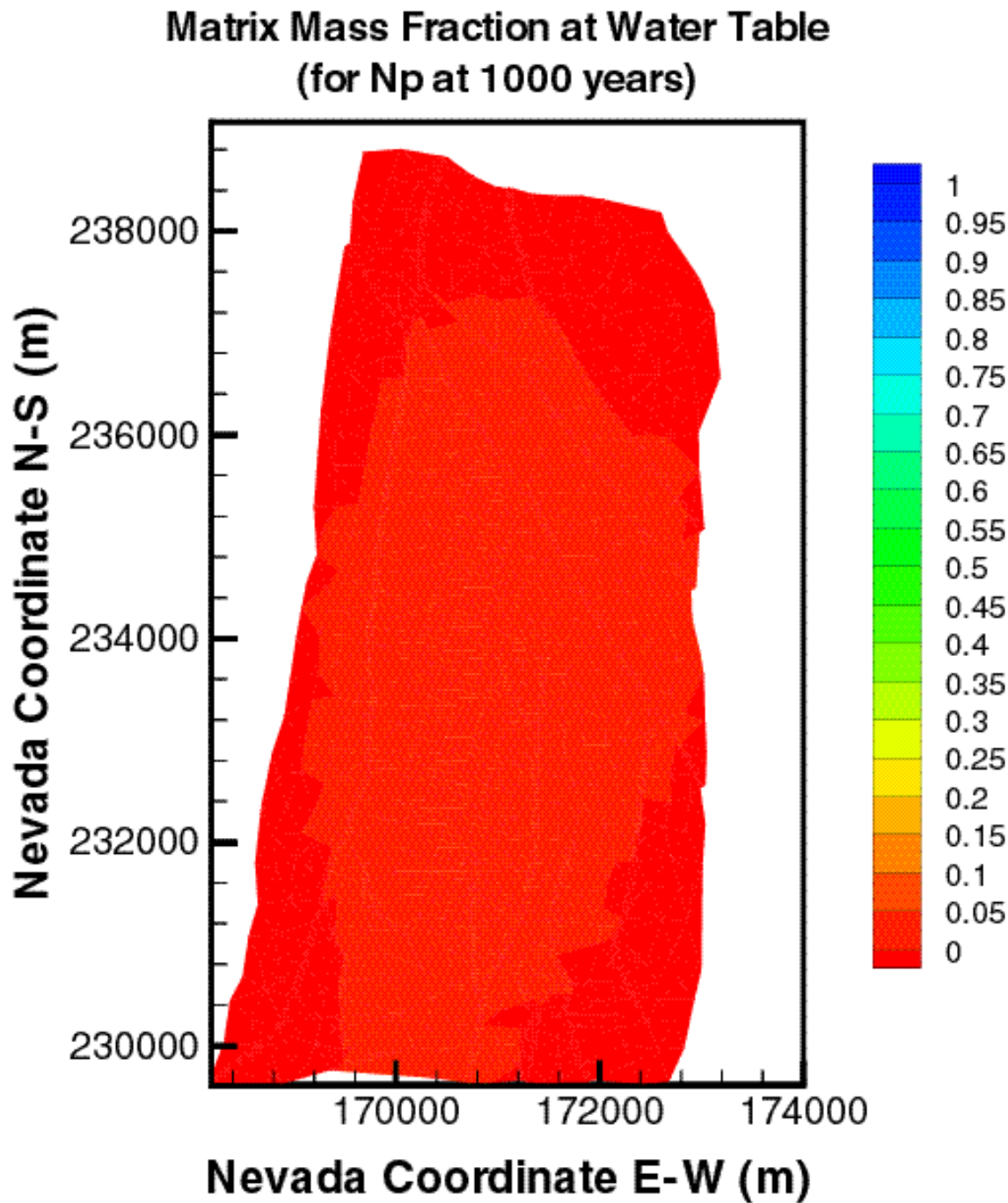


Figure VII.17. Distribution of the relative mass fraction X_R of ^{237}Np in the matrix immediately above the groundwater at $t = 1,000$ years for mean present-day infiltration (DTN: LB991220140160.012, data submitted with this AMR).

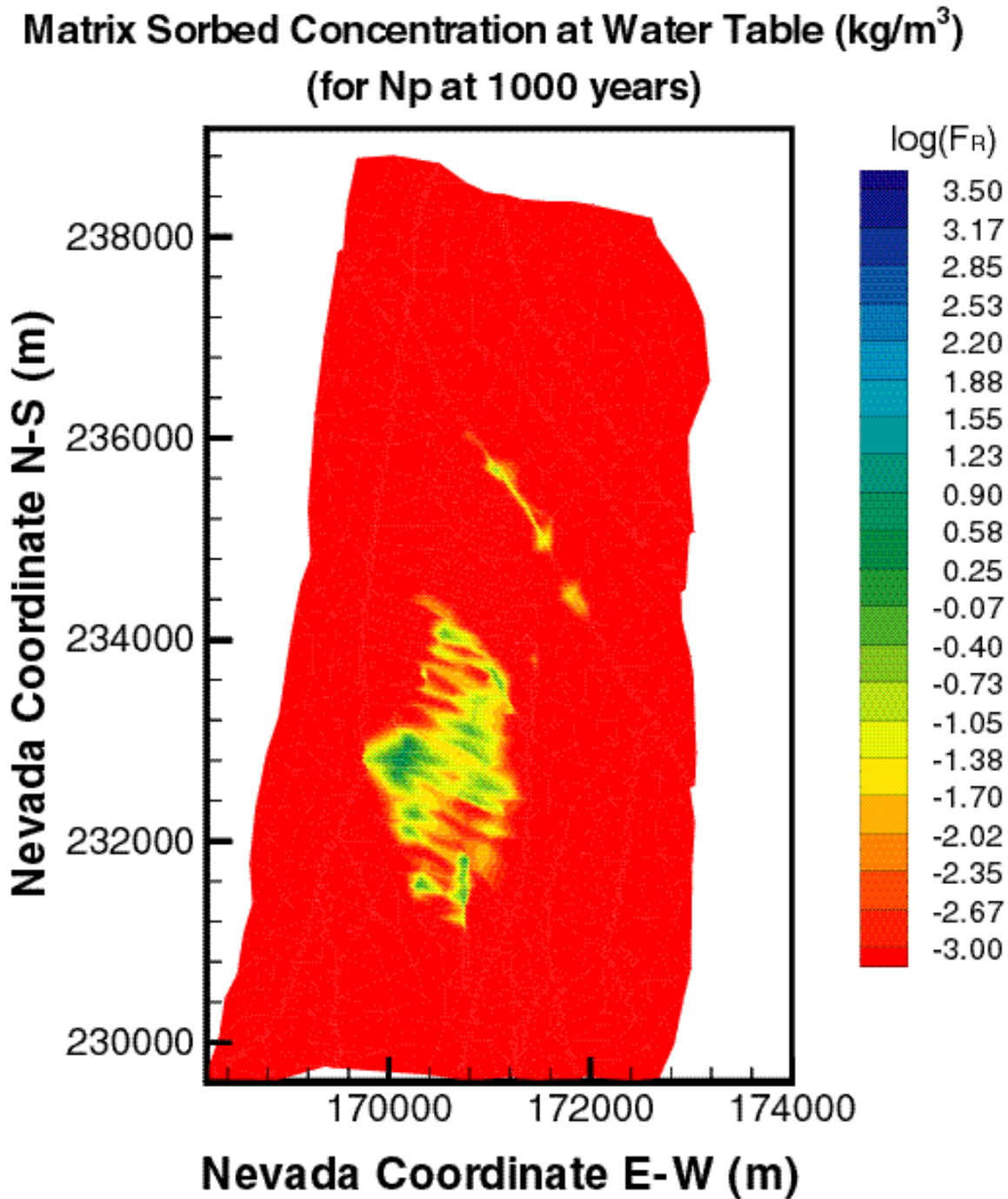


Figure VII.18. Distribution of the relative sorbed concentration F_R of ^{237}Np in the matrix immediately above the groundwater at $t=1,000$ years for mean present-day infiltration (DTN: LB991220140160.012, data submitted with this AMR).

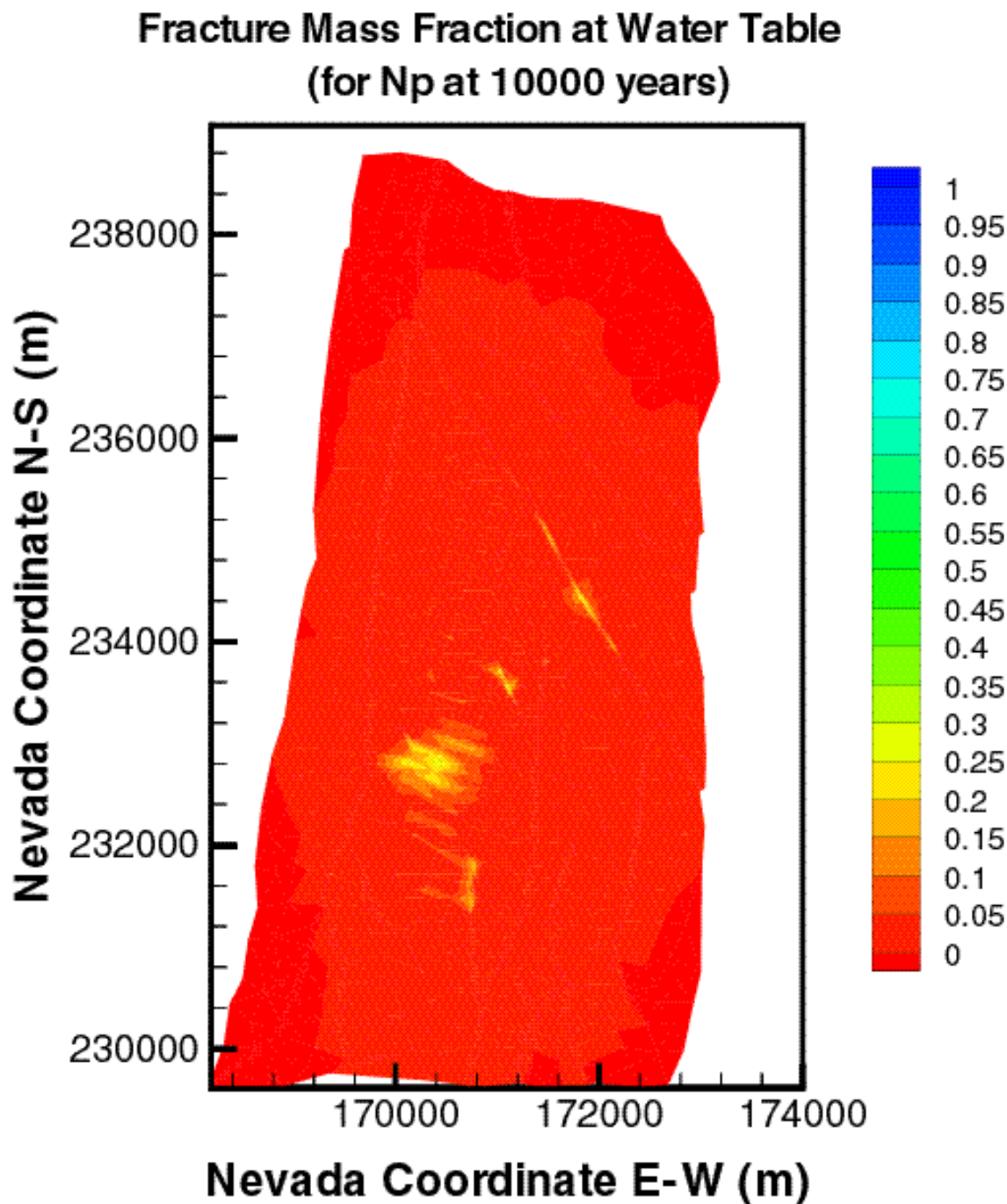


Figure VII.19. Distribution of the relative mass fraction X_R of ^{237}Np in the fractures immediately above the groundwater at $t = 10,000$ years for mean present-day infiltration (DTN: LB991220140160.012, data submitted with this AMR).

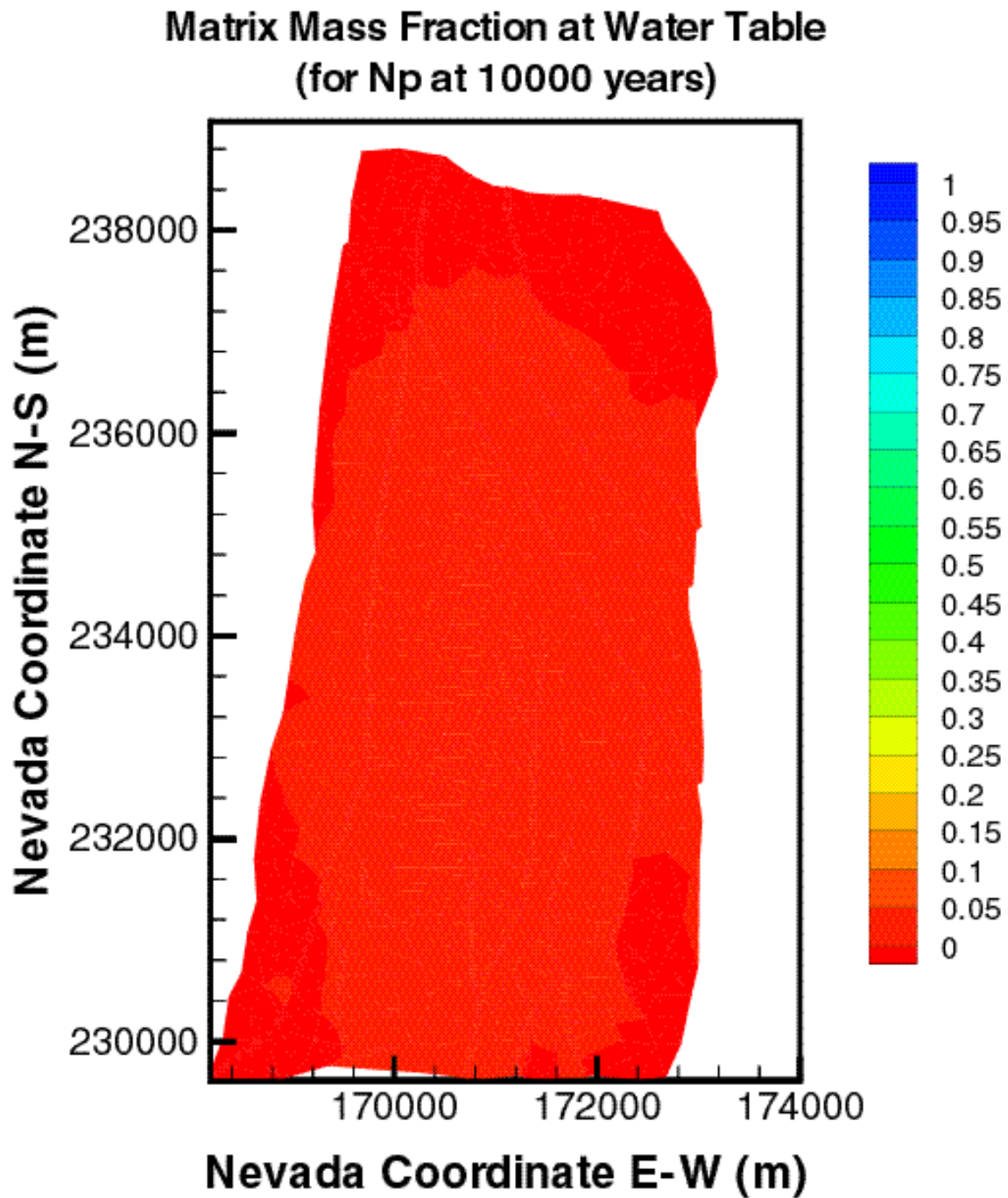


Figure VII.20. Distribution of the relative mass fraction X_R of ^{237}Np in the matrix immediately above the groundwater at $t = 10,000$ years for mean present-day infiltration (DTN: LB991220140160.012, data submitted with this AMR).

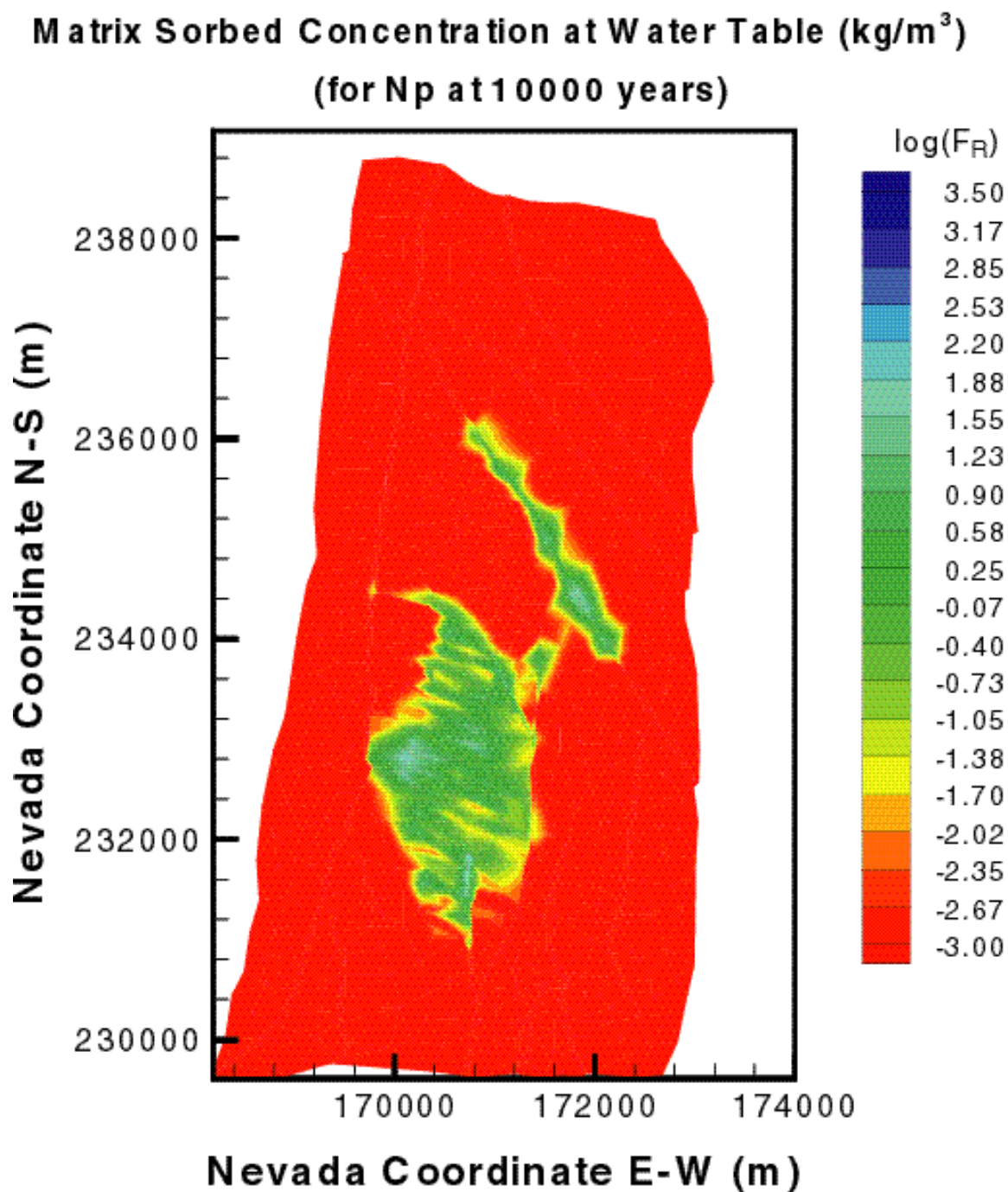


Figure VII.21. Distribution of the relative sorbed concentration F_R of ^{237}Np in the matrix immediately above the groundwater at $t = 10,000$ years for mean present-day infiltration (DTN: LB991220140160.012, data submitted with this AMR).

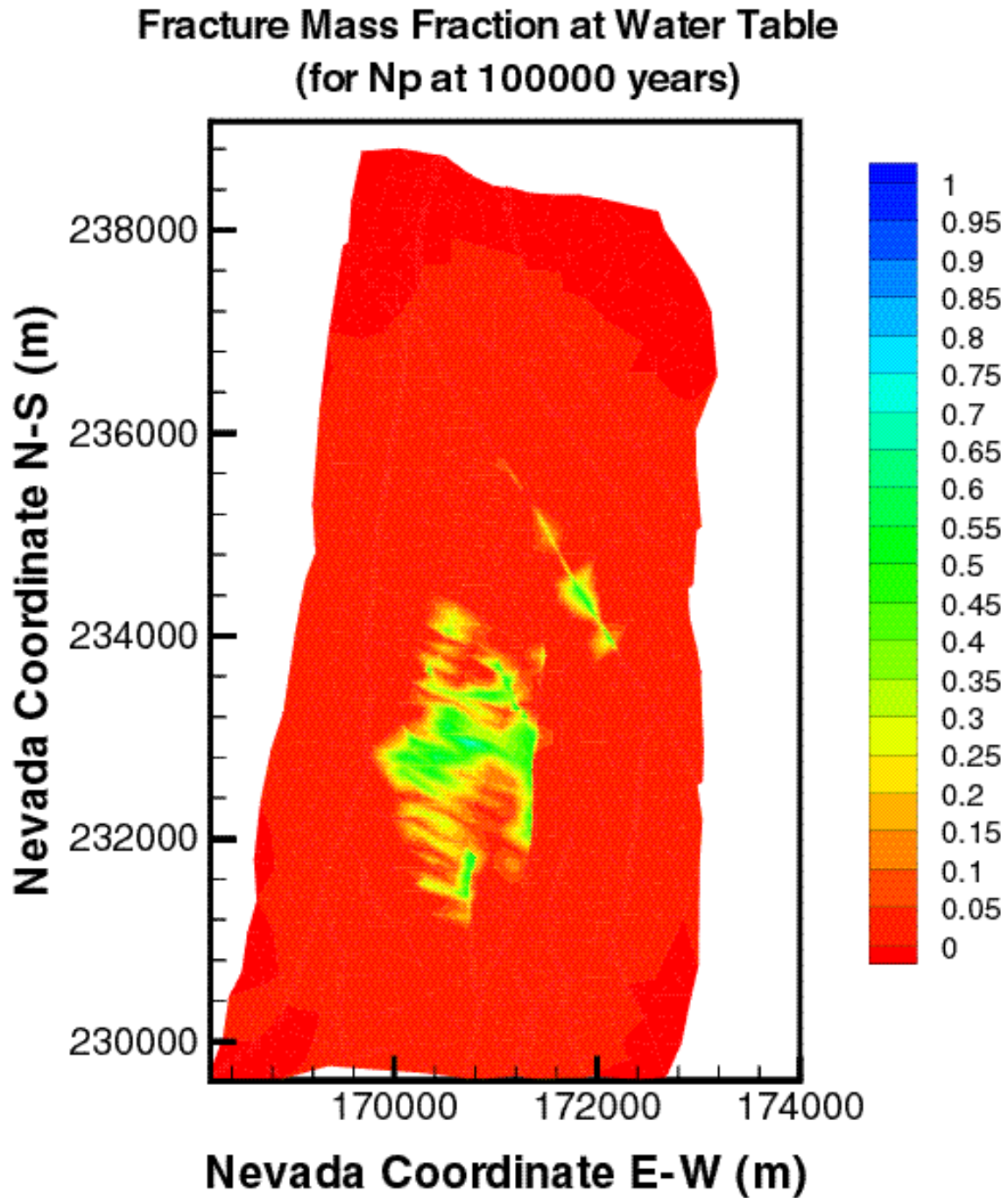


Figure VII.22. Distribution of the relative mass fraction X_R of ^{237}Np in the fractures immediately above the groundwater at $t = 100,000$ years for mean present-day infiltration (DTN: LB991220140160.012, data submitted with this AMR).

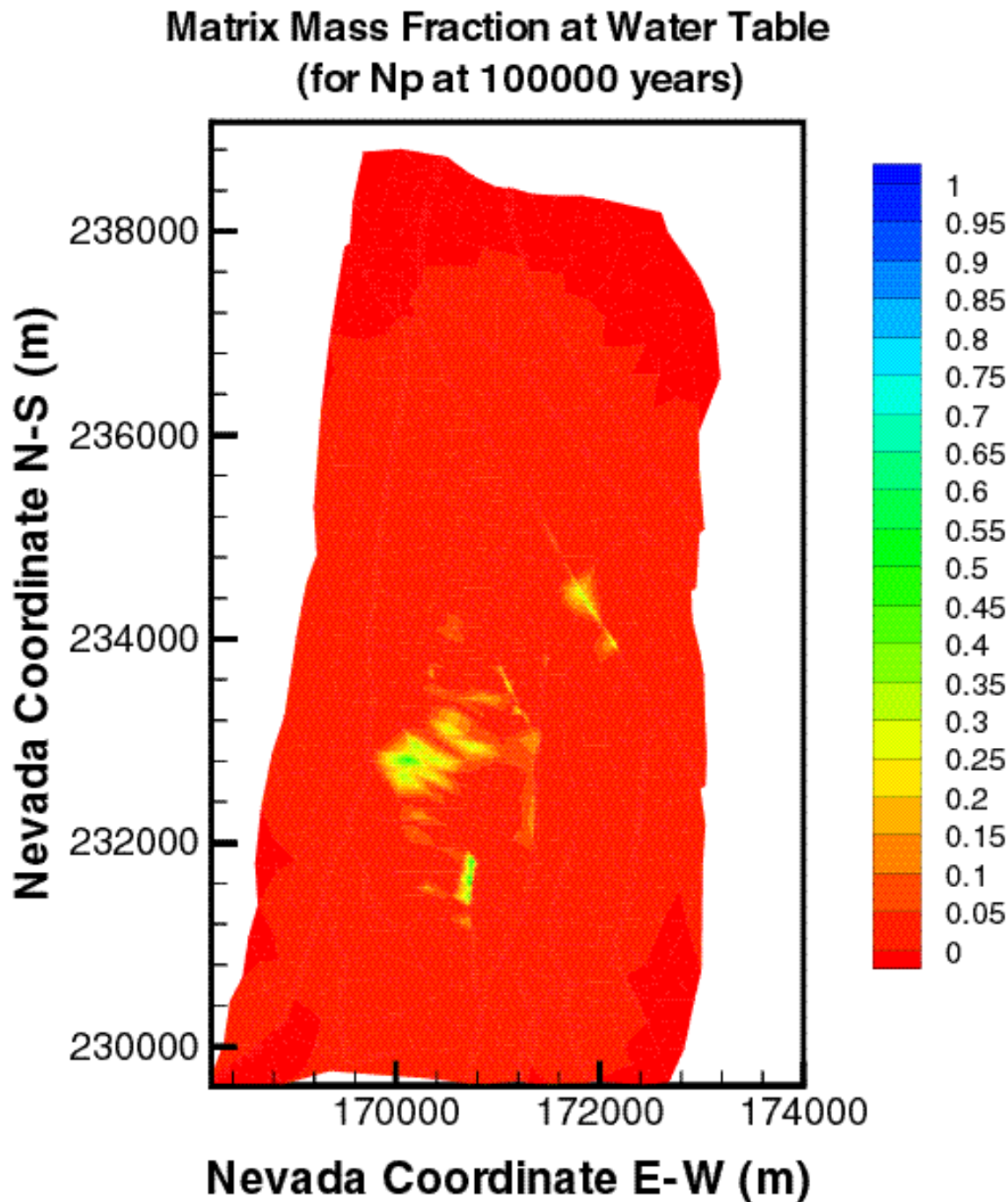


Figure VII.23. Distribution of the relative mass fraction X_R of ^{237}Np in the matrix immediately above the groundwater at $t = 100,000$ years for mean present-day infiltration (DTN: LB991220140160.012, data submitted with this AMR).

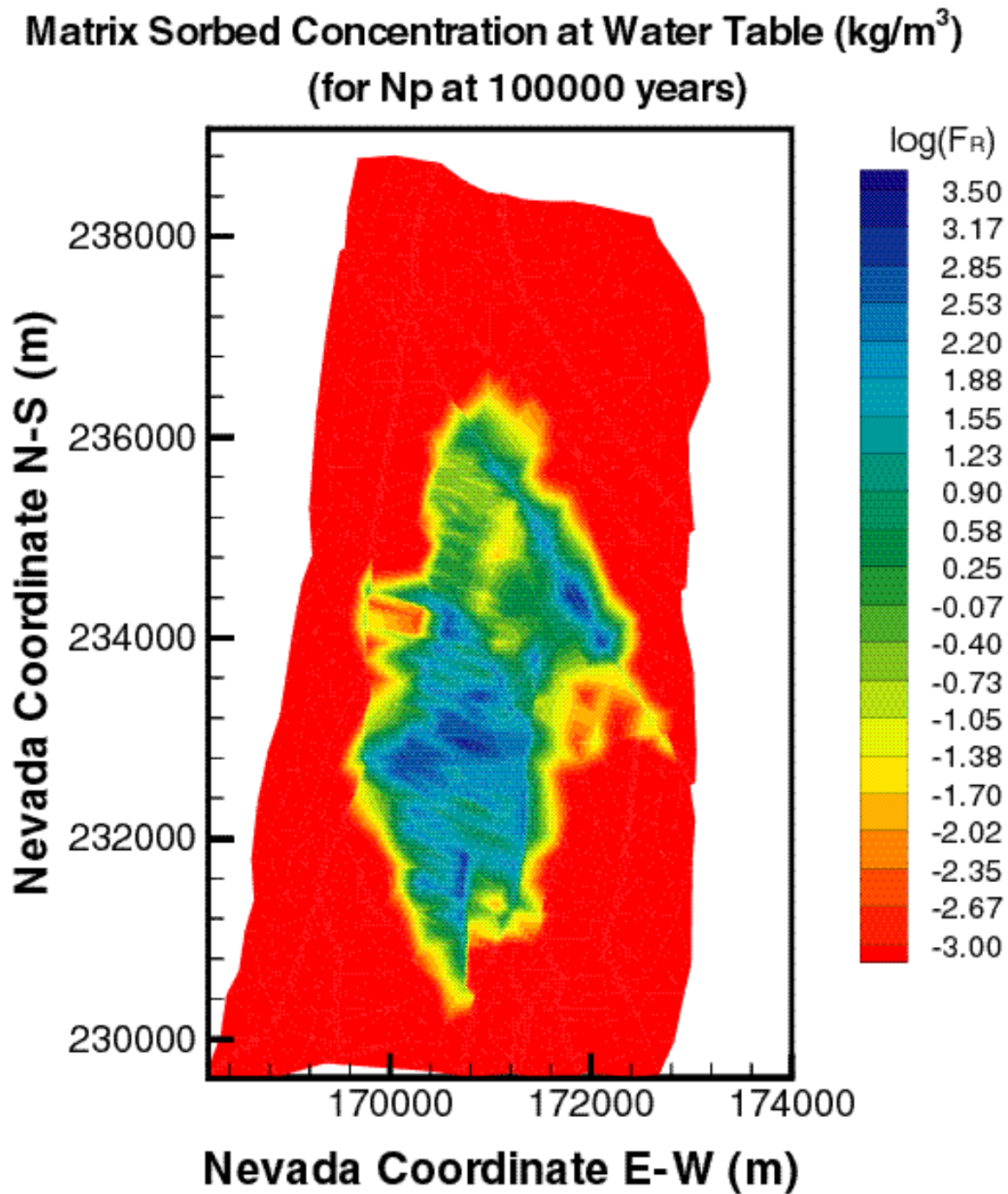


Figure VII.24. Distribution of the relative sorbed concentration F_R of ^{237}Np in the matrix immediately above the groundwater at $t = 100,000$ years for mean present-day infiltration (DTN: LB991220140160.012, data submitted with this AMR).

ATTACHMENT VIII.

FIGURES FROM THE ^{239}Pu 3-D TRANSPORT STUDIES

INTENTIONALLY LEFT BLANK

FIGURES

	Page
VIII.1. Distribution of the Relative Mass Fraction X_R of ^{239}Pu in the Fractures of the Tsw39 Layer at $t = 100$ Years for Mean Present-Day Infiltration.....	VIII-5
VIII.2. Distribution of the Relative Mass Fraction X_R of ^{239}Pu in the Matrix of the Tsw39 Layer at $t = 100$ Years for Mean Present-Day Infiltration.....	VIII-6
VIII.3. Distribution of the Relative Sorbed Concentration F_R of ^{239}Pu in the Matrix of the Tsw39 Layer at $t = 100$ Years for Mean Present-Day Infiltration.....	VIII-7
VIII.4. Distribution of the Relative Mass Fraction X_R of ^{239}Pu in the Fractures of the Tsw39 Layer at $t = 1,000$ Years for Mean Present-Day Infiltration.....	VIII-8
VIII.5. Distribution of the Relative Mass Fraction X_R of ^{239}Pu in the Matrix of the Tsw39 Layer at $t = 1,000$ Years for Mean Present-Day Infiltration.....	VIII-9
VIII.6. Distribution of the Relative Sorbed Concentration F_R of ^{239}Pu in the Matrix of the Tsw39 Layer at $t = 1,000$ Years for Mean Present-Day Infiltration.....	VIII-10
VIII.7. Distribution of the Relative Mass Fraction X_R of ^{239}Pu in the Fractures of the Tsw39 Layer at $t = 10,000$ Years for Mean Present-Day Infiltration.....	VIII-11
VIII.8. Distribution of the Relative Mass Fraction X_R of ^{239}Pu in the Matrix of the Tsw39 Layer at $t = 10,000$ Years for Mean Present-Day Infiltration.....	VIII-12
VIII.9. Distribution of the Relative Sorbed Concentration F_R of ^{239}Pu in the Matrix of the Tsw39 Layer at $t = 10,000$ Years for Mean Present-Day Infiltration.....	VIII-13
VIII.10. Distribution of the Relative Mass Fraction X_R of ^{239}Pu in the Fractures of the Tsw39 Layer at $t = 100,000$ Years for Mean Present-Day Infiltration.....	VIII-14
VIII.11. Distribution of the Relative Mass Fraction X_R of ^{239}Pu in the Matrix of the Tsw39 Layer at $t = 100,000$ Years for Mean Present-Day Infiltration.....	VIII-15
VIII.12. Distribution of the Relative Sorbed Concentration F_R of ^{239}Pu in the Matrix of the Tsw39 Layer at $t = 100,000$ Years for Mean Present-Day Infiltration.....	VIII-16
VIII.13. Distribution of the Relative Mass Fraction X_R of ^{239}Pu in the Fractures Immediately Above the Groundwater at $t = 100$ Years for Mean Present-Day Infiltration.....	VIII-17

FIGURES (Continued)

	Page
VIII.14. Distribution of the Relative Mass Fraction X_R of ^{239}Pu in the Matrix Immediately Above the Groundwater Table at $t = 100$ Years for a Mean Present-Day Infiltration.....	VIII-18
VIII.15. Distribution of the Relative Sorbed Concentration F_R of ^{239}Pu in the Matrix Immediately Above the Groundwater Table at $t = 100$ Years for a Mean Present-Day Infiltration.....	VIII-19
VIII.16. Distribution of the Relative Mass Fraction X_R of ^{239}Pu in the Fractures Immediately Above the Groundwater at $t = 1,000$ Years for Mean Present-Day Infiltration.....	VIII-20
VIII.17. Distribution of the Relative Mass Fraction X_R of ^{239}Pu in the Matrix Immediately Above the Groundwater Table at $t = 1,000$ Years for a Mean Present-Day Infiltration.....	VIII-21
VIII.18. Distribution of the Relative Sorbed Concentration F_R of ^{239}Pu in the Matrix Immediately Above the Groundwater Table at $t = 1,000$ Years for a Mean Present-Day Infiltration.....	VIII-22
VIII.19. Distribution of the Relative Mass Fraction X_R of ^{239}Pu in the Fractures Immediately Above the Groundwater at $t = 10,000$ Years for Mean Present-Day Infiltration.....	VIII-23
VIII.20. Distribution of the Relative Mass Fraction X_R of ^{239}Pu in the Matrix Immediately Above the Groundwater Table at $t = 10,000$ Years for a Mean Present-Day Infiltration.....	VIII-24
VIII.21. Distribution of the Relative Sorbed Concentration F_R of ^{239}Pu in the Matrix Immediately Above the Groundwater Table at $t = 10,000$ Years for a Mean Present-Day Infiltration.....	VIII-25
VIII.22. Distribution of the Relative Mass Fraction X_R of ^{239}Pu in the Fractures Immediately Above the Groundwater at $t = 100,000$ Years for Mean Present-Day Infiltration.....	VIII-26
VIII.23. Distribution of the Relative Mass Fraction X_R of ^{239}Pu in the Matrix Immediately Above the Groundwater Table at $t = 100,000$ Years for a Mean Present-Day Infiltration.....	VIII-27
VIII.24. Distribution of the Relative Sorbed Concentration F_R of ^{239}Pu in the Matrix Immediately Above the Groundwater Table at $t = 100,000$ Years for a Mean Present-Day Infiltration.....	VIII-28

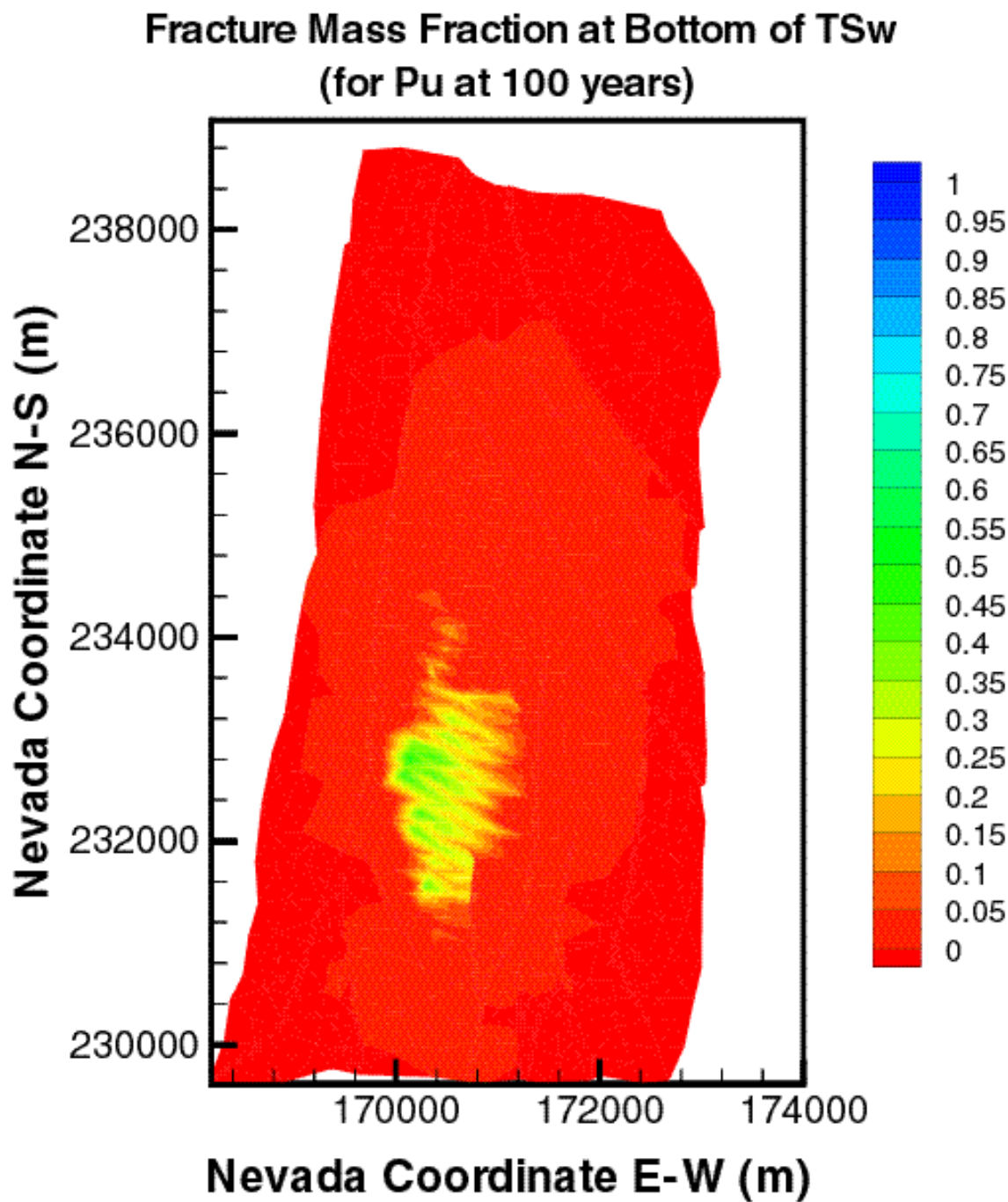


Figure VIII.1. Distribution of the relative mass fraction X_R of ^{239}Pu in the fractures of the tsw39 layer at $t = 100$ years for mean present-day infiltration (DTN: LB991220140160.012, data submitted with this AMR).

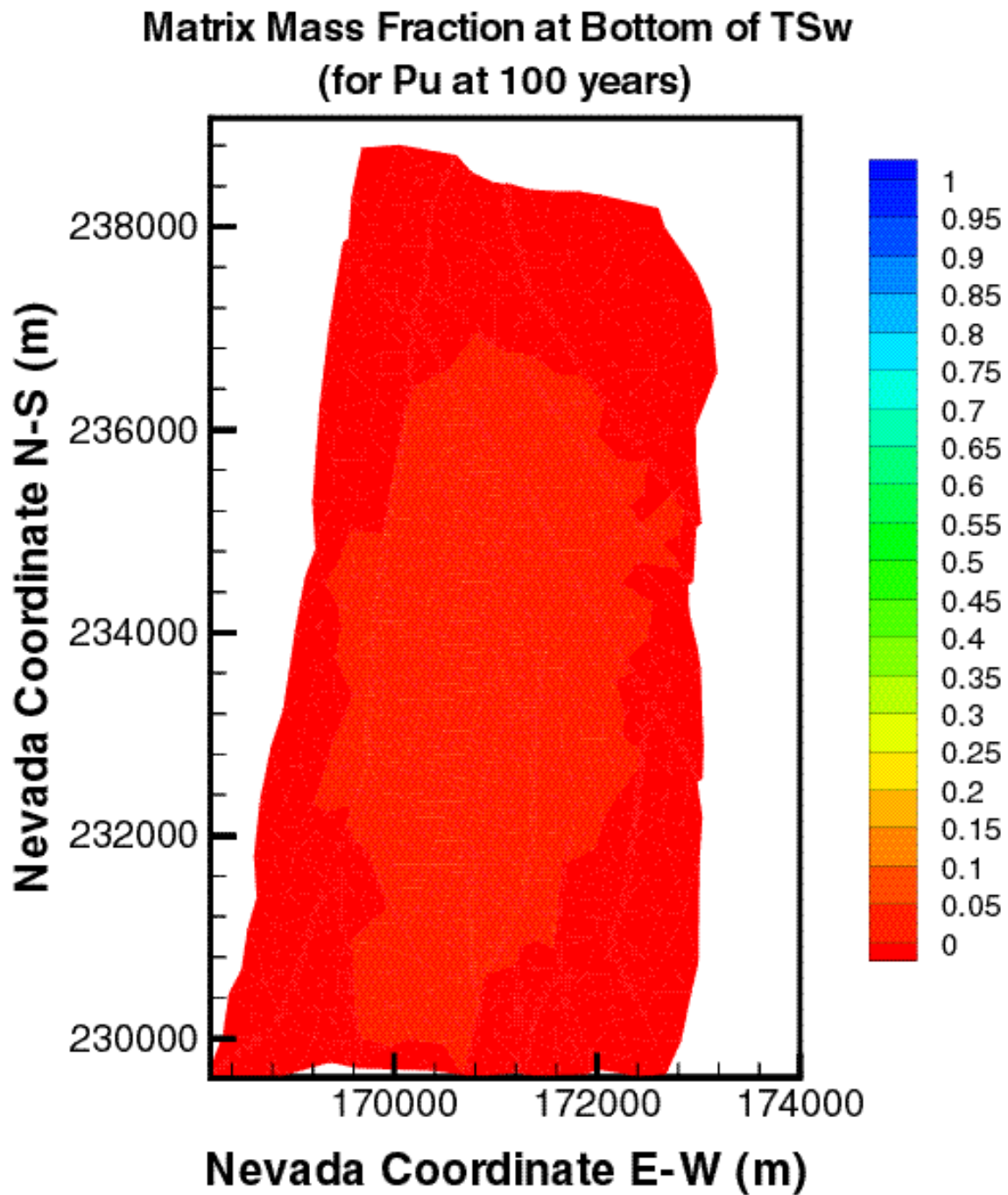


Figure VIII.2. Distribution of the relative mass fraction X_R of ^{239}Pu in the matrix of the TSw layer at $t = 100$ years for mean present-day infiltration (DTN: LB991220140160.012, data submitted with this AMR).

**Matrix Sorbed Concentration at Bottom of TSw (kg/m³)
(for Pu at 100 years)**

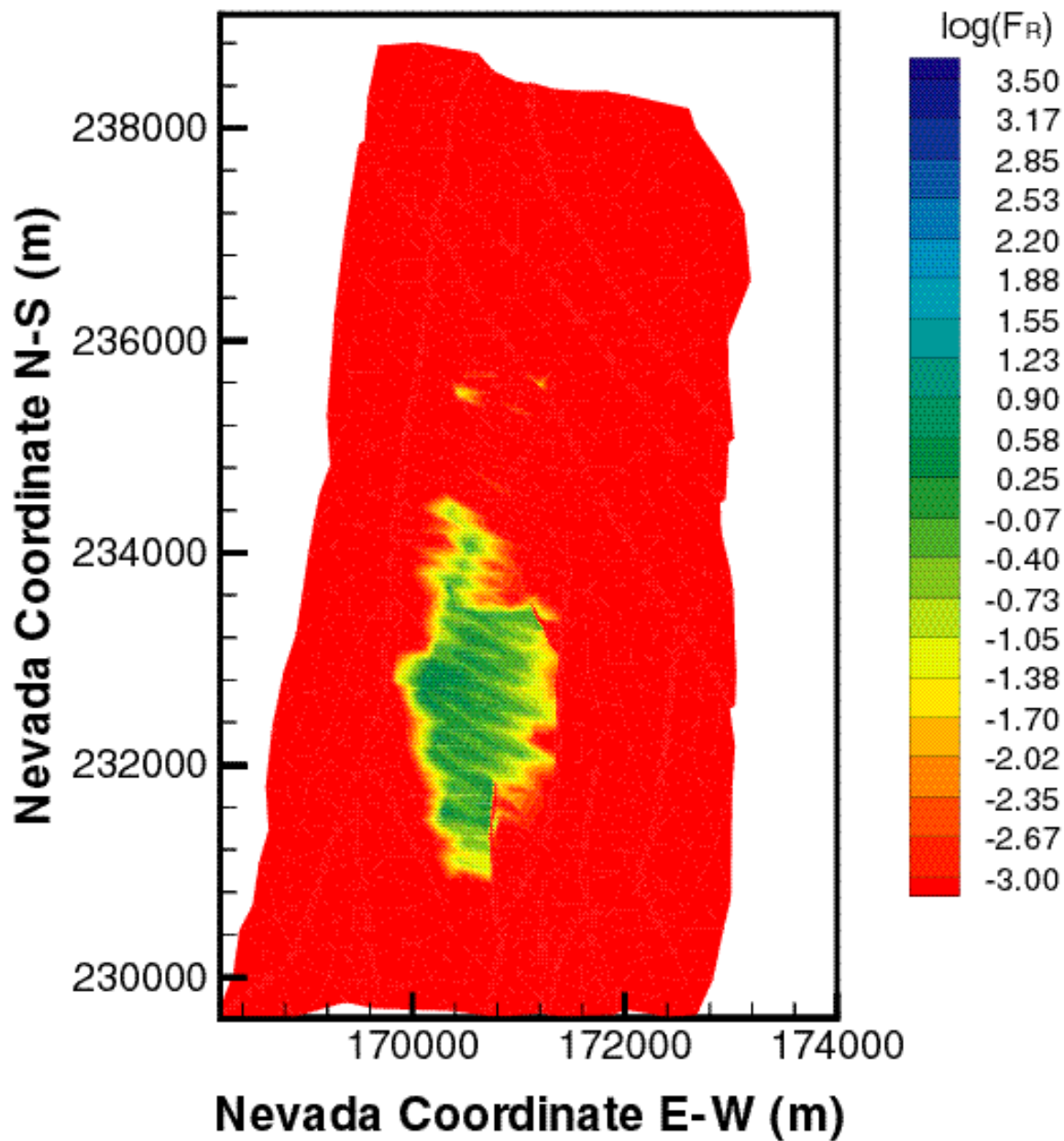


Figure VIII.3. Distribution of the relative sorbed concentration F_R of ^{239}Pu in the matrix of the tsw39 layer at $t = 100$ years for mean present-day infiltration (DTN: LB991220140160.012, data submitted with this AMR).

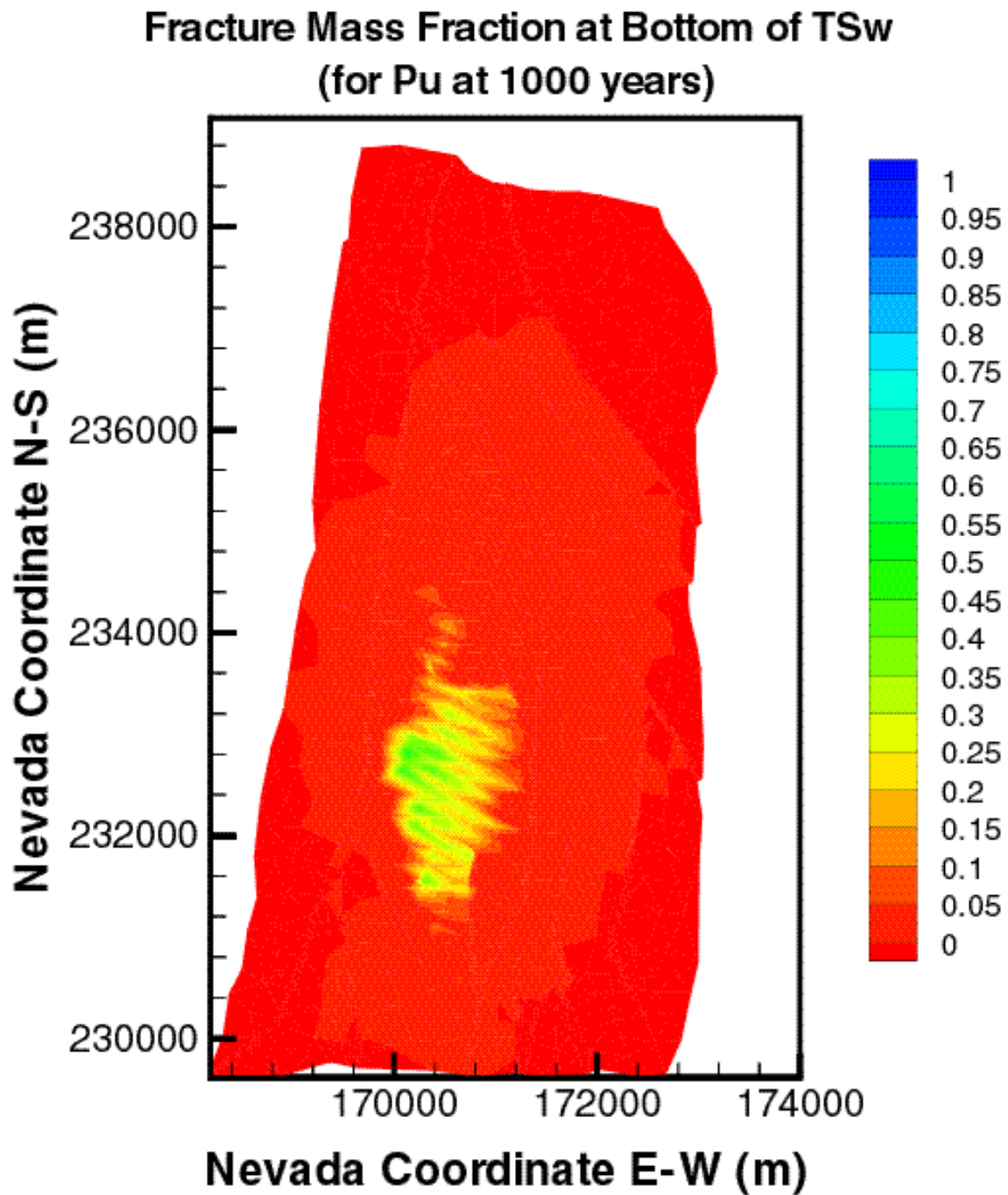


Figure VIII.4. Distribution of the relative mass fraction X_R of ^{239}Pu in the fractures of the tsw39 layer at $t = 1,000$ years for mean present-day infiltration (DTN: LB991220140160.012, data submitted with this AMR).

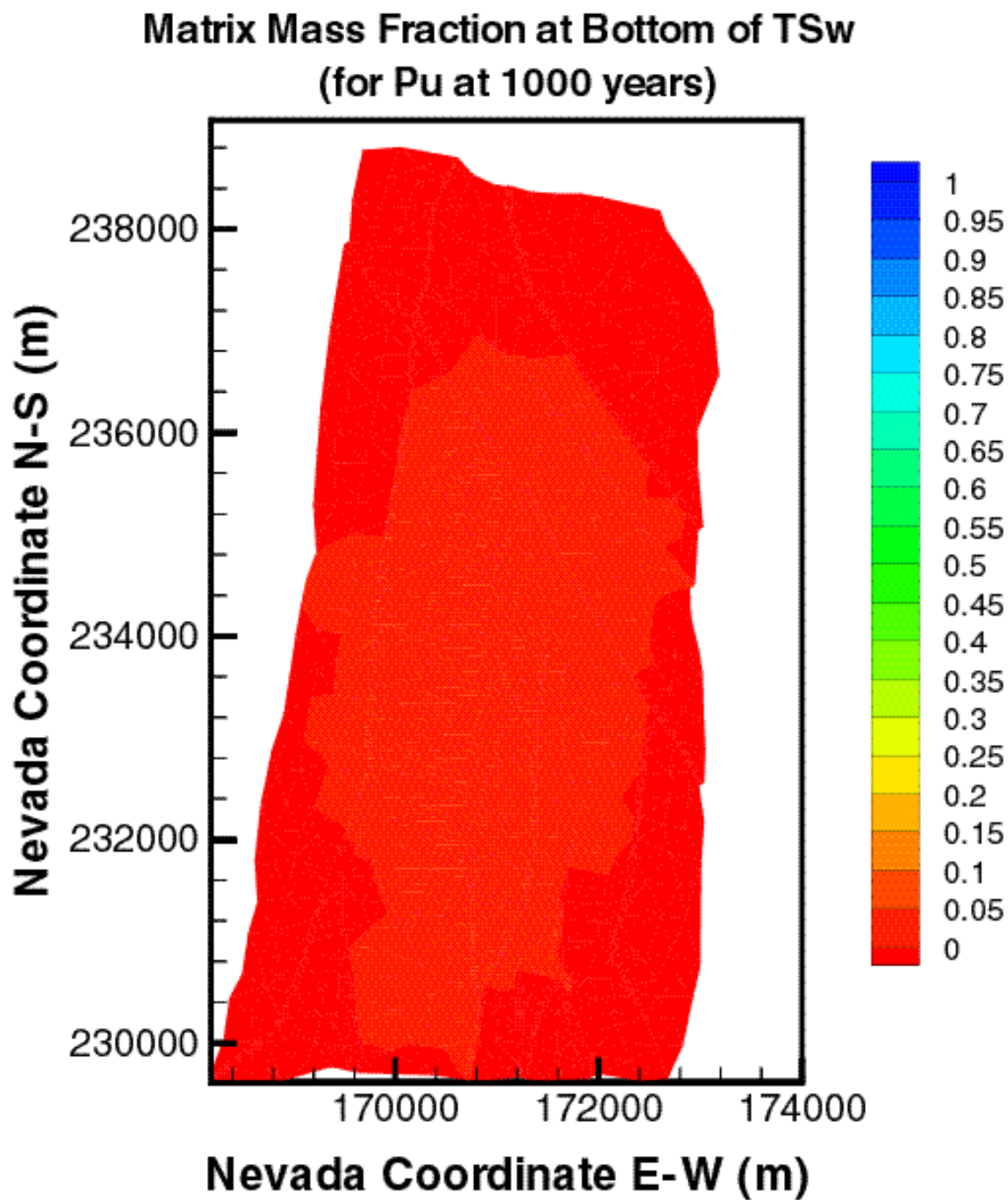


Figure VIII.5. Distribution of the relative mass fraction X_R of ^{239}Pu in the matrix of the tsw39 layer at $t = 1,000$ years for mean present-day infiltration (DTN: LB991220140160.012, data submitted with this AMR).

**Matrix Sorbed Concentration at Bottom of TSw (kg/m³)
(for Pu at 1000 years)**

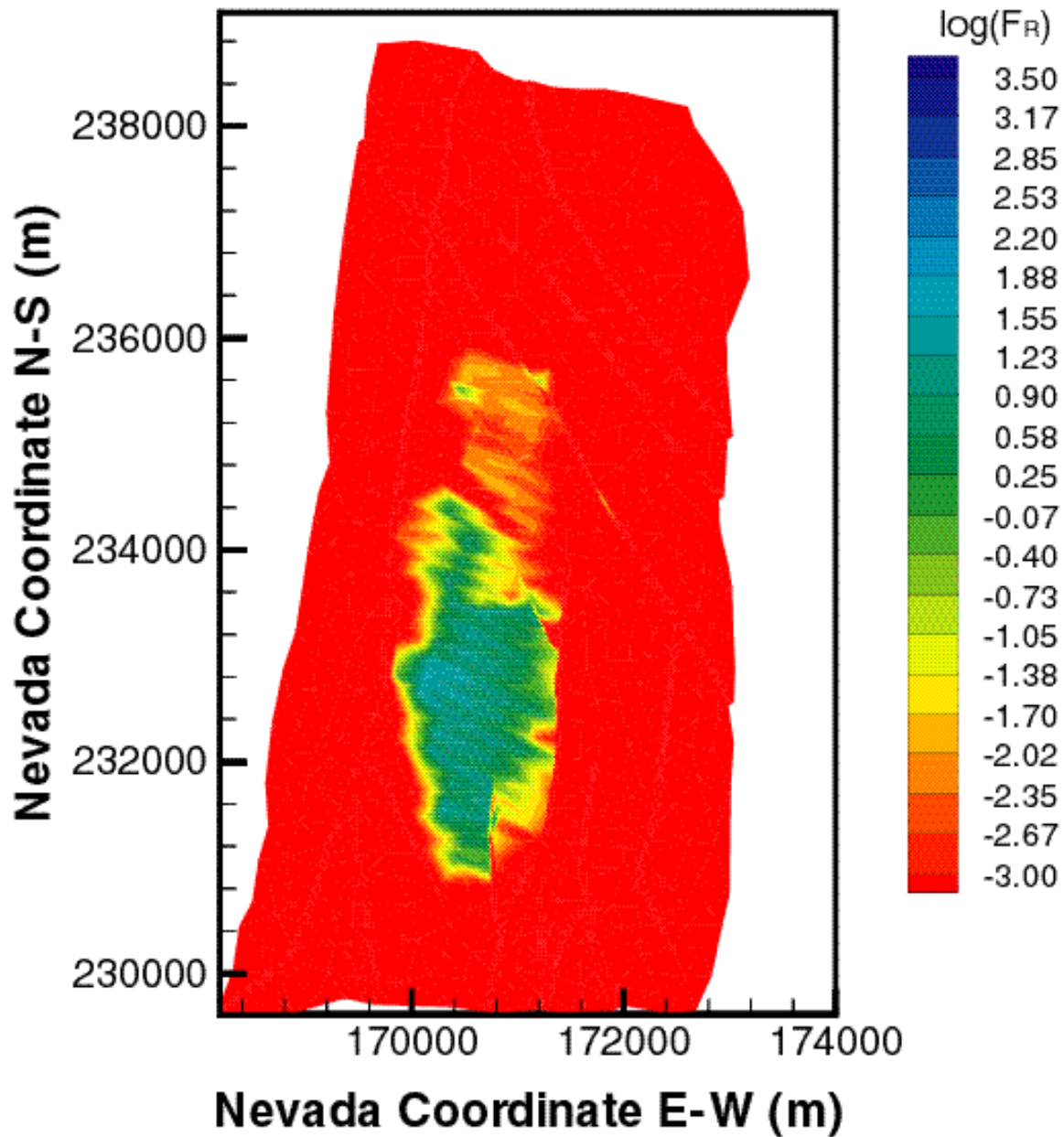


Figure VIII.6. Distribution of the relative sorbed concentration F_R of ^{239}Pu in the matrix of the tsw39 layer at $t = 1,000$ years for mean present-day infiltration (DTN: LB991220140160.012, data submitted with this AMR).

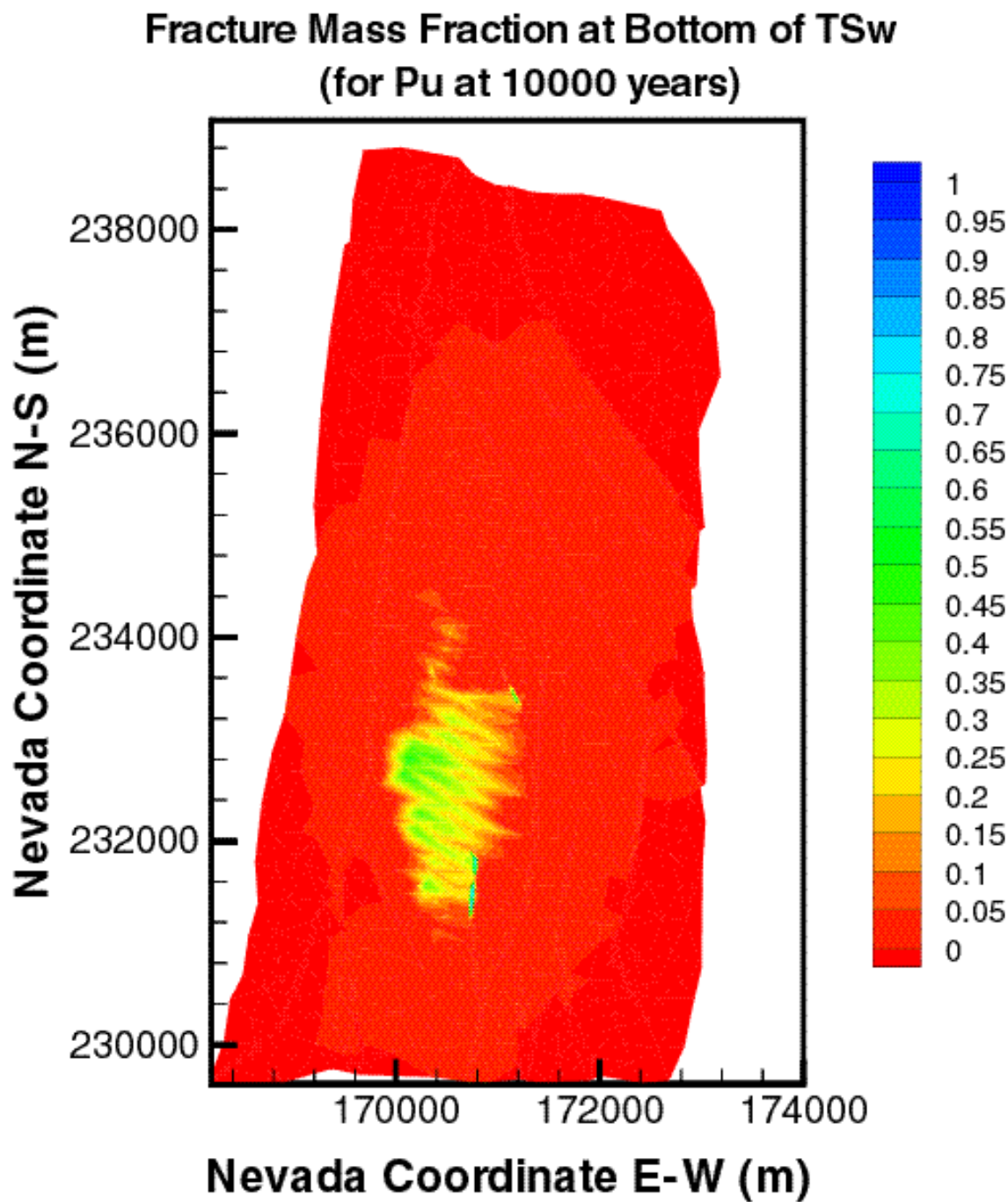


Figure VIII.7. Distribution of the relative mass fraction X_R of ^{239}Pu in the fractures of the tsw39 layer at $t = 10,000$ years for mean present-day infiltration (DTN: LB991220140160.012, data submitted with this AMR).

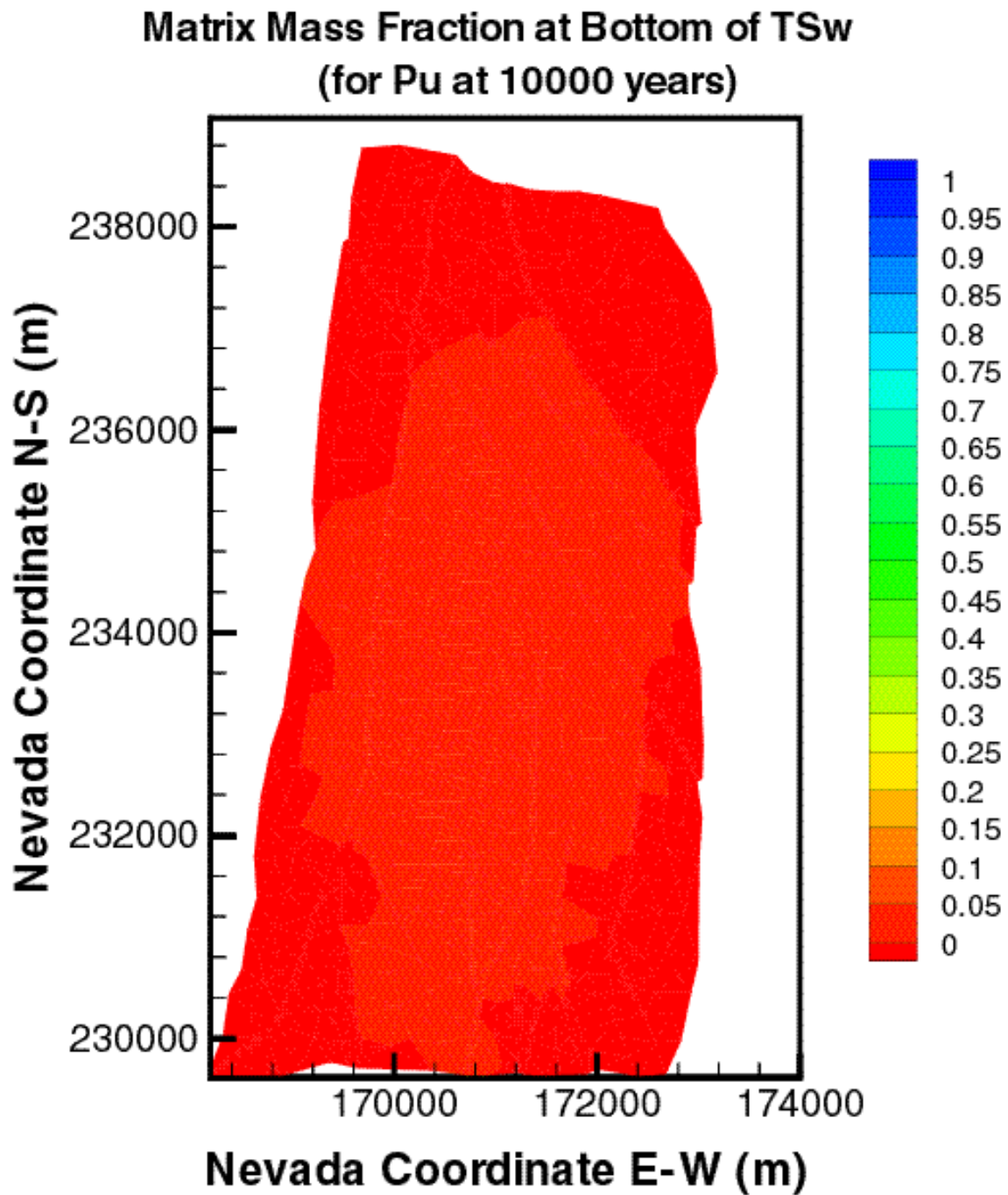


Figure VIII.8. Distribution of the relative mass fraction X_R of ^{239}Pu in the matrix of the tsw39 layer at $t = 10,000$ years for mean present-day infiltration (DTN: LB991220140160.012, data submitted with this AMR).

**Matrix Sorbed Concentration at Bottom of TSw (kg/m³)
(for Pu at 10000 years)**

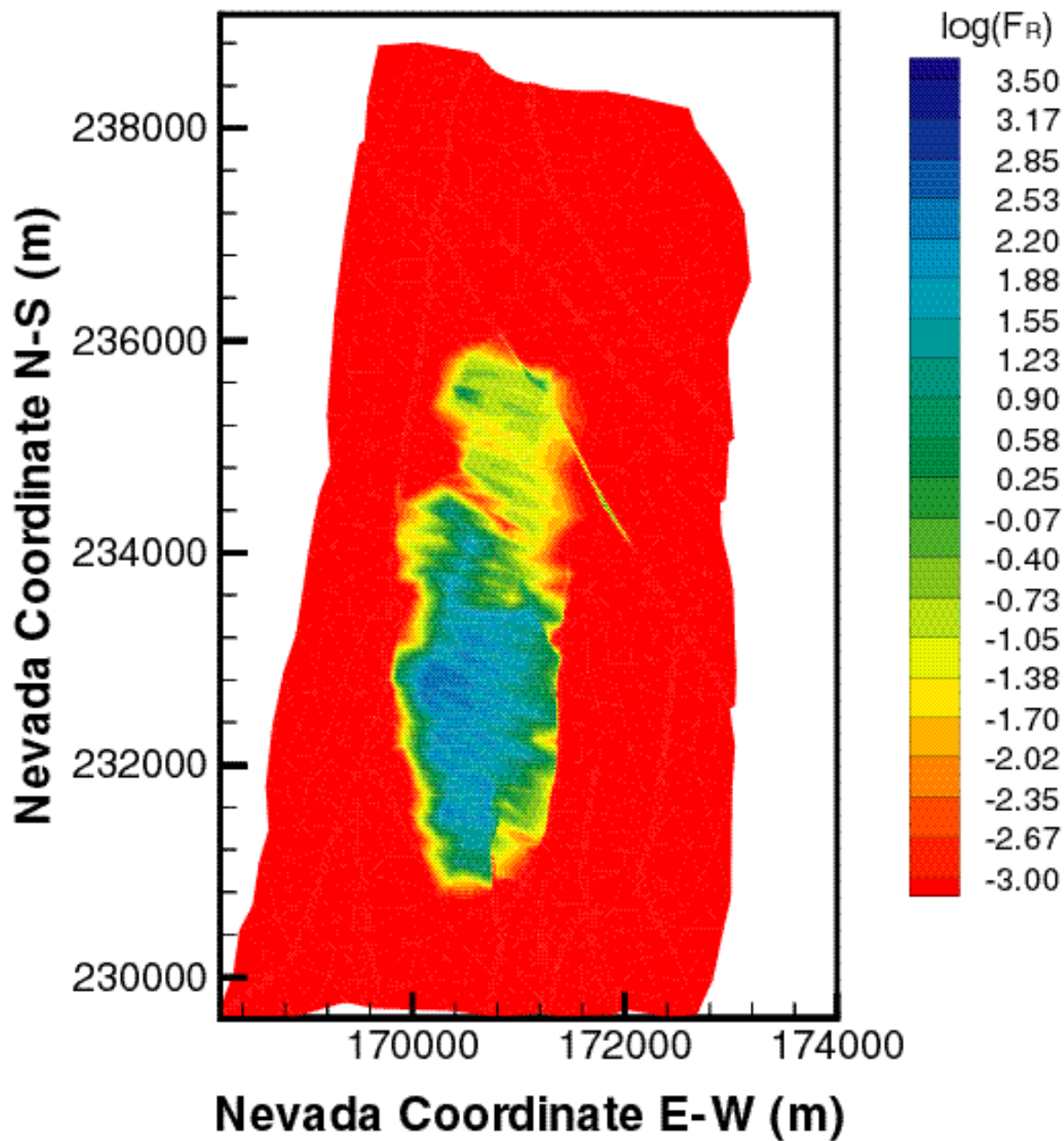


Figure VIII.9. Distribution of the relative sorbed concentration F_R of ^{239}Pu in the matrix of the tsw39 layer at $t = 10,000$ years for mean present-day infiltration (DTN: LB991220140160.012, data submitted with this AMR).

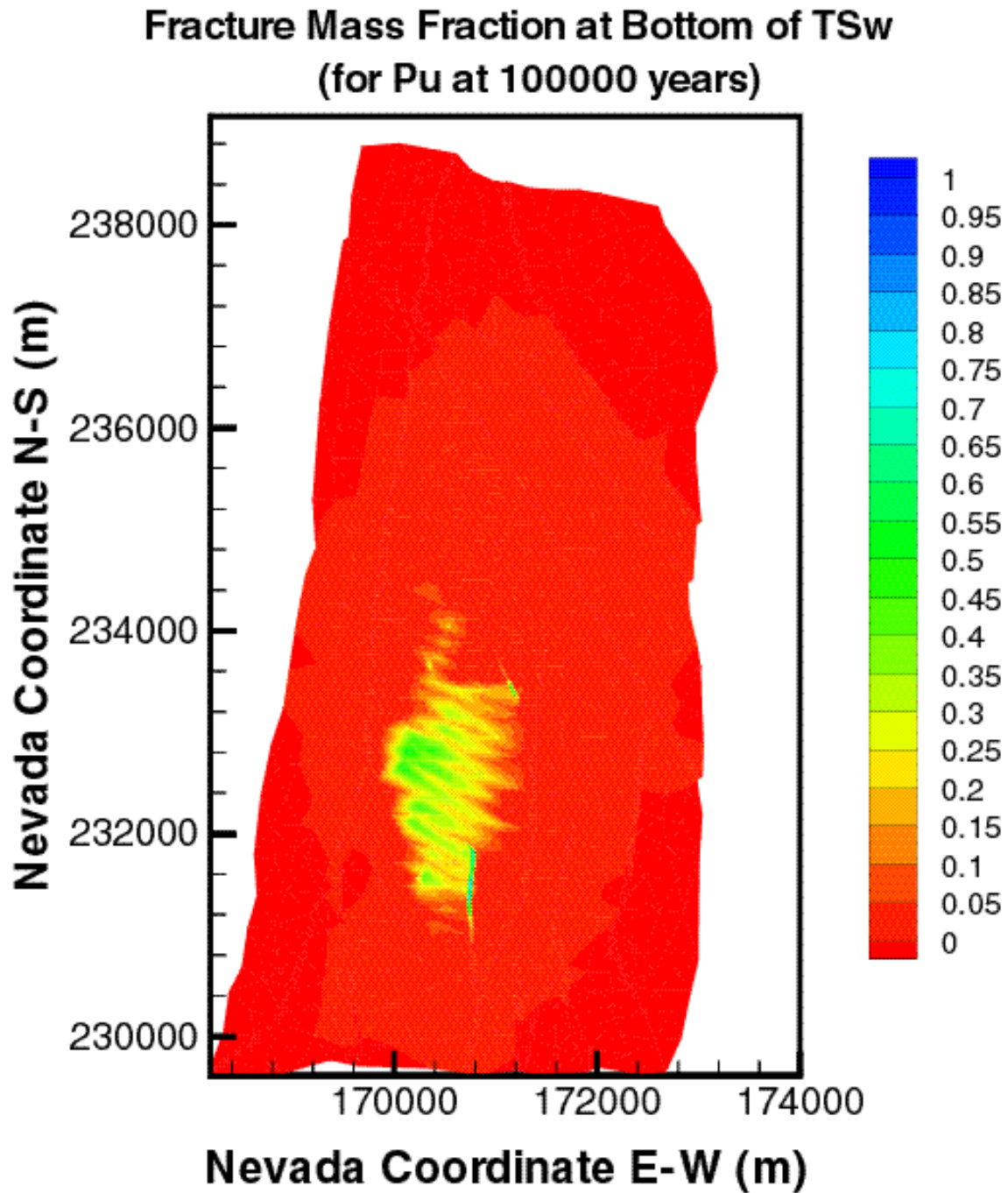


Figure VIII.10. Distribution of the relative mass fraction X_R of ^{239}Pu in the fractures of the tsw39 layer at $t = 100,000$ years for mean present-day infiltration (DTN: LB991220140160.012, data submitted with this AMR).

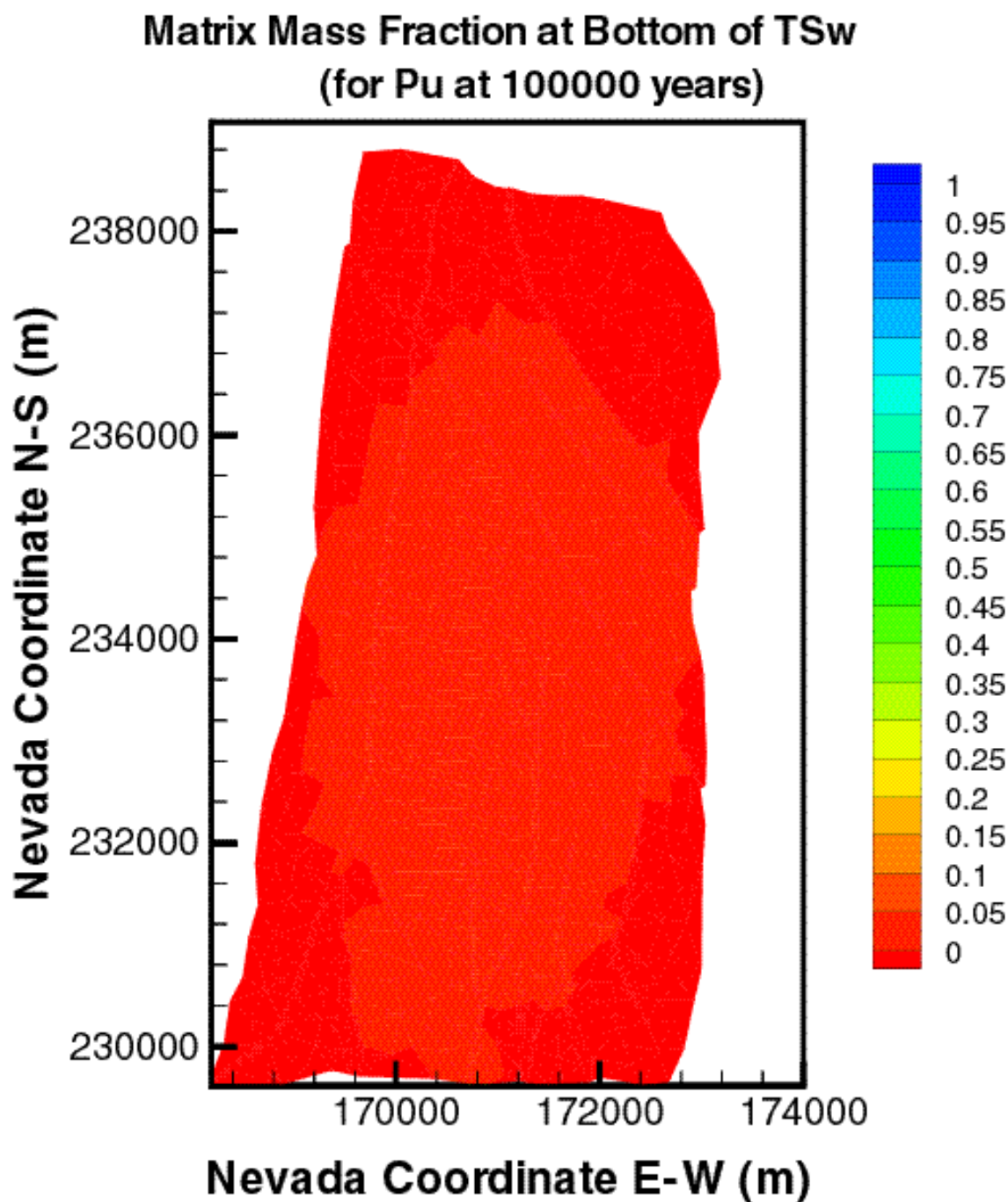


Figure VIII.11. Distribution of the relative mass fraction X_R of ^{239}Pu in the matrix of the tsw39 layer at $t = 100,000$ years for mean present-day infiltration (DTN: LB991220140160.012, data submitted with this AMR).

**Matrix Sorbed Concentration at Bottom of TSw (kg/m³)
(for Pu at 100000 years)**

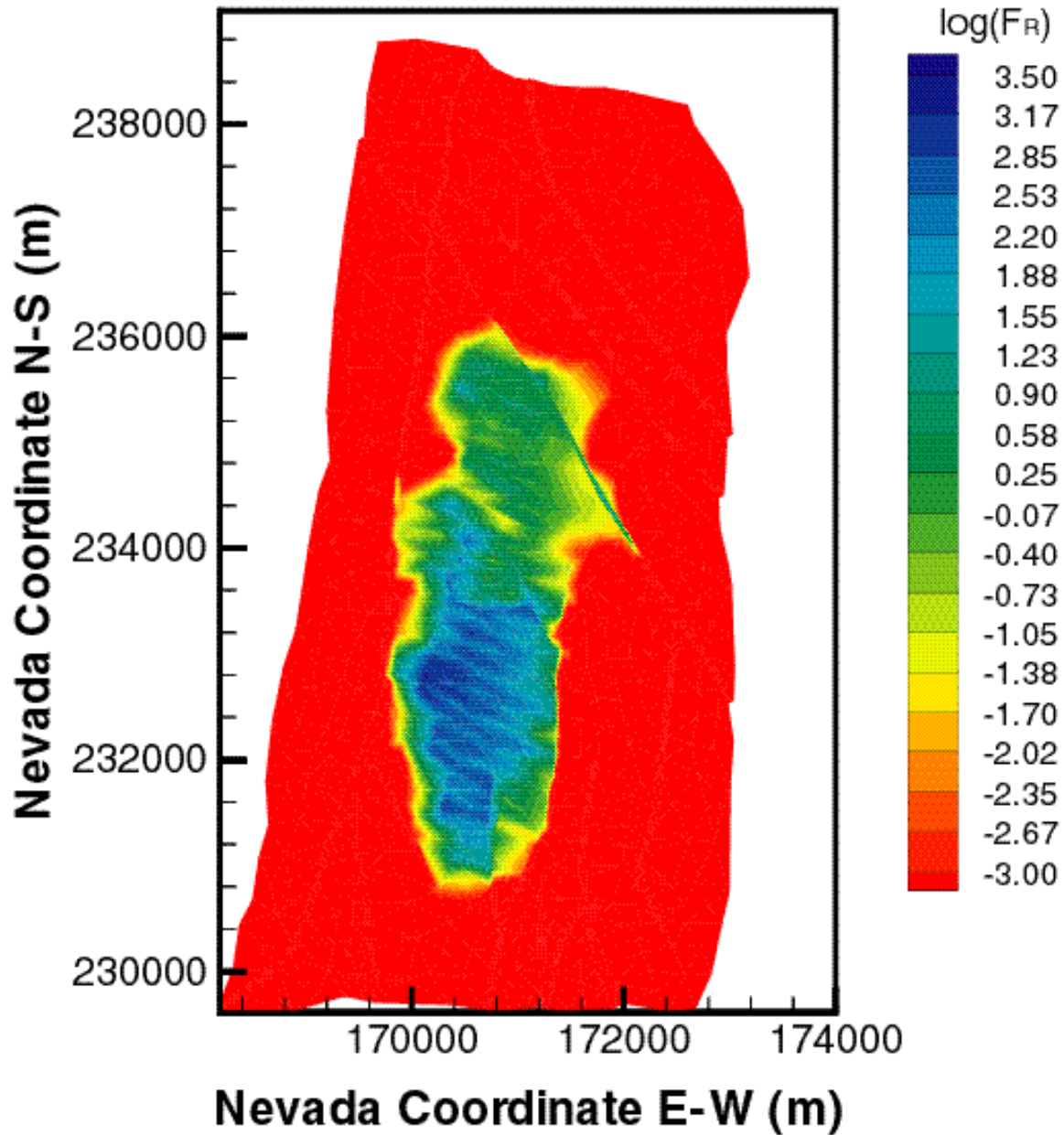


Figure VIII.12. Distribution of the relative sorbed concentration F_R of ^{239}Pu in the matrix of the tsw39 layer at $t = 100,000$ years for mean present-day infiltration (DTN: LB991220140160.012, data submitted with this AMR).

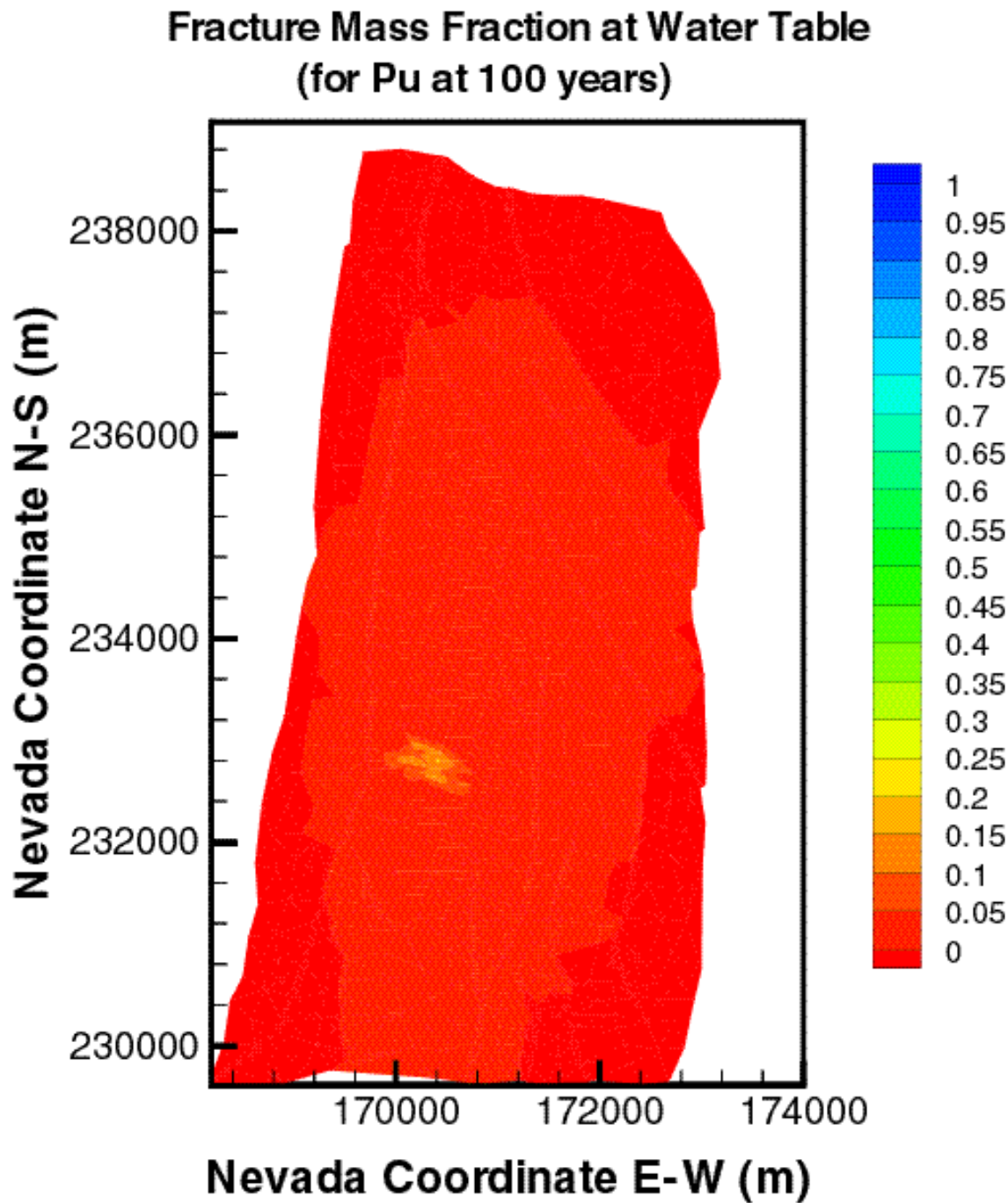


Figure VIII.13. Distribution of the relative mass fraction X_R of ^{239}Pu in the fractures immediately above the groundwater at $t = 100$ years for mean present-day infiltration (DTN: LB991220140160.012, data submitted with this AMR).

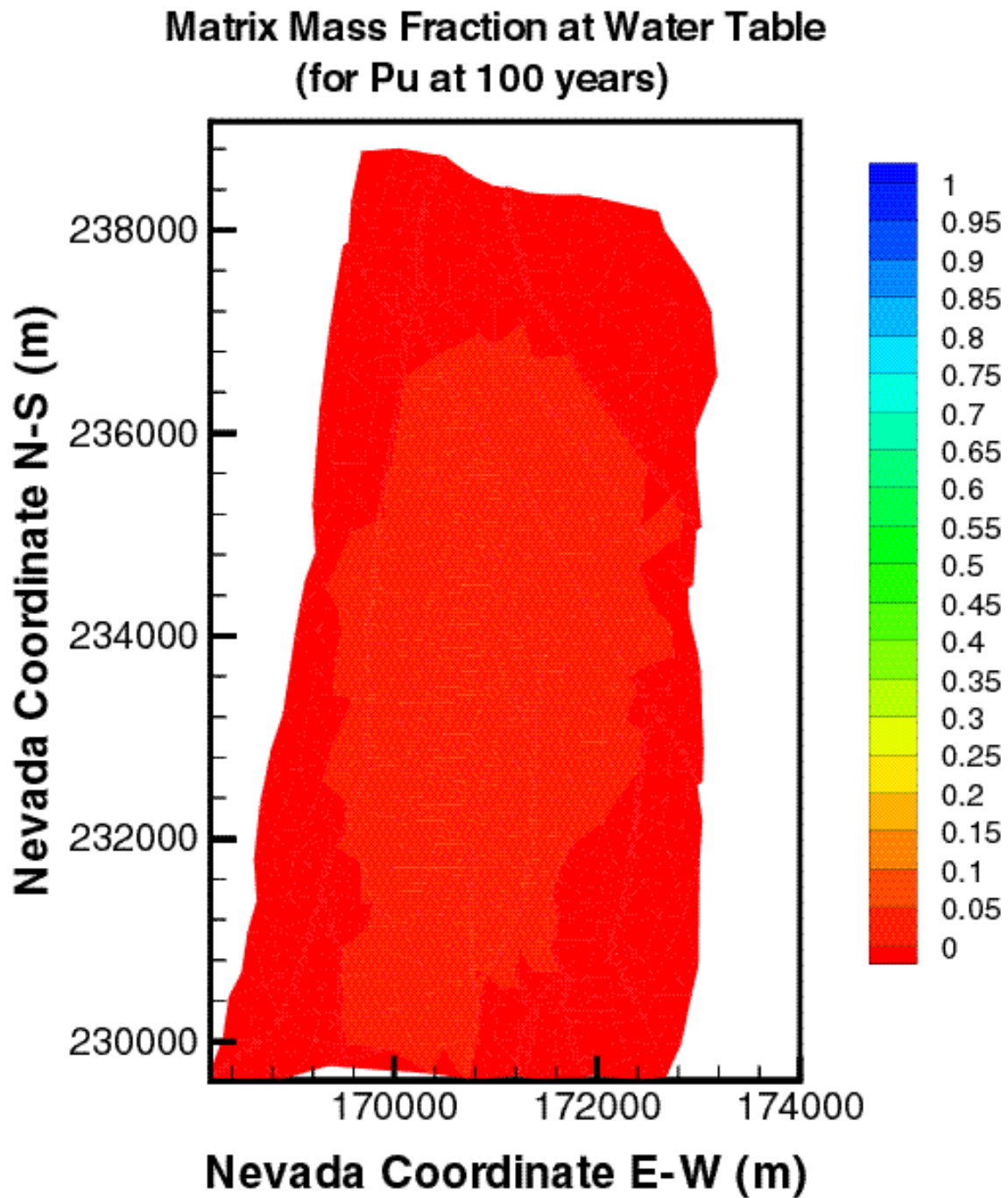


Figure VIII.14. Distribution of the relative mass fraction X_R of ^{239}Pu in the matrix immediately above the groundwater at $t = 100$ years for mean present-day infiltration (DTN: LB991220140160.012, data submitted with this AMR).

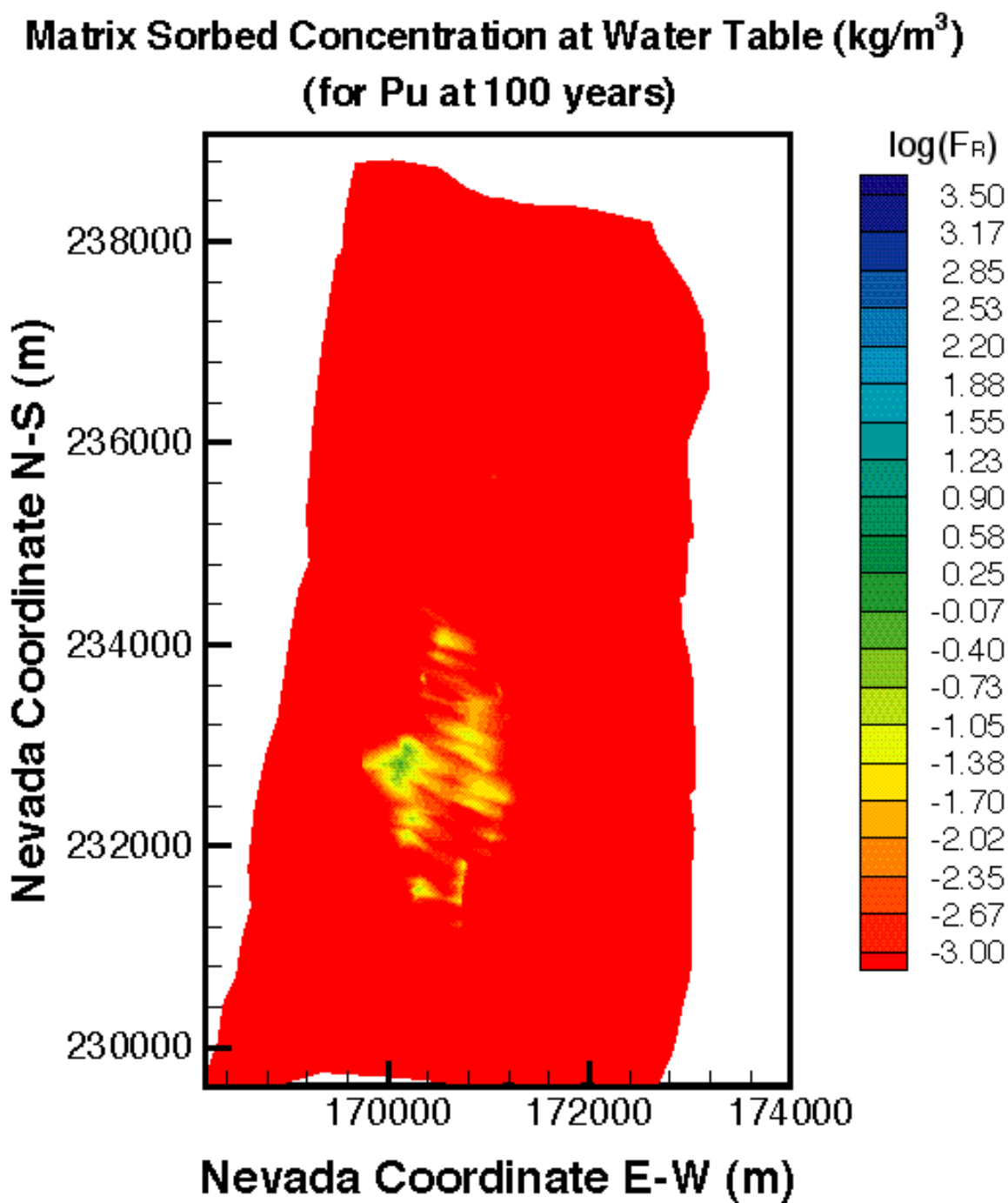


Figure VIII.15. Distribution of the relative sorbed concentration F_R of ^{239}Pu in the matrix immediately above the groundwater at $t = 100$ years for mean present-day infiltration (DTN: LB991220140160.012, data submitted with this AMR).

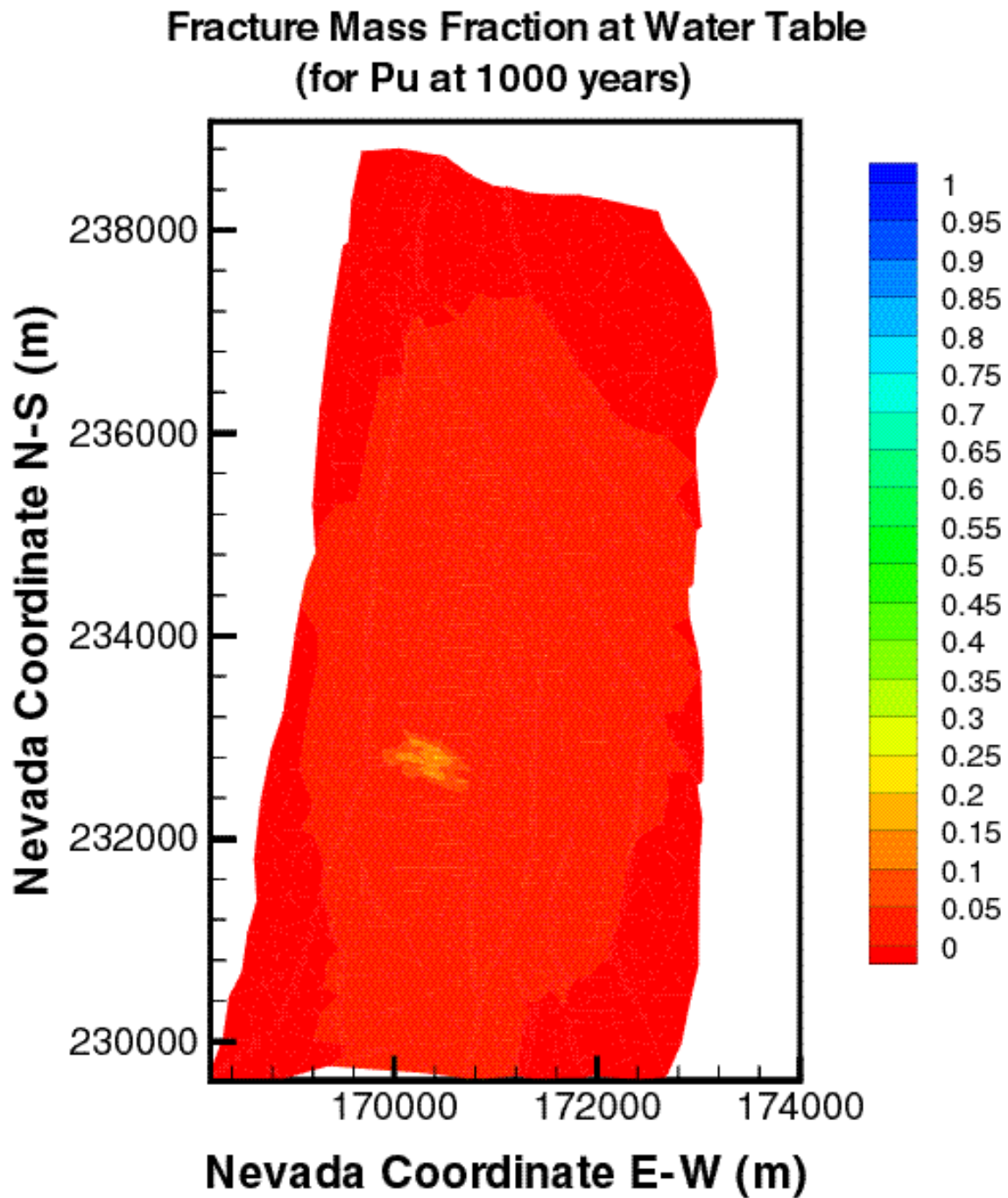


Figure VIII.16. Distribution of the relative mass fraction X_R of ^{239}Pu in the fractures immediately above the groundwater at $t = 1,000$ years for mean present-day infiltration (DTN: LB991220140160.012, data submitted with this AMR).

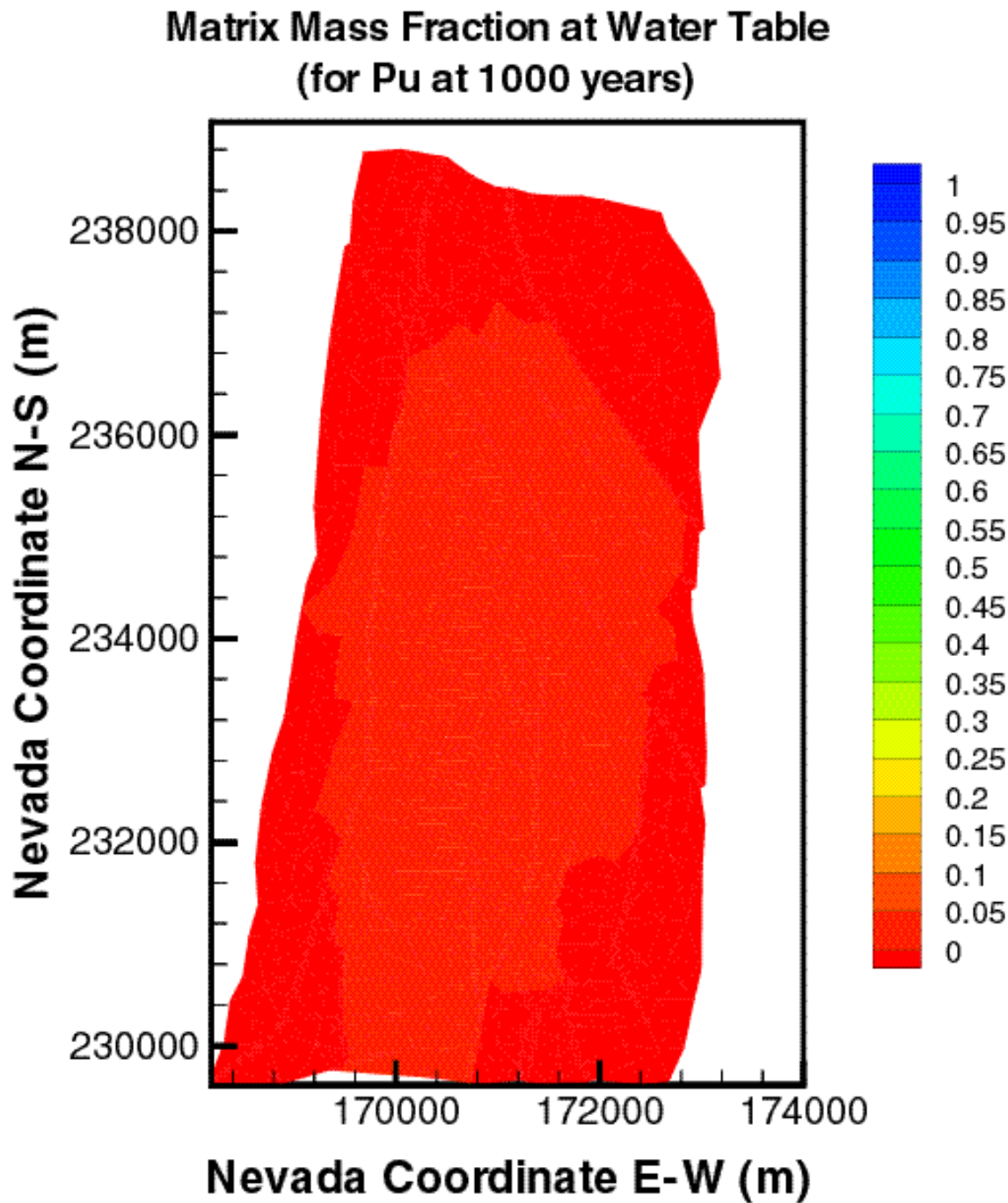


Figure VIII.17. Distribution of the relative mass fraction X_R of ^{239}Pu in the matrix immediately above the groundwater at $t = 1,000$ years for mean present-day infiltration (DTN: LB991220140160.012, data submitted with this AMR).

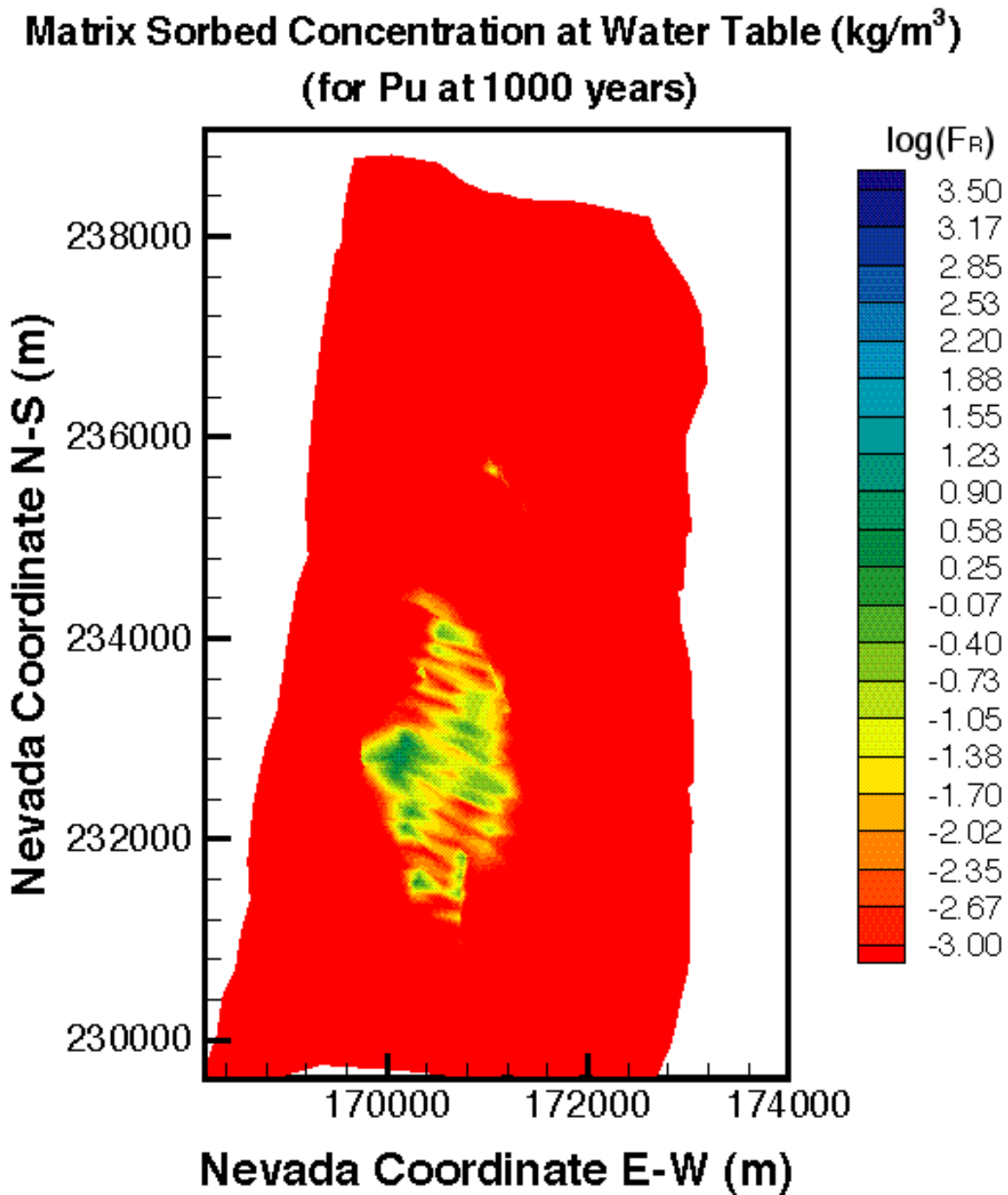


Figure VIII.18. Distribution of the relative sorbed concentration F_R of ^{239}Pu in the matrix immediately above the groundwater at $t = 1,000$ years for mean present-day infiltration (DTN: LB991220140160.012, data submitted with this AMR).

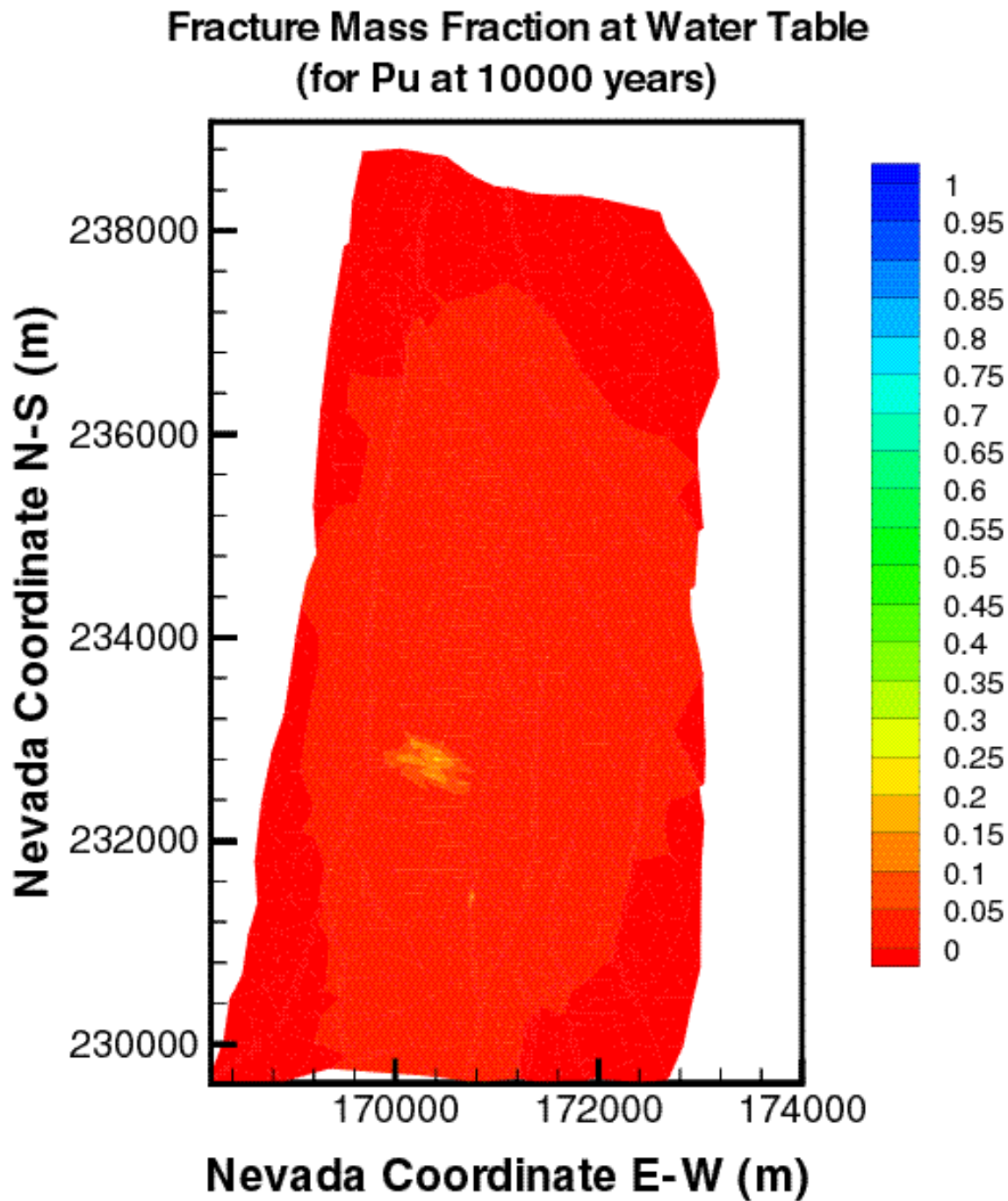


Figure VIII.19. Distribution of the relative mass fraction X_R of ^{239}Pu in the fractures immediately above the groundwater at $t = 10,000$ years for mean present-day infiltration (DTN: LB991220140160.012, data submitted with this AMR).

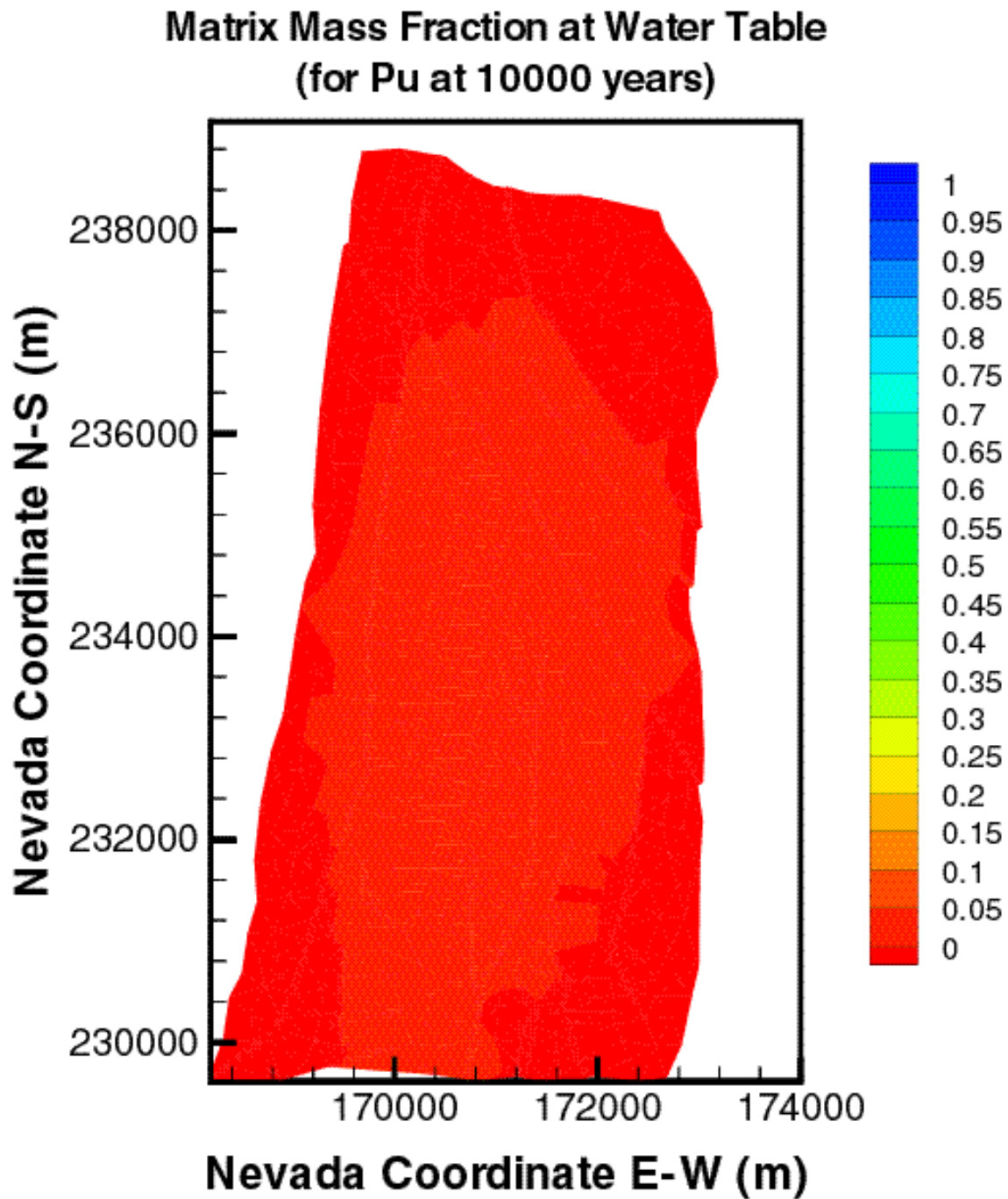


Figure VIII.20. Distribution of the relative mass fraction X_R of ^{239}Pu in the matrix immediately above the groundwater at $t = 10,000$ years for mean present-day infiltration (DTN: LB991220140160.012, data submitted with this AMR).

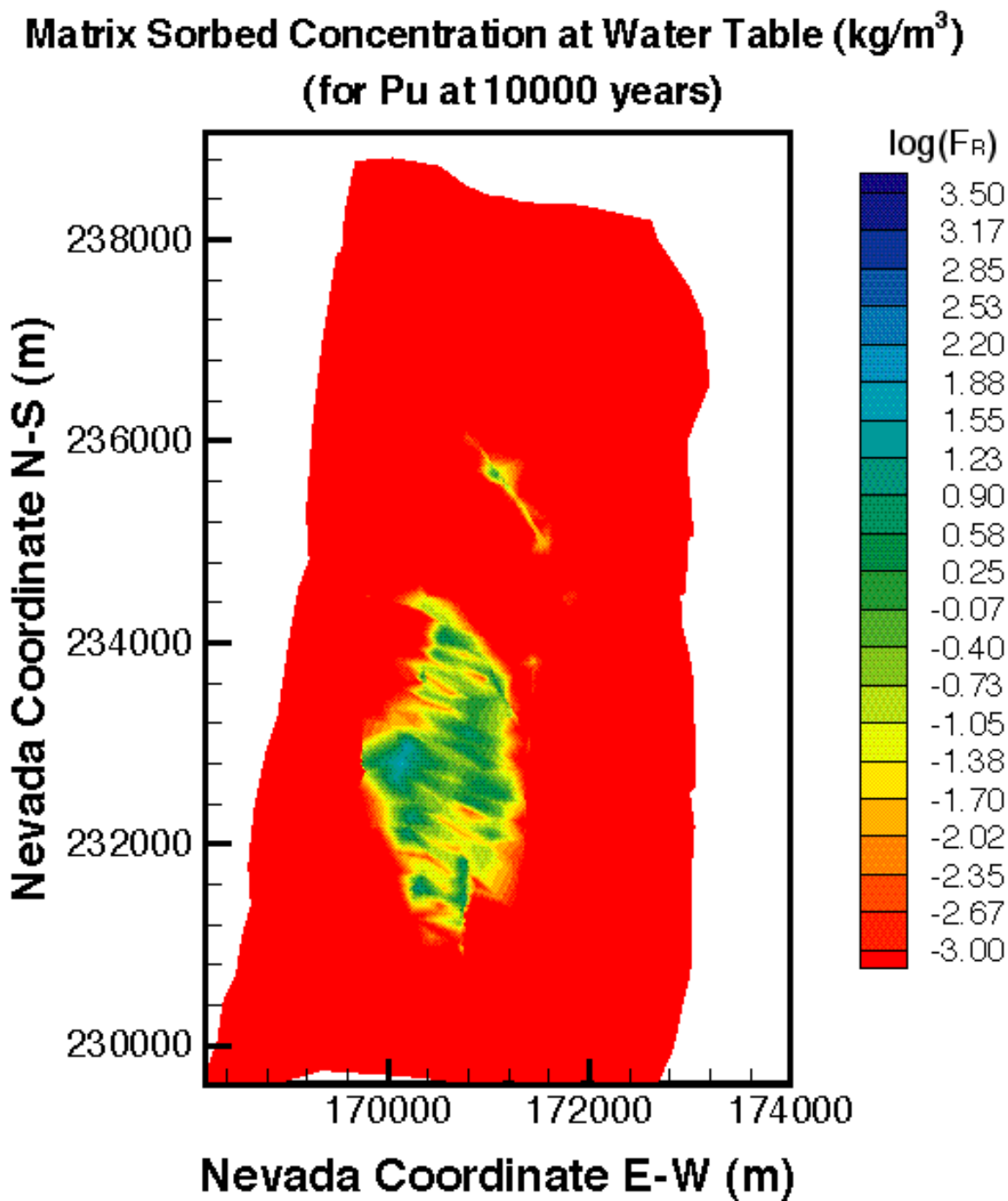


Figure VIII.21. Distribution of the relative sorbed concentration F_R of ^{239}Pu in the matrix immediately above the groundwater at $t = 10,000$ years for mean present-day infiltration (DTN: LB991220140160.012, data submitted with this AMR).

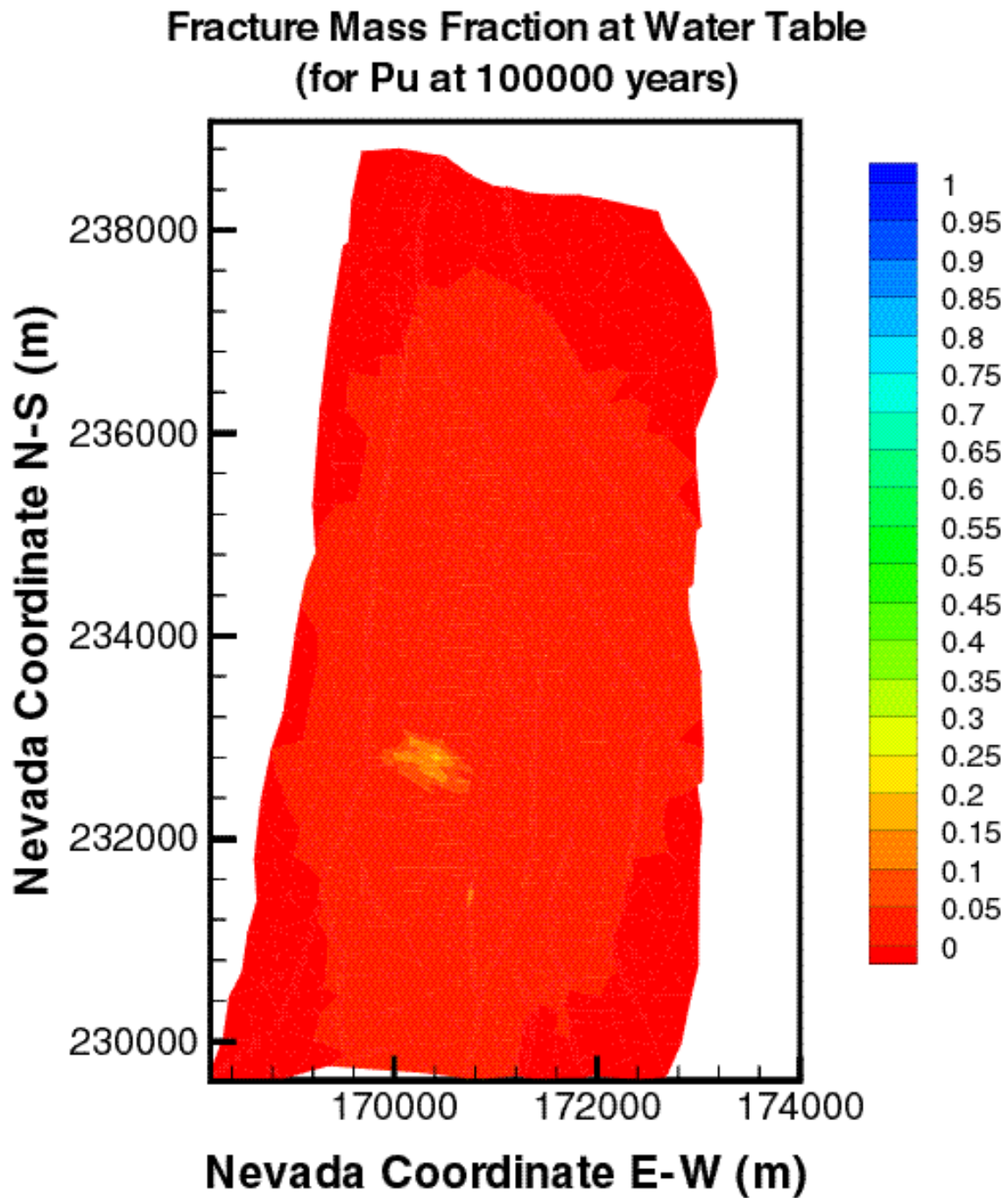


Figure VIII.22. Distribution of the relative mass fraction X_R of ^{239}Pu in the fractures immediately above the groundwater at $t = 100,000$ years for mean present-day infiltration (DTN: LB991220140160.012, data submitted with this AMR).

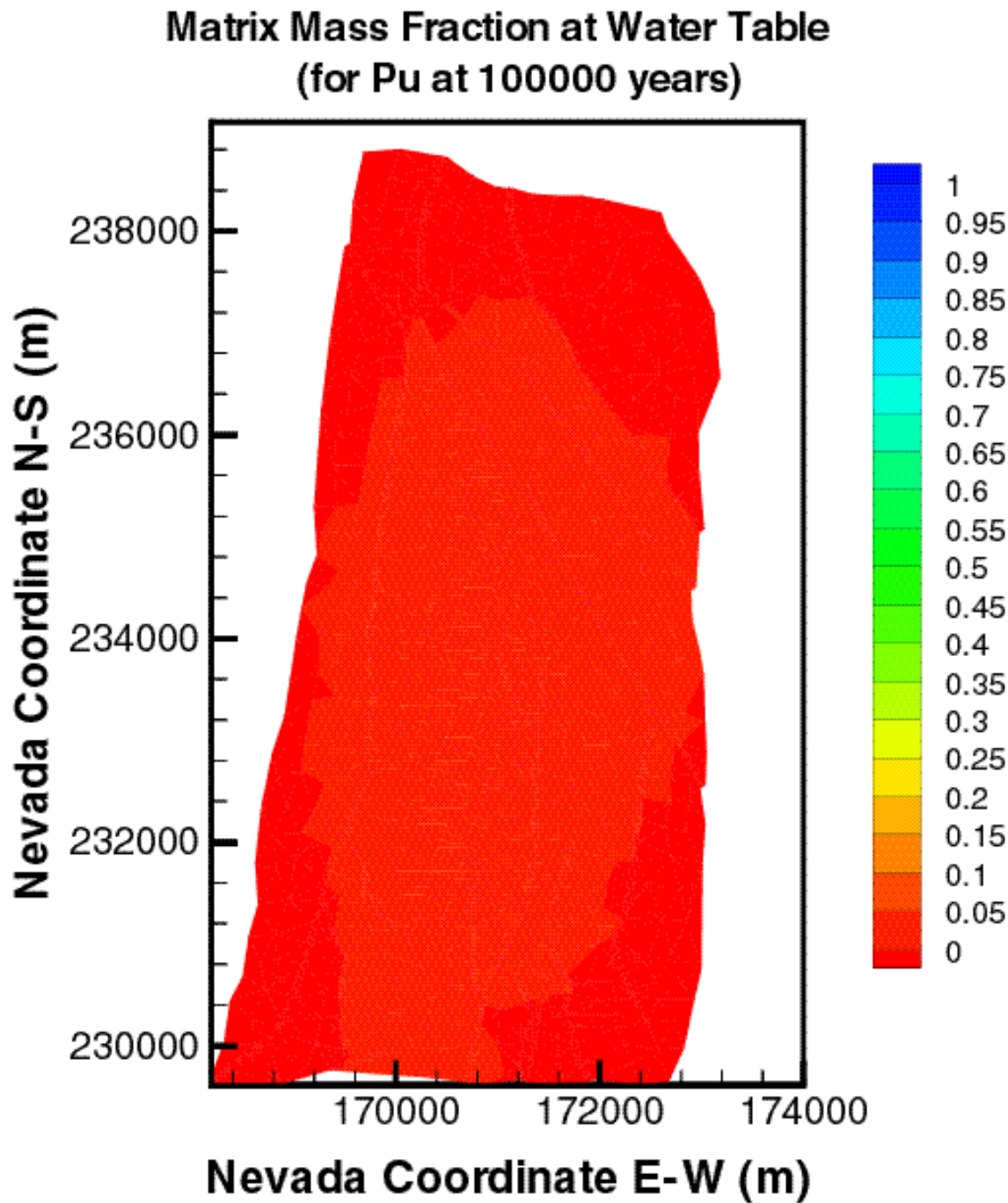


Figure VIII.23. Distribution of the relative mass fraction X_R of ^{239}Pu in the matrix immediately above the groundwater at $t = 100,000$ years for mean present-day infiltration (DTN: LB991220140160.012, data submitted with this AMR).

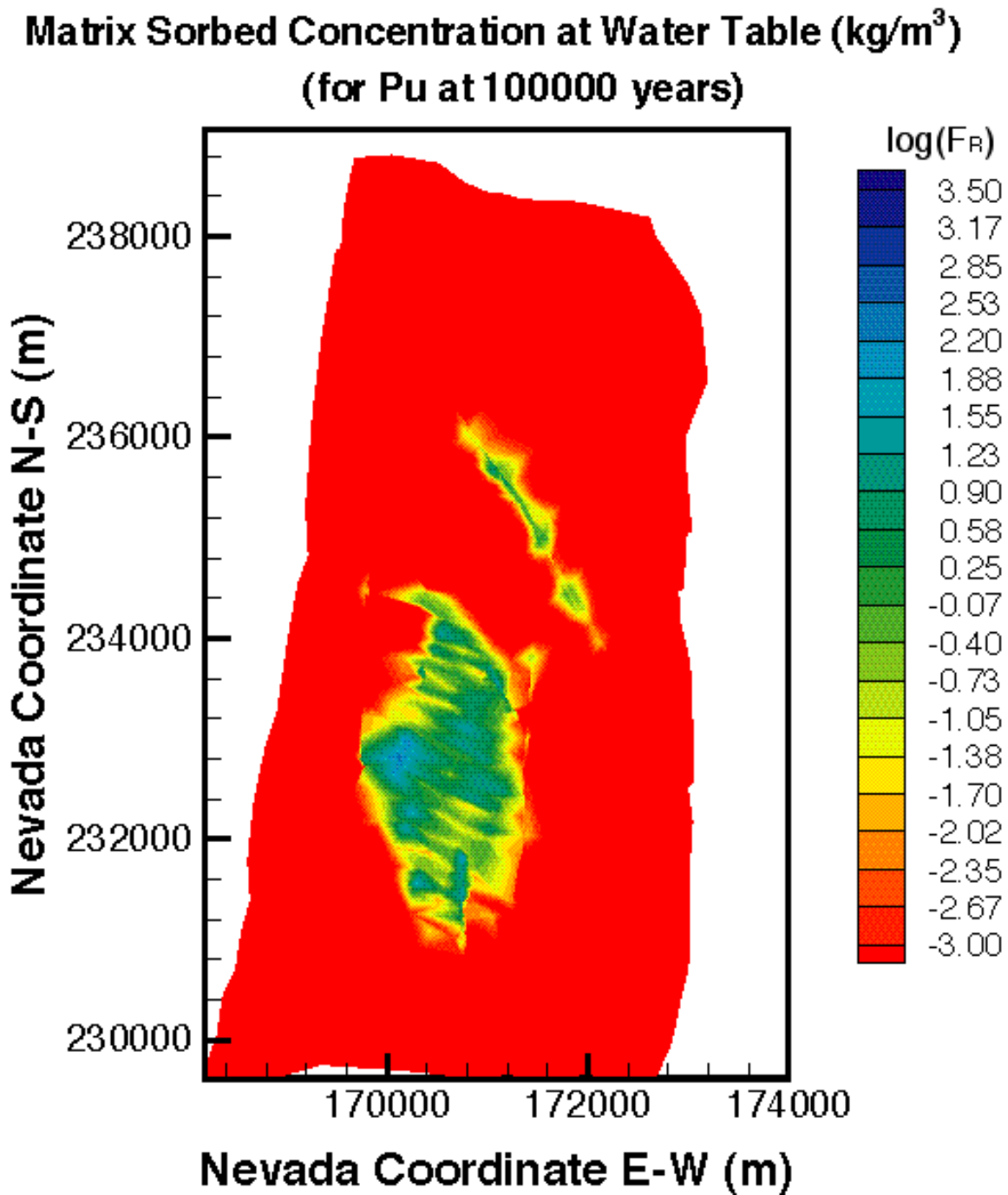


Figure VIII.24. Distribution of the relative sorbed concentration F_R of ^{239}Pu in the matrix immediately above the groundwater at $t = 100,000$ years for mean present-day infiltration (DTN: LB991220140160.012, data submitted with this AMR).

ATTACHMENT IX.

FIGURES FROM THE 3-D TRANSPORT STUDIES OF THE 6 nm COLLOID

INTENTIONALLY LEFT BLANK

FIGURES

	Page
IX.1. Distribution of the Relative Mass Fraction X_R of the 6 nm colloid in the Fractures of the Tsw39 Layer at $t = 10$ Years for Mean Present-Day Infiltration.....	IX-5
IX.2. Distribution of the Relative Mass Fraction X_R of the 6 nm colloid in the Matrix of the Tsw39 Layer at $t = 10$ Years for Mean Present-Day Infiltration.....	IX-6
IX.3. Distribution of the Relative Filtered Concentration F_R of the 6 nm colloid in the Matrix of the Tsw39 Layer at $t = 10$ Years for Mean Present-Day Infiltration.....	IX-7
IX.4. Distribution of the Relative Mass Fraction X_R of the 6 nm colloid in the Fractures of the Tsw39 Layer at $t = 100$ Years for Mean Present-Day Infiltration.....	IX-8
IX.5. Distribution of the Relative Mass Fraction X_R of the 6 nm colloid in the Matrix of the Tsw39 Layer at $t = 100$ Years for Mean Present-Day Infiltration.....	IX-9
IX.6. Distribution of the Relative Filtered Concentration F_R of the 6 nm colloid in the Matrix of the Tsw39 Layer at $t = 100$ Years for Mean Present-Day Infiltration.....	IX-10
IX.7. Distribution of the Relative Mass Fraction X_R of the 6 nm colloid in the Fractures of the Tsw39 Layer at $t = 1,000$ Years for Mean Present-Day Infiltration.....	IX-11
IX.8. Distribution of the Relative Mass Fraction X_R of the 6 nm colloid in the Matrix of the Tsw39 Layer at $t = 1,000$ Years for Mean Present-Day Infiltration.....	IX-12
IX.9. Distribution of the Relative Filtered Concentration F_R of the 6 nm colloid in the Matrix of the Tsw39 Layer at $t = 1,000$ Years for Mean Present-Day Infiltration.....	IX-13
IX.10. Distribution of the Relative Mass Fraction X_R of the 6 nm colloid in the Fractures of the Tsw39 Layer at $t = 10,000$ Years for Mean Present-Day Infiltration.....	IX-14
IX.11. Distribution of the Relative Mass Fraction X_R of the 6 nm colloid in the Matrix of the Tsw39 Layer at $t = 10,000$ Years for Mean Present-Day Infiltration.....	IX-15
IX.12. Distribution of the Relative Filtered Concentration F_R of the 6 nm colloid in the Matrix of the Tsw39 Layer at $t = 10,000$ Years for Mean Present-Day Infiltration.....	IX-16
IX.13. Distribution of the Relative Mass Fraction X_R of the 6 nm colloid in the Fractures Immediately Above the Groundwater at $t = 10$ Years for Mean Present-Day Infiltration.....	IX-17

FIGURES (Continued)

	Page
IX.14. Distribution of the Relative Mass Fraction X_R of the 6 nm colloid in the Matrix Immediately Above the Groundwater Table at $t = 10$ Years for a Mean Present-Day Infiltration.....	IX-18
IX.15. Distribution of the Relative Filtered Concentration F_R of the 6 nm colloid in the Matrix Immediately Above the Groundwater Table at $t = 10$ Years for a Mean Present-Day Infiltration.....	IX-19
IX.16. Distribution of the Relative Mass Fraction X_R of the 6 nm colloid in the Fractures Immediately Above the Groundwater at $t = 100$ Years for Mean Present-Day Infiltration.....	IX-20
IX.17. Distribution of the Relative Mass Fraction X_R of the 6 nm colloid in the Matrix Immediately Above the Groundwater Table at $t = 100$ Years for a Mean Present-Day Infiltration.....	IX-21
IX.18. Distribution of the Relative Filtered Concentration F_R of the 6 nm colloid in the Matrix Immediately Above the Groundwater Table at $t = 100$ Years for a Mean Present-Day Infiltration.....	IX-22
IX.19. Distribution of the Relative Mass Fraction X_R of the 6 nm colloid in the Fractures Immediately Above the Groundwater at $t = 1,000$ Years for Mean Present-Day Infiltration.....	IX-23
IX.20. Distribution of the Relative Mass Fraction X_R of the 6 nm colloid in the Matrix Immediately Above the Groundwater Table at $t = 1,000$ Years for a Mean Present-Day Infiltration.....	IX-24
IX.21. Distribution of the Relative Filtered Concentration F_R of the 6 nm colloid in the Matrix Immediately Above the Groundwater Table at $t = 1,000$ Years for a Mean Present-Day Infiltration.....	IX-25
IX.22. Distribution of the Relative Mass Fraction X_R of the 6 nm colloid in the Fractures Immediately Above the Groundwater at $t = 10,000$ Years for Mean Present-Day Infiltration.....	IX-26
IX.23. Distribution of the Relative Mass Fraction X_R of the 6 nm colloid in the Matrix Immediately Above the Groundwater Table at $t = 10,000$ Years for a Mean Present-Day Infiltration.....	IX-27
IX.24. Distribution of the Relative Filtered Concentration F_R of the 6 nm colloid in the Matrix Immediately Above the Groundwater Table at $t = 10,000$ Years for a Mean Present-Day Infiltration.....	IX-28

FRACTURE MASS FRACTION AT BOTTOM OF TSw (for Co006 at 10 years)

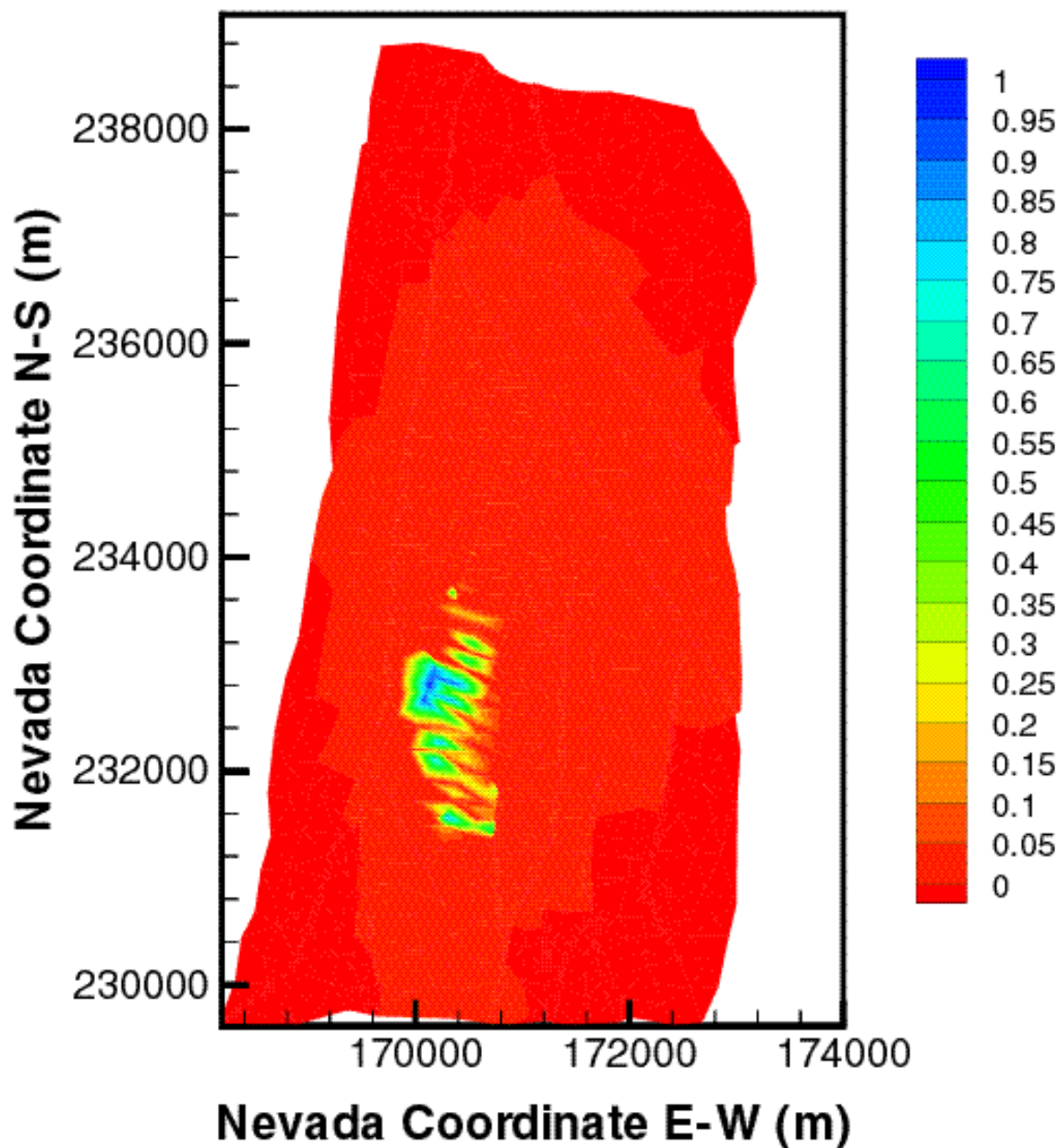


Figure IX.1. Distribution of the relative mass fraction X_R of the 6 nm colloid in the fractures of the tsw39 layer at $t = 10$ years for mean present-day infiltration (DTN: LB991220140160.017, data submitted with this AMR).

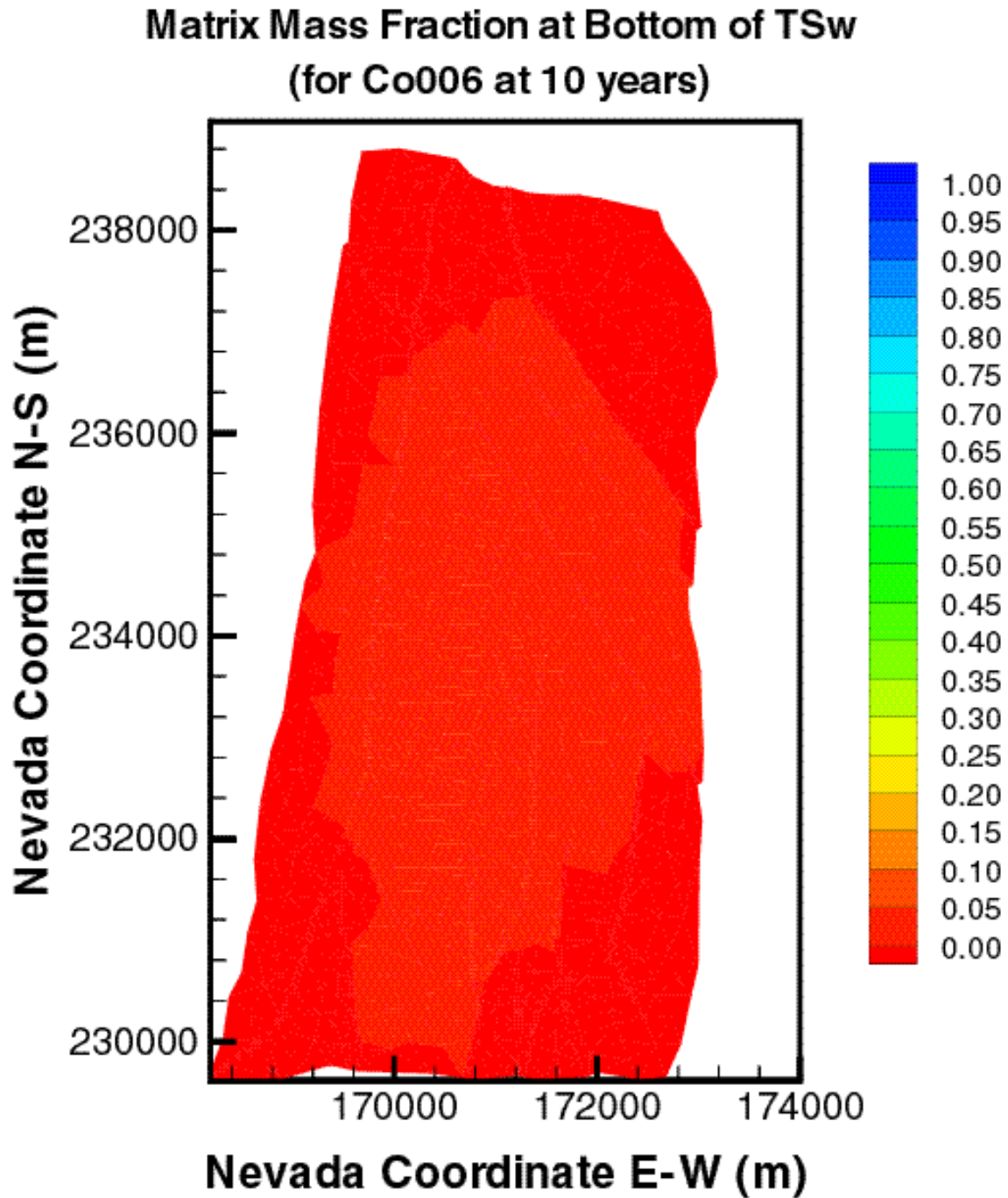


Figure IX.2. Distribution of the relative mass fraction X_R of the 6 nm colloid in the matrix of the tsw39 layer at $t = 10$ years for mean present-day infiltration (DTN: LB991220140160.017, data submitted with this AMR).

**Matrix Filtered Concentration at Bottom of TSw (kg/m³)
(for Co006 at 10 years)**

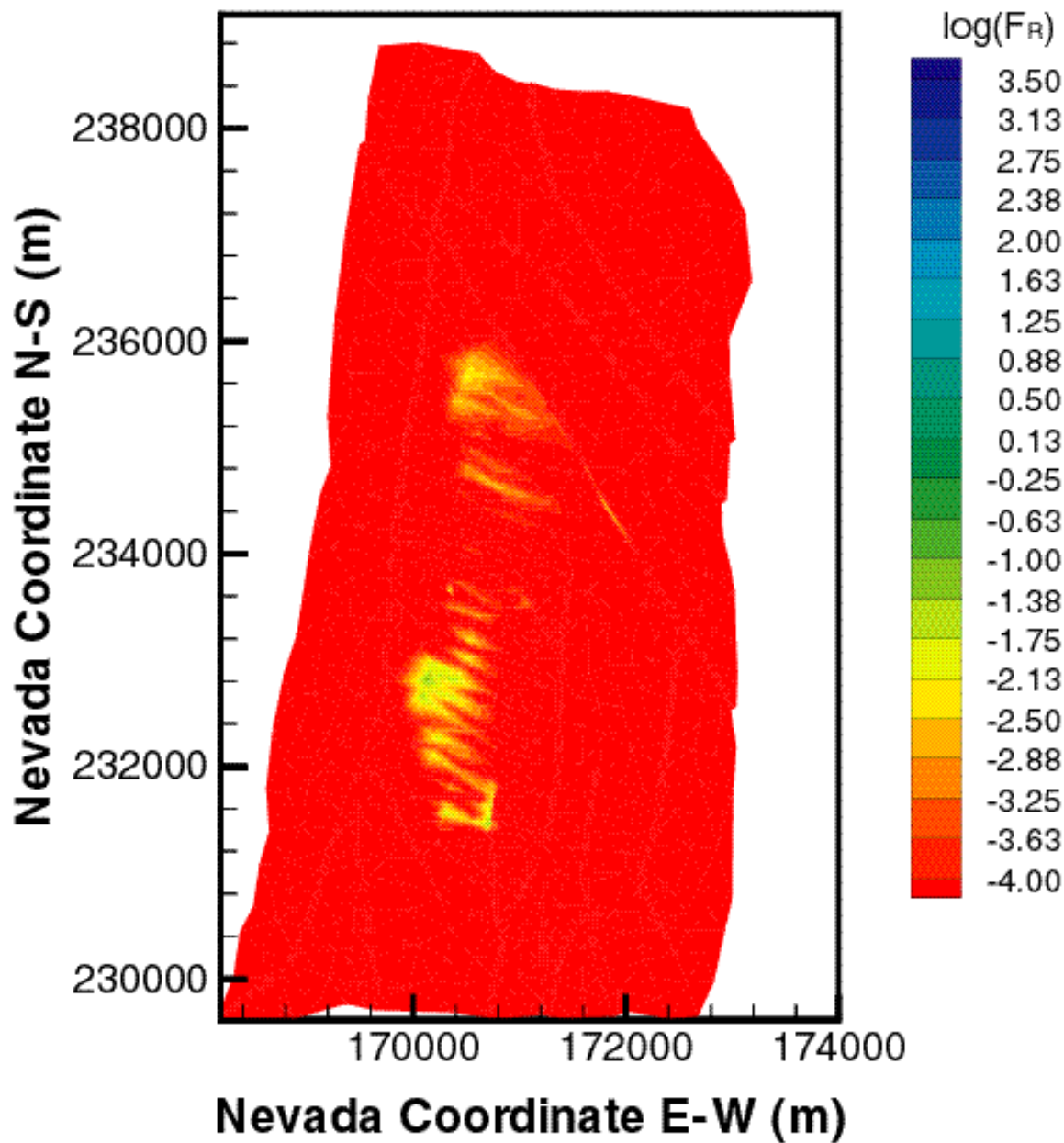


Figure IX.3. Distribution of the relative filtered concentration F_R of the 6 nm colloid in the matrix of the tsw39 layer at $t = 10$ years for mean present-day infiltration (DTN: LB991220140160.017, data submitted with this AMR).

FRACTURE MASS FRACTION AT BOTTOM OF TSw (for Co006 at 100 years)

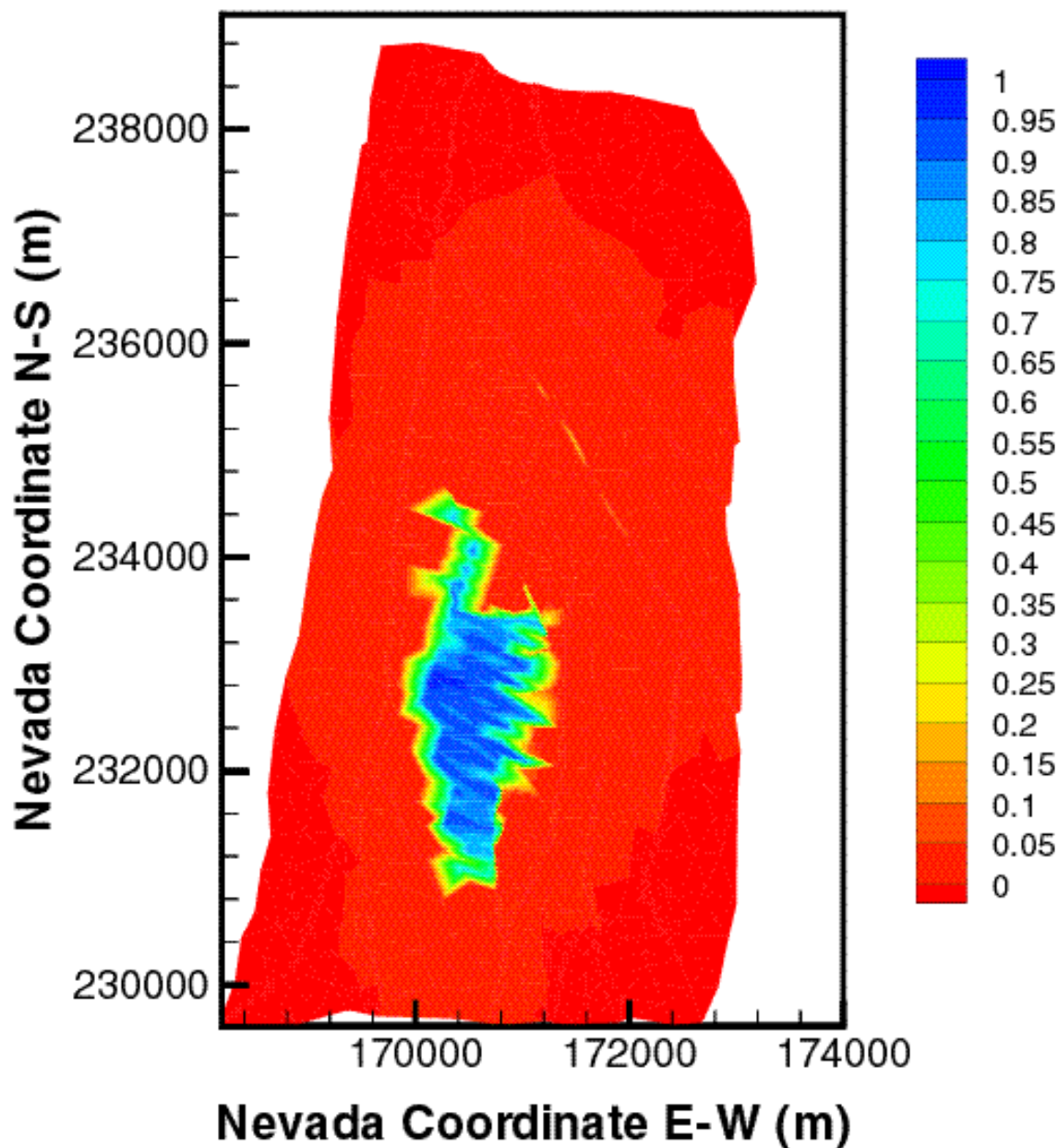


Figure IX.4. Distribution of the relative mass fraction X_R of the 6 nm colloid in the fractures of the tsw39 layer at $t = 100$ years for mean present-day infiltration (DTN: LB991220140160.017, data submitted with this AMR).

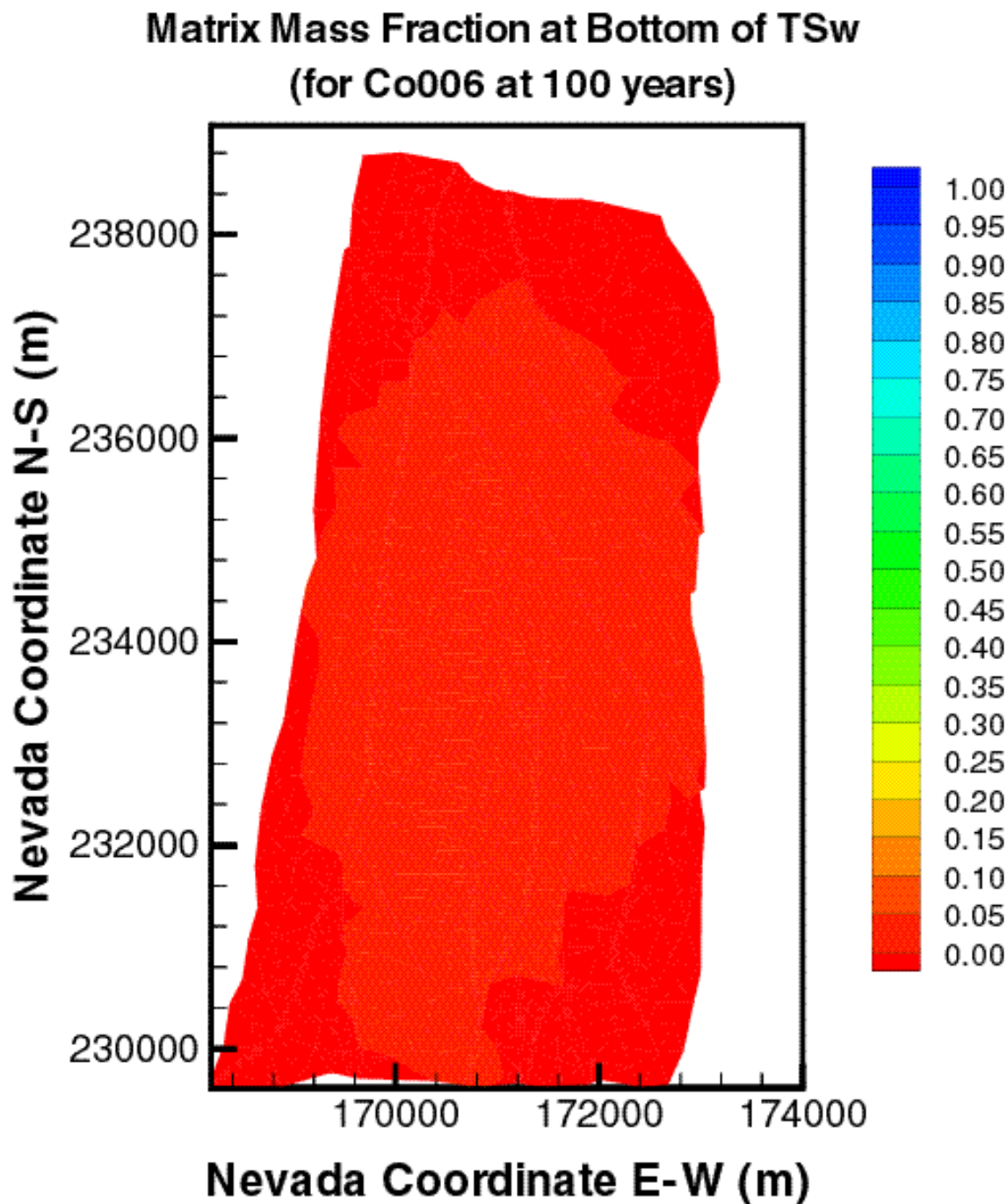


Figure IX.5. Distribution of the relative mass fraction X_R of the 6 nm colloid in the matrix of the tsw39 layer at $t = 100$ years for mean present-day infiltration (DTN: LB991220140160.017, data submitted with this AMR).

**Matrix Filtered Concentration at Bottom of TSw (kg/m³)
(for Co006 at 100 years)**

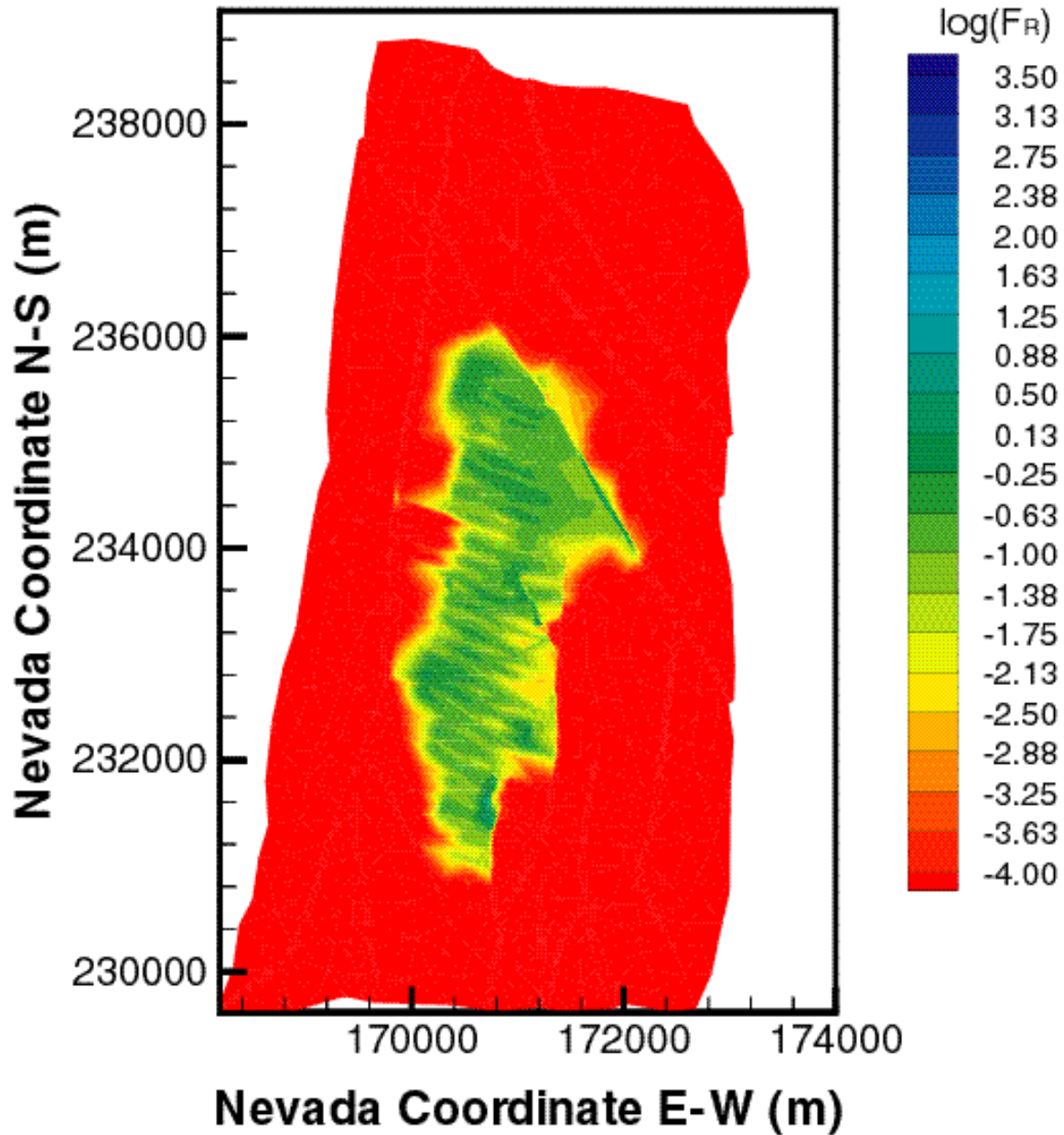


Figure IX.6. Distribution of the relative filtered concentration F_R of the 6 nm colloid in the matrix of the TSw layer at $t = 100$ years for mean present-day infiltration (DTN: LB991220140160.017, data submitted with this AMR).

FRACTURE MASS FRACTION AT BOTTOM OF TSw (for Co006 at 1000 years)

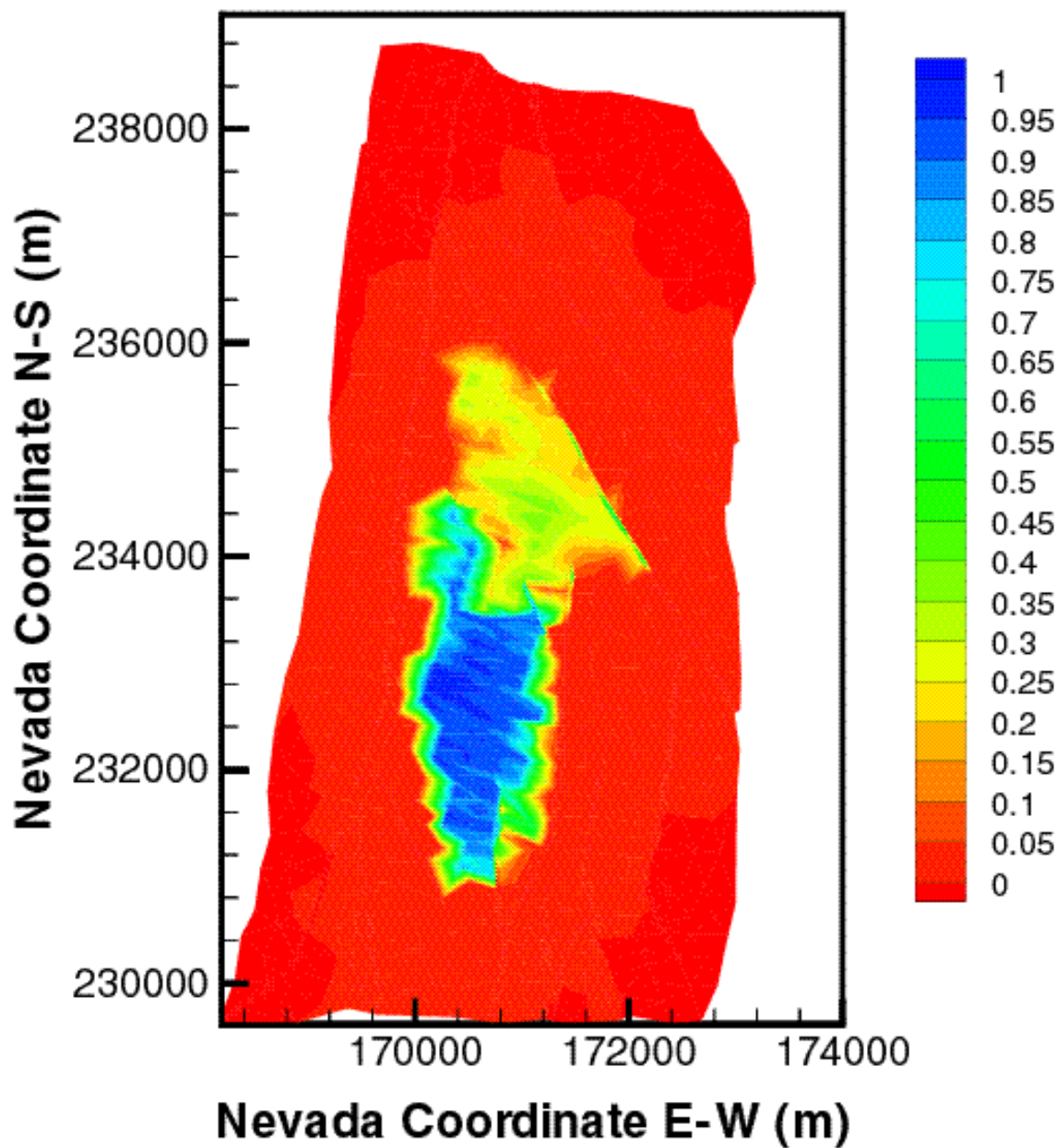


Figure IX.7. Distribution of the relative mass fraction X_R of the 6 nm colloid in the fractures of the tsw39 layer at $t = 1,000$ years for mean present-day infiltration (DTN: LB991220140160.017, data submitted with this AMR).

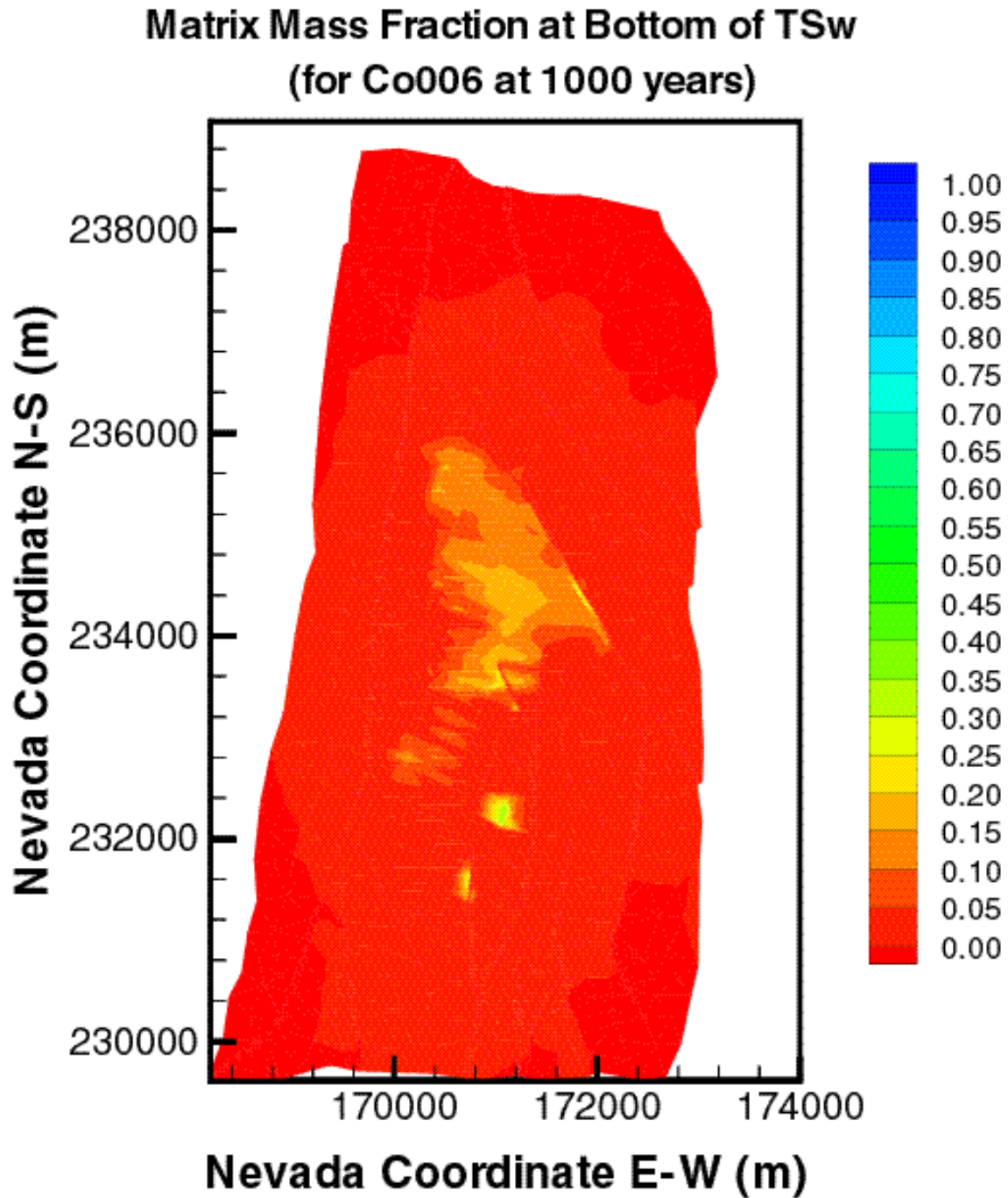


Figure IX.8. Distribution of the relative mass fraction X_R of the 6 nm colloid in the matrix of the tsw39 layer at $t = 1,000$ years for mean present-day infiltration (DTN: LB991220140160.017, data submitted with this AMR).

**Matrix Filtered Concentration at Bottom of TSw (kg/m³)
(for Co006 at 1000 years)**

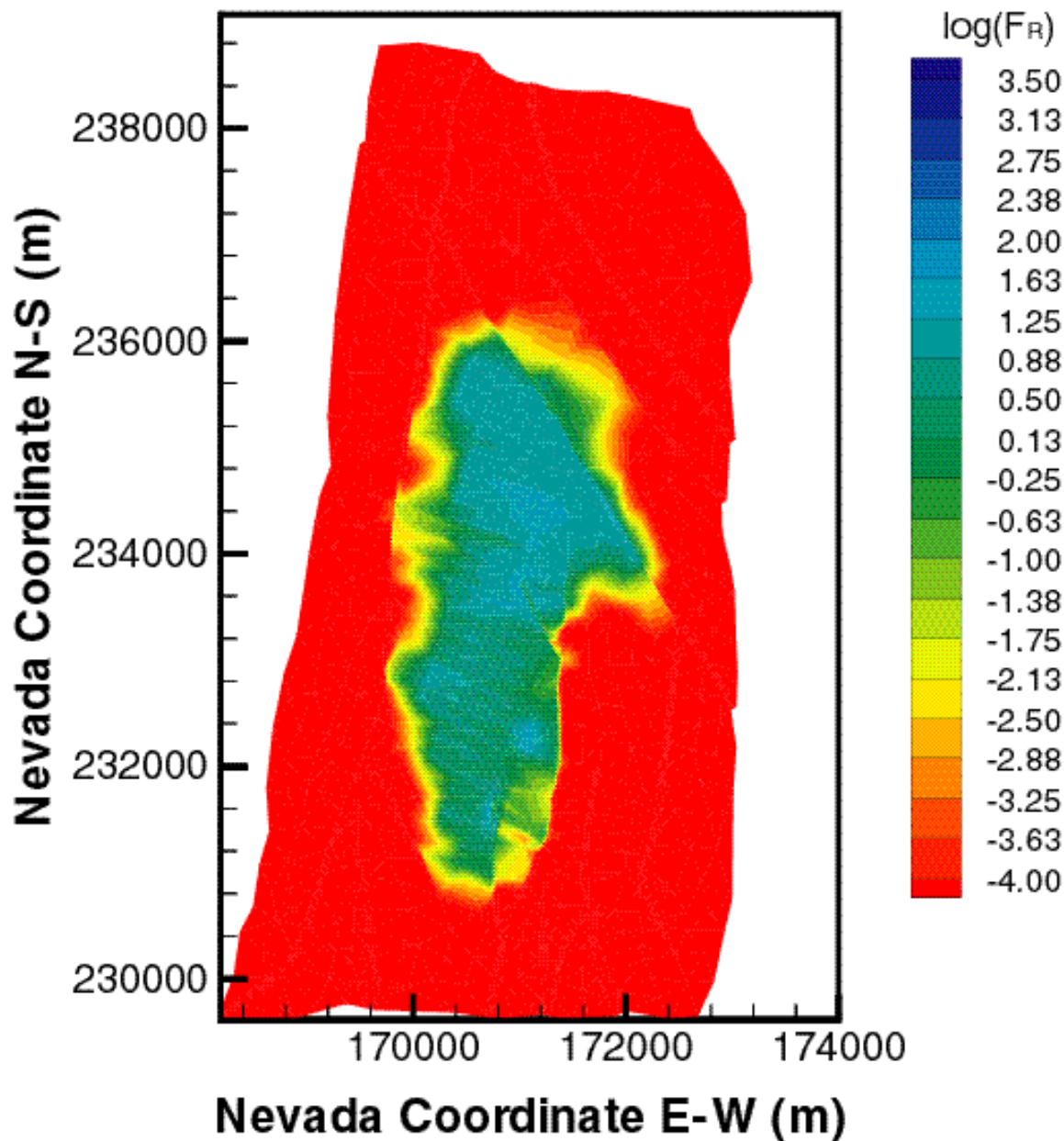


Figure IX.9. Distribution of the relative filtered concentration F_R of the 6 nm colloid in the matrix of the TSw layer at $t = 1,000$ years for mean present-day infiltration (DTN: LB991220140160.017, data submitted with this AMR).

FRACTURE MASS FRACTION AT BOTTOM OF TSw (for Co006 at 10000 years)

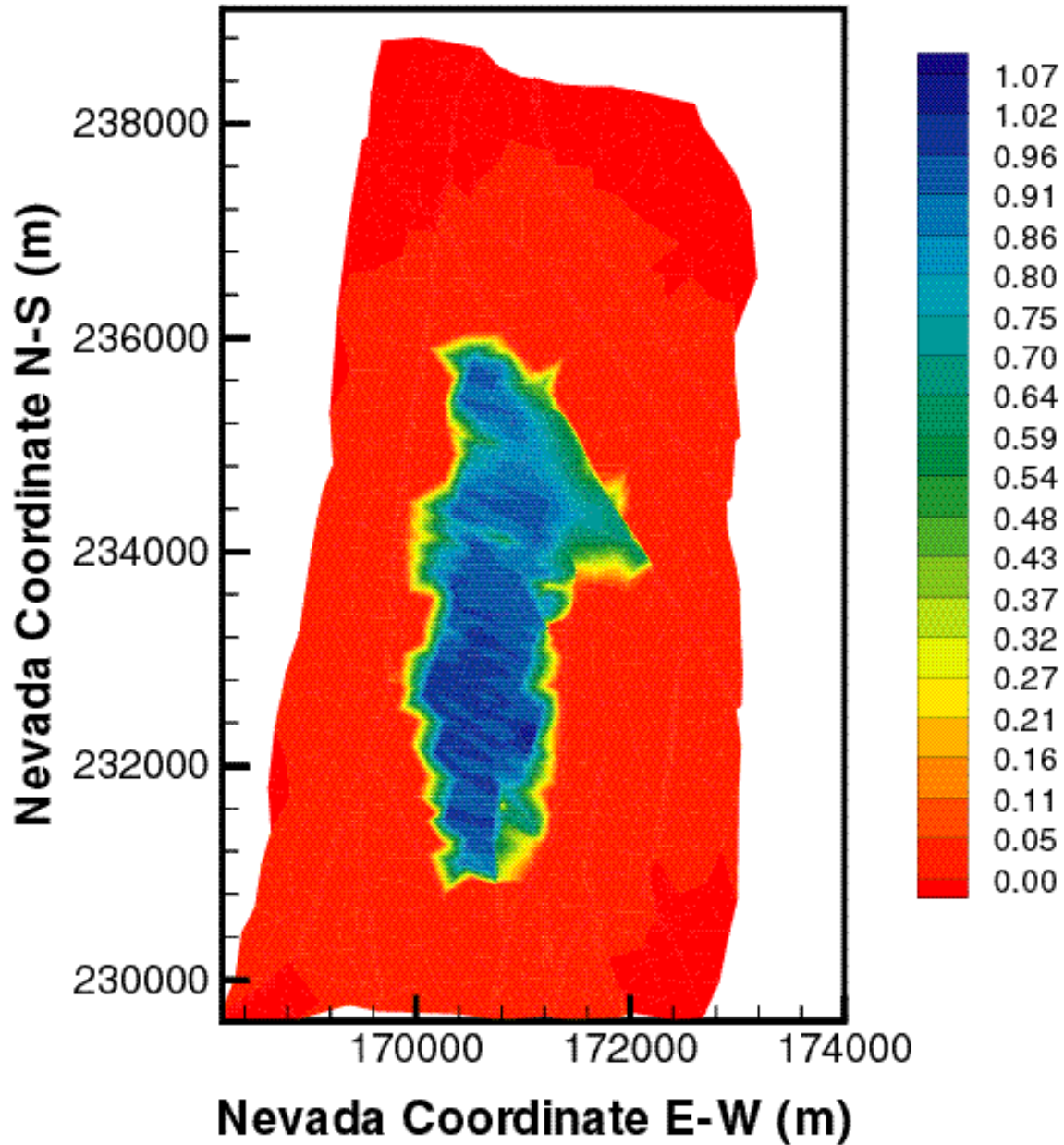


Figure IX.10. Distribution of the relative mass fraction X_R of the 6 nm colloid in the fractures of the tsw39 layer at $t = 10,000$ years for mean present-day infiltration (DTN: LB991220140160.017, data submitted with this AMR).

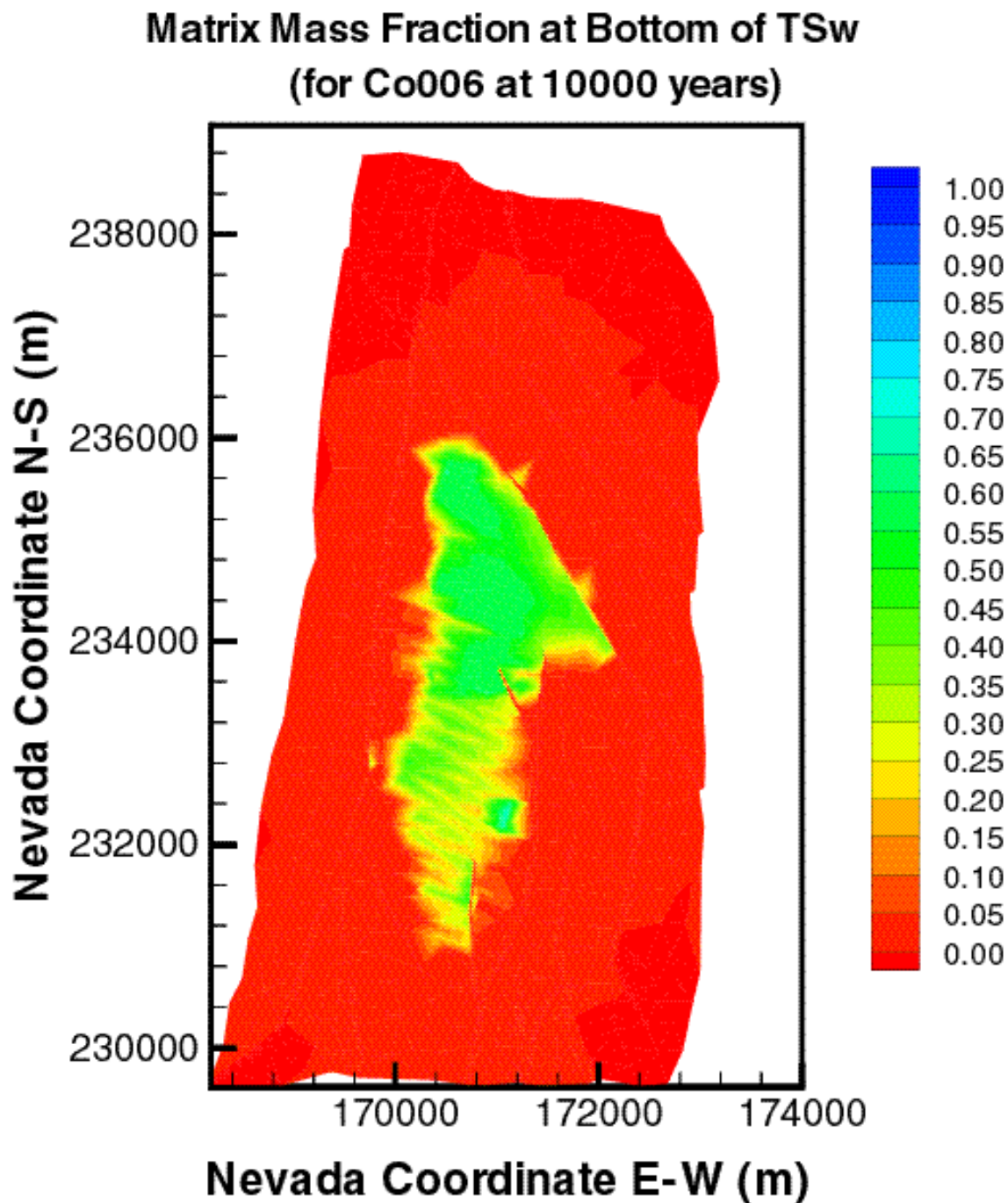


Figure IX.11. Distribution of the relative mass fraction X_R of the 6 nm colloid in the matrix of the tsw39 layer at $t = 10,000$ years for mean present-day infiltration (DTN: LB991220140160.017, data submitted with this AMR).

**Matrix Filtered Concentration at Bottom of TSw (kg/m³)
(for Co006 at 10000 years)**

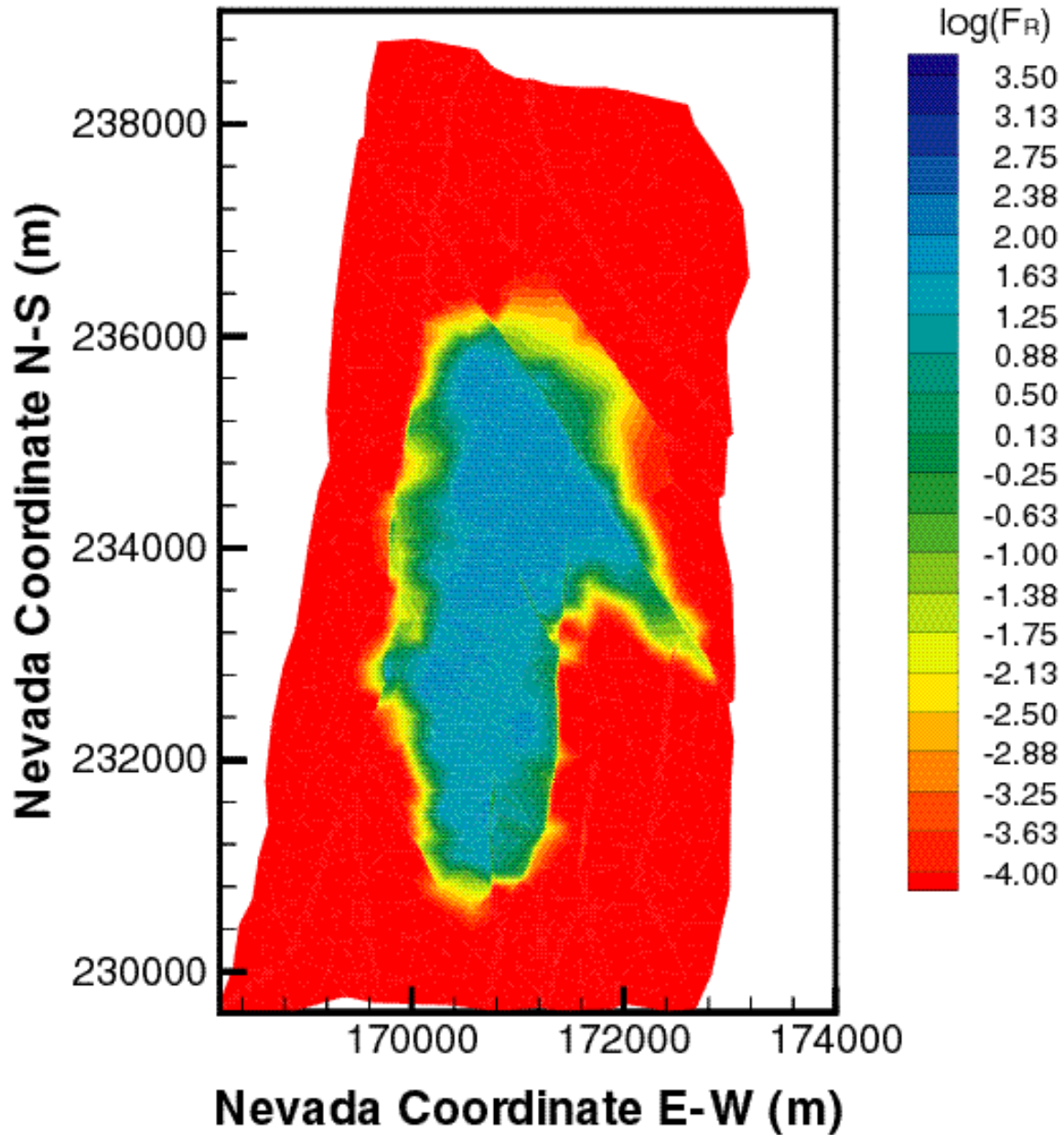


Figure IX.12. Distribution of the relative filtered concentration F_R of the 6nm colloid in the matrix of the TSw39 layer at $t = 10,000$ years for mean present-day infiltration (DTN: LB991220140160.017, data submitted with this AMR).

FRACTURE MASS FRACTION AT WATER TABLE (for Co006 at 10 years)

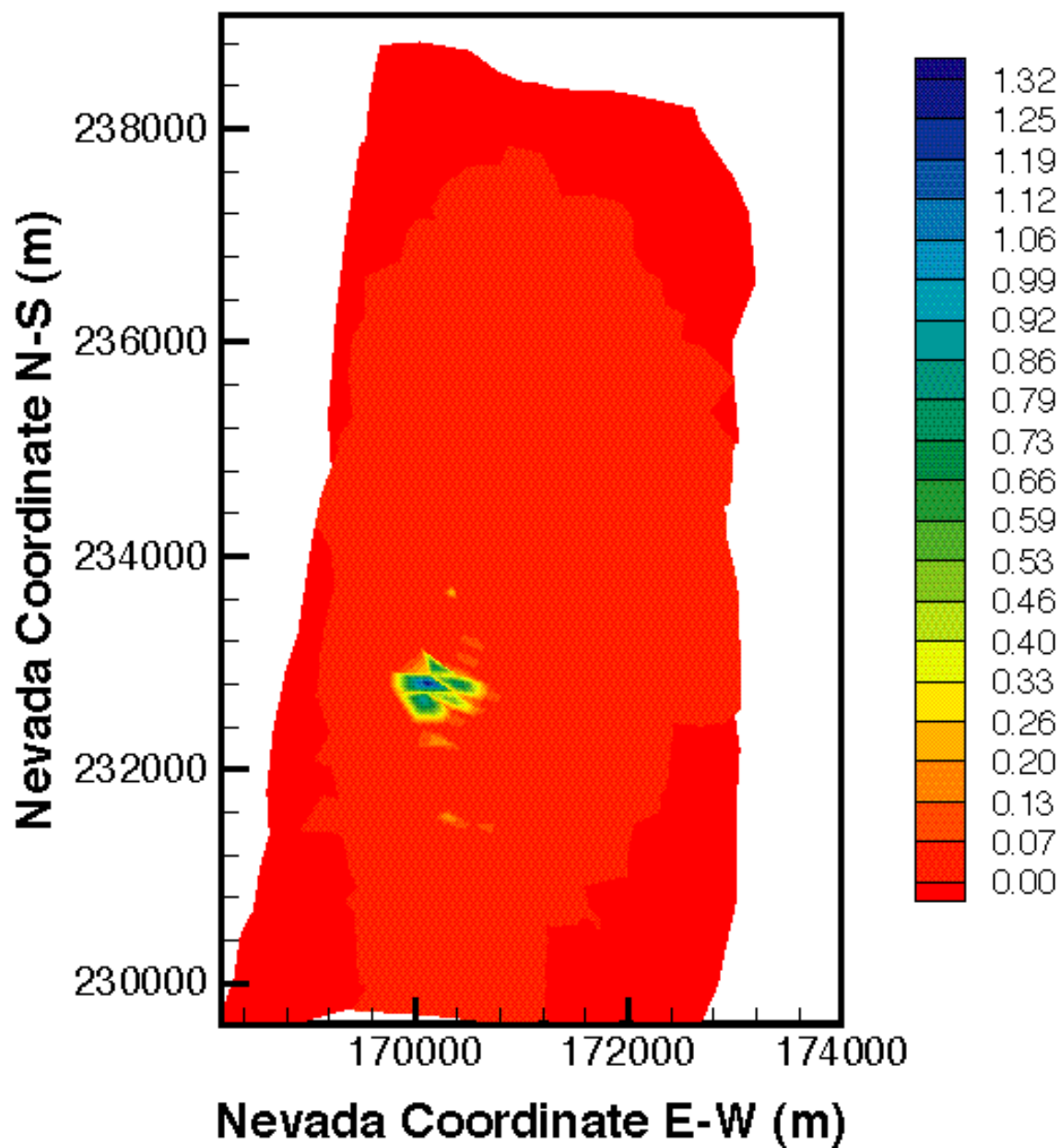


Figure IX.13. Distribution of the relative mass fraction X_R of the 6 nm colloid in the fractures immediately above the groundwater at $t = 10$ years for mean present-day infiltration (DTN: LB991220140160.017, data submitted with this AMR).

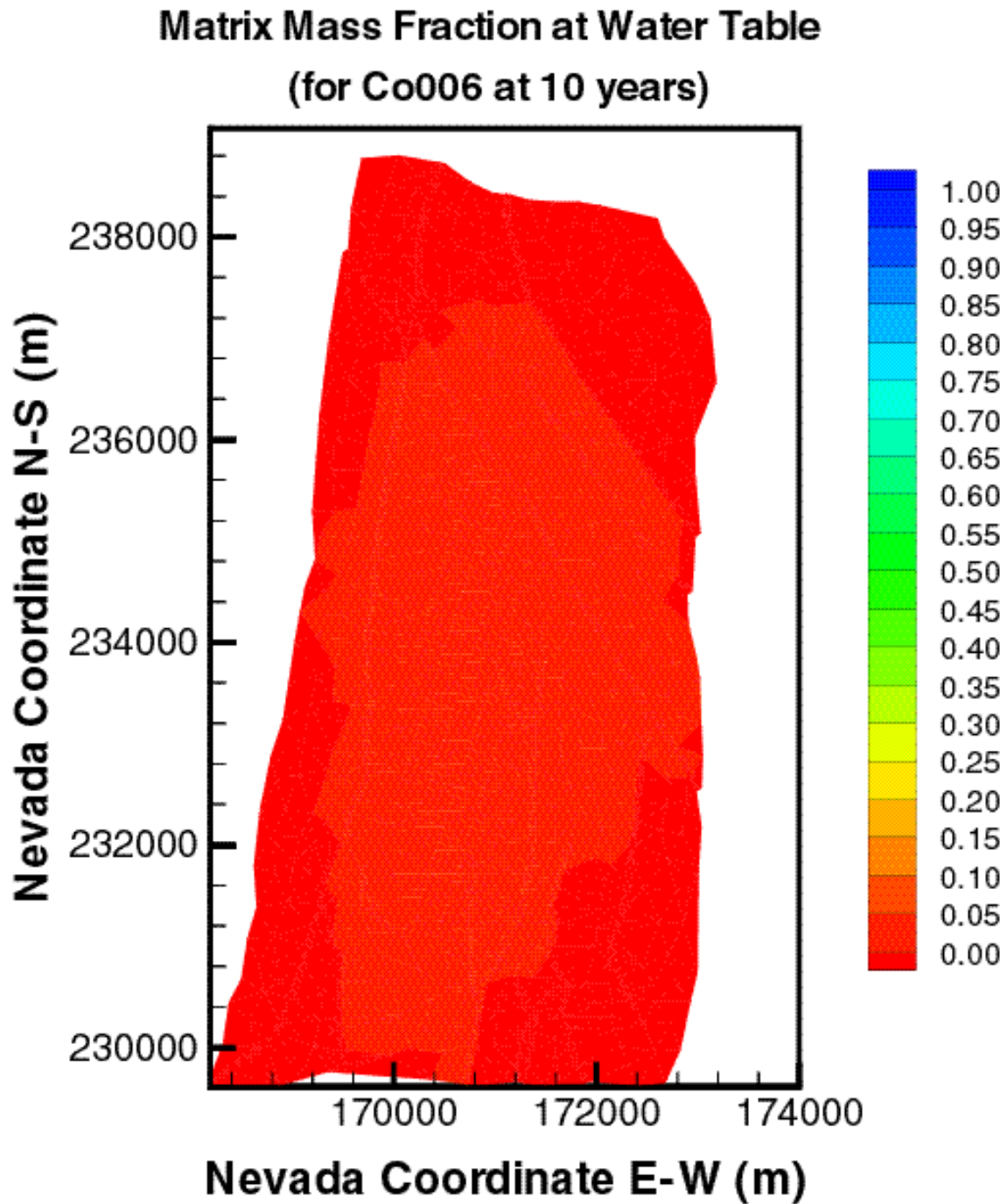


Figure IX.14. Distribution of the relative mass fraction X_R of the 6 nm colloid in the matrix immediately above the groundwater at $t = 10$ years for mean present-day infiltration (DTN: LB991220140160.017, data submitted with this AMR).

**Matrix Filtered Concentration at Water Table (kg/m^3)
(for Co006 at 10 years)**

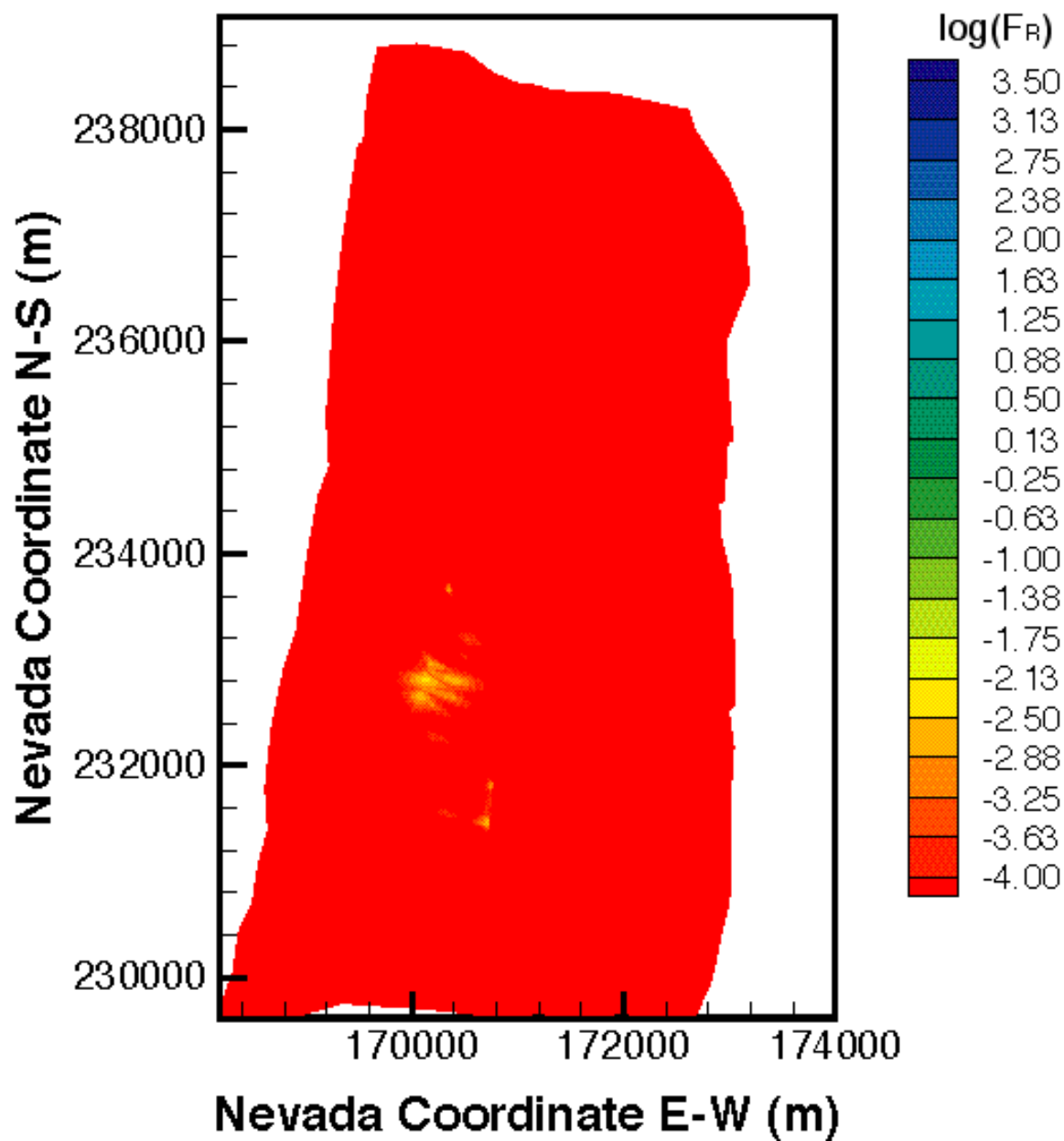


Figure IX.15. Distribution of the relative filtered concentration F_R of the 6 nm colloid in the matrix immediately above the groundwater at $t=10$ years for mean present-day infiltration (DTN:LB991220140160.017, data submitted with this AMR).

FRACTURE MASS FRACTION AT WATER TABLE (for Co006 at 100 years)

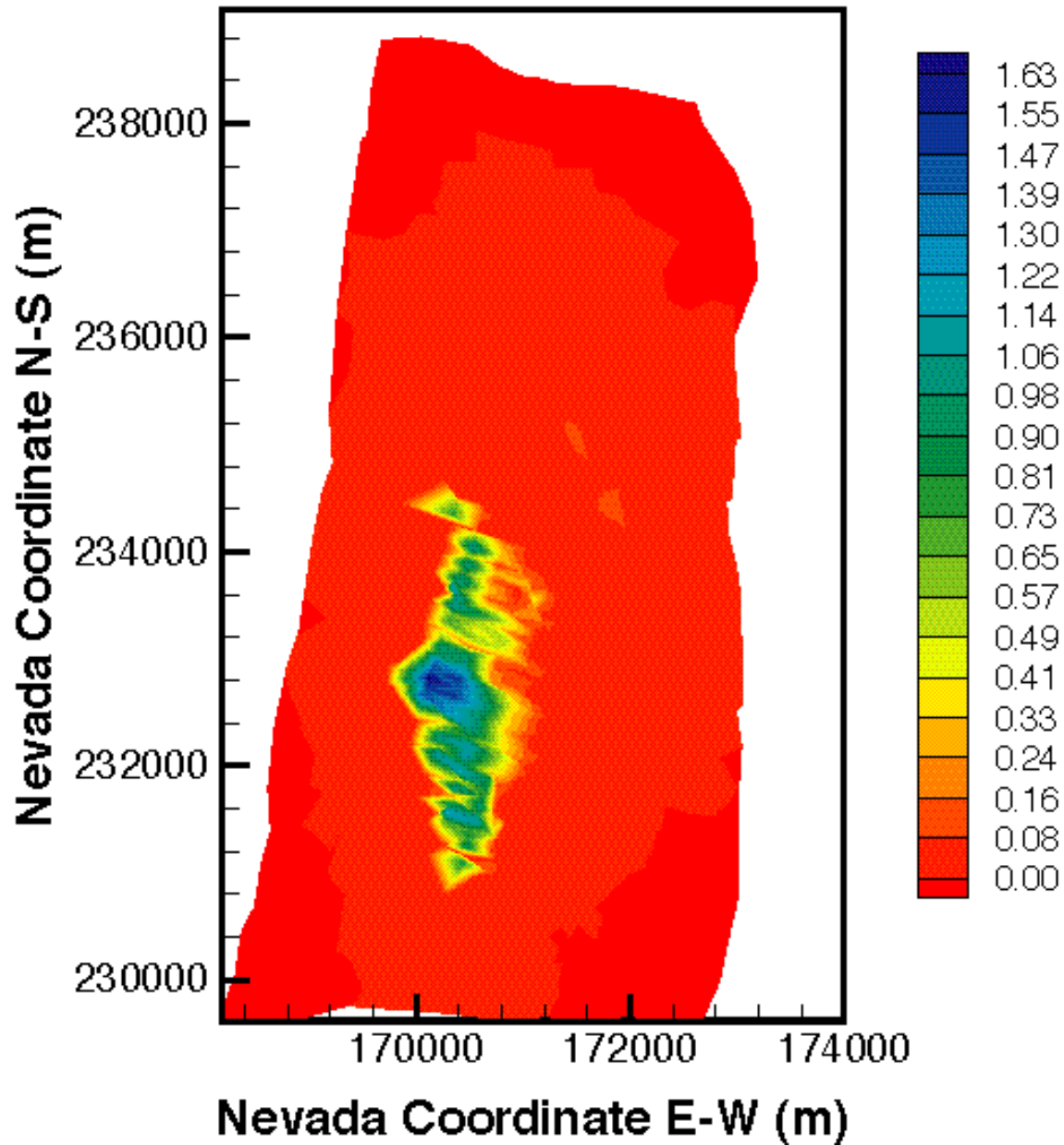


Figure IX.16. Distribution of the relative mass fraction X_R of the 6 nm colloid in the fractures immediately above the groundwater at $t = 100$ years for mean present-day infiltration (DTN: LB991220140160.017, data submitted with this AMR).

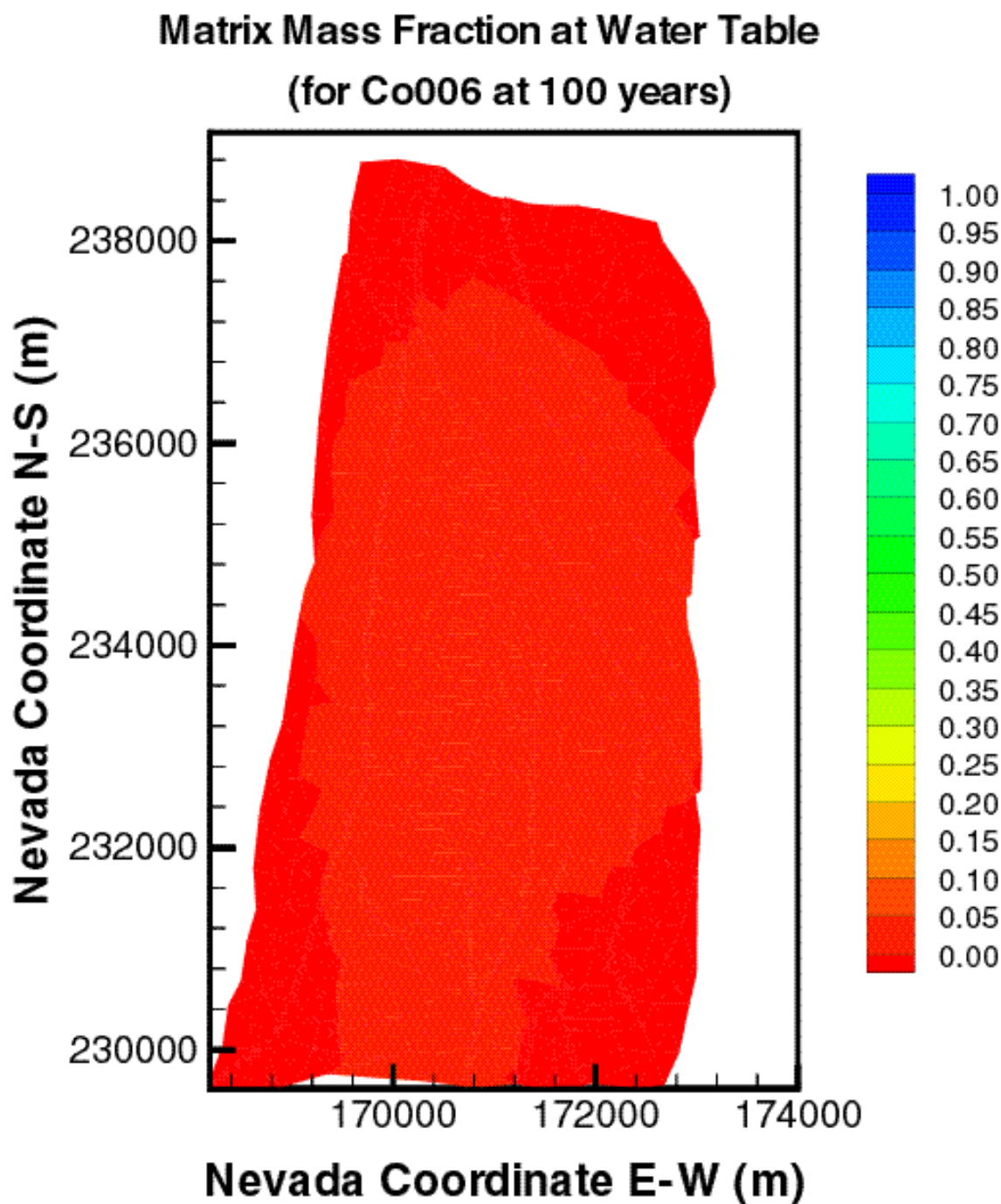


Figure IX.17. Distribution of the relative mass fraction X_R of the 6 nm colloid in the matrix immediately above the groundwater at $t = 100$ years for mean present-day infiltration (DTN: LB991220140160.017, data submitted with this AMR).

**Matrix Filtered Concentration at Water Table (kg/m^3)
(for Co006 at 100 years)**

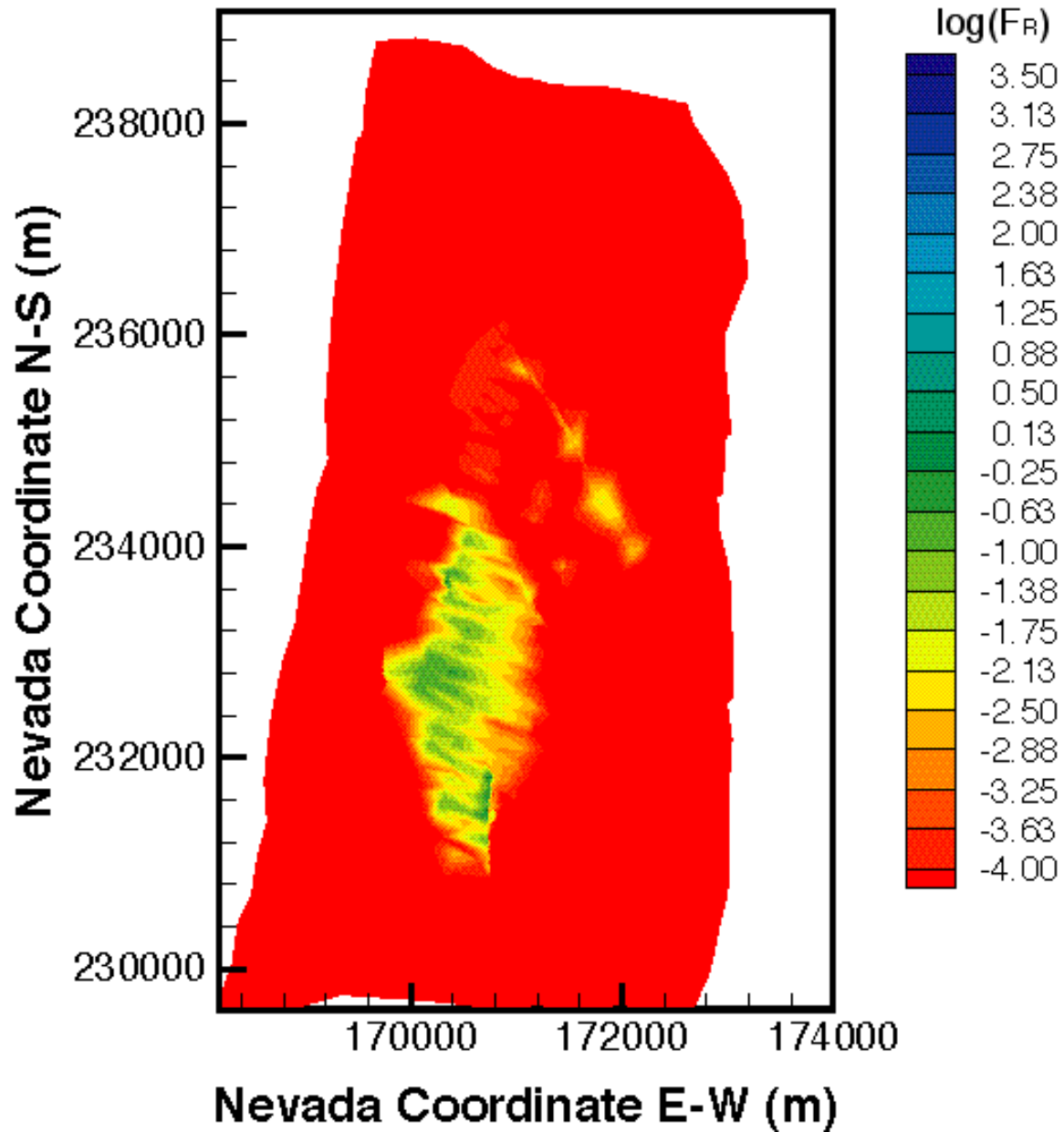


Figure IX.18. Distribution of the relative filtered concentration F_R of the 6 nm colloid in the matrix immediately above the groundwater at $t = 100$ years for mean present-day infiltration (DTN: LB991220140160.017, data submitted with this AMR).

FRACTURE MASS FRACTION AT WATER TABLE (for Co006 at 1000 years)

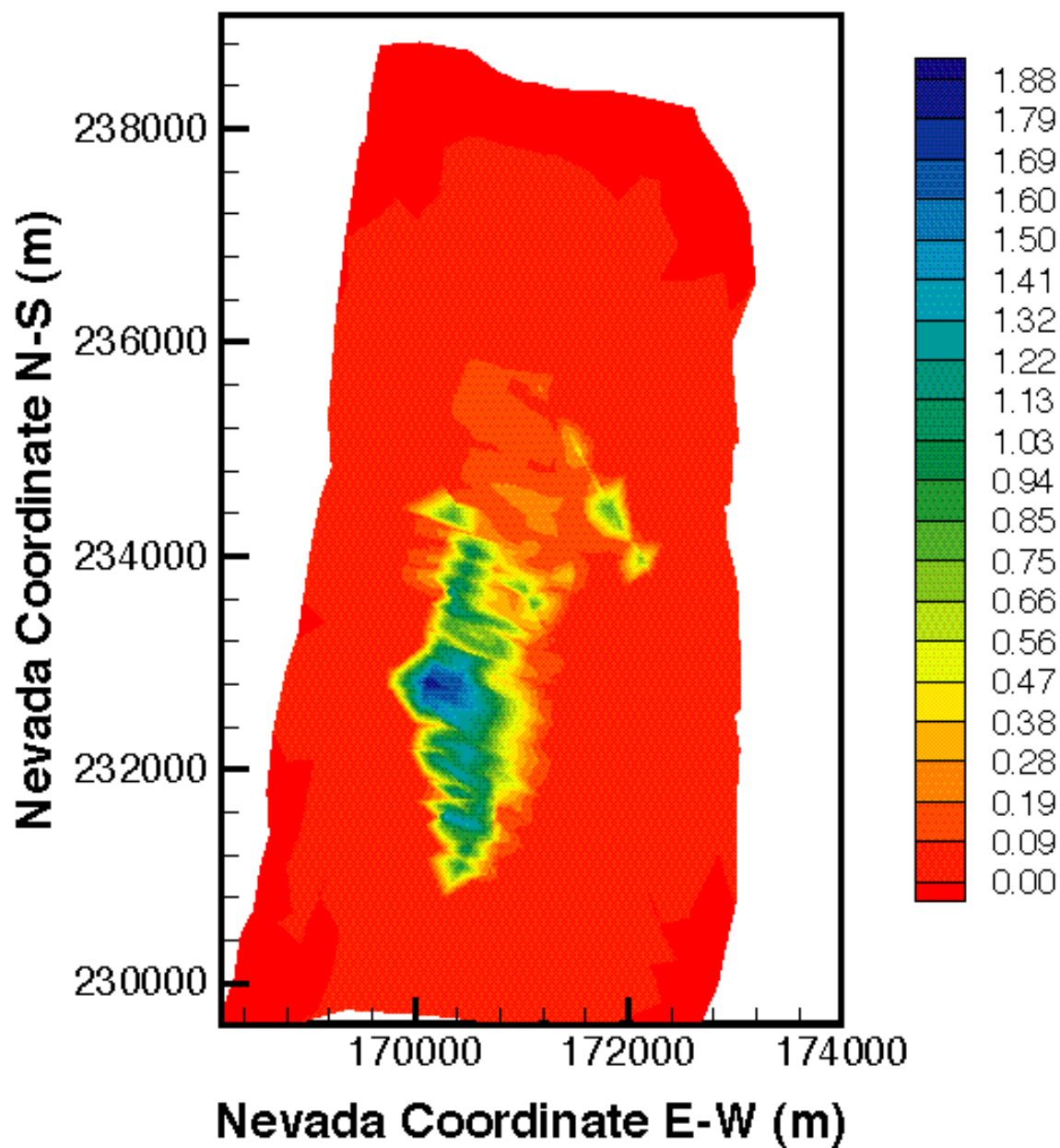


Figure IX.19. Distribution of the relative mass fraction X_R of the 6 nm colloid in the fractures immediately above the groundwater at $t = 1,000$ years for mean present-day infiltration (DTN: LB991220140160.017, data submitted with this AMR).

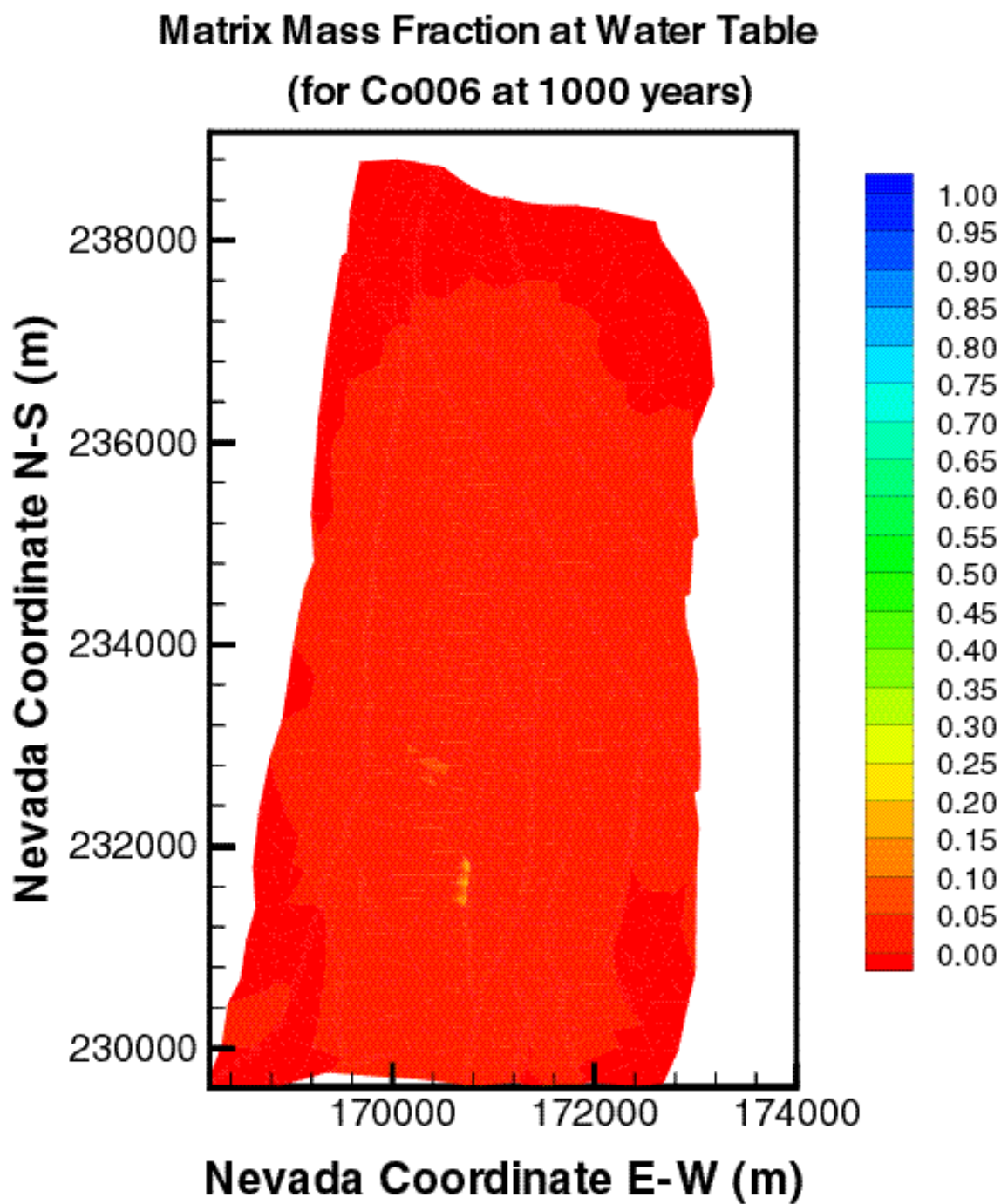


Figure IX.20. Distribution of the relative mass fraction X_R of the 6 nm colloid in the matrix immediately above the groundwater at $t = 1,000$ years for mean present-day infiltration (DTN: LB991220140160.017, data submitted with this AMR).

**Matrix Filtered Concentration at Water Table (kg/m^3)
(for Co006 at 1000 years)**

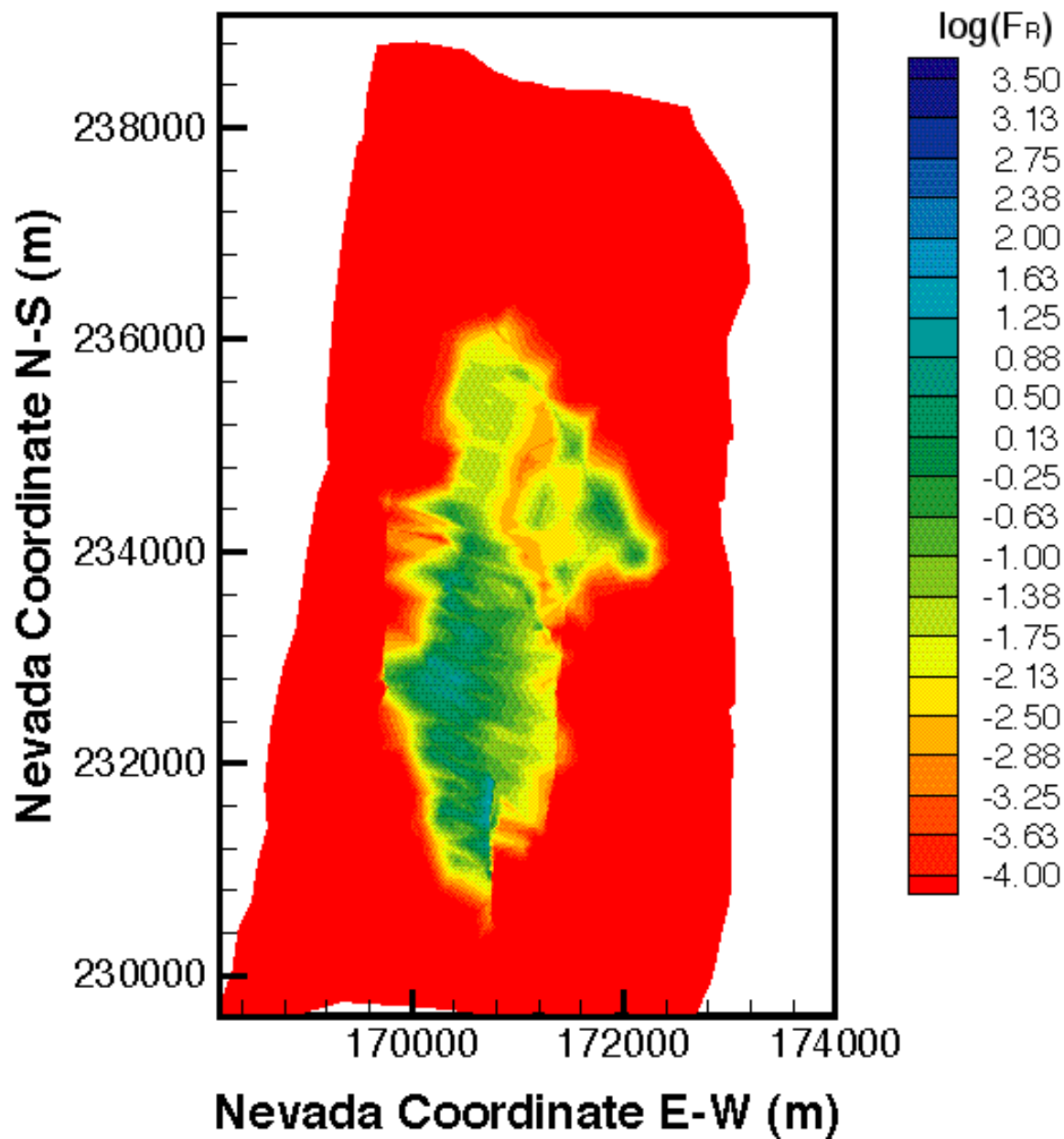


Figure IX.21. Distribution of the relative filtered concentration F_R of the 6 nm colloid in the matrix immediately above the groundwater at $t = 1,000$ years for mean present-day infiltration (DTN: LB991220140160.017, data submitted with this AMR).

FRACTURE MASS FRACTION AT WATER TABLE (for Co006 at 10000 years)

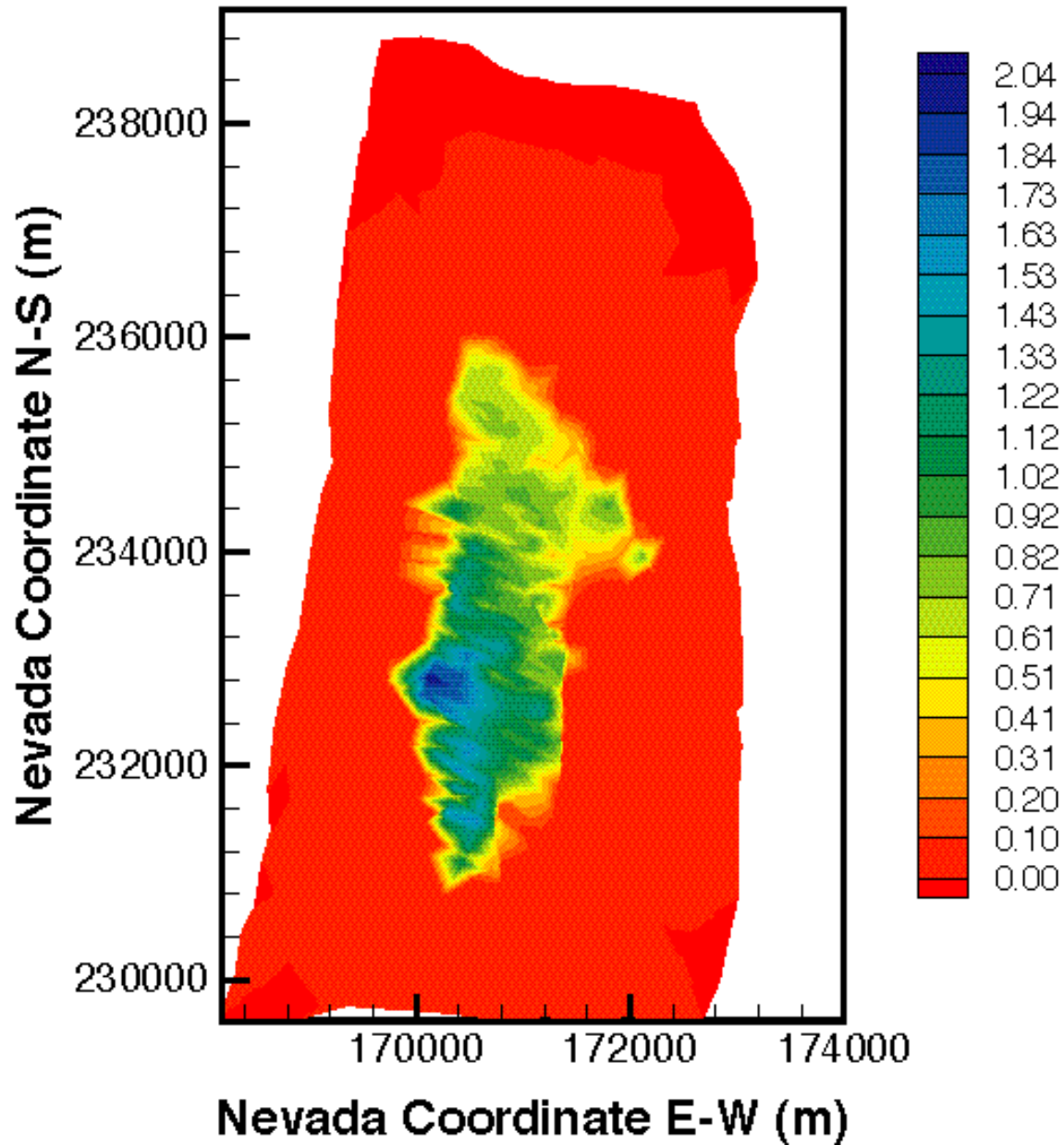


Figure IX.22. Distribution of the relative mass fraction X_R of the 6 nm colloid in the fractures immediately above the groundwater at $t = 10,000$ years for mean present-day infiltration (DTN: LB991220140160.017, data submitted with this AMR).

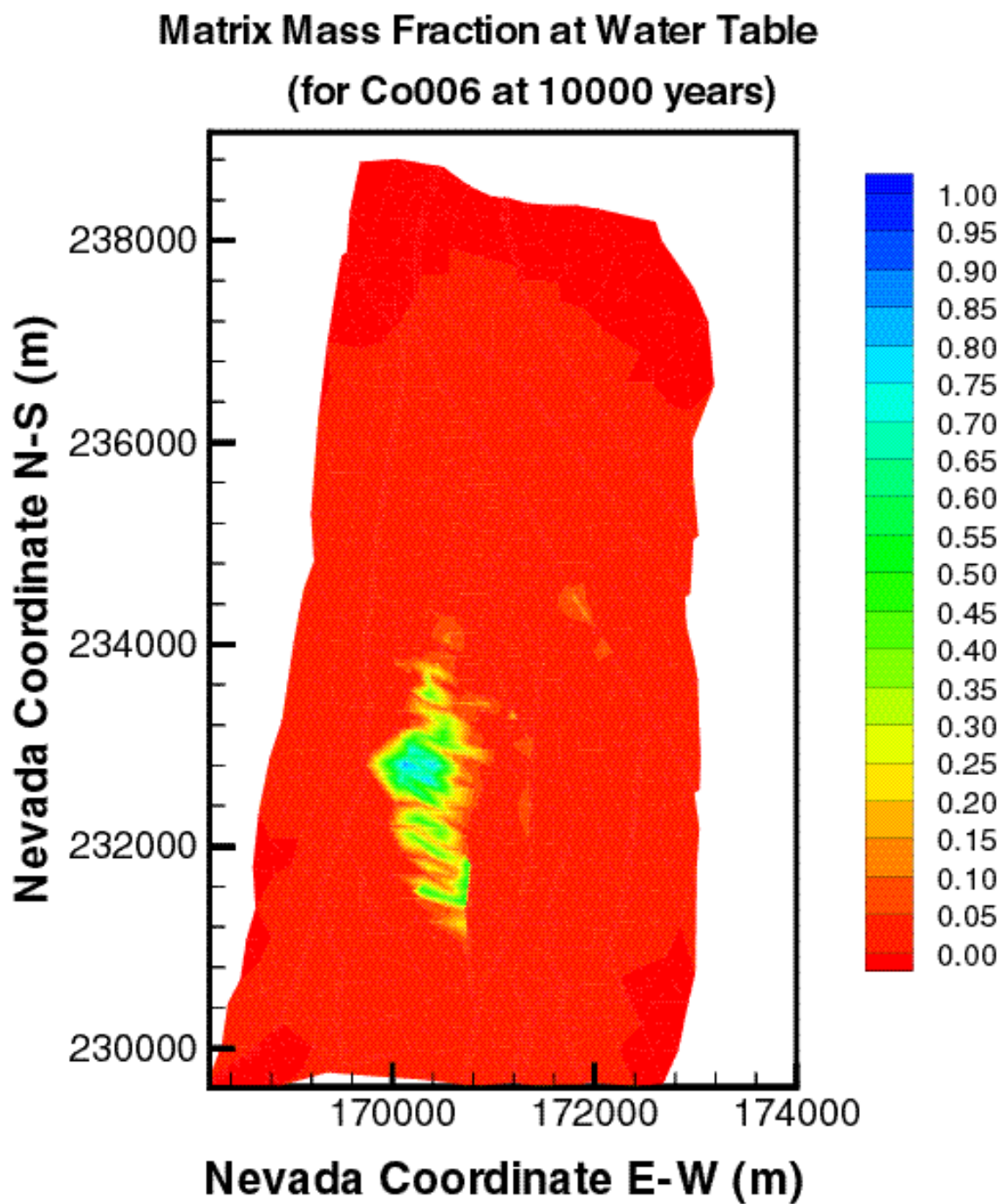


Figure IX.23. Distribution of the relative mass fraction X_R of the 6 nm colloid in the matrix immediately above the groundwater at $t = 10,000$ years for mean present-day infiltration (DTN: LB991220140160.017, data submitted with this AMR).

Matrix Filtered Concentration at Water Table (kg/m^3)
(for Co006 at 10000 years)

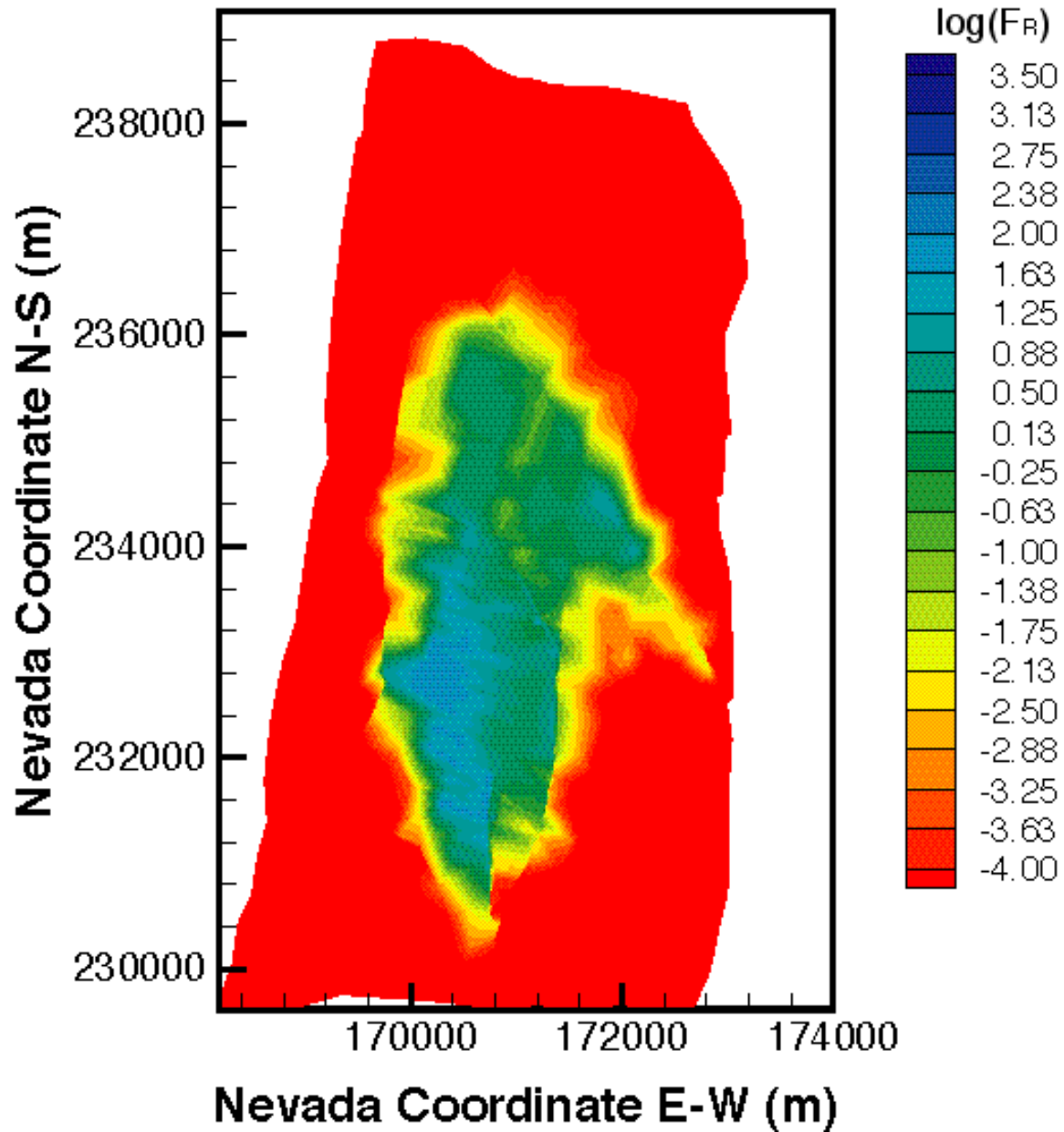


Figure IX.24. Distribution of the relative filtered concentration F_R of the 6 nm colloid in the matrix immediately above the groundwater at $t = 10,000$ years for mean present-day infiltration (DTN: LB991220140160.017, data submitted with this AMR).

ATTACHMENT X.

FIGURES FROM THE 3-D TRANSPORT STUDIES OF THE 450 nm COLLOID

INTENTIONALLY LEFT BLANK

FIGURES

	Page
X.1. Distribution of the Relative Mass Fraction X_R of the 450 nm colloid in the Fractures of the Tsw39 Layer at $t = 10$ Years for Mean Present-Day Infiltration.....	X-5
X.2. Distribution of the Relative Mass Fraction X_R of the 450 nm colloid in the Matrix of the Tsw39 Layer at $t = 10$ Years for Mean Present-Day Infiltration.....	X-6
X.3. Distribution of the Relative Filtered Concentration F_R of the 450 nm colloid in the Matrix of the Tsw39 Layer at $t = 10$ Years for Mean Present-Day Infiltration.....	X-7
X.4. Distribution of the Relative Mass Fraction X_R of the 450 nm colloid in the Fractures of the Tsw39 Layer at $t = 100$ Years for Mean Present-Day Infiltration.....	X-8
X.5. Distribution of the Relative Mass Fraction X_R of the 450 nm colloid in the Matrix of the Tsw39 Layer at $t = 100$ Years for Mean Present-Day Infiltration.....	X-9
X.6. Distribution of the Relative Filtered Concentration F_R of the 450 nm colloid in the Matrix of the Tsw39 Layer at $t = 100$ Years for Mean Present-Day Infiltration.	X-10
X.7. Distribution of the Relative Mass Fraction X_R of the 450 nm colloid in the Fractures of the Tsw39 Layer at $t = 1,000$ Years for Mean Present-Day Infiltration.....	X-11
X.8. Distribution of the Relative Mass Fraction X_R of the 450 nm colloid in the Matrix of the Tsw39 Layer at $t = 1,000$ Years for Mean Present-Day Infiltration.....	X-12
X.9. Distribution of the Relative Filtered Concentration F_R of the 450 nm colloid in the Matrix of the Tsw39 Layer at $t = 1,000$ Years for Mean Present-Day Infiltration.	X-13
X.10. Distribution of the Relative Mass Fraction X_R of the 450 nm colloid in the Fractures of the Tsw39 Layer at $t = 10,000$ Years for Mean Present-Day Infiltration.....	X-14
X.11. Distribution of the Relative Mass Fraction X_R of the 450 nm colloid in the Matrix of the Tsw39 Layer at $t = 10,000$ Years for Mean Present-Day Infiltration.	X-15
X.12. Distribution of the Relative Filtered Concentration F_R of the 450 nm colloid in the the Matrix of the Tsw39 Layer at $t = 10,000$ Years for Mean Present-Day Infiltration.....	X-16
X.13. Distribution of the Relative Mass Fraction X_R of the 450 nm colloid in the Fractures Immediately Above the Groundwater at $t = 10$ Years for Mean Present-Day Infiltration.....	X-17

FIGURES (Continued)

	Page
X.14. Distribution of the Relative Mass Fraction X_R of the 450 nm colloid in the Matrix Immediately Above the Groundwater Table at $t = 10$ Years for a Mean Present-Day Infiltration.....	X-18
X.15. Distribution of the Relative Filtered Concentration F_R of the 450 nm colloid in the Matrix Immediately Above the Groundwater Table at $t = 10$ Years for a Mean Present-Day Infiltration.....	X-19
X.16. Distribution of the Relative Mass Fraction X_R of the 450 nm colloid in the Fractures Immediately Above the Groundwater at $t = 100$ Years for Mean Present-Day Infiltration.....	X-20
X.17. Distribution of the Relative Mass Fraction X_R of the 450 nm colloid in the Matrix Immediately Above the Groundwater Table at $t = 100$ Years for a Mean Present-Day Infiltration.....	X-21
X.18. Distribution of the Relative Filtered Concentration F_R of the 450 nm colloid in the Matrix Immediately Above the Groundwater Table at $t = 100$ Years for a Mean Present-Day Infiltration.....	X-22
X.19. Distribution of the Relative Mass Fraction X_R of the 450 nm colloid in the Fractures Immediately Above the Groundwater at $t = 1,000$ Years for Mean Present-Day Infiltration.....	X-23
X.20. Distribution of the Relative Mass Fraction X_R of the 450 nm colloid in the Matrix Immediately Above the Groundwater Table at $t = 1,000$ Years for a Mean Present-Day Infiltration.....	X-24
X.21. Distribution of the Relative Filtered Concentration F_R of the 450 nm colloid in the Matrix Immediately Above the Groundwater Table at $t = 1,000$ Years for a Mean Present-Day Infiltration.....	X-25
X.22. Distribution of the Relative Mass Fraction X_R of the 450 nm colloid in the Fractures Immediately Above the Groundwater at $t = 10,000$ Years for Mean Present-Day Infiltration.....	X-26
X.23. Distribution of the Relative Mass Fraction X_R of the 450 nm colloid in the Matrix Immediately Above the Groundwater Table at $t = 10,000$ Years for a Mean Present-Day Infiltration.....	X-27
X.24. Distribution of the Relative Filtered Concentration F_R of the 450 nm colloid in the Matrix Immediately Above the Groundwater Table at $t = 10,000$ Years for a Mean Present-Day Infiltration.....	X-28

FRACTURE MASS FRACTION AT BOTTOM OF TSW (for Co450 at 10 years)

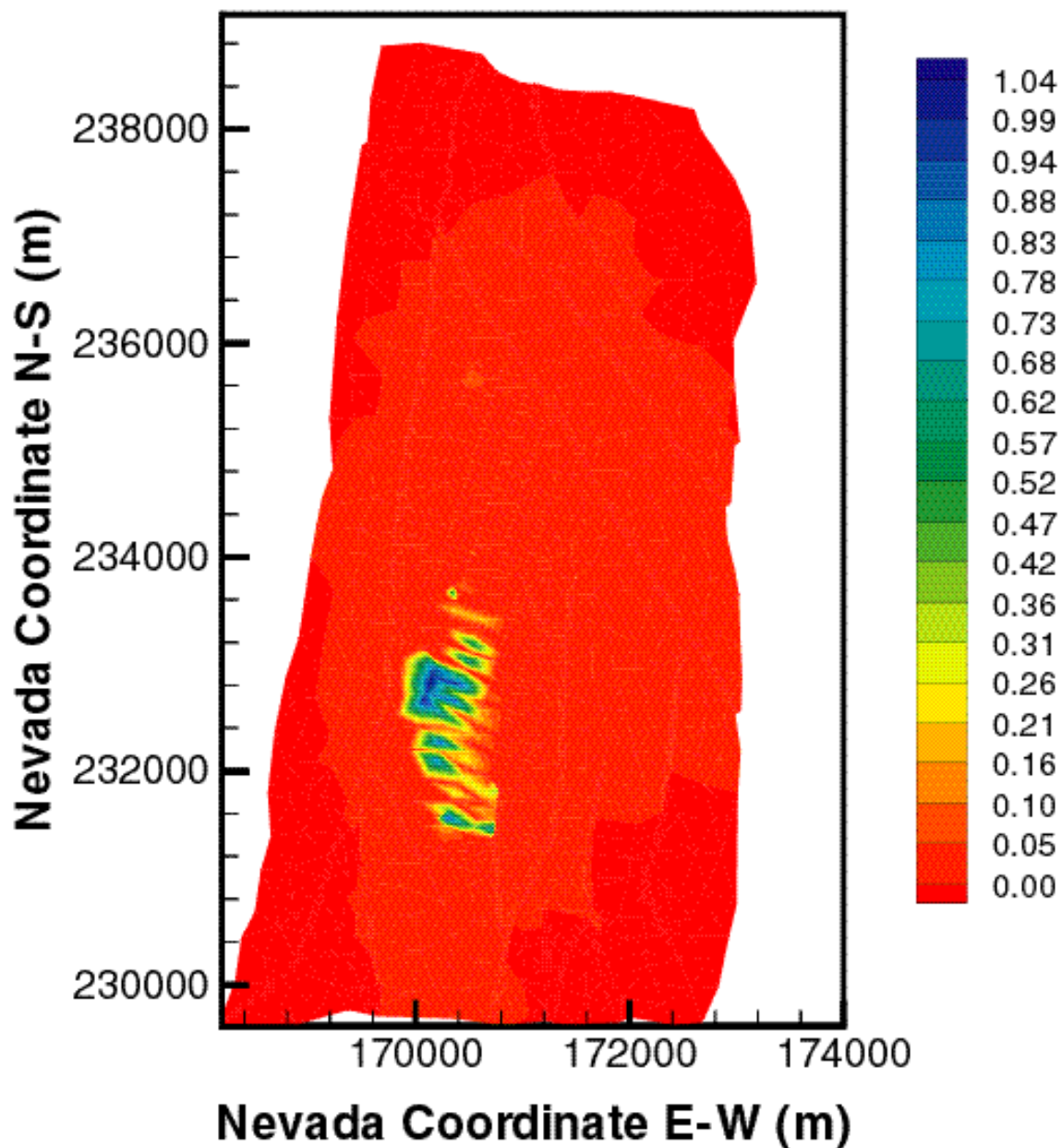


Figure X.1. Distribution of the relative mass fraction X_R of the 450 nm colloid in the fractures of the tsw39 layer at $t = 10$ years for mean present-day infiltration (DTN: LB991220140160.017, data submitted with this AMR).

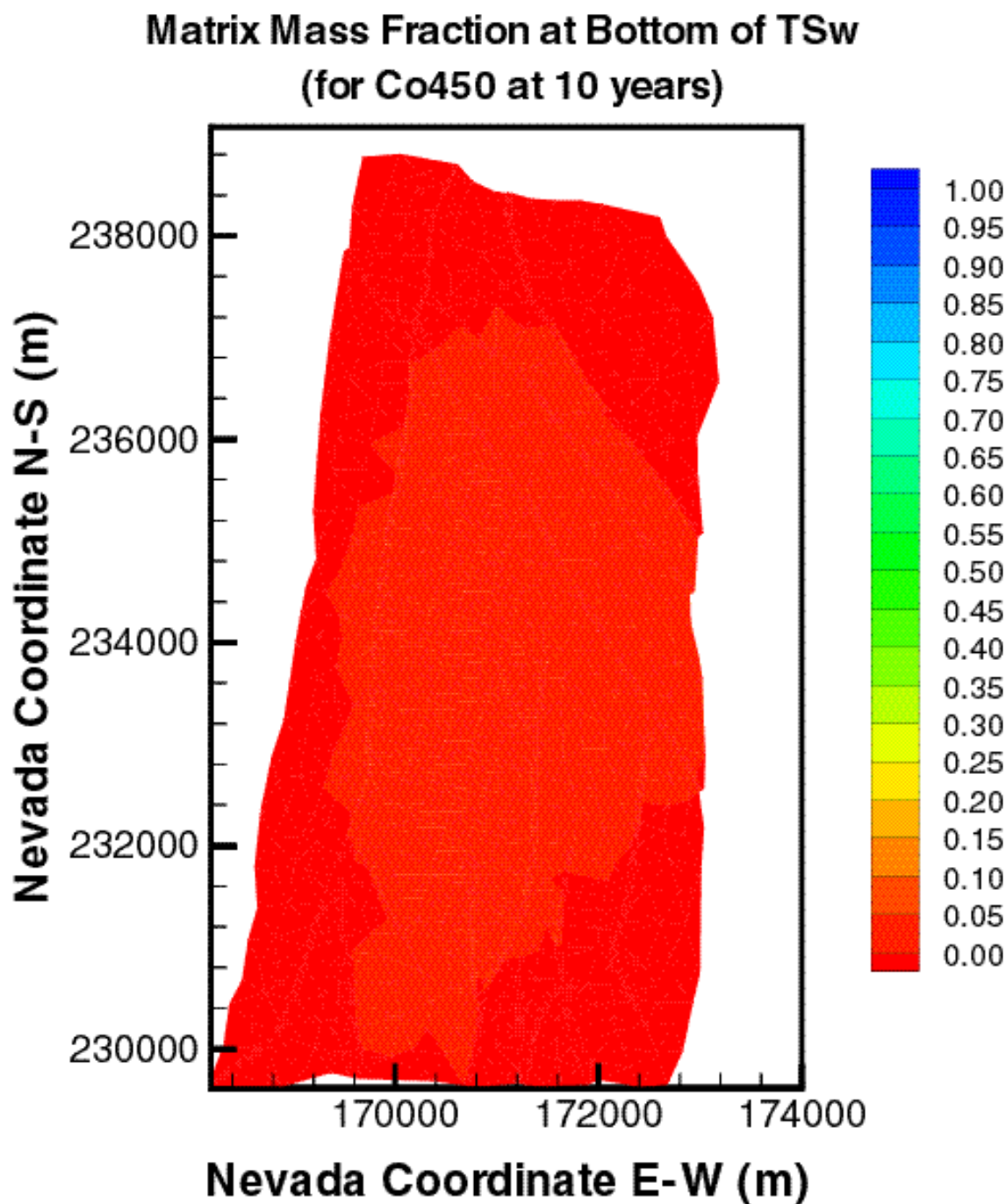


Figure X.2. Distribution of the relative mass fraction X_R of the 450 nm colloid in the matrix of the tsw39 layer at $t = 10$ years for mean present-day infiltration (DTN: LB991220140160.017, data submitted with this AMR).

**Matrix Filtered Concentration at Bottom of TSw (kg/m^3)
(for Co450 at 10 years)**

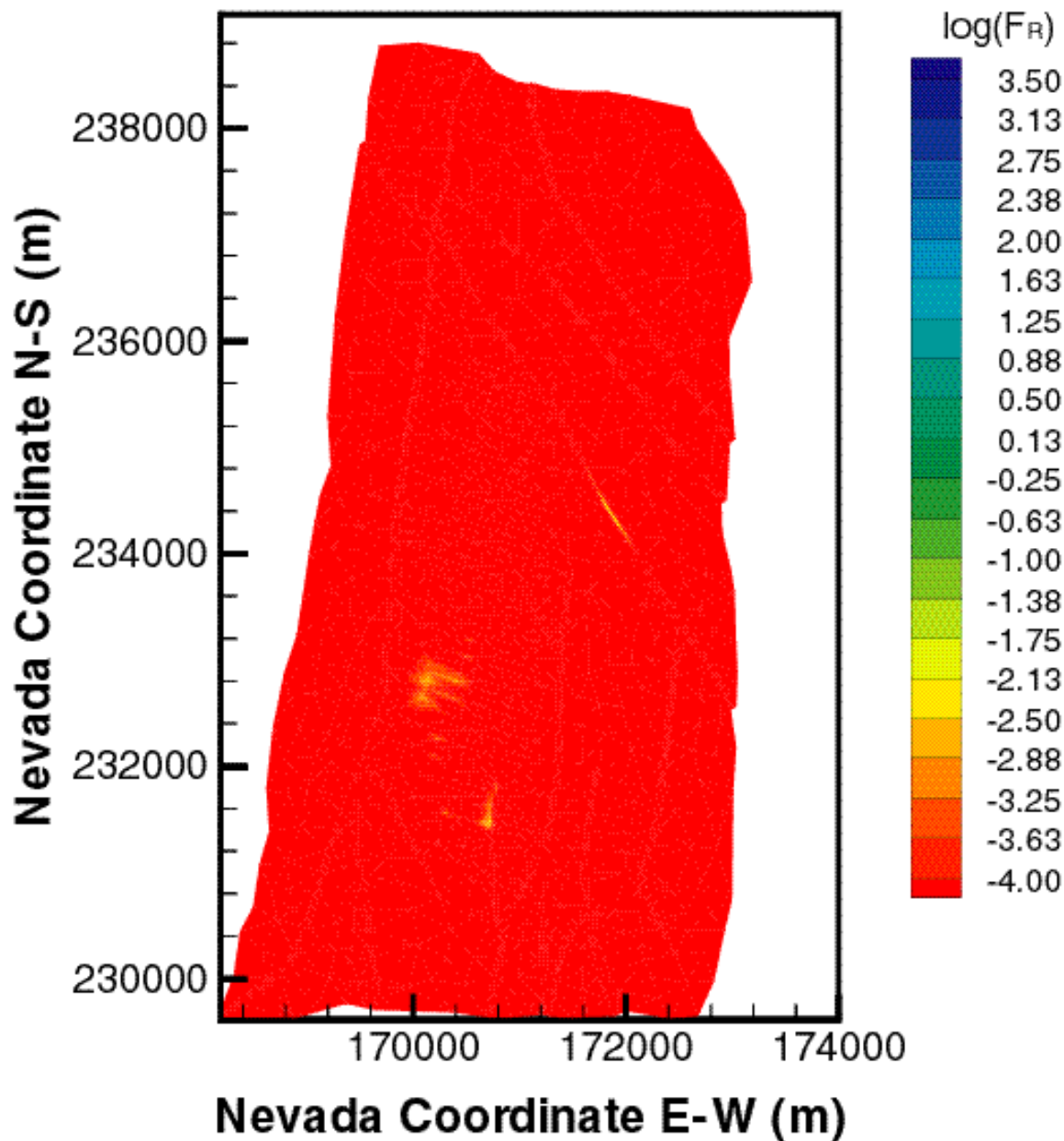


Figure X.3. Distribution of the relative filtered concentration F_R of the 450 nm colloid in the matrix of the tsw39 layer at $t = 10$ years for mean present-day infiltration (DTN: LB991220140160.017, data submitted with this AMR).

FRACTURE MASS FRACTION AT BOTTOM OF TSW (for Co450 at 100 years)

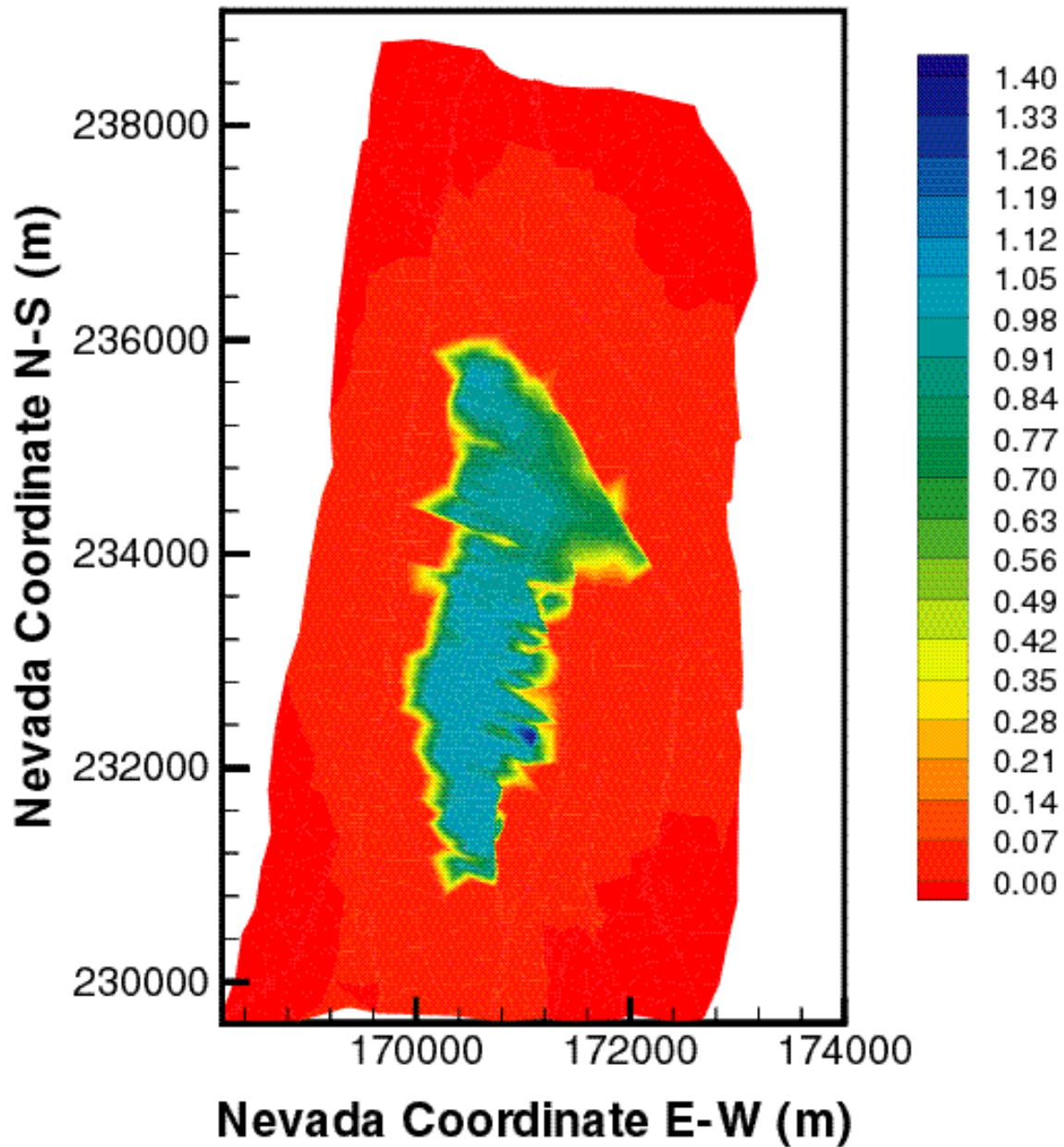


Figure X.4. Distribution of the relative mass fraction X_R of the 450 nm colloid in the fractures of the tsw39 layer at $t = 100$ years for mean present-day infiltration (DTN: LB991220140160.017, data submitted with this AMR).

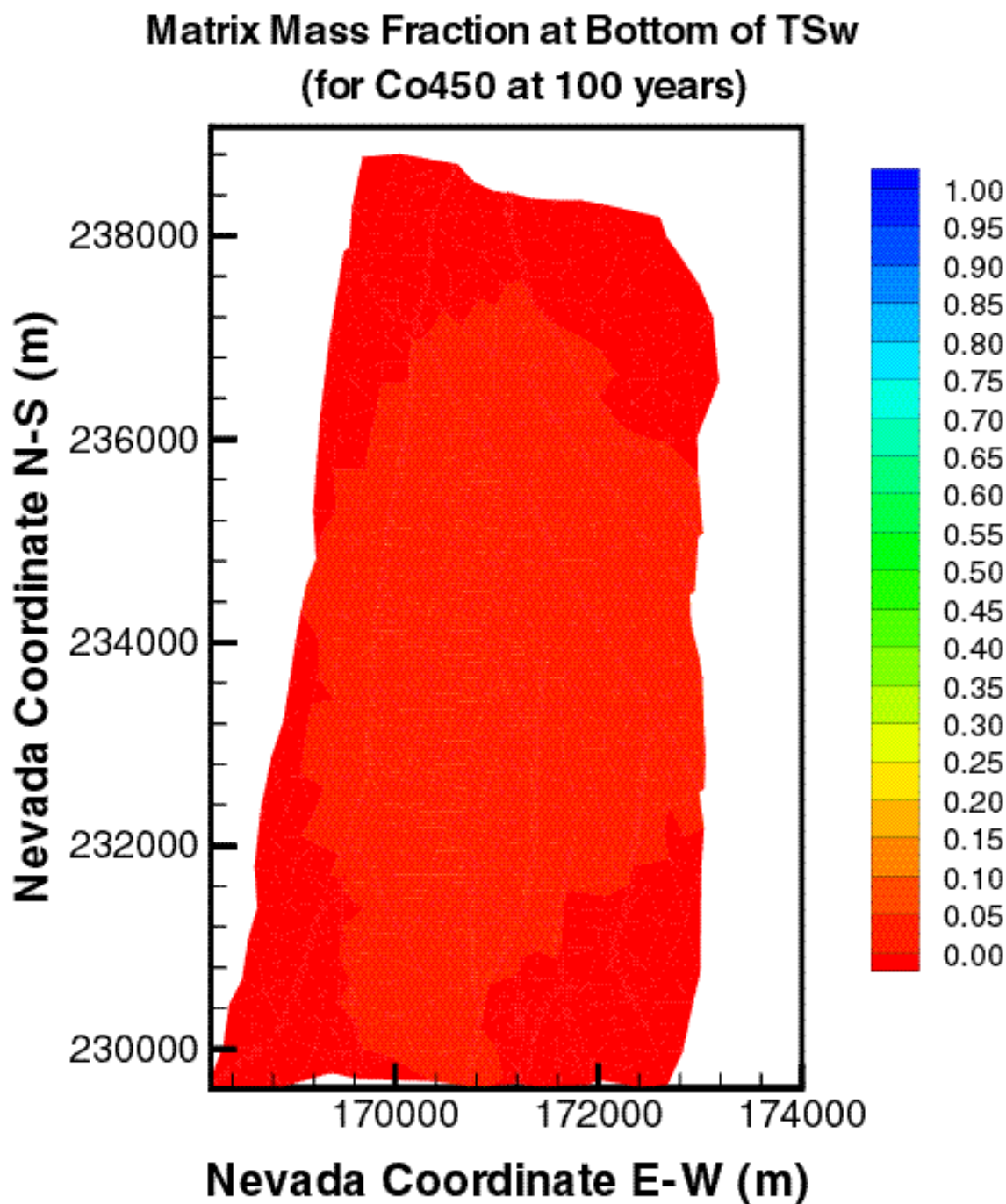


Figure X.5. Distribution of the relative mass fraction X_R of the 450 nm colloid in the matrix of the tsw39 layer at $t = 100$ years for mean present-day infiltration (DTN: LB991220140160.017, data submitted with this AMR).

**Matrix Filtered Concentration at Bottom of TSw (kg/m³)
(for Co450 at 100 years)**

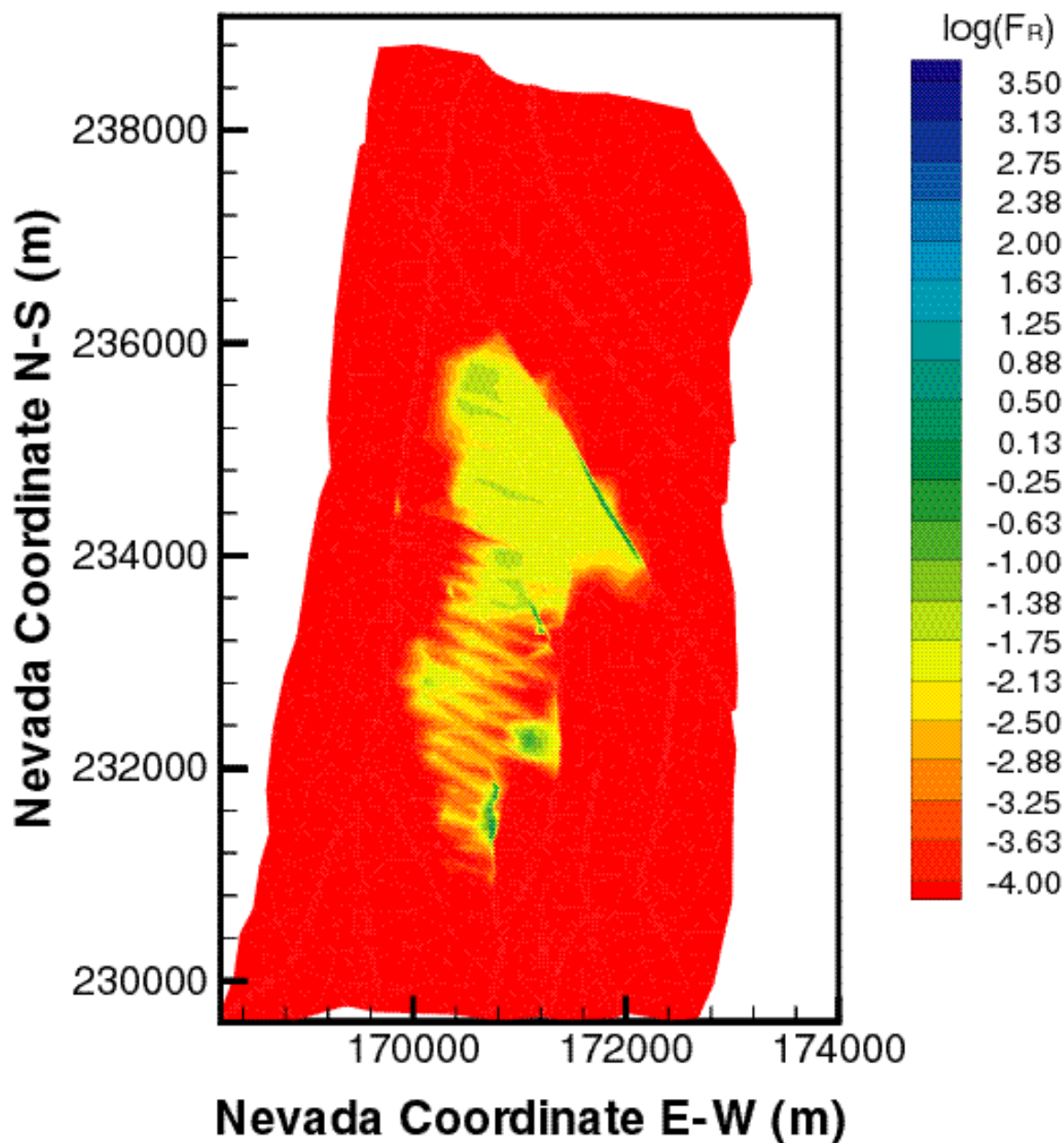


Figure X.6. Distribution of the relative filtered concentration F_R of the 450 nm colloid in the matrix of the tsw39 layer at $t = 100$ years for mean present-day infiltration (DTN: LB991220140160.017, data submitted with this AMR).

FRACTURE MASS FRACTION AT BOTTOM OF TSW (for Co450 at 1000 years)

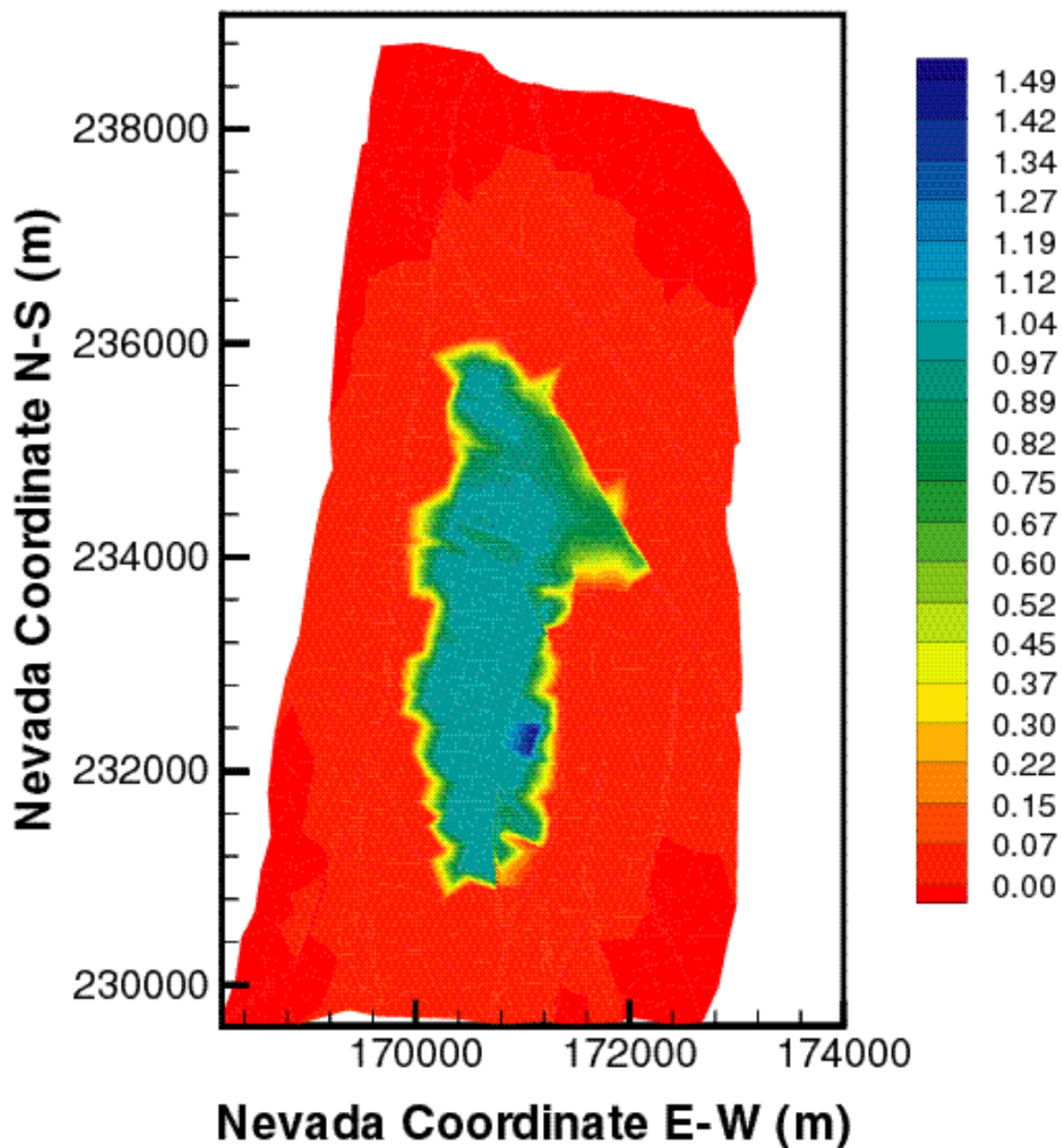


Figure X.7. Distribution of the relative mass fraction X_R of the 450 nm colloid in the fractures of the tsw39 layer at $t = 1,000$ years for mean present-day infiltration (DTN: LB991220140160.017, data submitted with this AMR).

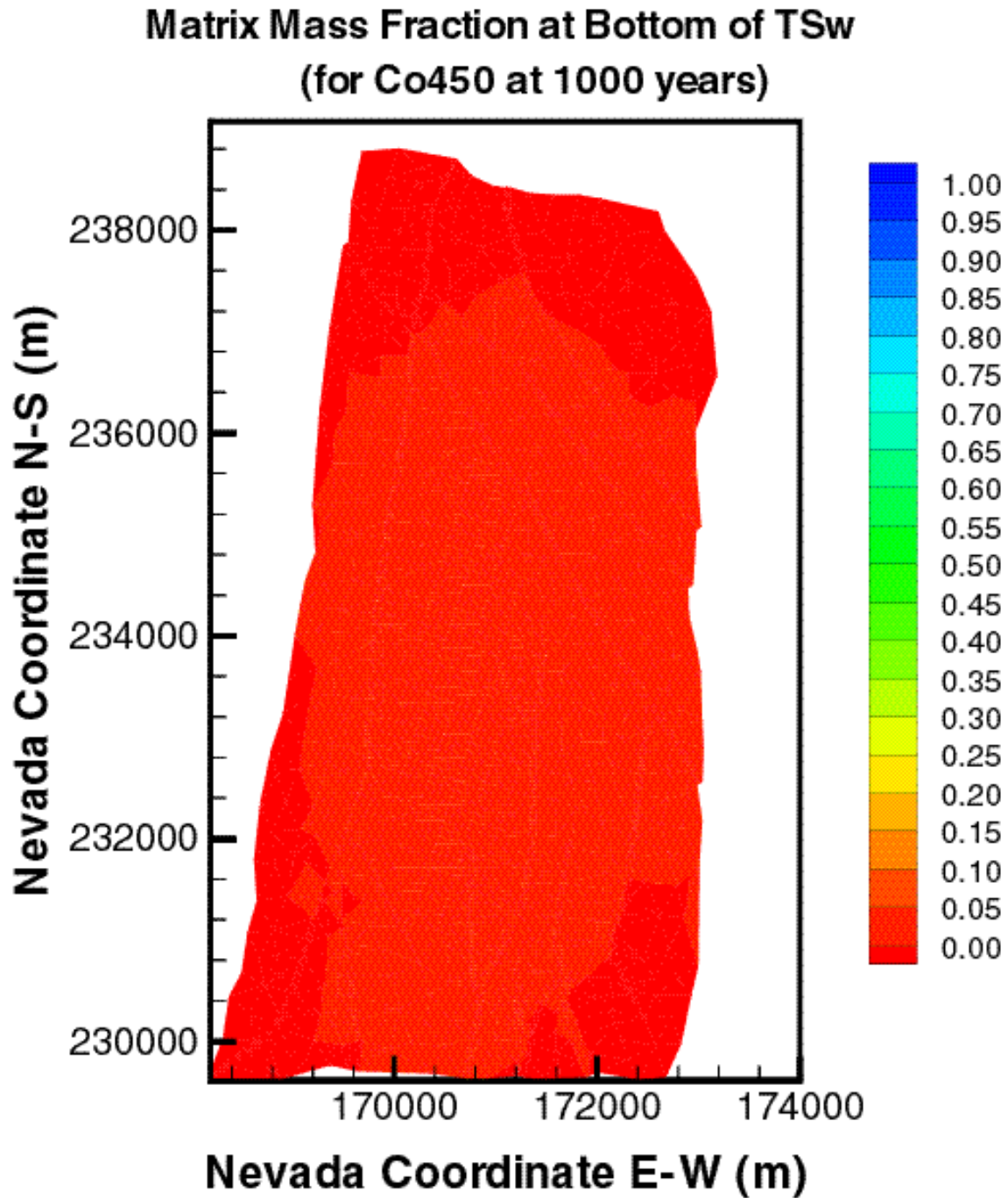


Figure X.8. Distribution of the relative mass fraction X_R of the 450 nm colloid in the matrix of the tsw39 layer at $t = 1,000$ years for mean present-day infiltration (DTN: LB991220140160.017, data submitted with this AMR).

**Matrix Filtered Concentration at Bottom of TSw (kg/m³)
(for Co450 at 1000 years)**

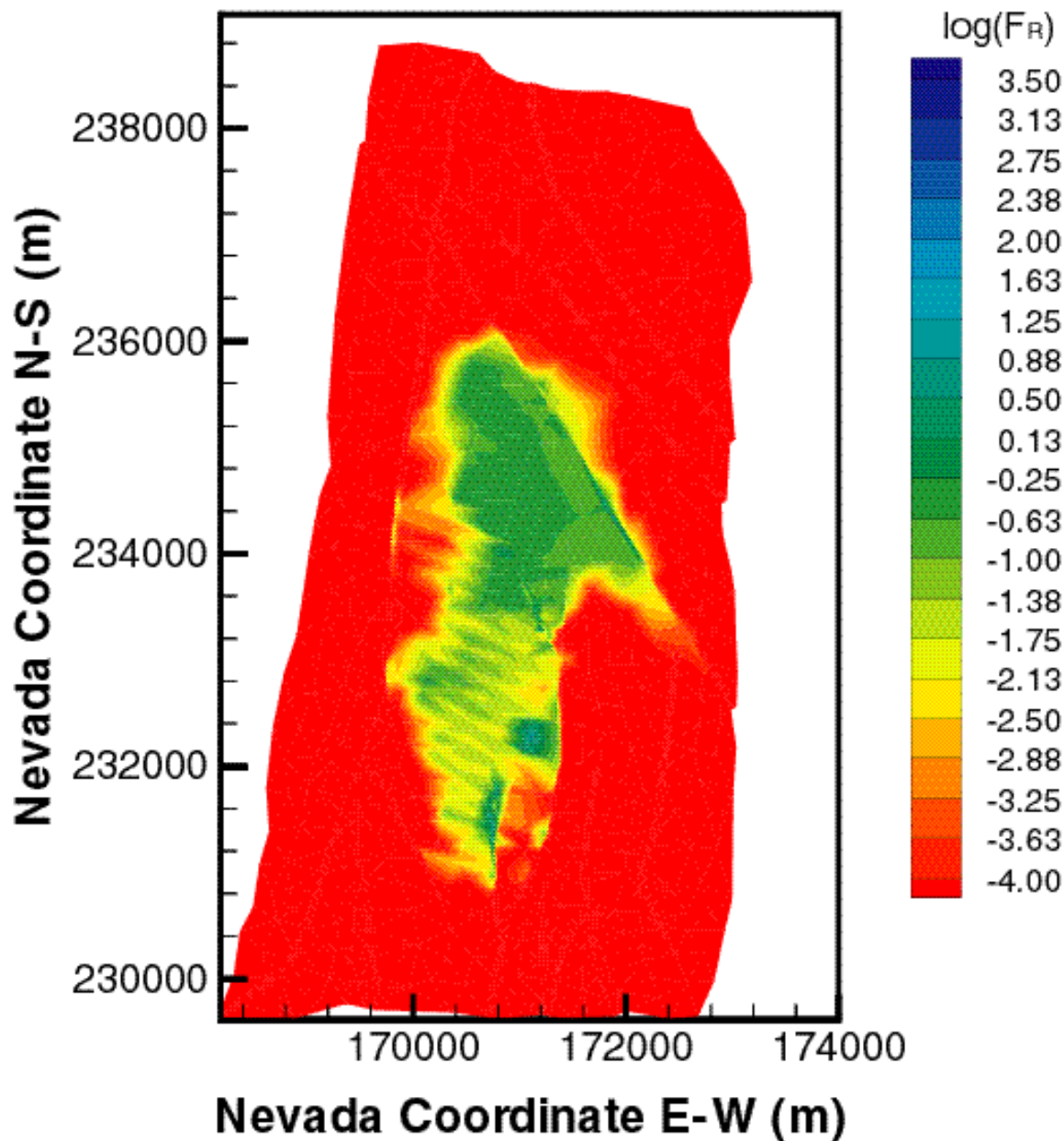


Figure X.9. Distribution of the relative filtered concentration F_R of the 450 nm colloid in the matrix of the tsw39 layer att =1,000yearsformean present-day infiltration (DTN: LB991220140160.017,datasubmitted with this AMR).

FRACTURE MASS FRACTION AT BOTTOM OF TSW (for Co450 at 10000 years)

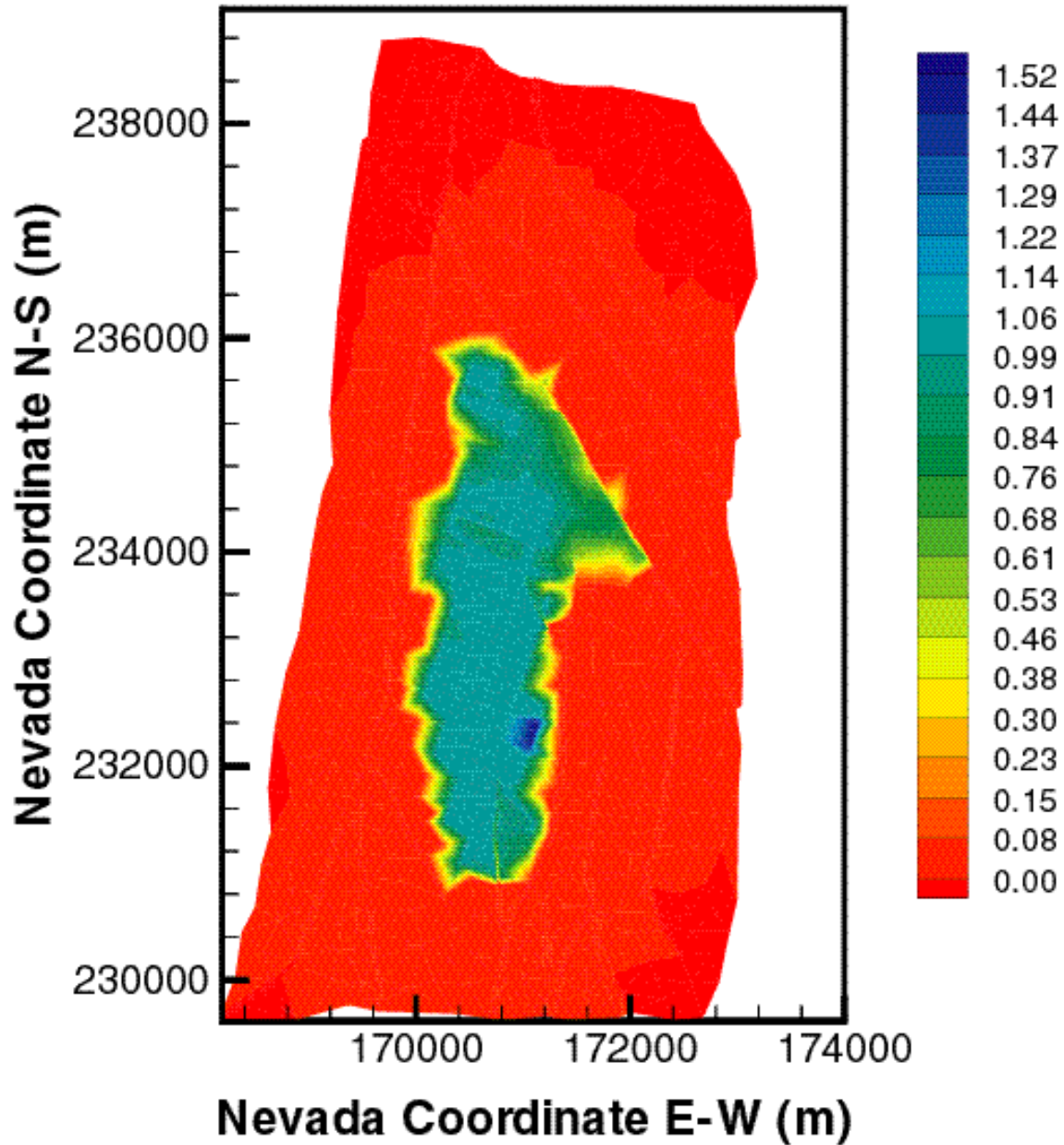


Figure X.10. Distribution of the relative mass fraction X_R of the 450 nm colloid in the fractures of the tsw39 layer at $t = 10,000$ years for mean present-day infiltration (DTN: LB991220140160.017, data submitted with this AMR).

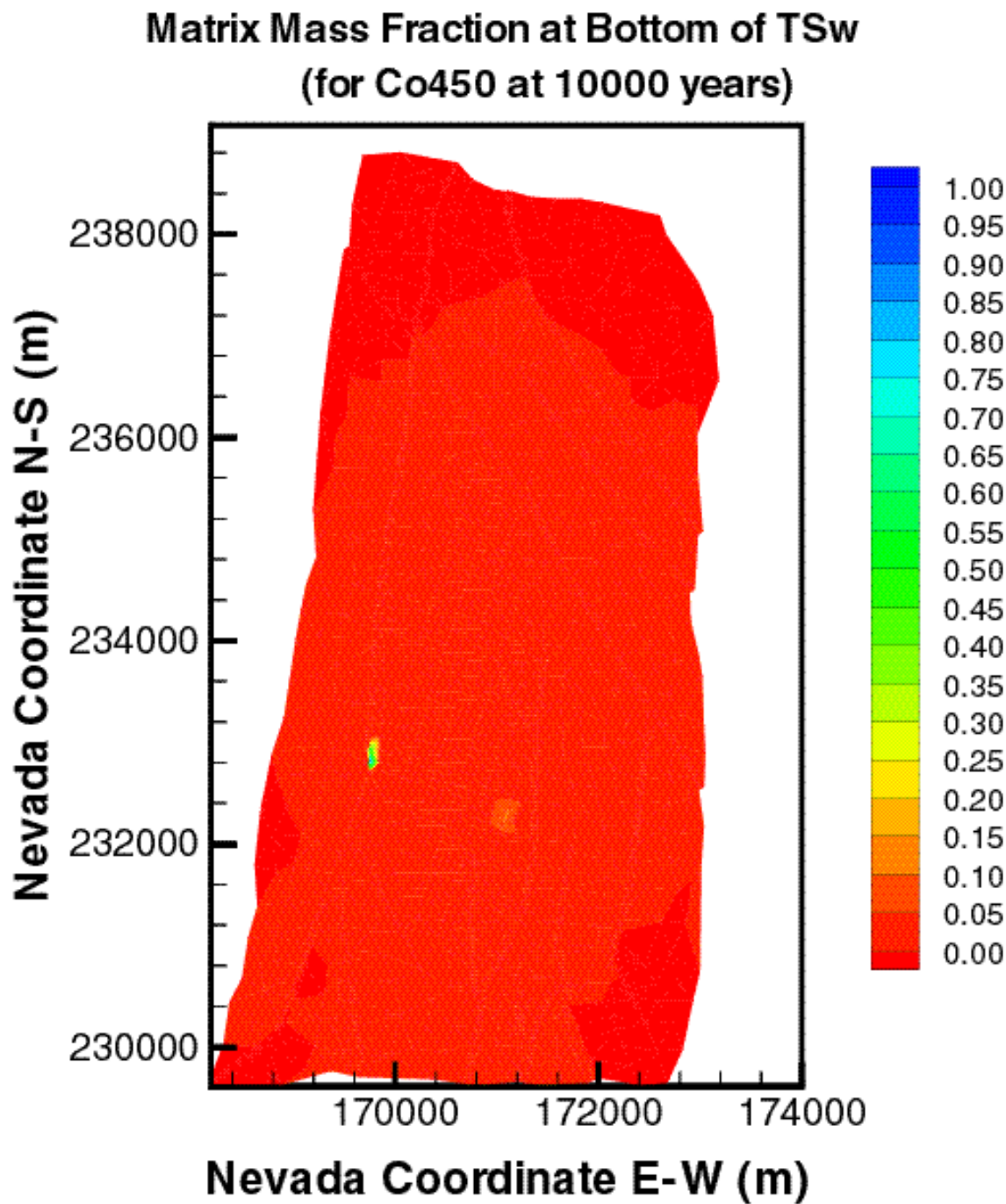


Figure X.11. Distribution of the relative mass fraction X_R of the 450 nm colloid in the matrix of the tsw39 layer at $t = 10,000$ years for mean present-day infiltration (DTN: LB991220140160.017, data submitted with this AMR).

**Matrix Filtered Concentration at Bottom of TSw (kg/m³)
(for Co450 at 10000 years)**

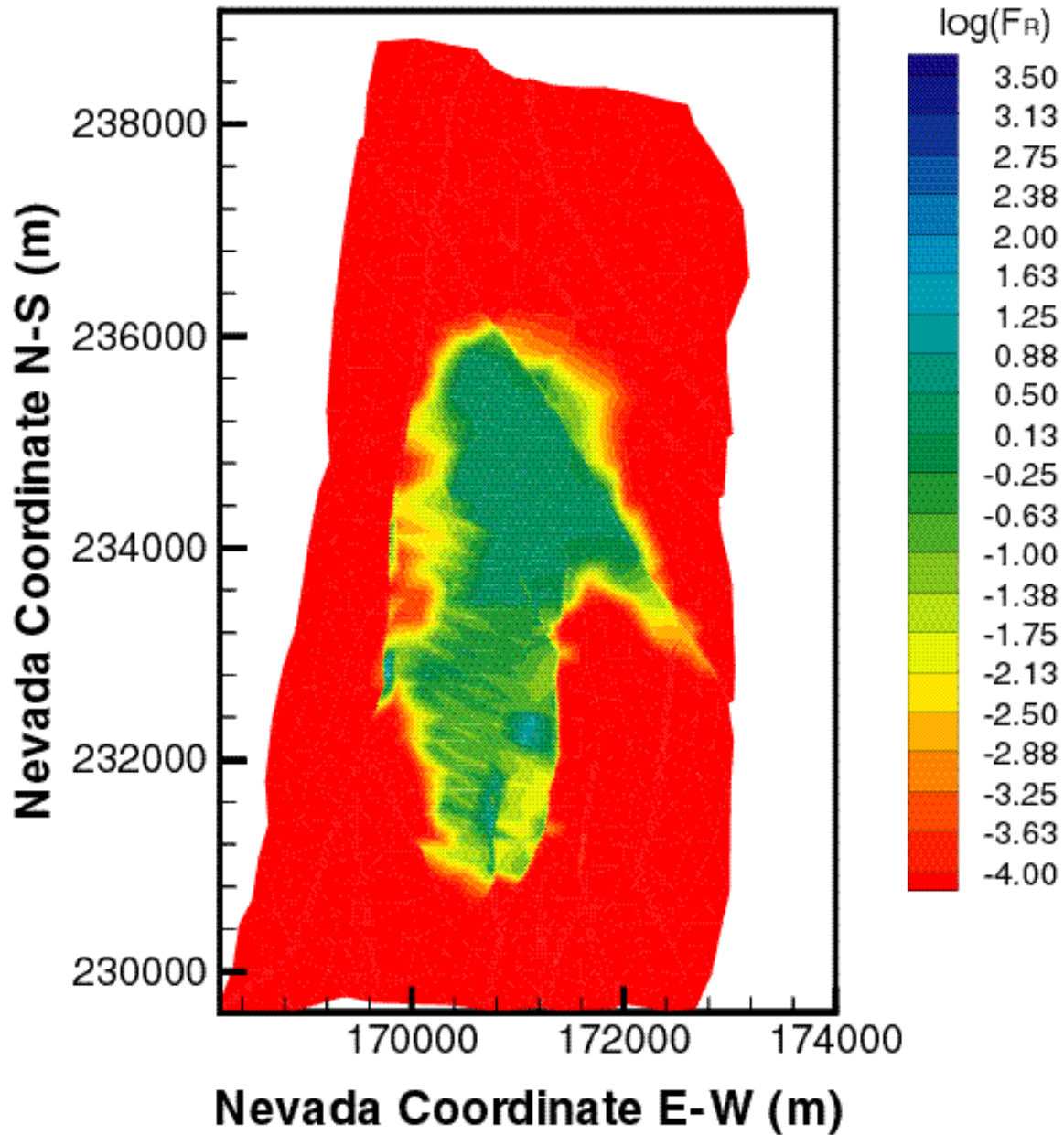


Figure X.12. Distribution of the relative filtered concentration F_R of the 450 nm colloid in the matrix of the tsw39 layer at $t = 10,000$ years for mean present-day infiltration (DTN: LB991220140160.017, data submitted with this AMR).

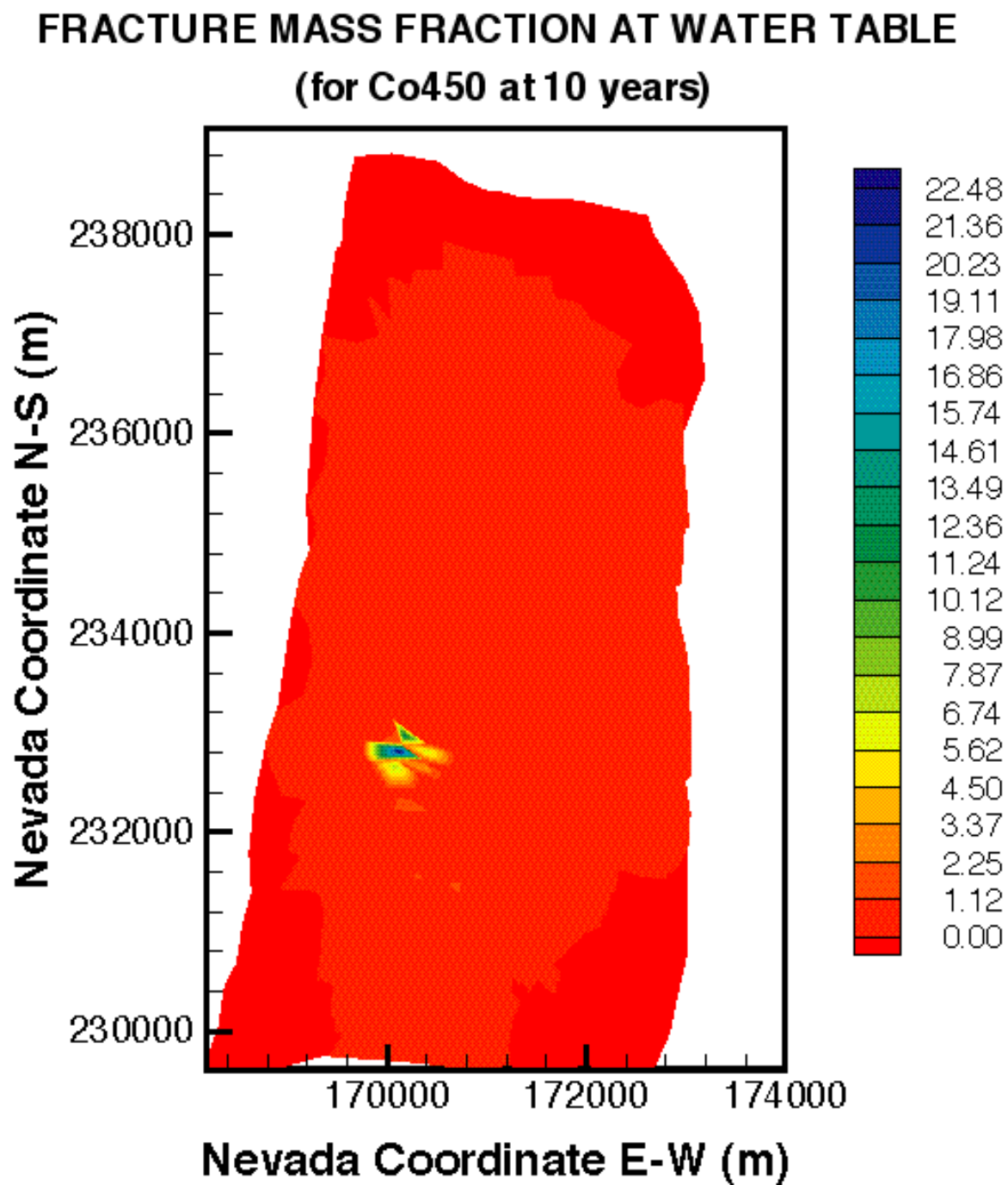


Figure X.13. Distribution of the relative mass fraction X_R of the 450 nm colloid in the fractures immediately above the groundwater at $t = 10$ years for mean present-day infiltration (DTN: LB991220140160.017, data submitted with this AMR).

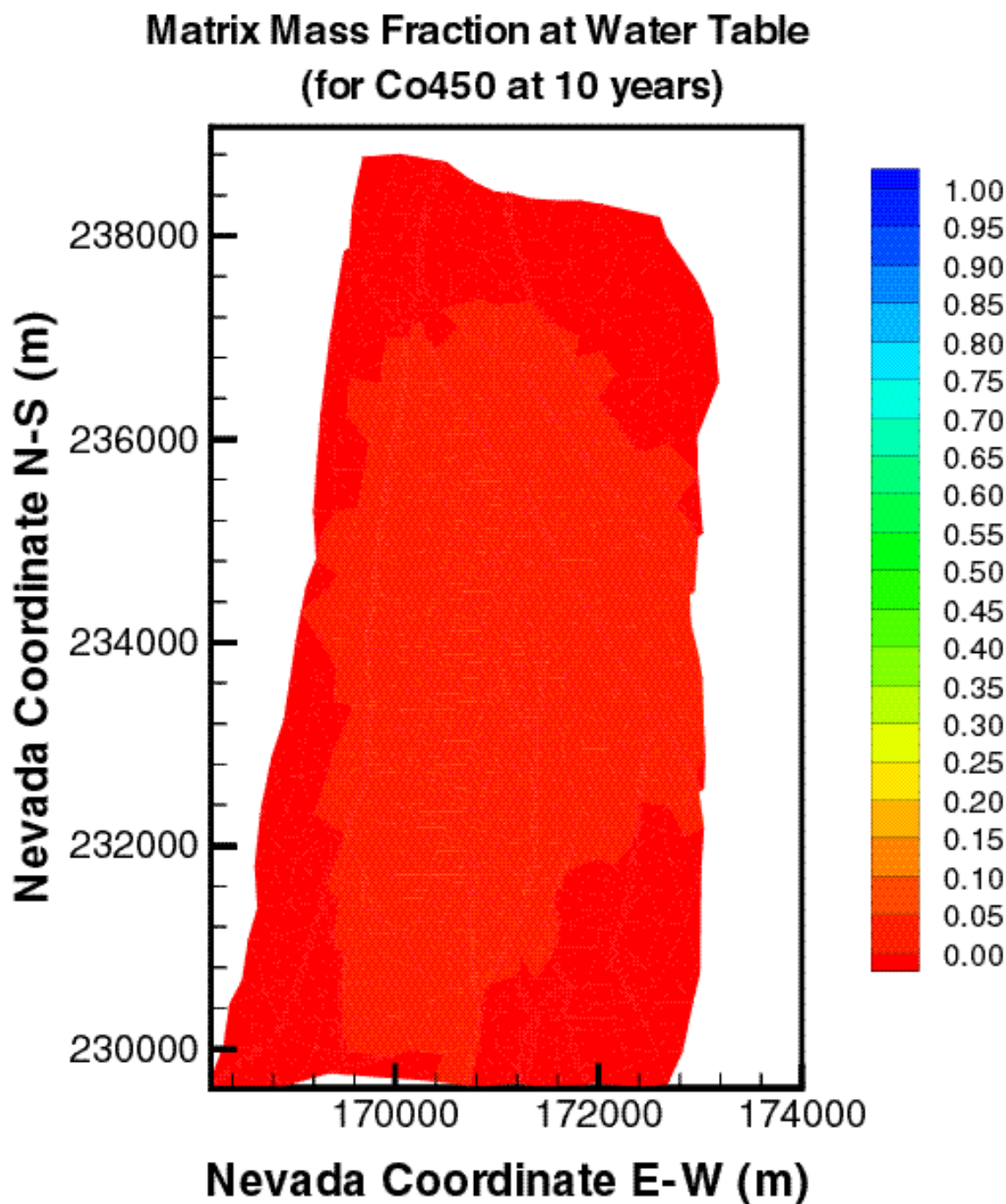


Figure X.14. Distribution of the relative mass fraction X_R of the 450 nm colloid in the matrix immediately above the groundwater at $t = 10$ years for mean present-day infiltration (DTN: LB991220140160.017, data submitted with this AMR).

**Matrix Filtered Concentration at Water Table (kg/m^3)
(for Co450 at 10 years)**

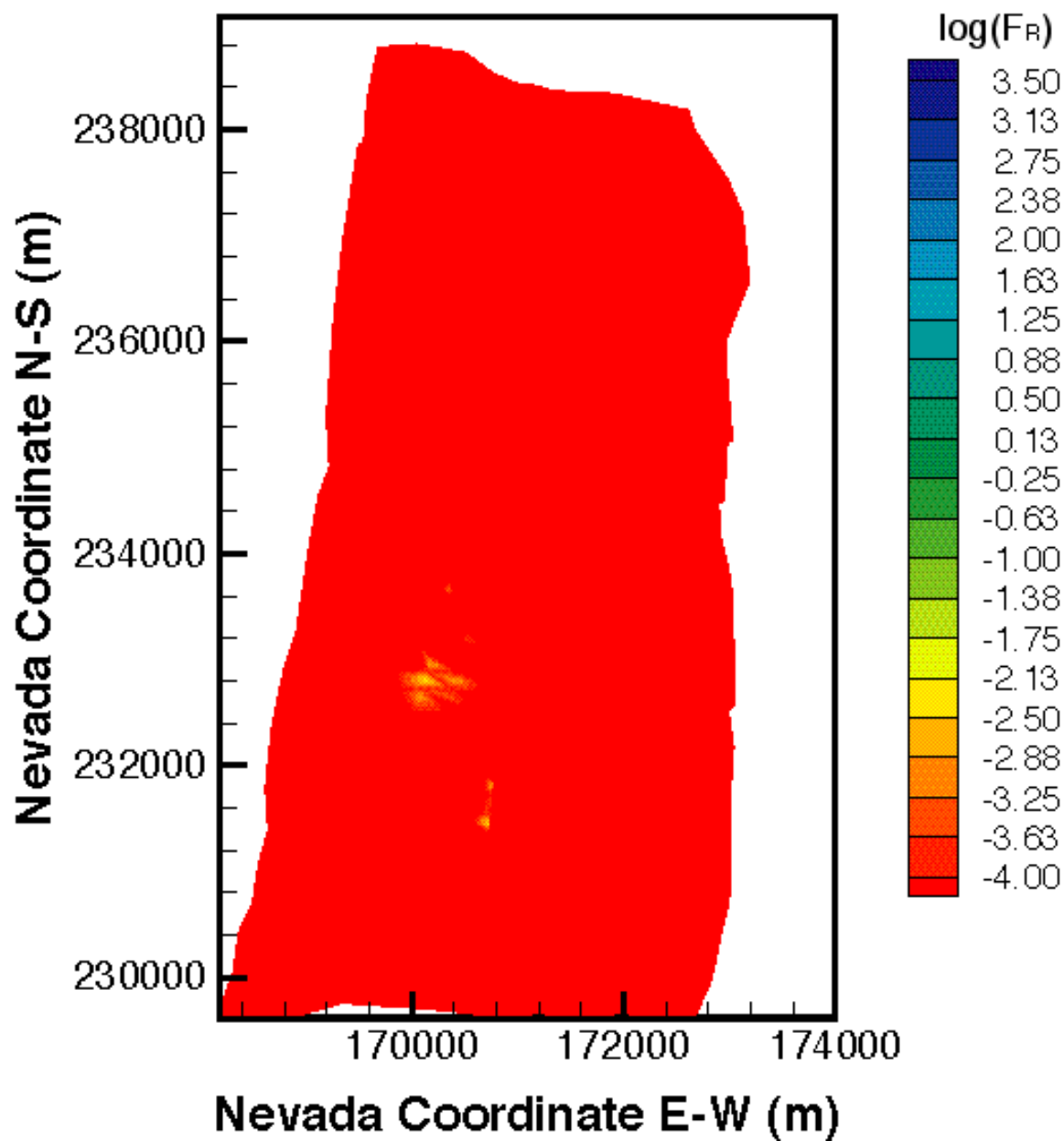


Figure X.15. Distribution of the relative filtered concentration F_R of the 450 nm colloid in the matrix immediately above the groundwater at $t=10$ years for mean present-day infiltration (DTN: LB991220140160.017, data submitted with this AMR).

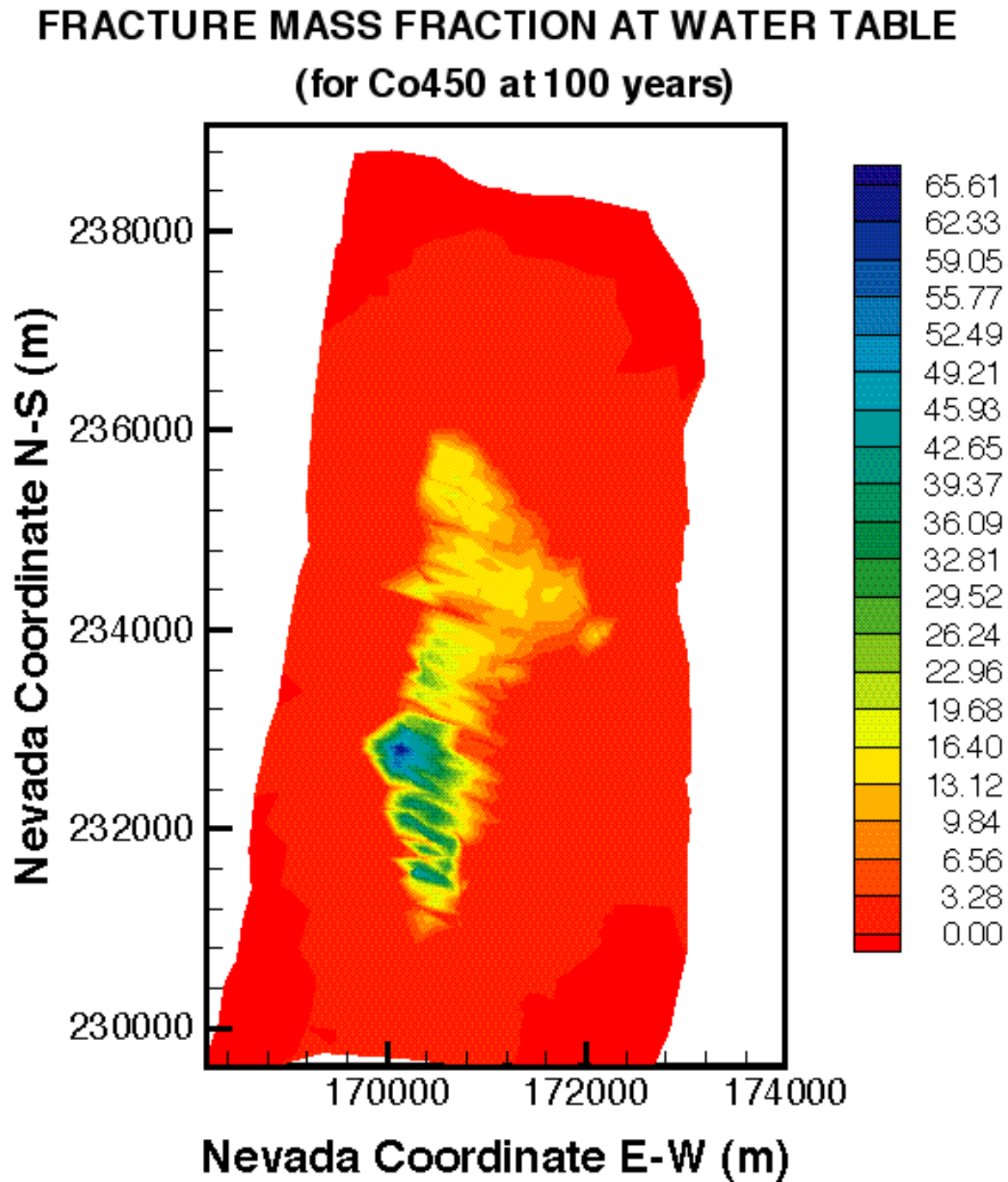


Figure X.16. Distribution of the relative mass fraction X_R of the 450 nm colloid in the fractures immediately above the groundwater at $t = 100$ years for mean present-day infiltration (DTN: LB991220140160.017, data submitted with this AMR).

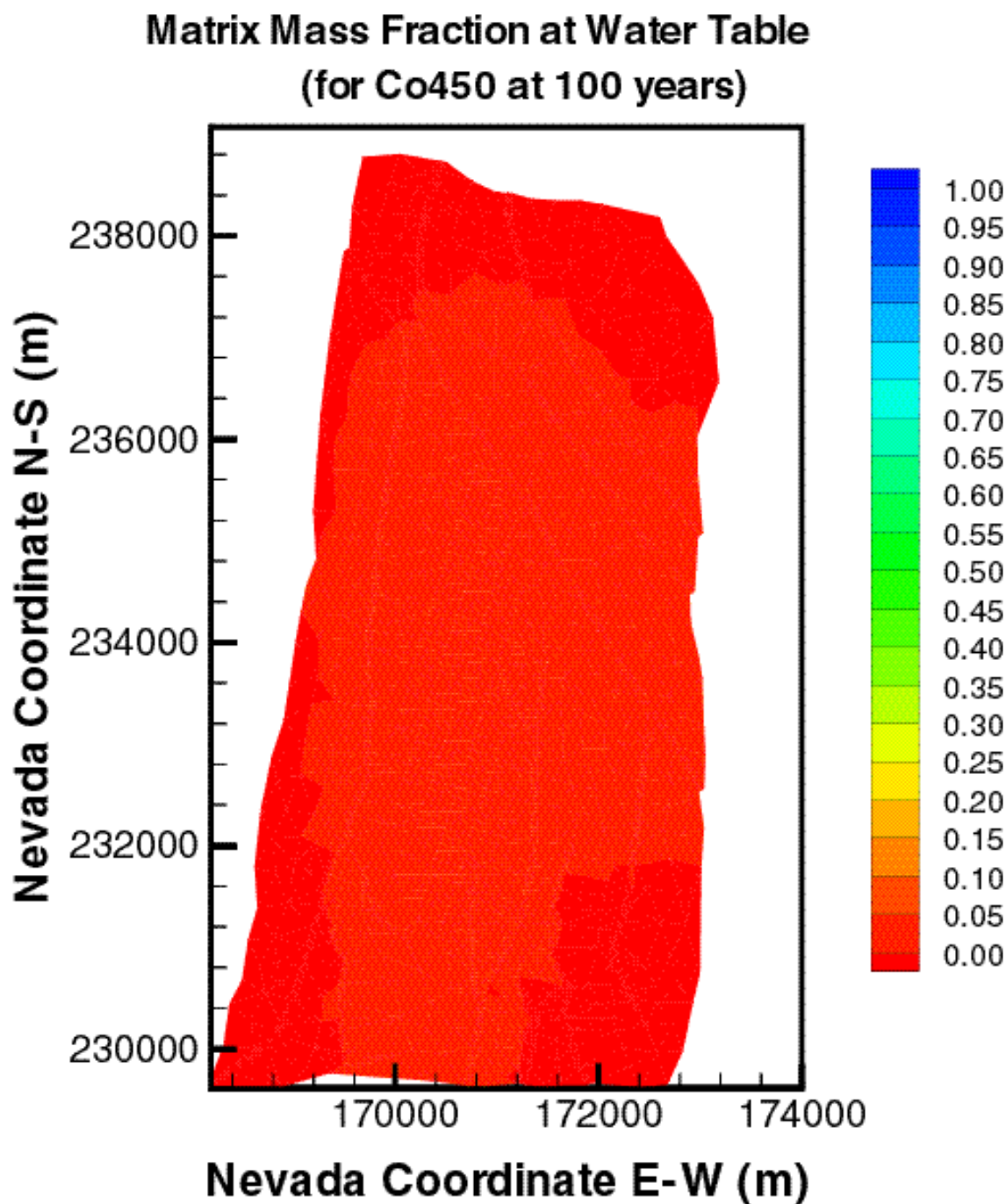


Figure X.17. Distribution of the relative mass fraction X_R of the 450 nm colloid in the matrix immediately above the groundwater at $t = 100$ years for mean present-day infiltration (DTN: LB991220140160.017, data submitted with this AMR).

**Matrix Filtered Concentration at Water Table (kg/m^3)
(for Co450 at 100 years)**

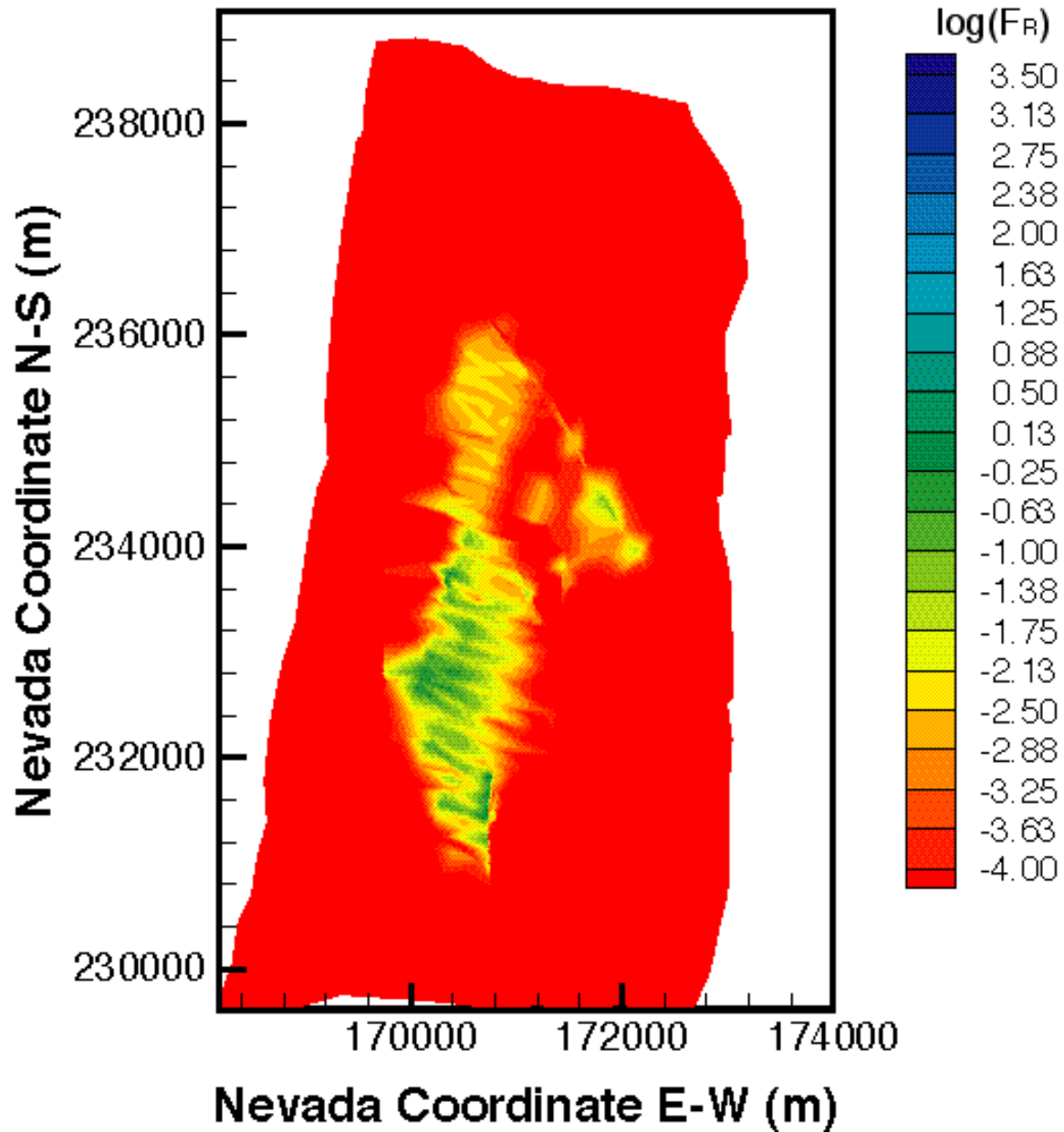


Figure X.18. Distribution of the relative filtered concentration F_R of the 450 nm colloid in the matrix immediately above the groundwater at $t=100$ years for mean present-day infiltration (DTN: LB991220140160.017, data submitted with this AMR).

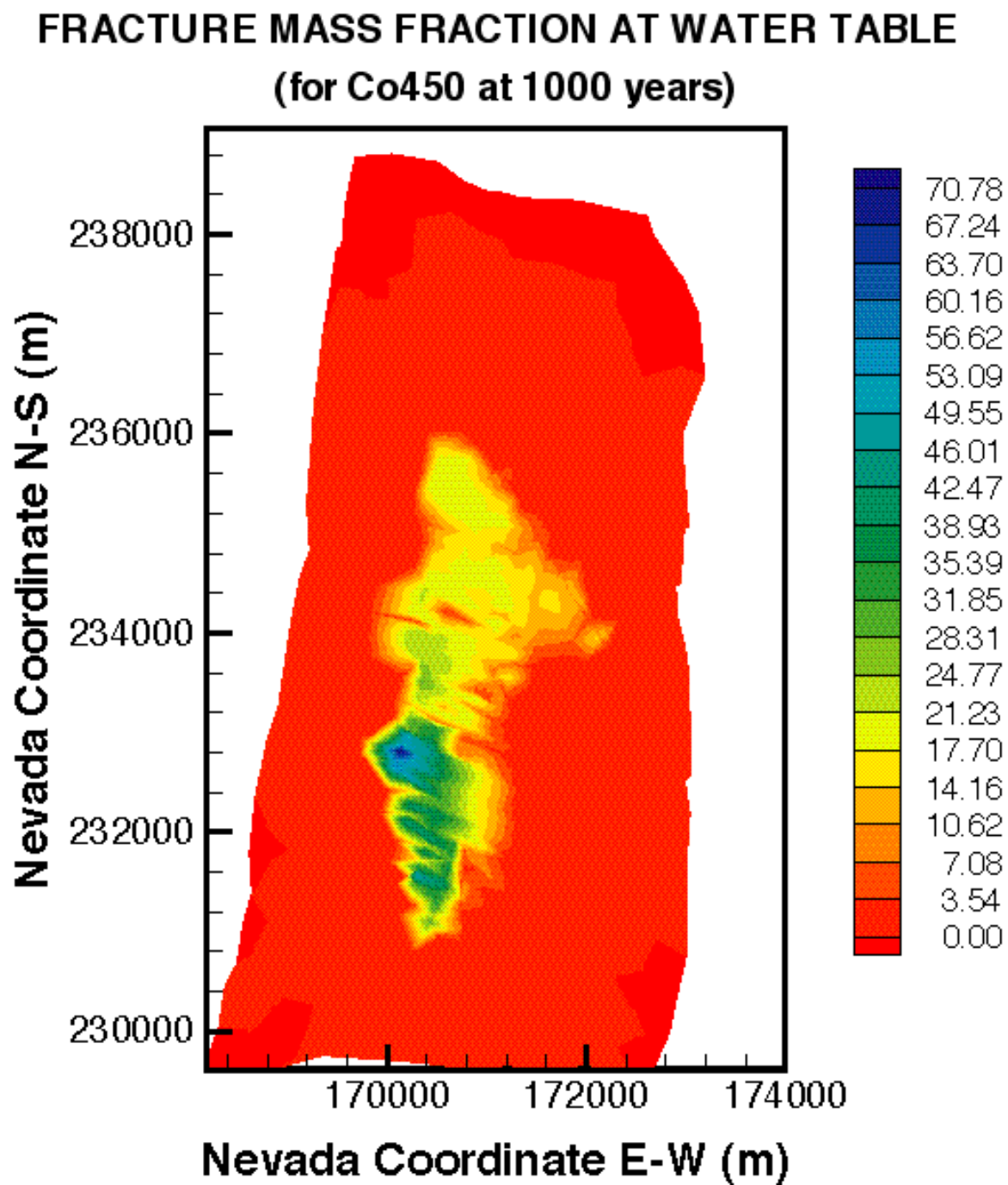


Figure X.19. Distribution of the relative mass fraction X_R of the 450 nm colloid in the fractures immediately above the groundwater at $t = 1,000$ years for mean present-day infiltration (DTN: LB991220140160.017, data submitted with this AMR).

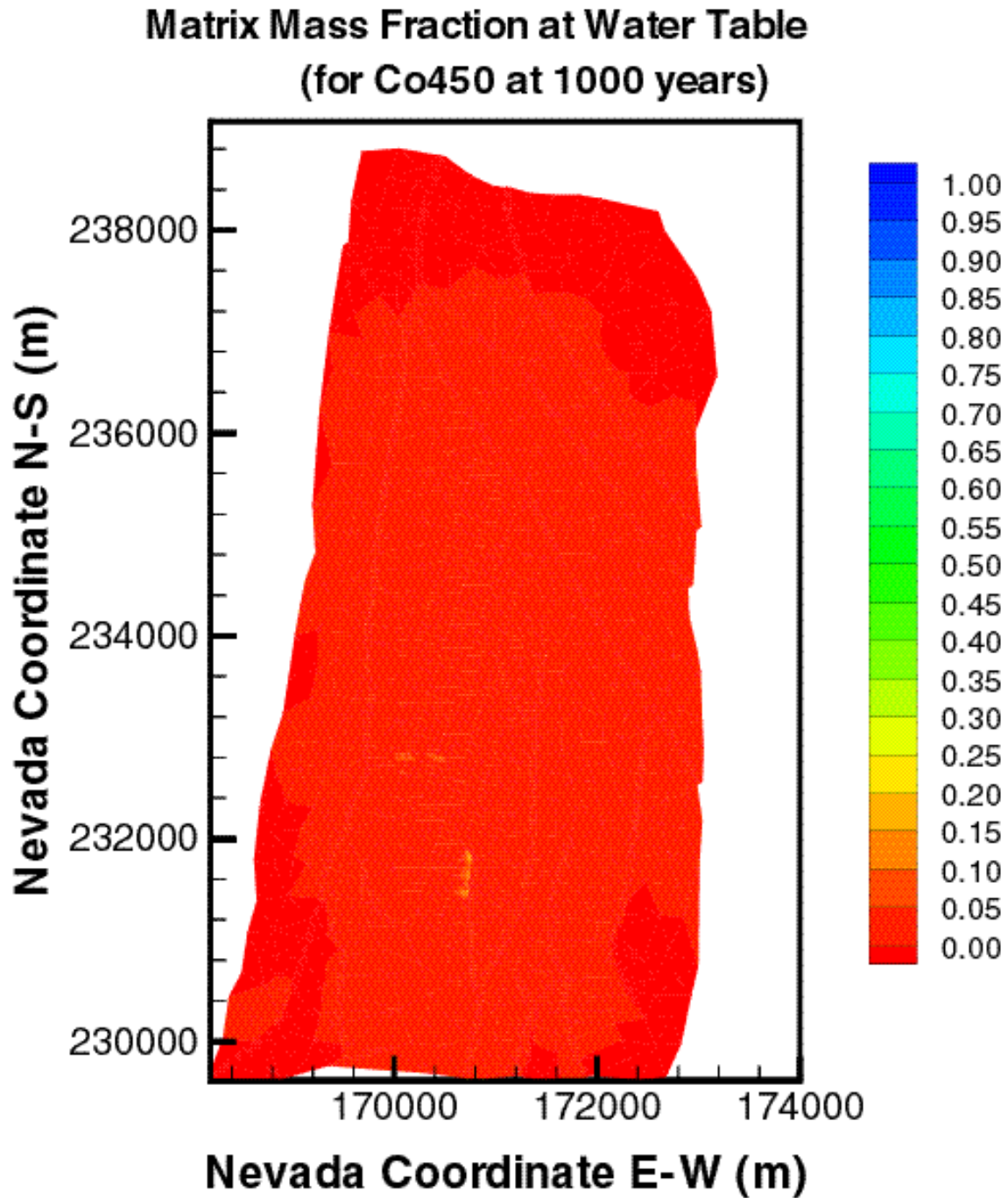


Figure X.20. Distribution of the relative mass fraction X_R of the 450 nm colloid in the matrix immediately above the groundwater at $t = 1,000$ years for mean present-day infiltration (DTN: LB991220140160.017, data submitted with this AMR).

**Matrix Filtered Concentration at Water Table (kg/m^3)
(for Co450 at 1000 years)**

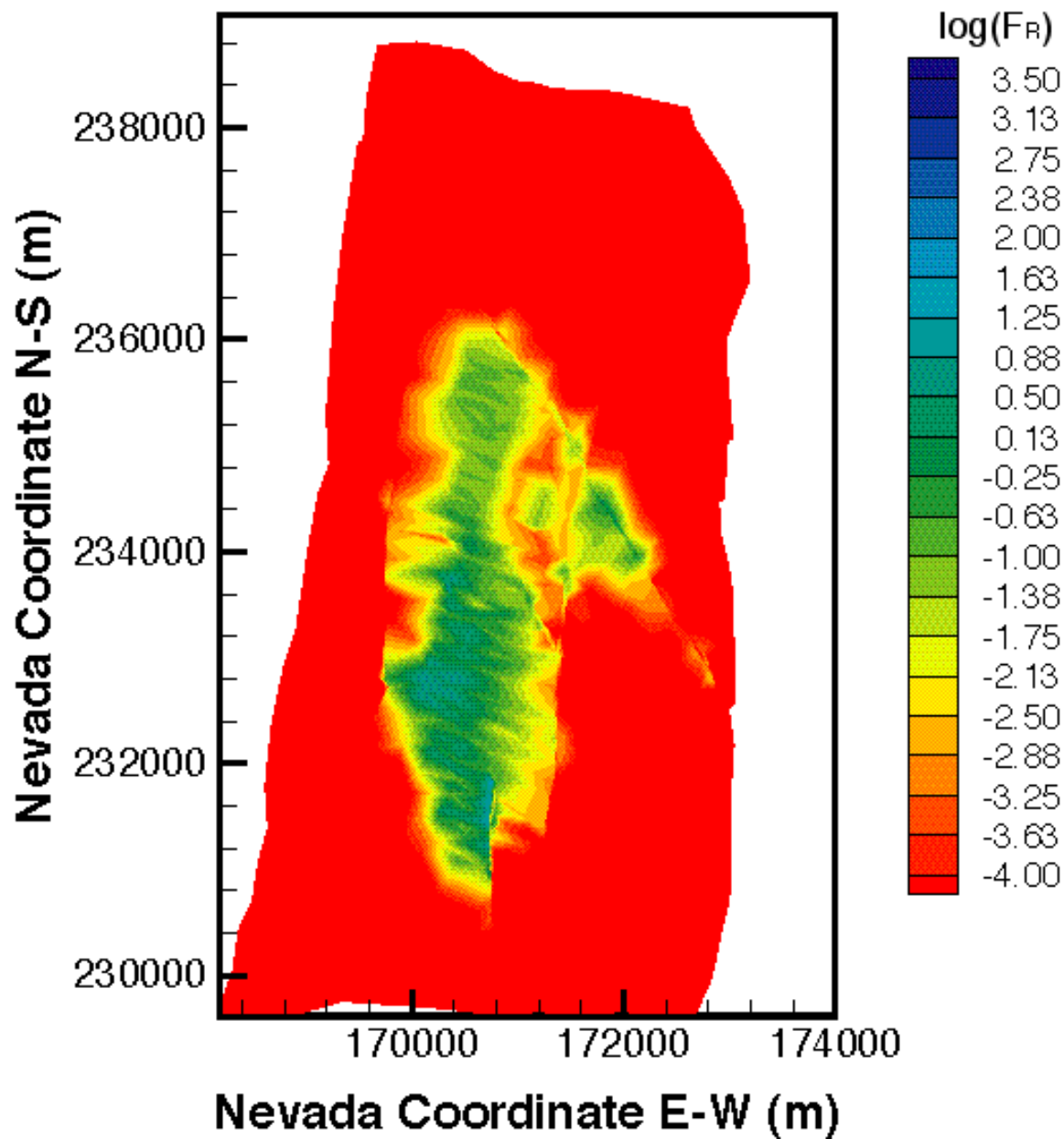


Figure X.21. Distribution of the relative filtered concentration F_R of the 450 nm colloid in the matrix immediately above the groundwater at $t = 1,000$ years for mean present-day infiltration (DTN: LB991220140160.017, data submitted with this AMR).

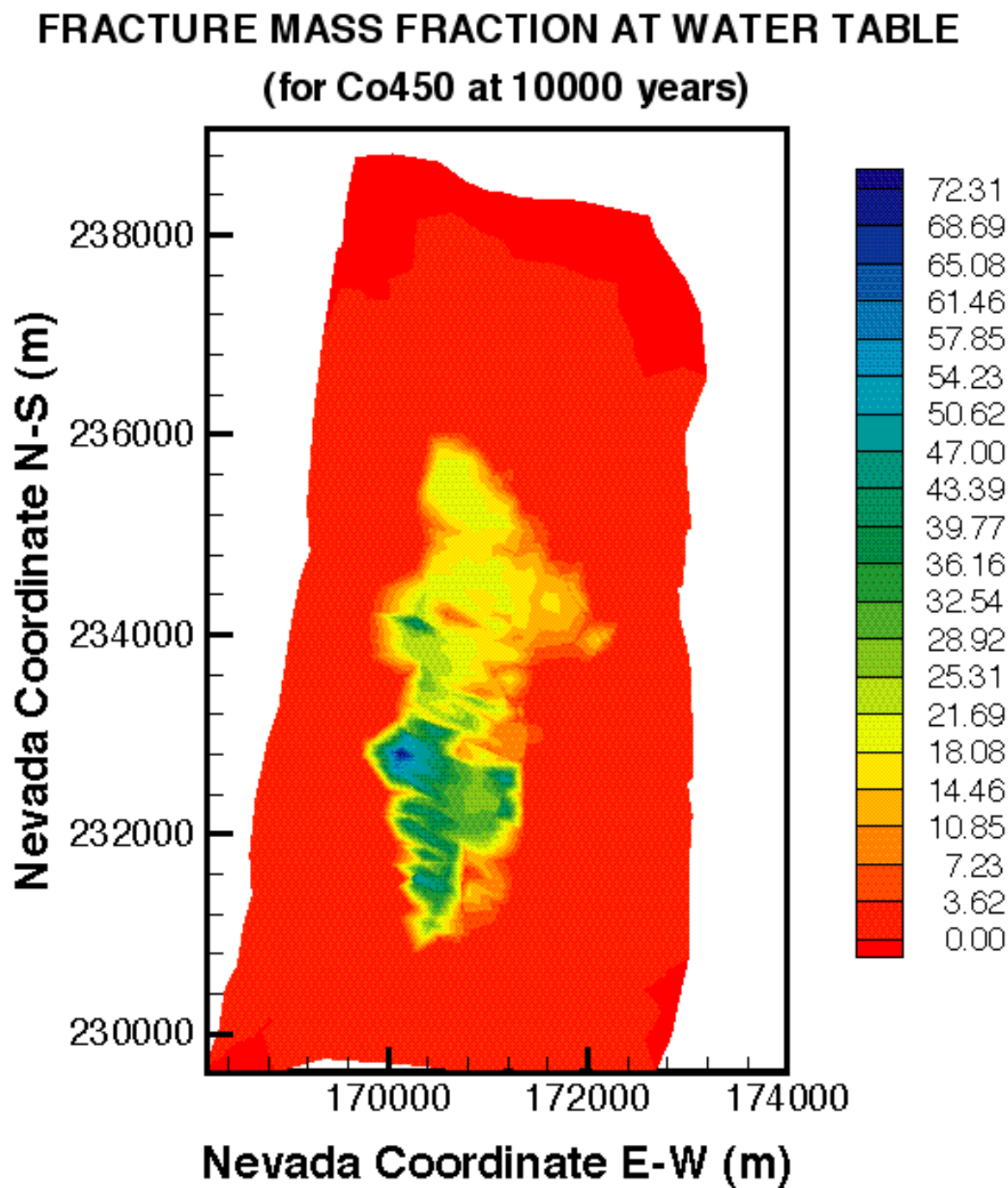


Figure X.22. Distribution of the relative mass fraction X_R of the 450 nm colloid in the fractures immediately above the groundwater at $t = 10,000$ years for mean present-day infiltration (DTN: LB991220140160.017, data submitted with this AMR).

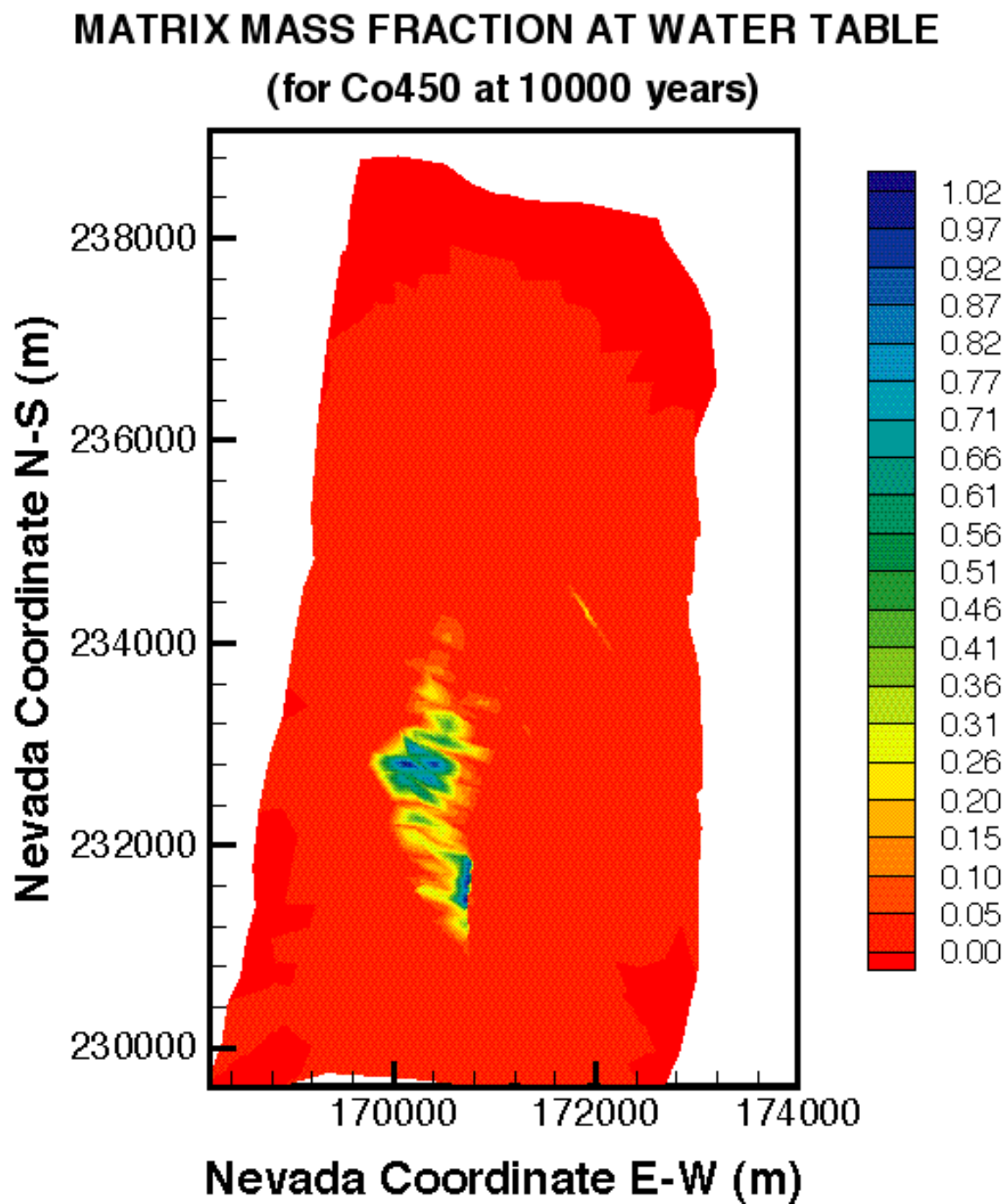


Figure X.23. Distribution of the relative mass fraction X_R of the 450 nm colloid in the matrix immediately above the groundwater at $t = 10,000$ years for mean present-day infiltration (DTN: LB991220140160.017, data submitted with this AMR).

Matrix Filtered Concentration at Water Table (kg/m^3)
(for Co450 at 10000 years)

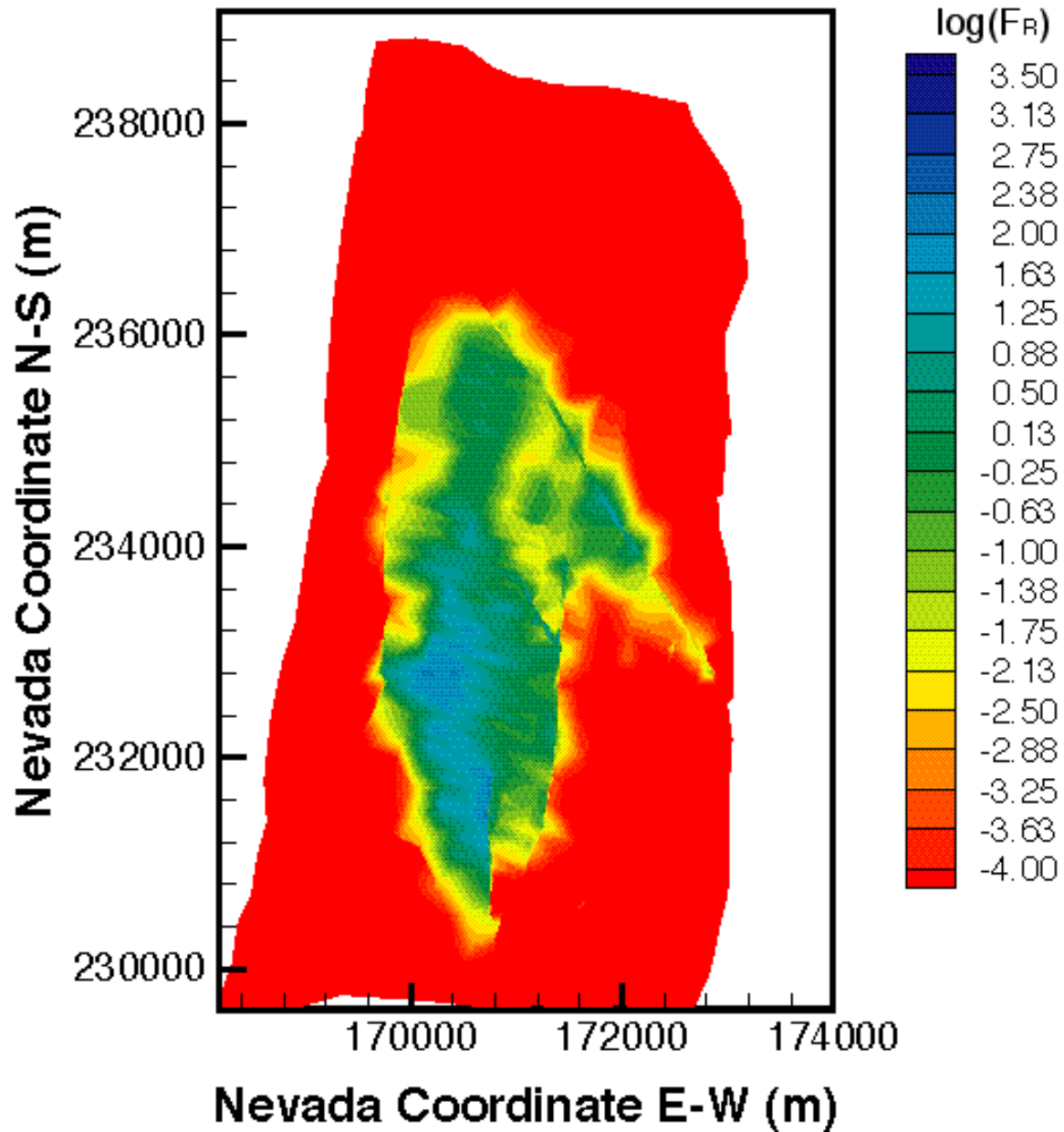


Figure X.24. Distribution of the relative filtered concentration F_R of the 450 nm colloid in the matrix immediately above the groundwater at $t = 10,000$ years for mean present-day infiltration (DTN: LB991220140160.017, data submitted with this AMR).

ATTACHMENT XI.
FORTTRAN ROUTINES

INTENTIONALLY LEFT BLANK

XI. FORTRAN ROUTINES USED IN THIS AMR

The software routines in this attachment have been documented according to AP-SI.1Q, Rev. 2, ICN 2, Section 5.1.1, and all documentation has been submitted to the Records Processing Center. The accession numbers for the software routine documentation are listed on Table 3.1, and also included in the short descriptions of each routine.

All the routines were written in FORTRAN77, and were all used for the rearrangement of data in the very large input or output files of the EOS9nT runs. The routines do not use any external input parameters and do not perform any computations. They simply open the data files indicated in the routines and rearrange the data to (a) meet the formatting requirements of EOS9nT input files or (b) extract a small portion of data at locations of interest.

XI.1. The xtract1.f Routine

The xtract1.f V1.0 routine (STN: 10213-1.0-00) is used to modify the grid system from the EOS9 runs for use in the EOS9nT runs. The modifications involve (a) determining the grid elements corresponding to the potential repository, (b) moving them to the end of the element file, where (c) the upper and lower boundary elements are also moved.

A listing of the xtract1.f routine follows.

```

PROGRAM xtract1
IMPLICIT DOUBLE PRECISION (A-H,O-Z)
CHARACTER*5 name(2000)
CHARACTER*5 onoma
CHARACTER*5 MA12
C
C
OPEN(UNIT=11,FILE='REPOS',STATUS='OLD')
OPEN(UNIT=12,FILE='ELEM',STATUS='OLD')
OPEN(UNIT=21,FILE='ELEMA')
OPEN(UNIT=22,FILE='ELEMI')
C
C
C
DO 100 n=1,2000
READ(11,6003) name(n)
IF(name(n).EQ.'+++ ') THEN
GO TO 101
ELSE
READ(11,6004) xx
END IF
100 CONTINUE
101 nsour = N-1
C
C

```

```

C
      nnaa = 0
      nnss = 0
      nnbb = 0
      jini = 1
      DO 1000 N=1,97976
        READ(12,6005) onoma,NSEQ,NADD,MA12,
&          VOLX,AHTX,zref,X,Y,Z
        DO 200 j8=jini,nsour
          IF(onoma.EQ.name(j8)) THEN
            nnss = nnss+1
            VOLX =1.0d55
            WRITE(22,6005) onoma,NSEQ,NADD,MA12,
&          VOLX,AHTX,zref,X,Y,Z
            jini = j8
            GO TO 1000
          END IF
200    CONTINUE
C
      IF(MA12.EQ.'topbd'.OR.MA12.EQ.'botbd') THEN
        nnbb = nnbb+1
        IF(nnnb.EQ.1) VOLX =-VOLX
        WRITE(22,6005) onoma,NSEQ,NADD,MA12,
&          VOLX,AHTX,zref,X,Y,Z
        GO TO 1000
      END IF
C
      nnaa = nnaa+1
      WRITE(21,6005) onoma,NSEQ,NADD,MA12,
&          VOLX,AHTX,zref,X,Y,Z
1000 CONTINUE
C
C
C
5000 FORMAT(3(A20))
6001 FORMAT(T5,'ENTER THE NAME OF THE DATA FILE')
6002 FORMAT(6(1pE15.8,2x))
6003 FORMAT(A5)
6004 FORMAT(4E20.13)
6005 FORMAT(A5,2I5,A5,3E10.4,2F10.3,F10.4)

999 STOP
      END

```

XI.2. The xtract2.f Routine

The xtract2.f V1.0 routine (STN: 10214-1.0-00) is used to obtain initial condition files (INCON) using the SAVE files from the EOS9 runs. The INCON files are then used for the EOS9nT simultaneous simulations of ^{99}Tc , ^{237}Np and ^{239}Pu transport.

A listing of the xtract2.f routine follows.

```

PROGRAM xtract2
IMPLICIT DOUBLE PRECISION (A-H,O-Z)
CHARACTER*5 name(2000)
CHARACTER*5 onoma
C
C
C
OPEN(UNIT=11,FILE='REPOS',STATUS='OLD')
OPEN(UNIT=12,FILE='BSAVE',STATUS='OLD')
OPEN(UNIT=22,FILE='INCON')
C
C
C
DO 100 n=1,2000
READ(11,6003) name(n)
IF(name(n).EQ.'+++ ') THEN
GO TO 101
ELSE
READ(11,6004) xx
END IF
100 CONTINUE
101 nsour = N-1
C
C
C
jini = 1
READ(12,6003) onoma
WRITE(22,6003) onoma
DO 1000 N=1,97976
READ(12,6004) onoma,NSEQ,NADD,PORX,ktracr
READ(12,6005) xxx,yyy
ktracr = 3
DO 200 j8=jini,nsour
IF(onoma.EQ.name(j8)) THEN
nnss = nnss+1
WRITE(22,6004) onoma,NSEQ,NADD,PORX,ktracr
WRITE(22,6005) xxx,yyy,0.0d0,0.0d0
WRITE(22,6005) 1.0d0,1.0d0,1.0d0
WRITE(22,6005) 0.0d0,0.0d0,0.0d0
WRITE(22,6005) 0.0d0,0.0d0,0.0d0
jini = j8
GO TO 1000
END IF
200 CONTINUE
C

```

```
        WRITE(22,6004) onoma,NSEQ,NADD,PORX,ktracr
        WRITE(22,6005) xxx,yyy,0.0d0,0.0d0
        WRITE(22,6005) 0.0d0,0.0d0,0.0d0
        WRITE(22,6005) 0.0d0,0.0d0,0.0d0
        WRITE(22,6005) 0.0d0,0.0d0,0.0d0
C
1000  CONTINUE
        WRITE(22,6006)
        WRITE(22,6006)
C
C
C
6003  FORMAT(A5)
6004  FORMAT(A5,2I5,E15.8,3I2)
6005  FORMAT(4E20.13)
6006  FORMAT(80(' '))

999  STOP
      END
```

XI.3. The xtract2a.f Routine

The xtract2a.f V1.0 routine (STN: 10215-1.0-00) is used to obtain initial condition files (INCON) using the SAVE files from the EOS9 runs. The INCON files are then used for the EOS9nT simulations of transport of the ^{237}Np and ^{239}Pu decay chains.

A listing of the xtract2a.f routine follows.

```

PROGRAM xtract2a
IMPLICIT DOUBLE PRECISION (A-H,O-Z)
CHARACTER*5 name(2000)
CHARACTER*5 onoma
C
C
C
OPEN(UNIT=11,FILE='REPOS',STATUS='OLD')
OPEN(UNIT=12,FILE='BSAVE',STATUS='OLD')
OPEN(UNIT=22,FILE='INCON')
C
C
C
DO 100 n=1,2000
READ(11,6003) name(n)
  IF(name(n).EQ.'+++ ') THEN
    GO TO 101
  ELSE
    READ(11,6004) xx
  END IF
100 CONTINUE
101 nsour = N-1
C
C
C
  jini = 1
  READ(12,6003) onoma
  WRITE(22,6003) onoma
  DO 1000 N=1,97976
    READ(12,6004) onoma,NSEQ,NADD,PORX,ktracr
    READ(12,6005) xxx,yyy
    ktracr = 3
    DO 200 j8=jini,nsour
      IF(onoma.EQ.name(j8)) THEN
        nnss = nnss+1
        WRITE(22,6004) onoma,NSEQ,NADD,PORX,ktracr
        WRITE(22,6005) xxx,yyy,0.0d0,0.0d0
        WRITE(22,6005) 1.0d0,0.0d0,0.0d0
        WRITE(22,6005) 0.0d0,0.0d0,0.0d0
        WRITE(22,6005) 0.0d0,0.0d0,0.0d0
        jini = j8
        GO TO 1000
      END IF
    200 CONTINUE

```

```
C
      WRITE(22,6004) onoma,NSEQ,NADD,PORX,ktracr
      WRITE(22,6005) xxx,yyy,0.0d0,0.0d0
      WRITE(22,6005) 0.0d0,0.0d0,0.0d0
      WRITE(22,6005) 0.0d0,0.0d0,0.0d0
      WRITE(22,6005) 0.0d0,0.0d0,0.0d0
C
1000 CONTINUE
      WRITE(22,6006)
      WRITE(22,6006)
C
C
C
6003 FORMAT(A5)
6004 FORMAT(A5,2I5,E15.8,3I2)
6005 FORMAT(4E20.13)
6006 FORMAT(80(' '))

999 STOP
END
```

XI.4. The xtract2b.f Routine

The xtract2b.f V1.0 routine (STN: 10216-1.0-00) is used to obtain initial condition files (INCON) using the SAVE files from the EOS9 runs. The INCON files are then used for the EOS9nT simulations of transport of ^{99}Tc , ^{237}Np and the ^{239}Pu decay chain.

A listing of the xtract2b.f routine follows.

```

PROGRAM xtract2b
IMPLICIT DOUBLE PRECISION (A-H,O-Z)
CHARACTER*5 name(2000)
CHARACTER*5 onoma
C
C
C
OPEN(UNIT=11,FILE='REPOS',STATUS='OLD')
OPEN(UNIT=12,FILE='BSAVE',STATUS='OLD')
OPEN(UNIT=22,FILE='INCON')
C
C
C
DO 100 n=1,2000
READ(11,6003) name(n)
  IF(name(n).EQ.'+++ ') THEN
    GO TO 101
  ELSE
    READ(11,6004) xx
  END IF
100 CONTINUE
101 nsour = N-1
C
C
C
  jini = 1
  READ(12,6003) onoma
  WRITE(22,6003) onoma
  DO 1000 N=1,97976
    READ(12,6004) onoma,NSEQ,NADD,PORX,ktracr
    READ(12,6005) xxx,yyy
    ktracr = 5
    DO 200 j8=jini,nsour
      IF(onoma.EQ.name(j8)) THEN
        nnss = nnss+1
        WRITE(22,6004) onoma,NSEQ,NADD,PORX,ktracr
        WRITE(22,6005) xxx,yyy,0.0d0,0.0d0
        WRITE(22,6005) 1.0d0,1.0d0,1.0d0,0.0d0,0.0d0
        WRITE(22,6005) 0.0d0,0.0d0,0.0d0,0.0d0,0.0d0
        WRITE(22,6005) 0.0d0,0.0d0,0.0d0,0.0d0,0.0d0
        jini = j8
        GO TO 1000
      END IF
    200 CONTINUE

```



```
C
      WRITE(22,6004) onoma,NSEQ,NADD,PORX,ktracr
      WRITE(22,6005) xxx,yyy,0.0d0,0.0d0
      WRITE(22,6005) 0.0d0,0.0d0,0.0d0,0.0d0,0.0d0
      WRITE(22,6005) 0.0d0,0.0d0,0.0d0,0.0d0,0.0d0
      WRITE(22,6005) 0.0d0,0.0d0,0.0d0,0.0d0,0.0d0
C
1000 CONTINUE
      WRITE(22,6006)
      WRITE(22,6006)
C
C
C
6003 FORMAT(A5)
6004 FORMAT(A5,2I5,E15.8,3I2)
6005 FORMAT(4E20.13)
6006 FORMAT(80(' '))

999 STOP
END
```

XI.5. The xtract5.f Routine

The xtract5.f V1.0 routine (STN: 10217-1.0-00) is used to obtain initial condition files (INCON) using the SAVE files from the EOS9 runs. The INCON files are then used for the EOS9nT simulations of Cl transport in the ESF.

A listing of the xtract5.f routine follows.

```

PROGRAM xtract5
IMPLICIT DOUBLE PRECISION (A-H,O-Z)
CHARACTER*5 onoma
C
C
C
OPEN(UNIT=12,FILE=' INCON_i ',STATUS='OLD')
OPEN(UNIT=22,FILE=' INCON_m ')
C
C
C
READ(12,6003) onoma
WRITE(22,6003) onoma
DO 1000 N=1,120000
  READ(12,6004) onoma,NSEQ,NADD,PORX,ktracr
  IF(onoma(1:3).EQ.'+++') GO TO 1001
  READ(12,6005) xxx,yyy
C
  ktracr = 1
C
  WRITE(22,6004) onoma,NSEQ,NADD,PORX,ktracr
  WRITE(22,6005) xxx,yyy,0.0d0,0.0d0
  WRITE(22,6005) 0.0d0
  WRITE(22,6005) 0.0d0
  WRITE(22,6005) 0.0d0
C
1000 CONTINUE
1001 WRITE(22,6006)
  WRITE(22,6006)
C
C
C
6003 FORMAT(A5)
6004 FORMAT(A5,2I5,E15.8,3I2)
6005 FORMAT(4E20.13)
6006 FORMAT(80(' '))

999 STOP
END

```

XI.6. The xtract6.f Routine

The xtract6.f V1.0 routine (STN: 10218-1.0-00) is used to extract the Cl concentrations corresponding to the ESF elements from the output of the EOS9nT simulation of Cl transport.

A listing of the xtract6.f routine follows.

```

PROGRAM xtract6
IMPLICIT DOUBLE PRECISION (A-H,O-Z)
DIMENSION tmf(2000),xx(2000)
CHARACTER*5 name(2000)
CHARACTER*5 onoma
C
C
OPEN(UNIT=11,FILE='esf',STATUS='OLD')
OPEN(UNIT=12,FILE='cl.out',STATUS='OLD')
OPEN(UNIT=22,FILE='ESF_Cl')
C
C
C
xmin = 1.0d6
DO 100 n=1,2000
  READ(11,6003) name(n),xx(n)
  IF(name(n).EQ.'+++ ') GO TO 101
100 CONTINUE
101 nsour = N-1
C
C
C
DO 1000 N=1,104156
  READ(12,6012) onoma,id,value
  DO 200 j8=1,nsour
    IF(onoma.EQ.name(j8)) THEN
      tmf(j8) = value
      GO TO 1000
    END IF
  200 CONTINUE
1000 CONTINUE
C
C
C
DO 2000 N=1,nsour
  WRITE(22,6022) xx(n),tmf(n)
2000 CONTINUE
C
C
C
6003 FORMAT(A5,7x,F9.4)
6004 FORMAT(4E20.13)
6005 FORMAT(A5,2I5,A5,3E10.4,2F10.3,F10.4)
6012 FORMAT(T3,A5,2x,I6,4x,1pe15.8,3x,2('(',i1,')',1pe15.8,2x),
&          1x,1pe15.8,2x,('(',i1,')',1pe15.8)

```

```
6020  FORMAT(T3,A5,2x,F9.4,2x,1pe15.8)
```

```
6022  FORMAT(T3,F9.4,2x,1pe15.8)
```

```
999  STOP
```

```
      END
```

INTENTIONALLY LEFT BLANK

ATTACHMENT XII.
INPUT AND OUTPUT FILES

INTENTIONALLY LEFT BLANK

XII. INPUT AND OUTPUT FILES

XII.1 FILES IN DTN: LB991220140160.001

This DTN includes the files involved in the 2-D numerical simulations for the EOS9nT validation (see Section 6.4). These files, located in the directory Val_num, are the following:

TestFMs	The input file for the simulation of the matrix-fracture transport problem using the coarse (2x320) grid.
TestFMs_T_out	Output corresponding to the TestFMs input file for conventional timestepping.
TestFMs_S_out	Output corresponding to the TestFMs input file for a Laplace transform formulation using the Stehfest algorithm (Stehfest 1970a;b).
TestFMs_H_out	Output corresponding to the TestFMs input file for a Laplace transform formulation using the DeHoog method (DeHoog et al. 1982).
TestFMb	The input file for the simulation of the matrix-fracture transport problem using the medium (5x320) grid.
TestFMb_T_out	Output corresponding to the TestFMb input file for conventional timestepping.
TestFMb_S_out	Output corresponding to the TestFMb input file for a Laplace transform formulation using the Stehfest algorithm (Stehfest 1970a;b).
TestFMb_H_out	Output corresponding to the TestFMb input file for a Laplace transform formulation using the DeHoog method (DeHoog et al. 1982).
TestFMx	The input file for the simulation of the matrix-fracture transport problem using the fine (12x320) grid.
TestFMx_T_out	Output corresponding to the TestFMx input file for conventional timestepping.
TestFMx_S_out	Output corresponding to the TestFMx input file for a Laplace transform formulation using the Stehfest algorithm (Stehfest 1970a;b).

TestFMx_H_out

Output corresponding to the TestFMx input file for a Laplace transform formulation using the DeHoog method (DeHoog et al. 1982).

The three outputs for each input file can be obtained by minor modifications of the input file. These modifications are the same for all three input files, and are introduced to the first line of the TRACR data block. Thus, the setting

```
TRACR----1----*-----2----*-----3----*-----4----*-----5----*-----6----*-----7----*-----8
      100010   05      steady0HOOG08      1.0e-14
```

leads to simulations using conventional timestepping. When it is changed to

```
TRACR----1----*-----2----*-----3----*-----4----*-----5----*-----6----*-----7----*-----8
      100010   05      steady1HOOG08      1.0e-14
```

the simulation uses a Laplace transform formulation based on the DeHoog method (DeHoog et al. 1982). Finally, modification to

```
TRACR----1----*-----2----*-----3----*-----4----*-----5----*-----6----*-----7----*-----8
      100010   05      steady1STFS18      1.0e-14
```

yields the solution based on a Laplace transform formulation following the Stehfest algorithm (Stehfest 1970a;b).

XII.2 FILES IN DTN: LB991220140160.002

This DTN includes the files involved in the 2-D semianalytical simulations for the FRACL validation (see Section 6.4). These files, located in the directory `Val_san`, are the following:

<code>Data_2h</code>	The input file for the simulation of a matrix-fracture transport problem involving three subdomains (two finite and one semi-infinite in z).
<code>Data_2h.C(z)_H</code>	Output corresponding to the <code>Data_2h</code> input file.
<code>Data_3h</code>	The input file for the simulation of a matrix-fracture transport problem involving a single domain (semi-infinite in z).
<code>Data_3h.C(z)_H</code>	Output corresponding to the <code>Data_3h</code> input file.

XII.3 FILES IN DTN: LB991220140160.003

This DTN includes the files involved in the 2-D semianalytical simulations of the Cl distribution in the UE-25 UZ#16 borehole. The FRACL simulations were conducted in support of the model validation (see Section 6.4). These files, located in the directory uz16_cl, are the following:

cl_10kyr	Input file to simulate chloride distribution at 10,000 years.
cl_10kyr.C(z)	Output corresponding to the cl_10kyr input file (vertical profile).
cl_10kyr.C(x)	Output corresponding to the cl_10kyr input file (horizontal profile).
cl_2500yr	Input file to simulate chloride distribution at 2,500 years.
cl_2500yr.C(z)	Output corresponding to the cl_2500yr input file (vertical profile).
cl_2500yr.C(x)	Output corresponding to the cl_2500yr input file (horizontal profile).
cl_1kyr	Input file to simulate chloride distribution at 1,000 years.
cl_1kyr.C(z)	Output corresponding to the cl_1kyr input file (vertical profile).
cl_1kyr.C(x)	Output corresponding to the cl_1kyr input file (horizontal profile).
cl_100yr	Input file to simulate chloride distribution at 100 years.
cl_100yr.C(z)	Output corresponding to the cl_100yr input file (vertical profile).
cl_100yr.C(x)	Output corresponding to the cl_100yr input file (horizontal profile).

XII.4 FILES IN DTN: LB991220140160.004

This DTN includes the files involved in the 3-D site-scale numerical simulations of Cl transport using a calibrated present-day infiltration regime. This simulation was conducted in support of verification (see Section 6.4), and was used to determine the Cl concentration distribution in the ESF. All the corresponding files are located in the directory `ESF_Cl`, and are listed below.

<code>MESH</code>	The file containing the mesh (grid geometry).
<code>INDEX</code>	Output and/or input file containing the global indices of the neighbors (active and/or inactive) of each grid cell.
<code>VELOC</code>	The input file containing the steady-state velocities across the cell boundaries.
<code>INCON</code>	Input file containing the initial conditions.
<code>chloride</code>	Input file for the EOS9nT simulation to determine the Cl distribution.
<code>chloride.out</code>	Output corresponding to the <code>chloride</code> input file.

XII.5 FILES IN DTN: LB991220140160.005

This DTN includes the files involved in the 2-D semianalytical FRACL simulations of the transport of three radionuclides (^{99}Tc , ^{237}Np , and ^{239}Pu) in the layers of the TSW hydrogeologic unit at three representative 2-D cross sections (i.e., Cross Sections 1, 2 and 3, see Section 6.5). The files in this DTN were used to obtain the results discussed in Section 6.6.

XII.5.1 Main Directory

All the files associated with this DTN are located in the directory `3crosssections_tsw`.

XII.5.2 Level 1 Directories

The `3crosssections_tsw` directory includes the three Level 1 directories `crosssection1`, `crosssection2`, and `crosssection3`. These correspond to Cross Sections 1, 2 and 3, respectively.

XII.5.3 Level 2 Directories

Each of the `crosssection1`, `crosssection2`, `crosssection3` directories includes the following Level 2 subdirectories:

<code>10kyear</code>	Input and output data for the 10,000-year simulation
<code>1kyear</code>	Input and output data for the 1,000-year simulation
<code>100year</code>	Input and output data for the 100-year simulation
<code>10year</code>	Input and output data for the 10-year simulation
<code>1year</code>	Input and output data for the 1-year simulation

XII.5.4 Files in Each Level 2 Directory

Each Level 2 directory includes the following files:

<code>tc</code>	Input file for the ^{99}Tc simulation.
<code>tc.C(z)</code>	Output corresponding to the <code>tc</code> input file (vertical profile).
<code>tc.C(x)</code>	Output corresponding to the <code>tc</code> input file (horizontal profile).
<code>np</code>	Input file for the ^{237}Np simulation.
<code>np.C(z)</code>	Output corresponding to the <code>np</code> input file (vertical profile).

np.C(x) Output corresponding to the np input file (horizontal profile).

pu Input file for the ^{239}Pu simulation.

pu.C(z) Output corresponding to the pu input file (vertical profile).

pu.C(x) Output corresponding to the pu input file (horizontal profile).

Note that the file names are the same in all level 2 directories, and only the name of the Level 1 and/or 2 directory changes.

XII.6 FILES IN DTN: LB991220140160.006

This DTN includes the files involved in the sensitivity analysis studies of transport of ^{99}Tc , ^{237}Np , and ^{239}Pu . These studies were conducted using the 2-D semianalytical FRACL model, and were conducted in the tsw35 layer of the TSw hydrogeologic unit. The files in this DTN were used to obtain the results discussed in Section 6.6.

XII.6.1 Main Directory

All the files associated with this DTN are located in the directory `analysis_tsw35`.

XII.6.2 Level 1 Directories

The `analysis_tsw35` main directory includes the following three Level 1 directories:

<code>aleffect</code>	Directory of the files corresponding to the study of the effect of longitudinal dispersivity α_L on transport.
<code>kieffect</code>	Directory of the files corresponding to the study of the effect of transfer coefficient K_i on transport.
<code>torteffect</code>	Directory of the files corresponding to the study of the effect of tortuosity τ on transport.

XII.6.3 Level 2 Directories of the `aleffect` Level 1 Directory

The `aleffect` level 1 directory includes the following three Level 2 directories:

<code>alf0.1</code>	Directory of the files corresponding to $\alpha_L = 0.1$ m.
<code>alf1</code>	Directory of the files corresponding to $\alpha_L = 1$ m.
<code>alf10</code>	Directory of the files corresponding to $\alpha_L = 10$ m.

XII.6.4 Level 2 Directories of the `kieffect` Level 1 Directory

The `aleffect` level 1 directory includes the following three Level 2 directories:

<code>ki0.1</code>	Directory of the files corresponding to $K_i = 0.1$.
<code>ki0.5</code>	Directory of the files corresponding to $K_i = 0.5$.

`ki1` Directory of the files corresponding to $K_i = 1$.

XII.6.5 Level 2 Directories of the `torteffect` Level 1 Directory

The `aleffect` level 1 directory includes the following three Level 2 directories:

`tort0.2phi` Directory of the files corresponding to $\tau = 0.2$ (: matrix porosity).

`tort1phi` Directory of the files corresponding to $\tau =$.

`tort5phi` Directory of the files corresponding to $\tau = 5$.

XII.6.6 Files in Each Level 2 Directory

Each Level 2 directory includes the following files:

`tc` Input file for the ^{99}Tc simulation.

`tc.C(z)` Output corresponding to the `tc` input file (vertical profile).

`tc.C(x)` Output corresponding to the `tc` input file (horizontal profile).

`np` Input file for the ^{237}Np simulation.

`np.C(z)` Output corresponding to the `np` input file (vertical profile).

`np.C(x)` Output corresponding to the `np` input file (horizontal profile).

`pu` Input file for the ^{239}Pu simulation.

`pu.C(z)` Output corresponding to the `pu` input file (vertical profile).

`pu.C(x)` Output corresponding to the `pu` input file (horizontal profile).

XII.7 FILES IN DTN: LB991220140160.007

This DTN includes the files involved in the 2-D semianalytical FRACL simulations of the transport of three radionuclides (^{99}Tc , ^{237}Np , and ^{239}Pu) in the layers of the CHn hydrogeologic unit at three representative 2-D cross sections (i.e., Cross Sections 1, 2 and 3, see Section 6.5). The files in this DTN were used to obtain the results discussed in Section 6.7.

XII.7.1 Main Directory

All the files associated with this DTN are located in the directory `3crosssections_chn`.

XII.7.2 Level 2 Directories

The `3crosssections_chn` directory includes the three Level 1 directories `crosssection1`, `crosssection2`, and `crosssection3`. These correspond to Cross Sections 1, 2 and 3, respectively.

XII.7.3 Level 3 Directories

Each of the `crosssection1`, `crosssection2`, and `crosssection3` directories includes the following Level 2 subdirectories:

<code>100kyear</code>	Input and output data for the 100,000-year simulation
<code>10kyear</code>	Input and output data for the 10,000-year simulation
<code>1kyear</code>	Input and output data for the 1,000-year simulation
<code>100year</code>	Input and output data for the 100-year simulation
<code>10year</code>	Input and output data for the 10-year simulation

XII.7.4 Files in Each Level 3 Directory

Each Level 2 directory includes the following files:

<code>tc</code>	Input file for the ^{99}Tc simulation.
<code>tc.C(z)</code>	Output corresponding to the <code>tc</code> input file (vertical profile).
<code>tc.C(x)</code>	Output corresponding to the <code>tc</code> input file (horizontal profile).
<code>np</code>	Input file for the ^{237}Np simulation.
<code>np.C(z)</code>	Output corresponding to the <code>np</code> input file (vertical profile).

np.C(x) Output corresponding to the np input file (horizontal profile).

pu Input file for the ^{239}Pu simulation.

pu.C(z) Output corresponding to the pu input file (vertical profile).

pu.C(x) Output corresponding to the pu input file (horizontal profile).

Note that the file names are the same in all level 2 directories, and only the name of the Level 1 and/or 2 directory changes.

XII.8 FILES IN DTN: LB991220140160.008

This DTN includes the files involved in the 2-D semianalytical FRACL simulations of the transport of three radionuclides (^{99}Tc , ^{237}Np , and ^{239}Pu) in the layers of the PP hydrogeologic unit at three representative 2-D cross sections (i.e., Cross Sections 1, 2 and 3, see Section 6.5). The files in this DTN were used to obtain the results discussed in Section 6.8.

XII.8.1 Main Directory

All the files associated with this DTN are located in the directory `3crosssections_pp`.

XII.8.2 Level 2 Directories

The `3crosssections_pp` directory includes the three Level 1 directories `crosssection1`, `crosssection2`, and `crosssection3`. These correspond to Cross Sections 1, 2 and 3, respectively.

XII.8.3 Level 3 Directories

Each of the `crosssection1`, `crosssection2`, `crosssection3` directories includes the following Level 2 subdirectories:

<code>100kyear</code>	Input and output data for the 100,000-year simulation
<code>10kyear</code>	Input and output data for the 10,000-year simulation
<code>1kyear</code>	Input and output data for the 1,000-year simulation
<code>100year</code>	Input and output data for the 100-year simulation
<code>10year</code>	Input and output data for the 10-year simulation

XII.8.4 Files in Each Level 3 Directory

Each Level 2 directory includes the following files:

<code>tc</code>	Input file for the ^{99}Tc simulation.
<code>tc.C(z)</code>	Output corresponding to the <code>tc</code> input file (vertical profile).
<code>tc.C(x)</code>	Output corresponding to the <code>tc</code> input file (horizontal profile).
<code>np</code>	Input file for the ^{237}Np simulation.
<code>np.C(z)</code>	Output corresponding to the <code>np</code> input file (vertical profile).

np.C(x) Output corresponding to the np input file (horizontal profile).

pu Input file for the ^{239}Pu simulation.

pu.C(z) Output corresponding to the pu input file (vertical profile).

pu.C(x) Output corresponding to the pu input file (horizontal profile).

Note that the file names are the same in all level 2 directories, and only the name of the Level 1 and/or 2 directory changes.

XII.9 FILES IN DTN: LB991220140160.009

This DTN includes the files involved in the 2-D semianalytical FRACL simulations of the transport of three radionuclides (^{99}Tc , ^{237}Np , and ^{239}Pu) in vertical cross sections that include all the hydrogeologic units from the potential repository horizon to the water table. Transport is studied in the three 2-D geological profiles of Cross Sections 1, 2 and 3 (see Section 6.5). The files in this DTN were used to obtain the results discussed in Section 6.9.

XII.9.1 Main Directory

All the files associated with this DTN are located in the directory `3rosssections`.

XII.9.2 Level 2 Directories

The `3rosssections` directory includes the two Level 1 directories `6mmyr` and `34mmyr`. The first corresponds to a mean present-day infiltration, and the second to a high glacial infiltration.

XII.9.3 Level 3 Directories

The `6mmyr` directory includes the four Level 2 directories `crosssection1`, `crosssection2`, `crosssection3`, and `crosssection3_perch`. The first three correspond to Cross Sections 1, 2, 3, respectively (with no perched water), while the fourth corresponds to Cross Section 3 with a perched water body.

The `34mmyr` directory includes the three Level 2 directories `crosssection1`, `crosssection2` and `crosssection3`. These correspond to Cross Sections 1, 2, 3, respectively (with no perched water).

XII.9.4 Level 4 Directories

Each of the Level 3 directories includes the following Level 4 subdirectories:

<code>100kyear</code>	Input and output data for the 100,000-year simulation
<code>10kyear</code>	Input and output data for the 10,000-year simulation
<code>1kyear</code>	Input and output data for the 1,000-year simulation
<code>100year</code>	Input and output data for the 100-year simulation
<code>10year</code>	Input and output data for the 10-year simulation

XII.9.5 Files in Each Level 4 Directory

Each Level 2 directory includes the following files:

<code>tc</code>	Input file for the ^{99}Tc simulation.
<code>tc.C(z)</code>	Output corresponding to the <code>tc</code> input file (vertical profile).
<code>tc.C(x)</code>	Output corresponding to the <code>tc</code> input file (horizontal profile).
<code>np</code>	Input file for the ^{237}Np simulation.
<code>np.C(z)</code>	Output corresponding to the <code>np</code> input file (vertical profile).
<code>np.C(x)</code>	Output corresponding to the <code>np</code> input file (horizontal profile).
<code>pu</code>	Input file for the ^{239}Pu simulation.
<code>pu.C(z)</code>	Output corresponding to the <code>pu</code> input file (vertical profile).
<code>pu.C(x)</code>	Output corresponding to the <code>pu</code> input file (horizontal profile).

Note that the file names are the same in all level 2 directories, and only the name of the level 1, 2 and/or 3 directory changes.

XII.10 FILES IN DTN: LB991220140160.010

This DTN includes the files involved in the T2R3D V1.4 (STN: 10006-1.4-00) 3-D simulations of the tracer injections in the Busted Butte field test. The files in this DTN were used to obtain the results discussed in Section 6.10. The files are located in two separate file directories that correspond to Phase 1A and Phase 1B tests.

XII.10.1 Directory bbphase1a

This directory corresponds to the simulations of the Phase 1A of the Busted Butte test, and includes the following files:

MESH	The mesh (grid geometry) file that is common to all the simulations listed under this file directory.
uz99bh1	Input file to simulate the borehole 1 test using the S1A flow parameters.
uz99bh1.out	Output corresponding to the uz99bh1 input file.
uz99bh3	Input file to simulate the borehole 3 test using the S1A flow parameters.
uz99bh3.out	Output corresponding to the uz99bh3 input file.
uz99bh4	Input file to simulate the borehole 4 test using the S1A flow parameters.
uz99bh4.out	Output corresponding to the uz99bh4 input file.
usgsbh3	Input file to simulate borehole 3 test using the S2A flow parameters.
usgsbh3.out	Output corresponding to the usgsbh3 input file.

XII.10.2 Directory bbphase1b

This directory corresponds to the simulations of the Phase 1B of the Busted Butte test, and includes the following files:

MESH	The mesh (grid geometry) file that is common to all the simulations listed under this file directory.
------	---

uz99_br	Input file to simulate bromide breakthrough curves using the S1A flow parameters.
uz99_br.out	Output corresponding to the uz99_br input file.
uz99_br.gasobs	Output containing simulation results in specific elements at specific times, corresponding to the uz99_br input file.
uz99_26dfba	Input file to simulate 2,6-DFBA breakthrough curves using the S1A flow parameters.
uz99_26dfba.out	Output corresponding to the uz99_26dfba input file.
uz99_26dfba.gasobs	Output containing simulation results in specific elements at specific times, corresponding to the uz99_26dfba input file.
uz99_li_kd1	Input file to simulate, using the S1A flow parameters, lithium breakthrough curves (use sorption coefficient $K_d=1$ mL/g).
uz99_li_kd1.out	Output corresponding to the uz99_li_kd1 input file.
uz99_li_kd1.gasobs	Output containing simulation results in specific elements at specific times, corresponding to the uz99_li_kd1 input file.
uz99_li_kd2	Input file to simulate, using the S1A flow parameters, lithium breakthrough curves (use sorption coefficient $K_d=2$ mL/g).
uz99_li_kd2.out	Output corresponding to the uz99_li_kd2 input file.
uz99_li_kd2.gasobs	Output containing simulation results in specific elements at specific times, corresponding to the uz99_li_kd2 input file.
usgs99_br	Input file to simulate bromide breakthrough curves using the S2B flow parameters.
usgs99_br.out	Output corresponding to the usgs99_br input file.
usgs99_br.gasobs	Output containing simulation results in specific elements at the specific times, corresponding to the usgs99_br input file.

XII.11 FILES IN DTN: LB991220140160.011

This DTN includes the files involved in the 3-D site-scale simulations of flow in the UZ of Yucca Mountain using the TOUGH2 V1.4 Module EOS9 V1.4 (STN: 10007-1.4-01) code. These simulations were conducted to generate the steady-state conditions, flow fields and velocities that are used as inputs for the 3-D site-scale simulations of solute and colloid transport through the UZ of Yucca Mountain (see Section 6.11).

XII.11.1 Main Directories

All the files associated with this DTN are located in the following directories:

<code>present</code>	Directory of the files corresponding to the present-day infiltration regime under the #1 perched water model.
<code>monsoon</code>	Directory of the files corresponding to the monsoon infiltration regime under the #1 perched water model.
<code>glacial</code>	Directory of the files corresponding to the glacial infiltration regime under the #1 perched water model.
<code>present_perch</code>	Directory of the files corresponding to the mean present-day infiltration regime for the #2 perched water model and the non-perched water model.
<code>esf_cl_flow</code>	Directory of the files corresponding to the flow regime for the study of chloride distribution in the ESF.

XII.11.2 Level 1 Directories

Each of the `present`, `monsoon` and `glacial` main directories includes the three Level 1 directories `lower`, `mean` and `upper`. These correspond to the lower, mean and upper infiltration of each climatic regime (see Table 6.11).

The main directory `present_perch` includes the two Level 1 directories `nonperch_mean` and `perch2_mean`. These correspond to the non-perched and the #2 perched water models, respectively. The main directory `esf_cl_flow` does not include any subdirectories.

XII.11.3 Files With Common Names in All Level 1 Directories and in the `esf_cl_flow` Main Directory

All Level 1 directories and the `esf_cl_flow` main directory include the following files:

MESH	The mesh (grid geometry) file.
INCON	The input file that records the initial thermodynamic conditions of a TOUGH2 simulation run.
VELOC	The output file containing the steady-state velocities across the cell boundaries.
SAVE	The output file that records thermodynamic conditions at the end of a TOUGH2 simulation run.

Note that although these files may share the same names, they include different data in the Level 1 directories and in the `esf_cl_flow` Main directory.

XII.11.4 Files With Common Names in the `lower` Level 1 Directories

All Level 1 directories with the name `lower` include the following files:

<code>lower</code>	Input file containing the initial conditions for the EOS9 simulation of flow under conditions of low infiltration of the corresponding regime (denoted by the main directory name).
<code>lower.out</code>	The output file corresponding to the <code>lower</code> input file.

Note that although these files may share the same names, they include different data in each Level 1 directory.

XII.11.5 Files With Common Names in the `mean` Level 1 Directories

All Level 1 directories with the name `lower` include the following files:

<code>mean</code>	Input file containing the initial conditions for the EOS9 simulation of flow under conditions of mean infiltration of the corresponding regime (denoted by the main directory name).
<code>mean.out</code>	The output file corresponding to the <code>mean</code> input file.

Note that although these files may share the same names, they include different data in each Level 1 directory.

XII.11.6 Files With Common Names in the `mean` Level 1 Directories

All Level 1 directories with the name `lower` include the following files:

`upper` Input file containing the initial conditions for the EOS9 simulation of flow under conditions of high infiltration of the corresponding regime (denoted by the main directory name).

`mean.out` The output file corresponding to the `upper` input file.

Note that although these files may share the same names, they include different data in each Level 1 directory.

XII.11.7 Files With Common Names in the `nonperch_mean` and `perch2_mean` Level 1 Directories, and in the `esf_cl_flow` Main Directory

The `nonperch_mean` and `perch2_mean` Level 1 directories and the `esf_cl_flow` main directory include the following files:

`flow` In the `nonperch_mean` and `perch2_mean` Level 1 directories, this is the input file containing the initial conditions for the EOS9 simulation of flow under conditions of mean present-day infiltration under the corresponding perched water conceptual model (denoted by the Level 1 directory name).
In the `esf_cl_flow` main directory, this is the input file containing the initial conditions for the EOS9 simulation of flow for the study of the chloride distribution in the ESF.

`flow.out` The output file corresponding to the `flow` input file.

Note that although these files may share the same names, they include different data in each Level 1 directory.

XII.12 FILES IN DTN: LB991220140160.012

This DTN includes the files involved in the 3-D site-scale simulations of solute transport for the #1 perched water model under the present-day climatic scenario (see Sections 6.12, 6.13 and 6.14). All these files are located in the directory `Present_case`.

XII.12.1 Input Files Common to Simulations

These files are common to all the simulations listed in this DTN. All these files are located in the subdirectory `Pr_mean` of the `Present_day` directory. These are the following:

MESH	The file containing the mesh (grid geometry).
INDEX	Output and/or input file containing the global indices of the neighbors (active and/or inactive) of each grid cell.
UNVEC	Output and/or input file containing the x,y and z components of the unit vectors normal to the cell interfaces.

XII.12.2 Files for Transport Simulations for a Mean Present-Day Infiltration Regime

All the files listed in this section are located in the subdirectory `Pr_mean` of the `Present_case` directory. These are the following:

VELOC	The input file containing the steady-state velocities across the cell boundaries.
INCON_3P	Input file containing the initial conditions of three parent radionuclides (^{99}Tc , ^{237}Np and ^{239}Pu).
INCON_3d	Input file containing the initial conditions of a parent and two daughter radionuclides.
M_pre_3P	Input file for the EOS9nT simulation of the three parent radionuclides. The output options in this file limit the simulation output to (a) species mass balances and (b) species mass fluxes across the repository and the groundwater boundaries.
M_pre_3P.out	Output corresponding to the <code>M_pre_3P</code> input file.
M_pre_3Pdis	Input file for the EOS9nT simulation of the three parent radionuclides. The output options lead to printouts of the

	concentration distributions of the three species in the liquid and solid phases.
M_pre_3Pdis.out	Output corresponding to the M_pre_3Pdis input file.
M_pre_3dNp	Input file for the EOS9nT simulation of ^{237}Np and its daughters (^{233}U and ^{229}Th). The output options are as in the M_pre_3P file.
M_pre_3dNp.out	Output corresponding to the M_pre_3dNp input file.
M_pre_3dPu	Input file for the EOS9nT simulation of ^{239}Pu and its daughters (^{235}U and ^{231}Pa). The output options are as in the M_pre_3P file.
M_pre_3dPu.out	Output corresponding to the M_pre_3dPu input file.
M_pre_3P_nD	Same as the M_pre_3P file, but with zero molecular diffusion for all species.
M_pre_3P_nD.out	Output corresponding to the M_pre_3P_nD input file.
M_pre_3dPu_nD	Same as the M_pre_3dPu file, but with zero molecular diffusion for all species.
M_pre_3dPu_nD.out	Output corresponding to the M_pre_3dPu_nD input file.

XII.12.3 Files for Transport Simulations for a Low Present-Day Infiltration Regime

All the files listed in this section are located in the subdirectory Pr_low of the Present_case directory. These are the following:

VELOC	The input file containing the steady-state velocities across the cell boundaries.
INCON_3P	Input file containing the initial conditions of the three parent radionuclides.
INCON_3d	Input file containing the initial conditions of a parent and two daughter radionuclides.
L_pre_3P	Input file for the EOS9nT simulation of the three parent radionuclides. The output options are as in the M_pre_3P file.
L_pre_3P.out	Output corresponding to the L_pre_3P input file.

L_pre_3dPu	Input file for the EOS9nT simulation of ^{239}Pu and its daughters. The output options are as in the M_pre_3P file.
L_pre_3dPu.out	Output corresponding to the L_pre_3dPu input file.

XII.12.4 Files for Transport Simulations for a High Present-Day Infiltration Regime

All the files listed in this section are located in the subdirectory Pr_high of the Present_case directory. These are the following:

VELOC	The input file containing the steady-state velocities across the cell boundaries.
INCON_3P	Input file containing the initial conditions of the three parent radionuclides.
INCON_3d	Input file containing the initial conditions of a parent and two daughter radionuclides.
H_pre_3P	Input file for the EOS9nT simulation of the three parent radionuclides. The output options are as in the M_pre_3P file.
H_pre_3P.out	Output corresponding to the H_pre_3P input file.
H_pre_3dPu	Input file for the EOS9nT simulation of ^{239}Pu and its daughters. The output options are as in the M_pre_3P file.
H_pre_3dPu.out	Output corresponding to the H_pre_3dPu input file.

XII.13 FILES IN DTN: LB991220140160.013

This DTN includes the files involved in the 3-D site-scale simulations of solute transport for the #1 perched water model under the monsoon climatic scenario (see Sections 6.12, 6.13 and 6.14). All these files are located in the directory `Monsoon_case`.

XII.13.1 Input Files Common to All Simulations

The files common to all the simulations listed in this DTN are `MESH`, `INDEX` and `UNVEC`. These files are identical to those discussed in Section XII.12.1, and can be found in the subdirectory `Pr_mean` of the `Present_day` directory.

XII.13.2 Files for Transport Simulations for a Mean Monsoon Infiltration Regime

All the files listed in this section are located in the subdirectory `Mns_mean` of the `Monsoon_case` directory. These are the following:

<code>VELOC</code>	The input file containing the steady-state velocities across the cell boundaries.
<code>INCON_3P</code>	Input file containing the initial conditions of the three parent radionuclides.
<code>INCON_3d</code>	Input file containing the initial conditions of a parent and two daughter radionuclides.
<code>M_mns_3P</code>	Input file for the EOS9nT simulation of the three parent radionuclides. The output options are as in the <code>M_pre_3P</code> file.
<code>M_mns_3P.out</code>	Output corresponding to the <code>M_mns_3P</code> input file.
<code>M_mns_3dPu</code>	Input file for the EOS9nT simulation of ^{239}Pu and its daughters. The output options are as in the <code>M_pre_3P</code> file.
<code>M_mns_3dPu.out</code>	Output corresponding to the <code>M_mns_3dPu</code> input file.

XII.13.3 Files for Transport Simulations for a Low Monsoon Infiltration Regime

All the files listed in this section are located in the subdirectory `Mns_low` of the `Monsoon_case` directory. These are the following:

<code>VELOC</code>	The input file containing the steady-state velocities across the cell boundaries.
--------------------	---

INCON_3P	Input file containing the initial conditions of the three parent radionuclides.
INCON_3d	Input file containing the initial conditions of a parent and two daughter radionuclides.
L_mns_3P	Input file for the EOS9nT simulation of the three parent radionuclides. The output options are as in the M_pre_3P file.
L_mns_3P.out	Output corresponding to the L_mns_3P input file.
L_mns_3dPu	Input file for the EOS9nT simulation of ^{239}Pu and its daughters. The output options are as in the M_pre_3P file.
L_mns_3dPu.out	Output corresponding to the L_mns_3dPu input file.

XII.13.4 Files for Transport Simulations for a High Monsoon Infiltration Regime

All the files listed in this section are located in the subdirectory Mns_high of the Monsoon_case directory. These are the following:

VELOC	The input file containing the steady-state velocities across the cell boundaries.
INCON_3P	Input file containing the initial conditions of the three parent radionuclides.
INCON_3d	Input file containing the initial conditions of a parent and two daughter radionuclides.
H_mns_3P	Input file for the EOS9nT simulation of the three parent radionuclides. The output options are as in the M_pre_3P file.
H_mns_3P.out	Output corresponding to the H_mns_3P input file.
H_mns_3dPu	Input file for the EOS9nT simulation of ^{239}Pu and its daughters. The output options are as in the M_pre_3P file.
H_mns_3dPu.out	Output corresponding to the H_mns_3dPu input file.

XII.14 FILES IN DTN: LB991220140160.014

This DTN includes the files involved in the 3-D site-scale simulations of solute transport for the #1 perched water model under the monsoon climatic scenario (see Sections 6.12, 6.13 and 6.14). All these files are located in the directory `Glacial_case`.

XII.14.1 Input Files Common to All Simulations

The files common to all the simulations listed in this DTN are `MESH`, `INDEX` and `UNVEC`. These files are identical to those discussed in Section XII.12.1, and can be found in the subdirectory `Pr_mean` of the `Present_day` directory.

XII.14.2 Files for Transport Simulations for a Mean Glacial Infiltration Regime

All the files listed in this section are located in the subdirectory `Gl_mean` of the `Glacial_case` directory. These are the following:

<code>VELOC</code>	The input file containing the steady-state velocities across the cell boundaries.
<code>INCON_3P</code>	Input file containing the initial conditions of the three parent radionuclides.
<code>INCON_3d</code>	Input file containing the initial conditions of a parent and two daughter radionuclides.
<code>M_gla_3P</code>	Input file for the EOS9nT simulation of the three parent radionuclides. The output options are as in the <code>M_pre_3P</code> file.
<code>M_gla_3P.out</code>	Output corresponding to the <code>M_gla_3P</code> input file.
<code>M_gla_3dPu</code>	Input file for the EOS9nT simulation of ^{239}Pu and its daughters. The output options are as in the <code>M_pre_3P</code> file.
<code>M_gla_3dPu.out</code>	Output corresponding to the <code>M_gla_3dPu</code> input file.

XII.14.3 Files for Transport Simulations for a Low Glacial Infiltration Regime

All the files listed in this section are located in the subdirectory `Gl_low` of the `Glacial_case` directory. These are the following:

<code>VELOC</code>	The input file containing the steady-state velocities across the cell boundaries.
--------------------	---

INCON_3P	Input file containing the initial conditions of the three parent radionuclides.
INCON_3d	Input file containing the initial conditions of a parent and two daughter radionuclides.
L_gla_3P	Input file for the EOS9nT simulation of the three parent radionuclides. The output options are as in the M_pre_3P file.
L_gla_3P.out	Output corresponding to the L_gla_3P input file.
L_gla_3dPu	Input file for the EOS9nT simulation of ^{239}Pu and its daughters. The output options are as in the M_pre_3P file.
L_gla_3dPu.out	Output corresponding to the L_gla_3dPu input file.

XII.14.4 Files for Transport Simulations for a High Glacial Infiltration Regime

All the files listed in this section are located in the subdirectory Gl_high of the Glacial_case directory. These are the following:

VELOC	The input file containing the steady-state velocities across the cell boundaries.
INCON_3P	Input file containing the initial conditions of the three parent radionuclides.
INCON_3d	Input file containing the initial conditions of a parent and two daughter radionuclides.
H_gla_3P	Input file for the EOS9nT simulation of the three parent radionuclides. The output options are as in the M_pre_3P file.
H_gla_3P.out	Output corresponding to the H_gla_3P input file.
H_gla_3dPu	Input file for the EOS9nT simulation of ^{239}Pu and its daughters. The output options are as in the M_pre_3P file.
H_gla_3dPu.out	Output corresponding to the H_gla_3dPu input file.

XII.15 FILES IN DTN: LB991220140160.015

This DTN includes the files involved in the 3-D site-scale simulations of solute transport for the #2-perched-water model under the mean present-day infiltration regime (see Section 6.15). All these files are located in the directory PER_2, and are listed below.

MESH	The file containing the mesh (grid geometry).
INDEX	Output and/or input file containing the global indices of the neighbors (active and/or inactive) of each grid cell.
VELOC	The input file containing the steady-state velocities across the cell boundaries.
INCON	Input file containing the initial conditions of the three parent radionuclides.
M_pre_3P_p2	Input file for the EOS9nT simulation of (a) the three parent radionuclides and (b) the daughters of ^{239}Pu . The output options are as in the M_pre_3P file.
M_pre_3P_p2.out	Output corresponding to the M_pre_3P_p2 input file.

XII.16 FILES IN DTN: LB991220140160.016

This DTN includes the files involved in the 3-D site-scale simulations of solute transport for the no-perched-water model under the mean present-day infiltration regime (see Section 6.15). All these files are located in the directory No_PER, and are listed below.

MESH	The file containing the mesh (grid geometry).
INDEX	Output and/or input file containing the global indices of the neighbors (active and/or inactive) of each grid cell.
VELOC	The input file containing the steady-state velocities across the cell boundaries.
INCON	Input file containing the initial conditions of the three parent radionuclides.
M_pre_3P_np	Input file for the EOS9nT simulation of (a) the three parent radionuclides and (b) the daughters of ^{239}Pu . The output options are as in the M_pre_3P file.
M_pre_3P_np.out	Output corresponding to the M_pre_3P_np input file.

XII.17 FILES IN DTN: LB991220140160.017

This DTN includes the files involved in the 3-D site-scale simulations of colloid transport for the #1 perched water model under the mean present-day infiltration regime (see Sections 6.16 and 6.17).. All these files are located in the subdirectory `Colloids` of the `Present_day` directory.

XII.17.1 Input Files Common to All Simulations

The files common to all the simulations listed in this DTN are `MESH`, `INDEX`, `UNVEC` and `VELOC`. These files are identical to those discussed in Sections XII.12.1 and XII.12.2, and can be found in the subdirectory `Pr_mean` of the `Present_day` directory.

XII.17.2 Files for Transport Simulations for a Mean Monsoon Infiltration Regime

All the files listed in this section are located in the subdirectory `Colloids` of the `Present_day` directory.. These are the following:

<code>INCON</code>	Input file containing the initial conditions of the three parent radionuclides.
<code>M_pre_4C_no</code>	Input file for the EOS9nT simulation of four colloids with different particle sizes for Case 1 (see Section 6.16). The output options are as in the <code>M_pre_3P</code> file.
<code>M_pre_4C_no.out</code>	Output corresponding to the <code>M_pre_4C_no</code> input file.
<code>M_pre_4Ca</code>	Input file for the EOS9nT simulation of four colloids with different particle sizes for Case 2 (see Section 6.16). The output options are as in the <code>M_pre_3P</code> file.
<code>M_pre_4Ca.out</code>	Output corresponding to the <code>M_pre_4Ca</code> input file.
<code>M_pre_4Ca_dis</code>	Input file for the EOS9nT simulation of four colloids with different particle sizes for Case 2 (see Section 6.16). The output options are as in the <code>M_pre_3P_dis</code> file.
<code>M_pre_4Ca_dis.out</code>	Output corresponding to the <code>M_pre_4Ca_dis</code> input file.
<code>M_pre_4Cb</code>	Input file for the EOS9nT simulation of four colloids with different particle sizes for Case 3 (see Section 6.16). The output options are as in the <code>M_pre_3P</code> file.
<code>M_pre_4Cb.out</code>	Output corresponding to the <code>M_pre_4Cb</code> input file.

M_pre_4Cc	Input file for the EOS9nT simulation of four colloids with different particle sizes for Case 4 (see Section 6.16). The output options are as in the M_pre_3P file.
M_pre_4Cc.out	Output corresponding to the M_pre_4Cc input file.
M_pre_4Ca_nD	Same as the M_pre_4Ca file, but with zero colloidal diffusion for all four species..
M_pre_4Ca_nD.out	Output corresponding to the M_pre_4Ca_nD input file.

XII.18 FILES IN DTN: LB991220140160.019

This DTN includes parameter values taken and/or computed from information in the scientific literature. Four data sets of parameter values are listed in the file `inputs_019`, along with the corresponding reference source.

ATTACHMENT XIII.

DOCUMENT INPUTS REFERENCE SYSTEM

INTENTIONALLY LEFT BLANK

OFFICE OF CIVILIAN RADIOACTIVE WASTE MANAGEMENT DOCUMENT INPUT REFERENCE SHEET									
1. Document Identifier No./Rev.: MDL-NBS-HS-000008/Rev. 00D			Change:	Title: Radionuclide Transport Models under Ambient Conditions					
Input Document			4. Input Status	5. Section Used in	6. Input Description	7. TBV/TBD Priority	8. TBV Due To		
2. Technical Product Input Source Title and Identifier(s) with Version		3. Section					Unqual.	From Uncontrolled Source	Un-confirmed
2a									
1.	DTN: GS950608312272.001. Chemical Data for Pore Water from Tuff Cores of USW NRG-6, NRG7/7A, UZ-14 AND UZ-N55, and UE-25 UZ#16. Submittal date: 05/30/1995.	S97476 _013, UZ#16	N/A-Reference only	Table 6.3 Figure 6.4.4	Calibration-Cl concentration in UE-25 UZ#16. For model verification. Comparison only.	N/A	N/A	N/A	N/A
2.	DTN: GS990308312242.007. Laboratory And Centrifuge Measurements Of Physical And Hydraulic Properties Of Core Samples From Busted Butte Boreholes UZTT-BB-INJ-1, UZTT-BB-INJ-3, UZTT-BB-INJ-4, UZTT-BB-INJ-6, UZTT-BB-COL-5 and UZTT-BB-COL-8. Submittal date: 03/22/1999. Initial use.	Entire	TBV-4001	6.10	Matrix porosity, permeability, initial saturation, and rock grain density of the field samples.	1	N/A	N/A	✓
3.	DTN: GS990708312242.008. Physical and Hydraulic Properties of Core Samples from Busted Butte Boreholes. Submittal date: 07/01/1999.	Entire	TBV-3620	6.10	Matrix porosity, permeability, initial saturation, and rock grain density of the field samples.	1	N/A	N/A	✓

OFFICE OF CIVILIAN RADIOACTIVE WASTE MANAGEMENT DOCUMENT INPUT REFERENCE SHEET									
1. Document Identifier No./Rev.: MDL-NBS-HS-000008/Rev. 00D			Change:	Title: Radionuclide Transport Models under Ambient Conditions					
Input Document			4. Input Status	5. Section Used in	6. Input Description	7. TBV/TBD Priority	8. TBV Due To		
2. Technical Product Input Source Title and Identifier(s) with Version		3. Section					Unqual.	From Uncontrolled Source	Un-confirmed
2a									
4.	DTN: LAIT831341AQ96.001. Radionuclide Retardation. Measurements of Batch Sorption Distribution Coefficients for Barium, Cesium, Selenium, Strontium, Uranium, Plutonium, and Neptunium. Submittal date: 11/12/1996.	Entire	N/A- Technical Product Output	6.5-6.9 6.11-6.15 6.17	Sorption coefficient K_d for Np, Pu, and U.	N/A	N/A	N/A	N/A
5.	DTN: LAJF831222AQ98.007. Chloride, Bromide, and Sulfate Analyses of Salts Leached from ECRB-CWAT#1, #2, and #3 Drill core. Submittal date: 09/09/1998. Initial use.	Entire	TBV-4002	6.4	Field chloride distribution data in the ESF	1	N/A	N/A	✓
6.	DTN: LA9909JF831222.010. Chloride, Bromide, Sulfate, and Chlorine-36 Analyses of ESF Porewaters. Submittal date: 09/29/1999. Initial use.	Entire	N/A- Qualified-Verification Level 2	6.4	Field distribution data in the ESF	N/A	N/A	N/A	N/A

OFFICE OF CIVILIAN RADIOACTIVE WASTE MANAGEMENT DOCUMENT INPUT REFERENCE SHEET									
1. Document Identifier No./Rev.: MDL-NBS-HS-000008/Rev. 00D			Change:	Title: Radionuclide Transport Models under Ambient Conditions					
Input Document			4. Input Status	5. Section Used in	6. Input Description	7. TBV/TBD Priority	8. TBV Due To		
2. Technical Product Input Source Title and Identifier(s) with Version		3. Section					Unqual.	From Uncontrolled Source	Un-confirmed
2a									
7.	DTN: LA9909JF831222.012. Chloride, Bromide, and Sulfate Analyses of Porewater Extracted from ESF Niche 3566 (Niche #1) and ESF 3650 (Niche #2) Drillcore. Submittal date: 09/29/1999. Initial use.	Entire	N/A- Qualified-Verification Level 2	6.4	Field distribution data in the ESF	N/A	N/A	N/A	N/A
8.	DTN: LA9909WS831372.001. Busted Butte UZ Transport Test: Phase I Collection Pad Extract Concentrations. Submittal date: 09/29/1999. Initial use.	Entire	N/A- Reference only	6.10	Measured tracer concentration.	N/A	N/A	N/A	N/A
9.	DTN: LA9909WS831372.002. Busted Butte UZ Transport Test: Phase I Collection Pad Tracer Loading And Tracer Concentrations. Submittal date: 09/30/1999. Initial use.	Entire	N/A- Reference only	6.10	Measured tracer concentration.	N/A	N/A	N/A	N/A

OFFICE OF CIVILIAN RADIOACTIVE WASTE MANAGEMENT DOCUMENT INPUT REFERENCE SHEET									
1. Document Identifier No./Rev.: MDL-NBS-HS-000008/Rev. 00D			Change:	Title: Radionuclide Transport Models under Ambient Conditions					
Input Document			4. Input Status	5. Section Used in	6. Input Description	7. TBV/TBD Priority	8. TBV Due To		
2. Technical Product Input Source Title and Identifier(s) with Version		3. Section					Unqual.	From Uncontrolled Source	Un-confirmed
2a									
10.	DTN: LB971212001254.001. DKM Basecase Parameter Set For UZ Model with Mean Fracture Alpha, Present Day Infiltration, and Estimated Welded, Non-Welded and Zeolitic FMX. Submittal date: 12/12/1997.	Entire	N/A-Reference only	6.10	Calibrated flow parameters for dual-permeability model base-case in the matrix of the ch1v and ch2v layers (porosity, permeability, van Genuchten α and m parameters, residual saturation, satiated saturation, rock grain density, tortuosity)	N/A	N/A	N/A	N/A
11.	DTN: LB990501233129.001. Fracture Properties for the UZ Model Grids and Uncalibrated Fracture and Matrix Properties for the UZ Model Layers for AMR U0090, "Analysis of Hydrologic Properties Data." Submittal date: 08/25/1999.	Entire	N/A-Technical Product Output	6.5-6.17	Fracture aperture	N/A	N/A	N/A	N/A
12.	DTN: LB990501233129.004. 3-D UZ Model Calibration Grids for AMR U0000, "Development of Numerical Grids of UZ Flow and Transport Modeling." Submittal date; 9/24/1999.	Entire	N/A-Technical Product Output	6.5-6.9	Hydrogeologic unit profiles	N/A	N/A	N/A	N/A

OFFICE OF CIVILIAN RADIOACTIVE WASTE MANAGEMENT DOCUMENT INPUT REFERENCE SHEET									
1. Document Identifier No./Rev.: MDL-NBS-HS-000008/Rev. 00D			Change:	Title: Radionuclide Transport Models under Ambient Conditions					
Input Document			4. Input Status	5. Section Used in	6. Input Description	7. TBV/TBD Priority	8. TBV Due To		
2. Technical Product Input Source Title and Identifier(s) with Version		3. Section					Unqual.	From Uncontrolled Source	Un-confirmed
2a									
13.	DTN: LB990701233129.002. 3-D Model Calibration Grid for Calculation of Flow Fields using #3 Perched Water Conceptual Model (Non-Perched Water Model). Submittal date: Will be submitted with AMR.		N/A- Technical Product Output	6.4	Chloride distribution modeling in borehole UE-25 UZ-16 3-D flow field (e.g. mesh)	N/A	N/A	N/A	N/A
14.	DTN: LB990801233129.001. TSPA Grid Flow Simulations for AMR U0050, "UZ Flow Models and Submodels." (Flow Field #1). Submittal date: 11/29/1999.		N/A- Technical Product Output	6.12-6.15	Present day infiltration – Lower bound, (perched water model #1)	N/A	N/A	N/A	N/A
15.	DTN: LB990801233129.003. TSPA Grid Flow Simulations for AMR U0050, "UZ Flow Models and Submodels." (Flow Field #3). Submittal date: 11/29/1999.		N/A- Technical Product Output	6.5-6.17	Steady-state fracture and matrix saturation Present day infiltration- mean (perched water model #1)	N/A	N/A	N/A	N/A
16.	DTN: LB990801233129.004. TSPA Grid Flow Simulations for AMR U0050, "UZ Flow Models and Submodels." Submittal date: 11/29/1999.		N/A- Technical Product Output	6.15	Present-day mean infiltration (perched-water model #2)	N/A	N/A	N/A	N/A

OFFICE OF CIVILIAN RADIOACTIVE WASTE MANAGEMENT DOCUMENT INPUT REFERENCE SHEET									
1. Document Identifier No./Rev.: MDL-NBS-HS-000008/Rev. 00D			Change:	Title: Radionuclide Transport Models under Ambient Conditions					
Input Document			4. Input Status	5. Section Used in	6. Input Description	7. TBV/TBD Priority	8. TBV Due To		
2. Technical Product Input Source Title and Identifier(s) with Version		3. Section					Unqual.	From Uncontrolled Source	Un-confirmed
2a									
17.	DTN: LB990801233129.005. TSPA Grid Flow Simulations for AMR U0050, "UZ Flow Models and Submodels." (Flow Field #5). Submittal date: 11/29/1999.	Entire	N/A- Technical Product Output	6.11-6.15	Present day infiltration-upper bound (perched water model #1)	N/A	N/A	N/A	N/A
18.	DTN: LB990801233129.007. TSPA Grid Flow Simulations for AMR U0050, "UZ Flow Models and Submodels." (Flow Field #7). Submittal date: 11/29/1999.	Entire	N/A- Technical Product Output	6.11-6.15	Glacial infiltration-lower bound (perched water model #1)	N/A	N/A	N/A	N/A
19.	DTN: LB990801233129.009. TSPA Grid Flow Simulations for AMR U0050, "UZ Flow Models and Submodels." (Flow Field #9). Submittal date: 11/29/1999.	Entire	N/A- Technical Product Output	6.11-6.15	Glacial infiltration-mean (perched water model #1)	N/A	N/A	N/A	N/A
20.	DTN: LB990801233129.011. TSPA Grid Flow Simulations for AMR U0050, "UZ Flow Models and Submodels." (Flow Field #11). Submittal date: 11/29/1999.	Entire	N/A- Technical Product Output	6.11-6.15	Glacial infiltration-upper bound (perched water model #1)	N/A	N/A	N/A	N/A
21.	DTN: LB990801233129.013. TSPA Grid Flow Simulations for AMR U0050, "UZ Flow Models and Submodels." (Flow Field #13). Submittal date: 11/29/1999.	Entire	N/A- Technical Product Output	6.11-6.15	Monsoon infiltration-lower bound (perched water model #1)	N/A	N/A	N/A	N/A

OFFICE OF CIVILIAN RADIOACTIVE WASTE MANAGEMENT DOCUMENT INPUT REFERENCE SHEET									
1. Document Identifier No./Rev.: MDL-NBS-HS-000008/Rev. 00D			Change:	Title: Radionuclide Transport Models under Ambient Conditions					
Input Document			4. Input Status	5. Section Used in	6. Input Description	7. TBV/TBD Priority	8. TBV Due To		
2. Technical Product Input Source Title and Identifier(s) with Version		3. Section					Unqual.	From Uncontrolled Source	Un-confirmed
2a									
22.	DTN: LB990801233129.015. TSPA Grid Flow Simulations for AMR U0050, "UZ Flow Models and Submodels." (Flow Field #15). Submittal date: 11/29/1999.	Entire	N/A- Technical Product Output	6.11- 6.15	Monsoon infiltration-mean (perched water model #1)	N/A	N/A	N/A	N/A
23.	DTN: LB990801233129.017. TSPA Grid Flow Simulations for AMR U0050, "UZ Flow Models and Submodels." (Flow Field #17). Submittal date: 11/29/1999.	Entire	N/A- Technical Product Output	6.11- 6.15	Monsoon infiltration-upper bound (perched water model #1)	N/A	N/A	N/A	N/A
24.	DTN: LB990801233129.019. TSPA Grid Flow Simulations for AMR U0050, "UZ Flow Models and Submodels." Flow Field #19: Present Day Mean Infiltration Map for Non-Perched Water Conceptual Model. Submittal date: will be submitted with AMR.	Entire	N/A- Technical Product Output	6.15	Present day mean infiltration (no perched water model)	N/A	N/A	N/A	N/A
25.	DTN: LB991131233129.003. Analytical and Simulation Results of Chloride and Chlorine-36 Analysis. Submittal date: Will be submitted with AMR U0050.	Entire	N/A- Technical Product Output	4.1, 6.4	Chloride concentration distribution	N/A	N/A	N/A	N/A

OFFICE OF CIVILIAN RADIOACTIVE WASTE MANAGEMENT DOCUMENT INPUT REFERENCE SHEET									
1. Document Identifier No./Rev.: MDL-NBS-HS-000008/Rev. 00D			Change:	Title: Radionuclide Transport Models under Ambient Conditions					
Input Document			4. Input Status	5. Section Used in	6. Input Description	7. TBV/TBD Priority	8. TBV Due To		
2. Technical Product Input Source Title and Identifier(s) with Version		3. Section					Unqual.	From Uncontrolled Source	Un-confirmed
2a									
26.	DTN: LB991220140160.019. Values from Refereed Literature Used as Input in AMR U0060. Submittal date: Will be submitted with AMR.	Entire	N/A- Technical Product Output	6.4-6.16	Simulation input parameters from literature.	N/A	N/A	N/A	N/A
27.	DTN: LB997141233129.001. Calibrated Basecase Infiltration 1-D Parameter Set for the UZ Flow and Transport Model, FY99. Submittal date: 07/21/1999.	Entire	N/A- Technical Product Output	6.11-6.15	Calibrated flow parameters for base-case infiltration in the matrix of the ch1v and ch2v layers (porosity, permeability, van Genuchten α and m parameters, residual saturation, saturated saturation, rock grain density, tortuosity)	N/A	N/A	N/A	N/A
28.	DTN: MO9901MWDISMMM.000. ISM3.1 MINERALOGIC MODELS. Submittal date: 01/22/1999.	Entire	N/A- Qualification Level 2	Table 4	Geologic profiles and rock properties at the three cross-sections	N/A	N/A	N/A	N/A
29.	DTN: MO9910MWDISMMM.003. ISM3.1 MINERALOGIC MODELS. Submittal date: 10/01/1999.	Entire	N/A- Reference only	6.12.1.3 Fig. 12.21	Mineralogy plots of % zeolites	N/A	N/A	N/A	N/A

OFFICE OF CIVILIAN RADIOACTIVE WASTE MANAGEMENT DOCUMENT INPUT REFERENCE SHEET									
1. Document Identifier No./Rev.: MDL-NBS-HS-000008/Rev. 00D			Change:	Title: Radionuclide Transport Models under Ambient Conditions					
Input Document			4. Input Status	5. Section Used in	6. Input Description	7. TBV/TBD Priority	8. TBV Due To		
2. Technical Product Input Source Title and Identifier(s) with Version		3. Section					Unqual.	From Uncontrolled Source	Un-confirmed
2a									
30.	Abdel-Salam, A. and C.V. Chrysikopoulos. 1995. "Modeling of colloid and colloid-facilitated contaminant transport in a two-dimensional fracture with spatially variable aperture." <i>Transport in Porous Media</i> , 20, 197-221. Dordrecht, The Netherlands: The Journal Editorial Office, Kluwer Academic Publishers. TIC: applied for.	pp.199-200	N/A-Reference only	6.2	N/A	N/A	N/A	N/A	N/A
31.	Bates, J.K.; Bradley, J.P.; Teetsov, A.; Bradley, C.R.; and ten Brink, M.B. 1992. "Colloid Formation during Waste Form Reaction: Implications for Nuclear Waste Disposal." <i>Science</i> , 256, 649-651. Washington, D.C.: American Association for the Advancement of Science. TIC: 239138.	Entire	N/A-Reference only	6.2	N/A	N/A	N/A	N/A	N/A
32.	Bear, J. 1972. <i>Dynamics of Fluid in Porous Media</i> . New York, New York: Dover Publications. TIC: 217568.	p.127	N/A-Reference only	5.1	N/A	N/A	N/A	N/A	N/A

OFFICE OF CIVILIAN RADIOACTIVE WASTE MANAGEMENT DOCUMENT INPUT REFERENCE SHEET									
1. Document Identifier No./Rev.: MDL-NBS-HS-000008/Rev. 00D			Change:	Title: Radionuclide Transport Models under Ambient Conditions					
Input Document			4. Input Status	5. Section Used in	6. Input Description	7. TBV/TBD Priority	8. TBV Due To		
2. Technical Product Input Source Title and Identifier(s) with Version		3. Section					Unqual.	From Uncontrolled Source	Un-confirmed
2a									
33.	Benson, C.F. and Bowman, R.S. 1994. "Tri- and Tetrafluorobenzoates as Nonreactive Tracers in Soil and Groundwater." <i>Soil Science Society of America Journal</i> , 58, 1123-1129. Madison, Wisconsin: Soil Science Society of America. TIC: applied for.	p.1125	N/A-Reference only	6.10	N/A	N/A	N/A	N/A	N/A
34.	Bird, R.B.; Stewart, W.E.; and Lightfoot, E.N. 1960. <i>Transport Phenomena</i> . New York: John Wiley & Sons. TIC: 208957.	p.514	N/A-Reference only	6.1	N/A	N/A	N/A	N/A	N/A
35.	Bodvarsson, G.S.; Boyle, W.; Patterson, R.; and Williams, D. 1999. "Overview of Scientific Investigations at Yucca Mountain the Potential Repository for High-Level Nuclear Waste." <i>Journal of Contaminant Hydrology</i> 38 (1-3), 3-24. Amsterdam, The Netherlands: Elsevier Science Publishers. TIC: 244160.	pp.8-15	N/A-Reference only	6.1	N/A	N/A	N/A	N/A	N/A

OFFICE OF CIVILIAN RADIOACTIVE WASTE MANAGEMENT DOCUMENT INPUT REFERENCE SHEET									
1. Document Identifier No./Rev.: MDL-NBS-HS-000008/Rev. 00D			Change:	Title: Radionuclide Transport Models under Ambient Conditions					
Input Document			4. Input Status	5. Section Used in	6. Input Description	7. TBV/TBD Priority	8. TBV Due To		
2. Technical Product Input Source Title and Identifier(s) with Version		3. Section					Unqual.	From Uncontrolled Source	Un-confirmed
2a									
36.	Boggs, J.M. and Adams, E.E. 1992. "Field Study in a Heterogeneous Aquifer. 4: Investigation of Adsorption and Sampling Bias." <i>Water Resources Research</i> , 28, 3325–3336. Washington, D.C.: American Geophysical Union. TIC: 246740.	Entire	N/A-Reference only	6.1	N/A	N/A	N/A	N/A	N/A
37.	Bowen, B.D. and Epstein, N. 1979. "Fine Particle Deposition in Smooth Parallel-Plate Channels." <i>Journal of Colloid and Interface Science</i> , 72, 81–97. Orlando, Florida: Academic Press. TIC: 224935.	Entire	N/A-Reference only	6.2	N/A	N/A	N/A	N/A	N/A
38.	Bradbury, M.H. and Stephen, I.G. 1985. "Diffusion and Permeability Based Sorption Measurements in Intact Rock Samples." <i>Scientific Basis for Nuclear Waste Management IX</i> , 81–90. Werme, L.O., ed. Boston, Massachusetts: Materials Research Society. TIC: 236384.	Entire	N/A-Reference only	6.1	N/A	N/A	N/A	N/A	N/A

OFFICE OF CIVILIAN RADIOACTIVE WASTE MANAGEMENT DOCUMENT INPUT REFERENCE SHEET									
1. Document Identifier No./Rev.: MDL-NBS-HS-000008/Rev. 00D			Change:	Title: Radionuclide Transport Models under Ambient Conditions					
Input Document			4. Input Status	5. Section Used in	6. Input Description	7. TBV/TBD Priority	8. TBV Due To		
2. Technical Product Input Source Title and Identifier(s) with Version		3. Section					Unqual.	From Uncontrolled Source	Un-confirmed
2a									
39.	Buddemeier, R.W. and Hunt, J.R. 1988. "Transport of Colloidal Contaminants in Groundwater: Radionuclide Migration at the Nevada Test Site." <i>Applied Geochemistry</i> , 3, 535–548. Amsterdam, The Netherlands: Elsevier Science Publishers. TIC: 224116.	Entire	N/A-Reference only	6.1	N/A	N/A	N/A	N/A	N/A
40.	Cameron, D.R. and Klute, A. 1977. "Convective-Dispersive Solute Transport with a combined Equilibrium and Kinetic Adsorption Model." <i>Water Resources Research</i> , 13 (1), 183–188. Washington, D.C.: American Geophysical Union. TIC: 246265.	Entire	N/A-Reference only	6.2	N/A	N/A	N/A	N/A	N/A
41.	Conca, J.L. and Wright, J. 1990. "Diffusion Coefficients in Gravel under Unsaturated Conditions." <i>Water Resources Research</i> , 26 (5), 1055–1066. Washington, D.C.: American Geophysical Union. TIC: 237421.	Entire	N/A-Reference only	6.1	N/A	N/A	N/A	N/A	N/A

OFFICE OF CIVILIAN RADIOACTIVE WASTE MANAGEMENT DOCUMENT INPUT REFERENCE SHEET									
1. Document Identifier No./Rev.: MDL-NBS-HS-000008/Rev. 00D			Change:	Title: Radionuclide Transport Models under Ambient Conditions					
Input Document			4. Input Status	5. Section Used in	6. Input Description	7. TBV/TBD Priority	8. TBV Due To		
2. Technical Product Input Source Title and Identifier(s) with Version		3. Section					Unqual.	From Uncontrolled Source	Un-confirmed
2a									
42.	Corapcioglu, M.Y.; Abboud, N.M.; and Haridas, A. 1987. "Governing Equations for Particle Transport in Porous Media." <i>Advances in Transport Phenomena in Porous Media</i> . Bear, J. and Corapcioglu, M.Y., eds. Series E.: Applied Sciences Series 128. Dordrecht, The Netherlands: Martinus Nijhoff. TIC: applied for.	pp.269-342	N/A-Reference only	6.2	N/A	N/A	N/A	N/A	N/A
43.	Cook, A.J. 1989. <i>A Desk Study of Surface Diffusion and Mass Transport in Clay</i> . Report WE/88/34. Luxembourg, Luxembourg: Commission of the European Communities. TIC: applied for.	Entire	N/A-Reference only	6.2	N/A	N/A	N/A	N/A	N/A

OFFICE OF CIVILIAN RADIOACTIVE WASTE MANAGEMENT DOCUMENT INPUT REFERENCE SHEET									
1. Document Identifier No./Rev.: MDL-NBS-HS-000008/Rev. 00D			Change:	Title: Radionuclide Transport Models under Ambient Conditions					
Input Document			4. Input Status	5. Section Used in	6. Input Description	7. TBV/TBD Priority	8. TBV Due To		
2. Technical Product Input Source Title and Identifier(s) with Version		3. Section					Unqual.	From Uncontrolled Source	Un-confirmed
2a									
44.	Crump, K.S. 1976. "Numerical Inversion of Laplace Transforms Using a Fourier Series Approximation." <i>Journal of the Association of Computing Machinery</i> , 23 (1), 89-96. New York, New York: The Association of Computing Machinery. TIC: 246764.	Entire	N/A-Reference only	Attachment I	N/A	N/A	N/A	N/A	N/A
45.	CRWMS M&O (Civilian Radioactive Waste Management System Management & Operating Contractor) 1999a. <i>M&O Site Investigations</i> . Activity Evaluation. Las Vegas, Nevada: CRWMS M&O. ACC: MOL.19990317.0330.	Entire	N/A – Reference only	2	Standards, Codes & Regulations	N/A	N/A	N/A	N/A
46.	CRWMS M&O 1999b. <i>M&O Site Investigations</i> . Activity Evaluation. Las Vegas, Nevada: CRWMS M&O. ACC: MOL.19990928.0224.	Entire	N/A - Reference only	2	Standards, Codes & Regulations	N/A	N/A	N/A	N/A

OFFICE OF CIVILIAN RADIOACTIVE WASTE MANAGEMENT DOCUMENT INPUT REFERENCE SHEET									
1. Document Identifier No./Rev.: MDL-NBS-HS-000008/Rev. 00D			Change:	Title: Radionuclide Transport Models under Ambient Conditions					
Input Document			4. Input Status	5. Section Used in	6. Input Description	7. TBV/TBD Priority	8. TBV Due To		
2. Technical Product Input Source Title and Identifier(s) with Version		3. Section					Unqual.	From Uncontrolled Source	Un-confirmed
2a									
47.	CRWMS M&O 1999c. <i>Analysis & Modeling Development Plan (DP) for U0060 , Radionuclide Transport Models under Ambient Conditions, Rev. 00.</i> TDP-NBS-HS-000013. Las Vegas, Nevada: CRWMS M&O. ACC: MOL.19990830.0381.	Entire	N/A - Reference only	2	Standards, Codes & Regulations	N/A	N/A	N/A	N/A
48.	CRWMS M&O 1999d. <i>UZ Flow Models and Submodels.</i> MDL-NBS-HS-000006. Las Vegas, Nevada: CRWMS M&O. ACC: MOL.19990721.0527. URN-0030.	6	N/A - Reference only	6.4, 6.10-6.16	N/A	N/A	N/A	N/A	N/A
49.	CRWMS M&O 1999e. <i>Unsaturated Zone and Saturated Zone Transport Properties.</i> ANL-NBS-HS-000019. Las Vegas, Nevada: CRWMS M&O. URN-0038.	6	N/A-Reference only	5.2, 6.1, 6.2, 6.10, 7.1	N/A	N/A	N/A	N/A	N/A
50.	CRWMS M&O 1999f. <i>UZ Colloid Transport Model.</i> ANL-NBS-HS-000028. Las Vegas, Nevada: CRWMS M&O. URN-0031.	6	N/A - Reference only	5.2, 5.4, 6.1, 6.16	N/A	N/A	N/A	N/A	N/A

OFFICE OF CIVILIAN RADIOACTIVE WASTE MANAGEMENT DOCUMENT INPUT REFERENCE SHEET									
1. Document Identifier No./Rev.: MDL-NBS-HS-000008/Rev. 00D			Change:	Title: Radionuclide Transport Models under Ambient Conditions					
Input Document			4. Input Status	5. Section Used in	6. Input Description	7. TBV/TBD Priority	8. TBV Due To		
2. Technical Product Input Source Title and Identifier(s) with Version		3. Section					Unqual.	From Uncontrolled Source	Un-confirmed
2a									
51.	CRWMS M&O 1999g. <i>Enhanced Design Alternative (EDA) II Repository Layout for 10 cm/s Ventilation Plan.</i> Las Vegas, Nevada: CRWMS M&O. ACC: MOL.19990409.0102.	Entire	N/A-Reference only	5.4, 6.1	N/A	N/A	N/A	N/A	N/A
52.	CRWMS M&O 1999h. <i>Development of Numerical Grids for UZ Flow and Transport Modeling.</i> ANL-NBS-HS-000015. Las Vegas, Nevada: CRWMS M&O. ACC: MOL.19990721.0517.	6	N/A-Reference only	6.1, 6.4, 6.5, 6.6, 6.11	N/A	N/A	N/A	N/A	N/A
53.	CRWMS M&O 2000a. <i>Calibrated Properties Model.</i> MDL-NBS-HS-000003. Las Vegas, Nevada: CRWMS M&O. ACC: MOL.19990721.0520. URN-0053.	6	N/A-Reference only	5.1, 6.7, 6.8, 6.9, 6.12	N/A	N/A	N/A	N/A	N/A
54.	CRWMS M&O 2000b. <i>Drift-Scale Coupled Processes (DST and THC Seepage) Models.</i> MDL-NBS-HS-000001. Las Vegas, Nevada: CRWMS M&O. ACC: MOL.19990721.0523. URN-0054.	6	N/A-Reference only	5.1, 5.2, 6.1	N/A	N/A	N/A	N/A	N/A

OFFICE OF CIVILIAN RADIOACTIVE WASTE MANAGEMENT DOCUMENT INPUT REFERENCE SHEET									
1. Document Identifier No./Rev.: MDL-NBS-HS-000008/Rev. 00D			Change:	Title: Radionuclide Transport Models under Ambient Conditions					
Input Document			4. Input Status	5. Section Used in	6. Input Description	7. TBV/TBD Priority	8. TBV Due To		
2. Technical Product Input Source Title and Identifier(s) with Version		3. Section					Unqual.	From Uncontrolled Source	Un-confirmed
2a									
55.	CRWMS M&O 2000c. <i>Seepage Calibration Model and Seepage Testing Data</i> . MDL-NBS-HS-000004. Las Vegas, Nevada: CRWMS M&O. ACC: MOL.19990721.0521.	6	N/A-Reference only	5.3	N/A	N/A	N/A	N/A	N/A
56.	CRWMS M&O 2000d. <i>Analysis of Hydrologic Properties Data</i> . ANL-NBS-HS-000002. Las Vegas, Nevada: CRWMS M&O. ACC: MOL.19990721.0519. URN-0055.	6	N/A-Reference only	6.1, 6.11	N/A	N/A	N/A	N/A	N/A
57.	CRWMS M&O 2000e. <i>Geologic Framework Model (GFM3.1) Analysis Model Report</i> . Las Vegas, Nevada: CRWMS M&O.. ACC: MOL.20000121.0115.	6	N/A-Reference only	6.11	N/A	N/A	N/A	N/A	N/A
58.	Cussler, E.L. 1984. <i>Diffusion: Mass Transfer in Fluid Systems</i> . Cambridge, United Kingdom: Cambridge University Press. TIC: on order.	p.147	N/A-Reference only	6.1	N/A	N/A	N/A	N/A	N/A

OFFICE OF CIVILIAN RADIOACTIVE WASTE MANAGEMENT DOCUMENT INPUT REFERENCE SHEET									
1. Document Identifier No./Rev.: MDL-NBS-HS-000008/Rev. 00D			Change:	Title: Radionuclide Transport Models under Ambient Conditions					
Input Document			4. Input Status	5. Section Used in	6. Input Description	7. TBV/TBD Priority	8. TBV Due To		
2. Technical Product Input Source Title and Identifier(s) with Version		3. Section					Unqual.	From Uncontrolled Source	Un-confirmed
2a									
59.	DeHoog, F.R.; Knight, J.H.; and Stokes, A.N. 1982. "An Improved Method for Numerical Inversion of Laplace Transforms." <i>SIAM Journal on Scientific and Statistical Computing</i> , 3 (3), 357-366. Philadelphia, Pennsylvania: Society for Industrial and Applied Mathematics. TIC: 246291.	Entire	N/A-Reference only	Attachment I	N/A	N/A	N/A	N/A	N/A
60.	de Marsily, G. 1986. <i>Quantitative Hydrogeology: Groundwater Hydrology for Engineers</i> . Orlando, Florida: Academic Press. TIC: 226335.	10, pp.228-283	N/A-Reference only	6.2	N/A	N/A	N/A	N/A	N/A
61.	DOE (U.S. Department of Energy) 1998. "Total System Performance Assessment." Volume 3 of <i>Viability Assessment of a Repository at Yucca Mountain</i> . DOE/RW-0508. Washington, D.C.: U.S. Department of Energy, Office of Civilian Radioactive Waste Management. ACC: MOL.19981007.0030	Entire	N/A-Reference only	6.1	N/A	N/A	N/A	N/A	N/A

OFFICE OF CIVILIAN RADIOACTIVE WASTE MANAGEMENT DOCUMENT INPUT REFERENCE SHEET									
1. Document Identifier No./Rev.: MDL-NBS-HS-000008/Rev. 00D			Change:	Title: Radionuclide Transport Models under Ambient Conditions					
Input Document			4. Input Status	5. Section Used in	6. Input Description	7. TBV/TBD Priority	8. TBV Due To		
2. Technical Product Input Source Title and Identifier(s) with Version		3. Section					Unqual.	From Uncontrolled Source	Un-confirmed
2a									
62.	Dyer, J.R. 1999. "Revised Interim Guidance Pending Issuance of New U.S. Nuclear Regulatory Commission (NRC) Regulations (Revision 01, July 22, 1999), for Yucca Mountain, Nevada." Letter from J.R. Dyer (DOE) to D.R. Wilkins (CRWMS M&O), September 9, 1999, OL&RC:SB-1714, with enclosure, "Interim Guidance Pending Issuance of New U.S. Nuclear Regulatory Commission (NRC) Regulations (Revision 01)." ACC: MOL.19990910.0079.	Entire	N/A-Reference only	4.2	Interim Guidance	N/A	N/A	N/A	N/A
63.	Dzombak, D.A. and Morel, F.M.M. 1990. <i>Surface Complexation Modeling: Hydrous Ferric Oxide</i> . New York, New York, John Wiley & Sons. TIC: 224089.	6	N/A-Reference only	6.1	N/A	N/A	N/A	N/A	N/A

OFFICE OF CIVILIAN RADIOACTIVE WASTE MANAGEMENT DOCUMENT INPUT REFERENCE SHEET									
1. Document Identifier No./Rev.: MDL-NBS-HS-000008/Rev. 00D			Change:	Title: Radionuclide Transport Models under Ambient Conditions					
Input Document			4. Input Status	5. Section Used in	6. Input Description	7. TBV/TBD Priority	8. TBV Due To		
2. Technical Product Input Source Title and Identifier(s) with Version		3. Section					Unqual.	From Uncontrolled Source	Un-confirmed
2a									
64.	EPRI (Electric Power Research Institute) 1999. <i>Colloids in Saturated and Partially Saturated Porous Media: Approached to the Treatment of Colloids in Yucca Mountain Total System Performance Assessment</i> . EPRI. TR-112135. Palo Alto, California: Electric Power Research Institute. TIC: 246964.	Entire	N/A-Reference only	6.1	N/A	N/A	N/A	N/A	N/A
65.	Farrell, J. and Reinhard, M. 1994. "Desorption of Halogenated Organics from Model Solids, Sediments, and Soil under Unsaturated Conditions. 2: Kinetics." <i>Environmental Science and Technology</i> , 28 (1), 63–72. Washington, D.C.: American Chemical Society. TIC: 246770.	p.64	N/A-Reference only	6.1	N/A	N/A	N/A	N/A	N/A
66.	Faure, G. 1977. <i>Principles of Isotope Geology</i> . New York, New York: John Wiley and Sons. TIC: 235628.	pp.288-289	N/A-Reference only	6.2, 6.10	N/A	N/A	N/A	N/A	N/A

OFFICE OF CIVILIAN RADIOACTIVE WASTE MANAGEMENT DOCUMENT INPUT REFERENCE SHEET									
1. Document Identifier No./Rev.: MDL-NBS-HS-000008/Rev. 00D			Change:	Title: Radionuclide Transport Models under Ambient Conditions					
Input Document			4. Input Status	5. Section Used in	6. Input Description	7. TBV/TBD Priority	8. TBV Due To		
2. Technical Product Input Source Title and Identifier(s) with Version		3. Section					Unqual.	From Uncontrolled Source	Un-confirmed
2a									
67.	Fetter, C.W. 1993. <i>Contaminant Hydrogeology</i> . Upper Saddle River, New Jersey: Prentice Hall. TIC: 240691	pp.65-66	N/A-Reference only	6.1	N/A	N/A	N/A	N/A	N/A
68.	Gelhar, L.W.; Welty, C.; and Rehfeldt, K.R. 1992. "A Critical Review of Data on Field-Scale Dispersion in Aquifers." <i>Water Resources Research</i> , 28 (7), 1955–1974. Washington, D.C.: American Geophysical Union. TIC: 235780.	Entire	N/A-Reference only	6.1	N/A	N/A	N/A	N/A	N/A
69.	Grathwohl, P. 1998. <i>Diffusion in Natural Porous Media: Contaminant Transport, Sorption/Desorption and Dissolution Kinetics</i> . Boston, Massachusetts: Kluwer Academic Publishers. TIC: applied for.	pp. 28-35	N/A-Reference only	6.1, 6.6, 6.12, 6.15	N/A	N/A	N/A	N/A	N/A

OFFICE OF CIVILIAN RADIOACTIVE WASTE MANAGEMENT DOCUMENT INPUT REFERENCE SHEET									
1. Document Identifier No./Rev.: MDL-NBS-HS-000008/Rev. 00D			Change:	Title: Radionuclide Transport Models under Ambient Conditions					
Input Document			4. Input Status	5. Section Used in	6. Input Description	7. TBV/TBD Priority	8. TBV Due To		
2. Technical Product Input Source Title and Identifier(s) with Version		3. Section					Unqual.	From Uncontrolled Source	Un-confirmed
2a									
70.	Harvey, R.W. and Garabedian, S.P. 1991. "Use of Colloid Filtration Theory in Modeling Movement of Bacteria through a Contaminated Sandy Aquifer." <i>Environmental Science and Technology</i> , 25 (1), 178–185. Washington, D.C.: American Chemical Society. TIC: 245733.	Entire	N/A-Reference only	6.2, 6.15-6.16	N/A	N/A	N/A	N/A	N/A
71.	Herzig, J.P.; Leclerc, D.M.; and Le Goff, P. 1970. "Flow of Suspension through Porous Media." <i>Industrial and Engineering Chemistry Research</i> , 62 (5), 129–157. Washington, D.C.: American Chemical Society. TIC: applied for.	Entire	N/A-Reference only	6.2	N/A	N/A	N/A	N/A	N/A

OFFICE OF CIVILIAN RADIOACTIVE WASTE MANAGEMENT DOCUMENT INPUT REFERENCE SHEET									
1. Document Identifier No./Rev.: MDL-NBS-HS-000008/Rev. 00D			Change:	Title: Radionuclide Transport Models under Ambient Conditions					
Input Document			4. Input Status	5. Section Used in	6. Input Description	7. TBV/TBD Priority	8. TBV Due To		
2. Technical Product Input Source Title and Identifier(s) with Version		3. Section					Unqual.	From Uncontrolled Source	Un-confirmed
2a									
72.	Holttä, P.; Siitani-Kauppi, M.; Huikuri, P.; Lindberg, A.; and Hautajarvi, A. 1997. "The Effect of Specific Surface Area on Radionuclides Sorption on Crushed Crystalline Rock." <i>Material Resources Society Symposium Proceedings</i> , 465, 789–796. Pittsburgh, Pennsylvania: Materials Resources Society of America. TIC: 238884.	Entire	N/A-Reference only	6.1	N/A	N/A	N/A	N/A	N/A
73.	Hu, Q. and Brusseau, M.L. 1994. "Effect of Solute Size on Diffusive-Dispersive Transport in Porous Media." <i>Journal Of Hydrology</i> , 158, 305–317. Amsterdam, The Netherlands: Elsevier Science Publishers. TIC: 246801.	Entire	N/A-Reference only	6.1	N/A	N/A	N/A	N/A	N/A
74.	Hu, Q. and Brusseau, M.L. 1995. "The Effect of Solute Size on Transport in Structured Porous Media." <i>Water Resources Research</i> , 31 (7), 1637–1646. Washington, D.C.: American Geophysical Union. TIC: 246800.	Entire	N/A-Reference only	6.1	N/A	N/A	N/A	N/A	N/A

OFFICE OF CIVILIAN RADIOACTIVE WASTE MANAGEMENT DOCUMENT INPUT REFERENCE SHEET									
1. Document Identifier No./Rev.: MDL-NBS-HS-000008/Rev. 00D			Change:	Title: Radionuclide Transport Models under Ambient Conditions					
Input Document			4. Input Status	5. Section Used in	6. Input Description	7. TBV/TBD Priority	8. TBV Due To		
2. Technical Product Input Source Title and Identifier(s) with Version		3. Section					Unqual.	From Uncontrolled Source	Un-confirmed
2a									
75.	Hu, Q. and Brusseau, M.L. 1996. "Transport of Rate-Limited Sorbing Solutes in an Aggregated Porous Medium: A Multiprocess Non-Ideality Approach." <i>Journal of Contaminant Hydrology</i> , 24 (1), 53–73. Amsterdam, The Netherlands: Elsevier Science Publishers. TIC: 246802.	Entire	N/A-Reference only	6.1	N/A	N/A	N/A	N/A	N/A
76.	Ibaraki, M. and Sudicky, E.A. 1995. "Colloid-Facilitated Contaminant Transport in Discretely Fractured Media: 1. Numerical Formulation and Sensitivity Analysis." <i>Water Resources Research</i> , 31 (12), 2945–2960. Washington, D.C.: American Geophysical Union. TIC: 245719.	Entire	N/A-Reference only	6.2	N/A	N/A	N/A	N/A	N/A
77.	Jacobsen, O.H.; Moldrup, P.; Larsen, C.; Konnerup, L.; and Peterson, L.W. 1997. "Particle Transport in Macropores of Undisturbed Soil Columns." <i>Journal Of Hydrology</i> , 196, 185–203. Amsterdam, The Netherlands: Elsevier Science Publishers. TIC: 246812.	pp.185-186	N/A-Reference only	6.1	N/A	N/A	N/A	N/A	N/A

OFFICE OF CIVILIAN RADIOACTIVE WASTE MANAGEMENT DOCUMENT INPUT REFERENCE SHEET									
1. Document Identifier No./Rev.: MDL-NBS-HS-000008/Rev. 00D			Change:	Title: Radionuclide Transport Models under Ambient Conditions					
Input Document			4. Input Status	5. Section Used in	6. Input Description	7. TBV/TBD Priority	8. TBV Due To		
2. Technical Product Input Source Title and Identifier(s) with Version		3. Section					Unqual.	From Uncontrolled Source	Un-confirmed
2a									
78.	Jahnke, F.M. and Radke, C.J. 1987. "Electrolyte Diffusion in Compacted Montmorillonite Engineered Barriers." <i>Coupled Processes Associated With Nuclear Waste Repositories</i> , 287–297. Orlando, Florida: Academic Press. TIC: 200325.	Entire	N/A-Reference only	6.2	N/A	N/A	N/A	N/A	N/A
79.	James, S.C. and Chrysikopoulos, C.V. 1999. "Transport of Polydisperse Colloid Suspensions in a Single Fracture." <i>Water Resources Research</i> , 35 (3), 707–718. Washington, D.C.: American Geophysical Union. TIC: 245938.	Entire	N/A-Reference only	6.2	N/A	N/A	N/A	N/A	N/A
80.	Johansson, H.; Byegard, J.; Skarnemark, G.; and Skalberg, M. 1997. "Matrix Diffusion of Some Alkali and Alkaline Earth Metals in Granitic Rock." <i>Material Resources Society Symposium Proceedings</i> , 465, 871–878. Pittsburgh, Pennsylvania: Materials Resources Society of America. TIC: 238884.	Entire	N/A-Reference only	6.1	N/A	N/A	N/A	N/A	N/A

OFFICE OF CIVILIAN RADIOACTIVE WASTE MANAGEMENT DOCUMENT INPUT REFERENCE SHEET									
1. Document Identifier No./Rev.: MDL-NBS-HS-000008/Rev. 00D			Change:	Title: Radionuclide Transport Models under Ambient Conditions					
Input Document			4. Input Status	5. Section Used in	6. Input Description	7. TBV/TBD Priority	8. TBV Due To		
2. Technical Product Input Source Title and Identifier(s) with Version		3. Section					Unqual.	From Uncontrolled Source	Un-confirmed
2a									
81.	Johansson, H.; Siitari-Kauppi, M.; Skalberg, M.; and Tullborg, E.L. 1998. "Diffusion Pathways in Crystalline Rock-Examples from Äspö-Diorite and Fine-Grained Granite." <i>Journal of Contaminant Hydrology</i> , 35, 41-53. Amsterdam, The Netherlands: Elsevier Science Publishers. TIC: 244160.	Entire	N/A-Reference only	6.1	N/A	N/A	N/A	N/A	N/A
82.	Kaplan, D.I. and Serne, R.J. 1995. <i>Distribution Coefficient Values Describing Iodine, Neptunium, Selenium, Technetium, and Uranium Sorption to Hanford Sediments</i> . PNL-10379. Richland, Washington: Pacific Northwest National Laboratory. TIC: 246721.	Entire	N/A-Reference only	6.1	N/A	N/A	N/A	N/A	N/A
83.	Kersting, A.B.; Efurud, D.W.; Finnegan, D.L.; Rokop, D.J.; Smith, D.K.; and Thompson, J.L. 1999. "Migration of Plutonium in Ground Water at the Nevada Test Site." <i>Nature</i> , 397, 56-59. London, England: Macmillan Magazines. TIC: 243597.	Entire	N/A-Reference only	6.1	N/A	N/A	N/A	N/A	N/A

OFFICE OF CIVILIAN RADIOACTIVE WASTE MANAGEMENT DOCUMENT INPUT REFERENCE SHEET									
1. Document Identifier No./Rev.: MDL-NBS-HS-000008/Rev. 00D			Change:	Title: Radionuclide Transport Models under Ambient Conditions					
Input Document			4. Input Status	5. Section Used in	6. Input Description	7. TBV/TBD Priority	8. TBV Due To		
2. Technical Product Input Source Title and Identifier(s) with Version		3. Section					Unqual.	From Uncontrolled Source	Un-confirmed
2a									
84.	Kretzschmar, R.; Robarge, W.P.; and Amoozegar, A. 1995. "Influence of Natural Organic Matter on Colloid Transport through Saproliite." <i>Water Resources Research</i> , 31 (3), 435–445. Washington, D.C.: American Geophysical Union. TIC: 246819.	p.435	N/A-Reference only	6.1	N/A	N/A	N/A	N/A	N/A
85.	Kretzschmar, R.; Barmettler, K.; Grolimund, D.; Yan, Y.; Borkovec, M.; and Sticher, H. 1997. "Experimental Determination of Colloid Deposition Rates and Collision Efficiencies in Natural Porous Media." <i>Water Resources Research</i> , 33 (5), 1129–1137. Washington, D.C.: American Geophysical Union. TIC: 246817.	p.1129	N/A-Reference only	6.1	N/A	N/A	N/A	N/A	N/A
86.	Lide, D.R. 1992. <i>CRC Handbook of Chemistry and Physics</i> . 73rd Edition. Boca Raton, Florida: CRC Press. TIC: 3595.	pp.11-53 to 11-126	N/A-Reference only	6.5-6.16	N/A	N/A	N/A	N/A	N/A

OFFICE OF CIVILIAN RADIOACTIVE WASTE MANAGEMENT DOCUMENT INPUT REFERENCE SHEET									
1. Document Identifier No./Rev.: MDL-NBS-HS-000008/Rev. 00D			Change:	Title: Radionuclide Transport Models under Ambient Conditions					
Input Document			4. Input Status	5. Section Used in	6. Input Description	7. TBV/TBD Priority	8. TBV Due To		
2. Technical Product Input Source Title and Identifier(s) with Version		3. Section					Unqual.	From Uncontrolled Source	Un-confirmed
2a									
87.	Liu, H.H.; Doughty, C.; and Bodvarsson, G.S. 1998. "An Active Fracture Model for Unsaturated Flow and Transport in Fractured Rocks." <i>Water Resources Research</i> , 34 (10), 2633–2646. Washington, D.C.: American Geophysical Union. TIC: 243012.	Entire	N/A-Reference only	6.6	N/A	N/A	N/A	N/A	N/A
88.	McCarthy, J.F. and Zachara, J.M. 1989. "Subsurface Transport of Contaminants." <i>Environmental Science and Technology</i> , 23 (5), 496–502. Washington, D.C.: American Chemical Society. TIC: 224876.	pp.496-498	N/A-Reference only	6.1	N/A	N/A	N/A	N/A	N/A
89.	McGraw, M.A. and Kaplan, D.I. 1997. <i>Colloid Suspension Stability and Transport Through Unsaturated Porous Media</i> . PNNL-11565. Richland, Washington: Pacific Northwest National Laboratory. TIC: 246723.	p.5.2	N/A-Reference only	6.1	N/A	N/A	N/A	N/A	N/A

OFFICE OF CIVILIAN RADIOACTIVE WASTE MANAGEMENT DOCUMENT INPUT REFERENCE SHEET									
1. Document Identifier No./Rev.: MDL-NBS-HS-000008/Rev. 00D			Change:	Title: Radionuclide Transport Models under Ambient Conditions					
Input Document			4. Input Status	5. Section Used in	6. Input Description	7. TBV/TBD Priority	8. TBV Due To		
2. Technical Product Input Source Title and Identifier(s) with Version		3. Section					Unqual.	From Uncontrolled Source	Un-confirmed
2a									
90.	Moridis, G. J. 1992. "Alternative Formulations of the Laplace Transform Boundary Element (LTBE) Numerical Method for the Solution of Diffusion-Type Equations." <i>Boundary Element Technology VII</i> , 815–833. Boston, Massachusetts: Computational Mechanics Publications. TIC: 246282.	pp.815-833	N/A-Reference only	Attachment I	N/A	N/A	N/A	N/A	N/A
91.	Moridis, G. J. 1999. "Semianalytical Solutions for Parameter Estimation in Diffusion Cell Experiments." <i>Water Resources Research</i> , 35 (6), 1729–1740. Washington, D.C.: American Geophysical Union. TIC: 246266.	Entire	N/A-Reference only	6.1	N/A	N/A	N/A	N/A	N/A
92.	Moridis, G.J., and Pruess, K. 1995. <i>Flow and Transport Simulations Using T2CG1, a Package of Conjugate Gradient Solvers for the TOUGH2 Family of Codes</i> . Report LBL-36235. Berkeley, California: Lawrence Berkeley National Laboratory. ACC: MOL.19960321.0035.	Entire	N/A-Reference only	Attachment I	N/A	N/A	N/A	N/A	N/A

OFFICE OF CIVILIAN RADIOACTIVE WASTE MANAGEMENT DOCUMENT INPUT REFERENCE SHEET									
1. Document Identifier No./Rev.: MDL-NBS-HS-000008/Rev. 00D			Change:	Title: Radionuclide Transport Models under Ambient Conditions					
Input Document			4. Input Status	5. Section Used in	6. Input Description	7. TBV/TBD Priority	8. TBV Due To		
2. Technical Product Input Source Title and Identifier(s) with Version	3. Section	Unqual.					From Uncontrolled Source	Un-confirmed	
2a									
93.	Moridis, G.J. and Pruess, K. 1998. "T2SOLV: An Enhanced Package of Solvers for the TOUGH2 Family of Reservoir Simulation Codes." <i>Geothermics</i> , 27 (4), 415-444. Amsterdam, The Netherlands: Elsevier Science Publications. TIC: 246902.	Entire	N/A-Reference only	Attachment I	N/A	N/A	N/A	N/A	N/A
94.	Moridis, G.J. and Bodvarsson, G.S. 1999. <i>Semianalytical Solutions of Radioactive or Reactive Tracer Transport in Layered Fractured Media</i> . LBNL-44155. Berkeley, California: Lawrence Berkeley National Laboratory. TIC: 246266.	Entire	N/A-Reference only	6.2-6.8	N/A	N/A	N/A	N/A	N/A
95.	Moridis, G.; Wu, Y.; and Pruess, K. 1999. <i>EOS9nT: A TOUGH2 Module for the Simulation of Flow and Solute/Colloid Transport</i> . Report LBL-42351. Berkeley, California: Lawrence Berkeley National Laboratory. TIC: 246520.	Entire	N/A-Reference only	6.2-6.4, 6.10-6.16	N/A	N/A	N/A	N/A	N/A

OFFICE OF CIVILIAN RADIOACTIVE WASTE MANAGEMENT DOCUMENT INPUT REFERENCE SHEET									
1. Document Identifier No./Rev.: MDL-NBS-HS-000008/Rev. 00D			Change:	Title: Radionuclide Transport Models under Ambient Conditions					
Input Document			4. Input Status	5. Section Used in	6. Input Description	7. TBV/TBD Priority	8. TBV Due To		
2. Technical Product Input Source Title and Identifier(s) with Version		3. Section					Unqual.	From Uncontrolled Source	Un-confirmed
2a									
96.	Mualem, Y. 1976. "A New Model for Predicting the Hydraulic Conductivity of Unsaturated Porous Media." <i>Water Resources Research</i> , 12, 513-522. Washington, D.C.: American Geophysical Union. TIC: 217339.	Entire	N/A-Reference only	5.1	N/A	N/A	N/A	N/A	N/A
97.	Nuttall, H.E.; Jain, R.; and Fertelli, Y. 1991. "Radiocolloid Transport in Saturated and Unsaturated Fractures." <i>High Level Radioactive Waste Management, Proceedings of the Second Annual International Conference, Las Vegas, Nevada, April 28-May 3, 1991</i> , 189-196. La Grange Park, Illinois: American Nuclear Society. TIC: 204272.	p.189	N/A-Reference only	6.1	N/A	N/A	N/A	N/A	N/A

OFFICE OF CIVILIAN RADIOACTIVE WASTE MANAGEMENT DOCUMENT INPUT REFERENCE SHEET									
1. Document Identifier No./Rev.: MDL-NBS-HS-000008/Rev. 00D			Change:	Title: Radionuclide Transport Models under Ambient Conditions					
Input Document			4. Input Status	5. Section Used in	6. Input Description	7. TBV/TBD Priority	8. TBV Due To		
2. Technical Product Input Source Title and Identifier(s) with Version		3. Section					Unqual.	From Uncontrolled Source	Un-confirmed
2a									
98.	Pigford, T. H.; Chambre, P. L.; Albert, M.; Foglia, M.; Harada, M.; Iwamoto, F.; Kanki, T.; Leung, D.; Masuda, S.; Muraoka, S.; and Ting, D. 1980. <i>Migration of Radionuclides through Sorbing Media, Analytical Solutions</i> . Report LBL-11616. Berkeley, California: Lawrence Berkeley National Laboratory. TIC: 211541.	Entire	N/A-Reference only	6.10	N/A	N/A	N/A	N/A	N/A
99.	Porter, L.K.; Kemper, W.D.; Jackson, R.D.; and Stewart, B.A. 1960. "Chloride Diffusion in Soils as Influenced by Moisture Content." <i>Soil Science Society of America Proceedings</i> , 24, 460–463. Madison, Wisconsin: Soil Science Society of America. TIC: 246854.	Entire	N/A-Reference only	6.1	N/A	N/A	N/A	N/A	N/A
100.	Pruess, K. 1987. <i>TOUGH User's Guide</i> . Nuclear Regulatory Commission, Report NUREG/CR-4645. Washington, D.C.: U.S. Nuclear Regulatory Commission. TIC: 217275.	Entire	N/A-Reference only	6.2	N/A	N/A	N/A	N/A	N/A

OFFICE OF CIVILIAN RADIOACTIVE WASTE MANAGEMENT DOCUMENT INPUT REFERENCE SHEET									
1. Document Identifier No./Rev.: MDL-NBS-HS-000008/Rev. 00D			Change:	Title: Radionuclide Transport Models under Ambient Conditions					
Input Document			4. Input Status	5. Section Used in	6. Input Description	7. TBV/TBD Priority	8. TBV Due To		
2. Technical Product Input Source Title and Identifier(s) with Version		3. Section					Unqual.	From Uncontrolled Source	Un-confirmed
2a									
101.	Pruess K. 1991. <i>TOUGH2—A General Purpose Numerical Simulator for Multiphase Fluid and Heat Flow</i> . Report LBL-29400, UC-251. Berkeley, California: Lawrence Berkeley National Laboratory. ACC: NNA.19940202.0088.	Entire	N/A-Reference only	6.2	N/A	N/A	N/A	N/A	N/A
102.	Richards, L.A. 1931. "Capillary Conduction of Liquids through Porous Mediums." <i>Physics, I</i> , 318–333. Washington, D.C.: American Physical Society. TIC: 225383.	Entire	N/A-Reference only	5.1	N/A	N/A	N/A	N/A	N/A
103.	Roberts, J.J. and Lin, W. 1997. "Electrical Properties of Partially Saturated Topopah Spring Tuff: Water Distribution as a Function of Saturation." <i>Water Resources Research</i> , 33 (4), 577–587. Washington, DC: American Geophysical Union. TIC: 239736.	pp.577-578	N/A-Reference only	6.1	N/A	N/A	N/A	N/A	N/A

OFFICE OF CIVILIAN RADIOACTIVE WASTE MANAGEMENT DOCUMENT INPUT REFERENCE SHEET									
1. Document Identifier No./Rev.: MDL-NBS-HS-000008/Rev. 00D			Change:	Title: Radionuclide Transport Models under Ambient Conditions					
Input Document			4. Input Status	5. Section Used in	6. Input Description	7. TBV/TBD Priority	8. TBV Due To		
2. Technical Product Input Source Title and Identifier(s) with Version		3. Section					Unqual.	From Uncontrolled Source	Un-confirmed
2a									
104.	Robin, M.J.L.; Gillham, R.W.; and Oscarson, D.W. 1987. "Diffusion of Strontium and Chloride in Compacted Clay-Based Materials." <i>Soil Science Society of America Journal</i> , 51, 1102–1108. Madison, Wisconsin: Soil Science Society of America. TIC: 246867.	pp.1105 -1106	N/A-Reference only	6.1	N/A	N/A	N/A	N/A	N/A
105.	Rogers, P.S.Z. and Meijer, A. 1993. "Dependence of Radionuclide Sorption on Sample Grinding Surface Area, and Water Composition." <i>High Level Radioactive Waste Management, Proceedings of the Fourth Annual International Conference, Las Vegas, Nevada</i> , 1509–1516. LaGrange Park, Illinois: American Nuclear Society. TIC: 226357.	Entire	N/A-Reference only	6.1	N/A	N/A	N/A	N/A	N/A

OFFICE OF CIVILIAN RADIOACTIVE WASTE MANAGEMENT DOCUMENT INPUT REFERENCE SHEET									
1. Document Identifier No./Rev.: MDL-NBS-HS-000008/Rev. 00D			Change:	Title: Radionuclide Transport Models under Ambient Conditions					
Input Document			4. Input Status	5. Section Used in	6. Input Description	7. TBV/TBD Priority	8. TBV Due To		
2. Technical Product Input Source Title and Identifier(s) with Version		3. Section					Unqual.	From Uncontrolled Source	Un-confirmed
2a									
106.	Sakthivadivel, R. 1969. <i>Clogging of Granular Porous Medium by Sediment</i> . Report No. HEL 15-7. Berkeley, California: Hydraulic Engineering Laboratory. TIC: applied for.	Entire	N/A-Reference only	6.2	N/A	N/A	N/A	N/A	N/A
107.	Saltelli, A.; Avogadro, A.; and Bidoglio, G. 1984. "Americium Filtration in Glauconitic Sand Columns." <i>Nuclear Technology</i> , 67, 245-254. LaGrange Park, Illinois: American Nuclear Society. TIC: 223230.	Entire	N/A-Reference only	6.2	N/A	N/A	N/A	N/A	N/A
108.	Seaman, J.C. 1998. "Retardation of Fluorobenzoate Tracers in Highly Weathered Soil and Groundwater Systems." <i>Soil Science Society of America Journal</i> , 62, 354-361. Madison, Wisconsin: Soil Science Society of America. TIC: 246908.	Entire	N/A-Reference only	6.1	N/A	N/A	N/A	N/A	N/A

OFFICE OF CIVILIAN RADIOACTIVE WASTE MANAGEMENT DOCUMENT INPUT REFERENCE SHEET									
1. Document Identifier No./Rev.: MDL-NBS-HS-000008/Rev. 00D			Change:	Title: Radionuclide Transport Models under Ambient Conditions					
Input Document			4. Input Status	5. Section Used in	6. Input Description	7. TBV/TBD Priority	8. TBV Due To		
2. Technical Product Input Source Title and Identifier(s) with Version		3. Section					Unqual.	From Uncontrolled Source	Un-confirmed
2a									
109.	Smith, P.A. and Degueldre, C. 1993. "Colloid-Facilitated Transport of Radionuclides through Fractured Media." <i>Journal of Contaminant Hydrology</i> , 13, 143–166. Amsterdam, The Netherlands: Elsevier Science Publishers. TIC: 224863.	Entire	N/A-Reference only	6.1	N/A	N/A	N/A	N/A	N/A
110.	Stehfest, H. 1970a. "Algorithm 368, Numerical Inversion of Laplace Transforms." <i>Journal of the Association of Computing Machinery</i> , 13 (1), 47–49. New York, New York: Association of Computing Machinery. TIC: 246873.	Entire	N/A-Reference only	Attachment I	N/A	N/A	N/A	N/A	N/A
111.	Stehfest, H. 1970b. "Algorithm 368, Remark on Algorithm 368 [D5], Numerical Inversion of Laplace Transforms. <i>Journal of the Association of Computing Machinery</i> , 13 (1), 56. New York, New York: Association of Computing Machinery. TIC: 246872.	Entire	N/A-Reference only	Attachment I	N/A	N/A	N/A	N/A	N/A

OFFICE OF CIVILIAN RADIOACTIVE WASTE MANAGEMENT DOCUMENT INPUT REFERENCE SHEET									
1. Document Identifier No./Rev.: MDL-NBS-HS-000008/Rev. 00D			Change:	Title: Radionuclide Transport Models under Ambient Conditions					
Input Document			4. Input Status	5. Section Used in	6. Input Description	7. TBV/TBD Priority	8. TBV Due To		
2. Technical Product Input Source Title and Identifier(s) with Version		3. Section					Unqual.	From Uncontrolled Source	Un-confirmed
2a									
112.	Sudicky, E.A. 1989. "The Laplace Transform Galerkin Method: A Time-Continuous Finite Element Theory and Application to Mass Transport in Groundwater." <i>Water Resources Research</i> , 25 (8), 1833–1846. Washington, D.C.: American Geophysical Union. TIC: 246878.	Entire	N/A-Reference only	Attachment I	N/A	N/A	N/A	N/A	N/A
113.	Sudicky, E.A.; Frind, E.O. 1982. "Contaminant Transport in Fractured Porous Media: Analytical Solutions for a System of Parallel Fractures." <i>Water Resources Research</i> , 18 (6), 1634–1642. Washington, D.C.: American Geophysical Union. TIC: 217475.	Entire	N/A-Reference only	6.4	N/A	N/A	N/A	N/A	N/A
114.	Tachi, Y.; Shibutani, T.; Sato, H.; and Yui, M. 1998. "Sorption and Diffusion Behavior of Selenium in Tuff." <i>Journal of Contaminant Hydrology</i> , 35 (1-3), 77–89. Amsterdam, The Netherlands: Elsevier Science Publications. TIC: 246891.	Entire	N/A-Reference only	6.1	N/A	N/A	N/A	N/A	N/A

OFFICE OF CIVILIAN RADIOACTIVE WASTE MANAGEMENT DOCUMENT INPUT REFERENCE SHEET									
1. Document Identifier No./Rev.: MDL-NBS-HS-000008/Rev. 00D			Change:	Title: Radionuclide Transport Models under Ambient Conditions					
Input Document			4. Input Status	5. Section Used in	6. Input Description	7. TBV/TBD Priority	8. TBV Due To		
2. Technical Product Input Source Title and Identifier(s) with Version		3. Section					Unqual.	From Uncontrolled Source	Un-confirmed
2a									
115.	van Genuchten, M. 1980. "A Closed-Form Equation for Predicting the Hydraulic Conductivity of Unsaturated Soils." <i>Soil Science Society of America Journal</i> , 44 (5), 892-898. Madison, Wisconsin: Soil Science Society of America. TIC: 217327.	Entire	N/A-Reference only	5.1	N/A	N/A	N/A	N/A	N/A
116.	Vilks, P. and Bachinski, D.B. 1996. "Colloid and Suspended Particle Migration Experiments in a Granite Fracture." <i>Journal of Contaminant Hydrology</i> , 21, 269-279. Amsterdam, the Netherlands: Elsevier Science Publishers. TIC: 245730.	pp.269, 272-278	N/A-Reference only	6.1	N/A	N/A	N/A	N/A	N/A
117.	Vilks, P.; Frost, L.H.; Bachinski, D.B. 1997. "Field-Scale Colloid Migration Experiments in a Granite Fracture." <i>Journal of Contaminant Hydrology</i> , 26, 203-214. Amsterdam, the Netherlands: Elsevier Science Publishers. TIC: 245732.	pp203, 212-213	N/A-Reference only	6.1	N/A	N/A	N/A	N/A	N/A

OFFICE OF CIVILIAN RADIOACTIVE WASTE MANAGEMENT DOCUMENT INPUT REFERENCE SHEET									
1. Document Identifier No./Rev.: MDL-NBS-HS-000008/Rev. 00D			Change:	Title: Radionuclide Transport Models under Ambient Conditions					
Input Document			4. Input Status	5. Section Used in	6. Input Description	7. TBV/TBD Priority	8. TBV Due To		
2. Technical Product Input Source Title and Identifier(s) with Version		3. Section					Unqual.	From Uncontrolled Source	Un-confirmed
2a									
118.	Viswanathan, H.S.; Robinson, B.A.; Valocchi, A.J.; and Triay, I.R. 1998. "A Reactive Transport Model of Neptunium Migration from the Potential Repository at Yucca Mountain." <i>Journal of Hydrology</i> , 209, 251–280. Amsterdam, the Netherlands: Elsevier Science Publishers. TIC: 243441.	Entire	N/A-Reference only	6.1	N/A	N/A	N/A	N/A	N/A
119.	Wan, J., and J.L. Wilson. 1994. "Colloid Transport in Unsaturated Porous Media." <i>Water Resources Research</i> , 30 (4), 857–864. TIC: 222359.	pp.857, 863	N/A-Reference only	6.1	N/A	N/A	N/A	N/A	N/A
120.	Wan, J. and Tokunaga, T.K. 1997. "Film Straining of Colloids in Unsaturated Porous Media: Conceptual Model and Experimental Testing." <i>Environmental Science and Technology</i> , 31 (8), 2413–2420. Washington, D.C.: American Chemical Society. TIC: 234804.	pp. 2413, 2419	N/A-Reference only	6.1	N/A	N/A	N/A	N/A	N/A

OFFICE OF CIVILIAN RADIOACTIVE WASTE MANAGEMENT DOCUMENT INPUT REFERENCE SHEET									
1. Document Identifier No./Rev.: MDL-NBS-HS-000008/Rev. 00D			Change:	Title: Radionuclide Transport Models under Ambient Conditions					
Input Document			4. Input Status	5. Section Used in	6. Input Description	7. TBV/TBD Priority	8. TBV Due To		
2. Technical Product Input Source Title and Identifier(s) with Version		3. Section					Unqual.	From Uncontrolled Source	Un-confirmed
2a									
121.	Wemheuer, R.F. 1999. "First Issue of FY00 NEPO QAP-2-0 Activity Evaluations." Interoffice correspondence from R.F. Wemheuer (CRWMS M&O) to R.A. Morgan (CRWMS M&O), October 1, 1999, LV.NEPO.RTPS.TAG.10/99-155, with attachments, Activity Evaluation for Work Package #1401213UM1. ACC: MOL.19991028.0162.	Work Package #1401213UM1	N/A-Reference only	4	N/A	N/A	N/A	N/A	N/A
122.	van de Weerd, H. and Leijnse, A. 1997. "Assessment of the Effect of Kinetics on Colloid Facilitated Radionuclide Transport in Porous Media." <i>Journal of Contaminant Hydrology</i> , 26, 245-256. Amsterdam, the Netherlands: Elsevier Science Publishers. TIC: 245731.	Entire	N/A-Reference only	6.1	N/A	N/A	N/A	N/A	N/A

OFFICE OF CIVILIAN RADIOACTIVE WASTE MANAGEMENT DOCUMENT INPUT REFERENCE SHEET									
1. Document Identifier No./Rev.: MDL-NBS-HS-000008/Rev. 00D			Change:	Title: Radionuclide Transport Models under Ambient Conditions					
Input Document			4. Input Status	5. Section Used in	6. Input Description	7. TBV/TBD Priority	8. TBV Due To		
2. Technical Product Input Source Title and Identifier(s) with Version		3. Section					Unqual.	From Uncontrolled Source	Un-confirmed
2a									
123.	Wu, Y.S.; Ritcey, A.C.; and Bodvarsson, G.S. 1999. "A Modeling Study of Perched Water Phenomena in the Unsaturated Zone at Yucca Mountain." <i>Journal of Contaminant Hydrology</i> , 38 (1-3), 157-184. Amsterdam, the Netherlands: Elsevier Science Publishers. TIC: 244160.	Entire	N/A-Reference only	6.1	N/A	N/A	N/A	N/A	N/A
124.	Wu, Y.S.; Ahlers, C.F.; Fraser, P.; Simmons, A.; and Pruess, K. 1996. <i>Software Qualification of Selected TOUGH2 Modules</i> . Report LBL-39490. Berkeley, California: Lawrence Berkeley National Laboratory. ACC: MOL.19970219.0104.	Entire	N/A-Reference only	6.2	N/A	N/A	N/A	N/A	N/A
125.	Software Code: TOUGH2 V1.4 Module EOS9 V1.4. STN: 10007-1.4-01	Entire	N/A-Qualified/Confirmed/Verified	6.10	General software use	N/A	N/A	N/A	N/A
126.	Software Code: TOUGH2 V1.11 Module EOS9nT V1.0. STN: 10065-1.11MEOS9NTV1.0-00.	Entire	TBV-4008	6.4-6.16	General software use	1	✓	N/A	N/A

OFFICE OF CIVILIAN RADIOACTIVE WASTE MANAGEMENT DOCUMENT INPUT REFERENCE SHEET									
1. Document Identifier No./Rev.: MDL-NBS-HS-000008/Rev. 00D			Change:	Title: Radionuclide Transport Models under Ambient Conditions					
Input Document			4. Input Status	5. Section Used in	6. Input Description	7. TBV/TBD Priority	8. TBV Due To		
2. Technical Product Input Source Title and Identifier(s) with Version		3. Section					Unqual.	From Uncontrolled Source	Un-confirmed
2a									
127.	Software Code: T2R3D V1.4. STN: 10006-1.4-00.	Entire	N/A- Qualified/ Confirmed/ Verified	6.10	General software use	N/A	N/A	N/A	N/A
128.	Software Code: FRACL V1.0. STN: 10191-1.0-00	Entire	N/A- Reference only	6.10	Comparison purposes only	N/A	N/A	N/A	N/A
129.	Software routine: xtract1.f V1.0. STN: 10213-1.0-00.	Entire	N/A- Qualified/ Confirmed/ Verified	6.10	General software use	N/A	N/A	N/A	N/A
130.	Software routine: xtract2.f V1.0. STN: 10214-1.0-00.	Entire	N/A- Qualified/ Confirmed/ Verified	6.10	General software use	N/A	N/A	N/A	N/A
131.	Software routine: xtract2a.f V1.0. STN: 10215-1.0-00.	Entire	N/A- Qualified/ Confirmed/ Verified	6.10	General software use	N/A	N/A	N/A	N/A
132.	Software routine: xtract2b.f V1.0. STN: 10216-1.0-00.	Entire	N/A- Qualified/ Confirmed/ Verified	6.10	General software use	N/A	N/A	N/A	N/A
133.	Software routine: xtract5.f V1.0. STN: 10217-1.0-00.	Entire	N/A- Qualified/ Confirmed/ Verified	6.10	General software use	N/A	N/A	N/A	N/A

OFFICE OF CIVILIAN RADIOACTIVE WASTE MANAGEMENT DOCUMENT INPUT REFERENCE SHEET									
1. Document Identifier No./Rev.: MDL-NBS-HS-000008/Rev. 00D			Change:	Title: Radionuclide Transport Models under Ambient Conditions					
Input Document			4. Input Status	5. Section Used in	6. Input Description	7. TBV/TBD Priority	8. TBV Due To		
2. Technical Product Input Source Title and Identifier(s) with Version		3. Section					Unqual.	From Uncontrolled Source	Un-confirmed
2a									
134.	Software routine: xtract6.f V1.0. STN: 10218-1.0-00.	Entire	N/A- Qualified/ Confirmed/ Verified	6.10	General software use	N/A	N/A	N/A	N/A

AP-3.15Q.1

Rev. 06/30/1999